SEISMIC STUDIES ON THE DERBYSHIRE DOME

DAVID EDWARD ROGERS

A Thesis submitted in fulfilment of the requirements for the degree of Doctor of Philosophy

Department of Earth Sciences
The University
Leeds LS2 9JT

February 1983

PhD Thesis February 1983

SEISMIC STUDIES ON THE DERBYSHIRE DOME

D.E. ROGERS
Dept Earth Sciences

ABSTRACT

The Derbyshire Dome is thought to have been a stable uplifted area since at least Lower Carboniferous times. This project is principally concerned with four 30km seismic refraction lines which crossed the limestone outcrop of Derbyshire and N. Staffordshire in order to investigate the Dome's upper crustal structure, using quarry blasts as seismic sources.

A time-term analysis of refracted arrival data defined basement structure more complicated than implied by the surface geology. The interpretation of these data was complicated by high (5.6-5.8km/s) velocity refractions from dolomitic horizons within the limestone sequence; the mean overburden velocity was determined to be about 5.2 km/s. The Dome could be divided into two pre-Carboniferous geological units separated approximately by the line of the NNW trending Bonsall Fault. To the north a broadly domal refractor of velocity 5.5-5.55km/s was mapped, and thought to correlate with both the shallow pre-Carboniferous volcanics encountered by the Woo Dale borehole and the Ordovician shales encountered by the Eyam borehole below 1.8km of limestone. This refractor accordingly deepens beneath the Carboniferous sedimentary basins flanking the Dome.

To the south of the Bonsall Fault zone, the Carboniferous was found to be underlain by a refractor of velocity 5.63-5.7km/s, thought to be of Precambrian material similar to the rocks of Charnwood Forest, Leicestershire, some 40km south. By analysing later arrivals, this refractor has been mapped to the north of the Bonsall Fault at a depth of 2.5-3.5km. The shallower Lower Palaeozoic refractor is thought to be no more than 500m thick, and underlain by lower velocity, possibly Cambrian, material.

This interpretation is consistent with the Bouguer anomaly map of the region, and sheds light on the structural control of Carboniferous sedimentation. The basement fault dividing the two pre-Carboniferous units is thought to have been active during the Dinantian as the northern unit tilted eastwards.

ACKNOWLEDGEMENTS

It would be impossible to mention individually everyone who helped with this project. I am most indebted to my two supervisors, Drs. Graham Stuart and David Whitcombe, for much encouragement and advice. I am particularly grateful to my colleague Andrew McDonald, with whom the brunt of the fieldwork was shared.

There are many to thank regarding the fieldwork: particularly Dennis Flaxington, John Lawes and Ray Dickinson; from the Global Seismology Unit, IGS Edinburgh, Dr. Paul Burton, Bob McGonigle, and Bob Jones for help with the equipment from the NERC Seismic Pool; from the University of Leicester, Drs. Peter Maguire and Aftab Khan for loan of the Geostore boxes and portable recording apparatus, and also the technical staff of the Department of Geology for help with the controlled shot at Shirley. None of the work would have been possible without the co-operation of the quarry managers and the farm owners of Derbyshire and Staffordshire, especially Mr. A. Moore of Fivewells Farm who put up with us for three successive autumns.

For use of the digitising facilities at GSU Edinburgh, I would like to thank Dr. Chris Browitt and Charlie Fyfe. Many thanks are also due to Dave Johnson and staff of the University of Leeds Computing Service.

Miscellaneous thanks are due to: Dr. John Samson for his hospitality in Edmonton, Canada; Drs. Roger Clark, Neil Aitkinhead, J. Chisholm, Trevor Ford and Michael Leeder for discussion on the geology and geophysics of the area; Sue Nemes for making such a neat job of typing this thesis; and also Dr. Doyle Watts, Pat Bermingham, Steve Brown, Dr. Jim Mechie.

This research was supported by a NERC studentship.

To Felicity,

I couldn't have wished for
a more loving wife.

CONTENTS

CHAPTER ONE

INTRODUCTION AND GEOLOGY

1.1 General Introduction

The Carboniferous limestone outcrop of Derbyshire and North-East Staffordshire, known as the White Peak district, has been economically important since Roman times (Lewis, 1971), originally for lead and zinc but more so during the last fifty years for limestone aggregate and fluorite. Consequently, the region has been of immense geological interest, at least for the last two centuries, as Ford's (1967, 1972) bibliographies show.

It is generally agreed that this outcrop, known as the Derbyshire Dome, represents a feature structurally positive since at least Lower Carboniferous times, when it had a strong influence on carbonate sedimentation. However, there are differing theories regarding the structure of the Dome itself and the nature of its sub-Dinantian basement: the Dome is one of several 'blocks' which hardly subsided during much of the Carboniferous, and which are thought to be underlain by Caledonian granites (Kent 1974). Granite beneath the eastern margin of the Dome is also thought to have caused the mineralisation of the limestone (Ford 1961, Evans and Maroof 1976), although Ineson and Ford (1982) now doubt this. Basement of different character is suggested by the interpretations of the LISPB (Bamford et al. 1978) and University of Leicester's Charnwood-Ballidon line (Whitcombe and Maguire 1981b), which terminated to the north and south of the Dome (see Fig. 1.1) and which respectively traced Lower Palaeozoic and Precambrian Charnian refractors to its flanks. Alternatively, the Dome is an integral part of the Pennine Anticline, which George (1963) considers tobe an entirely Tertiary feature, having had no effect on Carboniferous sedimentation.

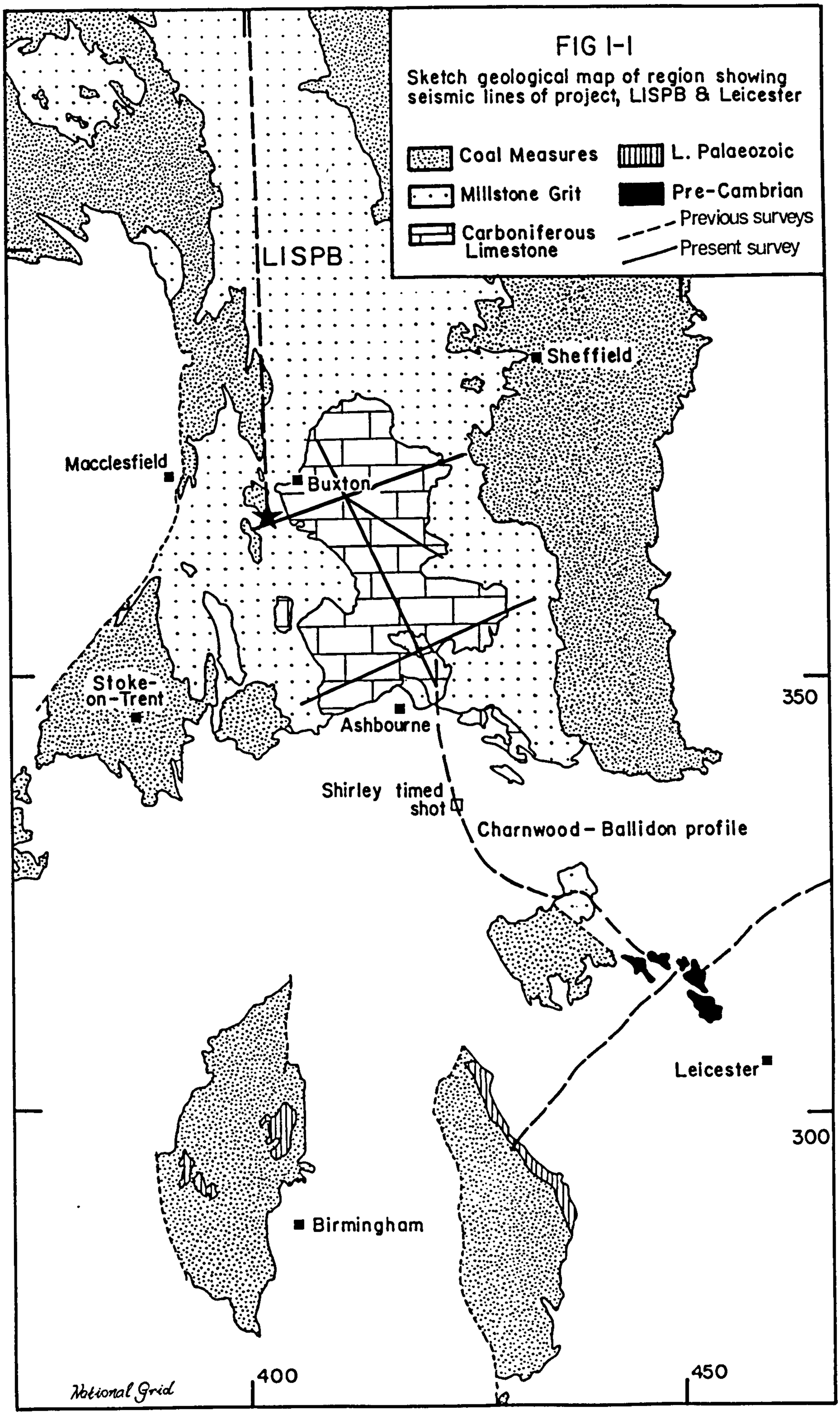
FIG 1-1
Sketch geological map of region showing seismic lines of project, LISPB & Leicester
Coal Measures
Millstone Grit
Carboniferous Limestone
L. Palaeozoic
Pre-Cambrian
Previous surveys
Present survey
LISPB
Sheffield
Macclesfield
Buxton
Stoke-on-Trent
Ashbourne
Shirley timed shot
Charnwood – Ballidon profile
Leicester
Birmingham
350
300
400
450
National Grid

The aim of this study is to investigate the upper crustal structure of the Derbyshire Dome by seismic refraction techniques, in order to differentiate between these various models. Quarry blasts have been used for seismic sources because they provide a free and abundant source of seismic energy. Despite the fact they are not ideal (because of irregular distribution over an area, complex source signals, etc.), quarry blasts have been used several times in previous crustal refraction work: the West German Upper Mantle Project (Bamford 1976), in the East Midlands (Whitcombe and Maguire 1980), and in South Wales (Bayerly and Brooks 1980). Additionally, the repetition of observations from some quarries has allowed signal processing techniques to be investigated.

Four refraction profiles were established in three years' successive field seasons to cover the Dome (Fig. 1.1): the first ran north-south to link the LISPB and Charnwood-Ballidon profiles, the second and third profiles were deployed orthogonally to this first line: one each to the north and south of the outcrop, and the fourth profile was established by McDonald (1982) at an angle of thirty degrees east of the first line.

1.2 Regional Geological Setting

The Derbyshire Dome is marked by an outcrop of Dinantian limestones at the southern axis of the Pennine Anticline (Fig. 1.1), and surrounded largely by Millstone Grit. The outcrop is characterised by low dips and gentle folding (George 1962) and mainly comprises massive bedded limestones indicative of clear, shallow water lagoonal conditions (Ford 1968). The absence of strata older than Chadian is traditionally thought to signify a late marine transgression during the Carboniferous (Benison and Wright 1969), and the Dome is one of several areas marked by attenuated Dinantian successions (George 1963; Fig. 1.2).

As such, the Dome is thought to have been a stable, high feature since at least the Dinantian, when it formed part of a

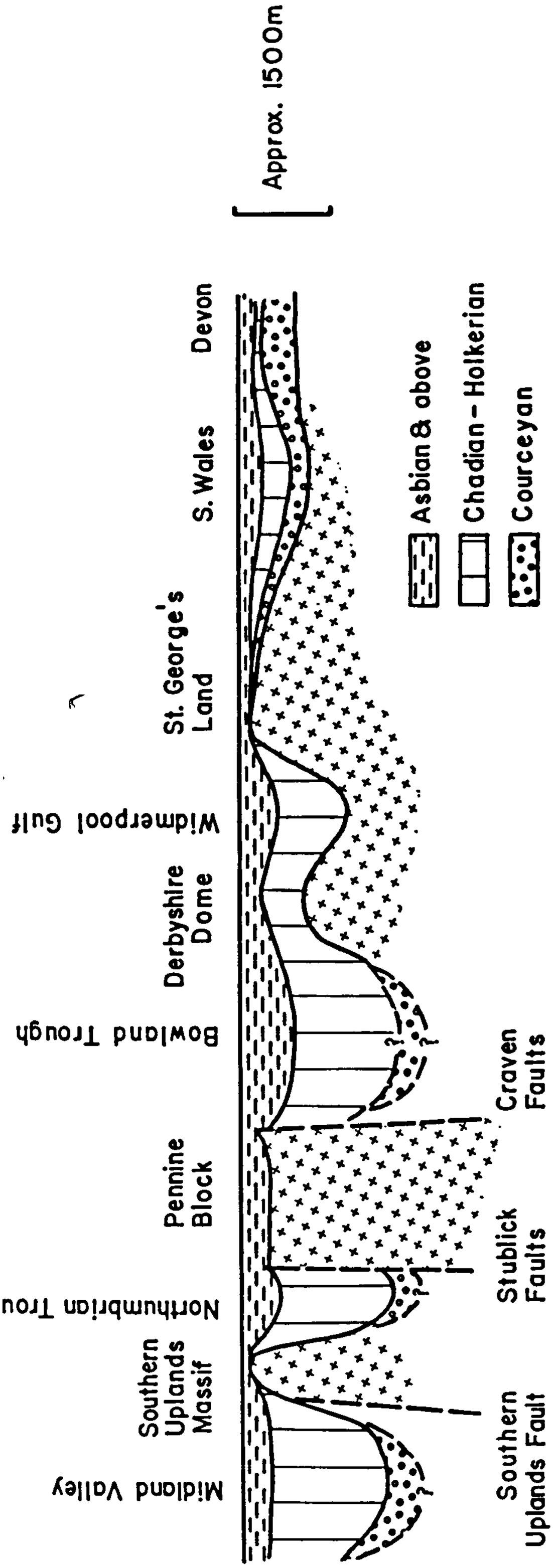

FIG 1-2 Variation of Dinantian thickness across Britain (after George(1963))

'block and basin' system controlling Carboniferous sedimentation (Falcon and Kent 1960; see Fig. 1.3). Leeder (1982) defines three sedimentary environments: A) the Northern British Caledonian molasse basins, whose location and subsidence were controlled by Caledonian tectonics; B) a central region where the blocks were stable remnants of the Caledonian landmass and whose basins subsided through crustal stretching caused by the Hercynian Orogeny; and C) the southerly Rheno-Hercynian back-arc basin system. The Derbyshire Dome occurs within the type B system of the 'Central Province' (Fig. 1.3), where blocks are characterised by reef-flanked carbonate platforms and the basins by deeper water mud-rich limestones and shales. Differential subsidence continued into the Namurian, and the Millstone Grit basins surrounding the Dome are thought to be underlain by thick Dinantian successions (Kent 1966).

The Askrigg and Alston Blocks on the northern margin of the Central Province are known to be underlain by pre-Carboniferous granites (Bott 1967, Dunham 1974), and are bounded by important fault systems which expedited the development of the surrounding basins (George 1958). No such fault system is obvious on the perimeter of the Dome (Fig. 1.4), but the north-west apron-reef complex is as well developed as that of the Craven-Cracoe belt on the southern margin of the Askrigg Block (Miller and Grayson 1982), and Kent (1974) supposes a similar granite support to the Dome.

The Dome is also thought to be related to the Midlands Barrier to the south, from which it forms a north-west facing promontory (Owen 1976). This trend is the characteristic strike of the Precambrian rocks of Charnwood Forest (Watts 1947; Evans (1979) thinks the strike due to Caledonian deformation), and underlies the structural fabric of the Dome and surrounding area (Frost and Smart 1979). The north-western continuation of a Precambrian basement is apparent from both the gravity (first noted by White (1948)) and magnetic maps of the region (see Section 1.3), although Evans and Maroof (1976) also postulate a north-north-western chain of buried Caledonian intrusions related to the Leicestershire granodiorites.

FIG 1-3 Dinantian palaeogeography (from Owen(1976))

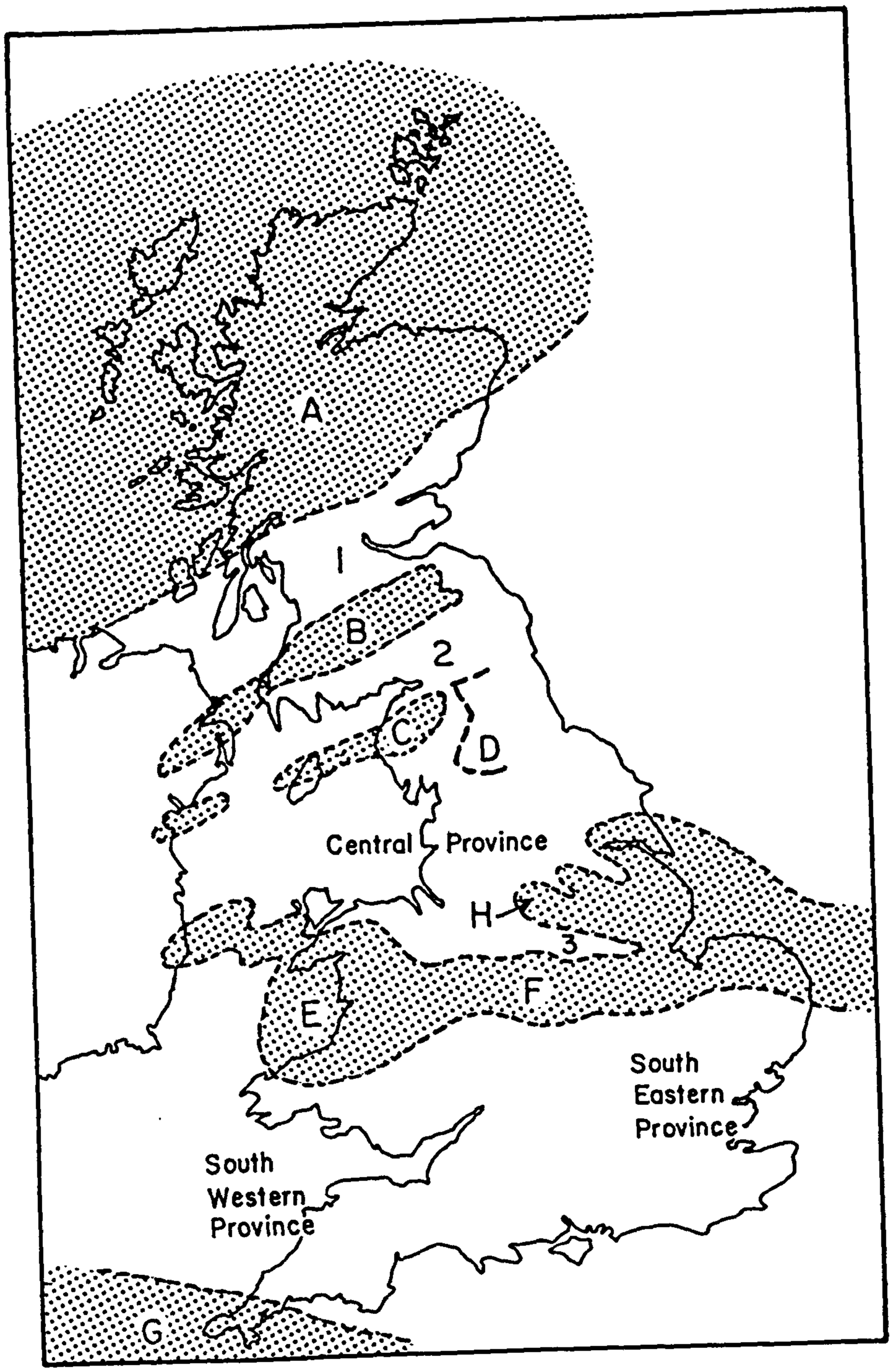

Non-depositional areas

A— Highland Massif B— Southern Uplands
C— Manx-Cumbrian Ridge D— Pennine Block
E— St. George's Land F— Midlands Barrier
G— Cornubrian Massif H— Derbyshire Dome

Depositional areas

1— Scottish Trough 2— Northumbrian Trough
3— Widmerpool Gulf

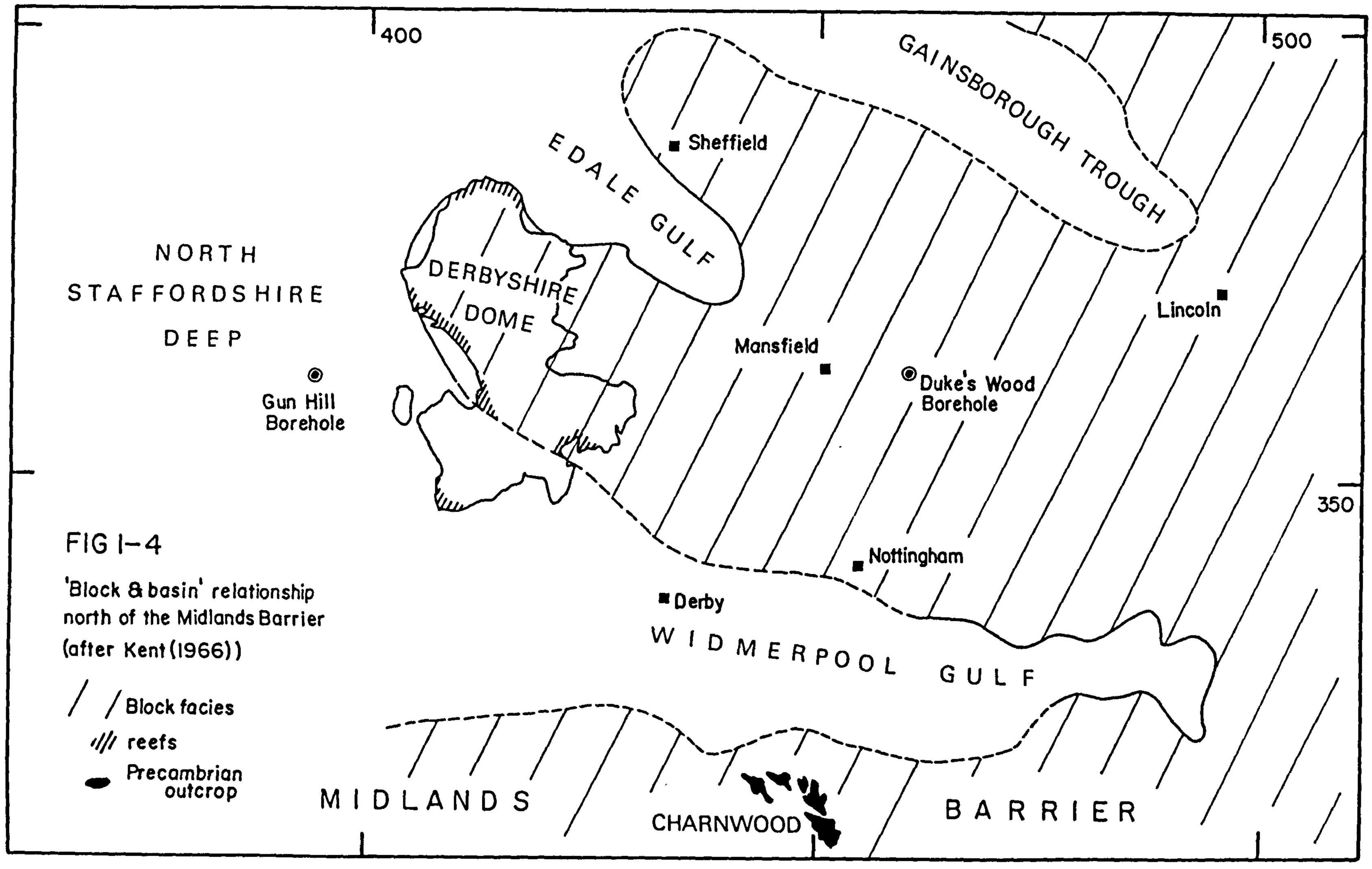

FIG I–4

'Block & basin' relationship north of the Midlands Barrier (after Kent (1966))

1.2.1 Geology of the Dinantian Inlier

Three distinct sedimentary facies can be identified within the limestone outcrop (Edwards and Trotter 1954; see Fig. 1.5):

a) Massif or Shelf: pale, well-bedded massive bioclastic limestones with a coral-brachioped fauna; rarely argillaceous and indicative of a clear, shallow water environment. There are local examples of extremely shallow water conditions: viz oolites, palaeokarst surfaces (Walkden 1974), (rare) current bedding and occasional non-sequence (Pigott 1965).

b) Basinal or Gulf: thin bedded limestones and shales with a goniatite-bivalve fauna; representative of a deeper water, mud rich environment.

c) Marginal or Gulf: well developed apron-reef complex which develops along the margin of the massif; dominantly shallow water fauna, though goniatites present. There is invariably a steep basinward dipping talus slope, although the difference in depth between massif and basin may only be tens of metres (Stevenson and Gaunt, 1971). The classic example at Castleton is well documented (e.g. Wolfenden 1958).

The main part of the outcrop comprises the massive bedded limestones of the massif facies, yet south and south-west of the Dovedale Transition (Fig. 1.5) basinal facies of the Widmerpool Gulf are encountered. These have been subsequently more deformed than the massif succession, and coupled with rapid lateral facies changes and poor fossil representation are only correlated with difficulty across the area (Parkinson 1950, Prentice 1951, Parkinson and Ludford 1964). The differing nomenclature between massif and basinal regions is summarised in Table 1-1. Most of the exposed succession is Asbian and Brigantian, with older strata being exposed along the western axis of the 'Dome'; on the massif these are of Holkerian age, but in Dovedale the Holkerian is largely missing and the Asbian has been deposited directly on Arundian or Chadian (George et al. 1976).

FIG 1-5 Sketch geological map

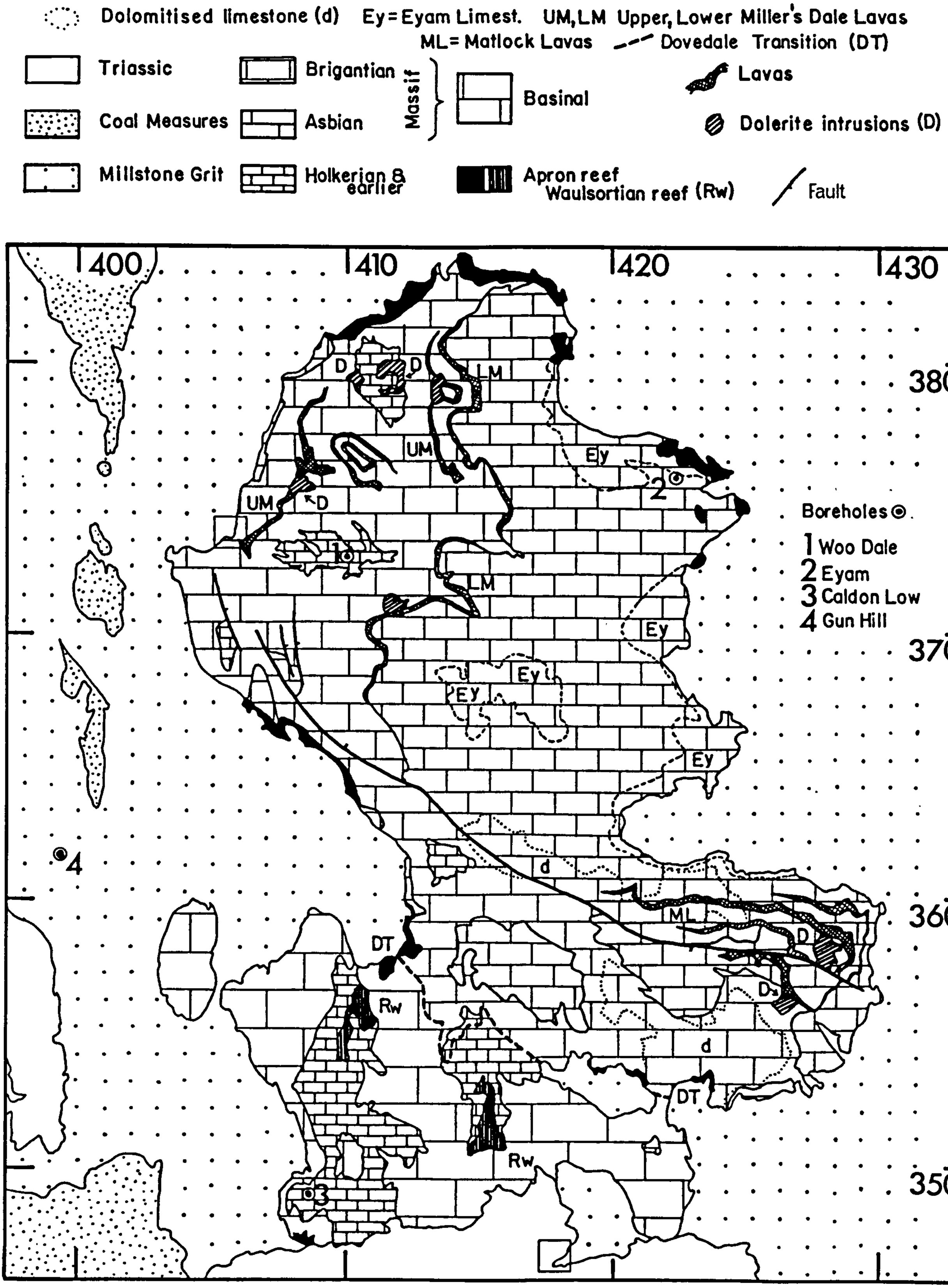

Table I-I Stratigraphy of region (after George et al. (1976))

	STAGES	VAUGHAN'S ZONES
D I N A N T I A N	BRIGANTIAN	Upper Posidonia (P_2)
		Upper Dibunophyllum (D_2)
	ASBIAN	Lower Dibunophyllum (D_1)
	HOLKERIAN	Seminula (S_2)
	ARUNDIAN	Upper Caninia (C_2 S_1)
	CHADIAN	
		Lower Caninia (C1)
	COURCEYAN	$C_1\gamma$

OFF-SHELF	SHELF
	LONGSTONE MUDSTONES
MIXON LIMESTONE-SHALES interbedded mid to dark grey limestones and shales with Onecote sandstones in the upper part	EYAM LIMESTONES dark thinly bedded limestones
ECTON LIMESTONES mainly thinly bedded limestones / HOPEDALE LIMESTONES mid to dark grey mainly thickly bedded limestones	MONSAL DALE LIMESTONES mainly pale thickly bedded limestones — Upper Millers Dale Lavas / Lower Millers Dale Lavas
	BEE LOW LIMESTONES pale thickly bedded chert free limestones
MILLDALE LIMESTONES mid grey-brown to dark grey limestones	WOO DALE LIMESTONES pale chert free limestones
	IRON TORS LIMESTONES pale chert free thickly bedded limestones / WOO DALE DOLOMITES grey and brown dolomitised limestones

The marginal reef complexes ring the massif facies, and are thought to have protected the lagoonal conditions from terrigenous sediment (Thach, 1965). Miller and Grayson (1982) distinguish between these apron-reef complexes and the Waulsortian-reef complexes which developed only in a basinal enviroment,, and which were well established south-west of the Dovedale Transition. Towards the end of the Brigantian, basinal conditions became established over the massif itself with the deposition of the Eyam Limestones and shales, during which patch-reefs developed in scattered areas. This period preluded the deltaic conditions of the Namurian, which must have originally covered the limestone outcrop, and which followed the Dinantian with only minor local unconformity (Smith et al. 1967).

About the Asbian-Brigantian boundary there are numerous volcanic horizons, including olivine-basalt lavas, tuffs, agglomerates and dolerite intrusions. These horizons have been correlated across the area by Walters and Ineson (1981), who postulate a centre of activity to the east of the limestone outcrop, perhaps near the thick basaltic pile in the Ashover Anticline. The more important horizons are the Lower and Upper Millers Dale Lavas, the latter of which occur at the base of the Brigantian (see Table 1-1). To the south-east of the area these are represented by the Lower and Upper Matlock Lavas. These lavas and tuffs generally thin to the south and west (the tuffs persevering as clay wayboards (Walkden 1972)), and are largely absent in the Dovedale region.

Two principal post-depositional features are associated with the limestone outcrop: dolomitisation and mineralisation, although syngenetic dolomitisation is evident from deep bore-holes. Kent (1957) thinks that most of the dolomitisation was due to the Permian marine trangression, and this is supported by the fact that limestones in the Dovedale region have largely been shielded by overlying shales (Ford 1968). Schoefield (University of Manchester, pers. comm. 1981) believes that dolomitisation was concentrated over basement highs where pore pressure was highest, and that beds such as the Woo Dale Dolomite are not laterally extensive.

The mineralisation of Derbyshire has, because of its economic importance, been discussed by many authors (e.g. Farey 1817, Mueller 1954, Ford and Serjeant 1964, Smith et al. 1967). The type of mineralisation is zoned subparallel to the eastern margin of the limestone outcrop so that minerals of lower temperature of emplacement are found further west (Fig. 1.6), suggesting a source close to the east of the Dome (Ford 1968), and commonly attributed to a buried granite (Ford 1961, Evans and Maroof 1976). Recently, Ineson and Ford (1982) have suggested that the hot mineralising fluids may have migrated from further east than supposed, and subsequently 'condensed' on the limestone massif. From isotopic work, Ineson and Al-Kufaishi (1970), and Ineson and Mitchell (1972) have concluded that the mineralisation was episodic from the Upper Carboniferous to the Jurassic.

1.2.2 Deep Boreholes

Three deep boreholes have penetrated the limestone outcrop: two, the Woo Dale (Cope 1973) and Eyam (Dunham 1973) were sunk within the massif, and the third at Caldon Low (IGS Report 78/21) in the Widmerpool facies (Fig. 1.7). The first two encountered a marked unconformity at the base of the Carboniferous, on which the Dinantian succession starts at Ramsbottom's (1973) second cycle (about the Courceyan-Chadian boundary). Both basal sequences infer subaerial exposure: Woo Dale with breccia derived the volcanoclastics in which the borehole terminated, and Eyam with a 70 m sequence of anhydrites and dolomites, following an initial 70 cm of green and red sandstones.

The Caldon Low borehole encounted much thicker red-brown and green sandstones, into which Chadian-Courceyan limestones and shales appear to pass conformably. These sandstones are presumed to be Devonian (Aitkinhead, IGS Leeds, pers. comm. 1981); however two other deep boreholes in the region penetrated similar clastic successions, but thought to be Dinantian: the Duke's Wood (Eakring 146) borehole (Lees and

FIG 1-6 Mineralisation with major veins (after Mueller (1954))

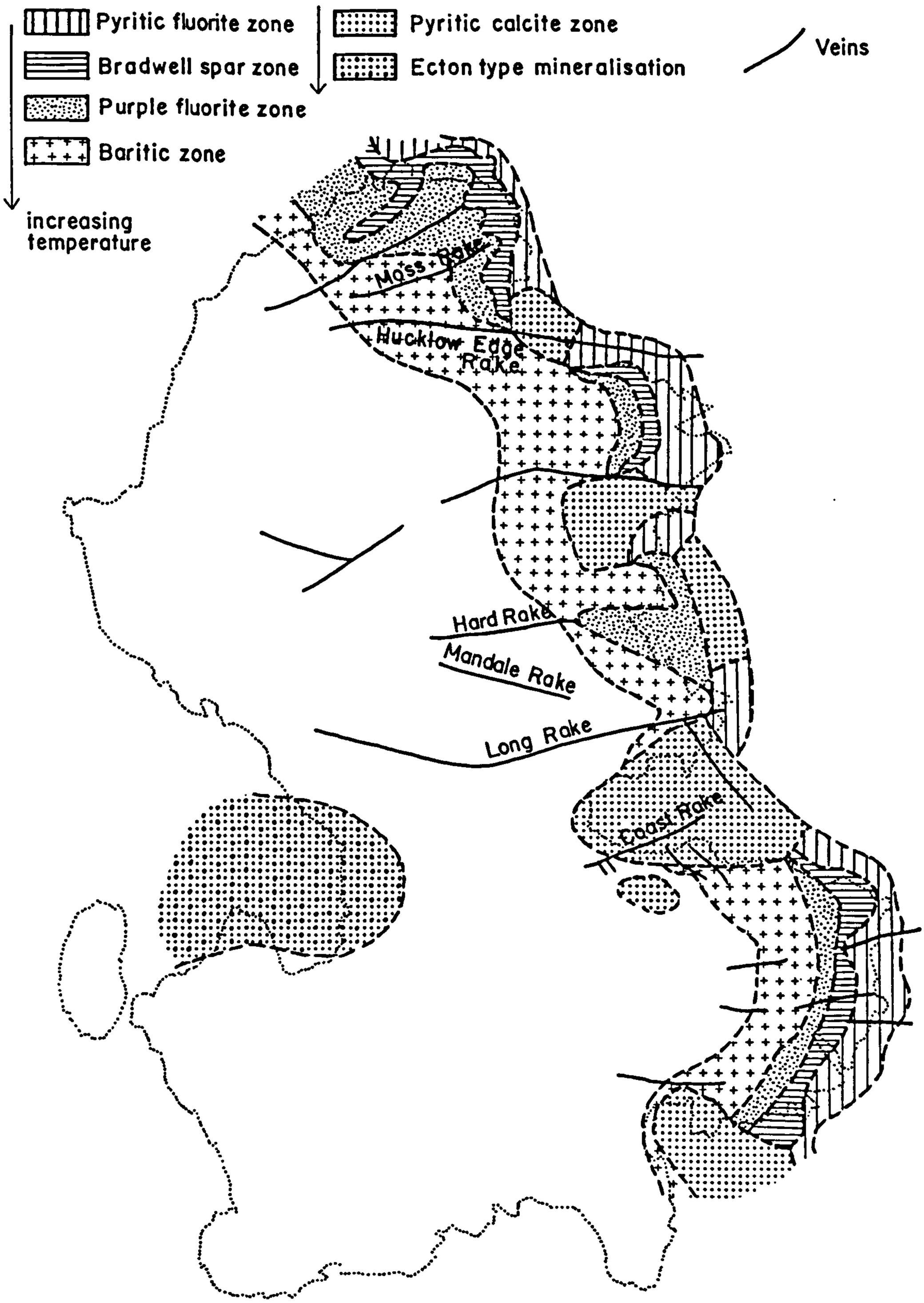

FIG I-7
DEEP BOREHOLES

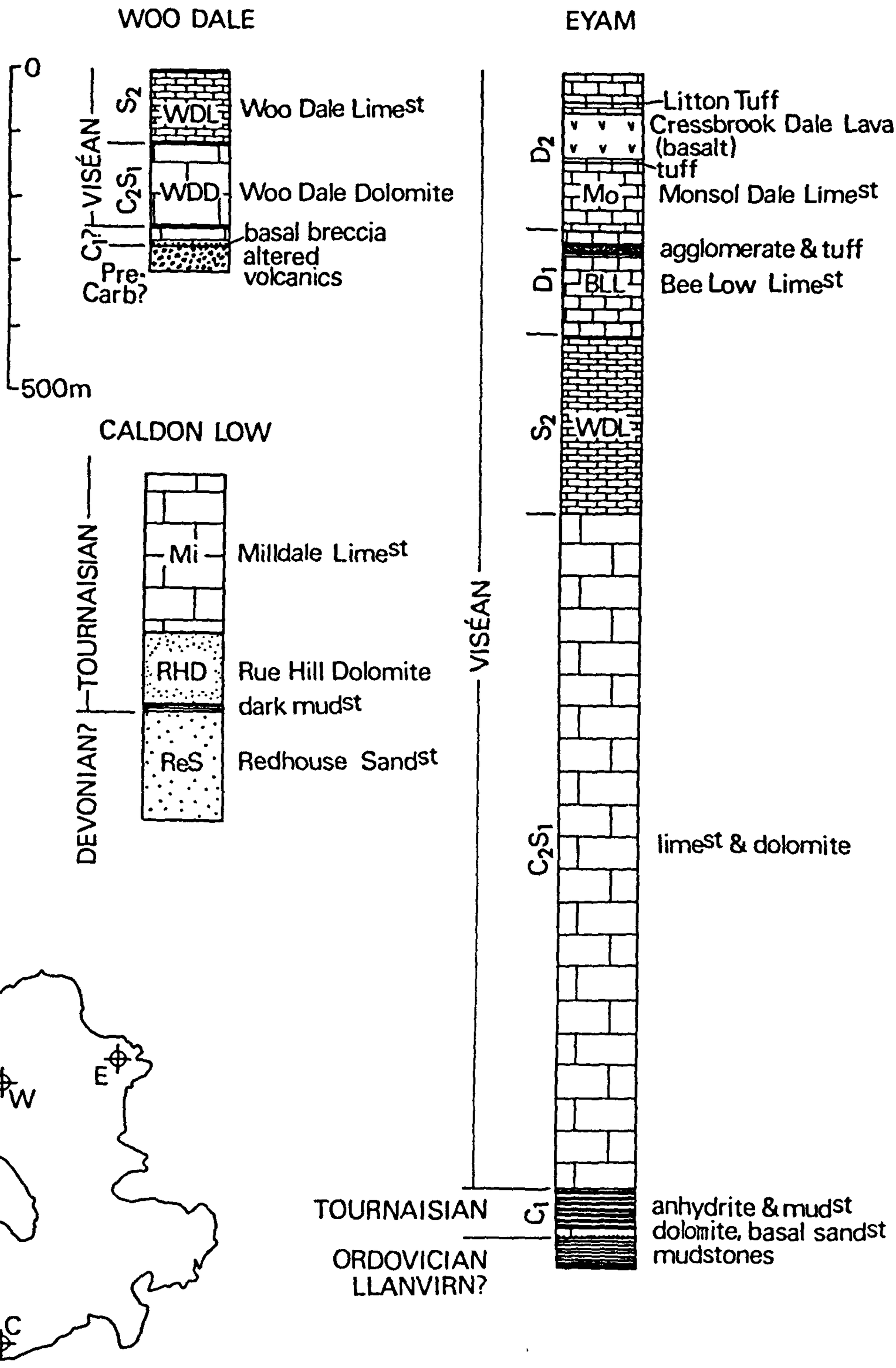

Taitt 1946), some 10 km east of Mansfield passed through a 550 m Carboniferous succession of red sandstones and conglomerates before ending in Cambrian quartzites and shales; and the Gun Hill borehole (Hudson and Cotton 1945; see Fig. 1.5), which pierced a thick sequence of basinal Chadian-Courceyan of the North Staffordshire Deep (Fig. 1.4), the ultimate 505 m of which comprised sandstones and conglomerates.

Chisholm and Butcher (1981) describe a shallow (100 m) borehole sunk on the massif near Matlock, which encountered increasing detrital quartz with depth, from which they presume that the base of the Dinantian to be quite shallow.

The mudstones in which the Eyam borehole terminated are irrefutably Ordovician, but the age of the pyroclastics in the Woo Dale borehole are uncertain. Originally they were thought to resemble the igneous rocks of Charnwood Forest and were thus assumed to be Precambrian (e.g. Edwards and Trotter 1954), but petrologically they are more likely to be Carbonif-erous (La Bas 1972). From isotopic dating, Cope (1979) observes that the sequence is either Devonian or, he prefers, Ordovician.

The most striking feature about the boreholes on the massif is the thickening of the pre-Holkerian succession east-wards: from 400 m in the Woo Dale borehole to about 1400 m at Eyam. The sequence in the Eyam borehole somewhat invalid-ates the notion of the Dome being a stable block covered by attenuated carbonate deposits (Miller and Grayson 1982). From the presence of numerous thin calcilutites, Cope (1973) notes that the Woo Dale sequence represents a condensed version of the Eyam succession rather than loss through over-lap, which suggests that the basement progressively tilted eastwards between Woo Dale and Eyam during Chadian-Arundian times.

This idea has prompted Miller and Grayson (1982) to formulate a 'tilt-block' model for the Derbyshire Dome, which they base on the distribution of apron- and Waulsortian-reef

complexes. The model (shown in Fig. 1.8), necessarily assumes that the Dome is cut by significant basement faults, largely defunct by the upper Brigantian.

1.2.3 Brief Structural History

At outcrop, the Derbyshire Dome attests to at least two major periods of deformation: during the Upper Carboniferous and during the Tertiary (respectively the Hercynian and Alpine orogenies; see structural map Fig. 1.9).

Much of the folding and faulting of the Carboniferous succession was instigated during the Hercynian (Frost and Smart 1979), early movements of which principally affected the marginal areas where local non-sequences and unconformities suggest at least four episodes during the Briganitan (Stevenson and Gaunt 1971). Deformation occurred throughout most of the Carboniferous, and reached a climax towards the end of the Westphalian. In the southern Pennines the compression was near east-west (Owen 1976), but on the Derbyshire Dome Hercynian features strike more north-westerly (Frost and Smart 1979). This implies a certain amount of basement control, and it is possible that older faults and folds were rejuvinated.

Alpine movements were mainly responsible for the broad uplift of the north-south trending Pennine Anticline during the Tertiary (George 1963), which accompanied slight accentuation of older faults and folds. Since this uplift, most of the Carboniferous cover has been removed, leaving the present, glacially carved surface.

Clearly the limestone inlier is not a simple dome, but a broad, north-south striking asymmetric anticline whose axis lies west of centre and whose margins dip steeply beneath the Millstone Grit. Most faulting has occurred along the western margin and south of the Bonsall Fault (Fig. 1.9), and the amplitude of folding increases south and west of the Dovedale Transition, with a marked NNW-SSE strike (Ford 1968).

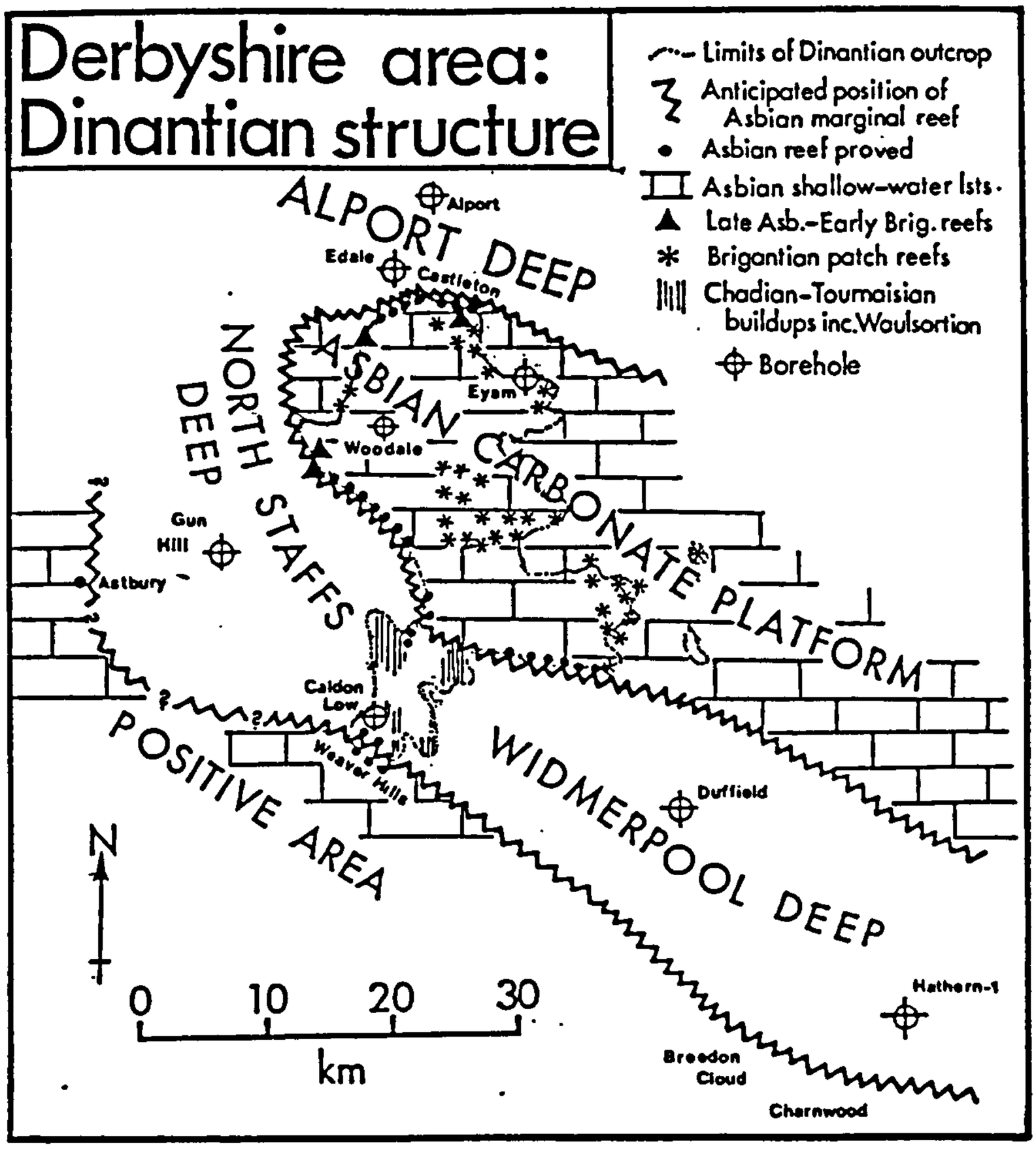

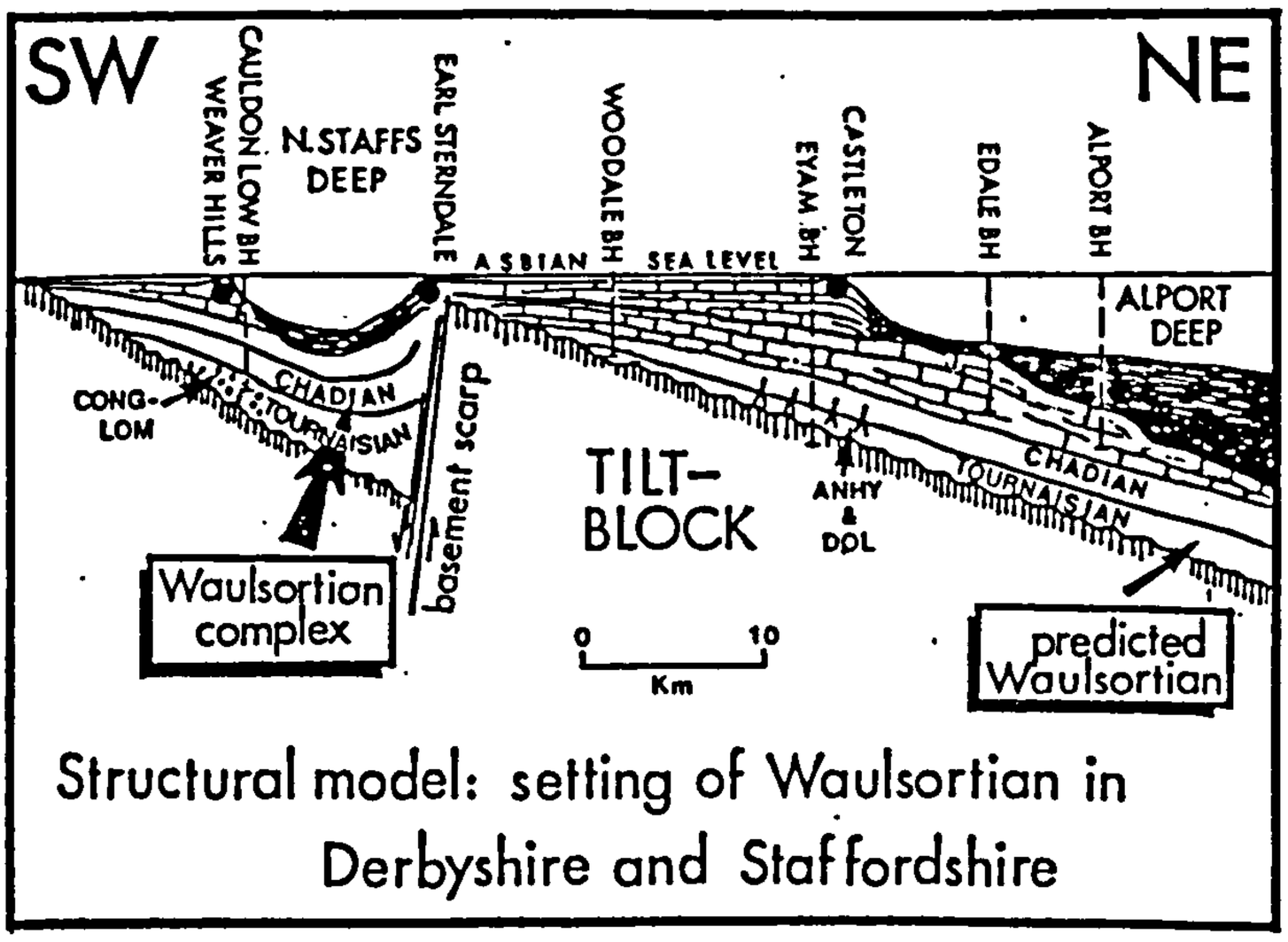

FIG 1-8 Tilt-Block model for the Derbyshire Dome (from Miller & Grayson (1982))

FIG 1-9 Sketch structural map

Key

—♦— Anticline —⧗— Syncline

——·—— Fault (tick on downthrow side)

—▷ Dip + Horizontal bedding

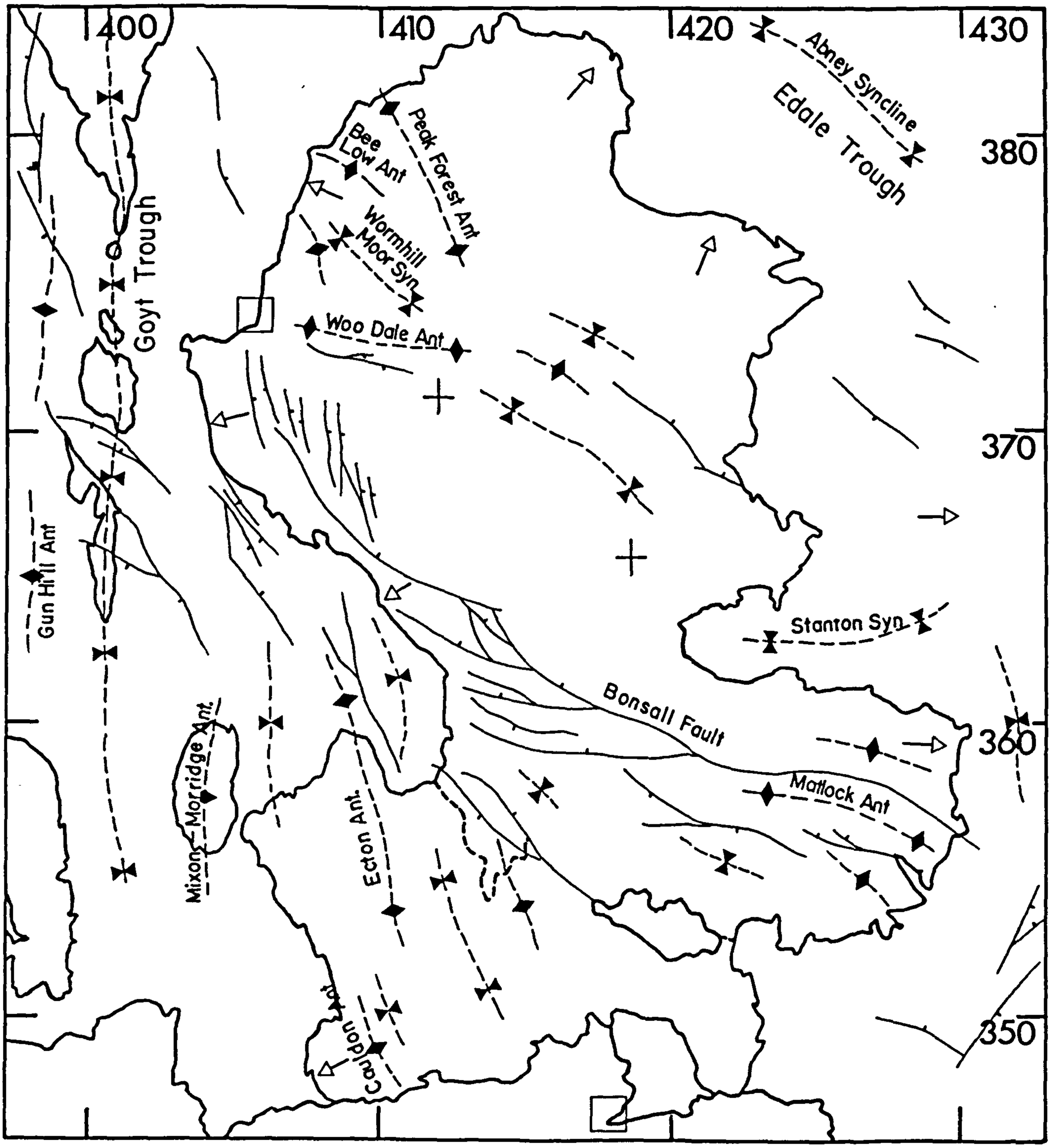

1.3 Previous Geophysical Work

1.3.1 Related Seismic Work

The region falls between two crustal refraction profiles: the Lithospheric Profile of Britain, LISPB (Bamford et al. 1978), which terminated to the north of the Dome at Buxton, and the University of Leicester's Charnwood-Ballidon profile (Whitcombe and Maguire 1981b), which ended on the southern flank of the limestone outcrop. Their respective interpretations are shown in Figs. 1.10a and 1.10b, and are plotted against a north-south geological section of the Dome in Fig. 1.10c.

The LISPB section traces a refractor a_o, of velocity 5.8 km/s, southwards from the Askrigg Block to a depth of about 1.0 km at the southern shotpoint, and which was interpreted as Lower Palaeozoic. This interpretation contrasts with the Charnwood-Ballidon profile which followed a continuous refractor of velocity 5.64-5.8 km/s northwards from outcrop in Charnwood Forest to a depth of approximately 2.0 km beneath Ballidon, and thought to be Charnian. The velocities of these refractors are similar, and so to assimilate a single refractor beneath the Dome either

a) The southern end of the LISPB line has defined a Charnoid refractor, such that Charnian basement exists beneath the Dome and eventually dips beneath, or is faulted against, Lower Palaeozoic somewhere under the Central Province, or

b) the northern end of the Charnwood-Ballidon profile has defined a Lower Palaeozoic refractor, such that the Dome is underlain by Lower Palaeozoic and the Charnian is faulted out somewhere within the Widmerpool Gulf.

Another possibility is that both interpretations are correct and that the Charnian dips below Lower Palaeozoic underneath the Dome itself. The Eyam borehole (Fig. 1.7), for example, validates a Lower Palaeozoic refractor at least to the north of the Dome.

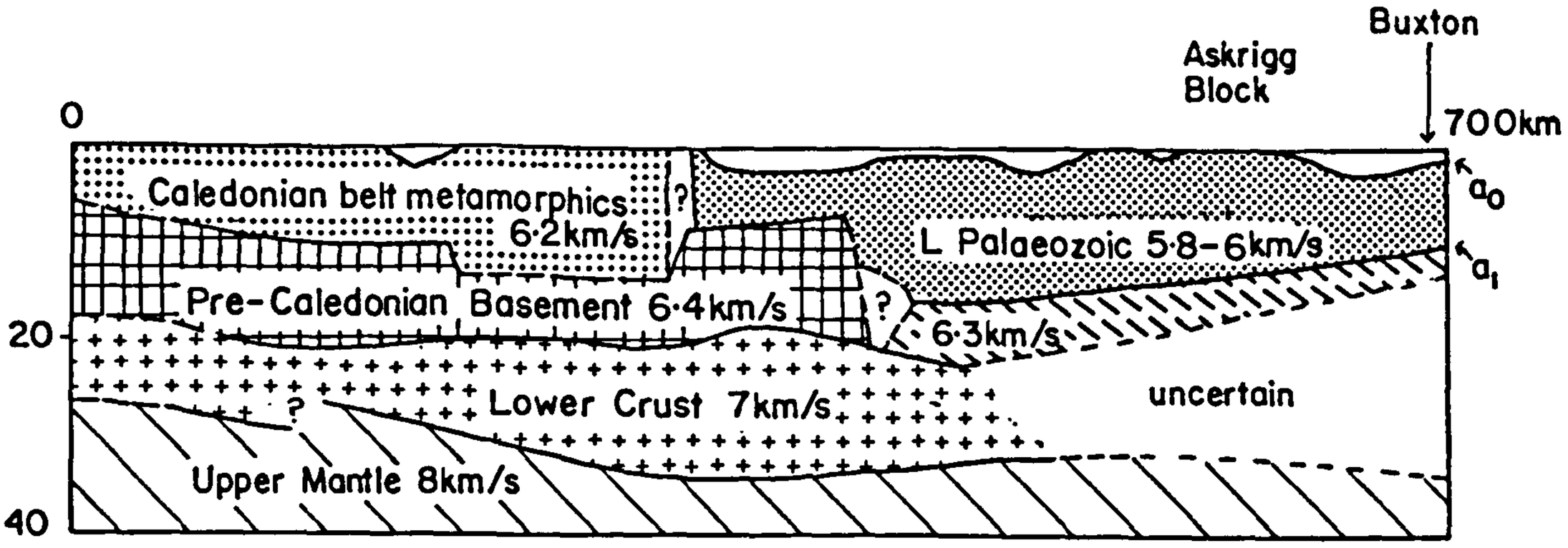

(a) LISPB

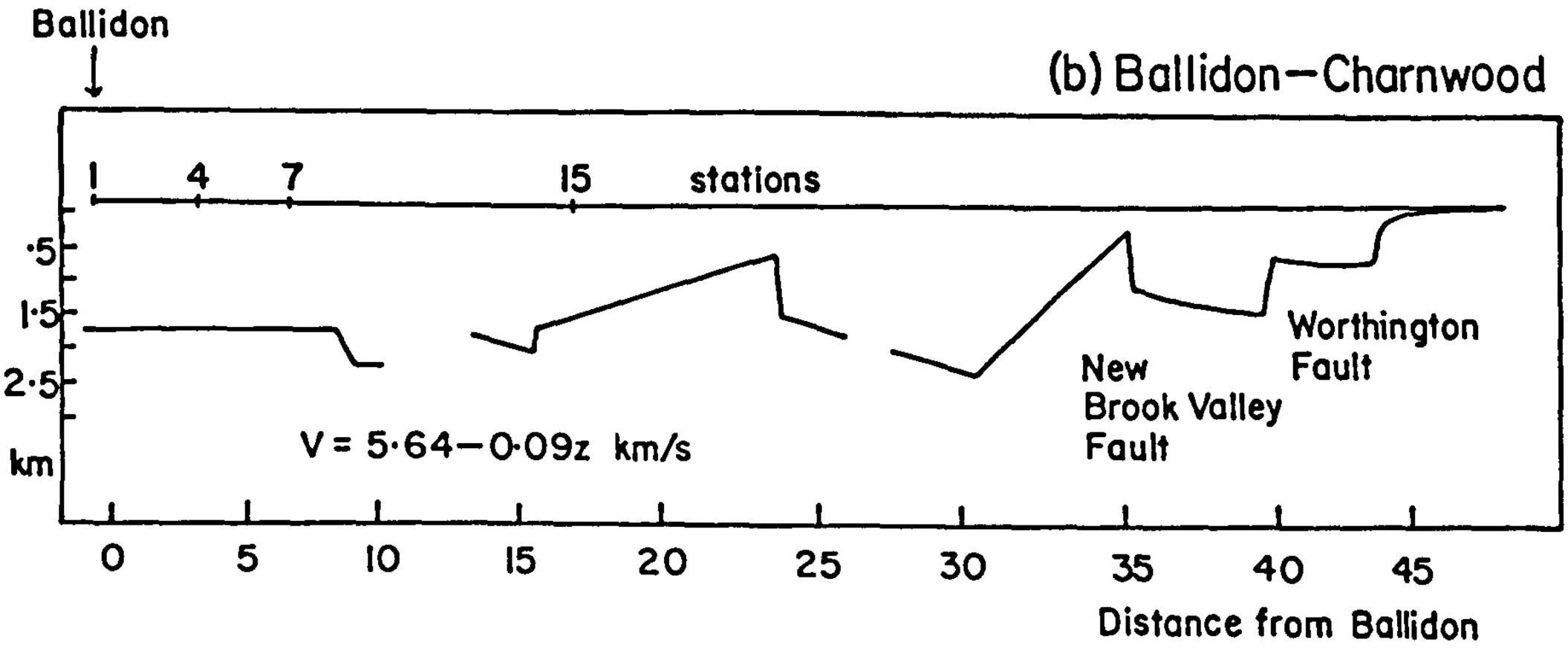

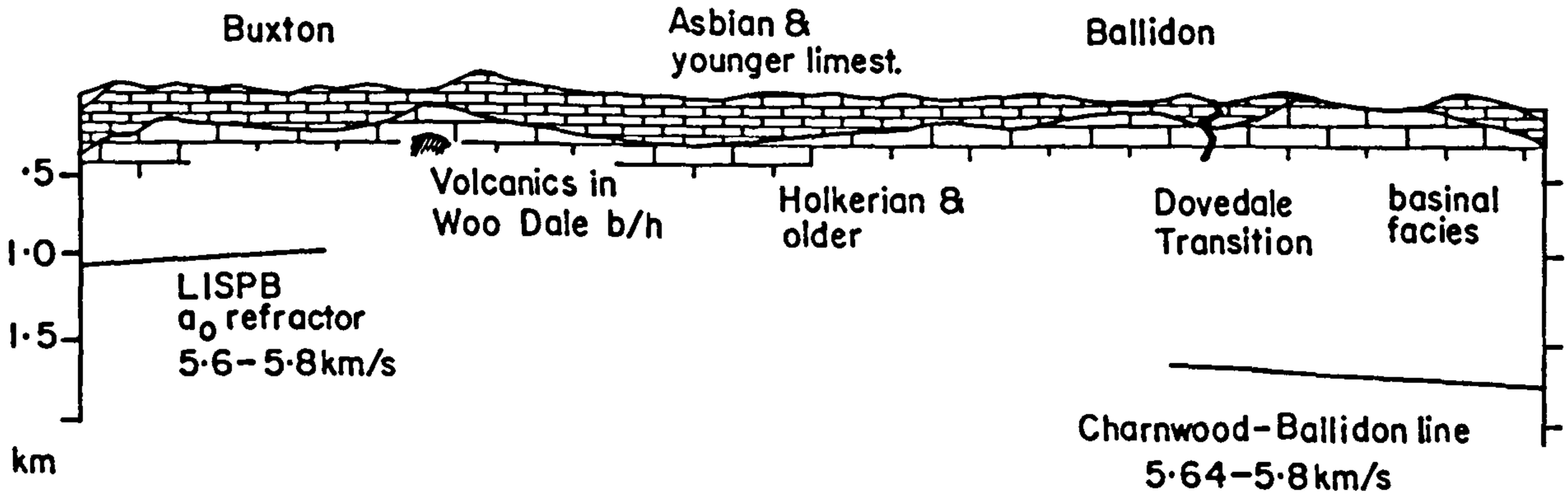

(c) North–south section of Dome

FIG 1-10

Previous seismic work on the limestone outcrop itself is scant. Cornwell (in Frost and Smart 1979), on refraction work south-east of Wirksworth, merely comments that the observed Dinantian velocities were lower than the 6.18 km/s determined from laboratory samples. A velocity of 5.95 km/s was assigned to the Dinantian for a refraction line shot east of Burton-upon-Trent (Bullerwell, in Stevenson and Mitchell 1955), but it is more likely that the observed refractor was Lower Palaeozoic or Precambrian.

Table 1-2 summarises velocities recently determined for strata related to the area. The high Dinantian velocities observed in South Wales were evident from direct arrivals which rapidly attenuated with distance and which were thought to be from dolomitic horizons. The Beckermonds Scar borehole was sunk about 5 km south-west of the Wensleydale Granite (under the Askrigg Block) to investigate the magnetic basement, and encountered at 260m a thick sequence of Ordovician siltstones and greywacke sandstones with a high magnetite content (Wilson and Cornwell 1982).

1.3.2 Gravity Field

Several important features are apparent on the Bouguer anomaly map of the region (IGS 1:250000 scale, 1977; Fig. 1.11), including two Precambrian trends: the Charnoid trend which sweeps across from the south-east, and the Malvernian trend which runs due north from the south-west. The steep gradient to the north-west defines the Red Rock Fault (west of which is the Cheshire Basin), and the Widmerpool Gulf can be distinguished running WNW-ESE.

The positive anomaly associated with the Dome is approximately defined by the 10mgal contour and is about 40 km north-south by 30 km east-west; its total amplitude is thus about 10mgal, although within the anomaly itself there are two distinct highs: one of about 20mgal to the south-west, and the other of about 16mgal to the north-east (Fig. 1.12).

Table 1-2

Recent Velocity Determinations

Strata	Velocity (km/s)	Means of Measurement	Reference
South Wales:			
Upper Carboniferous	4.3-4.7		
Dinantian Limestone	5.1-5.3	Least-squares	Bayerley & Brooks
(dolomitised)	5.6-5.7	(T-X plot)	(1980)
Old Red Sandstone	4.6-4.8		
Ordovician (Beckermonds Scar B/H)	5.4-6.1 (Mean 5.85)	Velocity Log	Wilson & Cornwell (1982)
Charnian (Charnwood Forest)			
Maplewell Series	5.65	Time-Term	Whitcombe & Maguire
Blackbrook Series	5.4	analysis	(1980)
Precambrian crystalline basement (East Anglia)	5.7-6.0	Various	Chroston & Sola (1982)

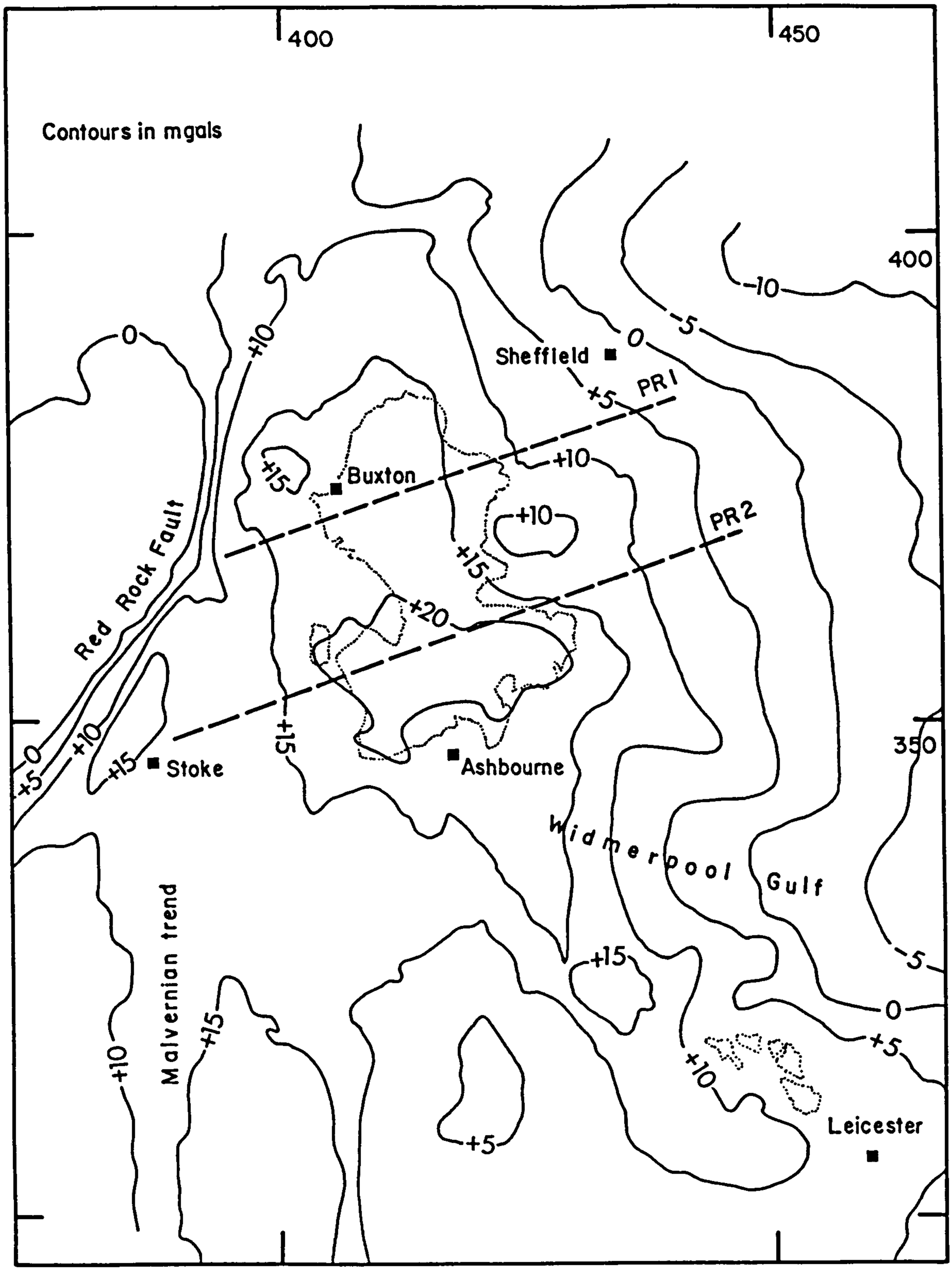

FIG I–II Bouguer anomaly map of region
PR1, PR2 Maroof's profiles

BOUGUER ANOMALY MAP

Contours in mgals

seismic station

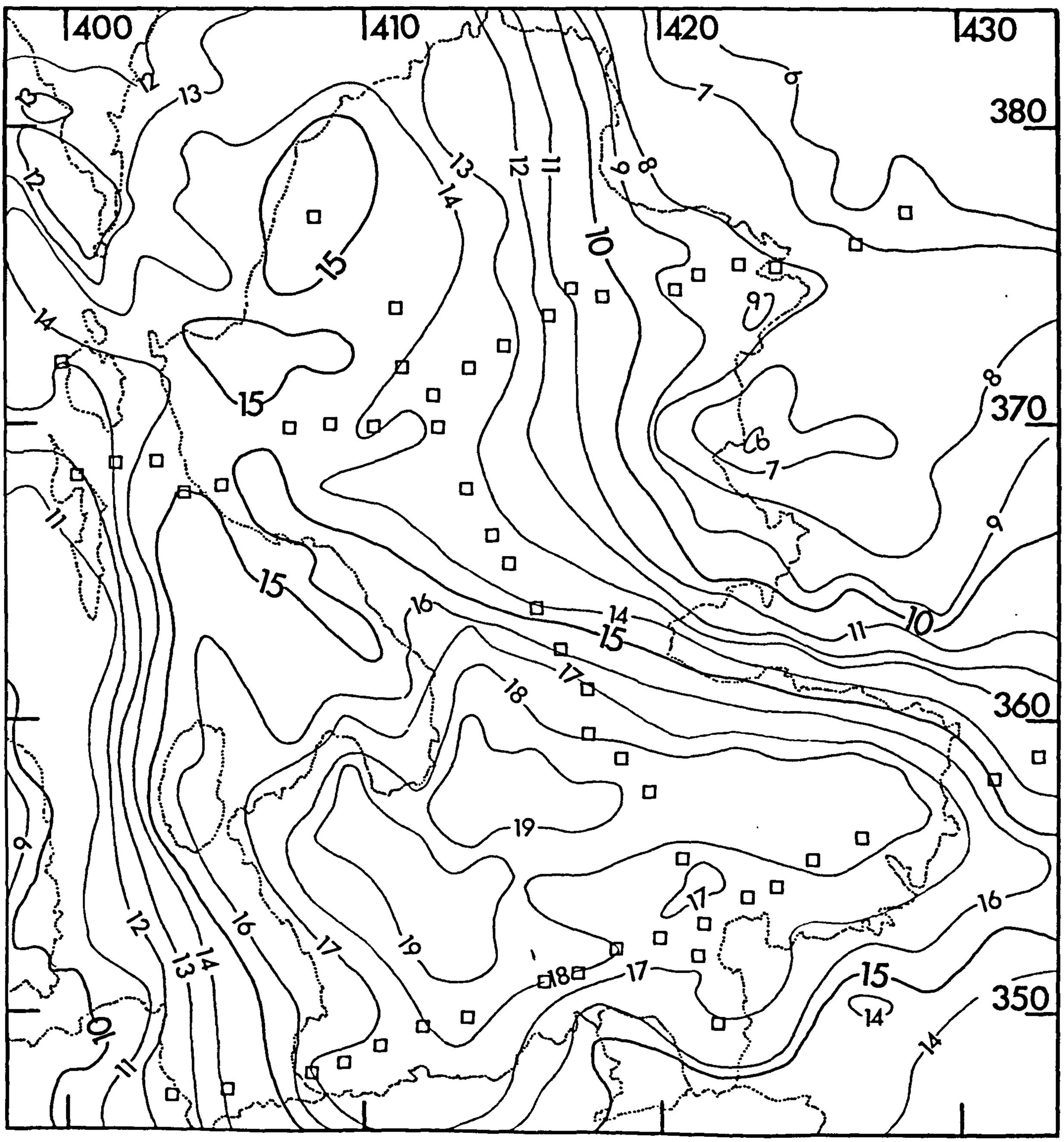

Table 1-3 lists densities for various formations in the region, determined by Bott (1967), Maroof (1973, 1976), Cornwell (in Frost and Smart 1979), and Wilson and Cornwell (1982):

The average limestone density in the Eyam borehole is about 2.72g/cc (Maroof, 1973), and it may be that the anomaly associated with the Dome is wholly due to a positive contrast between these limestones, and the surrounding Upper Carboniferous all underlain, say, by lower density granites. This model would suggest the limestones are thickest where the anomaly is greatest, to the south of the outcrop; however, the limestone sequence thickens between the Woo Dale and Eyam boreholes and this accompanies a decrease in anomaly which Dunham (1973) takes to indicate eastward dipping basement.

The total anomaly is more probably due to underlying higher density pre-Carboniferous basement. Maroof (1976) discusses three Bouguer anomaly sections he derived by digitising the published contoured map (IGS 1956) at 4 km intervals, two of which, PR1 and PR2, cross the limestone outcrop (Fig. 1.11). His interpretations of these sections are reproduced in Fig. 1.13, for which the average pre-Carboniferous density was taken to be 2.80g/cc, a value also assumed for similar work to the north of the area by Barker (University of Birmingham, pers. comm. 1982); Maroof further assumed a westward increasing regional of about 0.08mgal/km. These models suggest the basement to be shallower in the south than the north,

where the estimated depths to the base of the Carboniferous are 130-300 m and 200-530 m respectively.

The two gravity highs within the anomaly are divided approximately by Charnoid trending belt of contours across which the gradient increases easterly and which roughly coincides with the Bonsall Fault system (cf. Figs. 1.12 and 1.9). To the north of this belt the overall pattern swings from north-west to more northerly. Note that the Dome's north-south structural axis corresponds to where the two gravity highs merge; this region is marked by the older outcrops of

Table 1-3

Representative Densities

Formation	Density (g/cc)	Formation	Density (g/cc)
Upper Carboniferous	2.45	Precambrian	
Dinantian Limestone	2.70	Charnian:	
Carbo. dolerite	2.88	Brand series	2.76
Pennine Granites:		Maplewell series	2.70
Wensleydale	2.63	-- slate agglomerate	2.78
Weardale	2.59	Blackbrook series	2.65
Ordovician:		Pyroclastic rocks	2.83
Eyam Borehole	2.74	Phyllitic shale	2.84
Beckermonds Scar	2.78	Granodiorite	2.80
Cambrian:			
Stockingford shale	2.78		

PROFILE 1

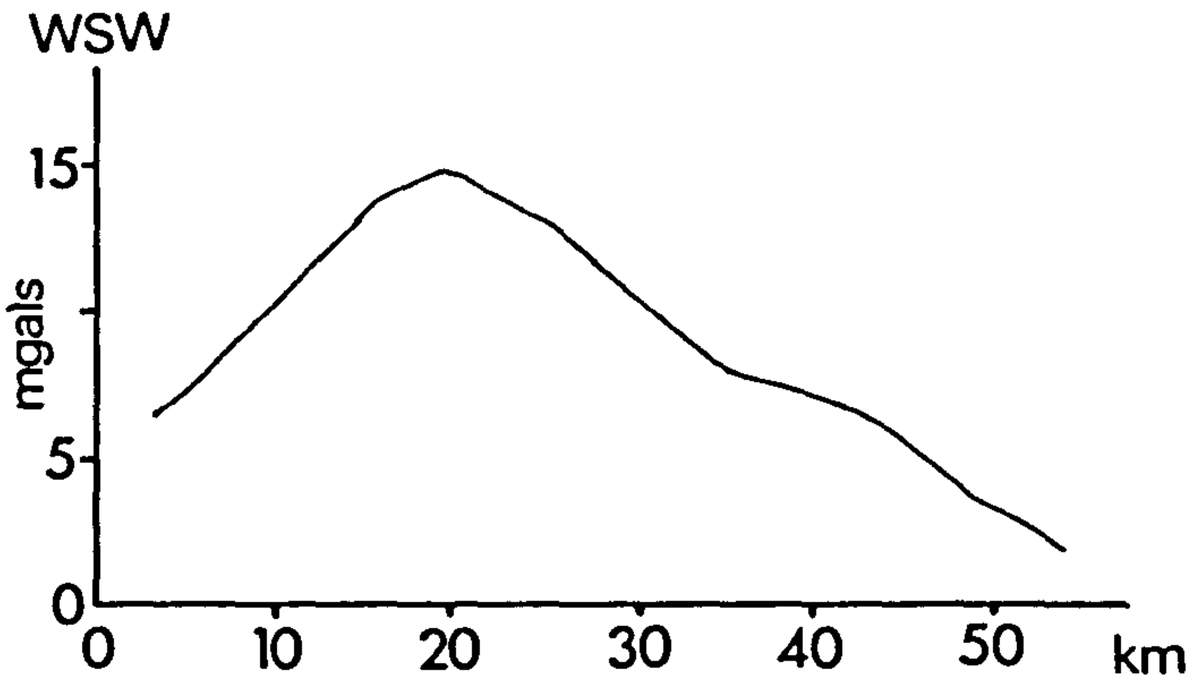

PROFILE 2

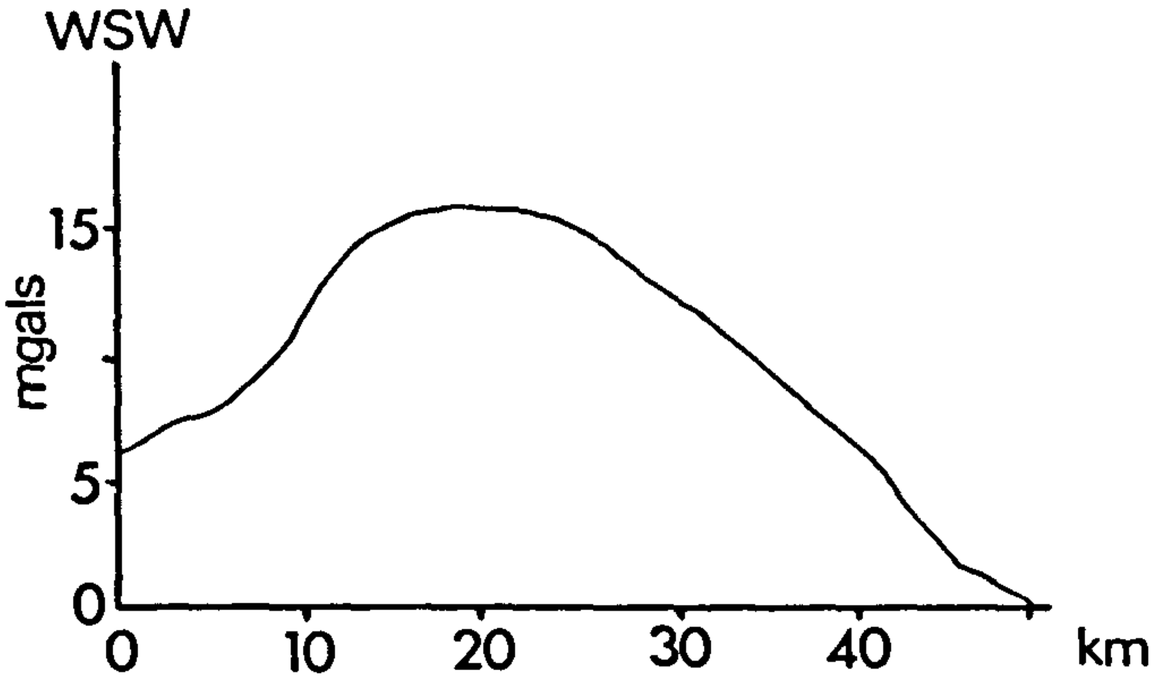

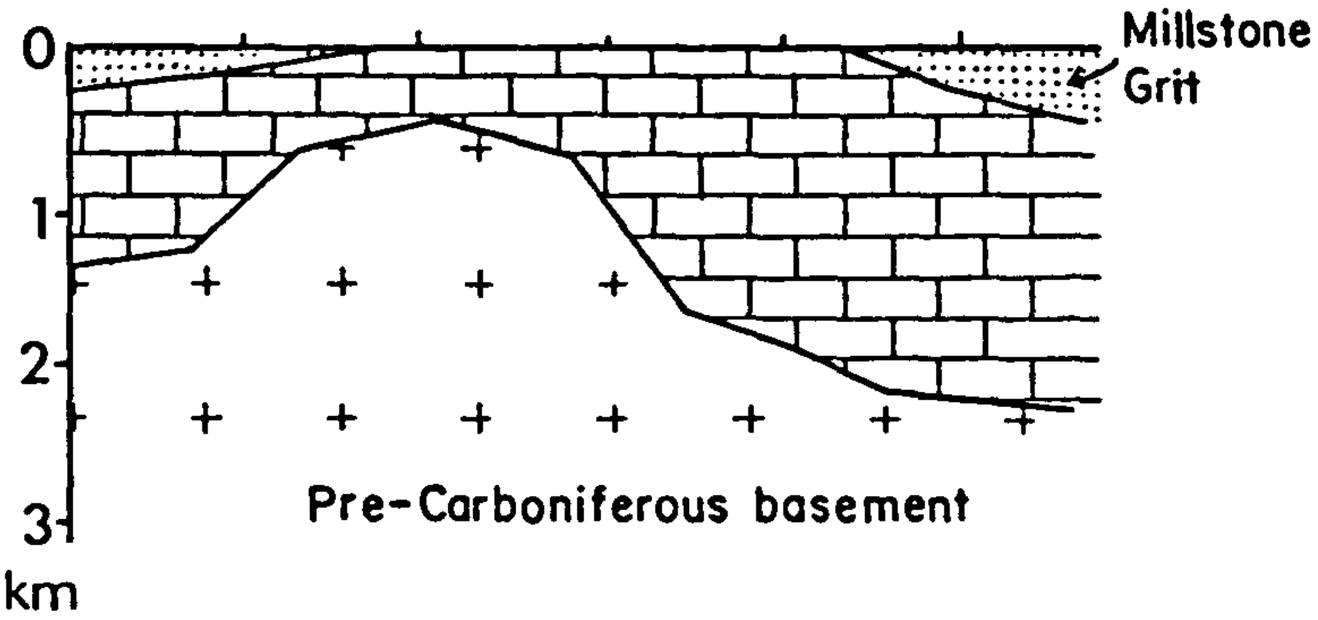

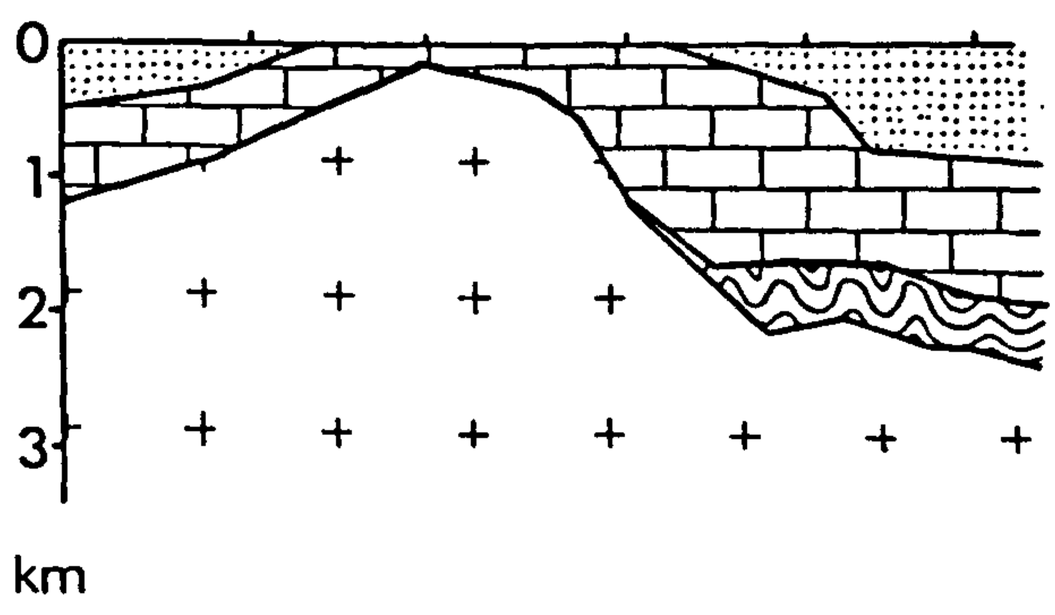

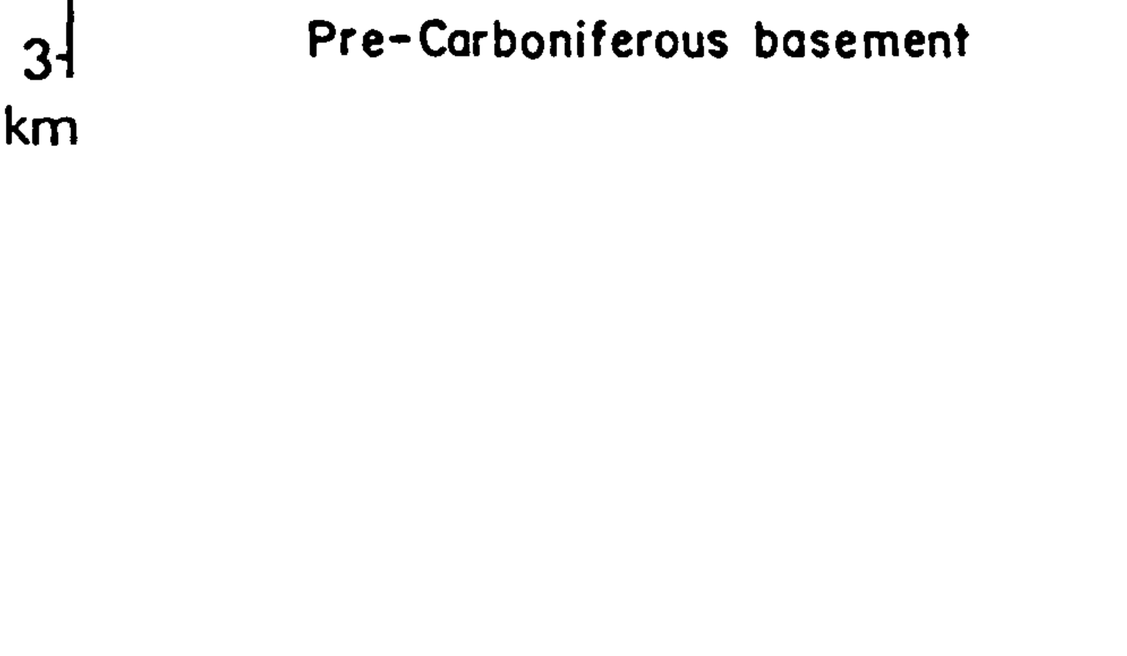

Fig 1-13 Maroof's models

the area, which also supports the notion of a high density pre-Carboniferous basement.

Bordering the massif, the only fault obvious from the Bouguer anomaly map is that to the west (discussed by Aitkinhead in Maroof (1976)). There is no fault apparent along the north-western margin of the massif, nor is there one marking the Dovedale Transition; this may be due to insufficient density contrast.

A couple of points may be made regarding the pre-Carboniferous basement:

a) the density contrast between the Dinantian limestones and the Charnian metasediments may not be sufficient to produce the whole anomaly. The Charnwood Forest inlier itself is marked by a smaller amplitude anomaly than the Dome (Fig. 1.11), though it is flanked by lower density tonalite and diorite intrusions, and El-Nikhely (1980) suggests that the outcrop is underlain by a metamorphosed and crystalline basement of density 2.85-2.9 g/cc at a depth of about 3 km, which agrees with the time-term interpretation of Whitcombe and Maguire (1980). It is therefore possible that such a deeper crystalline basement is also largely responsible for the broad Bouguer anomaly that characterises the Dome.

The same might be true if the Carboniferous were underlain by Lower Palaeozoic strata.

b) though the Carboniferous dolerites are more dense than the surrounding rocks, they are not obviously manifest on the Bouguer anomaly map and are therefore probably quite small and shallow.

1.3.3 Magnetic Field

The I.G.S aeromagnetic maps for the area are given in Figs. 1.14 and 1.15 (from Bullerwell 1965). The broad Charnoid trend north-westwards from the Leicestershire granodiorites (Fig. 1.14) led Evans and Maroof (1976) to postulate the north-

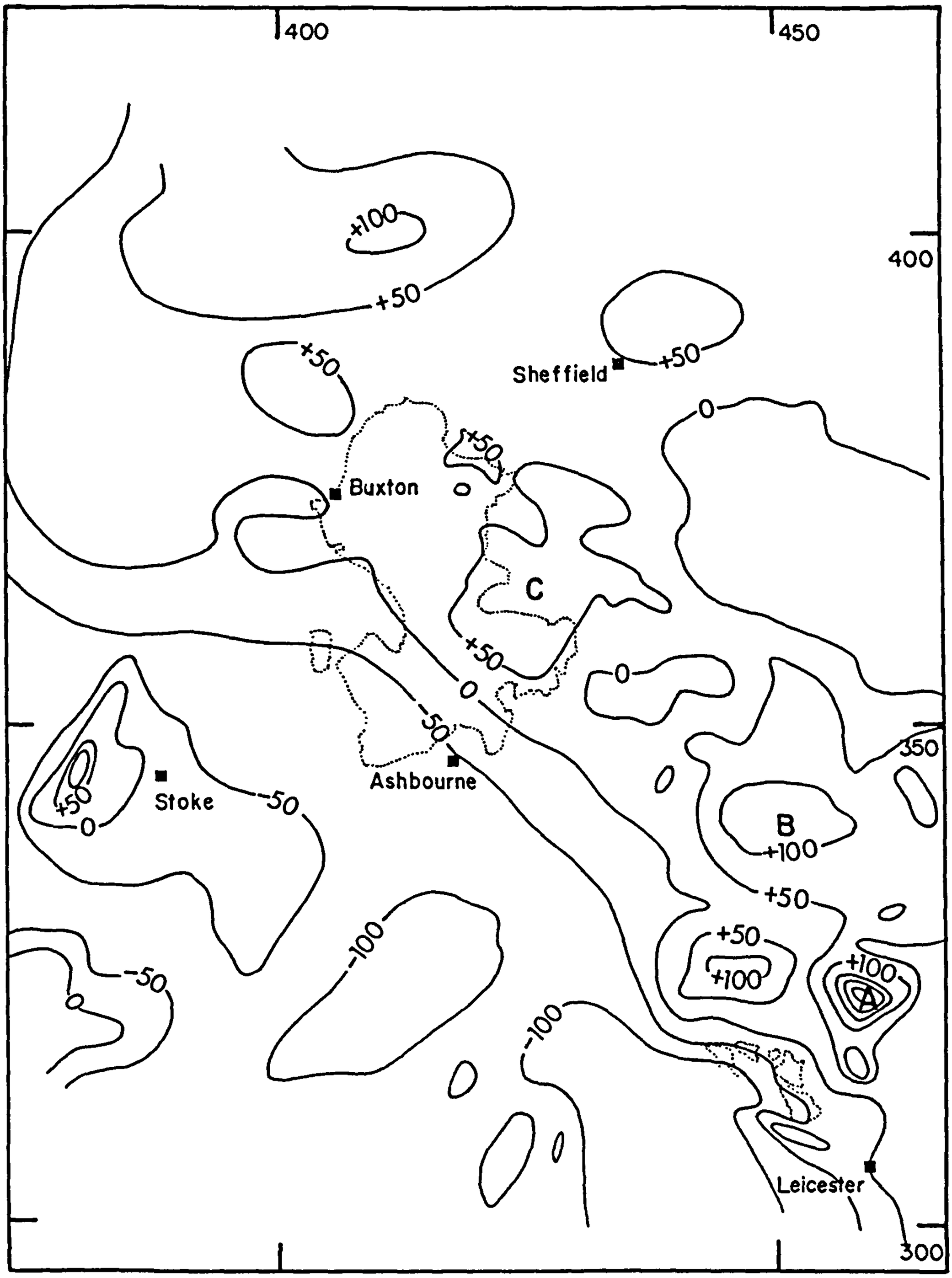

FIG 1–14 Aeromagnetic map
Contours in gammas

FIG I–15

AEROMAGNETIC MAP

Total field; contours every ten gammas

Local 'lows' shaded

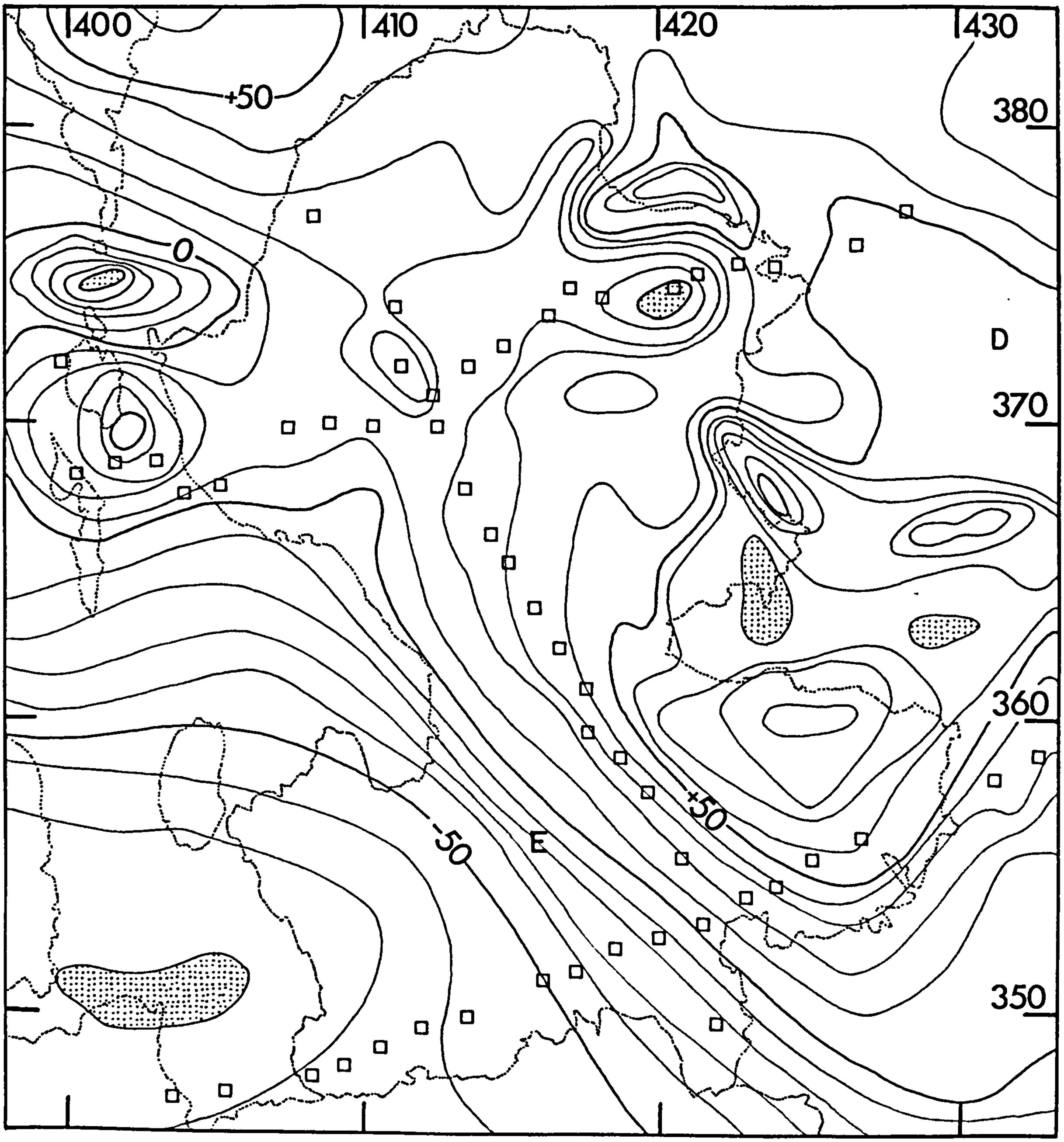

west continuation of Le Bas' (1972) Caledonian igneous province. If so, then the progressive decrease in amplitude and broadening of features A, B and C may imply the gradual deepening of this plutonic belt.

It is also possible that these anomalies to the east of the Dome are due to the Carboniferous volcanism: for example, anomaly D (Fig. 1.15) corresponds to the dolerite complex of the Ashover anticline, and the basinal region to the south-west of the Dome, largely without volcanism, is featureless. Since the gravity high to the south-west is not manifest in the aeromagnetic map, then any shallow pre-Carboniferous basement must be weakly magnetic, unlike the Precambrian and Caledonian granodiorites surrounding the Charnian outcrop (Maroof 1973, El-Nikhely 1980). Cornwell (in Frost and Smart 1979) notes that the smooth, widely spaced contours of gradient E are indicative of a Charnoid-trending structure at considerable depth, and Wills (1978) associates it with the Derby fault line, which he postulates to mark the western margin of the Precambrian massif (see Fig. 1.16).

1.3.4 Electrical Sounding

A deep resistivity sounding (Habberjam and Thanassoulos 1979) has been conducted on the Namurian at Big Moor, about six kilometres east of Stoney Middleton, by Stevens (1979; see Fig. 1.5). The favoured interpretation defines a layer of resistivity 3800 ohm m at between 1300-1500m depth, although Roxis (University of Leeds, pers. comm. 1982) doubts any interpretation of these data deeper than the base of the Namurian at about 600 m.

1.4 Summary - Ideas of the Sub Carboniferous basement

Structurally and sedimentologically, the Derbyshire limestone outcrop is more complicated than the simple term 'Dome' implies, and it is possible that the gently dipping

FIG 1-16

Palaeogeological map of region, beneath the Devonian (after Wills (1978))

Silurian
Ordovician
Cambrian
Pre-Cambrian
Charnian
Caledonide granites
fault
ridge of high magnetic anomaly

400
400
450
300
Sheffield
Eyam B/h
Buxton
Woo Dale B/h
Duke's Wood B/h
Red Rock Fault
Ridge of shallow P-C with Caledonide granitoid intrusions & L. Pal. outliers
Derby Fault Line
Stoke-on-Trent
Charnwood
Leicester
Birm'ham

Asbian and Brigantian strata disguise an even more complex geology. All three boreholes which pierced the Dinantian, for example, encountered differing strata, and the thickening of limestones between Woo Dale and Eyam belies a structurally stable basement during carbonate sedimentation.

If the Bouguer anomaly high associated with the Dome is due to a shallow, high density pre-Carboniferous basement, then this material must be weakly magnetic. The magnetic contours across the Dome suggest a deep magnetic basement with a Charnoid trend, which may correlate with the crystalline or metamorphic basement thought to be at a depth of about 3 km beneath the Charnwood Forest inlier, which was found to have a P wave velocity of about 6.4 km/s (Whitcombe and Maguire 1980).

That the Bouguer anomaly of the Dome is some 10mgals higher than that associated with Charnwood Forest may suggest that lower density Caledonide granodioritic intrusions are largely absent, at least within the upper crust. The Bouguer anomaly map suggests that the pre-Carboniferous basement is shallower to the south of the Dome than to the north, and that a north-westerly trending band of contours divides the Dome into two 'provinces', across which the underlying trend changes from Charnian (NW-SE) in the south to a more north-southerly direction to the north.

The sub-Carboniferous outcrop is unquestionably Ordovician in part from borehole evidence, and this may correspond with the Lower Palaeozoic refractor interpreted from the LISPB data. Although the Charnoid trend is apparent throughout the region, it seems to have a more dominant structural presence in the southern province, under which Whitcombe and Maguire (1981b) believe the basement to be of Charnoid-type material.

Thus the north-south profile set out to resolve the differences in interpretation between the LISPB and Charnwood-Ballidon lines, and to investigate the nature of the apparent division of the Dome. The northern east-west profile was planned to determine the nature of the basement tilting between

Woo Dale and Eyam, and the southern east-west line to investigate both the nature of the Dovedale Transition and the relationship of the sandstones of the Caldon Low borehole with the rest of the area.

CHAPTER TWO

THEORY

2.1 Introduction

The project is principally concerned with the analysis of first arrival data from quarry blast sources. Since these sources are unequally distributed over the area, and relatively few blasts have been accurately located and timed, the refracted data have been analysed using the time-term method of Scheidegger and Willmore (1957), which demands fewer conditions of the data than other delay-time or intercept-time techniques. This method is discussed in Section 2.2, along with simulated data studies of an anticlinal refractor, which is the suspected structure of the sub-Carboniferous surface of the Derbyshire Dome.

There then follows a brief discussion on amplitudes, signal analysis, and a short appraisal of the use of polarisation filters to enhance first arrivals.

2.1.1 General

The physical characteristics of different geological formations are expressed as the seismic properties of velocity of propagation and the attenuation of energy, which are loosely (but not necessarily) inversely related. Few rocks are homogeneous and isotropic: P wave velocities within any medium are a function of position, depth, azimuth (anisotropy) and frequency (dispersive effects). Lateral variations occur because of facies changes in sedimentary rocks or because of anomalous zones of mineralisation (e.g. diagenetic dolomitisation of limestones, ore bodies etc.). Velocity gradients occur in sedimentary rock where the consolidation increases with depth (Wyrobek 1959), and also within the top five kilometres or so

for shallow plutonic bodies (Birch 1959). Azimuthal velocity anisotropy has received much attention in the literature since Hess (1964) discussed anisotropy in oceanic mantle; in crystalline rocks anisotropy arises through the preferred orientation of crystals (Meissner and Fakhini 1977), and in sedimentary rocks through the parallelism of cracks and fractures (Crampin, McGonigle and Bamford 1980). Vertical velocity anisotropy can also occur in sedimentary rocks due to facies change with depth.

To some degree all these effects are probably present in any geological situation although individual media are normally assumed to have a constant seismic velocity unless some other feature (anisotropy, velocity gradient, etc.) is pronounced enough to determine from the observed data. This simplification pervades nearly all seismic refraction interpretation procedures, which usually start from the notion of a constant velocity stratified earth. Furthermore, the analyses can only easily distinguish those interfaces across which there is a velocity increase, and horizons for which this is not so can only be investigated through additional observations such as reflections and amplitude information.

The velocity structure of the Dinantian limestones of the Derbyshire Dome, for example, may be similar to the Carboniferous limestones in South Wales investigated by Bayerly and Brooks (1980): viz generally 5.1-5.3km/s with dolomitic bands of velocity 5.6-5.7km/s. If so, then beneath such high velocity overburden and above the basement, thought to be of velocity 5.6-5.8km/s, there may be

(a) a hidden layer (Fig. 2.1a), which is either too thin to produce headwaves, or whose velocity contrast is too small for headwaves to precede refractions from a deeper horizon with a larger velocity contrast, or even

(b) a velocity inversion (Fig. 2.1b), where the depth of the lower velocity medium is best estimated by plotting T^2-X^2 curves for the reflected phases.

The sandstones beneath the limestone at Caldon Low (Section 1.2.3) suggest at least one example in the region where a low

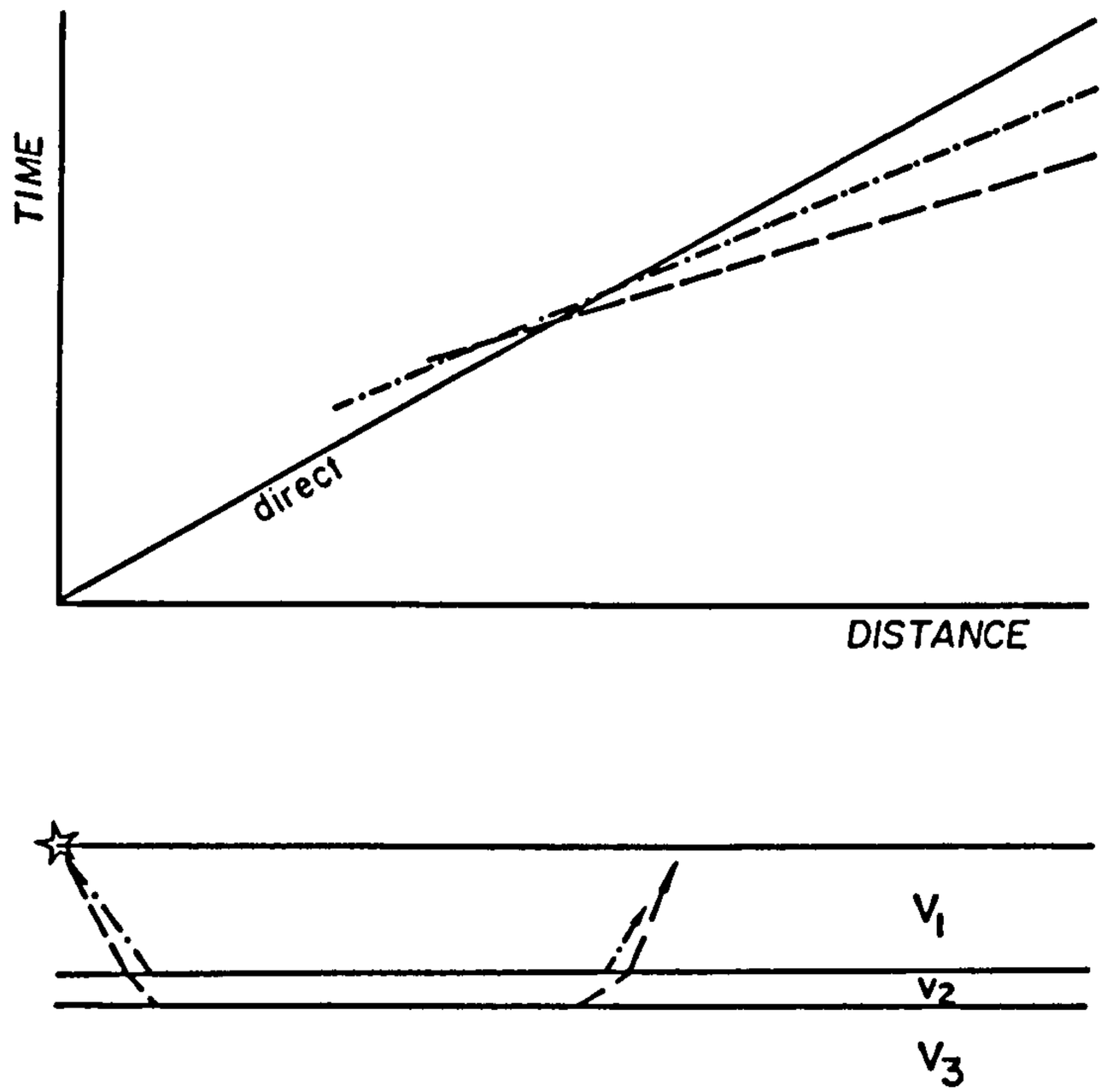

(a) Hidden second layer $V_1 < V_2 < V_3$

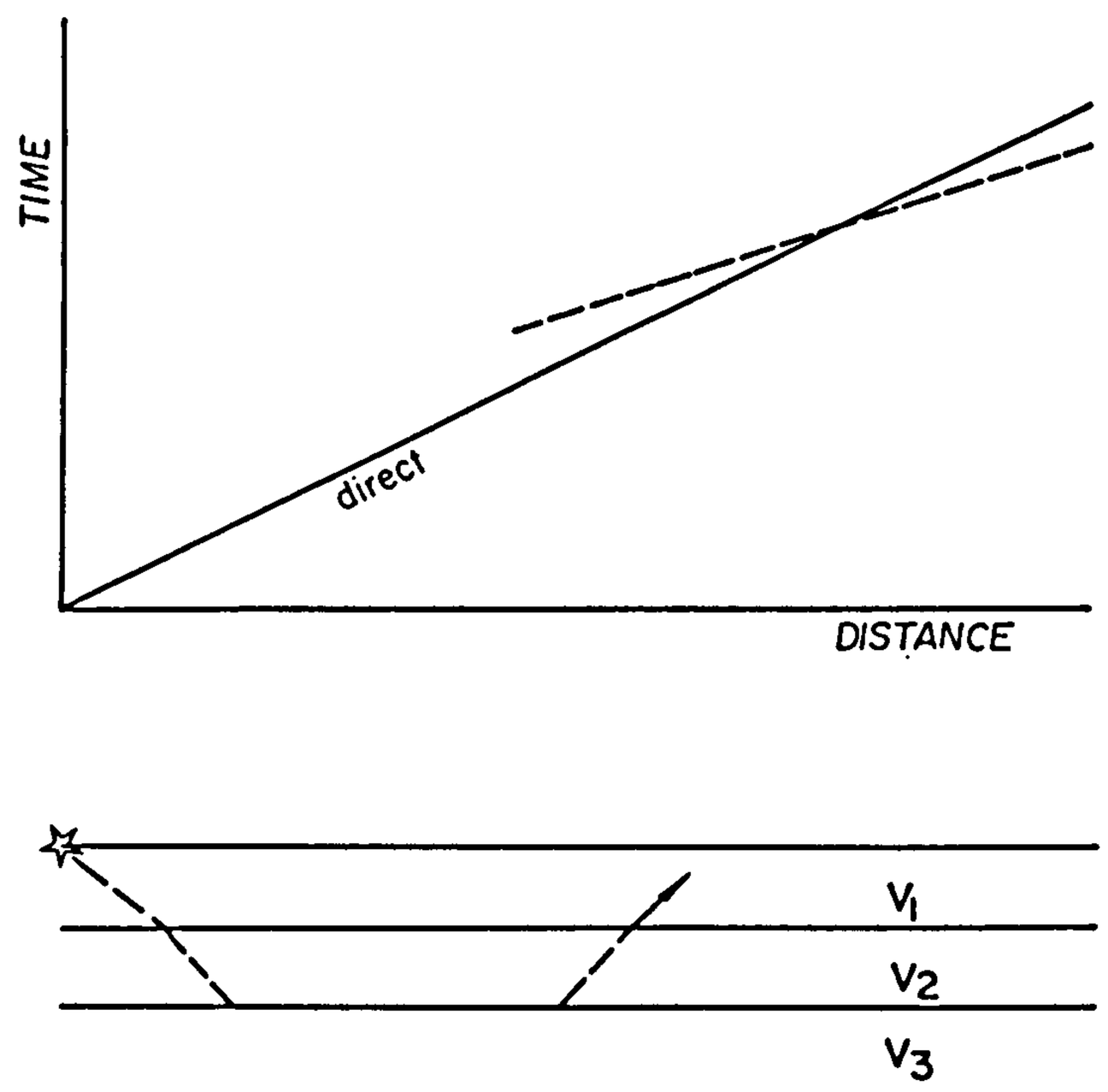

(b) Low velocity second layer $V_2 < V_1 < V_3$

FIG 2-1

velocity layer may be present. Schmöller (1982) has recently published simple nomographs to interpret cases similar to those above, given an estimate of the masked layer velocity.

Refractions from high velocity dolomitic layers may screen a deeper refractor. To investigate the effects of thin shallow masking layers, Trostle (1967) made the following studies by considering both scaled models and similar cases in the field:

a) Thin, shallow screening layer (Fig. 2.2a): two sets of arrivals at the same velocity were observed to succeed the direct waves, the first which was of lower amplitude and about twice the frequency than the second, and which eventually attenuated out. The later arrival, which attenuated at a rate consistent with spherical spreading, was interpreted to be a true headwave from the lower interface rather than a reflection.

b) Thin, high velocity overburden (Fig. 2.2b): two cases were investigated, with the piezoelectric source above, and then below the overburden. Each time the effects of the anomaly (Q) were observed at the same detector positions to prove that the arrivals were refracted from the lower boundary. The case is similar to the screening layer in that direct waves in the overburden attenuated rapidly, and that the refracted arrivals were of much lower frequency.

Trostle conducted refraction surveys over similar field cases to conclude that: a) deep refractions are consistently observed beneath screening layers, b) the wavelength of the deep refraction is about equal to the thickness of the screening layer (although the nature of the hidden layer also contributes to the filtering), and c) the deeper refraction can be easily identified as a second arrival.

2.2 The Time-Term Method - Introduction

The time-term method (Scheidegger and Willmore 1957, Willmore and Bancroft 1960) is a least-squares approach to solving refractor velocities and delay-times (time-terms).

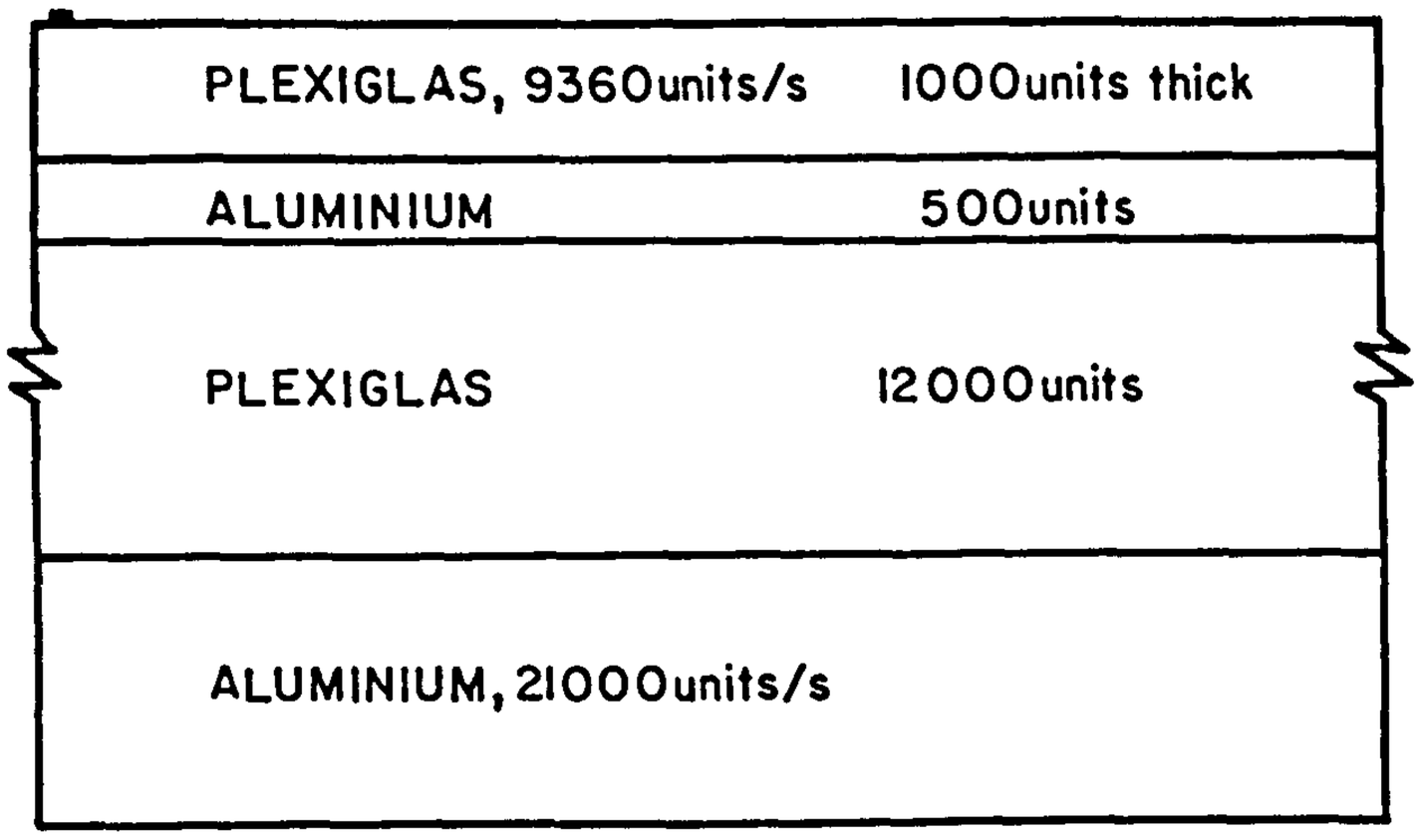

(a)

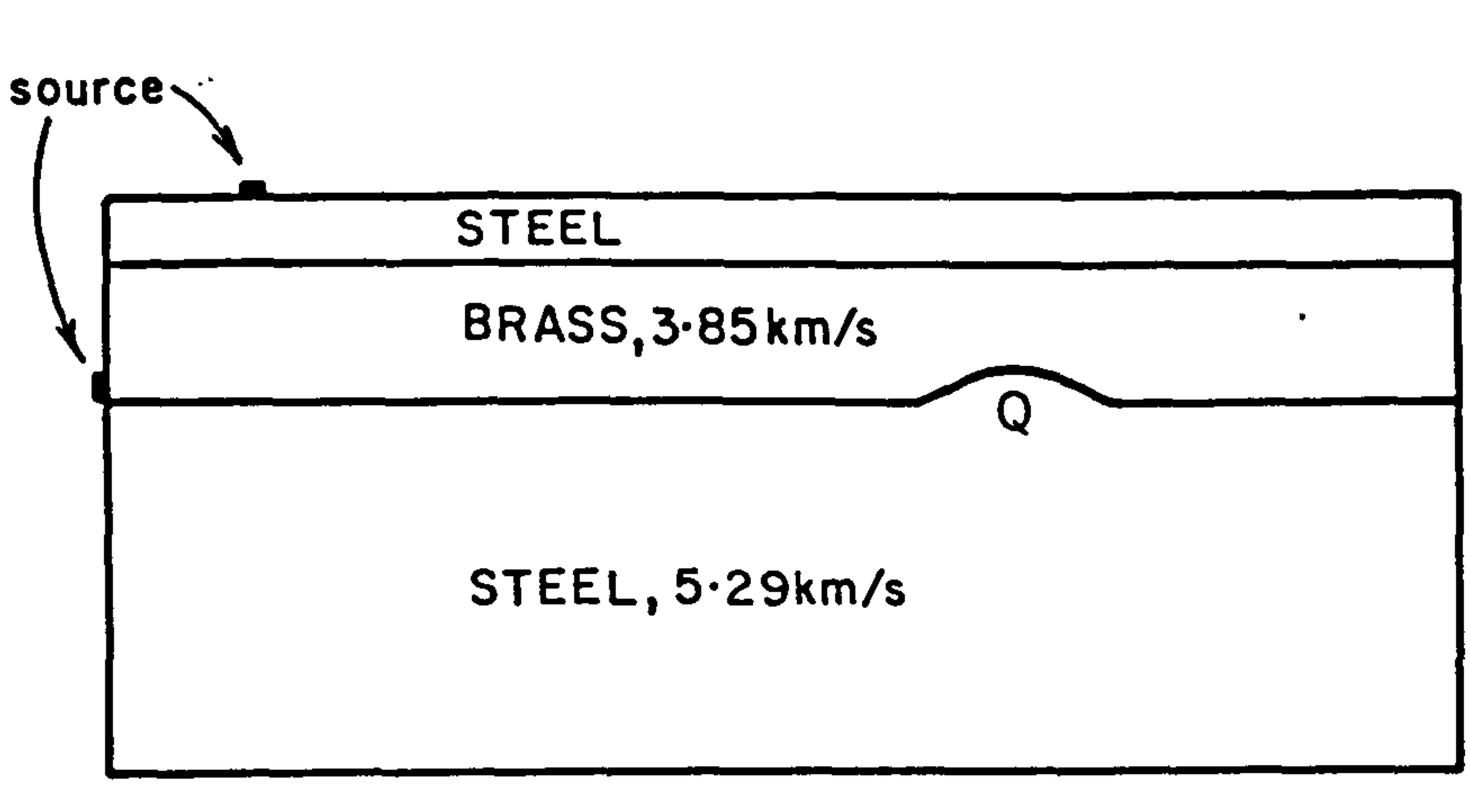

(b)

FIG 2-2 Models used by Trostle (1967) to investigate high velocity screening layers

Unlike other delay-time methods (e.g. Gardner 1939, Barry 1967), intercept-time methods (e.g. Wyrobek 1956) or plus-minus methods (Hagedoorn 1959), the time-term technique does not require a linear configuration of stations and well controlled shots. The method is well suited to an areally distributed pattern of shots and stations, and only one observation linking two shot-points is required to solve the unknowns uniquely.

Extensions to the method have come with application: for the Lake Superior seismic refraction project, Berry and West (1966) generalised the depth conversion of time-terms for several layers, and introduced a weighting function to simplify the algorithm. For data from the same project, Smith, Steinhart and Aldrich (1966) included the solution for vertical velocity gradients. Raitt et al. (1969) extended the method to determine velocity anisotropy for experiments in the Pacific, and also used a delay-time-function method to overcome the problems of unevenly distributed observations by fitting a polynomial surface to the solution rather than solve each time-term uniquely, thus reducing the number of unknowns. In considering similar poorly distributed data in West Germany, Bamford (1976) assumed groups of stations to have the same time-term (the MOZAIC method), thus reducing the number of unknowns before, rather than after, the data were inverted.

2.2.1 The Time Term Method

Consider the simple refraction example of Fig. 2.3. The travel time t_{ij} between shot i and station j can be written

$$t_{ij} = \frac{ip}{V_o} + \frac{pq}{V_r} + \frac{qj}{V_o} = \frac{h_i+h_j}{V_o\cos\theta_c} + \frac{X_{ij}\cos\phi - (h_i+h_j)\tan\theta_c}{V_r} \qquad (2.1)$$

for the critical angle $\theta_c=\sin^{-1}(V_o/V_r)$. However, the time can also be written

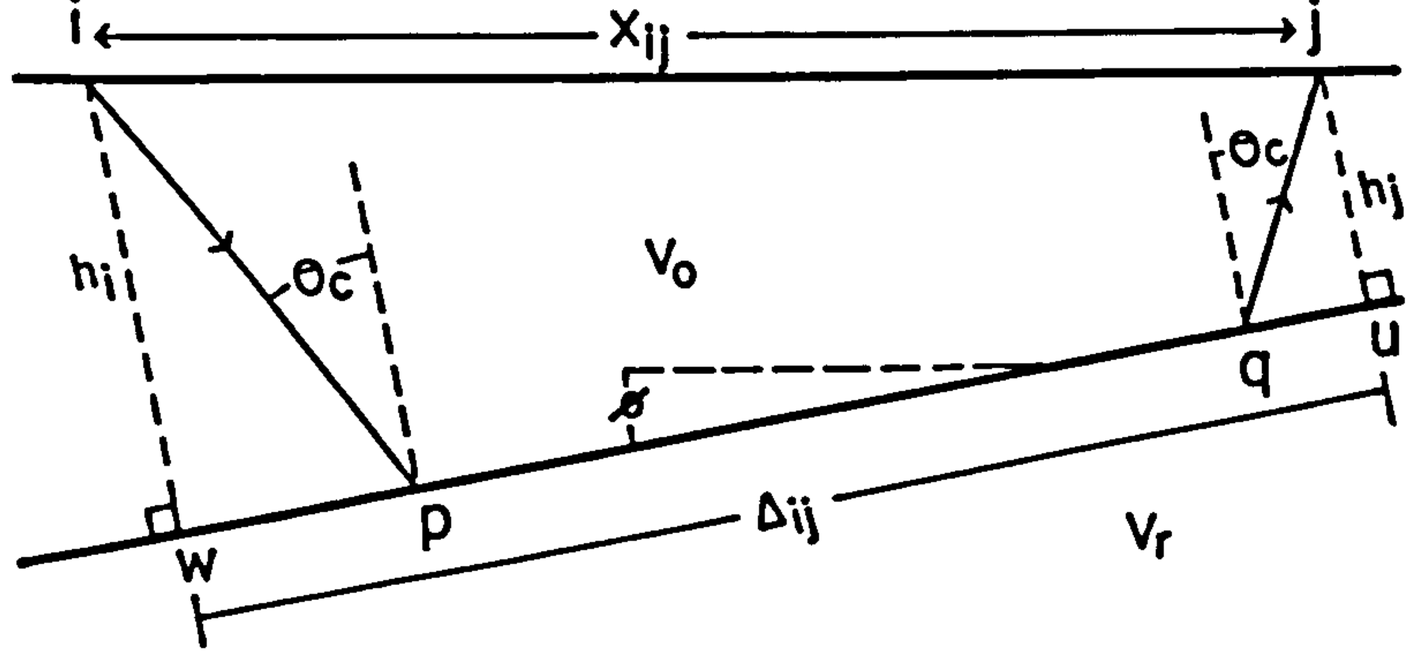
i
X_{ij}
j
h_i
θ_c
V_o
θ_c
h_j
ϕ
q
u
p
Δ_{ij}
V_r
w

FIG 2-3

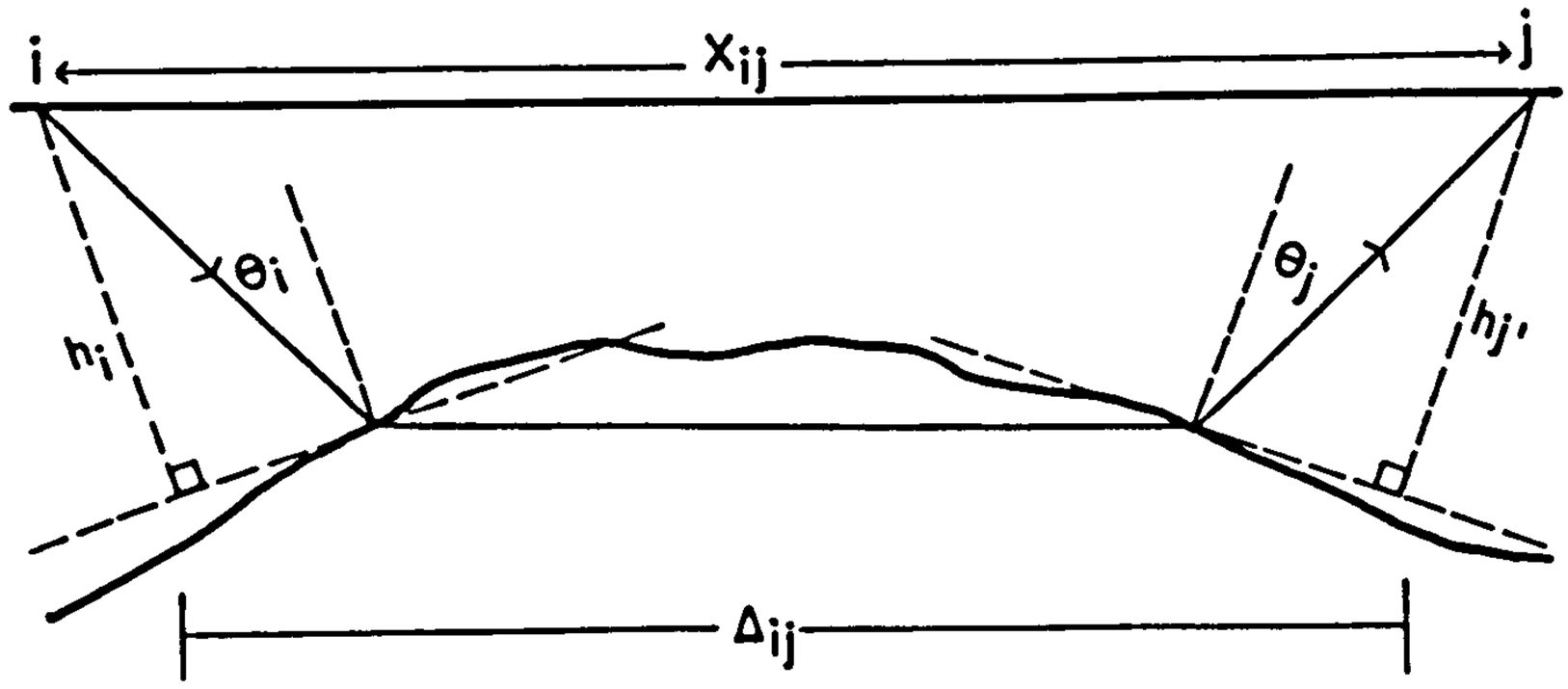
i
X_{ij}
j
h_i
θ_i
θ_j
h_j
Δ_{ij}

FIG 2-4

$$t_{ij} = \left(\frac{ip}{V_o} - \frac{wp}{V_r}\right) + \left(\frac{qj}{V_o} - \frac{qu}{V_r}\right) + \frac{wu}{V_r}$$

$$= \frac{h_i \cos\theta_c}{V_o} + \frac{h_j \cos\theta_c}{V_o} + \frac{X_{ij} \cos\phi}{V_r}$$

$$= ai + aj + \Delta_{ij}/V_r \qquad (2.2)$$

where ai, aj are known as the delay times associated with shot and station respectively, and Δ_{ij} the distance between perpendicular drops from stations to refactor. The time-term technique employs observation Equation 2.2 as one of a set of simultaneous equations from which the solution delay times (time-terms) can be estimated by least-squares analysis; this reduces the effect of azimuth on the observed station delay times and is particularly suited to a patchwork of shots and observations. A more general approximation to this equation is,

$$t_{ij} = \frac{h_i \cos\theta_i}{V_o} + \frac{h_j \cos\theta_j}{V_o} + \frac{\Delta_{ij}}{V_r} \qquad (2.3)$$

where θ_i, θ_j are the angles of incidence at the refractor boundary, and hi, hj the lengths of perpendicular drops to the tangents drawn normal to the points of incidence (see Fig. 2.4). Δ_{ij} is the distance between the perpendicular intercepts. Obviously the angles of incidence vary from one shot-station connection to another, so the time-terms are usually defined for critical incidence:

$$a(h) = \int_0^h \frac{[V_r(h)^2 - V_o(z)^2]^{\frac{1}{2}}}{V_r(h) V_o(z)} \qquad (2.4)$$

(after Berry and West 1966), where a(h) is the time-term of the refractor at depth h, $V_r(h)$ the refractor velocity immediately below the interface, and $V_o(z)$ the velocity structure of the overburden.

By using Equation 2.3 it is usually assumed that the points of refraction below any station lie close to a common plane such that the effect of offset (wp, qu in Fig. 2.1) is accounted for (Bamford 1976). In general, however, both overburden and refractor velocities may vary laterally, azimuthally and with depth and the true station delay times may be highly azimuthally dependent (Whitcombe and Maguire 1979) so that too few parameters are known to apply Equation 2.3 literally. The distance Δ_{ij} is unlikely to be known before the analysis proceed so that the first assumption made is:

$$\Delta_{ij} = X_{ij}$$

so that

$$t_{ij} = a_i + a_j + \frac{X_{ij}}{V_o} + d_{ij} \qquad (2.5)$$

where

$$d_{ij} = e_{ij} + g_{ij}$$

for observational error e_{ij} and a structurally dependent error variable g_{ij}. The solution to Equation 2.5 may be written

$$T_{ij} = a_{si} + a_{sj} + \frac{X_{ij}}{V_s} + r_{ij} \qquad (2.6)$$

where the solution residual r_{ij},

$$r_{ij} = t_{ij} - T_{ij}$$

for solution time-term a_{si}, a_{sj} and solution velocity V_s.

For n shots and m stations there will be $L = n \times m$ equations of the form 2.6, and $N = n+m+1$ unknowns, including the refractor velocity. Thus for a least-squares solution to be possible, $L \geq N$. Writing Equation 2.6 in vector form (after Whitcombe 1979),

$$[t] = [A][a_s] + [X]/V_s + [r] \qquad (2.7)$$

where the L×1 vectors [t], [X] and [r] contain the observation times, distances and residuals, $[a_s]$ an N×1 vector containing the model time-terms, and [A] an L×N matrix which links the shots and stations for all observations. Now, each solution time-term and residual may be split,

$$a_{si} = e_i - \frac{f_i}{V_s} \qquad r_i = g_i - \frac{h_i}{V_s} \tag{2.8}$$

where e_i, g_i are elements of [t] and f_i, h_i elements of [X]. Substituting these in Equation 2.7 and re-arranging,

$$[A][e] - \frac{[A][f]}{V_s} = [t] - \frac{[X]}{V_s} - [g] - \frac{[h]}{V_s} \tag{2.9}$$

The least-squares solution is that where the residual terms are a minimum; thus by setting [g] and [h] to zero and separating elements of time and distance,

$$\begin{aligned} [A][e] &= [t] \\ [A][f] &= [X] \end{aligned}$$

which may be solved by inverting matrix [A].

To solve for a least-squares velocity, consider the sum of squared residuals, I,

$$I = \sum_{i=1}^{n} \sum_{j=1}^{m} r_{ij}\, \gamma_{ij} = \sum_{i=1}^{n} \sum_{j=1}^{m} \left(t_{ij} - \frac{X_{ij}}{V_s} - a_i - a_j\right)^2 \gamma_{ij}$$

(where γ_{ij} is unity if t_{ij} exists, and zero if not (after Berry and West 1966))

$$= \sum_i \sum_j \left(t_{ij} - \frac{X_{ij}}{V_s} - e_i + \frac{f_i}{V_s} - e_j + \frac{f_j}{V_s}\right)^2 \gamma_{ij}$$

which on differentiating with respect to $1/V_s$ and equating the result to zero, reduces to

$$V_s = \frac{\sum_{ij} d_{ij}^{\,2}\, \gamma_{ij}}{\sum_{ij} c_{ij} d_{ij}\, \gamma_{ij}} \tag{2.10}$$

where

$$d_{ij} = X_{ij} - f_i - f_j$$

$$c_{ij} = t_{ij} - e_i - e_j$$

Thus the solution values e_i, f_i, V_s, etc. can be substituted into Equations 2.8 to solve the solution time-terms. Note that for Equation 2.6 an arbitrary constant α may be added to all the station time-terms and subtracted from all the shot time-terms without affecting the observations (Willmore and Bancroft 1960). Thus to prevent the singularity of the observations matrix [A] at least one observation must be a shot-to-shot time, or one time-term be assigned an arbitrary value (Berry and West 1966).

2.2.2 Quality of the solution

A measure of the solution fit to the data is the solution variance, σ_s^2 where

$$\sigma_s^2 = \frac{\sum_{j=1}^{n} \sum_{j=1}^{m} r_{ij} \gamma_{ij}}{L-N-1}$$

(Berry and West 1966), where L,N are the number of observations and unknowns respectively. For a least-squares solution σ_s^2 is a minimum, and obviously the greater σ_s^2 the worse the fit of the solution to the data. The solution residuals are due to both observational error and the differences between the model and the real earth (due to the assumptions of the method), that is

$$\sigma_s^2 = \frac{\sum_{i=1}^{n} \sum_{j=1}^{m} e_{ij}^2 \gamma_{ij}}{L} + \frac{\sum_{i=1}^{n} \sum_{j=1}^{m} g_{ij}^2 \gamma_{ij}}{L-N-1}$$

where g_{ij} is the structurally related residual due to the approximations of the model. Thus a good fit to the data is when the solution variance is similar to the observational error variance, σ_e^2, estimated from the data. This may be tested by the F ratio

$$F = \frac{\sigma_s^2}{\sigma_e^2}$$

(Whitcombe and Maguire 1979), where the nearer the ratio to unity the more statistically similar the populations for which the variances have been calculated (Davis 1973). Lack of fit is evident when F exceeds the critical value at the 95 per cent confidence level (read from the relevant F distribution chart), or when 1/F exceeds a similar critical value (i.e., the solution is overmodelled and not justified by the data). Though the F ratio is a good indicator of the quality of a solution, a decrease of value does not necessarily indicate that the solution is any more correct, and must not be used as the only criterion to judge a result (Whitcombe and Rogers 1981).

The F ratio can also be used to compare the variances of two solutions (Whitcombe, pers. comm.), where if their ratio is insignificantly different from unity at the critical value, then they can be considered indistinguishable on the basis of variance.

The variance for a time-term may be defined as

$$\sigma_j^2 = \frac{\sum_{i=1}^{n} r_{ij}^2 \gamma_{ij}}{N-1}$$

and the mean deviation by

$$\bar{\sigma}_j = \frac{\sigma_j}{\sqrt{N(N-1)}}$$

where σ_j^2 is the variance of all the solution residuals containing a_j; however, because each observation links two stations, this estimate necessarily contains residuals due to other stations, and thus can only be an approximation. Another means of estimating the error of individual time-terms is by considering the diagonals of the inverted matrix [A], which contain the inverse weights of the unknowns; however, this assumes that all the observations have the same weight which

is clearly not the case where the data from some stations will obviously be better than others.

Assuming that all the solution residuals are due to uncertainties in the solution velocity, Willmore and Bancroft (1960) derive

$$\sigma\left(\frac{1}{V}\right)^2 = \frac{\sigma_s^2}{\sum_{ij} d_{ij}\, \gamma_{ij}}$$

from which the standard solution velocity variance σ_v^2 can be estimated.

2.2.3 Refractor with a Vertical Velocity Gradient

Commonly the velocities of refractive media are not constant but vary with depth, z. The simplest function of this kind is the constant velocity gradient, g where

$$V(z) = V_o + gz \qquad (2.11)$$

As shown in BOX 1, a velocity structure of this type results in a suite of circular raypaths the locus for the centres of which is a plane at a height V_o/g above the surface of the refractor. The distance the ray travels is dependent upon the angle at which the ray enters the medium, i_o, such that the smaller i_o the larger the radius of curvature of the raypath and the higher the velocity sampled.

A refinement to such a velocity structure can be considered by which the refractor velocity increases until it reaches a maximum, V_{max}. The distance at which V_{max} is sampled by a raypath, X_{max}, is

$$X_{max} = \frac{2}{g}\left(V_{max}^2 - V_o^2\right)^{\frac{1}{2}}$$

So that for $X_{ij} < X_{max}$, the travel time T_{ij} is given by Equation B(v) of BOX 1, while for $X_{ij} \geq X_{max}$,

$$T_{ij} = \frac{2}{g} \ln \left(\frac{V_{max} + (V_{max}^2 - V_o^2)^{\frac{1}{2}}}{V_o} \right) + \frac{(X_{ij} - X_{max})}{V_{max}} \qquad (2.12)$$

V_{max} constrains the solution velocity structure and may be set to a chosen value. Both the constrained and unconstrained (unbounded) vertical velocity gradients may be solved after the inversion of the observations matrix [A] and the best values for V_o and g found by minimising

$$\sum_{ij}^{L} \left[t_{ij} - T_{ij} - e_i + \frac{f_i}{V_{ij}} - e_j + \frac{f_j}{V_{ij}} \right]^2 \gamma_{ij}$$

whether T_{ij} is defined by Equation B(v) or 2.12.

The effect of a vertical velocity gradient is to cause the apparent station delay times to decrease with distance from the shot as the mean velocity of the raypath in the refractor increases. The time-term will also be affected as the angles of incidence steepen with distance from the shot.

2.3 The Effect of Structure on the Time-Term Solution

Several simulated data studies have tested the time-term technique and illustrated how a solution can be affected through its inherent approximations. Willmore and Bancroft (1960) graphically constructed raypaths through a domal refractor to illustrate the method of time-term analysis; Reiter (1970) considered the relationships between refractor topography and array configurations; Bamford (1971) investigated model topographies and velocity anisotropy in application to the 1969 south-west Britain Continental Margin experiment. Whitcombe and Maguire (1979) quantitatively studied the effects of dipping, anticlinal and synclinal refractors by ray-tracing 2D models, and more recently Whitcombe and Rogers (1981) considered the effects of refractor topography in producing velocity anisotropy in the time-term solution, using model studies incorporating 3D ray-tracing.

Principally these studies illustrate the dangers of failing to iterate the time-term solution; that is, assuming Δ_{ij} equals X_{ij} and proceeding no further. If the refractor topography has a wavelength greater than the scale of the survey there may be a systematic difference between Δ_{ij} and X_{ij}, and the solution time-terms and velocities will not be exact. Willmore and Bancroft (1960) use their model to show the significance of estimating Δ_{ij} values from the structure evident from the first solution; these were employed as a first iteration of the solution, which yielded a much closer fit to the true refractor.

Considering the first-time-term solutions for simple two-dimensional structures, Whitcombe and Maguire (1979) surmised that:

a) for a re ractor dipping at an angle α, the solution velocity will be $V_r/\cos\alpha$ (i.e., greater than the true refractor velocity, V_r, by $V_r\{1/\cos\alpha-1\}$); this is because Δ_{ij} is equal to $X_{ij}\cos\alpha$. The effect is minimal for a refractor dipping at less than ten degrees, but may induce a solution velocity error of greater than 6 per cent for dips of twenty degrees or more.

b) the solution velocity for anticlinal refractors is always greater than the true refractor velocity, and the solution portrays a radius of curvature larger than the true. These differences are because Δ_{ij} is always less than X_{ij} (see Fig. 2.4). For example, for an anticline of radius of curvature 30km and overburden, refractor velocities of 3.5,6km/s, the solution gave a radius of 44km and a velocity of 6.404km/s, which was in error by 6 per cent.

c) time-term solutions for synclinal refractors yielded velocities lower than the true refractor velocity, and portrayed radii of curvature less than the true. The reason is the converse of the anticlinal case: that is, Δ_{ij} is always greater than X_{ij}. For the same model as above, the solution yielded a radius of curvature of about 21km and a velocity of 4.86km/s, which was in error by 19 per cent.

These ideas were extended by Whitcombe and Rogers (1981) to three-dimensional structures and their generation of apparent velocity anisotropy in the non-iterated time-term solution. For an anticlinal refractor, for example (Fig. 2.5a), the maximum solution velocity will be perpendicular to the strike, while along strike the refractor is horizontal and the solution velocity will be exact. The model of Fig. 2.5a was ray-traced by a 3D 'shooting' ray method and the travel times were best fitted by a time-term solution which incorporated a 4.4 per cent velocity anisotropy, while the isotropic velocity solution yielded a somewhat distorted picture of the basement (Fig. 2.5b). The converse effect will result for synclinal topography, so the most pronounced solution anisotropy will occur for a saddle-shaped refractor (Fig. 2.6). In general, any azimuthally dependent refractor topography will generate false anisotropy.

Distrust of velocities defined by the time-term method dates back to Willmore and Bancroft (1960) who preferred to assume a plausible refractor velocity to solve time-terms. The effect of dipping interfaces on the observed refractor velocity have been discussed by Sjögren (1979) and Palmer (1974), both of whom suggest that the apparent velocity must be corrected once the refractor structure is known; that is, the solution must be iterated.

The effect of iterating a time-term solution was illustrated by Bamford (1973) who re-interpreted the non-iterated solution by Berry and West (1966) of data from the 1963 Lake Superior experiment. Similarly, the apparent anisotopy of the anticlinal model of Fig. 2.5a almost totally disappears after one iteration, by estimating Δ_{ij} from the solution model.

2.3.1 Anticlinal Refractors - Model Studies

As it is possible for an anticlinal refractor to induce a velocity higher than the true velocity into the non-iterated

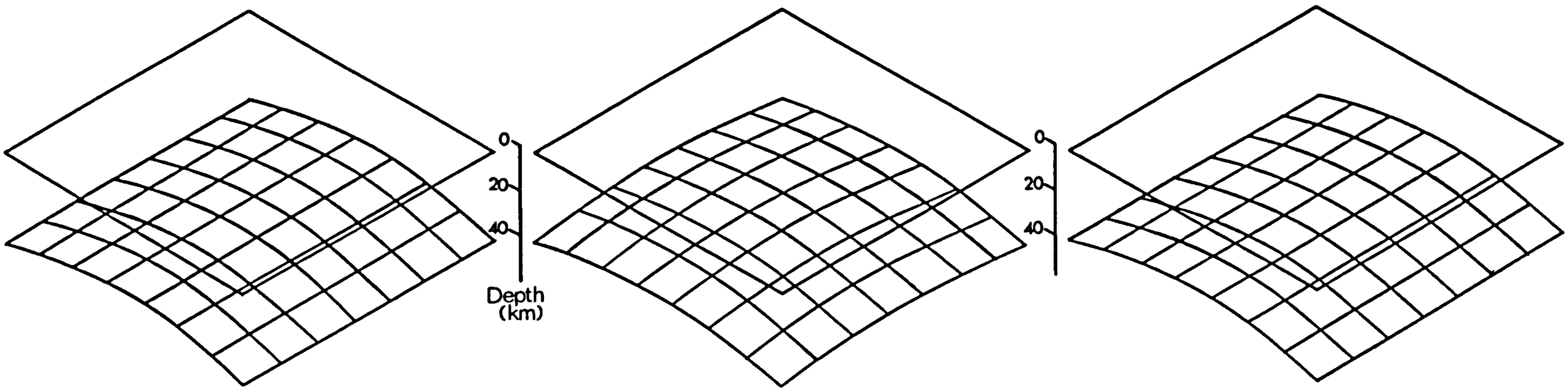

STARTING MODEL
Isotropic crust
Isotropic upper mantle
(a)

ISOTROPIC SOLUTION
(F ratio = 10·23)
(b)

ANISOTROPIC SOLUTION
(F ratio = 1·06)
(c)

FIG 2-5

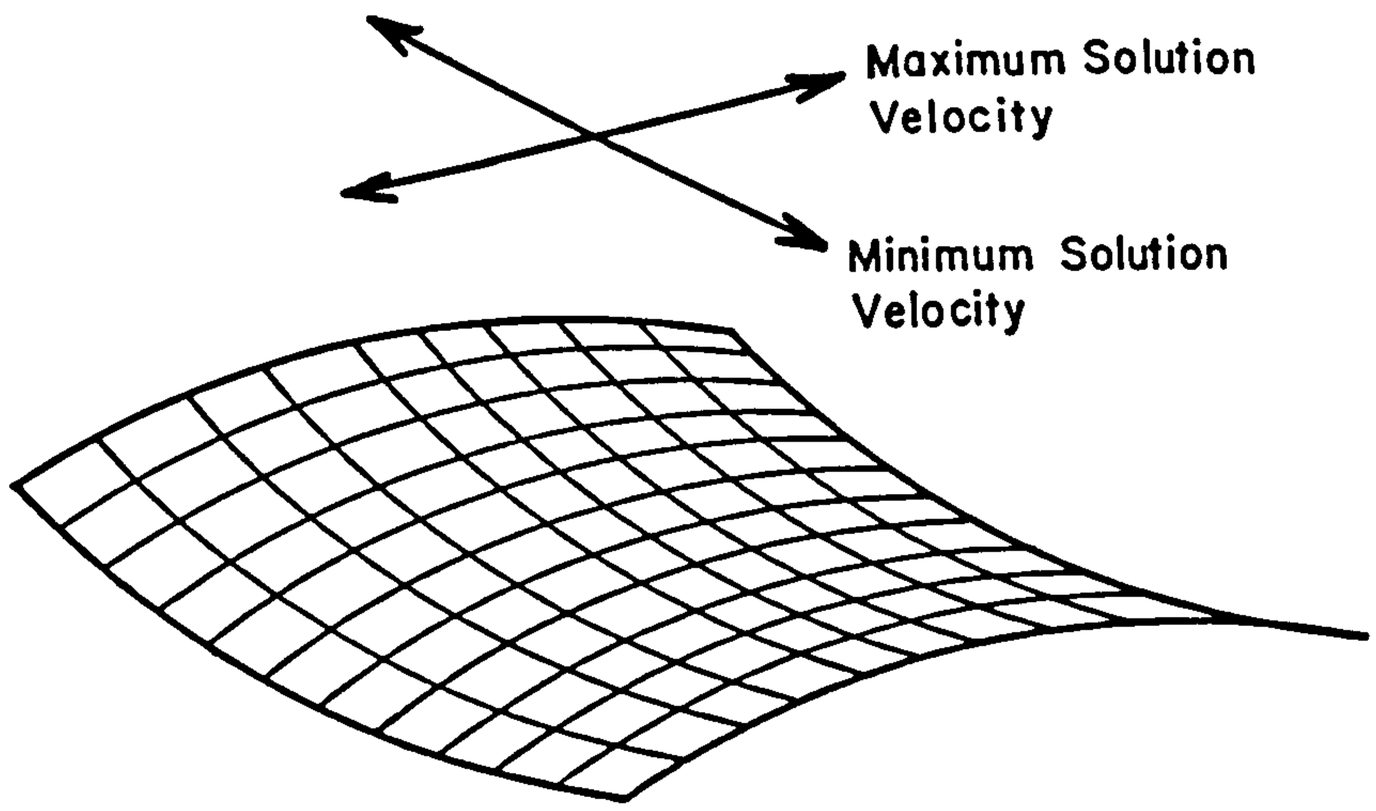

FIG 2-6 Saddle-shaped refractor

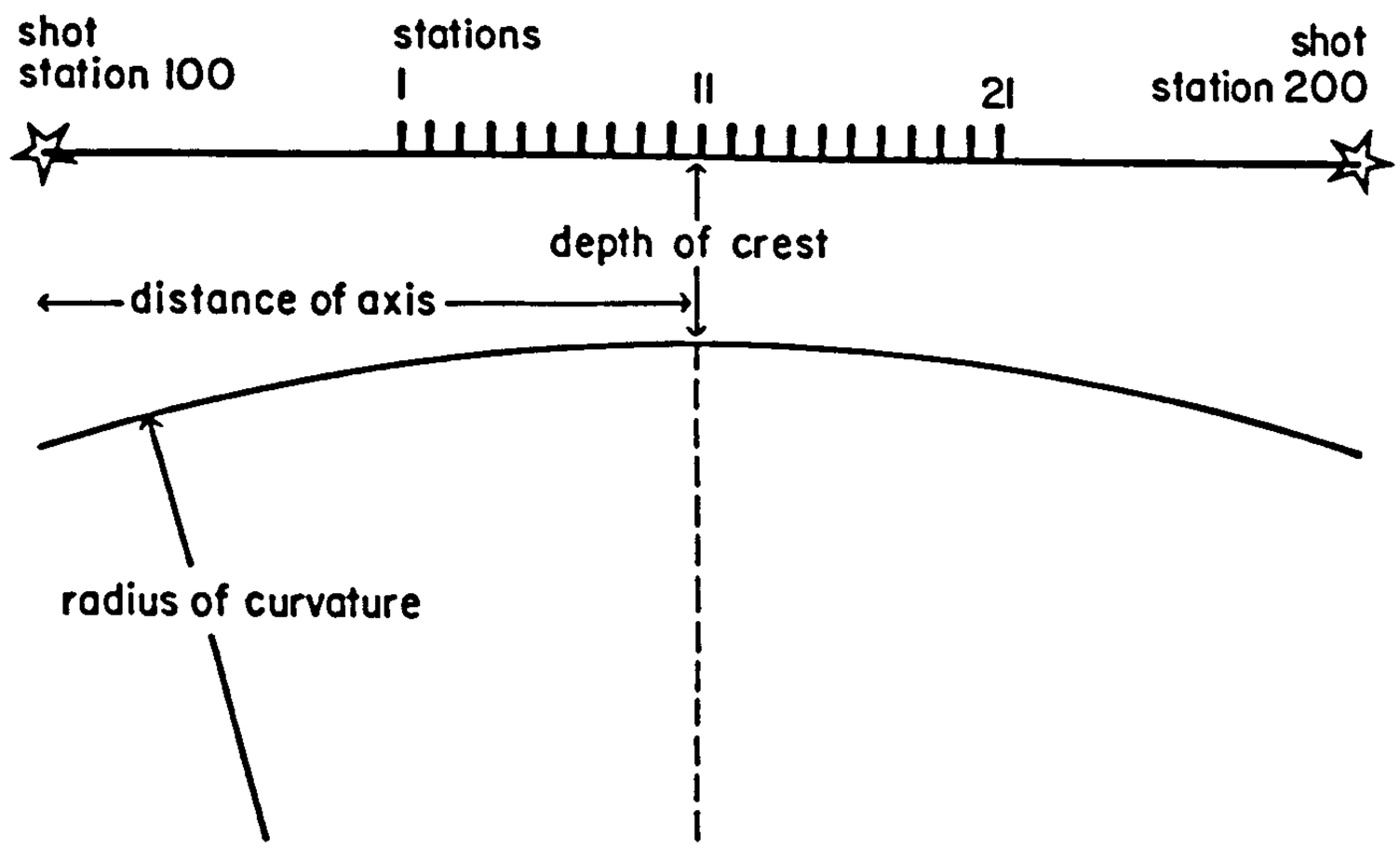

FIG 2-7 Model anticline

time-term solution, it may also be possible for a false velocity gradient to be observed. This is so because not only does the difference between X_{ij} and Δ_{ij} increase with distance, but $d(X_{ij}-\Delta_{ij})/dx$ also increases with distance. It is therefore important to be able to distinguish between the effect of a structurally induced velocity gradient in the solution, and the presence of a real velocity gradient in the basement refractor: for example, the Derbyshire Dome is broadly anticlinal, but may be underlain by granodiorites.

To illustrate the effect, four anticlinal refractor models have been ray-traced and the travel times analysed using the computer programmes TTINV and TTERM described in Section 6.2. All the models use an overburden velocity, V_o, of 3.5km/s and a refractor velocity, V_r, of 6.0km/s; these models are illustrated by the schema of Fig. 2.7, and comprise:

	Depth of overburden at crest (km)	Radius of Curvature (km)	Distance of axis from shot (km)	Distance of station 1 from shot (km)	spacing (km)
MODEL 1	.5	15	10	5	.5
MODEL 2	.5	20	15	10	.5
MODEL 3	1	30	15	5	1
MODEL 4	1	40	20	10	1

All the models are such that station 11 lies at the axis of the anticline, and ten stations lie on each limb. Since part of the exercise was to iterate back to the starting models as accurately as possible, no observational errors were synthesised.

Raytracing

There are two sets of refracted raypaths through an anticlinal structure: those which are refracted into the anticline, and define a chord across the feature (the non-critical raypath), and those which may be critically refracted along the surface of the anticline (the critical raypath). Both are considered here.

1) The non-critical ray (see Fig. 2.8a)

The required raypath linking shot $[X_i,Y_i]$ and station $[X_j,Y_j]$ is SPUG. Since it is difficult to determine this path analytically, an iterative 'shooting' process has been adopted by minimising the end point error $(X'-X_j)^2$ by varying the position of point P on the anticline surface, rather than varying the starting angle as used by most ray-tracers. The algorithm is given in BOX 2, and the NAG routine E04JAF was used to minimise the end point error. No travel was given where X' differed from X_j by more than 1m; in fact, successful rays were traced to an accuracy better than 5mm, which is negligible. Unsuccessfully traced rays were always for a near critical angle of incidence, for which the solutions failed to converge. The travel time is given by

$$T_{ij} = (SP + UG)/V_o \quad + \quad D/V_r \qquad (2.13)$$

2) The Critically Refracted Ray (see Fig. 2.8b)

Again, the required raypath linking shot $[X_i,Y_i]$ and station $[X_j, X_j]$ is SPUG, only the ray segment PU is an arc, and not a chord. In this case the ray segments linking shot and station with the refractor surface may be determined independently because the angle of incidence is constant; the shot ray segment need only be defined once. Again, the raypath was determined by varying point P on the anticline surface, using E04JAF to minimise the end point error. The algorithm is given in BOX 3. The total travel time is given by equation 2.13, with arc PU substituted for chord D.

Each ray was generated to an accuracy of ±5mm; if the solution for X_j was such that $U>X_j$, then no solution time was given.

Model Travel Times - Discussion

The travel times and solution details for all four models are given in Tables 2-1 to 2-4. One obvious difference between the raypaths considered is that the critically refracted rays always arrive later than those non-critically refracted

(a)

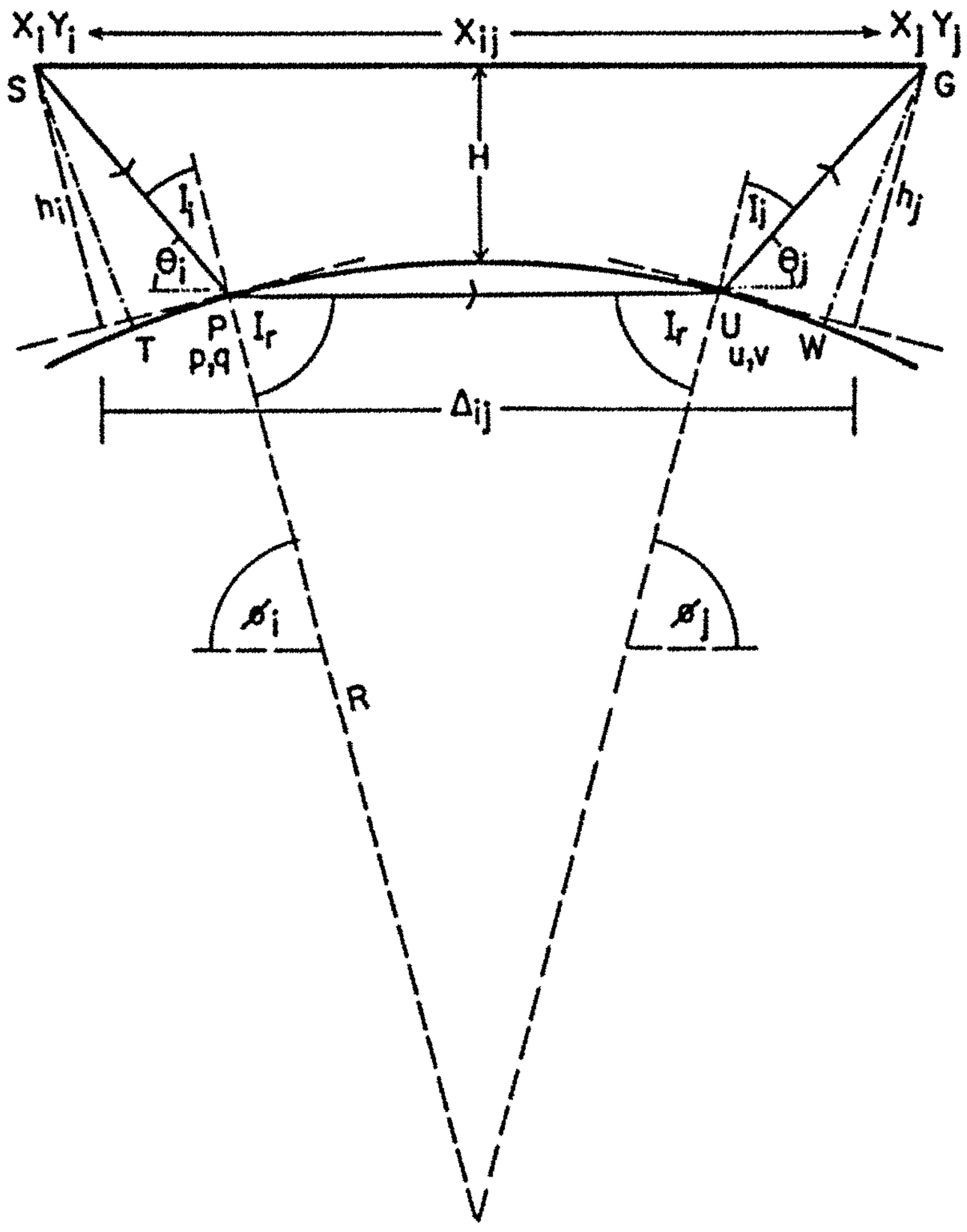
$X_i Y_i$
X_{ij}
$X_j Y_j$
S
G
H
h_i
h_j
I_i
I_j
θ_i
θ_j
T
P
p,q
I_r
I_r
U
u,v
W
Δ_{ij}
ϕ_i
ϕ_j
R

(b)

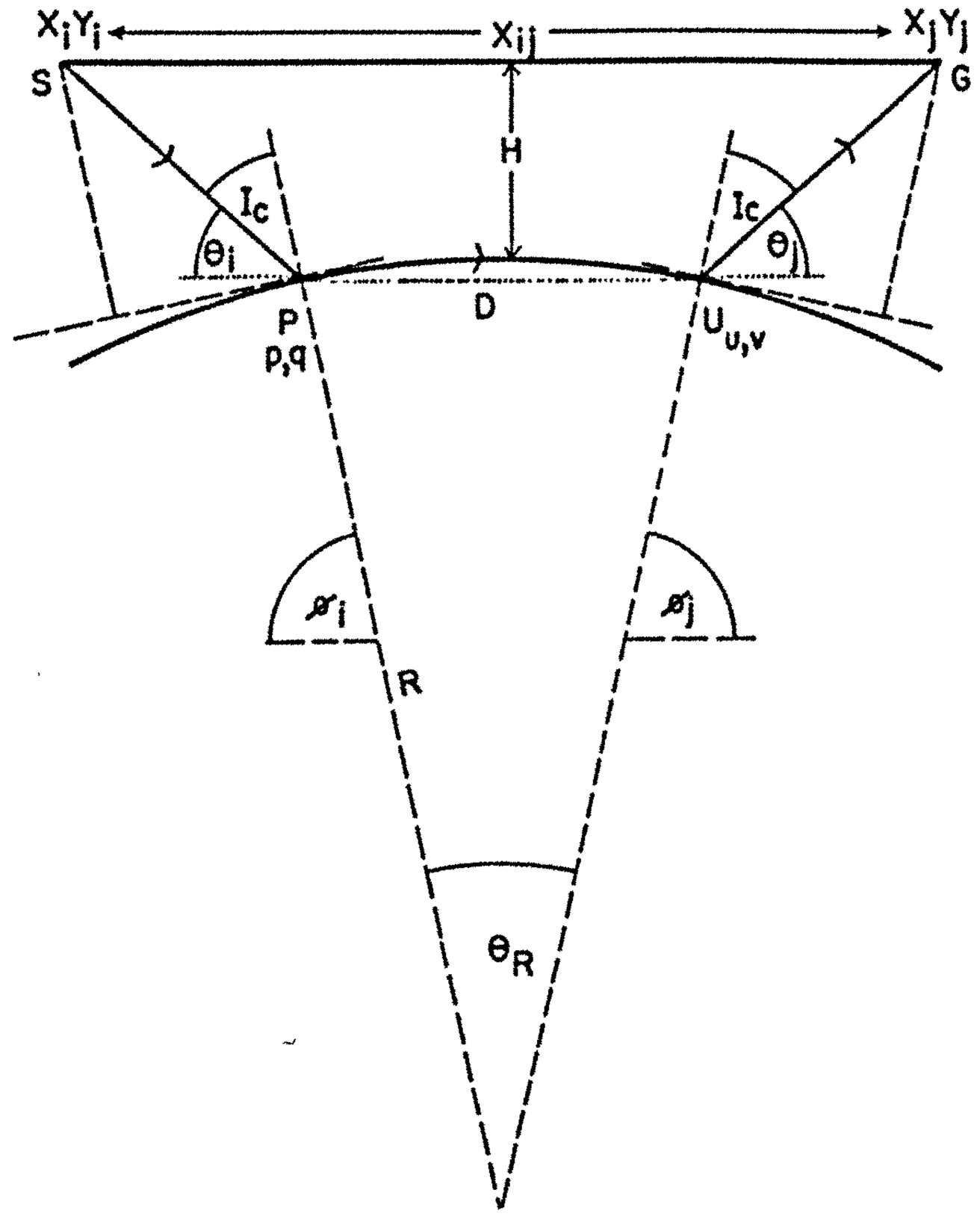
$X_i Y_i$
X_{ij}
$X_j Y_j$
S
G
H
I_c
I_c
θ_i
θ_j
P
p,q
D
$U_{u,v}$
ϕ_i
ϕ_j
R
θ_R

FIG 2-8

Table 2-I

Non-Critically Refracted Ray

Table of Times, Distances and Velocities

(For detailed explanation of column headings see Text)

MODEL 1 -- RADIUS OF CURVATURE 15KM

St	Xij	True Time	TTi (Oi)	TTj (Oi)	Δ ij (Oi)	T-T (Oi)	Xij-Δ ij	Vap Xij/TT	Vit Dj/TT	Dtt	Xj-Dtt
1	0.0000	0.0000	0.0000	0.0000	0.0000	0.0000	0.0000	0.0000	0.0000	0.0000	0.0000
2	0.0000	0.0000	0.0000	0.0000	0.0000	0.0000	0.0000	0.0000	0.0000	0.0000	0.0000
3	0.0000	0.0000	0.0000	0.0000	0.0000	0.0000	0.0000	0.0000	0.0000	0.0000	0.0000
4	0.0000	0.0000	0.0000	0.0000	0.0000	0.0000	0.0000	0.0000	0.0000	0.0000	0.0000
5	0.0000	0.0000	0.0000	0.0000	0.0000	0.0000	0.0000	0.0000	0.0000	0.0000	0.0000
6	7.5000	2.0324	0.7683	0.1614	6.6204	2.0331	0.8796	6.8015	6.0038	6.6694	0.8306
7	8.0000	2.0936	0.7694	0.1452	7.0787	2.0944	0.9213	6.7859	6.0045	7.1415	0.8585
8	8.5000	2.1589	0.7707	0.1325	7.5402	2.1600	0.9598	6.7695	6.0051	7.6181	0.8819
9	9.0000	2.2283	0.7721	0.1235	8.0034	2.2295	0.9966	6.7534	6.0056	8.0980	0.9020
10	9.5000	2.3016	0.7737	0.1181	8.4673	2.3030	1.0327	6.7386	6.0061	8.5798	0.9202
11	10.0000	2.3786	0.7753	0.1165	8.9306	2.3802	1.0694	6.7257	6.0064	9.0624	0.9376
12	10.5000	2.4592	0.7770	0.1185	9.3921	2.4605	1.1079	6.7151	6.0066	9.5447	0.9553
13	11.0000	2.5431	0.7788	0.1244	9.8509	2.5449	1.1491	6.7073	6.0066	10.0256	0.9744
14	11.5000	2.6303	0.7806	0.1340	10.3059	2.6322	1.1941	6.7025	6.0066	10.5044	0.9956
15	12.0000	2.7206	0.7825	0.1473	10.7564	2.7225	1.2436	6.7008	6.0064	10.9801	1.0199
16	12.5000	2.8137	0.7844	0.1643	11.2017	2.8156	1.2983	6.7023	6.0061	11.4523	1.0477
17	13.0000	2.9096	0.7863	0.1850	11.6410	2.9114	1.3590	6.7069	6.0058	11.9203	1.0797
18	13.5000	3.0080	0.7883	0.2092	12.0738	3.0098	1.4262	6.7147	6.0053	12.3839	1.1161
19	14.0000	3.1089	0.7902	0.2370	12.4998	3.1106	1.5002	6.7255	6.0048	12.8428	1.1572
20	14.5000	3.2120	0.7922	0.2683	12.9186	3.2136	1.5814	6.7393	6.0043	13.2968	1.2032
21	15.0000	3.3173	0.7942	0.3029	13.3300	3.3187	1.6700	6.7559	6.0037	13.7459	1.2541
200	20.0000	4.4622	0.8121	0.8121	17.0282	4.4622	2.9718	7.0471	6.0000	18.0125	1.9875

Table 2-I continued

Critically Refracted Ray

Table of Times and Distances

(For cetailed explanation of colusn headings see Text)

MODEL 1 -- RADIUS OF CURVATURE 15KM

St	Xij	Tdir	TT	TTi	TTj	Δcij	TTc(t-t)	Xij-Δcij	TTshot	TTst	TTmin
1	5.0000	1.4286	1.7940	0.7643	0.2927	4.4192	1.7936	0.5808	0.7997	0.2986	1.7487
2	5.5000	1.5714	1.8324	0.7643	0.2599	4.8442	1.8316	0.6558	0.7997	0.2646	1.7877
3	6.0000	1.7143	1.8758	0.7643	0.2302	5.2784	1.8743	0.7216	0.7997	0.2339	1.8312
4	6.5000	1.8571	1.9239	0.7643	0.2037	5.7209	1.9215	0.7791	0.7997	0.2066	1.8790
5	7.0000	2.0000	1.9767	0.7643	0.1805	6.1704	1.9732	0.8296	0.7997	0.1828	1.9311
6	7.5000	2.1429	2.0341	0.7643	0.1607	6.6257	2.0293	0.8743	0.7997	0.1625	1.9875
7	8.0000	2.2857	2.0961	0.7643	0.1444	7.0856	2.0896	0.9144	0.7997	0.1459	2.0480
8	8.5000	2.4286	2.1624	0.7643	0.1316	7.5488	2.1541	0.9512	0.7997	0.1328	2.1125
9	9.0000	2.5714	2.2330	0.7643	0.1224	8.0140	2.2224	0.9860	0.7997	0.1235	2.1809
10	9.5000	2.7143	2.3078	0.7643	0.1169	8.4800	2.2946	1.0200	0.7997	0.1179	2.2530
11	10.0000	2.8571	2.3865	0.7643	0.1151	8.9455	2.3703	1.0545	0.7997	0.1160	2.3286
12	10.5000	3.0000	2.4690	0.7643	0.1169	9.4096	2.4495	1.0904	0.7997	0.1179	2.4076
13	11.0000	3.1429	2.5552	0.7643	0.1224	9.8710	2.5319	1.1290	0.7997	0.1235	2.4898
14	11.5000	3.2857	2.6448	0.7643	0.1316	10.3285	2.6174	1.1711	0.7997	0.1328	2.5750
15	12.0000	3.4286	2.7377	0.7643	0.1444	10.7824	2.7058	1.2176	0.7997	0.1459	2.6630
16	12.5000	3.5714	2.8337	0.7643	0.1607	11.2309	2.7968	1.2691	0.7997	0.1625	2.7537
17	13.0000	3.7143	2.9326	0.7643	0.1805	11.6736	2.8904	1.3264	0.7997	0.1828	2.8467
18	13.5000	3.8571	3.0343	0.7643	0.2037	12.1102	2.9864	1.3898	0.7997	0.2066	2.9420
19	14.0000	4.0000	3.1385	0.7643	0.2302	12.5402	3.0846	1.4598	0.7997	0.2339	3.0392
20	14.5000	4.1429	3.2452	0.7643	0.2599	12.9635	3.1848	1.5365	0.7997	0.2646	3.1384
21	15.0000	4.2857	3.3542	0.7643	0.2927	13.3797	3.2870	1.6203	0.7997	0.2986	3.2392
200	20.0000	5.7143	4.5390	0.7643	0.7643	17.1682	4.3900	2.8318	0.7997	0.7997	4.3100

Table 2-2

Non-Critically Refracted Ray

Table of Times, Distances and Velocities

(For detailed explanation of column headings see Text)

MODEL 2 -- RADIUS OF CURVATURE 20KM

St	Xij	True Time	TTi (Oi)	TTj (Oi)	Δij (Oi)	T-T (Oi)	Xij-Δij	Vap Xij/TT	Vit Dj/TT	Dtt	Xj-Dtt
1	0.0000	0.0000	0.0000	0.0000	0.0000	0.0000	0.0000	0.0000	0.0000	0.0000	0.0000
2	0.0000	0.0000	0.0000	0.0000	0.0000	0.0000	0.0000	0.0000	0.0000	0.0000	0.0000
3	0.0000	0.0000	0.0000	0.0000	0.0000	0.0000	0.0000	0.0000	0.0000	0.0000	0.0000
4	0.0000	0.0000	0.0000	0.0000	0.0000	0.0000	0.0000	0.0000	0.0000	0.0000	0.0000
5	12.0000	3.1051	1.2011	0.1664	10.4379	3.1071	1.5621	6.9057	6.0068	10.5596	1.4404
6	12.5000	3.1681	1.2028	0.1513	10.8980	3.1703	1.6020	6.8905	6.0075	11.0397	1.4603
7	13.0000	3.2342	1.2046	0.1369	11.3599	3.2367	1.6401	6.8755	6.0081	11.5229	1.4771
8	13.5000	3.3033	1.2065	0.1292	11.8228	3.3061	1.6772	6.8611	6.0086	12.0083	1.4917
9	14.0000	3.3754	1.2085	0.1223	12.2860	3.3785	1.7140	6.8475	6.0091	12.4953	1.5047
10	14.5000	3.4503	1.2106	0.1183	12.7488	3.4536	1.7512	6.8350	6.0095	12.9831	1.5169
11	15.0000	3.5280	1.2128	0.1170	13.2106	3.5315	1.7894	6.8238	6.0098	13.4710	1.5290
12	15.5000	3.6263	1.2132	0.1187	13.6859	3.6101	1.8141	6.8190	6.0099	13.5627	1.5428
13	16.0000	3.6912	1.2173	0.1231	14.1285	3.6952	1.8715	6.8062	6.0101	14.4449	1.5551
14	16.5000	3.7766	1.2197	0.1304	14.5836	3.7807	1.9164	6.7999	6.0101	14.9296	1.5704
15	17.0000	3.8643	1.2221	0.1405	15.0353	3.8685	1.9647	6.7954	6.0101	15.4123	1.5877
16	17.5000	3.9544	1.2246	0.1535	15.4831	3.9586	2.0169	6.7928	6.0099	15.8925	1.6075
17	18.0000	4.0466	1.2271	0.1693	15.9268	4.0509	2.0732	6.7920	6.0097	16.3697	1.6303
18	18.5000	4.1409	1.2296	0.1875	16.3659	4.1452	2.1341	6.7930	6.0094	16.8438	1.6562
19	19.0000	4.2372	1.2321	0.2083	16.8001	4.2415	2.1999	6.7959	6.0091	17.3145	1.6855
20	19.5000	4.3355	1.2346	0.2315	17.2291	4.3396	2.2709	6.8006	6.0086	17.7815	1.7185
21	20.0000	4.4356	1.2371	0.2603	17.6526	4.4396	2.3474	6.8071	6.0082	18.2448	1.7552
200	30.0000	6.7159	1.2822	1.2822	24.9096	6.7159	5.0904	7.2261	6.0000	26.8366	3.1634

Table 2-2continued

Critically Refracted Ray

Table of Times and Distances

(For detailed explanation of column headings see Text)

MODEL 2 -- RADIUS OF CURVATURE 20KM

St	Xij	Tdir	TT	TT1	TTj	Δcij	TTc(t-t)	Xij-Δcij	TTshot	TTst	TTmin
1	10.0000	2.8571	2.8872	1.1912	0.2521	8.6365	2.8827	1.3635	1.2536	0.2555	2.8089
2	10.5000	3.0000	2.9375	1.1912	0.2266	9.0838	2.9317	1.4162	1.2536	0.2293	2.8583
3	11.0000	3.1429	2.9914	1.1912	0.2035	9.5360	2.9840	1.4640	1.2536	0.2057	2.9109
4	11.5000	3.2857	3.0488	1.1912	0.1831	9.9924	3.0397	1.5076	1.2536	0.1849	2.9667
5	12.0000	3.4286	3.1096	1.1912	0.1652	10.4523	3.0985	1.5477	1.2536	0.1667	3.0256
6	12.5000	3.5714	3.1737	1.1912	0.1501	10.9149	3.1604	1.5851	1.2536	0.1513	3.0876
7	13.0000	3.7143	3.2412	1.1912	0.1376	11.3794	3.2253	1.6206	1.2536	0.1386	3.1525
8	13.5000	3.8571	3.3119	1.1912	0.1279	11.8452	3.2932	1.6548	1.2536	0.1288	3.2204
9	14.0000	4.0000	3.3858	1.1912	0.1209	12.3114	3.3640	1.6886	1.2536	0.1217	3.2910
10	14.5000	4.1429	3.4626	1.1912	0.1167	12.7775	3.4375	1.7225	1.2536	0.1174	3.3644
11	15.0000	4.2857	3.5425	1.1912	0.1153	13.2427	3.5136	1.7573	1.2536	0.1160	3.4404
12	15.5000	4.4286	3.6252	1.1912	0.1167	13.7064	3.5923	1.7936	1.2536	0.1174	3.5189
13	16.0000	4.5714	3.7107	1.1912	0.1209	14.1675	3.6734	1.8321	1.2536	0.1217	3.5999
14	16.5000	4.7143	3.7989	1.1912	0.1279	14.6268	3.7568	1.8732	1.2536	0.1288	3.6831
15	17.0000	4.8571	3.8896	1.1912	0.1376	15.0825	3.8425	1.9175	1.2536	0.1386	3.7686
16	17.5000	5.0000	3.9827	1.1912	0.1501	15.5346	3.9303	1.9654	1.2536	0.1513	3.8561
17	18.0000	5.1429	4.0782	1.1912	0.1652	15.9826	4.0202	2.0174	1.2536	0.1667	3.9456
18	18.5000	5.2857	4.1761	1.1912	0.1831	16.4262	4.1119	2.0738	1.2536	0.1849	4.0370
19	19.0000	5.4286	4.2761	1.1912	0.2035	16.8651	4.2056	2.1349	1.2536	0.2057	4.1301
20	19.5000	5.5714	4.3781	1.1912	0.2266	17.2990	4.3009	2.2010	1.2536	0.2293	4.2249
21	20.0000	5.7143	4.4821	1.1912	0.2521	17.7277	4.3979	2.2723	1.2536	0.2555	4.3213
200	30.0000	8.5714	6.8515	1.1912	1.1512	25.2045	6.5831	4.7955	1.2536	1.2536	6.4439

Table 2-3

Non-Critically Refracted Ray

Table of Times, Distances and Velocities

(For detailed explanation of column headings see Text)

MODEL 3 -- RADIUS OF CURVATURE 30KM

St	Xij	True Time	TTi (Oi)	TTj (Oi)	Δij (Oi)	T-T (Oi)	Xij-Δ ij	Vap Xij/TT	Vit Dj/TT	Dtt	Xj-Dtt
1	0.0000	0.0000	0.0000	0.0000	0.0000	0.0000	0.0000	0.0000	0.0000	0.0000	0.0000
2	0.0000	0.0000	0.0000	0.0000	0.0000	0.0000	0.0000	0.0000	0.0000	0.0000	0.0000
3	0.0000	0.0000	0.0000	0.0000	0.0000	0.0000	0.0000	0.0000	0.0000	0.0000	0.0000
4	0.0000	0.0000	0.0000	0.0000	0.0000	0.0000	0.0000	0.0000	0.0000	0.0000	0.0000
5	9.0000	2.7305	0.9992	0.3614	8.2212	2.7308	0.7788	6.5692	6.0008	8.2390	0.7610
6	10.0000	2.8450	1.0000	0.3220	9.1397	2.8453	0.8603	6.5660	6.0011	9.1675	0.8325
7	11.0000	2.9681	1.0010	0.2856	10.0682	2.9686	0.9318	6.5569	6.0015	10.1079	0.8921
8	12.0000	3.0998	1.0021	0.2642	11.0041	3.1004	0.9959	6.5450	6.0018	11.0576	0.9424
9	13.0000	3.2397	1.0034	0.2461	11.9449	3.2404	1.0551	6.5322	6.0021	12.0141	0.9859
10	14.0000	3.3874	1.0049	0.2353	12.8882	3.3882	1.1118	6.5201	6.0023	12.9748	1.0252
11	15.0000	3.5427	1.0065	0.2319	13.8315	3.5436	1.1685	6.5095	6.0024	13.9374	1.0626
12	16.0000	3.7052	1.0082	0.2360	14.7725	3.7063	1.2275	6.5013	6.0025	14.8997	1.1003
13	17.0000	3.8746	1.0100	0.2475	15.7092	3.8757	1.2908	6.4957	6.0025	15.8597	1.1403
14	18.0000	4.0505	1.0118	0.2665	16.6396	4.0516	1.3604	6.4932	6.0024	16.8156	1.1844
15	19.0000	4.2326	1.0138	0.2929	17.5619	4.2337	1.4381	6.4938	6.0023	17.7661	1.2339
16	20.0000	4.4205	1.0158	0.3266	18.4746	4.4215	1.5254	6.4977	6.0021	18.7097	1.2903
17	21.0000	4.6139	1.0179	0.3676	19.3764	4.6145	1.6236	6.5048	6.0019	19.6455	1.3545
18	22.0000	4.8124	1.0200	0.4157	20.2662	4.8133	1.7338	6.5151	6.0016	20.5727	1.4273
19	23.0000	5.0159	1.0221	0.4708	21.1431	5.0167	1.8569	6.5284	6.0013	21.4908	1.5092
20	24.0000	5.2239	1.0242	0.5327	22.0063	5.2245	1.9937	6.5447	6.0011	22.3995	1.6005
21	25.0000	5.4362	1.0263	0.6012	22.8553	5.4367	2.1447	6.5639	6.0008	23.2987	1.7013
200	30.0000	6.5531	1.0366	1.0366	26.8795	6.5531	3.1205	6.6966	6.0000	27.6591	2.3409

Table 2-3 continued

Critically Refracted Ray

Table of Times and Distances

(For detailed explanation of column headings see Text)

MODEL 3 -- RADIUS OF CURVATURE 30KM

St	Xij	Tdir	TT	TTi	TTj	Δcij	TTc(t-t)	Xij-Δcij	TTshot	TTst	TTmin
1	5.0000	1.4286	0.0000	0.9978	0.0000	0.0000	0.0000	0.0000	1.0300	0.0000	0.0000
2	6.0000	1.7143	2.4427	0.9978	0.5198	5.5501	2.4426	0.4499	1.0300	0.5291	2.3987
3	7.0000	2.0000	2.5293	0.9978	0.4604	6.4244	2.5289	0.5756	1.0300	0.4678	2.4867
4	8.0000	2.2857	2.6255	0.9978	0.4074	7.3161	2.6245	0.6839	1.0300	0.4132	2.5836
5	9.0000	2.5714	2.7312	0.9978	0.3610	8.2227	2.7292	0.7773	1.0300	0.3656	2.6893
6	10.0000	2.8571	2.8460	0.9978	0.3214	9.1420	2.8429	0.8580	1.0300	0.3250	2.8037
7	11.0000	3.1429	2.9699	0.9978	0.2887	10.0715	2.9651	0.9285	1.0300	0.2917	2.9264
8	12.0000	3.4286	3.1026	0.9978	0.2632	11.0086	3.0958	0.9914	1.0300	0.2657	3.0574
9	13.0000	3.7143	3.2439	0.9978	0.2449	11.9508	3.2345	1.0492	1.0300	0.2470	3.1962
10	14.0000	4.0000	3.3934	0.9978	0.2338	12.8956	3.3809	1.1044	1.0300	0.2358	3.3426
11	15.0000	4.2857	3.5508	0.9978	0.2302	13.8406	3.5347	1.1594	1.0300	0.2321	3.4963
12	16.0000	4.5714	3.7159	0.9978	0.2338	14.7836	3.6956	1.2164	1.0300	0.2358	3.6569
13	17.0000	4.8571	3.8882	0.9978	0.2449	15.7223	3.8631	1.2777	1.0300	0.2470	3.8241
14	18.0000	5.1429	4.0674	0.9978	0.2632	16.6550	4.0368	1.3450	1.0300	0.2657	3.9973
15	19.0000	5.4286	4.2532	0.9978	0.2887	17.5795	4.2165	1.4201	1.0300	0.2917	4.1764
16	20.0000	5.7143	4.4451	0.9978	0.3214	18.4954	4.4018	1.5046	1.0300	0.3250	4.3607
17	21.0000	6.0000	4.6430	0.9978	0.3610	19.4004	4.5922	1.5996	1.0300	0.3656	4.5500
18	22.0000	6.2857	4.8463	0.9978	0.4074	20.2937	4.7875	1.7063	1.0300	0.4132	4.7438
19	23.0000	6.5714	5.0545	0.9978	0.4604	21.1746	4.9873	1.8254	1.0300	0.4678	4.9418
20	24.0000	6.8571	5.2683	0.9978	0.5198	22.0425	5.1914	1.9575	1.0300	0.5291	5.1436
21	25.0000	7.1429	5.4862	0.9978	0.5854	22.8969	5.3994	2.1031	1.0300	0.5971	5.3489
200	30.0000	8.5714	6.6337	0.9978	0.9978	26.9637	6.4895	3.0363	1.0300	1.0300	6.4156

Table 2-4

Non-Critically Refracted Ray

Table of Times, Distances and Velocities

(For detailed explanation of column headings see Text)

MODEL 4 -- RADIUS OF CURVATURE 40KM

St	Xij	True Time	TTi (0i)	TTj (0i)	Δ ij (0i)	T-T (0i)	Xij-Δ ij	Vap Xij/TT	Vit Dj/TT	Dtt	Xj-Dtt
1	0.0000	0.0000	0.0000	0.0000	0.0000	0.0000	0.0000	0.0000	0.0000	0.0000	0.0000
2	11.0000	3.3931	1.2661	0.4536	10.0415	3.3932	0.9585	6.5734	6.0007	10.0591	0.9409
3	12.0000	3.5004	1.2667	0.4077	10.9578	3.5007	1.0422	6.5717	6.0009	10.9837	1.0163
4	13.0000	3.6146	1.2675	0.3669	11.8833	3.6150	1.1167	6.5651	6.0012	11.9191	1.0809
5	14.0000	3.7354	1.2685	0.3314	12.8169	3.7360	1.1831	6.5555	6.0015	12.8638	1.1362
6	15.0000	3.8628	1.2695	0.3012	13.7569	3.8635	1.2431	6.5441	6.0018	13.8164	1.1836
7	16.0000	3.9965	1.2707	0.2764	14.7019	3.9974	1.2981	6.5319	6.0020	14.7751	1.2249
8	17.0000	4.1365	1.2720	0.2570	15.6504	4.1374	1.3496	6.5198	6.0022	15.7387	1.2613
9	18.0000	4.2824	1.2734	0.2433	16.6011	4.2835	1.3989	6.5082	6.0024	16.7056	1.2944
10	19.0000	4.4341	1.2748	0.2351	17.5524	4.4353	1.4476	6.4976	6.0025	17.6745	1.3255
11	20.0000	4.5914	1.2764	0.2325	18.5031	4.5928	1.4969	6.4883	6.0026	18.6440	1.3560
12	21.0000	4.7542	1.2781	0.2356	19.4517	4.7556	1.5483	6.4805	6.0027	19.6129	1.3871
13	22.0000	4.9222	1.2798	0.2444	20.3972	4.9237	1.6028	6.4744	6.0027	20.5801	1.4199
14	23.0000	5.0952	1.2816	0.2588	21.3382	5.0967	1.6618	6.4702	6.0027	21.5444	1.4556
15	24.0000	5.2730	1.2835	0.2788	22.2738	5.2746	1.7262	6.4678	6.0026	22.5050	1.4950
16	25.0000	5.4554	1.2854	0.3045	23.2030	5.4570	1.7970	6.4674	6.0025	23.4611	1.5389
17	26.0000	5.6423	1.2873	0.3358	24.1248	5.6439	1.8752	6.4689	6.0024	24.4118	1.5882
18	27.0000	5.8334	1.2893	0.3726	25.0386	5.8349	1.9614	6.4724	6.0022	25.3567	1.6433
19	28.0000	6.0286	1.2913	0.4148	25.9435	6.0300	2.0565	6.4778	6.0020	26.2951	1.7049
20	29.0000	6.2276	1.2933	0.4625	26.8390	6.2290	2.1610	6.4850	6.0018	27.2268	1.7732
21	30.0000	6.4304	1.2953	0.5155	27.7245	6.4316	2.2755	6.4941	6.0016	28.1513	1.8487
200	40.0000	8.6263	1.3153	1.3153	35.9734	8.6263	4.0266	6.6716	6.0000	37.0026	2.9974

Table 2-4 continued

Critically Refracted Ray

Table of Times and Distances

(For detailed explanation of column headings see Text)

MODEL 4 -- RADIUS OF CURVATURE 40KM

St	Xij	Tdir	TT	TTi	TTj	Δcij	TTc(t-t)	Xij-Δcij	TTshot	TTst	TTmin
1	10.0000	2.8571	3.2925	1.2647	0.5043	9.1370	3.2918	0.8630	1.3037	0.5110	3.2427
2	11.0000	3.1429	3.3935	1.2647	0.4532	10.0425	3.3917	0.9571	1.3037	0.4586	3.3437
3	12.0000	3.4286	3.5013	1.2647	0.4071	10.9598	3.4984	1.0402	1.3037	0.4115	3.4513
4	13.0000	3.7143	3.6160	1.2647	0.3662	11.8862	3.6119	1.1138	1.3037	0.3697	3.5654
5	14.0000	4.0000	3.7376	1.2647	0.3305	12.8206	3.7320	1.1794	1.3037	0.3334	3.6859
6	15.0000	4.2857	3.8660	1.2647	0.3001	13.7616	3.8584	1.2384	1.3037	0.3026	3.8127
7	16.0000	4.5714	4.0009	1.2647	0.2752	14.7078	3.9912	1.2922	1.3037	0.2772	3.9457
8	17.0000	4.8571	4.1423	1.2647	0.2557	15.6576	4.1300	1.3424	1.3037	0.2575	4.0846
9	18.0000	5.1429	4.2900	1.2647	0.2418	16.6097	4.2748	1.3903	1.3037	0.2434	4.2294
10	19.0000	5.4286	4.4438	1.2647	0.2334	17.5625	4.4252	1.4375	1.3037	0.2349	4.3797
11	20.0000	5.7143	4.6035	1.2647	0.2306	18.5148	4.5811	1.4852	1.3037	0.2321	4.5355
12	21.0000	6.0000	4.7689	1.2647	0.2334	19.4652	4.7423	1.5348	1.3037	0.2349	4.6965
13	22.0000	6.2857	4.9399	1.2647	0.2418	20.4125	4.9086	1.5875	1.3037	0.2434	4.8625
14	23.0000	6.5714	5.1162	1.2647	0.2557	21.3555	5.0797	1.6445	1.3037	0.2575	5.0333
15	24.0000	6.8571	5.2976	1.2647	0.2752	22.2933	5.2555	1.7067	1.3037	0.2772	5.2087
16	25.0000	7.1429	5.4840	1.2647	0.3001	23.2248	5.4356	1.7752	1.3037	0.3026	5.3883
17	26.0000	7.4286	5.6751	1.2647	0.3305	24.1491	5.6200	1.8509	1.3037	0.3334	5.5720
18	27.0000	7.7143	5.8707	1.2647	0.3662	25.0655	5.8085	1.9345	1.3037	0.3697	5.7596
19	28.0000	8.0000	6.0706	1.2647	0.4071	25.9733	6.0007	2.0267	1.3037	0.4115	5.9509
20	29.0000	8.2857	6.2747	1.2647	0.4532	26.8720	6.1965	2.1280	1.3037	0.4586	6.1455
21	30.0000	8.5714	6.4826	1.2647	0.5043	27.7611	6.3958	2.2389	1.3037	0.5110	6.3433
200	40.0000	11.4286	8.7395	1.2647	1.2647	36.0795	8.5427	3.9205	1.3037	1.3037	8.4531

(where successfully traced), and that the delay between the two arrivals increases with distance from the shotpoint. This is not surprising as the critically refracted rays have further to travel around the perimeter of the anticline, while the non-critically refracted rays take the shortest possible route across it. Since the non-critically refracted rays therefore constitute the first arrivals, their travel times will be used in the following time-term analysis.

The respective columns contain the following information:

St, X_{ij} — Station numbers and horizontal shot-station separation, as shown in Fig. 2.7. The values given for X_{ij} are those calculated as X'.

True Time, T_{dir}, TT — True time (non-critically refracted), T_{dir} (direct ray), and TT (critically refracted ray): calculated travel times through model. Values of zero indicate that no ray was traced for that station.

$TT_{i,j}(\theta_i)$ $TT_{i,j}(\theta_c)$ — Time-terms calculated from the perpendicular drops for each shot (i) and station (j) pair onto the tangent at the point of entry of the ray into the anticline. Note that for the non-critically refracted rays (θ_i) the shot time-terms gradually increase as the angle of incidence decreases, and that the station time-terms are larger on the opposing limb of the anticline. Predictably, the time-terms for the shot points (stations 100, 200) are equal as the path is symmetrical about the anticline axis. The critically refracted station time-terms are symmetrical about the anticline axis (at station 11), and are consistantly slightly smaller than the non-critically refracted time-terms, the shot time-term is constant for all raypaths.

$\Delta_{ij}(\theta_i)$ Δ_{cij} — The respective distances between the feet of the perpendular drops from shot and station. $\Delta_{ij}(\theta_i)$ for the non-critically refracted ray is slightly less than that for the critically refracted ray, by that the larger the angle of incidence the closer P to the anticline axis, and the more horizontal the tangent (cf. Figs. 2.8a and 2.8b).

$T-T(\theta_i)$
$TT_c(tt)$

The travel times reconstructed from the time-term approximation, for non-critical and critical ray-paths respectively. Note that for the non-critical case these values match the first arrivals almost exactly while the critical angle time-term travel times progressively under-estimate the true time.

$X_{ij}-\Delta_{ij}$

The differences between the perpendicular drop connections and the horizontal shot-station distances; those values for the non-critically refracted case have been plotted against X_{ij} in Fig. 2.9 for all four models. It is obvious from these plots that $X_{ij}-\Delta_{ij}$ is not linearly dependent upon distances from the shot (here plotted at the origin), but that the gradient of the curve increases away from the axis of the anticline. Thus if the shot were on one limb of the anticline, and all stations on the other, an apparent velocity gradient would be observed. Similarly a least-squares straight line could be drawn through the data to give an overestimated refractor velocity.

V_{ap}, V_{it}

For each connection, an estimate of the refractor velocity, V, can be made from the calculated travel time T_{ij} by rearranging Equation 2.2:

$$V_r = \frac{X}{(T_{ij} - TT_i - TT_j)} \qquad (2.14)$$

where TT_i, TT_j are the calculated time-terms. V_{ap} is derived by using X_{ij} for X, and V_{it} the iterated version by substituting Δ_{ij}. V_{ap} is predictably higher than the true refractor velocity, but note the apparent velocities decrease towards a mid-line minimum, offset away from the shot. (The degree of offset is dependent upon not only the depth of the refractor and the velocity contrast, but also increases with increasing distance of the shot). For similarly scaled models (1 and 3, 2 and 4), V_{ap} is smaller for larger radii of curvature, and, as expected, once iterated nearly all structural effects disappear.

FIG 2-9 X−Δ vs distance from shot

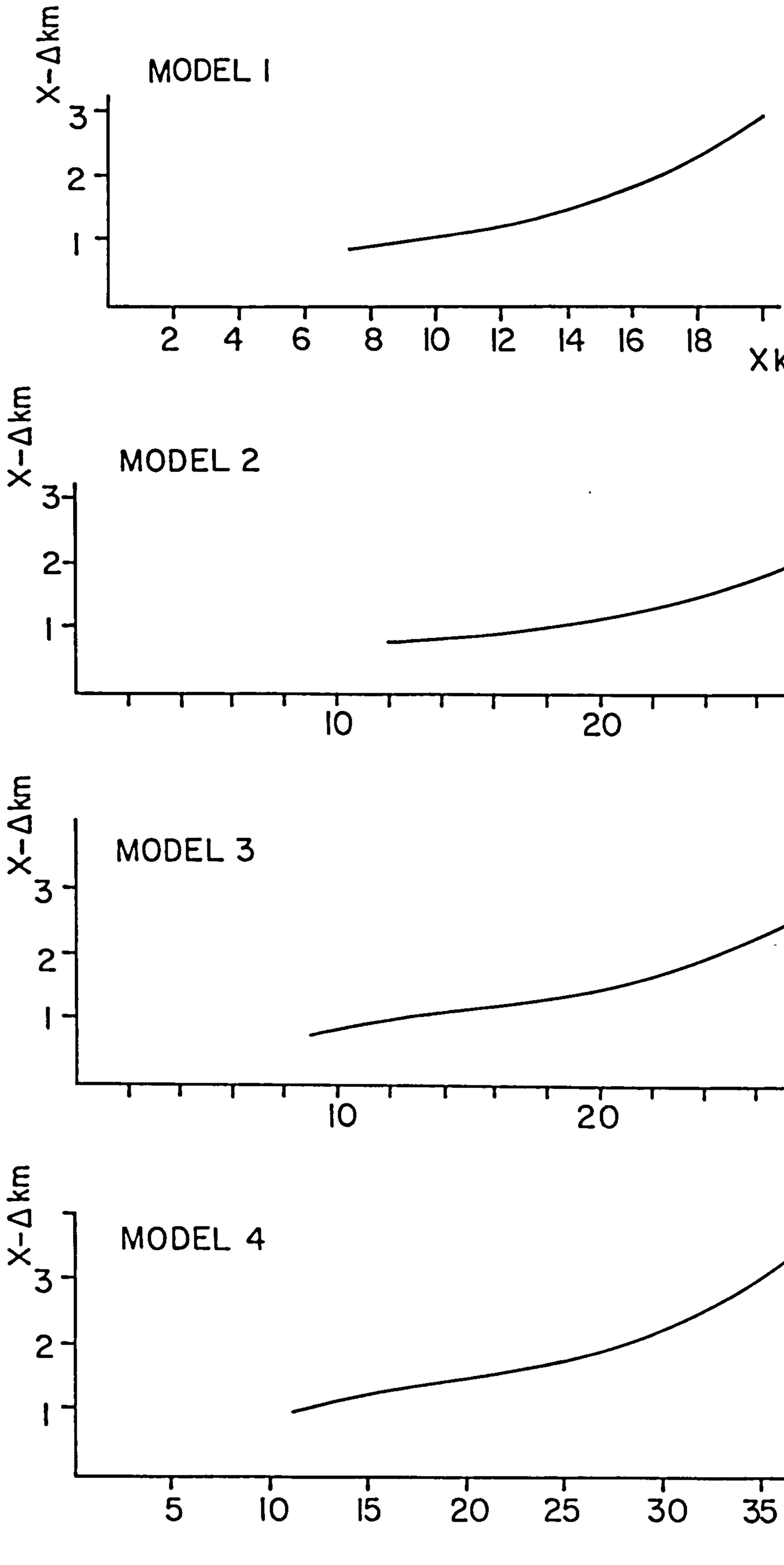

TT_{shot}, TT_{st}, TT_{min}, The time-term for each station calculated from the shortest distance between station and surface of the anticline, that is the tangential drops ST, GW in Fig. 2.8a. These constitute the 'absolute' time-terms as arcs of radius h_i, h_j will only touch the refractor for stations at the axis. However, the raypath SPUG cannot be approximated by STWG as the basic triangulation of the delay-time concept is violated, and thus it would be difficult to solve for the 'absolute' time-terms. To illustrate this, the travel-times TT_{min} are reconstituted from

$$TT_{min} = \frac{h_i \cos\theta_c}{V_o} + \frac{h_j \cos\theta_c}{V_o} + \frac{X'_{ij}}{V_r}$$

where h_i, h_j are the lengths of the perpendiculars to the refractor surface, and X'_{ij} the distance between their feet. The resultant travel times consistantly underestimate the true travel time, but are only slightly smaller than TT(t-t). However, it is doubted whether X'_{ij} could be reliably used as an iteration upon X_{ij}.

D_{tt}, $X_{ij}-D_{tt}$, see below

Solving Model Time-Terms

The non-critically refracted arrival times have been considered for two time-term solutions: one assuming a constant velocity refractor, and the other assuming an unconstrained linear vertical velocity gradient. Two computer programmes TTINV and TIMET were used in the analysis, the first of which inverts the observations matrix [A], and the second solves for the solution velocities and time-terms; the matrix inversion need only be executed once for both solutions (for a full description, see Section 6.2).

Since the method necessarily requires two shotpoints, the profiles have been 'reversed' by regenerating the travel times and reversing the station numbers. No profile contains non-critically refracted times at every station, so that some unreversed observations (asterisked) have been included in the analyses, without contaminating the results. The solutions are summarised in Tables 2-5 to 2-8.

Non-Iterated Solutions

The first two columns of each table list the mean time-term for each station pair symmetric about the anticline axis, for both the non-critical (θ_i) and critical (θ_c) cases. Note that the latter portray a minutely shallower and flatter anti-form. The shot time-terms for the non-critical cases have been taken from the shot-shot travel time, although the (smaller) mean shot time-term could equally have been used.

As expected from Whitcombe and Maguire (1979), the least-squares velocity solutions overestimate the true refractor velocity, an effect which decreases with increasing radius of curvature. The solution time-terms also imply refractors of greater radius of curvature than the starting models (see Fig. 2.10). However, on examination of the solution time-term residuals (columns 4 and 5 for differences with the non-critical and critical time-terms respectively), it appears that the solution topography is not circular as the model but that the implied radius of curvature increases with increasing distance from the axis. Thus the greatest distortion occurs at the ends of the profile where $X_{ij}-\Delta_{ij}$ is greatest: i.e., the shot-to-shot linkage.

As suggested by the non-linearity of the $X_{ij}-\Delta_{ij}$ curves of Fig. 2.9, the geometry of the anticline allows a substantial vertical velocity gradient to occur in the time-term solution where the analysis permits. Both the gradient and initial velocity, V_o, are greatest for the smaller radii of curvature. In contrast with the constant velocity solutions, the anticline radii here appear to have been accentuated (Fig. 2.10), and this effect increases for the longer wavelength models. The

Table 2-5

Time-Term Solutions Model 1

St	Time-Terms Calculated from Input Model (* unreversed)		Time-Terms from Non-Iterated Least-squares Velocity Solution			Time Terms from Non-Iterated Linear Vertical Velocity Gradient Solution		
	aj	ac	as	(as-aj)	(as-ac)	as	(as-aj)	(as-ac)
1	.303*	.293	.303*	0*	.01*	.215*	-.088*	-.078*
2	.268*	.26	.276*	.008*	.016*	.181*	-.087*	-.079*
3	.237*	.23	.251*	.014*	.021*	.150*	-.087*	-.08*
4	.209*	.204	.229*	.02*	.025*	.122*	-.087*	-.082*
5	.185*	.181	.209*	.024*	.028*	.097*	-.088*	-.084*
6	.163	.161	.192	.029	.031	.077	-.086	-.084
7	.146	.144	.176	.03	.032	.058	-.088	-.086
8	.133	.132	.164	.031	.032	.043	-.09	-.089
9	.124	.122	.155	.031	.033	.032	-.092	-.09
10	.118	.117	.149	.031	.032	.026	-.092	-.091
11	.117	.115	.148	.031	.033	.024	-.093	-.091
12	.118	.117	.149	.031	.032	.026	-.092	-.091
13	.124	.122	.155	.031	.033	.032	-.092	-.09
14	.133	.132	.164	.031	.032	.043	-.09	-.089
15	.146	.144	.176	.03	.032	.058	-.088	-.086
16	.163	.161	.192	.029	.031	.077	-.086	-.084
17	.185*	.181	.209*	.024*	.028*	.097*	-.088*	-.084*
18	.209*	.204	.229*	.02*	.025*	.122*	-.087*	-.082*
19	.237*	.23	.251*	.014*	.021*	.150*	-.087*	-.08*
20	.268*	.26	.276*	.008*	.016*	.181*	-.087*	-.079*
21	.303*	.293	.303*	0*	.01*	.215*	-.088*	-.078*
100	.812	.764	.665	-.147	-.099	.686	-.126	-.078
200	.812	.764	.665	-.147	-.099	.686	-.126	-.078
			V lsq = 6.384			V grad = 5.818+.524z		

St	Iterated Time-Term Solution (Type 1)			Iterated Time-Term Solution (Type 2)			Iterated Time-Term Solution (Type 3)		
	as	(as-aj)	(as-ac)	as	(as-aj)	(as-ac)	as	(as-aj)	(as-ac)
1	.256*	-.038*	-.028*	.273*	-.03*	-.02*	.312*	.009*	.019*
2	.230*	-.038*	-.030*	.238*	-.03*	-.022*	.280*	.012*	.02*
3	.198*	-.039*	-.032*	.207*	-.03*	-.023*	.251*	.014*	.021*
4	.170*	-.039*	-.034*	.175*	-.03*	-.025*	.225*	.016*	.021*
5	.145*	-.04*	-.036*	.154*	-.031*	-.027*	.203*	.018*	.022*
6	.124	-.39	-.037	.134	-.029	-.027	.183	.02	.022
7	.107	-.039	-.037	.117	-.029	-.027	.167	.021	.023
8	.094	-.039	-.038	.103	-.03	-.029	.155	.022	.023
9	.084	-.04	-.038	.094	-.03	-.028	.146	.022	.024
10	.078	-.04	-.039	.088	-.03	-.029	.140	.022	.023
11	.076	-.041	-.039	.086	-.031	-.029	.138	.021	.023
12	.078	-.04	-.039	.088	-.03	-.029	.140	.022	.023
13	.084	-.04	-.038	.094	-.03	-.028	.146	.022	.024
14	.094	-.039	-.038	.103	-.03	-.029	.155	.022	.023
15	.107	-.039	-.037	.117	-.029	-.027	.167	.021	.023
16	.124	-.039	-.037	.134	-.029	-.027	.183	.02	.022
17	.145	-.04*	-.036*	.154*	-.031*	-.027*	.203*	.018*	.022*
18	.170	-.039*	-.034*	.179*	-.03*	-.025*	.225*	.016*	.021*
19	.198	-.039*	-.032*	.207*	-.03*	-.023*	.251*	.014*	.02*
20	.230	-.038*	-.03*	.238*	-.03*	-.022*	.280*	.012*	.02*
21	.265	-.038*	-.028*	.273*	-.03*	-.02*	.312*	.009*	.01*
100	.779	-.033	-.015	.775	-.037	-.011	.760	-.052	-.004
200	.779	-.033	-.015	.775	-.037	-.011	.760	-.052	-.004
	V lsq = 5.865 V grad = 5.865+.0024z			V lsq = 5.896 V grad = 5.896+.001z			V lsq = 6.122 V grad = 6.122+.005z		

Table 2-6

Time-Term Solutions Model 2

St	Time-Terms Calculated from Input Model (* unreversed)		Time-Terms from Non-Iterated Least-squares Velocity Solution			Time Terms from Non-Iterated Linear Vertical Velocity Gradient Solution		
	ai	ac	as	(as-ai)	(as-ac)	as	(as-ai)	(as-ac)
1	.26*	.252	.291*	.031*	.039*	.131*	-.129*	-.121*
2	.234*	.227	.270*	.036*	.043*	.106*	-.128*	-.121*
3	.209*	.204	.250*	.041*	.046*	.082*	-.127*	-.122*
4	.188*	.183	.233*	.045*	.05*	.061*	-.127*	-.122*
5	.168	.165	.218	.05	.053	.044	-.124	-.121
6	.152	.15	.203	.051	.053	.027	-.125	-.123
7	.14	.138	.191	.051	.053	.013	-.127	-.125
8	.13	.128	.182	.052	.054	.002	-.128	-.126
9	.123	.121	.175	.052	.054	.006	-.129	-.127
10	.118	.117	.171	.053	.054	.011	-.129	-.128
11	.117	.115	.170	.053	.055	.012	-.129	-.127
12	.118	.117	.171	.053	.054	.011	-.129	-.128
13	.123	.121	.175	.052	.054	.006	-.129	-.127
14	.13	.128	.182	.052	.054	.002	-.128	-.126
15	.14	.138	.191	.051	.053	.013	-.127	-.125
16	.152	.15	.203	.051	.053	.027	-.125	-.123
17	.168	.165	.218	.05	.053	.044	-.124	-.121
18	.188*	.183	.233*	.045*	.05*	.061*	-.127*	-.122*
19	.209*	.204	.250*	.041*	.046*	.082*	-.127*	-.122*
20	.234*	.227	.270*	.036*	.043*	.106*	-.128*	-.121*
21	.26*	.252	.291*	.031*	.039*	.131*	-.129*	-.121*
100	1.28	1.191	.599	-.281	-.192	1.029	-.251	-.162
200	1.28	1.191	.599	-.281	-.182	1.029	-.251	-.162
			V lsq = 6.359			V grad = 5.799+.347z		

St	Iterated Time-Term Solution (Type 1)			Iterated Time-Term Solution (Type 2)			Iterated Time-Term Solution (Type 3)		
	as	(as-ai)	(as-ac)	as	(as-ai)	(as-ac)	as	(as-ai)	(as-ac)
1	.186*	-.074	-.066*	.205*	-.055*	-.047*	.296*	.036*	.044*
2	.159*	-.075	-.068*	.178*	-.056*	-.049*	.271*	.037*	.044*
3	.134*	-.075	-.07*	.154*	-.055*	-.05*	.248*	.039*	.044*
4	.112*	-.076	-.071*	.132*	-.056*	-.051*	.223*	.035*	.04*
5	.093	-.075	-.072	.113	-.055	-.05	.210	.042	.045
6	.077	-.075	-.073	.097	-.055	-.053	.196	.044	.046
7	.064	-.076	-.074	.084	-.056	-.054	.183	.043	.045
8	.054	-.076	-.074	.074	-.056	-.054	.174	.044	.046
9	.046	-.077	-.075	.067	-.056	-.054	.167	.044	.046
10	.042	-.076	-.075	.062	-.056	-.055	.163	.045	.046
11	.040	-.077	-.075	.061	-.056	-.054	.162	.045	.047
12	.042	-.076	-.075	.062	-.056	-.055	.163	.045	.046
13	.046	-.077	-.075	.067	-.056	-.054	.167	.044	.046
14	.054	-.076	-.074	.074	-.056	-.054	.174	.044	.046
15	.064	-.076	-.074	.084	-.056	-.054	.183	.043	.045
16	.077	-.075	-.073	.097	-.055	-.053	.196	.044	.046
17	.093	-.075	-.072	.113	-.055	-.05	.210	.042	.045
18	.112*	-.076*	-.071*	.132*	-.056*	-.051*	.223*	.035*	.04*
19	.134*	-.075*	-.07*	.154*	-.055*	-.05*	.248*	.039*	.044*
20	.159*	-.075*	-.068*	.178*	-.056*	-.045*	.271*	.037*	.044*
21	.186*	-.074*	-.066*	.205*	-.055*	-.047*	.296*	.036*	.044*
100	1.222	-.058	.031	1.213	-.067	.022	1.184	-.096	.007
200	1.222	-.058	.031	1.213	-.067	.022	1.184	-.096	.007
	V lsq = 5.813			V lsq = 5.875			V lsq = 6.17		
	V grad = 5.813+.0037z			V grad = 5.875+.003z			V grad = 6.17+.001z		

Table 2-7

Time-Term Solutions Model 3

St	Time-Terms Calculated from Input Model (* unreversed)		Time-Terms from Non-Iterated Least-squares Velocity Solution			Time Terms from Non-Iterated Linear Vertical Velocity Gradient Solution		
			as	(as-ai)	(as-ac)	as	(as-ai)	(as-ac)
1	.061*	.585	.584*	-.017*	-.001*	.491*	-.11*	-.094*
2	.533*	.520	.529*	-.004*	.009*	.418*	-.115*	-.102*
3	.471*	.46	.479*	.008*	.019*	.351*	-.12*	-.109*
4	.416*	.407	.433*	.017*	.026*	.291*	-.125*	-.116*
5	.365	.361	.396	.031	.035	.242	-.123	-.119
6	.324	.321	.356	.032	.035	.193	-.131	-.128
7	.291	.289	.324	.033	.035	.153	-.138	-.136
8	.265	.263	.299	.034	.036	.121	-.144	-.142
9	.247	.245	.281	.034	.036	.099	-.148	-.146
10	.236	.234	.270	.034	.036	.085	-.151	-.149
11	.232	.23	.266	.034	.036	.081	-.151	-.149
12	.236	.234	.270	.034	.036	.085	-.151	-.149
13	.247	.245	.281	.034	.036	.099	-.148	-.146
14	.265	.263	.299	.034	.036	.121	-.144	-.142
15	.291	.289	.324	.033	.035	.153	-.138	-.136
16	.324	.321	.356	.032	.035	.193	-.131	-.128
17	.365	.361	.396	.031	.035	.242	-.123	-.119
18	.416*	.407	.433*	.017*	.026*	.291*	-.125*	-.116*
19	.471*	.46	.479*	.008*	.019*	.351*	-.12*	-.109*
20	.533*	.52	.529*	-.004*	.009*	.418*	-.115*	-.102*
21	.601*	.585	.584*	-.017*	-.001*	.491*	-.91*	-.094*
100	1.037	.998	.513	-.093	-.085	.541	-.096	-.57
200	1.037	.598	.513	-.093	-.085	.541	-.096	-.57
			V lsq = 6.347			V grad = 5.769+.345z		

St	Iterated Time-Term Solution (Type 1)			Iterated Time-Term Solution (Type 2)			Iterated Time-Term Solution (Type 3)		
	as	(as-aj)	(as-ac)	as	(as-ai)	(as-ac)	as	(as-ai)	(as-ac)
1	.571*	-.03*	-.014*	.574*	-.027*	-.011*	.596*	-.005*	.011*
2	.502*	-.031*	-.018*	.505*	-.028*	-.015*	.532*	-.001*	.012*
3	.439*	-.029*	-.021*	.444*	-.027*	-.018*	.474*	.003*	.014*
4	.384*	-.032*	-.023*	.388*	-.028*	-.019*	.422*	.006*	.015*
5	.335	-.03	-.026	.340	-.025	-.021	.376	.011	.015
6	.294	-.03	-.027	.299	-.025	-.022	.337	.013	.016
7	.260	-.031	-.029	.266	-.025	-.023	.305	.014	.016
8	.234	-.031	-.029	.240	-.025	-.023	.280	.015	.017
9	.215	-.032	-.03	.221	-.026	-.024	.262	.015	.017
10	.204	-.032	-.03	.209	-.027	-.025	.251	.015	.017
11	.200	-.032	-.03	.206	-.026	-.024	.247	.015	.017
12	.204	-.032	-.03	.209	-.027	-.025	.251	.015	.017
13	.215	-.032	-.03	.221	-.026	-.024	.262	.015	.017
14	.234	-.031	-.029	.240	-.025	-.023	.280	.015	.017
15	.260	-.031	-.029	.266	-.025	-.023	.305	.014	.016
16	.294	-.03	-.027	.295	-.025	-.022	.337	.013	.016
17	.335	-.03	-.026	.340	-.025	-.021	.376	.011	.015
18	.348*	-.032*	-.023*	.388*	-.028*	-.019*	.422*	.006*	.015*
19	.439*	-.029*	-.021*	.444*	-.027*	-.018*	.474*	.003*	.014*
20	.502*	-.031*	-.018*	.505*	-.028*	-.015*	.532*	-.001*	.012*
21	.571*	-.03*	-.014*	.574*	-.027*	-.011*	.596*	-.005*	.011*
100	1.008	-.029	.01	1.006	-.031	.008	.994	-.043	-.004
200	1.008	-.029	.01	1.006	-.031	.008	.994	-.043	-.004
	V lsq = 5.925			V lsq = 5.937			V lsq = 6.055		
	V grad = 5.925+.001z			V grad = 5.937+.0016z			V grad = 6.055+.002z		

Table 2-8

Time-Term Solutions Model 4

St	Time-Terms Calculated from Input Model (* unreversed) a1	ac	Time-Terms from Non-Iterated Least-squares Velocity Solution as	(as-a1)	(as-ac)	Time Terms from Non-Iterated Linear Vertical Velocity Gradient Solution as	(as-a1)	(as-ac)
1	.516*	.504	.534*	.018*	.03*	.352*	-.164*	-.152*
2	.458	.453	.497	.039	.044	.302	-.156	-.151
3	.411	.407	.451	.04	.044	.245	-.166	-.162
4	.37	.366	.411	.041	.045	.194	-.176	-.172
5	.334	.331	.376	.042	.045	.150	-.184	-.181
6	.303	.3	.346	.043	.046	.113	-.19	-.187
7	.278	.275	.322	.044	.047	.083	-.195	-.192
8	.258	.256	.303	.045	.047	.059	-.199	-.197
9	.244	.242	.289	.045	.047	.042	-.202	-.2
10	.235	.233	.281	.046	.048	.032	-.203	-.201
11	.233	.231	.278	.045	.047	.029	-.205	-.203
12	.235	.233	.281	.046	.048	.032	-.203	-.201
13	.244	.242	.289	.045	.047	.042	-.202	-.2
14	.258	.256	.303	.045	.047	.059	-.199	-.197
15	.278	.275	.322	.044	.047	.083	-.195	-.192
16	.303	.3	.346	.043	.046	.113	-.19	-.187
17	.334	.331	.376	.042	.045	.150	-.184	-.181
18	.37	.366	.411	.041	.045	.194	-.176	-.172
19	.411	.407	.451	.04	.044	.245	-.166	-.162
20	.458	.453	.497	.035	.044	.302	-.156	-.151
21	.516*	.504	.534*	.018*	.03*	.352*	-.164*	-.152*
100	1.315	1.265	1.146	-.169	-.119	1.184	-.131	-.081
200	1.315	1.265	1.146	-.169	-.119	1.184	-.131	-.081
			V lsq = 6.316			V grad = 5.736+.261z		

St	Iterated Time-Term Solution (Type 1) as	(as-aj)	(as-ac)	Iterated Time-Term Solution (Type 2) as	(as-a1)	(as-ac)	Iterated Time-Term Solution (Type 3) as	(as-a1)	(as-ac)
1	.475*	-.041*	-.029*	.481*	-.035*	-.023*	.517*	.001*	.013*
2	.421	-.037	-.032	.427	-.031	-.026	.467	.009	.014
3	.373	-.038	-.034	.379	-.032	-.028	.421	.01	.014
4	.331	-.039	-.035	.337	-.033	-.029	.381	.011	.015
5	.294	-.04	-.037	.301	-.033	-.03	.345	.011	.014
6	.263	-.04	-.037	.270	-.033	-.03	.315	.012	.015
7	.237	-.041	-.038	.244	-.034	-.031	.290	.012	.015
8	.217	-.041	-.039	.224	-.034	-.032	.271	.013	.015
9	.203	-.041	-.039	.210	-.034	-.032	.257	.013	.015
10	.194	-.041	-.039	.201	-.034	-.032	.249	.014	.016
11	.191	-.042	-.04	.198	-.035	-.033	.246	.013	.015
12	.194	-.041	-.039	.201	-.034	-.032	.249	.014	.016
13	.203	-.041	-.039	.210	-.034	-.032	.257	.013	.015
14	.217	-.041	-.039	.224	-.034	-.032	.271	.013	.015
15	.237	-.04	-.02	.244	-.034	-.031	.290	.012	.015
16	.263	-.04	-.037	.270	-.033	-.03	.315	.012	.015
17	.294	-.04	-.037	.301	-.033	-.03	.345	.011	.014
18	.331	-.039	-.035	.337	-.033	-.029	.381	.011	.015
19	.373	-.038	-.034	.379	-.032	-.028	.421	.01	.014
20	.421	-.037	-.032	.427	-.031	-.026	.467	.009	.014
21	.475*	-.041*	-.029*	.481*	-.035*	-.023*	.517*	.001*	.013*
100	1.279	-.036	-.014	1.276	-.039	.011	1.260	-.055	-.005
200	1.279	-.036	-.014	1.276	-.039	.011	1.260	-.055	-.00
	V lsq = 5.929 V grad = 5.929+.001z			V lsq = 5.939 V grad = 5.939+.001z			V lsq = 6.056 V grad = 6.039+.04z		

FIG 2-10 Solution time-terms for models

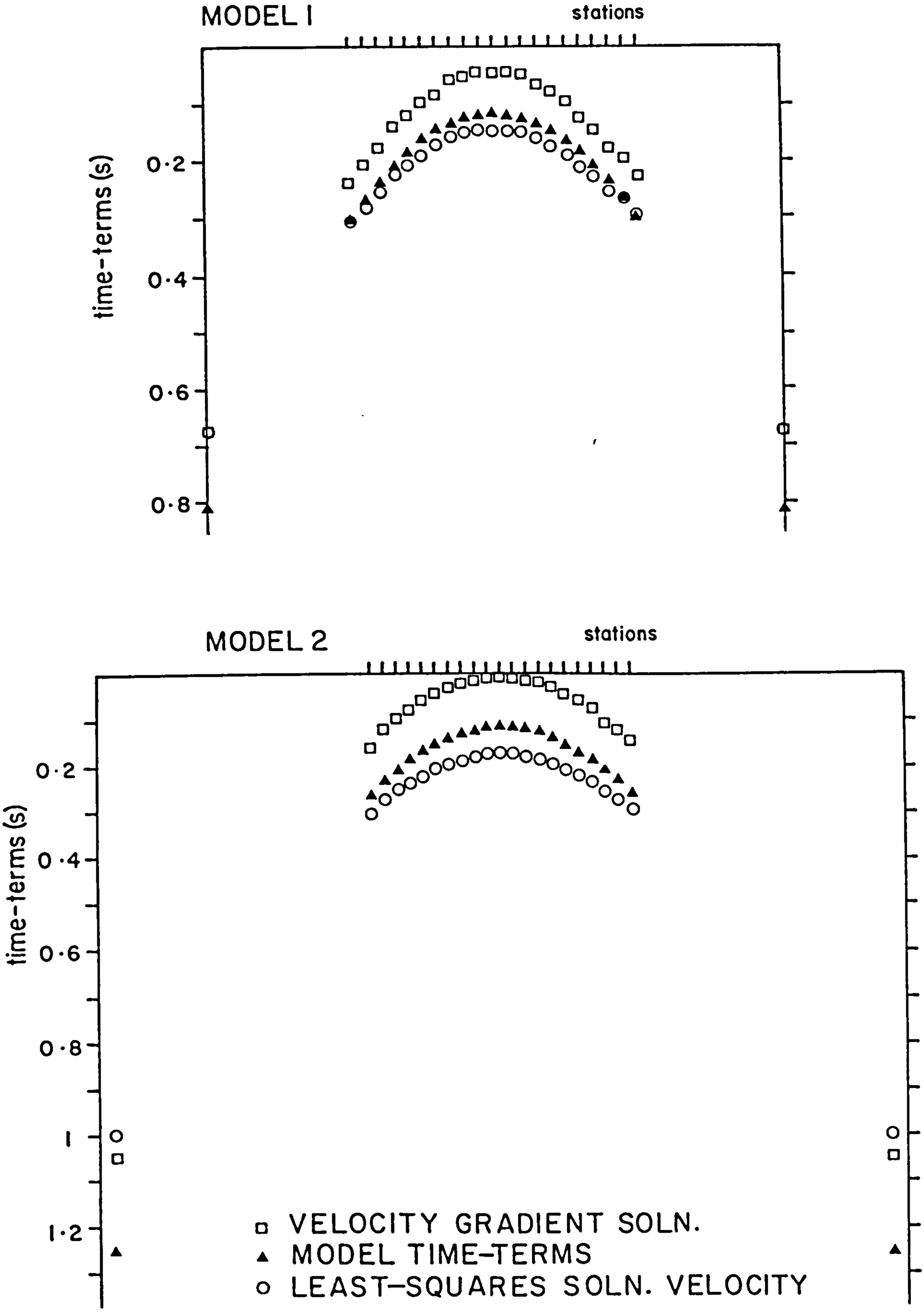

FIG 2-10 cont.

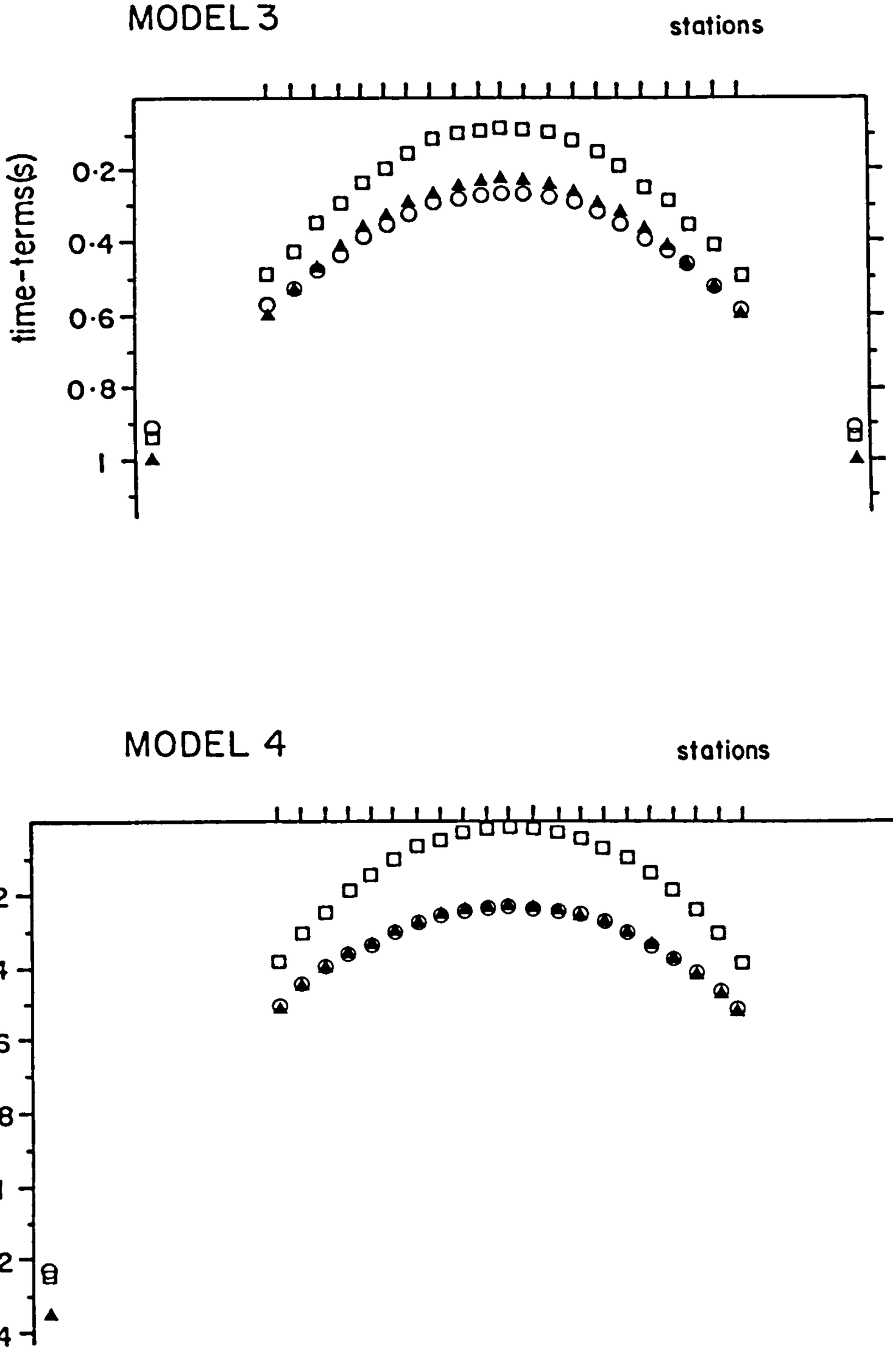
MODEL 3
stations
time-terms(s)
0·2
0·4
0·6
0·8
1
MODEL 4
stations
time-terms(s)
0·2
0·4
0·6
0·8
1
1·2
1·4
VELOCITY GRADIENT SOLn.
MODEL TIME-TERMS
LEAST-SQUARES VELOCITY SOLn

most noticeable feature of these solutions is that a constant seems to have been subtracted from all the solution time-terms, and that the value of this constant is greatest for the smaller radii of curvature.

To illustrate the relative distortion of the model by each solution, the time-terms have been superimposed at the axis of the anticline (Fig. 2.11). Thus while the effect of structure on the shape of the solution topography is greatest for the constant velocity solution at the smaller radii of curvature, the converse is true for solutions allowing a vertical velocity gradient. Both solution velocities depart furthest from the true velocity for the 15km radius model. It is obvious that the refractor structure has greatest influence upon the solution time-terms where $X_{ij}-\Delta_{ij}$ is greatest, that is for the end-to-end linkage, which immediately discredits the value of the solution time-terms, which are solved uniquely from the shot-shot travel time.

Consider the time-term solutions for a simple flat refractor for which there will be no structural effects (Fig. 2.12). The travel-times are generated from Equation 2.2, where ϕ is zero. With the correct end-to-end time and distances all the true time-terms are 0.232s. Now,

a) When .464s are subtracted from the end-to-end times, the error is divided equally between the station and shot time-terms, such that

$$t_{ij} = (a_i - 0.232) + (a_j + 0.232) + \frac{X}{V}$$

so that station time-terms increase to 0.464s, the shot time-terms fall to zero, but the solution velocity and refractor structure implied by the stations are the same as the model. For an over-estimated travel time the corrections are applied in the opposite sense.

b) When 2.784km are added to shot-shot distances (i.e. 0.464s at 6km/s, or equivalent to the end-to-end travel time too small by 0.464s), the error is again equally divided between shot and station time-terms without affecting the solution

FIG 2-11 Solution time-terms normalised to central station (without shotpoints)

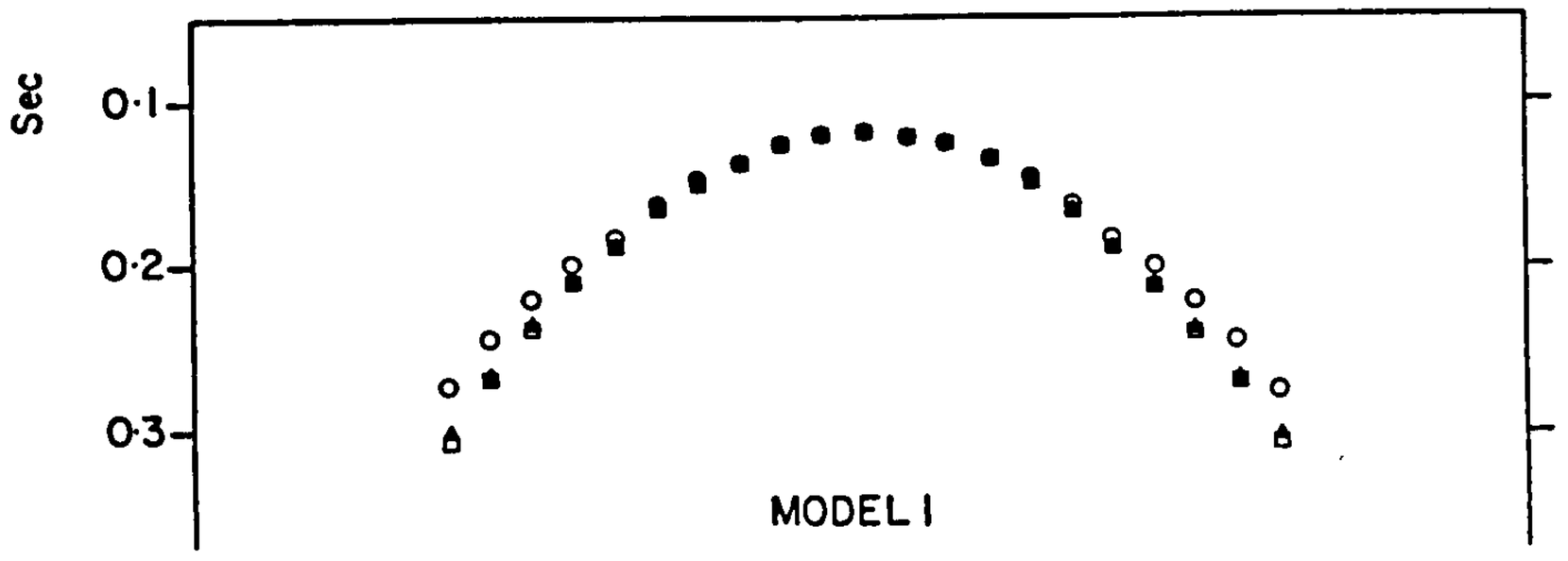

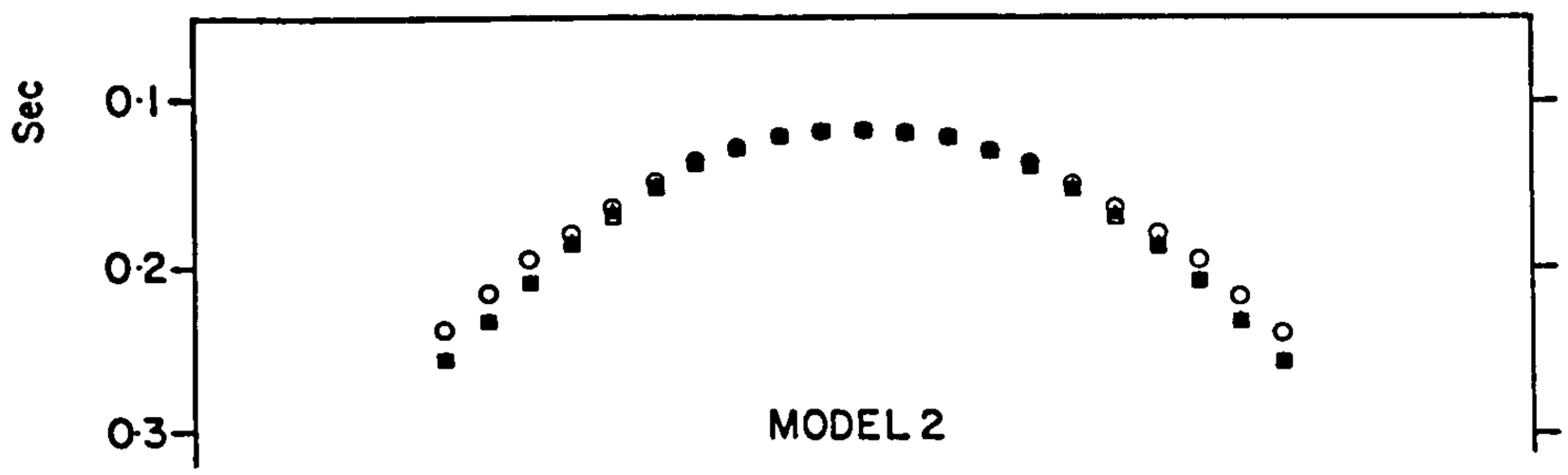

○ CONSTANT VELOCITY SOLN. ▲ MODEL TIME-TERMS □ VELOCITY GRADIENT SOLN.

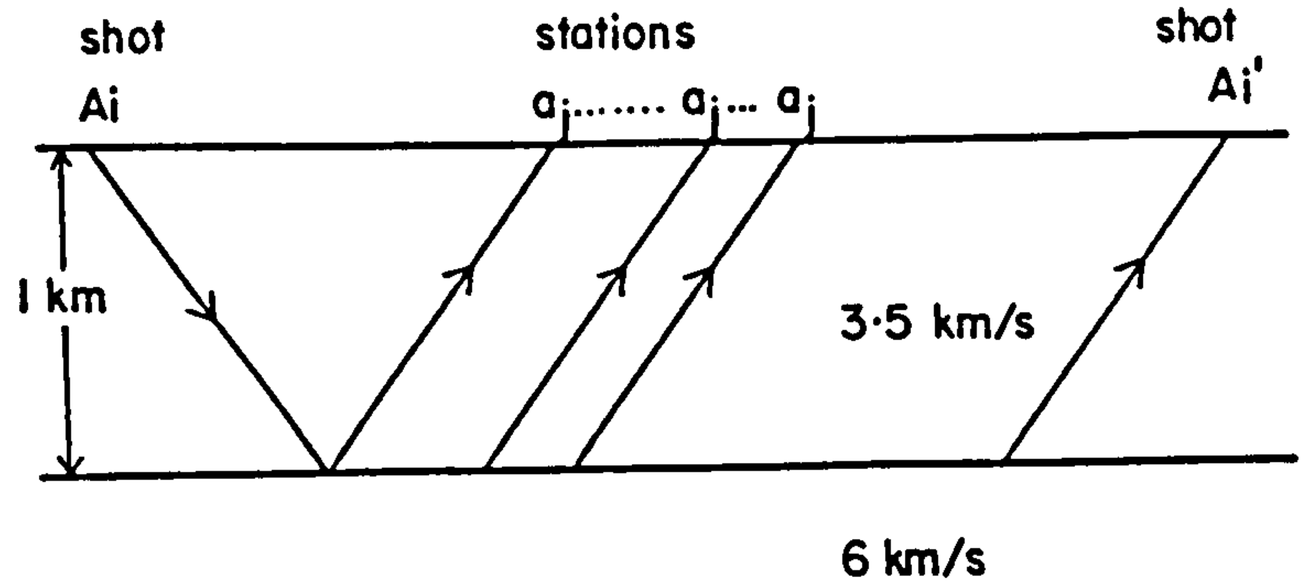

FIG 2-12 Flat refractor

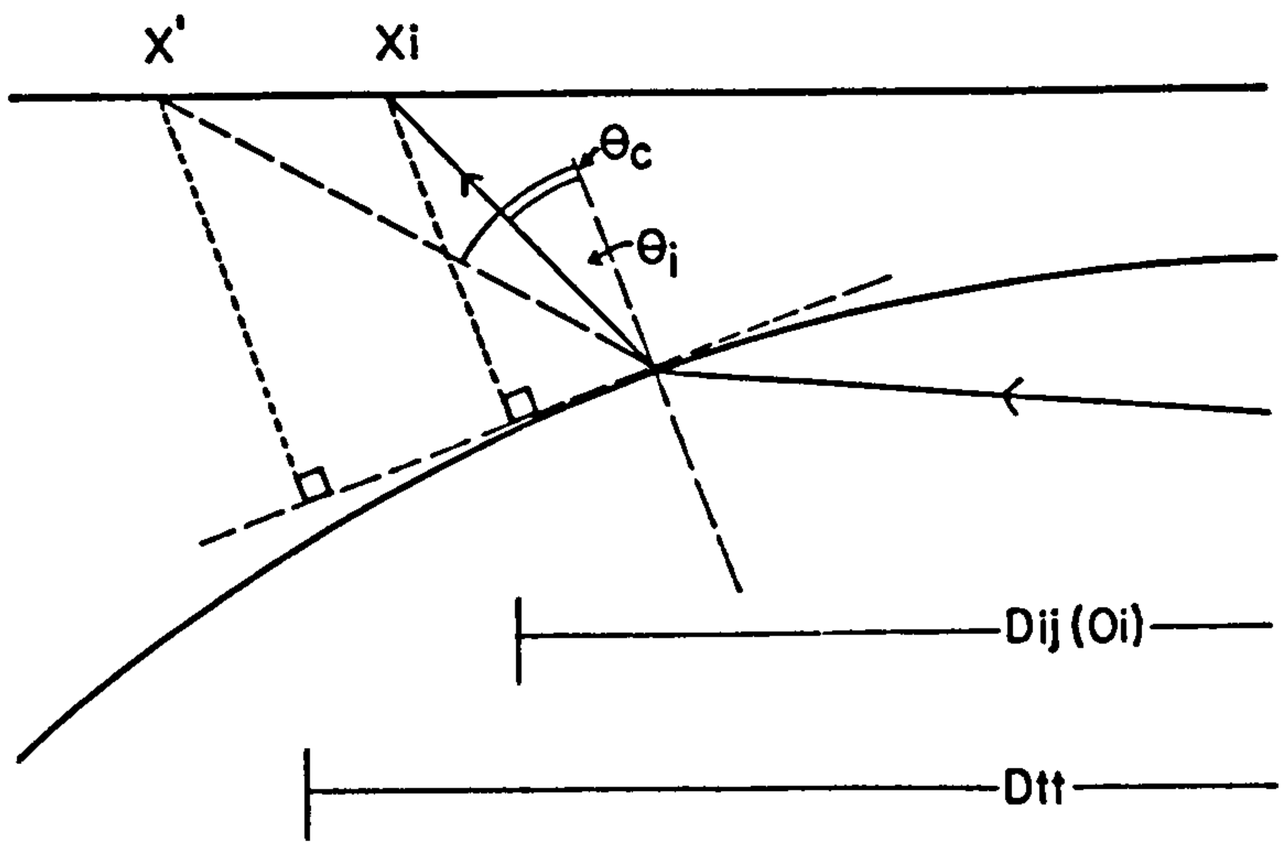

FIG 2-13 Type 3 iteration

Text cut off in original

velocity or shape of the refractor between the stations. Thus an error in shot-shot distance is equivalent to an error in shot-shot travel time, which results in half the net error being added to the station time-terms, and half subtracted from the shot time-terms.

Thus the incorrect assumption of X_{ij} for Δ_{ij} is a double source of error: firstly on the station time-terms themselves, and secondly by introducing relative error between shot and station time-terms, which further exaggerates the broadening of the delay-time surface (like above, X_{ij} is larger than Δ_{ij}). The error introduced between shot and station time-terms also occurs for the solution incorporating a velocity gradient, only the anticlinal structure is additionally accentuated for the station time-terms; thus the two effects result in the apparent d.c. shift of the solution time-terms.

Iterated Solutions

The solutions were iterated by using both Δ_{ij} (θ_i) (Type 1) and Δ_{cij} (Type 2) for X_{ij}, for each of which a single iteration was carried out. The results of both are given in Tables 2.5 to 2.8; the quality of the solution is much improved by either iteration, and any structually induced velocity gradient has almost totally been eliminated, leaving the default velocity gradient of 0.001 per sec in the solution. However, both solutions have slightly overcorrected the data such that

a) The solution velocities defined by the iterations are too low,

b) The solution time-terms are too low by some constant, and

c) The implied refractor topographies are slightly accentuate (the axial station time-terms are marginally less than at the profile extremes).

Generally the Type 2 iterations are slightly more accurate than Type 1. These features are indicative of the iterated distances being too small, which is surprising because the theoretical non critical time-term travel times approximated the true travel times so closely.

To attempt to improve the solution, a third iteration (Type 3) was executed employing characteristics of both critical and non-critical time-term approximations: at the point of incidence for the non-critically refracted raypath, a line was extended to the surface at the critical angle and a new perpendicular intersection onto the tangent constructed from this point (see Fig. 2.13). Thus, Dtt is the distance between these perpendicular drops, and $(X_{ij} - Dtt)$ the correction used for the Type 3 iteration (see tables 2-1 to 2-4). (There is no geometrical reason for this construction apart from that the correction is easy to calculate and is proportional to the position of the station with respect to the axis of the anticline. Within a first approximation, Δ_{ij} increases by a factor of $2 \tan\theta_c / \tan\theta_i$).

The solutions of the Type 3 iteration are given in the final three columns of Tables 2.5 to 2.8. Although the true model time-terms have not been obtained, the results are a little closer to the true, but in the opposite sense to either Types 1 or 2 iteration: the refractor velocity is slightly overestimated and the implied refractor topographies have been broadened (Fig. 2.14). Obviously the best values of Δ_{ij} upon which to iterate are somewhat between this and the Type 2 iteration. This Type 3 iteration has worked best for the longer wavelength models where the time-term residuals are of the order of 10ms. Again, no structurally induced velocity gradient occurs.

Conclusions

The models demonstrate how antiform refractors can induce an apparent vertical velocity gradient into the non-iterated time-term solution. As Willmore and Bancroft (1960) conclude, the time-term method is more efficient in defining refractor structure than velocity character, and for these models the lack of fit caused by the assumptions made about the refractor were absorbed into the velocity gradient term (Whitcombe and Maguire 1979). Whether or not a vertical velocity gradient exists in the refractor can be tested by

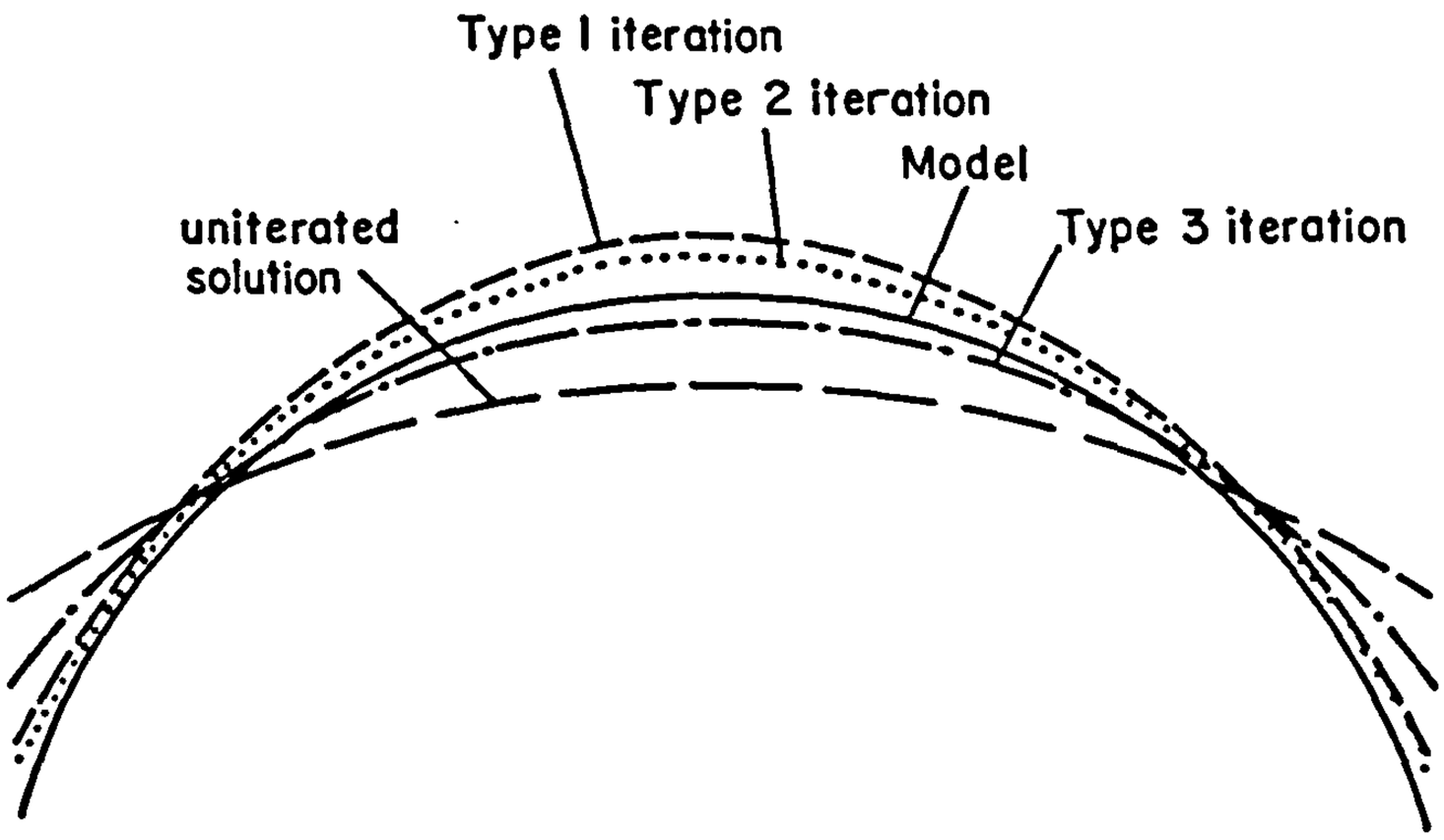

FIG 2-14 Scheme of iterated time-term solutions (not to scale)

comparing the variances of solutions which assume uniform or velocity gradient; if the F test is significant then the inclusion of a gradient term may be justified.

Since a least-squares velocity time-term solution for a horizontal refractor with a vertical velocity gradient implies a synclinal refractor (Smith et al. 1966), then presumably a velocity gradient time-term solution for a synclinal refractor will yield a horizontal refractor with an apparent velocity gradient. Strictly speaking, the refractor must have a velocity gradient for refracted waves to be observed from a synclinal structure, in which case the two effects may complement each other: supressing the synclinal shape and accentuating the solution gradient.

The interchangeable effects of refractor topography and velocity structure present a dilemma with regard to the iterated solution, for the assumptions of one feature will mitigate the effects of the other. The difficulty in achieving an accurate solution by iterating synthetic data must also discredit the need for numerous iterations upon data which may not justify the quality of the solution. Generally one or two iterations are sufficient for the solution to converge to a point that refractor structure no longer has significant effect upon the solution velocity (or vice versa).

To constrain the solution time-terms, the velocity is best estimated separately (Willmore and Bancroft 1960, Smith et al. 1966). Regarding the problems of shot point time-terms evident from these models, satisfactory time-terms for the stations would result if they were allowed to 'float' according to, say, geological control, without the need for time-consuming iteration. In their simulated data studies of a domal refractor, for example, Willmore and Bancroft (1960) tethered the solution to an outcrop of the dome at the centre of the array. Owing to the approximations of the method, 'absolute' distance from station to refractor surface can only be determined for a horizontal refractor.

Unlike structurally induced velocity anisotropy, the inducement of an apparent velocity gradient will be greatest for an azimuthally independent feature, such as a dome.

Conversely, for orthogonal profiles across an azimuthally dependent feature the effect might average out, although a false velocity gradient may be generated by a saddle-shaped refractor.

2.3.2 Reduced Time Plots

Equation 2.2 can be re-arranged:

$$t_{ij} - \frac{X_{ij}}{V_r} = a_i + a_j = T_{rij} \qquad (2.15)$$

for the reduced travel time T_{rij}. Thus by estimating V_r the observed travel times t_{ij} can be easily treated to derive a quantity related to the sum of delay times at shot and station. Furthermore, for a suite of observations from the same shot, the shot time-term a_i will be common to each, so that the relative values of T_{rij} are directly related to a_j.

There are two main advantages with this method: firstly reduced times provide an easy means of qualitatively analysing the delay-time surface, and secondly the compression of the travel times enables seismic records to be more easily handled. When the reduced times are plotted against X_{ij}, arrivals with the reducing velocity will tend to lie parallel to the zero time axis, while those with a velocity less than V_r will have increasingly positive reduced times. Thus to avoid distortion of the implied delay-time surface, the reducing velocity must be carefully chosen.

Fig. 2.15 illustrates the reduced times obtained by plotting the travel times from each of the four anticline models with three reducing velocities: 5.5km/s, 6.0km/s (the true refractor velocity) and 6.5km/s. Both forward and reversed times have been considered, and the reduced times have been plotted positive down to give the effect of depth. The principal differences between the reducing velocities are:

FIG 2-15 Reduced time graphs for anticline models (reduced times in seconds)

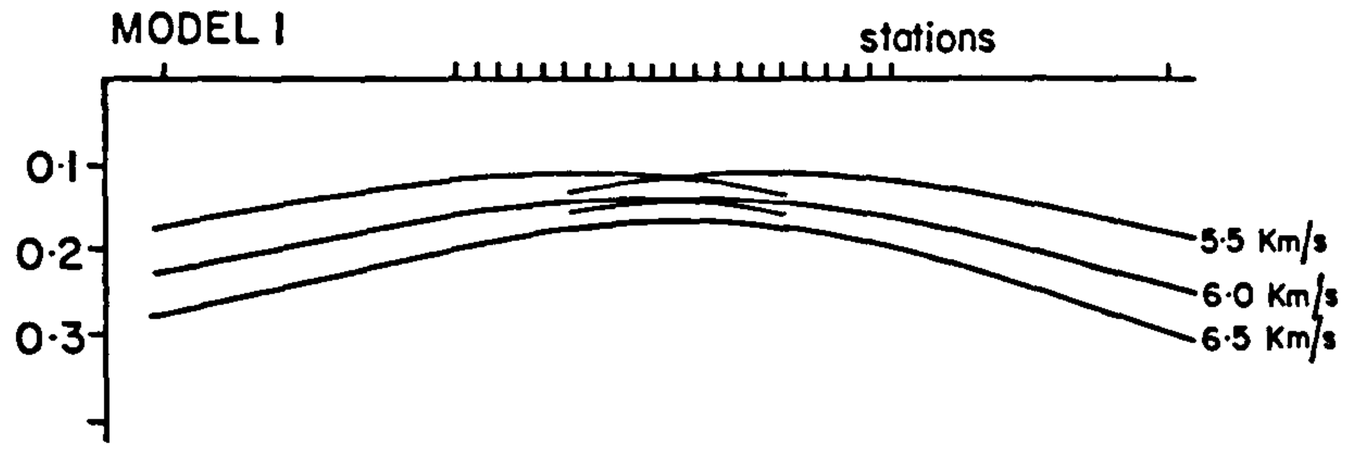

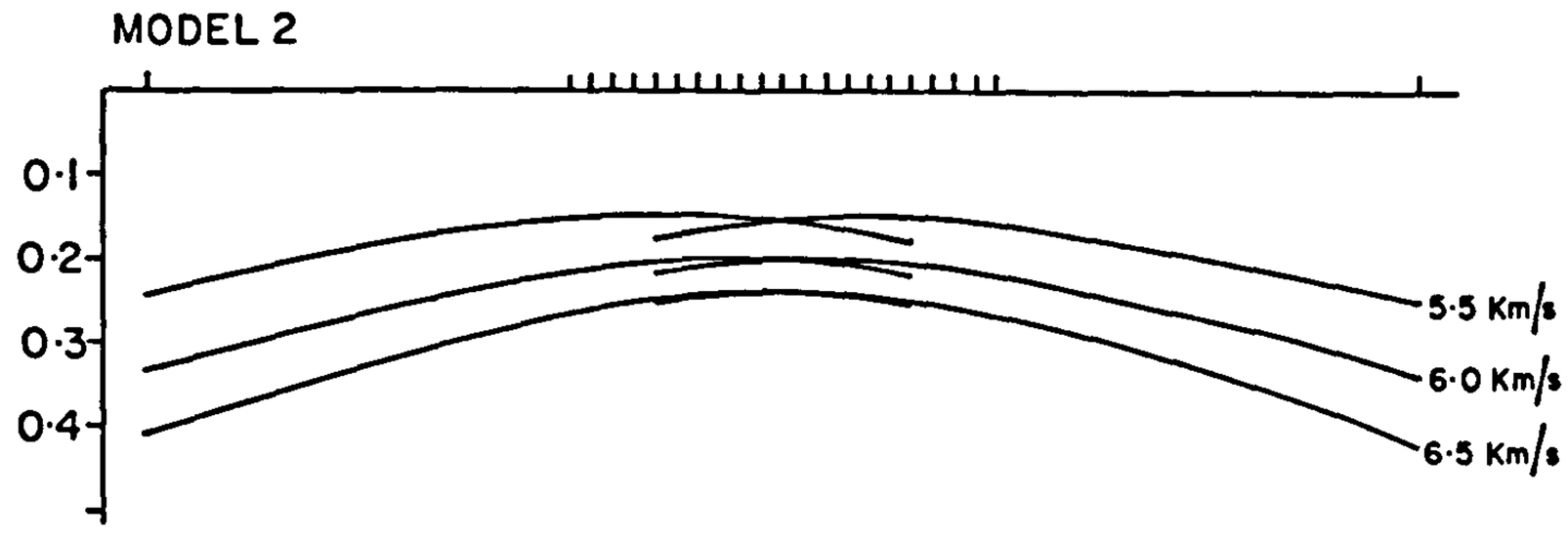

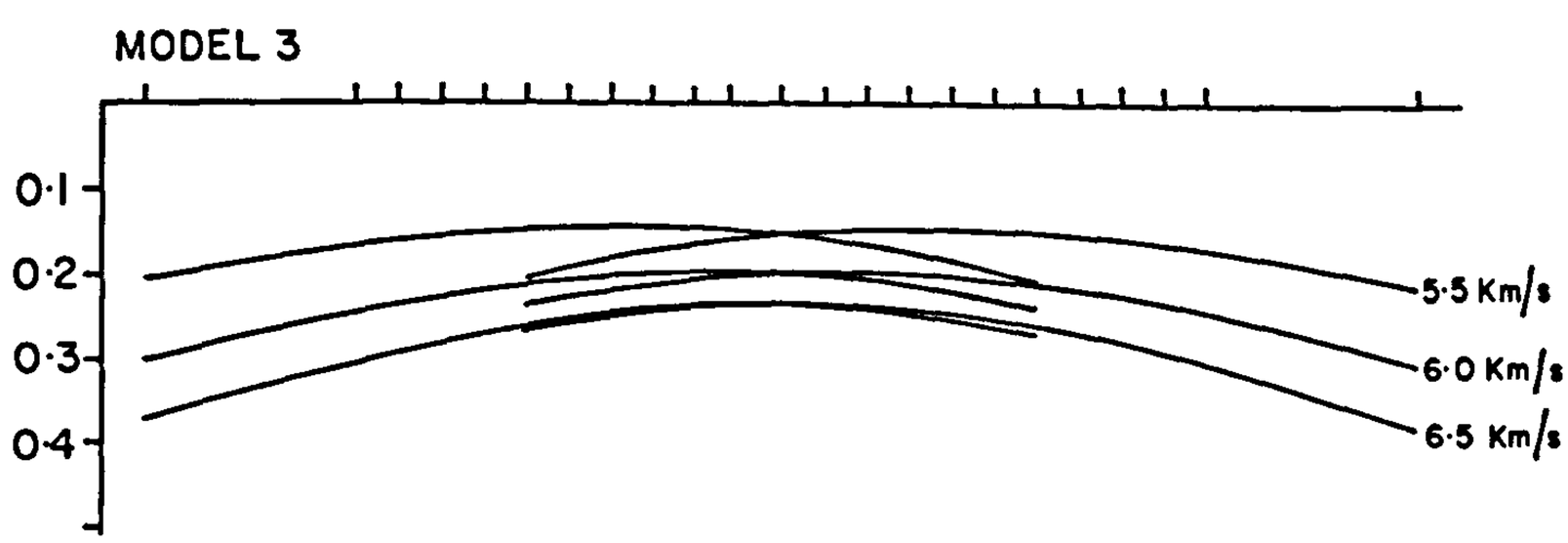

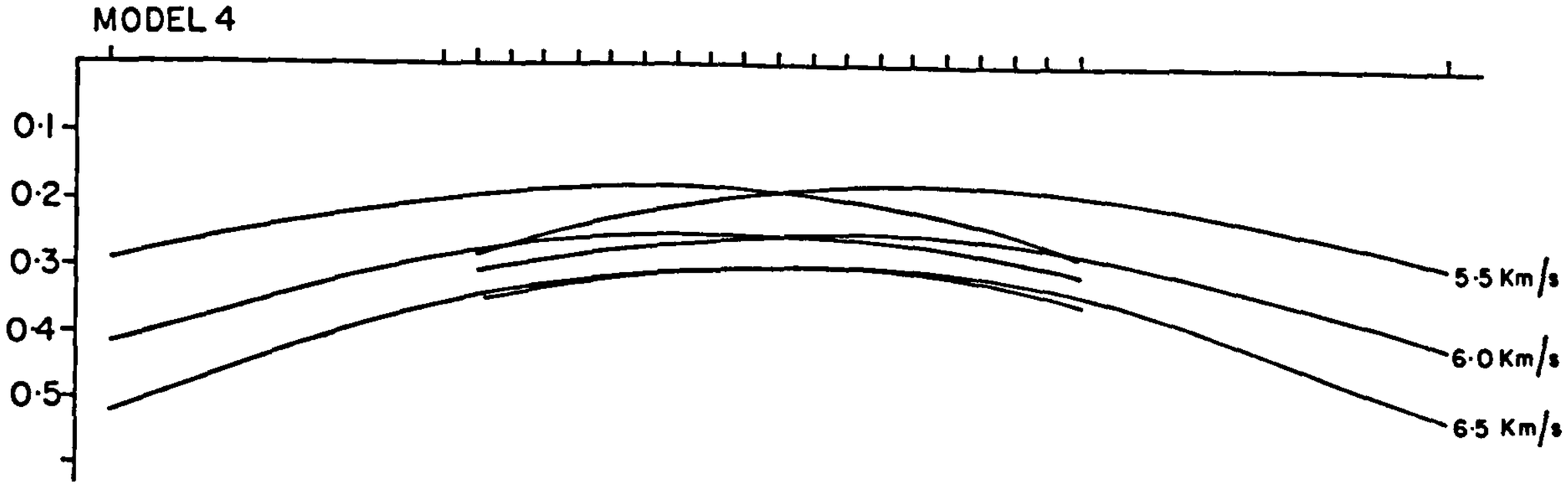

a) The larger V_r the deeper the implied surface: this is because T_{rij} is inversely proportional to V_r, such that the greater X_{ij} the greater the reduced time.

b) The smaller V_r the greater the apparent offset, where 'offset' is here defined as the horizontal distance travelled by the ray between leaving the refractor and striking the surface. Thus the reduced time surface is migrated away from the shot. The degree of offset, o_i, is related to the velocity contrast and the depth of the refractor, h, by

$$o_i = h\tan\theta_i = \frac{hV_o}{(V_r^2 - V_o^2)^{\frac{1}{2}}} \qquad (2.16)$$

The smaller the velocity contrast the greater the offset, hence the closing of the reduced time surface for the larger reducing velocities.

Equation 2.16 can be used to estimate mean overburden velocities (Smith et al. 1966): if some feature occurs in both forward and reversed reduced times, then its relative displacement between the two is twice the absolute offset. The mean overburden velocity V_o may be estimated if h and V_r are known (or h may be calculated once o_i, V_o and V_r are known).

2.4 Amplitudes and Frequency Analysis of P waves

This section discusses two supplementary, but nevertheless important aids to refraction data interpretation: relative amplitudes, and the frequency content of P waves.

2.4.1 Amplitudes of P Waves

The factors that influence the observed amplitude at a station include (O'Brien 1967):

a) the strength of the source, and its geological situation

b) attenuation along the travel path

c) the angle of approach (for a vertical instrument, the steeper the angle of incidence the greater the response)
d) the seismometer location, including local geology, the thickness and consolidation of the topsoil (which on the limestones in Derbyshire is a metre or less), and the installation of the instrument (whether buried, housed in a pit, etc)
e) the recording system, in particular the amplitude response of the individual seismometers (which need to be calibrated in situ)
f) the means of measurement (which phase is considered, whether peak to peak etc., see Section 4.4.4), including observational errors.

Relative amplitudes between instruments can be readily determined, for which the effects of (a), (e) and (f) are either known or constant for all observations from any one event, and therefore cancel. Similarly, after analysing several events, systematic differences between stations should become apparent, and thus allowances can be made for (d). It is normally assumed that the variation due to (c) is no more than about 10 per cent, and for refracted arrivals the angle of incidence will be approximately critical and thus constant over large distances.

Therefore, the differences in relative amplitude between stations is largely diagnostic of the attenuation along the respective raypaths, and sudden changes in relative amplitude with distance may be indicative of different phases being considered. Heelan (1953) showed that the amplitude of the refracted wave is normally expected to decay with $1/(X^{\frac{1}{2}}Xr^{3/2})$ for shot-station distance X, and distance travelled in the refractor X_r; note that this cannot hold for stations very close to the critical distance (O'Brien 1967). For uninterpreted data X_r is difficult to determine, and since over large distances X_r is almost equal to X, the amplitude can be assumed to decay by $1/X^2$.

In general, attenuation is dependent upon:

a) the thickness of the medium: for a refractor only a wavelength or so thick the attenuation may be several decibels per dominant wavelength, while waves from a much thicker refractor may only attenuate by fractions of a decibel
b) the lithology of the medium: waves through porous or fractured rocks attenuate quicker than those transmitted through more consolidated media, and
c) the presence of a vertical velocity gradient, which will focus up energy and thus reduce the rate of attenuation.

Rates of amplitude decay can be a useful discriminant between refractors of the same velocity, but differing attenuation characteristics. Additionally, direct waves can be distinguished from refractor arrivals because they travel predominantly horizontal raypaths, and thus are observed to attenuate quickly using vertical seismometers, unless there is a vertical velocity gradient in the overburden.

2.4.2 Frequency Analysis of P waves

The frequency content of P waves depend upon factors at source, at detector and during transmission. Greenhalgh (1980) has discussed the effects of quarry blasting on P wave spectra, with the conclusions that:
a) complexities in P and S wave coda are largely due to multiple delay shooting; synthetic seismogram studies attest that this complexity increases with the number of shots and the length of the delays (for example, a blast of 25 holes with 17ms delays lasts for 0.425s).
b) the shape of P wave spectra appear remarkably consistent between blasts from the same mine or quarry, despite the differing shot configurations, and
c) the amplitude of the 4Hz peak was found to correlate directly with the total size of the blast.

The recorded frequency content of a P wave will mainly depend upon the frequency response of the seismometer (see Section 3.2.1), and the situation of the instrument: for example,

if it lies on poorly consolidated material some high frequency content will be lost (O'Brien 1967).

Since it is difficult to separate individual P wave phases from noise, instrument response and the source function, the effects of transmission upon the frequency content are treated easiest by qualitatively comparing arrivals at instruments relative to each other. Generally, the further a ray travels the more attenuated its higher frequencies, which results in the waveform becoming progressively lower frequency. The less consolidated the media through which the ray passes, the greater this effect.

Assessment of Polarisation Filters

During the month of March 1982 the author was sponsored by NERC to work with J. Samson at the University of Alberta, Edmonton, Canada on the application of multichannel polarisation filters to seismic data. The trip followed the successful treatment of teleseismic data from the West African Seismic Project (Briden et al. 1981), discussed in Samson and Olson (1981).

The technique essentially uses the degree of linear polarisation as an optimising criterion for the design of a filter which operates in the frequency domain on each channel separately. The process is data-adaptive since the filtering window is slid through the data, at each position of which the degree of polarisation is recalculated and the filter redesigned. The advantage of this technique over most other multichannel filters is that for n channels of input there will be n channels of filtered output, rather than one best filtered channel.

The method is discussed in detail in Appendix B, but the test example plotted in Fig. 2.16 serves to illustrate the filter's effect. Six identical channels containing the first four seconds of a quarry blast digitised at 50 samples per second were considered (Fig. 2.16a), to which artificial noise was randomly added with a peak-to-peak amplitude about half that of the signal (Fig. 2.16b). These data were then filtered by sliding a window two wavelengths long through the signal,

TEST DATA

TEST DATA PLUS NOISE

TEST DATA PLUS NOISE, OPTFIL FILTERED

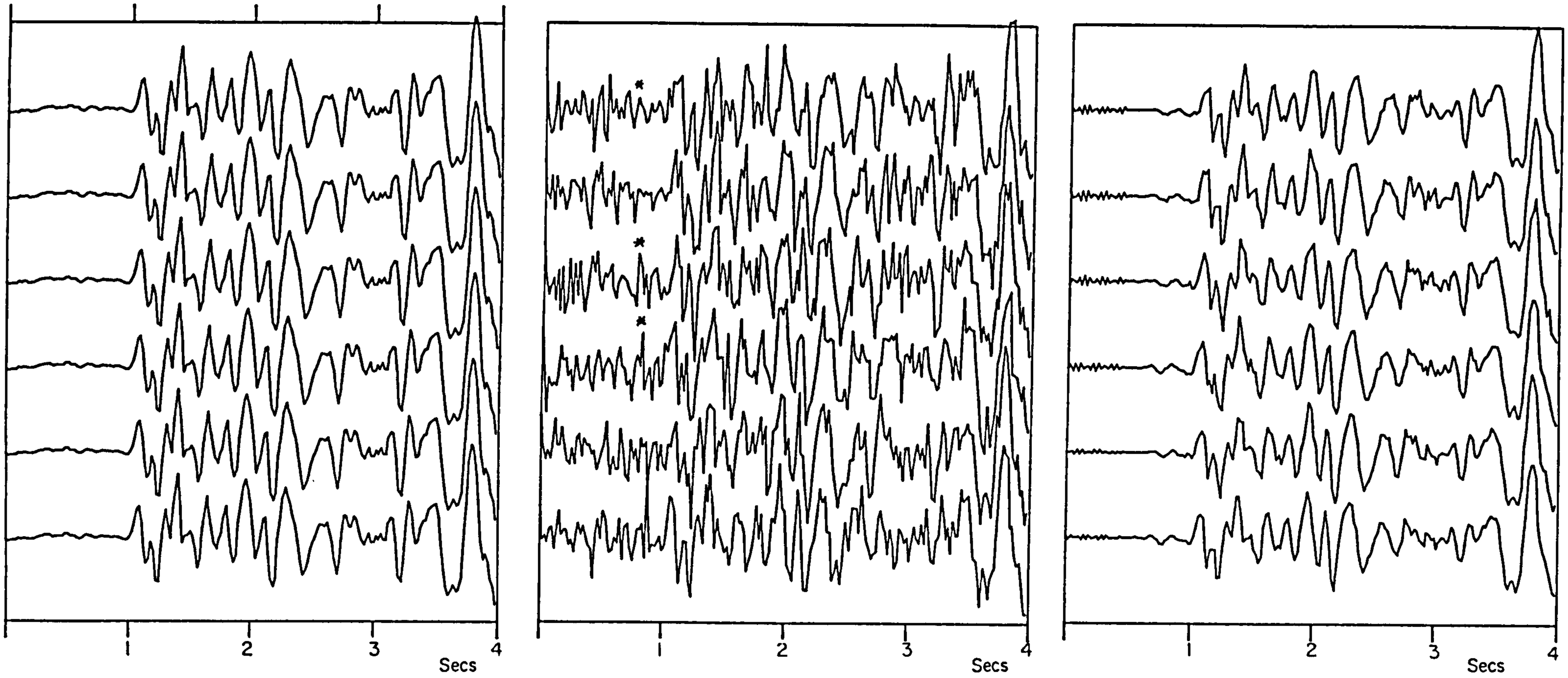

(a) (b) (c)

FIG 2-16

with two samples between adjacent positions; the shorter the increment between filter positions the less the edge effects at the extremes of the window.

The filtered data are plotted in Fig. 2.16c. The high frequency chatter at the start of the filtered output denotes the window within which the characteristic of the ambient noise was estimated and an auxilliary filter designed; consequently within this window nearly all seismic energy (linearly polarised or not) was filtered out. Since each channel contained the same signal, the seismic data are extremely well polarised and consequently recovery is good. However, because the technique is unbiased and the artificial noise not ideally random, any linearly polarised or correlated (asterisked) component of the ambient noise remains.

BOX 1

Calculation of a Raypath Through a Layer of Constant Vertical Velocity Gradient.

Consider the case of a ray being refracted downwards through a sequence of n very thin, constant velocity horizons:

At the n^{th} interface, $\frac{\sin i_n}{V_n} = \frac{\sin i_o}{V_o} = \frac{\sin i}{V} = p$ constant

(ray parameter)

Now, $\frac{dx}{dz} = \tan i_n$ and $\frac{dt}{dz} = \frac{1}{V_n \cos i_n}$

So, consider ray at (x,z) at a time t for infinitesimally thin beds, and

$$x = \int_o^z \frac{\rho V(z)}{(1-\rho^2 V^2(z))^{\frac{1}{2}}} \quad \text{and} \quad t = \int_o^z \frac{dz}{V(z)(1-\rho^2 V^2(z))^{\frac{1}{2}}}$$

Now, for linear velocity gradient $V(z) = V_o + gz$ for gradient g. Therefore $dz = \frac{dV}{g}$. Also, let $u = pV$ such that $dV = \frac{du}{p}$

$$x = \frac{1}{gp} \int_{pV_o}^{pV} \frac{udu}{(1-u^2)^{\frac{1}{2}}} \quad \text{and} \quad t = \frac{1}{g} \int_{pV_o}^{V} \frac{du}{u(1-u^2)^{\frac{1}{2}}}$$

Hence

$$x = -\frac{1}{gp} \left| (1-u^2)^{\frac{1}{2}} \right|_{pV_o}^{pV} \quad \text{and} \quad t = -\frac{1}{g} \left| \ln\left(\frac{1}{u}\{1+u^2\}^{\frac{1}{2}}\right) \right|_{pV_o}^{pV}$$

By substituting limits of integration and including $V=V_o + gz$ and $u = PV$,

$$x = \frac{1}{gp} \left[\{1 - p^2 V_o^2\}^{\frac{1}{2}} + \{1 - p^2 (V_o + gz)^2\}^{\frac{1}{2}}\right] \qquad B(i)$$

and

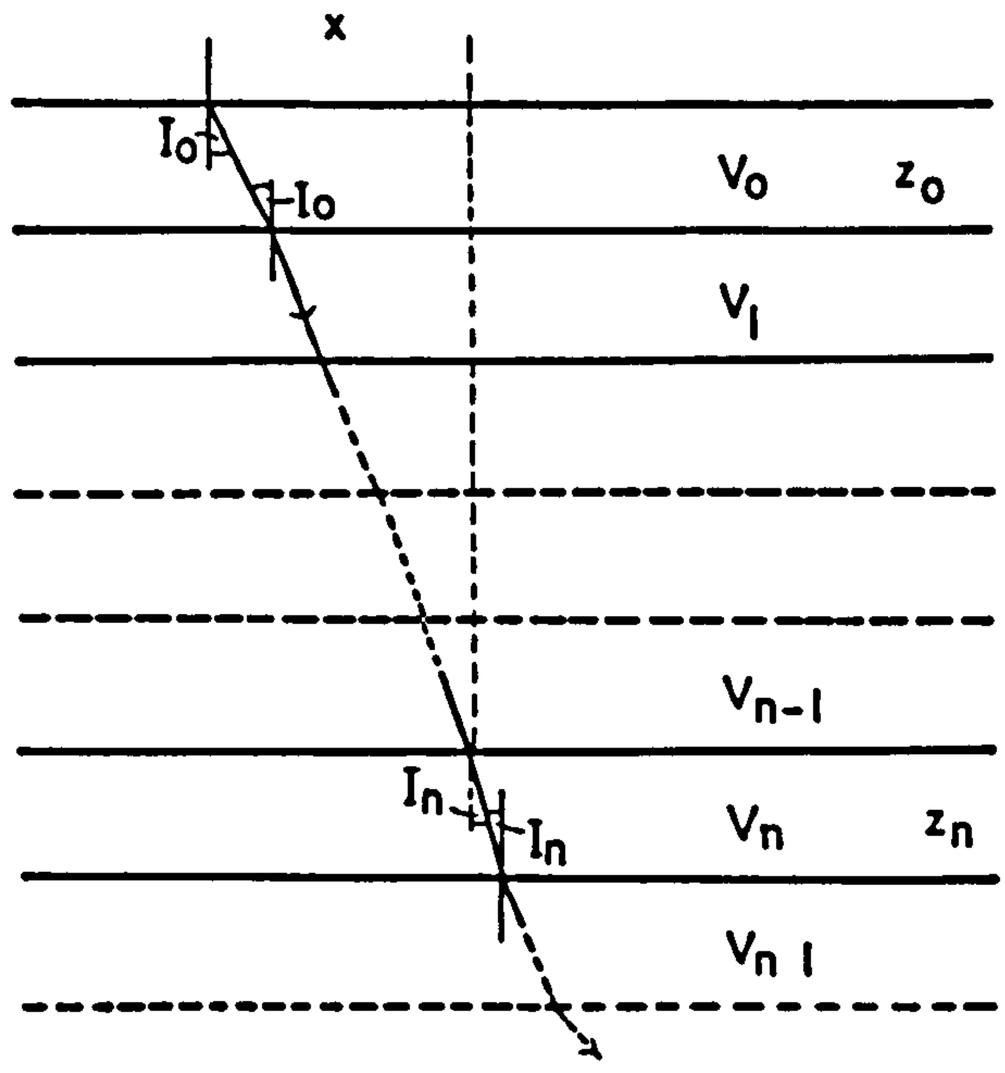

FIG BI-1

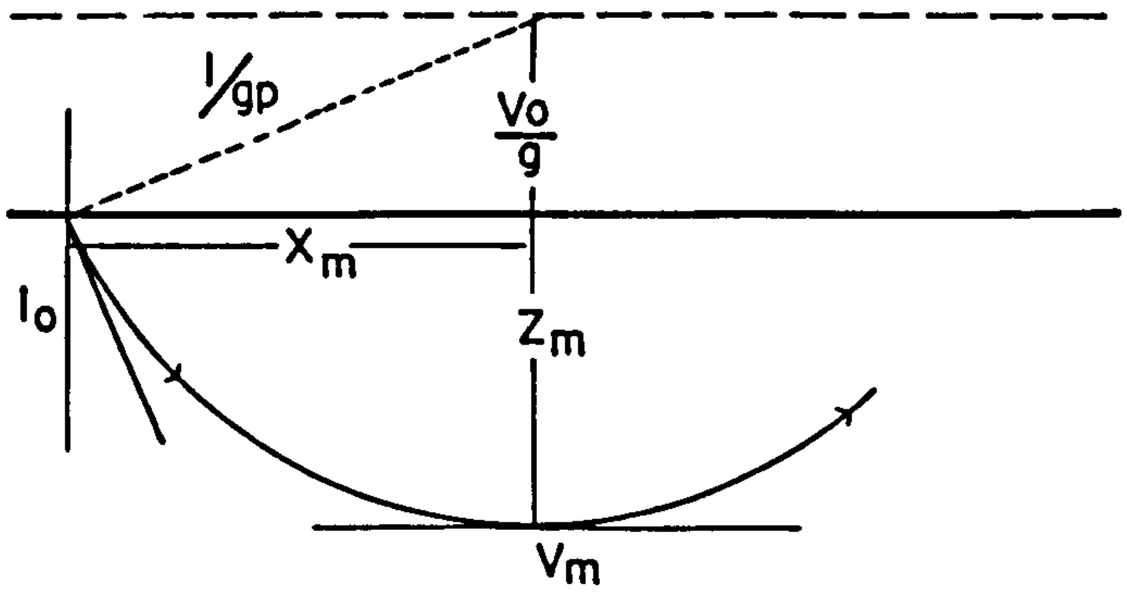

FIG BI-2

$$t = \frac{1}{g} \ln \left[\frac{(V_o + gz)(1 + \{1-p^2V_o^2\}^{\frac{1}{2}})}{V_o(1+\{1 - p^2[V_o+gz]^2\}^{\frac{1}{2}}}\right] \qquad \text{B(ii)}$$

The solution for x can be re-arranged to give

$$\left[x - \frac{(1 - p^2\ V_o^2)^{\frac{1}{2}}}{gp}\right]^2 + \left(z + \frac{V_o}{g}\right)^2 = \frac{1}{g^2p^2}$$

which is the equation of a circle of radius $(\frac{1}{gp})$ and centre at

$$\left[\frac{(1-p^2\ V_o^2)^{\frac{1}{2}}}{gp}\ ,\quad -\frac{V_o}{g}\right]$$

Let the deepest point of the ray be at $[x_m, z_m]$, at which

$$p = \frac{\sin i}{V} = \frac{1}{V_{max}} \qquad \text{B(iii)}$$

$$z_m = \frac{(V_{max} - V_o)}{g}$$

Normally we wish to calculate the travel time of a ray between shot and station X_{ij} apart. By substituting B(iii) into B(i) and B(ii),

$$V_m = \left[\frac{X_{ij}^2 g^2}{4} + V_o^2\right]^{\frac{1}{2}} \qquad \text{B(iv)}$$

and

$$T_{ij} = \frac{2}{g} \ln \left[\frac{V_m + (V_m^2 - V_o^2)^{\frac{1}{2}}}{V_o}\right] \qquad \text{B(v)}$$

(Proof after Slotnick (1959)).

BOX 2

Iterative Determination of a Non-critical Ray Through Anticlinal Refractor

Consider point P on the surface of the anticline, coordinates p,q (see Fig. B2.8a)

$$q = (r^2 - p^2)^{\frac{1}{2}}$$

$$\phi_i = \tan^{-1} \left(\frac{q}{p}\right)$$

$$\theta_i = \tan^{-1}\left[\frac{R + H - q}{X_i - p}\right]$$

Therefore the angle of incidence I_i, and refraction, I_r

$$I_i = |\phi_i - \theta_i|$$

$$I_r = \frac{V_r}{V_o} \sin I_i$$

Since the raypath through the anticline is the chord of a circle, the ray will be incident at both boundaries at the angle I_r. So, the length of the chord,

$$PU = 2R \cos I_r$$

and the slope of the chord,

$$\phi_{PU} = I_r - |\phi_i|$$

Thus the co-ordinates of the point U (u,v),

$$u = p + PU|\cos(\phi_{PU})|$$

$$v = q + PU.\sin(\phi_{PU})$$

So that,

$$\phi_j = \tan^{-1} \left(\frac{v}{u}\right)$$

And incline of ray segment UG, θ_j,

for $\phi_j < 0$ $\quad \theta_j = 180 - |\phi_j| - I_i$

$\phi_j = 0$ $\quad \theta_j =$ infinity (tan I_c used)

$\phi_j > 0$ $\quad \theta_j = \phi_j - I_i$

So we may calculate (X', Y_j) on the line $y=\tan\theta_j + C$, where

$$c = v - u.\tan\theta_j$$

Thus we may minimise X' w.r.t X.

BOX 3

Iterative Determination of Raypath Critically Refracted Along Surface of Anticline

Consider any point K on surface of anticline, co-ordinates n,m

$$m = (R^2 - n^2)^{\frac{1}{2}}$$

Angle of normal to surface at K, $\phi = \tan^{-1} (\frac{m}{n})$

Critical angle θ_c given by $\theta_c = \sin^{-1} (\frac{V_o}{V_r})$

So for the shot, the gradient of the incidence ray, $\theta_i = \theta_c - \phi_i$

And for the station where u<O

$$X_j < O \quad \theta_i = |\phi_j| + \theta_c - 180$$

$$X_j > O \quad \theta_i = 180 - |\phi_j| - \theta_c$$

and for u>O

$$\theta_i = \phi_j - \theta_c$$

So, gradient of ray segment SP $= \frac{(Y_i - q)}{(X_i - p)} = \tan \theta_i$

gradient of ray segment UG $= \frac{(Y_j - v)}{(X_j - u)} = \tan \theta_j$

Therefore $X'_{shot} = \frac{(Y_i - q + p \tan \theta_j)}{\tan \theta_j}$

and $X'_{station} = \frac{(Y_j - v + u \tan \theta_j)}{\tan \theta_j}$

Whence $(X' - X_{i,j})^2$ may be minimised to give the correct position of p,q and u,v.

Chord length D $D = \sqrt{(p-u)^2 + (q-v)^2}$

Angle bisected at centre, $\theta_r = 2\sin^{-1}(\frac{D}{2R})$

Therefore length of arc $PU = \theta_r(\text{rads}) - R$

CHAPTER THREE

DATA COLLECTION

3.1 Introduction

In all, four seismic refraction lines were deployed across the Derbyshire Dome (Fig. 3.1). These occupied three separate field seasons, each of about two months, during successive autumns from September 1979. This chapter discusses these experiments from inception to the acquisition of the raw data analysed in Chapter Four, and interpreted in Chapter Five. It falls into two main sections: firstly the general strategy of the method, and secondly the details of each of the four lines.

The equipment used throughout was largely supplied by the N.E.R.C. Seismic Pool. Two boxes for housing the Geostore recorders in the field and the portable recording apparatus were kindly supplied by the Geology Department of the University of Leicester.

3.2 The Method

Profiles of between 20 and 40 km long with seismic stations at intervals of 1.5 - 2.0 km were used, with due regard to possible depth and structure of the basement refractor, length and topography of the line, and the amount of equipment available. Obviously it would have been impractical to link such distances by cable, and extravagant to have recording apparatus at every station, so a system of central recording sites and telemetred outstations was adopted (see cartoon Fig. 3.2). This method also facilitated maintainance as the transmissions from the remote stations could be checked for reception at the recording sites. For the UHF radios used, the outstations had to be in line-of-sight for their signals to be received, so the recording stations were invariably situated on high ground.

FIG 3-1

SKETCH GEOLOGICAL MAP WITH STATIONS

Key

- Triassic
- Westphalian
- Namurian
- D_1 & above (Viséan)
- S_2 & earlier (Viséan)
- Line of Widmerpool Transition

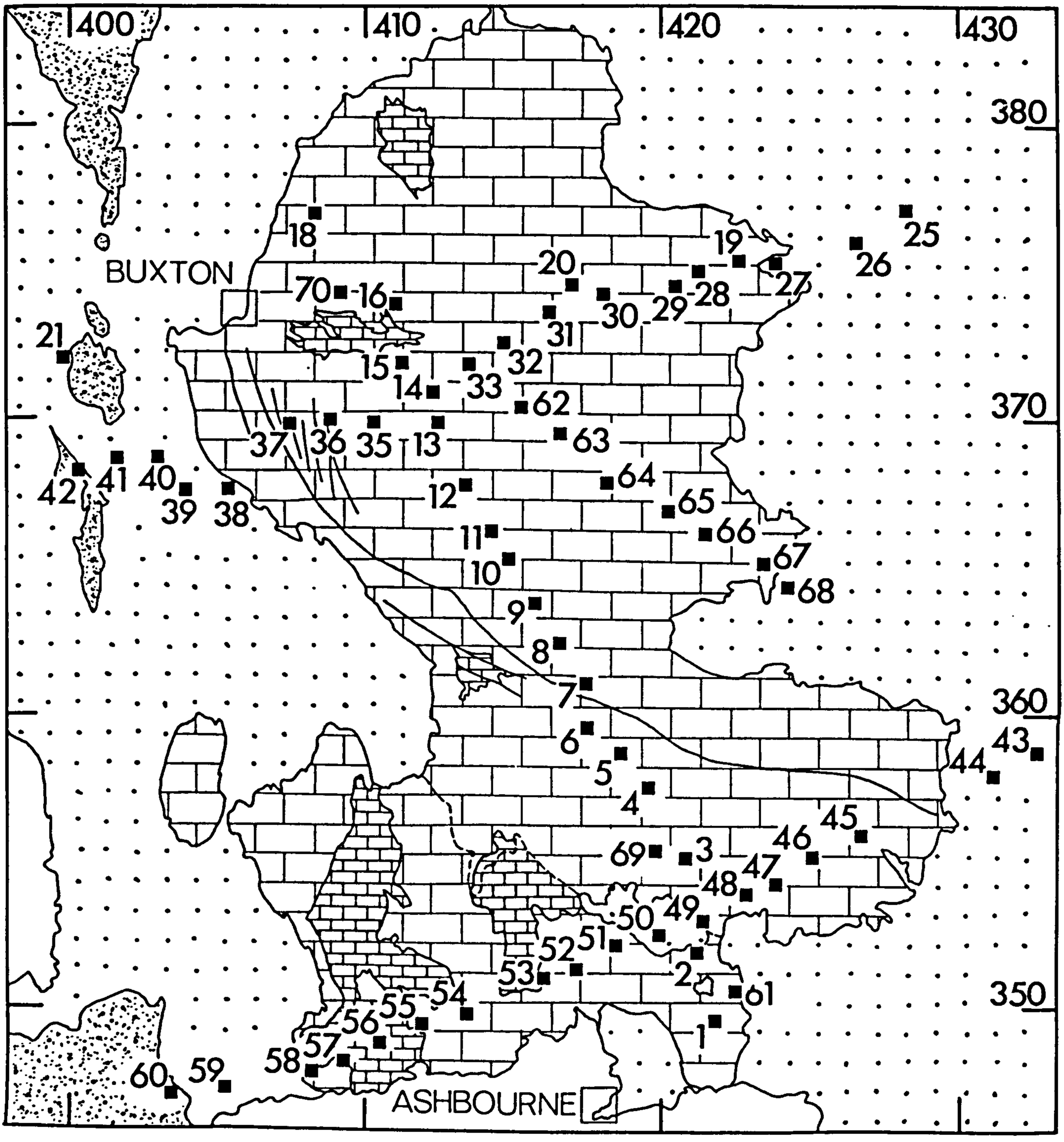

FIG 3-2 Scheme of experiment

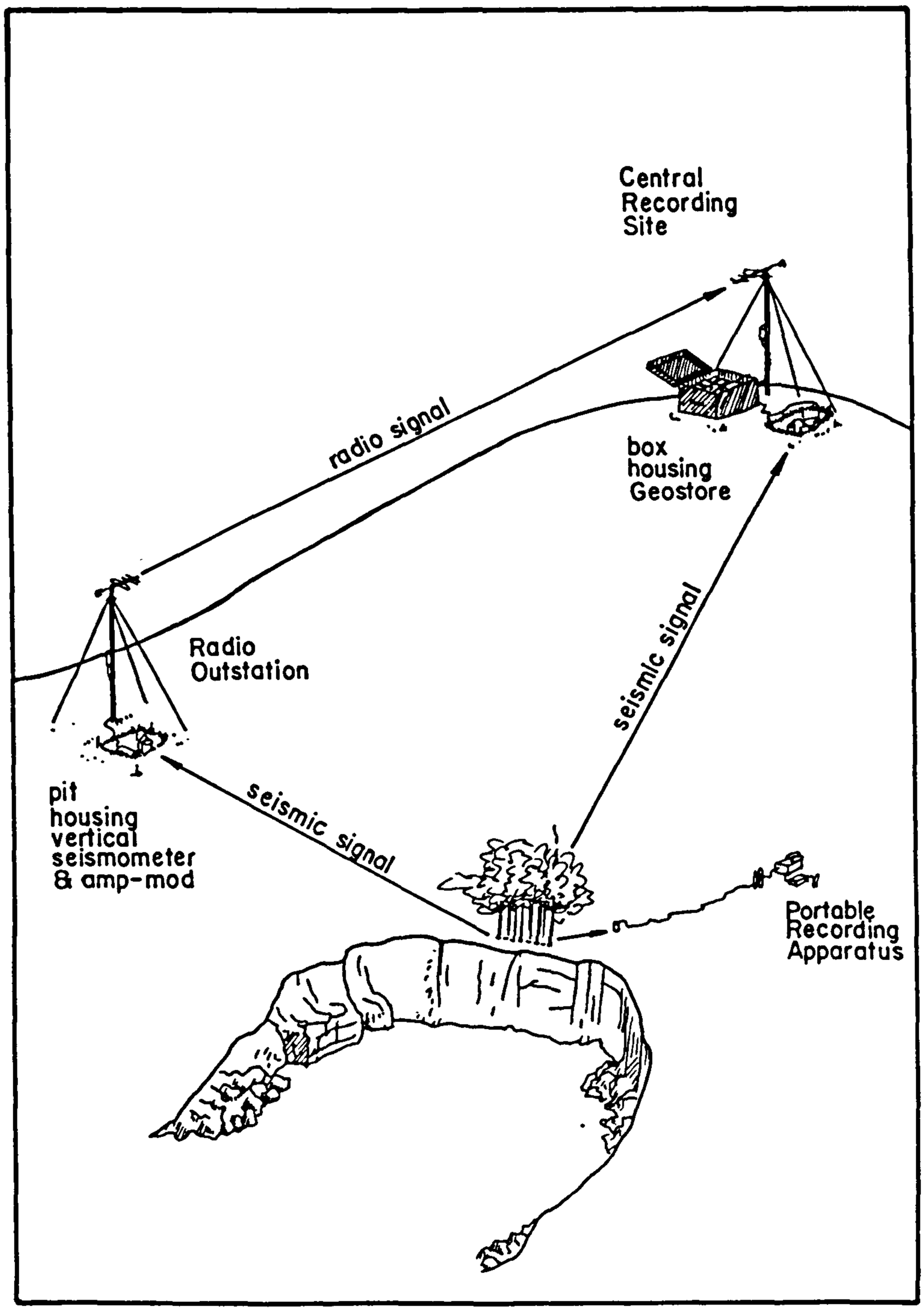

3.2.1 Equipment

Normally each station had a single vertical component Willmore MkIIIa seismometer whose resonant frequency was calibrated to 1Hz, the amplitude response for which is shown in Fig. 3.3 (Sensonics publ. no. HB 064). For the 1981 experiment, which was primarily a surface wave study designed by A McDonald (IGS Edinburgh), some three-component sets were used and the seismometer periods set to 1.5 Hz. Each seismometer had an Amplifier Modulator (amp-mod) which amplifies the signal according to one of ten possible gain settings (see Table 3-1; Racal Thermionic publ. no. DS102-1), and frequency modulates it at 676 Hz. For an outstation this signal was then transmitted betwee a UHF radio pair preset at one frequency between 458.5 and 458.75 MHz. All the seismometers were placed in covered pits: firstly to protect the instrument from the elements and reduce wind noise, and secondly to minimise waveform differences between stations due to poor seismometer coupling (O'Brien 1967). For the 1979 and 1980 seasons, the seismometers merely stood on soil, but in 1981 the base of each pit was concreted, and three-component sets placed on base-plates. To protect the terminal connections from moisture, the transmitter, receiver and amp-mod were covered with plastic bags and housed in the pit where possible.

The equipment was powered by 12V heavy duty batteries. The recording instrument used was the 14-channel Geostore (Racal Thermionic publ. no. D5104-1; Fig. 3.4), which can accommodate ten channels of data with two channels each for flutter and time. The recorder is designed for low power consumption and slow recording speeds; at a rate of 15/320 ips an analogue magnetic tape runs for about six days in unidirectional mode, which is a convenient interval at which to check the site (twice this recording period is obtained for half the maximum data channels when recording bimodally). At this speed the recording is made with a high frequency cut-off at about 16 Hz, as shown in Fig. 3.5. For security and protection from weather and livestock, the Geostores were locked in sturdy boxes.

Table 3-1

Amplifier Modulator Gains

Input voltages required to give full output deviation of ±40%

Gain setting	Voltage (±mV)	Gain setting	Voltage (±mV)
1	250	6	5
2	100	7	2.5
3	50	8	1
4	25	9	0.5
5	10	10	0.25

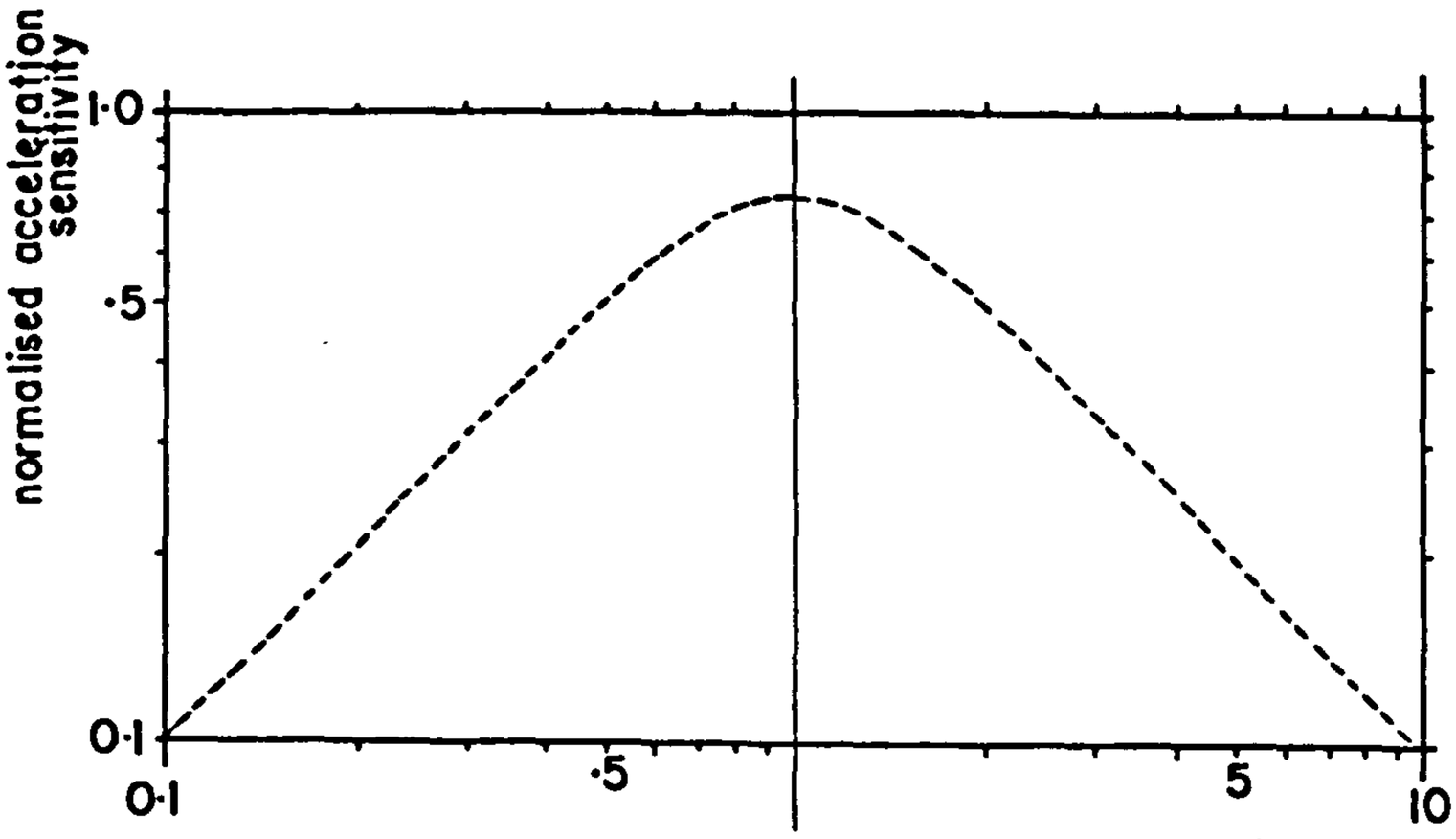

FIG 3-3 Amplitude response for Willmore Mk IIIa, damping factor 0·7, centre frequency 1Hz (from Sensonics publ. no. HB 064)

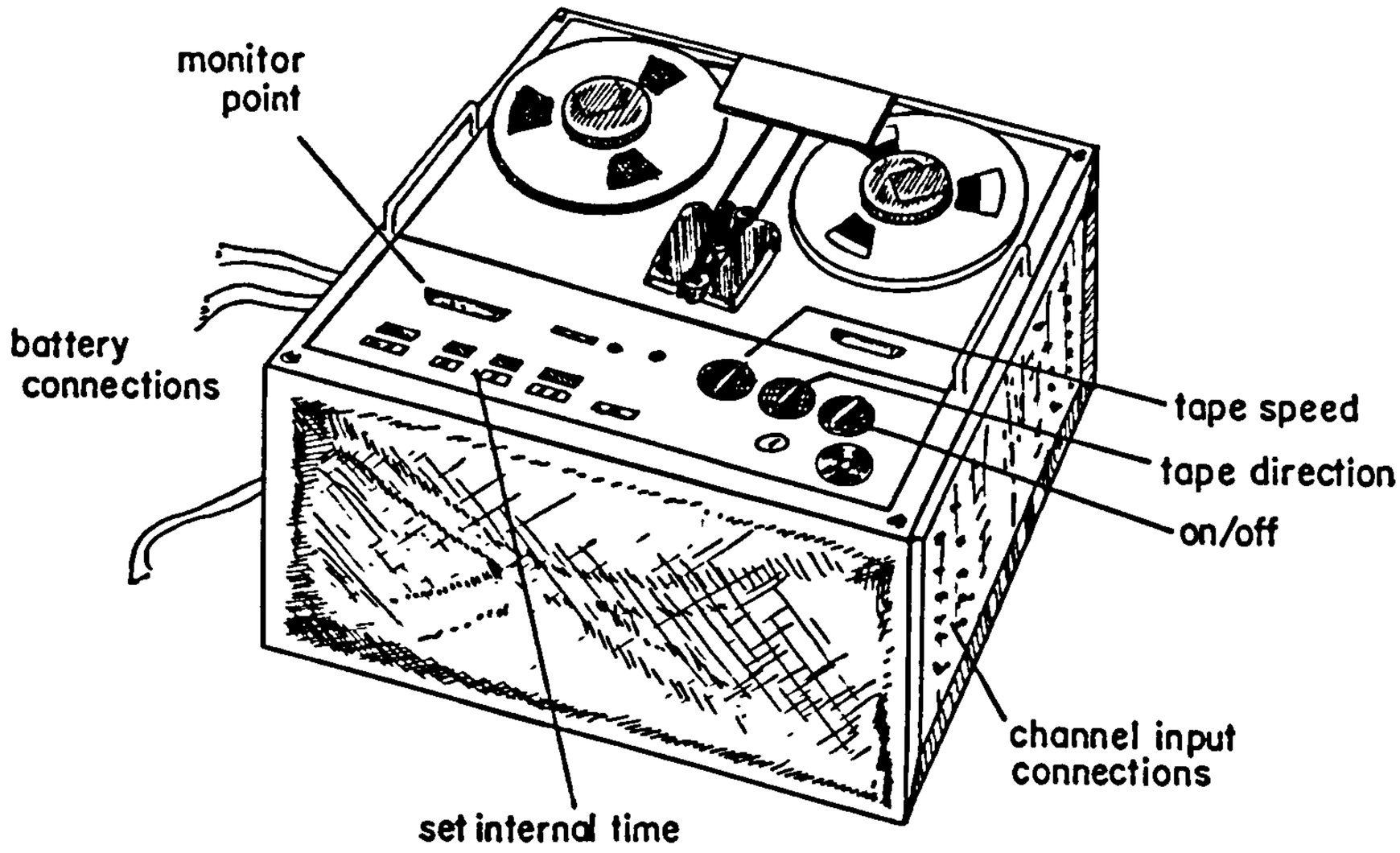

FIG 3-4 Geostore field recorder (schematic)

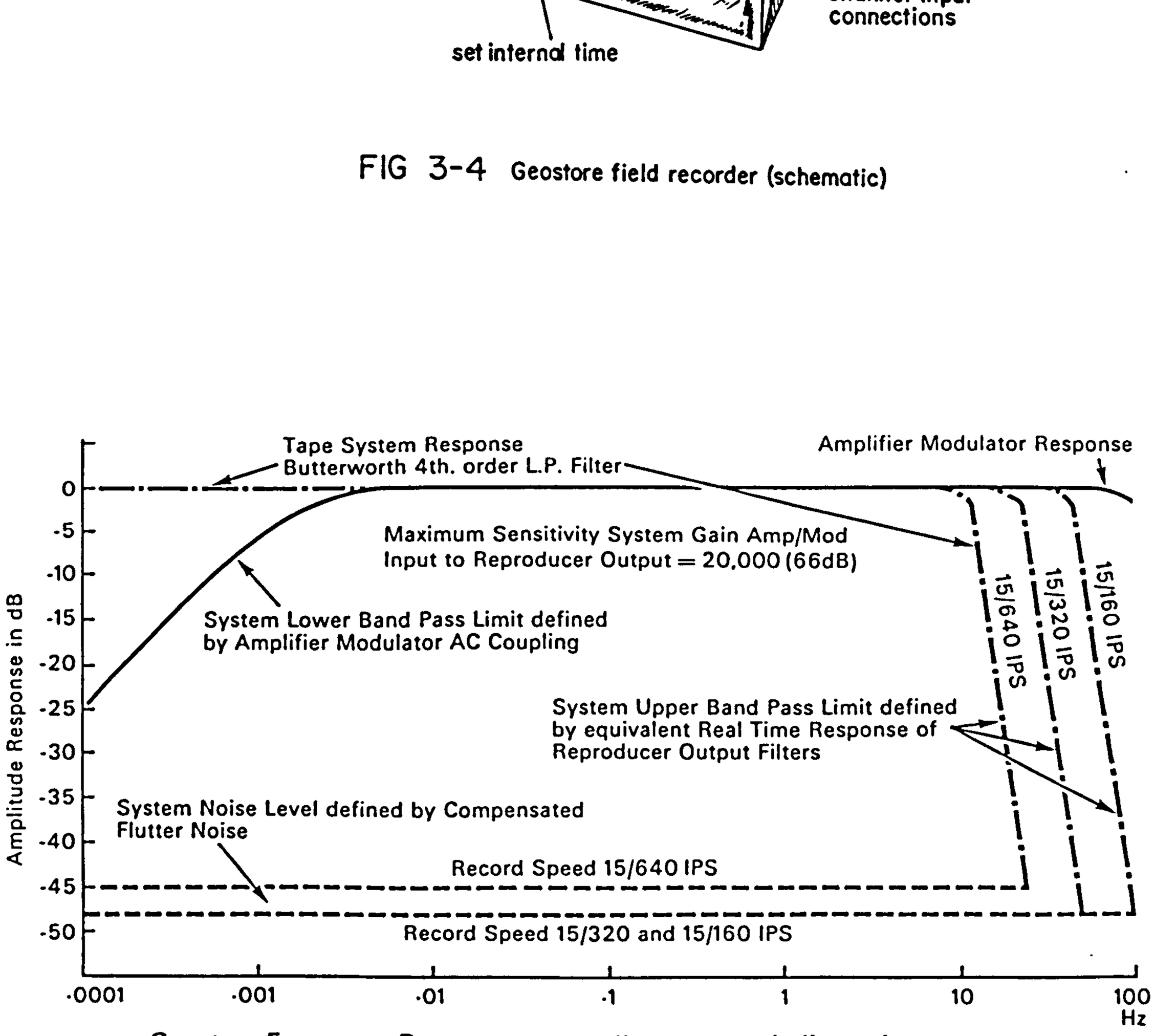

Geostore Frequency Response – overall system excluding seismometer

FIG 3-5 (from Racal-Thermionic publ.3027-2)

In addition to seismic data, two time channels were recorded: the Geostore internal clock, which is standard Vela encoded, and the MSF time broadcast from Rugby, which is also encoded (Wireless World, July 1978; see Fig. 3.6) and for which a small receiver is required. Consequently MSF time was recorded by all Geostores, and has thus been used as the standard clock. When each Geostore was started, the internal clock was set as closely as possible to MSF time so that events on contemporaneously recorded tapes could be easily found on playback.

Once deployed, the instruments were maintained for the duration of the experiment, data being recorded continuously. During this period, quarries were visited for timing and locating blasts. The portable timing apparatus comprised a small tape recorder, an HS10 seismometer, an amp-mod and a good length of cable to separate the equipment from the shotpoint. For the 1979 season, a Uher reel-to-reel tape recorder was used, and in subsequent seasons a cassette-based system. The time was recorded from an MSF receiver.

3.2.2 Design of Profiles

The profiles were mainly chosen on geological grounds, although other factors had to be taken into consideration, including

a) Reversal of the line, ideally by shot points at each end. This study is limited by the distribution of working quarries on and close to the limestone outcrop, shown in Fig. 3.7. There are about thirty quarries which blast regularly, half of which shoot more than once weekly.

b) Geological control, from deep boreholes (see Fig. 1.7), etc.

c) Geophysical control: for this survey key stations were re-occupied to tie profiles into one another, particularly station 14 (34) which was operative for all the lines. Furthermore, two stations on the 1979 north-south line re-occupied

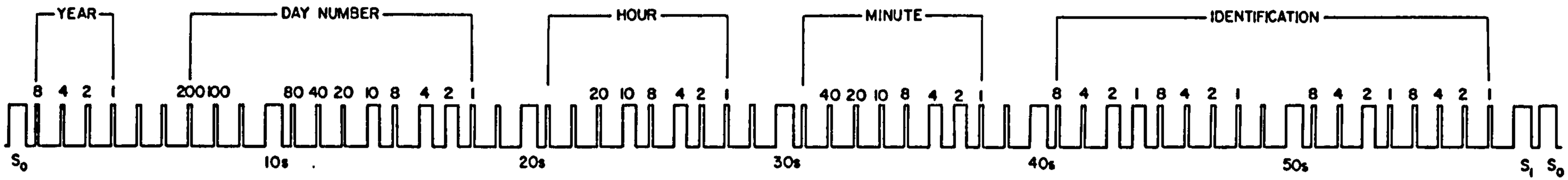

Internal clock-Vela code

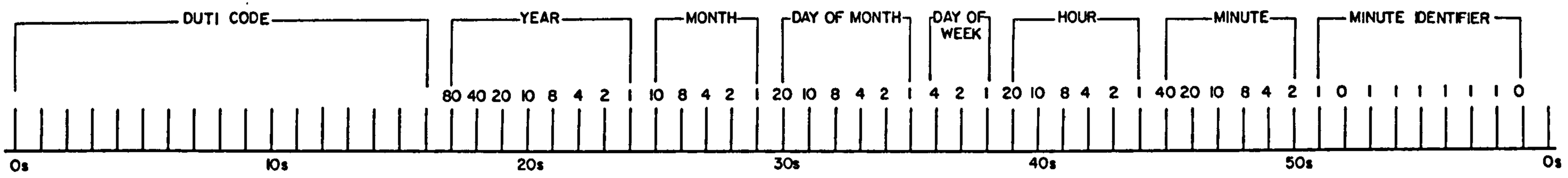

MSF slow code

FIG 3-6

FIG 3-7

QUARRY DISTRIBUTION

Boreholes

C Caldon Low E Eyam W Woo Dale

sites on the University of Leicester's Charnwood-Ballidon profile (see Section 3.3.1).

d) Geography: urban areas like Buxton and Ashbourne were far too noisy, while the hilly terrain of the Dark Peak District to the north and west of the limestone outcrop was largely avoided because suitable stations in line-of-sight would have been difficult to find.

The length and direction of the profiles having been decided, the positions of central recording sites and outstations were chosen in that order from the 1:50,000 O.S. map, from which topographic sections were drawn to test lines-of-sight. Potentially noisy sites were avoided: viz close to large farmsteads, main roads, windy copses, etc., and where possible stations were planned where most accessible by road or track: with insufficient manpower, for example, it would have been totally impracticable to carry the artifacts of a Geostore site more than 500m, or an outstation more than 2 km.

For ease of interpretation, the profiles were designed to be as straight as possible with equi-spaced stations, but where this was difficult to achieve, it was thought better to tolerate slightly crooked profiles than include substantial gaps between adjacent stations, especially where the lines were perpendicular to the geological structure.

3.2.3 Deployment of line

The first stage concerned the permissioning of sites chosen from the map, at the same time as which the pits were prepared and lines-of-sight tested (where questionable) using a spare radio pair. Since the Geostore receiving sites were central to the strategy of each line, and required greater security, they were normally established first.

Station locations changed between map and field for several reasons: the quantity of equipment required was sometimes not available, some sites were not easily accessible, landowners were not found, and permission was (rarely) refused.

More often than not, the station position was determined for maximum protection from livestock; the mast is the most exposed item of an outstation, for which reason it was commonly placed against a wall, hedge or even old farm machinery. Dry stone walls provided excellent ties for mast guys.

Before installation the equipment was checked and radio frequencies were assigned to outstations. In the case of duplicated frequencies, the transmitters were placed as far apart as possible and beamed in opposite directions; since the receivers have a phase-lock loop only the stronger signals received at each Geostore were recorded. For transmission over long distances, or for poor lines-of-sight, more powerful ten element Yagi antennae were used instead of the usual three element.

The amp-mods were normally set to a gain as high as the ambient noise would allow. For stations on the Carboniferous the gains were invariably set to seven, while the noisier stations on the Permo-Triassic to the west required lower amp-mod gains (see Section 3.3.2). These gains were sufficient to record quarry blasts, local earthquakes and teleseisms alike, although for some timed shots the gains at stations nearest the quarry were temporarily turned down in order to prevent overloading.

Every outstation was checked using a field test box as soon as it was installed, whereupon any mis-connections were soon discovered. Battery voltages and power drain were also checked with an avometer, and the aerial direction noted before leaving the site, although for a good line-of-sight the system can easily tolerate a ten degree mis-alignment. However, the ultimate test of operation is made at the Geostore itself, where the test box can monitor the channels being recorded. This was the easiest means of checking a group of outstations and was done every time the recording site was visited, saving considerable travel.

3.2.4 Maintainance of the Experiment

Maintainance divided between upkeep of the profile and visiting quarries with the portable shot-time recording equipment. Most of the upkeep comprised changing batteries and Geostore tapes; the central recording sites were visited at least every six days, while, depending upon the state of the batteries, outstations were visited every seven days or so. Any outstations found not being received, however, were investigated immediately. Most instrumental problems occurred during the initial stages of each profile, while later failures were often due to bad weather: for example, flooded pits and masts blown down by the wind. With the experience, diagnostic ailments were quickly recognised, and it was normally more efficient to replace faulty equipment with spares, where available, than attempt repair in the field.

When possible, the magnetic tapes were monitored as soon as they were recorded by playing them back on a Racal Storel4 replay system. Thus station performances and problems could be judged straightaway, and the necessary steps taken to improve poor sites, essential during the early stages of each profile.

For timing quarry blasts arrangements were always made beforehand with manager and foreman. Usually the appointments were made days in advance so that a time-table could be constructed. However, bad weather often brought forward or postponed shot times, and occasionally arrangements conflicted with essential on-line maintainance.

The normal shot configuration is a line of equal-spaced holes parallel to, and a couple of metres behind the quarry face (see section 3.2.6 and Fig. 3.2); the HSlO seismometer was usually placed about ten metres behind the holes, depending upon the size of the blast, and beside the shot nearest the profile. Its amp-mod was set to the lowest gain so that the first ground motion could be recorded without overloading. The location of each blast was determined to within 50m through taking compass bearings on local landmarks.

3.2.5 Dismantling the Array - Calibrations

Obviously stations were not dismantled before their positions were known; the 1:25,000 O.S. maps with field boundaries were sufficiently accurate to locate sites to within 10 m, which is equivalent to a timing error of about 2ms.

Before each station was dismantled, the seismometer was first calibrated in situ to normalise the amplitude response by passing a 4mA step impulse into the amp-mod at each of the gains used. These calibrations were then recorded at the Geostore before each site was taken out, leaving those seismometers at the Geostore site itself to be calibrated last.

Finally, because Geostore recording heads may be orientated slightly differently from Storel4 playback heads (see Section 4.3), an impulse was recorded via an amp-mod on either pairs of channels, or all channels simultaneously for each Geostore. These signals were later played out on the Storel4 used for digitising, so that the required corrections could be determined.

3.2.6 Quarry Blasts as Seismic Sources

Quarry blasts are not ideal seismic sources for a variety of reasons, including,

a) their distribution and times of occurrence cannot be controlled to suit the experiment,

b) most of the energy is used in fragmenting the rock, and

c) the source signature is normally quite complicated.

A typical quarry blast in the area comprises 10-20 holes linearly and equi-distantly spaced parallel to the working face (see Fig. 3.2); the shot holes are commonly 10-30m deep, 12-16m apart and 10m behind the face. Only few quarries fire the shots simultaneously, while most 'ripple' shoot by inserting a small (17-34ms) delay between each detonation; this

minimises ground vibration (and hence effect on the environment), and helps to fracture the rock more efficiently. Ripple shooting may result in a blast lasting several tenths of a second, the effects of which on P waves have been investigated by Greenhalgh (1980).

The size of blasts varies between tens of kilogrammes for stump shooting (clearing the remnants of a previous shot), to several tonnes in the larger quarries such as Tunstead and Dow Low.

3.3 Seismic Refraction Profiles Across the Derbyshire Dome

In total, about seventy stations were established in the area (see Fig. 3.1). These were occupied per profile as follows:

Season	Profile	Station nos.
Autumn 1979	North-South	1 - 18
"	Stoney-Middleton-Holmes Chapel	19 - 24
Autumn 1980	Northern East-West	25 - 42, 51
"	Southern East-West	43 - 60, 34
Autumn 1981	DASED 1 & 2	61,49,69,4,6,8,10 12,14,70
		62 - 68

(For the 1980 experiments, station 34 re-occupied the 1979 station 14). The co-ordinates, heights and station names for all these sites are given in Table 3-2.

Table 3-2 Station details

Station	Site	Easting	Northing	Height (m)
1	Madge Hill	421.7	349.67	289
2	Haven Hill	421.13	351.94	274
3	Ballidon Moor	420.6	355.18	264
4	Roystone Grange	419.47	357.5	326
5	Gotham	418.53	358.67	354
6	Aleck Low	417.38	359.52	400
7	Frieden Grange	417.38	361.	289
8	Roman Road	416.46	362.38	337
9	Arbor Low	415.73	363.79	354
10	Highlow Farm	414.72	365.3	341
11	Endmoor Lane	414.21	366.16	314
12	Moor Lane	413.37	367.71	309
13	Townhead	412.5	369.83	301
14	Fivewells Farm	412.28	370.86	430
15	Calton Farm	411.21	371.88	343
16	Old Moor	410.78	373.88	337
18	Bibbington	408.32	376.99	351
19	Stoney Middleton	422.54	375.38	234
20	Litton	416.93	374.52	305
21	Cat & Fiddle Inn	399.79	372.1	485
22	Moss House	390.07	370.29	155
23	Gorsley Farm	384.87	369.26	100
24	Twemlow	378.3	369.19	65
25	Barbrook Res.	428.15	377.12	327
26	Big Moor	426.5	376.0	355
27	Knouchley Farm	423.8	375.63	180
28	Highfields	421.24	375.37	310
29	Black Harry Hs.	420.34	374.49	321
30	Wardlow Hay	417.98	374.21	320
31	Littonslack	416.18	373.58	290
32	Bull Tor	414.55	372.53	305
33	Priestcliffe	413.46	371.83	367
34	Fivewells Farm	412.28	370.86	447
35	Fardtich Farm	410.24	369.9	328
36	Brierlow Bar	408.9	370.1	310
37	Hillhead Farm	407.46	369.77	385
38	Booth Farm	405.52	367.89	387
39	Sycamore Bank	403.96	367.64	445
40	Axe Edge	403.02	368.66	503
41	Three Shire Head	401.55	369.56	427
42	Cut-thorn Hill	400.36	369.06	391
43	Dethick	432.53	358.78	206
44	Bilberry Knoll	431.02	357.9	383
45	Old Quarry	426.67	355.86	358
46	Harborough Hill	425.08	356.15	360
47	Western Lane	423.725	354.27	320
48	Brassington	422.715	353.86	229
49	Bradbourne	421.355	352.99	221
50	Lea Hall	419.83	352.5	160
51	Wibben Hill	418.375	352.23	249
52	Blue Bell Inn	417.07	351.4	229
53	Thorpe	415.98	351.025	210
54	Blore Hall	413.34	349.82	227
55	Waterings Farm	411.85	349.5	319
56	Miles Knoll	410.45	348.9	304
57	Rue Hill	409.12	348.1	293
58	Cauldon Low	407.67	347.71	360
59	Blakely Farm	405.18	347.27	291
60	Evesford	403.39	347.03	180
61	Winn Farm	422.25	350.969	291
62	Taddington	415.425	370.169	362
63	Manor House	416.775	369.293	331
64	Bole Hill	418.368	367.61	354
65	Over Haddon	420.407	366.769	253
66	Haddon fields	421.738	366.14	203
67	Bowers Hall	423.775	365.04	113
68	Stanton-in-the-Peak	424.53	364.375	263
69	Ballidon	419.73	355.06	240
70	Tunstead	409.42	373.72	335

3.3.1 The North-South Profile

The line was principally planned to link the Charnwood-Ballidon profile with the southern termination of LISPB (see Fig. 1.1). It was designed to pass the Woo Dale borehole, and to be reversed between Doveholes and Ballidon quarries (Fig. 3.7). As such, the profile was 31km long and comprised seventeen single, vertical component stations all on the limestone outcrop.

The geological section of the line is shown in Fig. 3.8. Much of the profile lies within the massif facies; stations 1 and 2 alone were south of the Dovedale Transition. The line crossed the Bonsall Fault between stations 6 and 7, and Woo Dale lay between stations 15 and 16.

Sources along the line of the profile included Doveholes, Tunstead and Ballidon quarries. Eldon, Dow Low and Longcliffe were close broadside quarries, while those of Cauldon, Matlock and Wirksworth formed more distant broadside sources (see Fig. 3.7). Since no quarries lay immediately south of stations 1 and 2 (and those of Leicestershire were too far south to record), a controlled shot at Shirley was detonated in collaboration with the Geology Department of the University of Leicester in order to reverse this section of the line. The shot at [42329 33889] (see Fig. 1.1), comprised three 20m deep drill holes, each containing 40kg of explosive.

Since the topography was fairly gentle along this section, only two receiving sites were required for the line: at Fivewells Farm (station 14), which recorded data from stations 9 to 18, and at Aleck Low (station 6), which was central to stations 1 to 8, but which was slightly off line. (Station 17 was planned, but was never installed.)

Stations 1 and 2 re-occupied stations 7 and 4 of the Charnwood-Ballidon profile, for which reason they were established a little off line. Stations 3, 15, and 18 were close to Ballidon, Topley Pike and Doveholes quarries respectively, and were therefore a little noisy at times; for an unknown

FIG 3-8

GEOLOGICAL SECTION – NORTH-SOUTH LINE

Vertical exaggeration x2

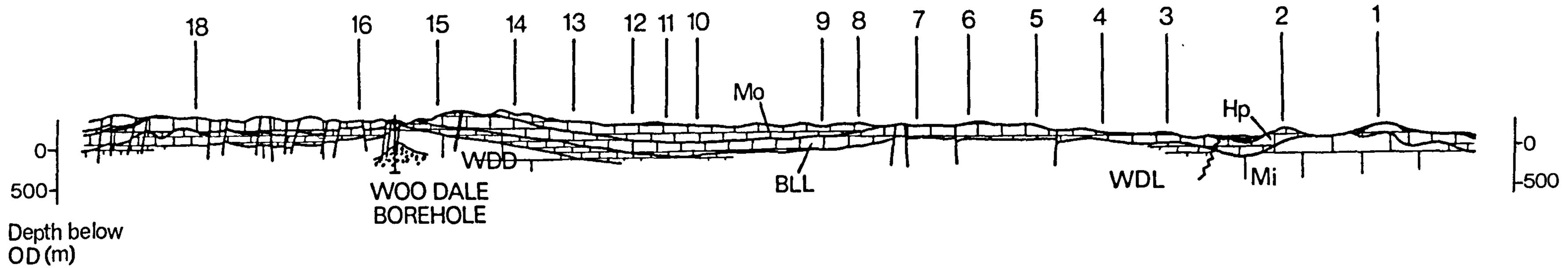

(WDD Woo Dale Dolomite WDL Woo Dale Limest. BLL Bee Low Limest. Mo Monsal Dale Limest. Hp Hopedale Limest Mi Milldale Limest)

reason, station 18 was atypically sensitive and commonly gave an anomalous signal. Other noisy stations were 7 and 9; the former of which was near the Freiden Grange brickworks, and the latter beside a windy copse. Station 16 never worked satisfactorily owing to instrument problems, but all the other sites proved to yield excellent signal-to-noise ratios.

The area was found seismically quiet enough for the amp-mods to be normally set at gain seven. Gains of four were set at the nearest stations for one timed shot each from Tunstead and Ballidon; there were two other timed shots at Wardlow and Hindlow. The experiment ran from 6th September to the 13th October 1979, during which each Geostore recorded six tapes.

3.3.2 Stoney Middleton-Holmes Chapel Line

This profile (see Fig. 3.9) was intended firstly to provide a cross-arm with the North-South profile for a teleseismic T-shaped array, and secondly to test the feasibility of a sixty kilometre refraction line from the Derbyshire Dome into the Permo-Triassic Cheshire Basin (see Fig. 1.1), intended to be deployed the following season but which was never followed up.

The line consisted of six stations about seven kilometres apart, with a substantial gap across Buxton. Stations 22 to 24 lay west of the Red Rock Fault, and transmitted eastwards to a Geostore at station 21, much higher up near the Cat and Fiddle Inn. Stations 19 and 20 both broadcast north to an offline receiving site at Eyam Edge, which had no seismometer.

All stations employed a single, vertical seismometer with amp-mods set at gain seven for stations on the Carboniferous, while west of the Red Rock Fault the stations required gains of only four, though they were established in fairly secluded surroundings. Therefore the ambient noise was approximately ten times greater in the Cheshire Basin.

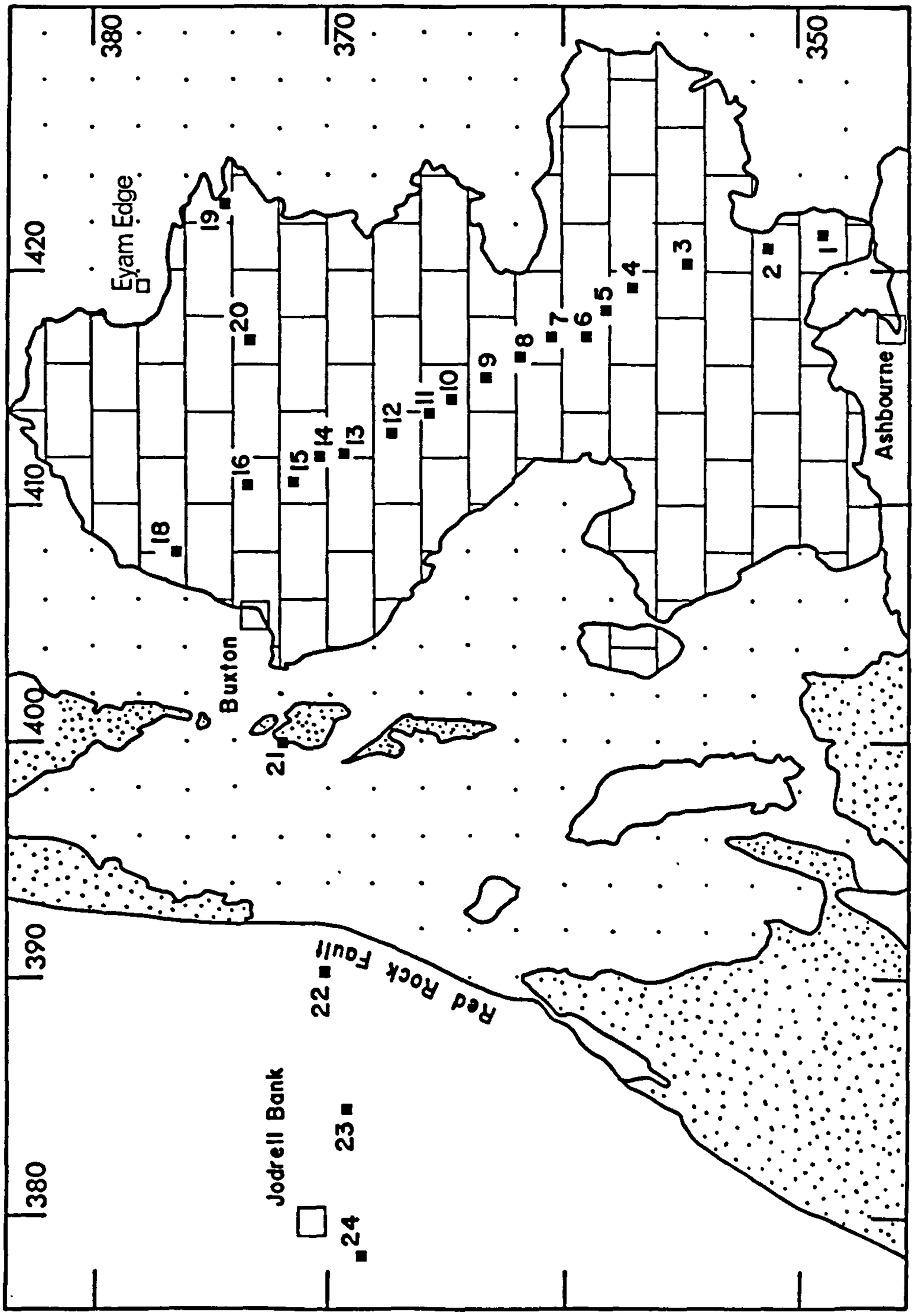

FIG 3-9 Stoney Middleton—Holmes Chapel line

The profile was maintained in full from 25th September to 13th October. From the 14th to 28th October four single station Geostore sites were retained at stations 1, 12, 19 and 24 in order to record teleseisms, for which reason a three-component station was further maintained at Moor Lane barn (station 12) from November 1979 to April 1980.

3.3.3 Northern East-West (NEW) Profile

This profile was established to investigate the structure of the Dome orthogonal to the north-south line, and between the Woo Dale and Eyam boreholes. The section was reversed between Stoney Middleton and Hind Low quarries, and station 34 re-occupied station 14 of the 1979 experiment. This line was the first of two east-west profiles of the Dome deployed during the 1980 season.

Being 33 km long, the profile completely spanned the limestone outcrop (section Fig. 3.10), and of its eighteen stations five were located on the Millstone Grit. The outer stations were deployed over postulated deep Dinantian basins: the Edale Gulf in the east (stations 25 and 26), and the Goyt Trough to the west (stations 40-42). Like the north-south profile, a basement high was expected in the region of Woo Dale.

Four Geostore recording sites spanned the line: on Big Moor (station 25) which received station 26, on Eyam Edge (without seismometer) which accommodated stations 27 to 30, at Fivewells Farm (station 34) which recorded stations 32 to 37, and on Axe Edge (station 40) for stations 38 to 42. A further single-site Geostore was at station 51 on the Southern line (see Fig. 3.1), for purposes of linking both lines, aiding the location of untimed blasts, and to form a wider aperture teleseismic array.

The profile was kinked about station 39 because of the difficult topography on the Millstone Grit. Stations 37 and 28 were situated near Hindlow and Stoney Middleton quarrie

FIG 3-10

GEOLOGICAL SECTION – NORTHERN LINE

Vertical exaggeration x2

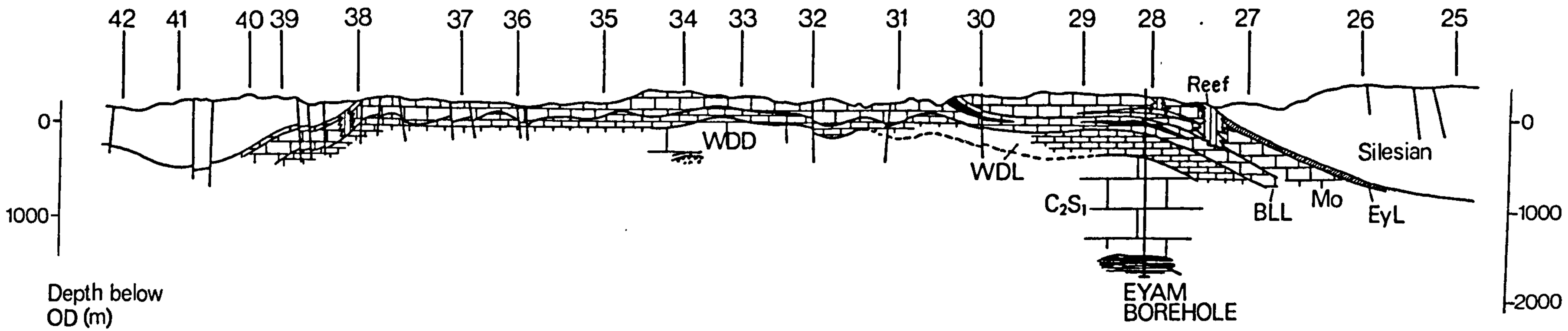

respectively, although these, in common with all the other stations, were relatively quiet and yielded excellent signal to noise ratios.

All the sites were occupied by single, vertical component seismometers; the amp-mod gains were permanently set to seven. The line was maintained from the 7th to the 28th October 1980, during which time three tapes were recorded at each Geostore, and eight blasts were timed and positioned: from Cauldon, Stoney Middleton, Dene, Middlepeak, Ballidon, Tunstead, Longcliffe and Dow Low.

3.3.4 Southern East-West (SEW) Profile

The southern East-West profile was planned to investigate the geology across the Dovedale Transition (Fig. 3.1), and the nature of the sandstones in which the Caldon Low borehole terminated. As such the line was designed to span the entire limestone outcrop, and to be reversed between the quarries of Dene (Wirksworth) and Cauldon (Fig. 3.7). As the Bouguer anomaly map suggests (see Section 1.3.2), the profile was expected to cross shallow basement. The geological section is drawn in Fig. 3.11.

The line was deployed during the same field season and directly after the NEW profile, with one station (34) maintained in common for the same reasons as station 51 was previously. This profile also comprised eighteen stations, and was 33km long. The topography along line was quite gentle and a straight profile was easily planned. Four Geostore sites were sufficient: at Bilberry Knoll (station 44) to which station 43 broadcast, the Old Quarry (station 46) which recorded stations 45 to 48, Wibben Hill (station 51) for stations 49 to 53, and Cauldon Low (station 58) which served stations 54 to 60.

The gap between stations 44 and 45 was to avoid Wirksworth, and that between stations 53 and 54 was due to the Manifold Valley. As for the northern line, all amp-mod

FIG 3-11

GEOLOGICAL SECTION — SOUTHERN LINE

Vertical exaggeration x2

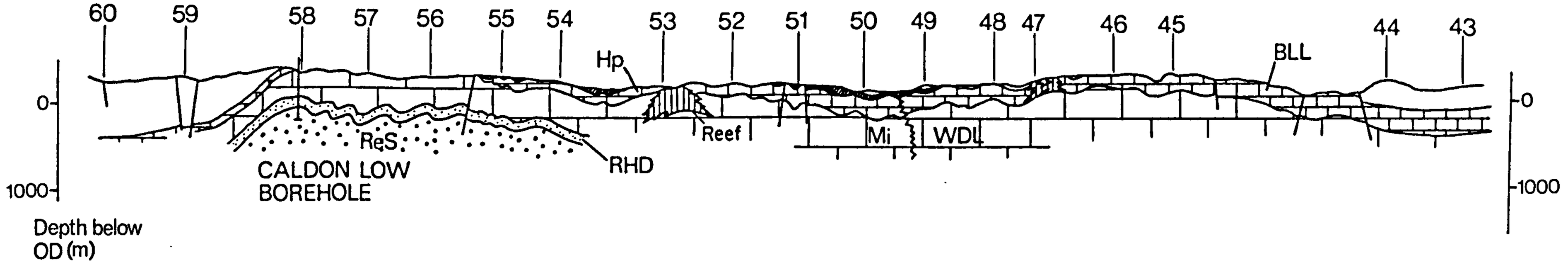

gains were permanently set at seven, and each station had a single vertical seismometer.

Five quarry blasts were timed and recorded during the three weeks this line was maintained, from 30th October to 19th November 1980. The northern quarries provided distant broadside sources, while all the sourthern quarries were either on-line or closely on-line.

Unfortunately, this line was plagued with bad weather and instrument problems. Of the stations on the Millstone Grit, only station 59 ever worked; stations 54 and 55 never operated satisfactorily, and the Old Quarry Geostore only worked during the last week. The only complete records, therefore, are for the Cauldon Low and Wibben Hill Geostores.

Additionally the poor weather also affected quarry blasting, and several quarries reduced their programmes.

3.3.5 DASED1 and DASED2

This experiment was primarily designed by A McDonald (University of Leeds, and IGS Edinburgh; his acronyms for these profiles are retained for convenience) for the study of surface waves; thus the seismometer periods were extended to 1.5s, and the average station interval to about two kilometres. DASED1 and DASED2 radiated south from Tunstead Quarry, DASED2 being about thirty degrees east of DASED1 (see Fig. 3.1) DASED1 largely re-occupied the even numbered stations of the 1979 north-south line, but with the southern end straightened out with three new stations: 69, 49 (in common with SEW), and 61. DASED2 was a shorter profile (only 14km long), and was reversed between Tunstead and Shining Bank quarries.

The lines comprised five Geostore sites: Winn Farm (station 61, for stations 61, 49 and 69), Aleck Low (for stations 4, 6 and 8), Fivewells Farm (for stations 10, 12, 14 and 70), Blore Hill (recording stations 62 to 65), and Stanton-in-the-Peak (for stations 66 to 68). Three component sets were installed at stations 61, 6, 14 and 64. Station 70

comprised an HS10 seismometer situated on the western perimeter of Tunstead Quarry, to aid location of Tunstead shots and to record other quarries for shot-shot reciprocal times.

The experiment ran from 20th October to 10th December 1981. The amp-mod gain history was varied to prevent over-loading of surface waves recorded from timed and located shots, of which there were twenty-one from various quarries, including ten from Tunstead alone.

CHAPTER FOUR

DATA PROCESSING

4.1 Introduction

The three years' experiments were recorded on seventy-five analogue magnetic tapes, comprising about 10,800 Geostore hours' data. In all, about 950 separate, good quality events were detected, of which about 850 were quarry blasts, 29 global earthquakes and the remainder local earthquakes (most of which were from the Mansfield region). Of the total, 800 or so events were digitised, multiplexed and written to digital tape at IGS Global Seismology Unit (GSU), Edinburgh. This chapter describes the processing of these data into a form suitable for their interpretation and the discussion of velocity-depth models in Chapter Five.

Essentially, this chapter comprises five sections:

1. The data set
2. Digital processing
3. Picking of onset times
4. Location of untimed events
5. Global earthquake data.

All sections except 4 apply to the teleseismic data recorded during the experiments.

4.2 The Data Set

In basic form the data exists on the analogue magnetic tapes recorded in the field; a listing of these per Geostore per experiment is given in Table 4-1. The first step in processing these data was the compilation of an events catalogue: a tape by tape listing of events recorded, including times of occurrence, types of signal and quality of recording. After each field season the tapes were monitored on a system originally

Table 4-1 Summary of Geostore tapes per experiment
Tape codes include experiment number; N is the number of good quality events recorded

1979			NEW			SEW			1981		
Tape codes	Day numbers	N	Tape codes	Day numbers	N	Tape codes	Day numbers	N	Tape codes	Day numbers	N
A1,F1,MG1	248-251	32	AX11,E11,F11, B11	281-288	29	C21,W21,F21	304-311	21	F31,A31,BH31, WN31,S31	293-300	56
A2,F2	253-259	66	AX12,E12,F12, B12,W12	288-295	33	C22,W22,F22	311-318	33	F32,A32,BH32, WN32,S32	300-307	41
A3,F3	259-265	60	AX13,E13,F13, B13,W13	295-302	24	C23,W23,Q23, BK23	318-323	22	F33,A33,BH33, WN33,S33	307-313	52
A4,F4,E4,CF4	265-272	75	AX14,F14,W14	302-305	15				F34,A34,BH34, WN34,S34	313-320	44
A5,F5,E5	272-278	98							F35,A35,BH35, WN35,S35	320-327	40
A6,F6	278-281	62							F36,A36,BH36, WN36,S36	327-335	46
A7,F7	281-286	86							F37,A37,BH37, WN37,S37	335-342	40
ML1,MG2	286-296	135							F38,A38,BH38, WN38,S38	342-344	16

Tapes: A Aleck Low, AX Axe Edge, B Barbrook Reservoir, BH Bole Hill, BK Bilberry Knoll, C Cauldon Low, E Eyam Edge, F Fivewells Farm, MG Madge Hill, ML Moor Lane, Q Old Quarry, S Stanton-in-the-Peak, W Wibben Hill, WN Winn Farm

devised by G. Neilson (GSU Edinburgh), shown in Fig. 4.1. Normally tapes from the Geostore site with the most complete recording history and the quietest stations were chosen to be monitored; this assumed that any event not detected at this site was not worth considering.

Four seismic channels could be monitored during replay: two on the oscilloscope screen, and one to each channel of the stereo headphones (see Fig. 4.1). The ear is far more sensitive in discriminating between noise and signal than the eye and demands less concentration: an event is perceived when a signal is heard simultaneously in both channels, and with experience the listener can distinguish between types of event. For example, a quarry blast is heard as a single gunshot, and an earthquake as protracted cannon fire. The detection was so sensitive that a good number of events perceived were seen only with difficulty on the paper playouts, made on the jet pen recorder.

Most events recorded were quarry blasts which occurred during the normal working week. An overall guide to the frequency of blasting in Derbyshire is presented in Table 4-2, which is based on the results from a questionnaire sent to every known working quarry in 1979, primarily to aid the location of untimed blasts.

After each season, the data were digitised on the PDP11/70 facilities at GSU Edinburgh, by which the records were flutter compensated, digitised at 50 samples per second and multiplexed onto digital magnetic tape. Since the upper frequency cut-off for the analogue recording at 15/320ips and replay is 16Hz (see Fig. 3.5), and the highest frequency component of P waves from quarry blasts only about 12Hz (observed from the analogue playbacks), there was little seismic energy above the Nyquist frequency of 25Hz.

All quarry blasts were digitised for a window of one or two minutes (starting on the minute, or the half-minute). Teleseismic and local earthquakes were digitised for up to five minutes. To save on tape, only those channels with seismic

FIG 4-1 Tape monitoring system (schematic)

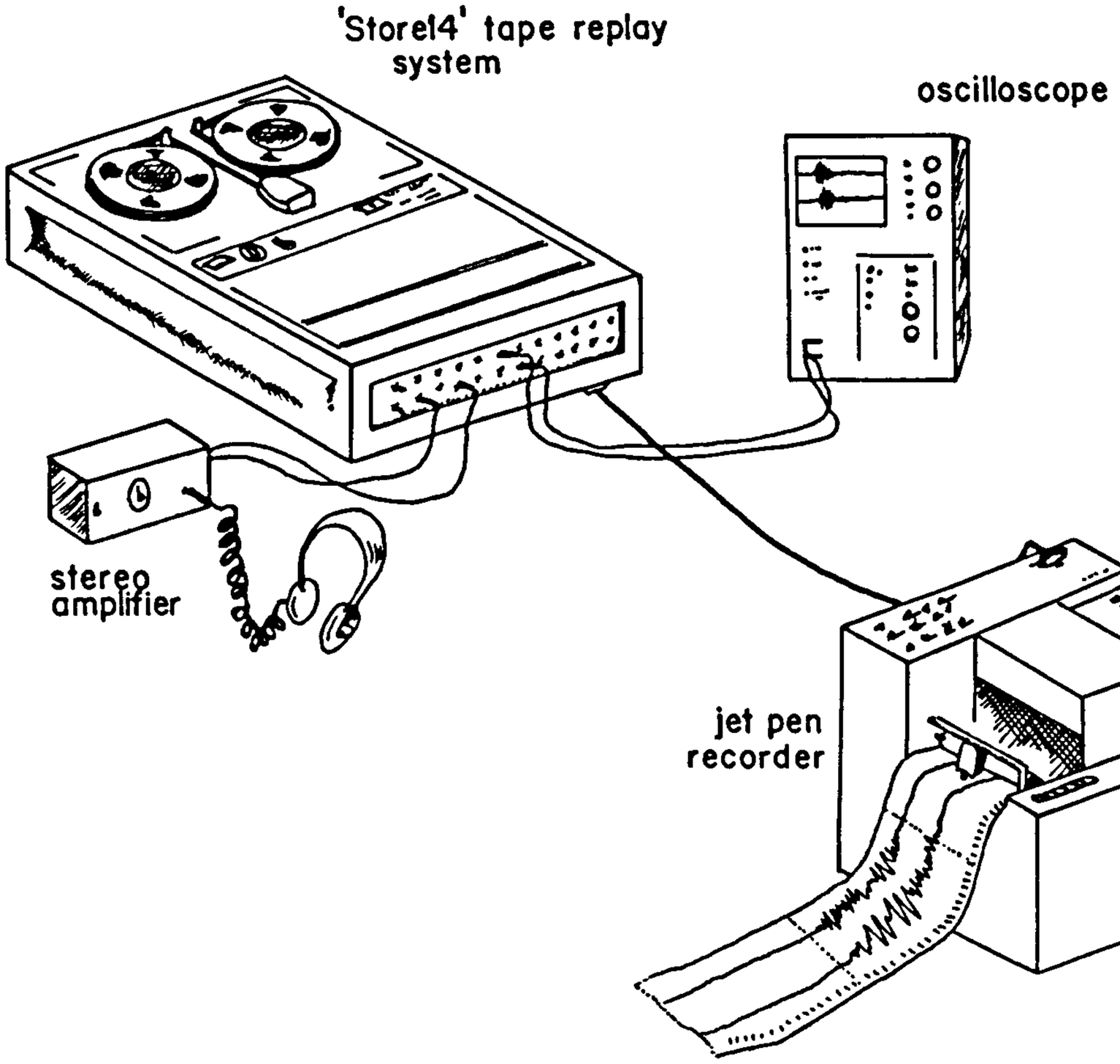

9am	10am	11am	12pm	1pm	2pm	3pm	4pm	5pm
Moneystone (9-20) Ramshorn (9-25)	Ballidon (10-00) Tunstead (10-05) Doveholes (10-15) Middlepeak (10-30, 10-45)	Grange Bar (11-00) Dene(11-25) Middlepeak (11-30) Hindlow (11-45, 11-55)	Dene (12-00) Doveholes (12-00) Hindlow (12-00) Water-swallows (12-00, 12-20) Longcliffe (12-15) Dow Low (12-30) Stoney Middleton (12-30) Ramshorn (12-50)	Ballidon (1-00) Wardlow (1-00) Stoney Middleton (1-30)	Stoney Middleton (2-04) Tunstead (2-05) Middlepeak (2-00,2-50) Brierlow (2-30) Hindlow (2-30)	Doveholes (3-00) Hope Valley (3-00) Stoney Middleton (3-00,3-35) Cauldon (3-03,3-20) Ashwood Dale(3-10) Moneystone (3-30)	Doveholes (4-00,4-10) Hope Valley (4-00) Stoney Middleton (4-00) Wardlow (4-00,4-35) Eldon (4-04) Ramshorn (4-35)	Topley Pike (5-05, 5-32) Middleton Mine (5-30)

Table 4-2 Typical quarry blasting schedule

data were digitised, along with the Geostore internal clock on the first digital channel and MSF always on the last. The digitiser afforded four gain settings between 2.5mV and 20mV, with which the output was scaled between +1024 and -1024 digital units. In order to prevent clipping of the signals, most of the data were digitised at a low gain, nominally 5mV.

In total, the digitised data comprised 300, 165 and 320 events recorded during the 1979, 1980 and 1981 seasons respectively. These were written on twelve 3600 foot digital tapes, for each of which a file by file catalogue was compiled, and a jet pen playout of the complete contents made for future reference. At this stage, unique catalogue numbers were assigned to each digital file with the following code: a letter for the Geostore (e.g. A for Aleck Low, E for Eyam, etc.), a single digit each for the experiment number (see below) and the analogue tape number, and three digits for the event number, counted from zero for each analogue tape. For example

F22034 -- Recorded at Fivewells (F)
Experiment 2 (Southern East-West line)
Tape 2 (which ran for Days 321 to 327)
Event number 034 (34th digitised from Tape 2)

The experiment numbers were: 1979-no number, NEW-1, SEW-2 and 1981-3. Events recorded at several Geostores were assigned the same event numbers, and differed only by the Geostore prefix. The numbers of events digitised from each tape are included in Table 4-1.

4.3 Digital Processing

From digital tape to producing records suitable for picking onset times, a Digital Tape Analysis Package (DTAP) has been developed on the University of Leeds Amdahl V7 designed to make the process as easy and efficient as possible. At the core of this package are the programmes originally written by D.N. Whitcombe specifically to handle data digitised at G.S.U. Edinburgh, and further developed by the present author: DECODED, FSTOR and PLOTTER.

The data on tape were written in a specially coded, highly packed format (C. Fyfe, G.S.U. Edinburgh), which DTAP reads using the subroutine SEIREC, developed by D.K. Johnson of the Computing Service, the University of Leeds.

The four stages of processing a digital tape were:

1. Checking the Contents of a Tape (programme DECODED)

It was necessary to define the exact start time of each digitised window before further processing, and also to check the contents of the tape in case of null files or errors in the documentation. DECODED automatically provides a file by file log of the tape; by decoding the Geostore internal clock it lists the precise start and end time of each digitised window.

2. Creating Event Data Files (programme FSTOR)

The computer at the University of Leeds stores files on two levels: in the permanent FILESTOR, and on temporary Disk which is used as work space.

The programme FSTOR reads an event from the tape, demultiplexes it, and writes the data to Disk with headings specifying details of recording and digitising. This Disk file is then automatically transferred to FILESTOR, and saved under the same name as its catalogue number. Only a window containing the relevant signal need be copied: typically for a quarry blast about 25secs, and for a teleseism about 40secs. Once a window was written to Disk, a standard plot of its contents was made on a Calcomp drum plotter.

3. Merging Demultiplexed Files

Most events were recorded on between two and five Geostores, for each of which there was a separate demultiplexed file created by FILESTOR. To reduce the number of data files on the computer, and to facilitate processing, these were normally combined into single event files. For consistency, the order by which Geostore records were combined was the same for each experiment. The name of the merged file was usually taken to be that of the first file of the set: for example, the

files F35024, A35024, WH35024, BH35024 and S35024 were combined in that order and saved as F35024. Data from 1979 were an exception in that merged files had the prefix M.

4. Display of Data (programme PLOTTER)

Steps 1 to 3 were repeated with little variation for all data transferred from the digital tape. By contrast, the programme PLOTTER used to display the data is a general package and as such may be employed for a variety of uses; a flow chart summarising its functions is shown in Fig. 4.2.

For basic processing, PLOTTER was most frequently used for two purposes:

(a) to produce standard plots of the raw data, and
(b) to plot the data in a form suitable for picking onset times: a 'fast replay' with an extended time base.

Case (a) arose where the FSTOR plot was lost or the contents of a file needed checking. For case (b), the output required large gains, well-spaced channels and a broad time base: the normal form for quarry blast data comprised channels separated by 4 cm with amplitudes normalised to fit their assigned plotting window, and five seconds of data plotted at 5cm/sec. Both time channels were plotted. Although it was possible to apply a bandpass filter to the data (see Fig. 4.2), none of the fast replays were filtered. This was partly due to the high quality of the events considered, but also because for the picking of first breaks as little distortion of the signal as possible was desired.

i) Time Corrections

Three time corrections were applied to the signals plotted:

A. Clock Corrections

These are the relative differences in start time of the demultiplexed windows between Geostores (see Fig. 4.3). The corrections are determined either by using the output from DECODED, or by plotting the first five seconds of each time channel on a fast replay and measuring the differences relative

FIG 4-2

(a) Running PLOTTER from FILESTOR

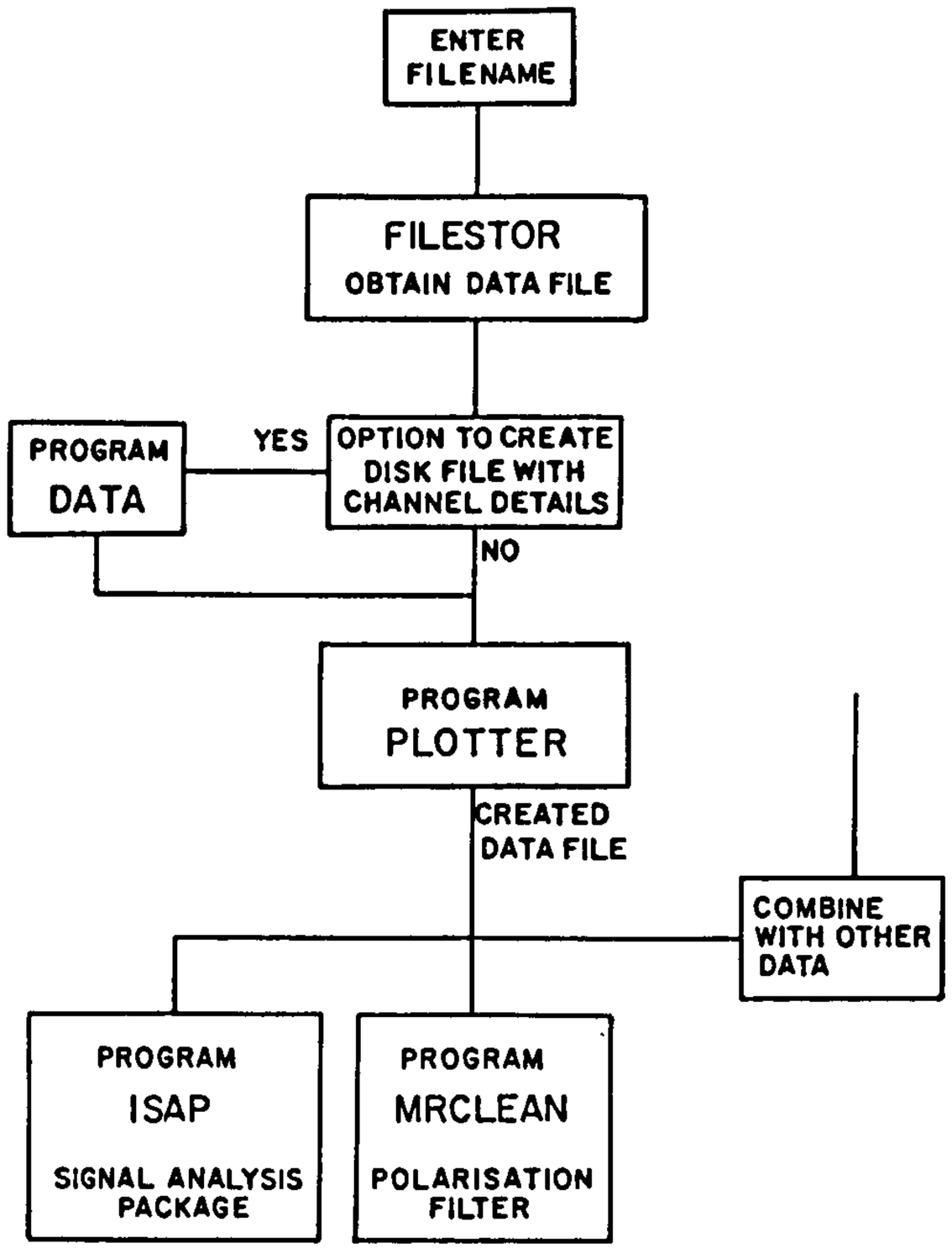

(b) Flow chart for PLOTTER

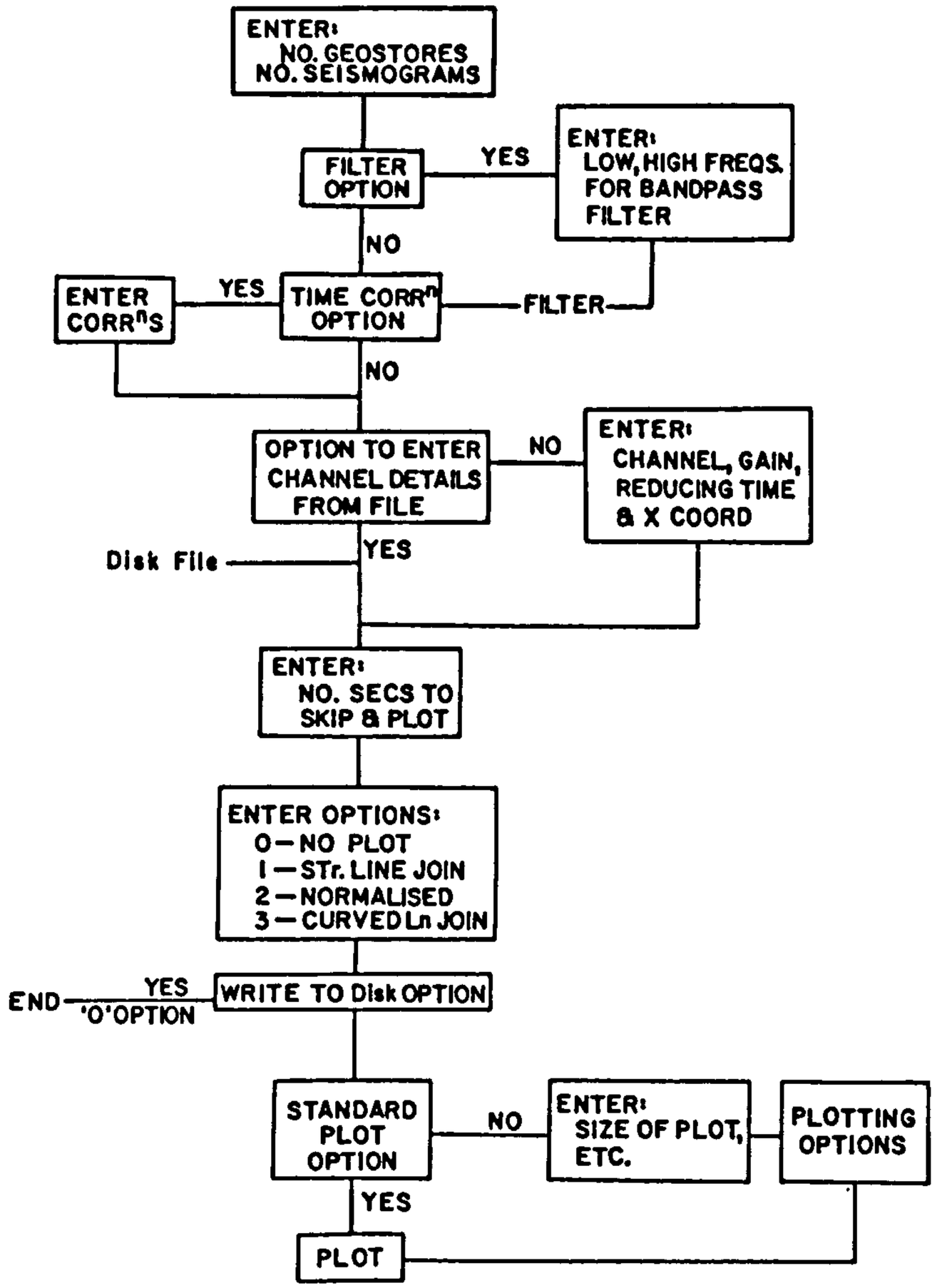

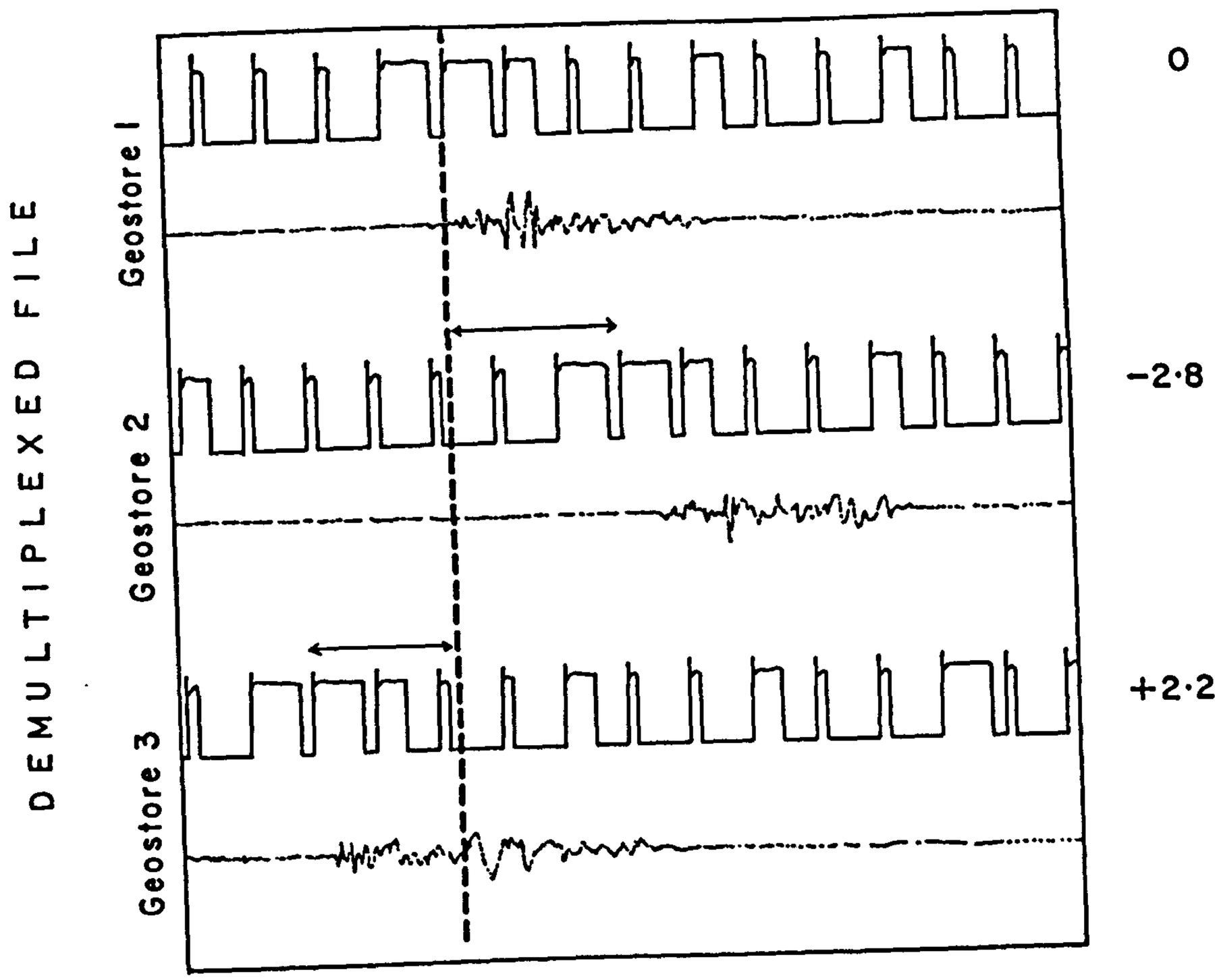

FIG 4-3 Clock corrections

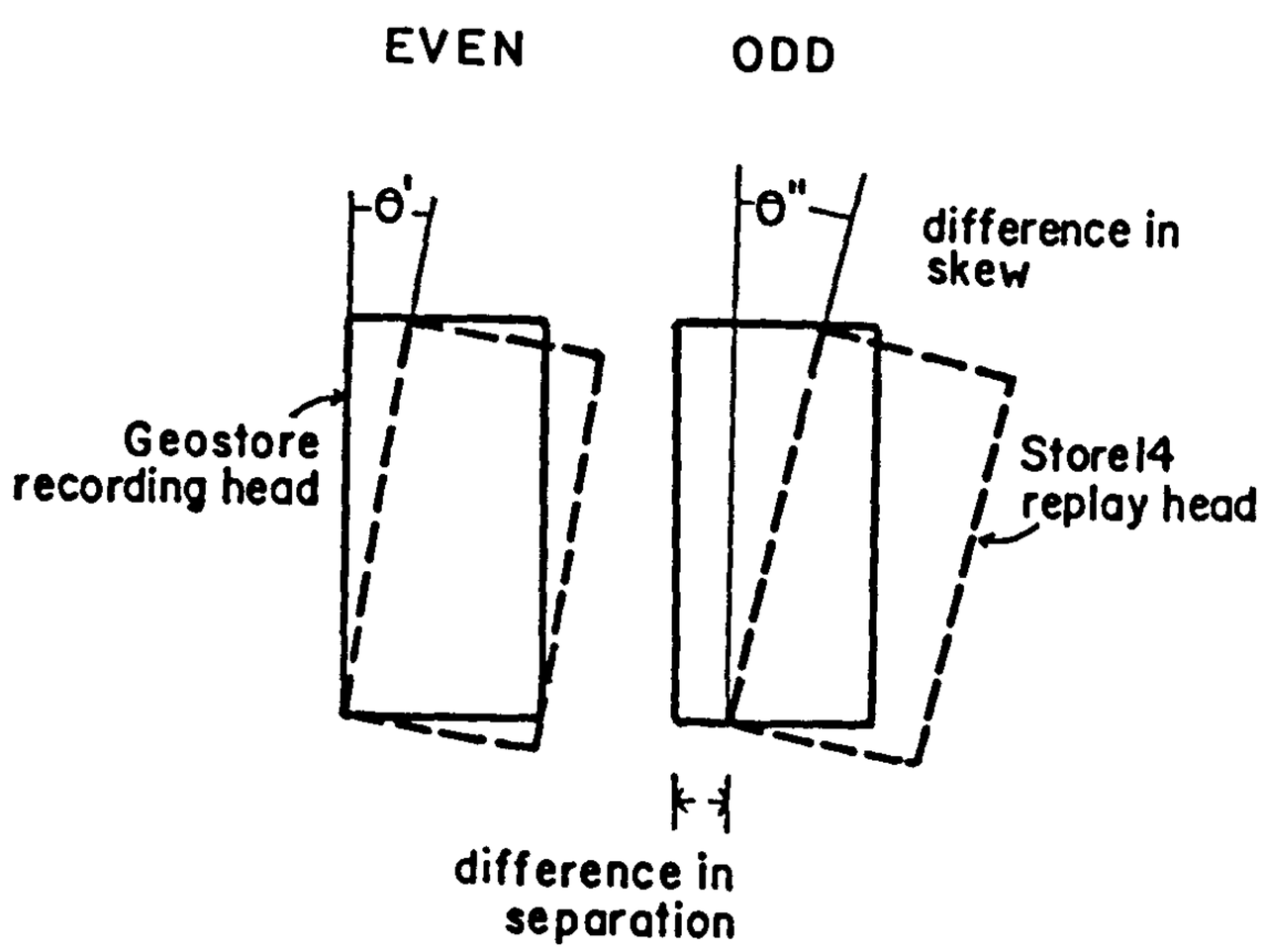

FIG 4-4 Channel corrections

to the first Geostore. Clock corrections accurate to better than ± 10ms were required for the reduced time sections (see (ii) below).

B. Head Corrections

Head corrections negate the time error due to the difference in alignment between various Geostore recording heads and Storel4 replay heads, and thus a suite of corrections was required for each Geostore-Storel4 combination used. There are two components to the correction (see Fig. 4.4):

(a) difference in separation between the heads which record odd and even channels. This was often the largest correction to apply, and varied between ± 50 ms. (For this reason, whenever half the total number of data channels are used, they should all be recorded on either even or odd channels, rather than mixed between the two).

(b) difference in skew, θ, for each of the heads. This error was found to be normally smaller, up to ± 10ms for channels at either end of the same head.

The corrections were measured from the calibration pulses recorded on each Geostore specifically for this purpose (see Section 3.2.5). The signals were replayed by the Storel4 used for digitising and played out with an extended time scale using a jet pen. The time differences were then measured relative to the MSF clock on channel 14, to an accuracy of ± 1ms.

C. Channel Corrections

During multiplexing, it takes 72 microsecs for the digitiser to sweep from channels 1 to 14 for every sample digitised, and each channel's correction will be a proportion of this value. This correction is negligible compared with the head correction, or picking error.

ii) Reduced Time Sections

PLOTTER was often employed to produce time sections where each seismogram was shifted towards the origin by a reduction time T_r given by

$$T_r = X/V_r \quad .$$

where X is the distance of the station from the source, and V_r the reducing velocity (cf. Equation 2.15). All phases travelling at velocity V_r line up parallel to the time axis, so that if V_r corresponds to the velocity of the arrival of interest, the reduced time section conveniently displays the data without needing to compress the time scale.

These reduced time seismograms sections were plotted either against true distance from the source, or against station distance along each profile. The records were usually plotted to as large a gain as possible without overlapping adjacent first arrivals.

4.4 Picking Onset Times

At each stage of the digital processing the best quality data were progressively selected: thus of the total 800 events digitised, 400 were copied by FSTOR and saved in FILESTOR, of which 250 were plotted as fast replays and picked. Timed and positioned quarry blasts, most of the local tremors and all of the global earthquakes were processed by default.

These records form the 'raw data' of this section, although all the teleseismic data from stations outside the Dome (viz. Charnwood Forest, Haverah Park and Stroke-on-Trent) have been picked from jet pen records with an extended time base.

4.4.1 Method

All the data have been picked by eye which is more accurate, efficient and versatile than any automatic means. A cross-correlation technique was investigated using an Interactive Signal Analysis Package (ISAP, see Fig. 4.2), but without constant user supervision the derived arrival times were found to be questionable, which rendered the method both time consuming

and cumbersome. Furthermore, considering the high quality of most of the raw data, the development of such a computer-based system was unjustified.

Rather, traced waveforms were used to correlate P waves between pairs of stations, whereby a well-defined arrival was traced and superimposed on a less well recorded signal in order to judge the onset. Usually this process worked outwards from stations nearest the shot, for as the amplitude of the wave decreased the signal became more contaminated by noise. However, there was no set approach: normally the stations nearest the source did not require interstation correlation since the direct arrivals were extremely well defined; and frequently the refracted phase was best recorded at the more distant stations from the shot, whereupon the correlation worked inwards.

'Onset' here refers to the earliest point of a signal correlated from station to station. There are various points on a wavelet than can be picked, as Fig. 4.5 illustrates. If this wavelet were incident without change along a profile, then any of these points may be used without affecting the relative arrival times. However, because of P wave dispersion, filtering of the signal with distance, interference by later arrivals, etc, the signal waveform changes between stations and the later into the signal the point used for correlation the less reliable the picks will be. Therefore, where possible, the first point of displacement, A, in Fig. 4.5 has been used.

Generally, the quality of the 'pick' is dependent upon: (a) the signal to noise ratio, (b) the frequency of the waveform, and (c) the interstation coherency of the signal.

(a) Noise comprises any seismic energy apart from the signal of interest, and may be either random or correlated between stations. Random noise encompasses both ambient and system noise; ambient noise (wind, cultural, livestock, etc.) was observed to differ in amplitude and frequency according to geology and proximity to habitation, and also to increase in level during the working day for stations near quarries, etc.

FIG 4-5

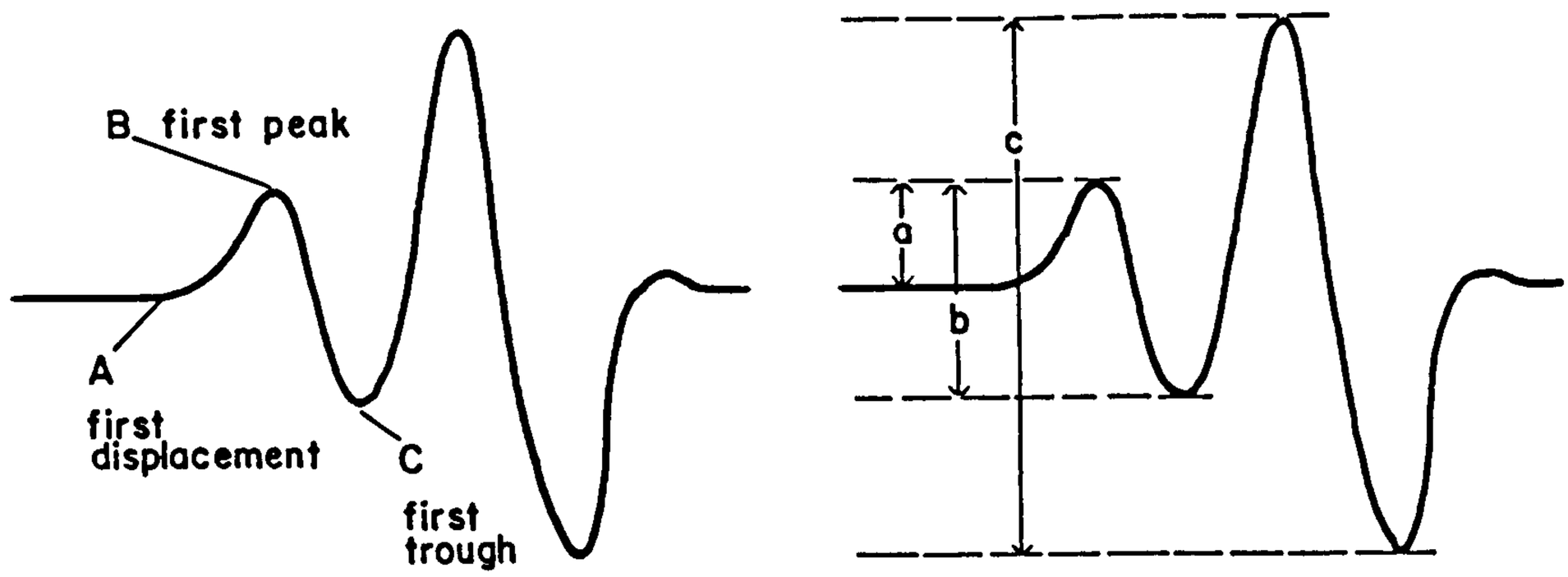

FIG 4-6 Different wavelength arrivals

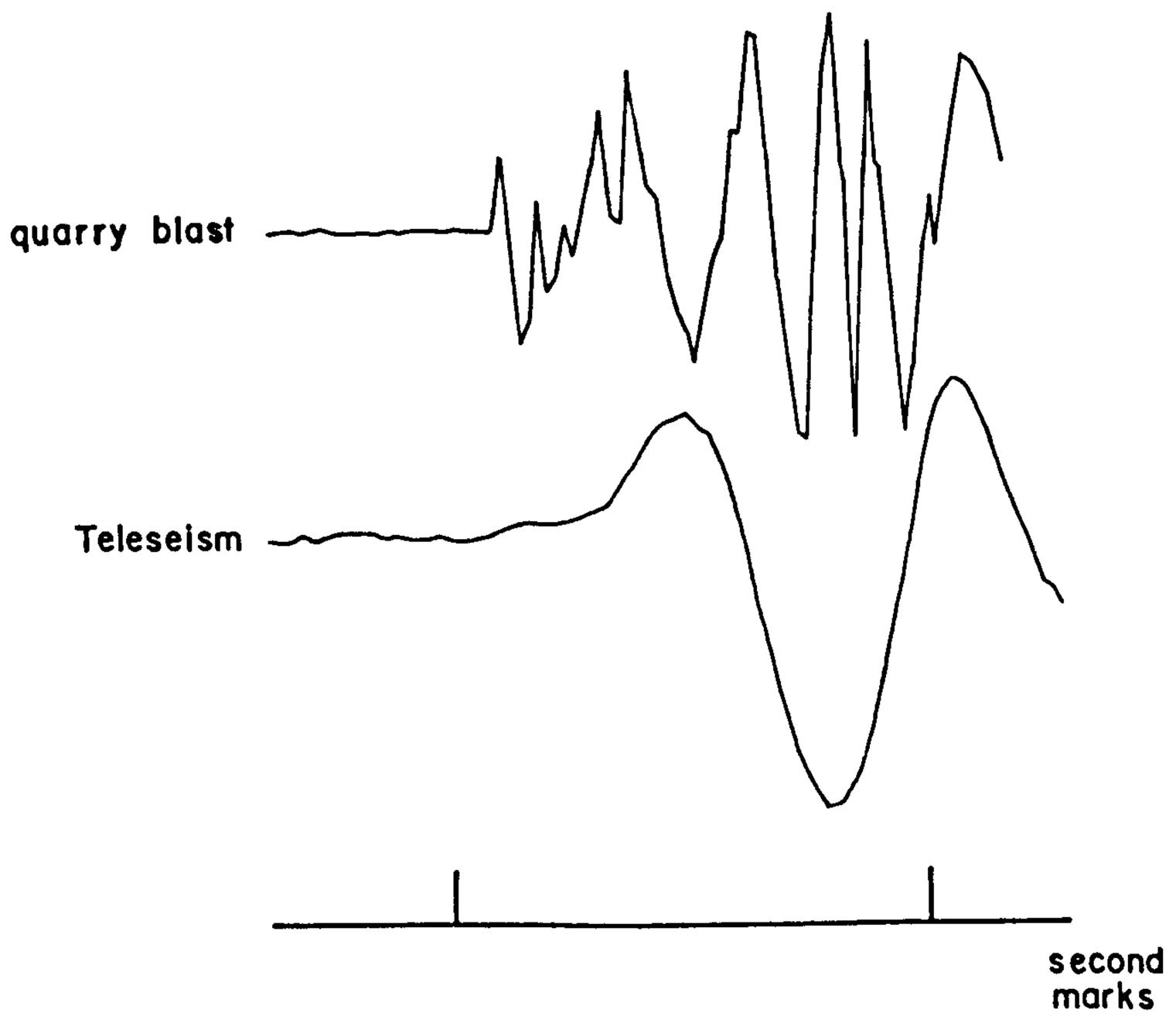

Correlated noise mainly comprises seismic energy from the same source as the arrival of interest: for example, precursory ripple to the picked 'direct' wave, or the coda of the first arrival itself for a later phase.

At various levels noise is always present, and has greatest effect when prevalent at similar frequencies to the signal concerned. Where the signal to noise ratio is less than unity the first break is unlikely to be reliably determined, unless the frequency of the ambient noise is distinctly different from the signal. When noise and signal are similar in amplitude and frequency it is easy to pick on the wrong cycle and the trace correlation must be carefully made.

In order to combat the problem of ambient noise of similar frequency to signal, multichannel polarisation filters have been assessed to enhance first arrivals (see Section 2.4.1 and Appendix B). The filters essentially discriminate against incoherent energy between the data channels.

(b) The effect of wavelength on the quality of picking is illustrated in Fig. 4.6, which contrasts quarry blast with teleseism. Obviously the broader the take-off slope, the more difficult it is to estimate its origin. Thus there is a trade-off between the frequency of the signal (on the fast replay) and the length of the time scale, for the greater the distance between second marks, the more accurately the pick can be measured. Thus for quarry blasts, the P waves for which were commonly between 3 and 6 Hz, a time scale of 5 cms/sec was used, whereas for teleseismic data, where the first arrival was often 1Hz or less, a scale of 2.5cm/sec was employed.

(c) The more a signal waveform changes down a profile, the more difficult it becomes to correlate traces, and therefore judge onset times. Noise apart, such changes between stations may be due to: differing station characteristics, differing angles of incidence (where the steeper the angle of incidence the less the arrival will be affected by near-surface irregularities, and the larger the amplitude response of a vertical seismometer), or through the interference of various arrivals:

for example, where headwaves overtake direct waves, where either phase can be considered as noise. It is unwise to force a correlation between stations where their first breaks correspond to differing arrivals.

In cases where, because of noise and changes of waveform, no two stations satisfactorily correlated, picking became a protracted, iterative process whereby most of the signals were traced and correlated with each other. For emergent teleseismic arrivals the first break was sometimes indefinable, in which case the first peak or trough was used instead; this was justifiable as the first arrivals are normally coherent along the profile, and only the relative delay times were required.

Not only was it possible to pick arrivals between stations for the same event, but it was also possible to correlate arrivals into the same station for different events from the same source. This could not be done until the sources had been located, but it was one means of improving the quality of the pick, especially for less reliable observations. However, different shot configurations can yield differing source signatures, and this had to be taken into consideration.

4.4.2 Time Measurement

All arrival times have been measured against the MSF clock (Fig. 3.6), although absolute MSF time was only used for timed quarry blasts and global earthquakes; for untimed blasts relative arrival times were merely required, so that the seconds were arbitrarily numbered.

There were two areas where measurement error occurred:

(a) Estimation of the start of the second mark

Fig. 4.7 illustrates the true shape of a received second pulse and three variants after digitisation. None of the MSF receivers seemed to have exactly the same response, so the coded widths varied slightly. The onset of each second mark

FIG 4-7 Digitised second marks

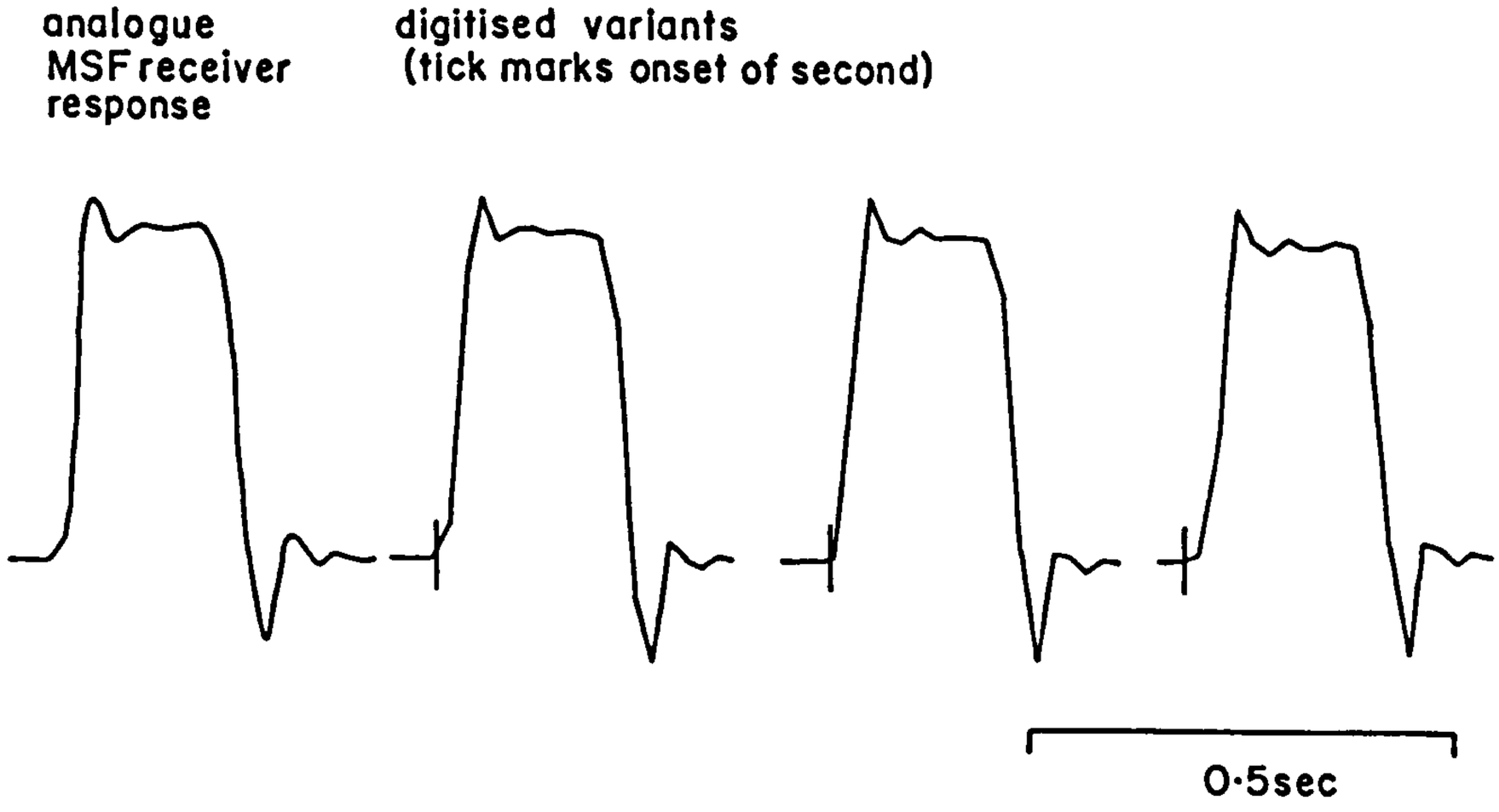

FIG 4-8

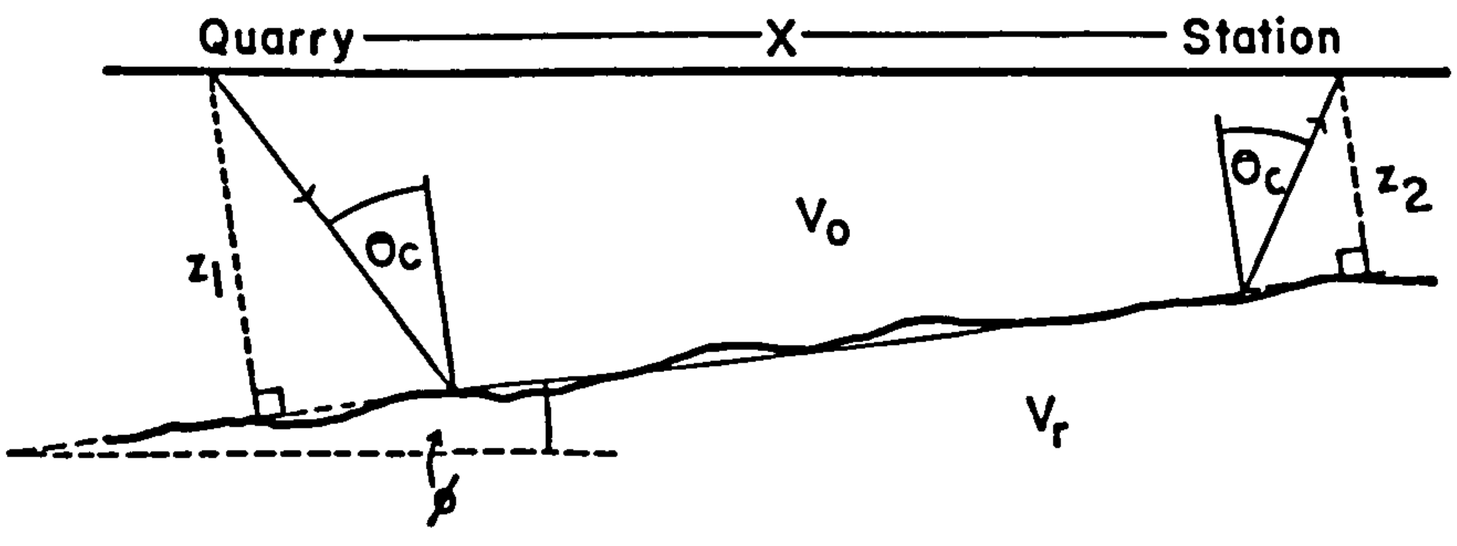

was taken to be the sample before deviation from the baseline, which, as shown, was rarely more than about 10ms out.

This error increased for noisy or faulty time channels. Where the MSF channel was unusable the Geostore internal clock was employed, in which instance it was calibrated against MSF time. Since the Geostore clock has been known to drift irregularly, particularly in cold weather (when it was observed to differ from MSF by 0.4s within a week), this calibration was preferably made using the previous and succeeding records with MSF, whereupon the required correction was interpolated between the two.

(b) Measurement of arrival

The picks were measured with a ruler from the left hand margin of the fast replay; since the time scale is known, only one trace need be measured against the clock per Geostore, as all the other arrival times can be calculated directly. Thus the measuring error between signals of the same Geostore was no more than the accuracy of a ruler, say about ± 0.1 mm, equivalent to ± 2 ms for a 5 cms/sec time scale.

Thus the total measurement error is potentially greater between groups of stations due to (a), than between adjacent stations due to (b).

4.4.3 Observational Error

All the effects upon the quality of pick add uncertainty to the derived arrival time. Whitcombe (1979) suggests blind repicking to estimate the error variance of the jth observation, σ_j^2, so:

$$\sigma_j^2 = \sum_{n=1}^{K} \frac{(t_j - t_n)^2}{K-1}$$

for k pickings for mean time t_j. With trace correlation, however, it was found more efficient to estimate observational error by moving the trace to either side of the pick, thus

actually estimating the limits of correlation. This could be done at the same time as picking, and was a direct reflection on the quality of each individual pick, as opposed to the above variance method.

Where trace correlation is used to determine an onset time, the observational error of this pick necessarily contains (a) the error in estimating the onset due to noise, etc., (b) the error due to the difference in waveform between the two traces, and (c) any observational error in defining the onset of the correlating trace. In the case where the signal waveform, say, progressively broadens with distance from the shot and the same correlating signal is used throughout, then the error due to (b) will increase away from the shot while that for (c) is constant for each pick. Alternatively, if the event is picked by correlating adjacent pairs of stations and working away from the source, then the error due to (c) may well accumulate with distance, while that for (b) will be minimal. In most instances, several correlating traces were used to estimate an onset, in which case the estimated observational error was an ensemble average.

The observational error estimates were found to fall into three distinct groups:

1. 0-10ms: for strong, high frequency signals with an excellent signal to noise level. Here the observational error is not due to the pick itself, but the errors in time measurement, discussed above. Obviously, it is possible that the true first break occurs between adjacent sample points, so that the observational error is at most 10ms.
2. 10-50ms: (minor picking error): most observational error estimates for noisy signals fall into this range. The total error also includes the measurement error (above).
3. >50ms (major picking error): errors of this magnitude were normally not obvious during picking (although the picks were known to be questionable), and became apparent when either the data were plotted

or the source location was considered unsatisfactory. These errors arose where the ambient noise was similar in amplitude and frequency to the signal, and the pick was made on the wrong cycle. Such observations were either ignored, or a repick attempted.

Other miscellaneous errors include inaccurate head corrections, noisy time channels, and a poorly calibrated internal clock (if used). Combined, these additional errors are generally small, less than 5ms, especially compared to most estimated observational errors.

4.4.4 Measurement of Relative Amplitudes

The first arrival amplitudes were measured from the fast replay records using a magnifying lens and graticule, accurate to ± 0.05 mm. For the same reasons as the first break was picked at point, A, in Fig. 4.5a (see Section 4.5.1), the amplitudes were measured peak-to-peak between first peak and trough where possible (see Fig. 4.5b). These amplitudes were expressed relative to the maximum digital range (i.e. 2048 units = 1.0).

The accuracy of measurement increases with: the signal to noise ratio, the frequency of the first arrival, the accuracy of the pick, the interstation coherence, and the closeness of the first arrival waveform to the ideal wavelet (i.e. Fig. 4.5b). Note that the correction for Heelan's law gives more weight to observations more distant from the shot whose amplitudes are small and most effected by ambient noise. Normally such small observations are either ignored, or overestimated.

4.4.5 Location of Untimed Quarry Blasts

Unlike almost all seismic refraction surveys, the vast majority of events recorded by this experiment were untimed and of uncertain origin: of the two hundred or so quarry blasts

picked, less than forty were timed or positioned. Thus a reliable efficient means of estimating a shot location from relative arrival times was required.

There is a finite number of shot locations in the area: the working quarry faces on and around the limestone outcrop (see Fig. 3.7). The grid references for these have been determined by considering points about 100m apart along each face. The most simple means of locating an untimed quarry blast was therefore to generate travel times from each of these co-ordinates to the observing stations using a suitable velocity-depth model, and select the solution by least-squares best fit with the observed travel times. The source is assumed to lie on the surface.

4.5.1 Method

Consider Fig. 4.8 where shot S and station G overly an irregular refractor. The line PQ is an average of the refractor slope between the stations where the depths z_1, z_2 are small compared to the station distance, X. The travel time for the approximated raypath SPQG is then given by using Equation 2.2 (terms as given in Fig. 4.8):

$$T = \frac{(z_1 + z_2)\cos\theta}{V_o}\, c + \frac{X\cos\phi}{V_r}$$

Without knowing the detailed structure at depth, a simple two layer model can be assumed whereby the Carboniferous overlies a continuous refractor the length of the Dome (e.g. Whitcombe and Maguire 1981b). To use Equation 2.2 the depths to a refractor had to be estimated for all stations and quarries. Initially this was done through examining the timed and positioned shots from the 1979 experiment, and subsequently revised after the first time-term solution (see Section 6.3.1). The depths were calculated for overburden and refractor velocities of 5.2km/s and 5.6km/s respectively: those for the quarries were estimated by interpolation from gravity and bore-hole information.

The travel times using this simple model were calculated using the computer programme MODFIT (see flow chart, Fig. 4.9). A suite of travel times is calculated from every co-ordinate specified and the closest set to the observed arrival times printed along with a printout of the best thirty locations. A least-squares velocity was also derived for (arbitrarily) the nearest six stations to the located shot point, and this value is used as the overburden velocity for an iterated solution.

Since most picked times are from linear arrays of instruments, the quality of a location may depreciate where the source is collinear with the profile but not within its ends, EE' (see Fig. 4.10), as the relative arrival times will be least dependent on the distance of the source. A poor location may also arise for a distant source perpendicular to the line, where the difference in arrival times will be very small and more dependent upon refractor structure beneath the line than difference in distance from the source.

To test the routine, timed and positioned events from the 1979 season were 'located'; the results are summarised in Table 4-3. Given that the structural and velocity variations along each raypath were largely unknown, these locations are quite satisfactory, and predictably the error in position increases for the more distant shots from the line. Clearly it is unnecessary to attempt to define an accurate model for this purpose, for the object is to discern the refractor structure once the location is known!

The accuracy of the method was found to be less dependent upon error in the velocity-depth model than picking error in the first arrival time data. Changing the overburden or refractor velocity by 0.2km/s rarely changed a solution. However, while the system could handle one bad observation, several could steer the location to a nearby quarry and further for noisy data from a distance broadside source. Occasionally suspect locations were checked against other diagnostic features (below, Section 4.5.2), but this was only required when the

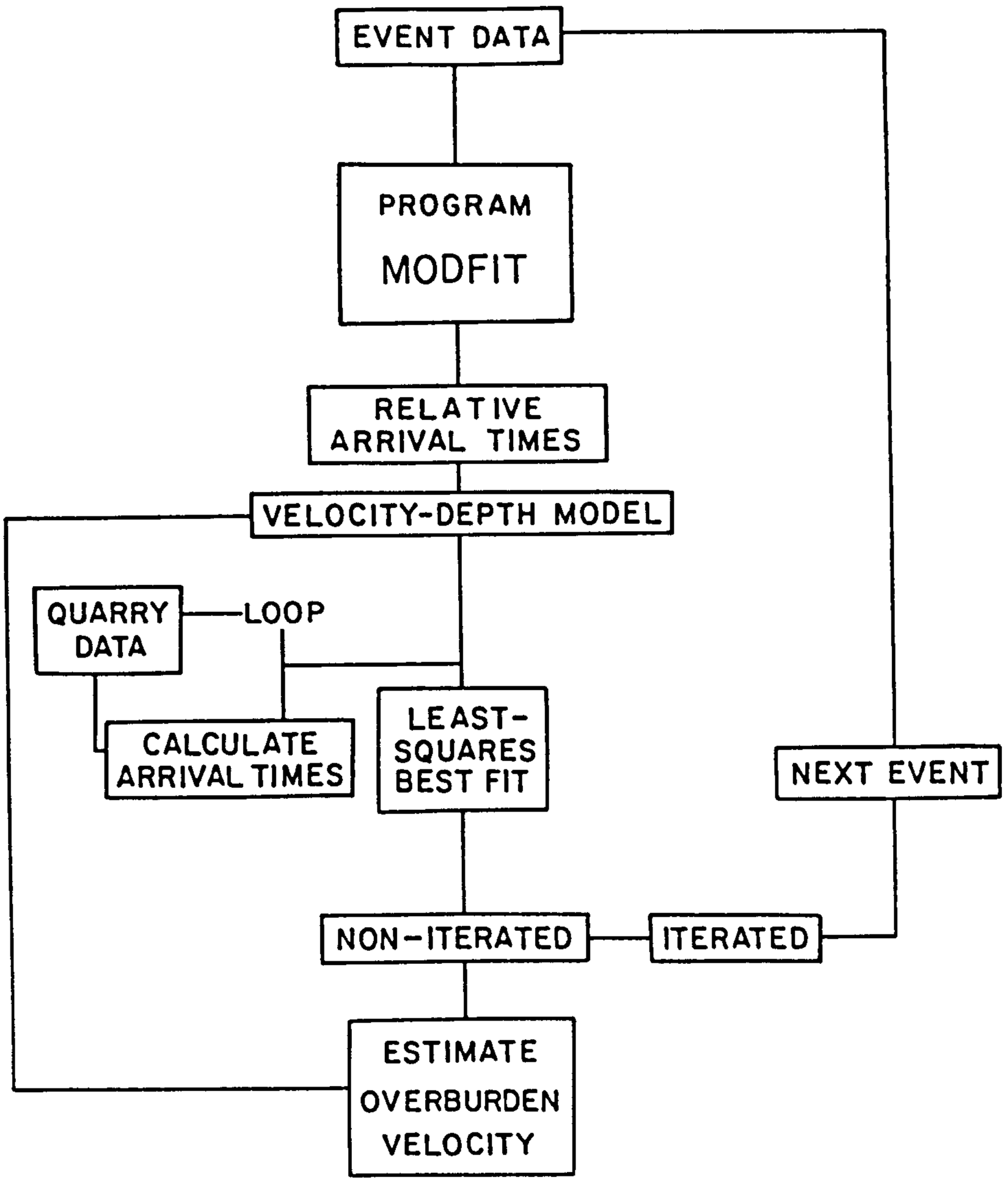

FIG 4-9 Flow chart for MODFIT

FIG 4-10

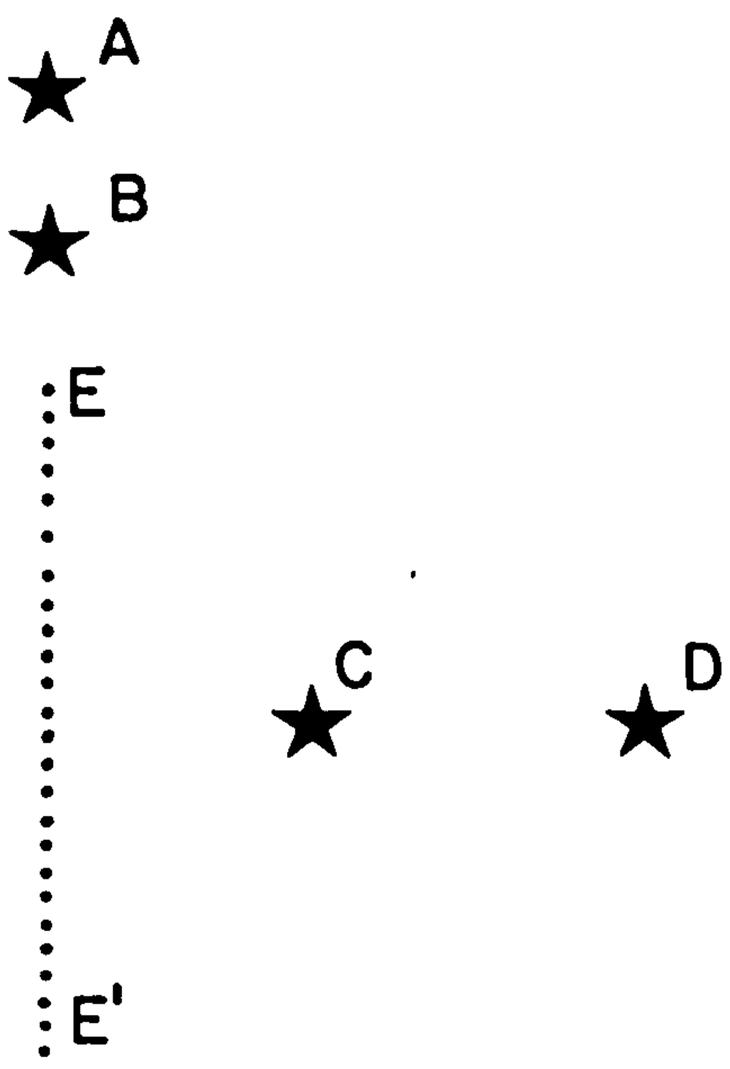

Table 4-3

Testing location programme
using timed events from 1979 expt.

Quarry	Co-ords (km)		Location (km)		Error
Ballidon	419.86	355.58	419.71	355.53	0.16
Tunstead	409.87	373.79	410.1	373.5	0.37
Brierlow	408.97	368.62	409.21	368.93	0.39
Wardlow	408.36	347.28	408.64	346.88	0.49

data were poor, and it was rare that the true shot point lay outside the thirty best locations (most of which usually comprised co-ordinates of the same, or closely adjacent quarries).

4.5.2 Other Aids to Location

The blasting schedule of Table 4-2 is a fair check on the location. P-S times also vindicate or contradict a solution, and so do amplitudes and signal waveforms, especially for the closest stations to the source. The shape of the reduced time graph (see Section 2.3.2) was often an effective quality control check and gross mis-pickings were sometimes evident from discrepancies between the observed and best-fit arrival times.

Instead of using a sequence of quarry faces, MODFIT can be used with a network of points. Thus the location for a local earthquake may be obtained by considering a regular grid generated approximately about the source, assuming that a simple two-layer model can still be applied, and that the focus is on the surface. For the Mansfield and Stoke-on-Trent tremors, for example, depths to the basement were first estimated from the Duke's Wood (Lees and Taitt 1946) and Gun Hill (Hudson and Cotton 1945) boreholes respectively, and a 2km mesh drawn about the region. Having obtained a coarse solution, smaller grids of interval 200m were used to estimate the final locations; within the limits of the model, any finer solution would not be justified.

Similarly, a 50m grid was generated within the perimeter of Tunstead quarry in order to refine the location of untimed shots for the 1981 season. This was possible as station 70 was located on the western boundary of the quarry itself (see Fig. 3.7).

4.5.3 Summary of Locations

Table 4-4 summarises the distribution of the timed and untimed quarry blasts picked. A full listing of the locations is given in Appendix A. Predictably, most events listed are from quarries nearest to each line, and particularly from the northern quarry groups which are well represented because they fire larger shots more often. Long distance broadside shots are least represented as their lower amplitude P arrivals were frequently at noise level.

Of special interest are the local earthquakes recorded from three different regions, during successive experiments: both the Mansfield and Stoke-on-Trent tremors occurred within 45 km of any station to yield strong P waves, and the Flamborough Head event, about 180km from the Dome, was sufficiently distant for Pn phases to be recorded.

i) The Mansfield Events

This sequence of shocks was recorded over a period of thirty days from 26th September 1979, with activity concentrated on Sunday 7th October (Fig. 4.11), when thirty-six events were detected between 04.00 and 10.00 (Fig. 4.12). In all, forty-three events were identified from P-S times and signal waveform, the largest of which, magnitude about ML 3.7, shook people from their Sunday morning slumber at 8.10am. (Fig. 4.12 plots surface wave log(A/T) magnitudes relative to the smallest detectable event, arbitrarily assigned a magnitude of 1.0).

Six tremors have been located using MODFIT using a grid system, for which data recorded on the Charnwood Forest (CWF) arrays (Maguire, Whitcombe and Francis 1982) have been kindly supplied by D.J. Francis. A minimum depth of 2.3km for the refractor beneath Mansfield has been estimated from the Duke's Wood borehole, and depths beneath the CWF stations have been taken from Whitcombe and Maguire (1981a and 1981b).

The solution locations are shown in Fig. 4.13. Although these epicentres do not correspond with a fault at surface, the implied trend is subparallel to the principal strike of faults

Table 4-4

Number of untimed quarry blasts
located by MODFIT

Quarry	1979	NEW	SEW	1981
Eldon Hill	2			1
Hope Valley	1	1		
Smalledale		5		
Bee Low	2			
Doveholes	10	5		6
Waterswallows	5	4		1
Tunstead	10	11	2	16
Topley Pike	2	2	2	1
Stoney Midd.	1	1		1
Hindlow	1	1		1
Brierlow	6	6	3	6
Dow Low	5	3		4
Sterndale	4	2		2
Masson	2			
Upperwood	5		1	1
Middlepeak[1]	6			1
Dene	1			
Middleton			1	
Ballidon	7		1	4
Longcliffe				1
Grange Bar	4			2
Cauldon	4	1	4	2
Wardlow	4	1	4	
Ramshorn[2]	4			

1 For 1979, may include Middleton shots
2 For 1979, may include Cauldon shots

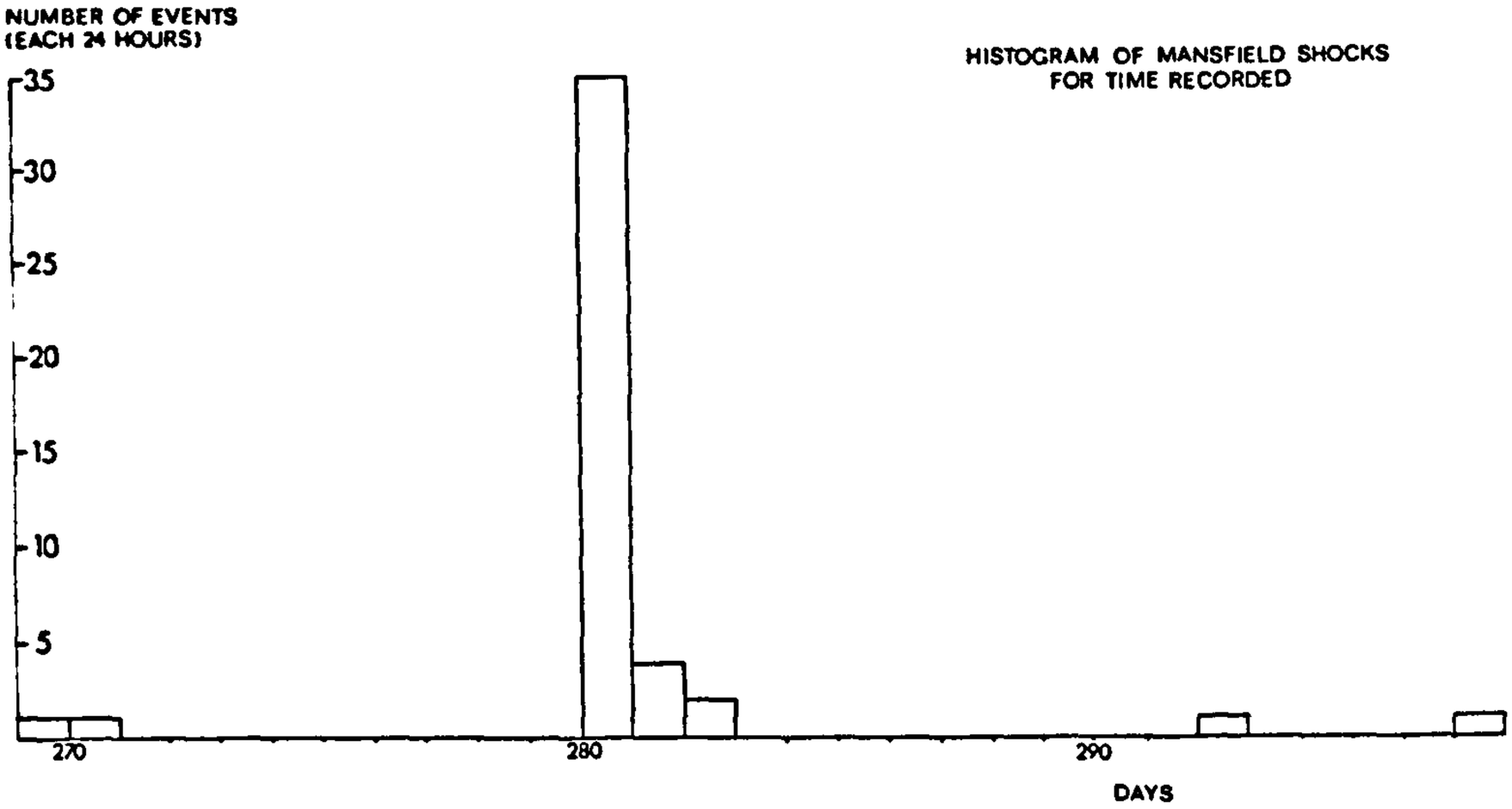

FIG 4-11

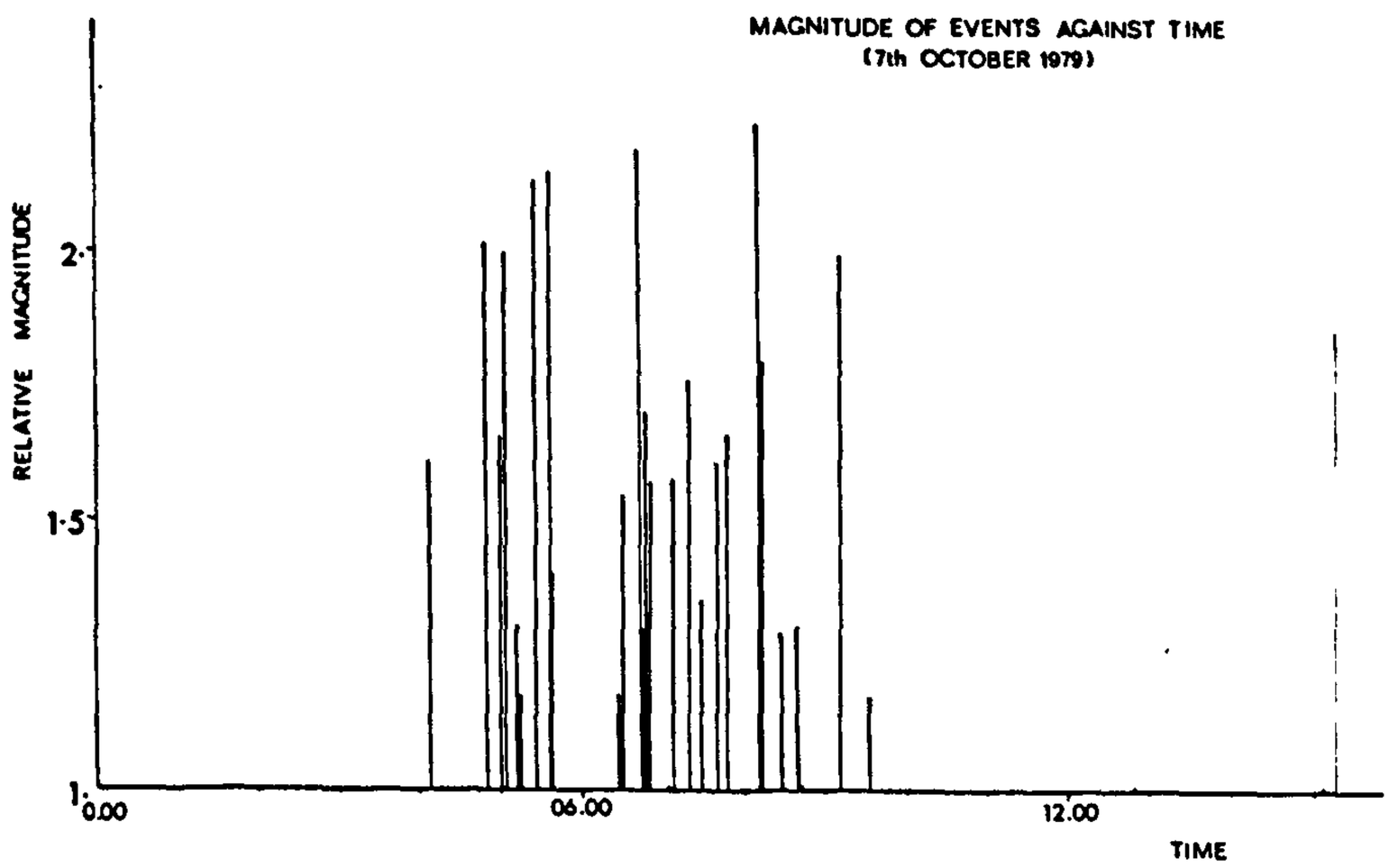

FIG 4-12

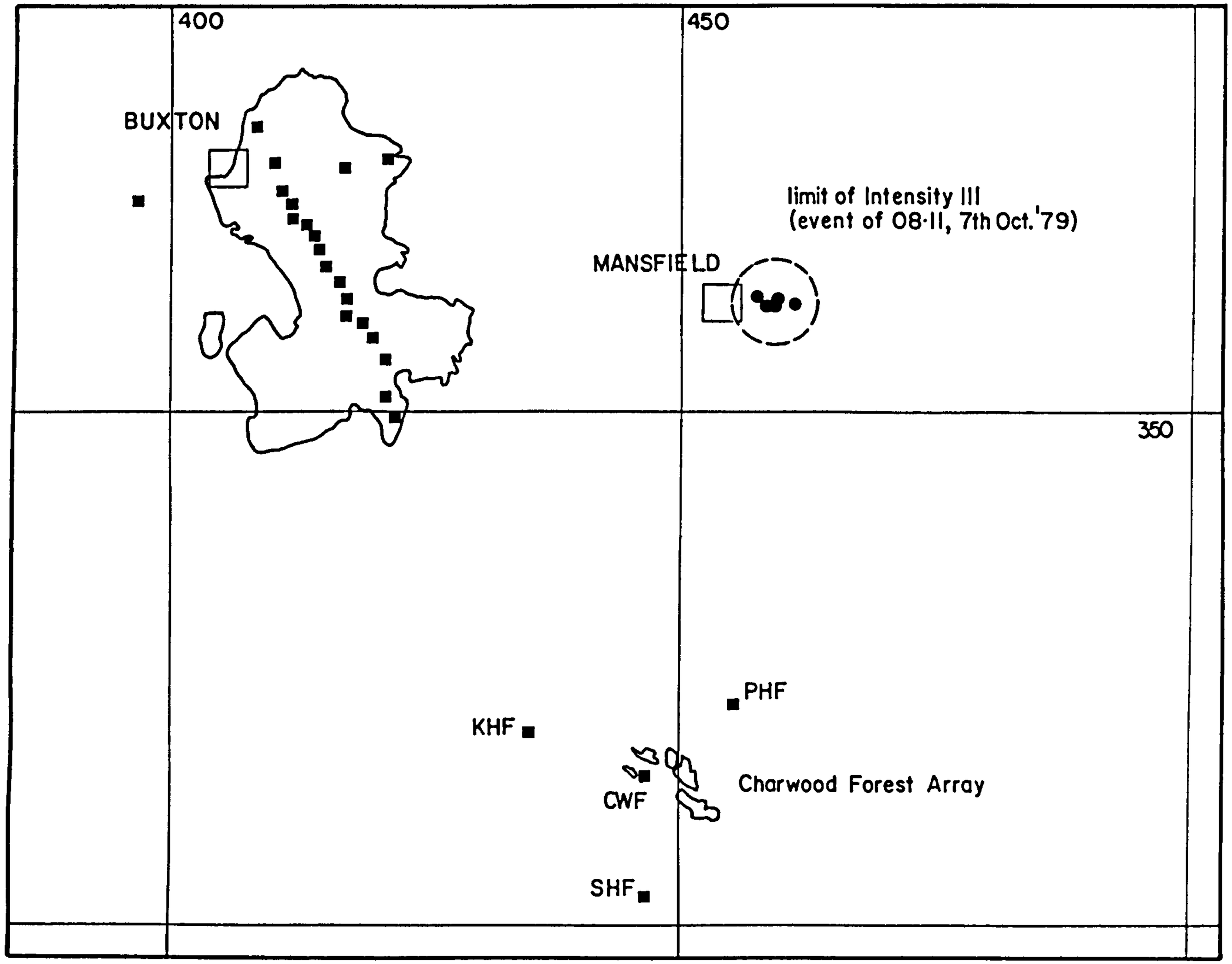

FIG 4-13

Location of Mansfield tremors

■ seismic station

● solution location

in the underlying Coal Measures. These locations correspond with the centre of a circle drawn around the limits of Intensity III, provided by J. Barker (GSU Edinburgh, pers. comm. 1983).

ii) The Stoke-on-Trent Events

Of the twenty-two identified tremors during the period 26th September to 20th November 1980 by the Stoke-on-Trent (STM) network (specifically deployed to study events in this area; N. Kusznir, University of Keele), at least seven were recorded by this experiment: one (very weak) event by the northern east-west profile, and six by the southern east-west line. The largest event of the series was of magnitude ML 3.6, and all but one of the seven were greater than ML 2.3. Mining induced activity has long been known in the region (e.g. Kusznir et al. 1980), and, like the Mansfield tremors, this sequence was concentrated within quite a short period, about thirteen hours (Fig. 4.14; C. Browitt, GSU Edinburgh, pers. comm. 1982).

iii) The Flamborough Earthquakes

These two events of ML 2.4 and ML 4.4 occurred off the North Yorks coast on the 26th and 27th October 1981, the second of which was detected by the combined DASED array (event F31055). These were too distant to use MODFIT, and their location [55012 47854] has been provided by GSU Edinburgh.

These events were approximately 175km from the Dome, and Pn phases were expected. The picked first arrival times yield a least-squares apparent velocity of 8.4km/s across the array, but since the azimuth of approach was around 40 degrees, this value reduces to about 6.2km/s (P* rather than Pn?).

4.6 Global Earthquake Data

Twenty-nine global earthquakes were recorded during the running of the refraction profiles, of which eleven were recorded in 1979, eight during 1980 (including four successive tremors from Algeria), and ten during 1981. A summary of

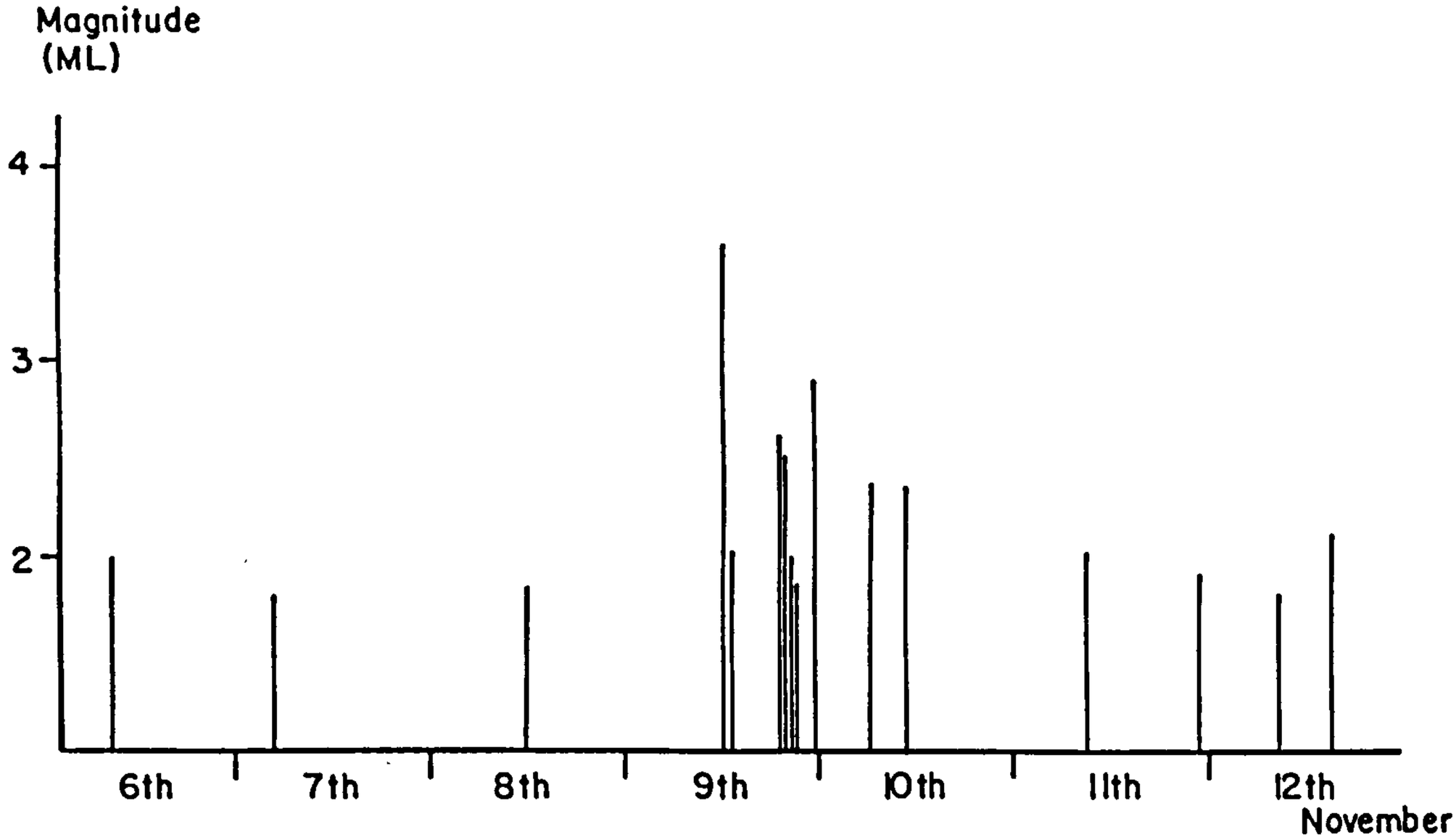

FIG 4-14 Magnitudes of the Stoke tremors, November 1980

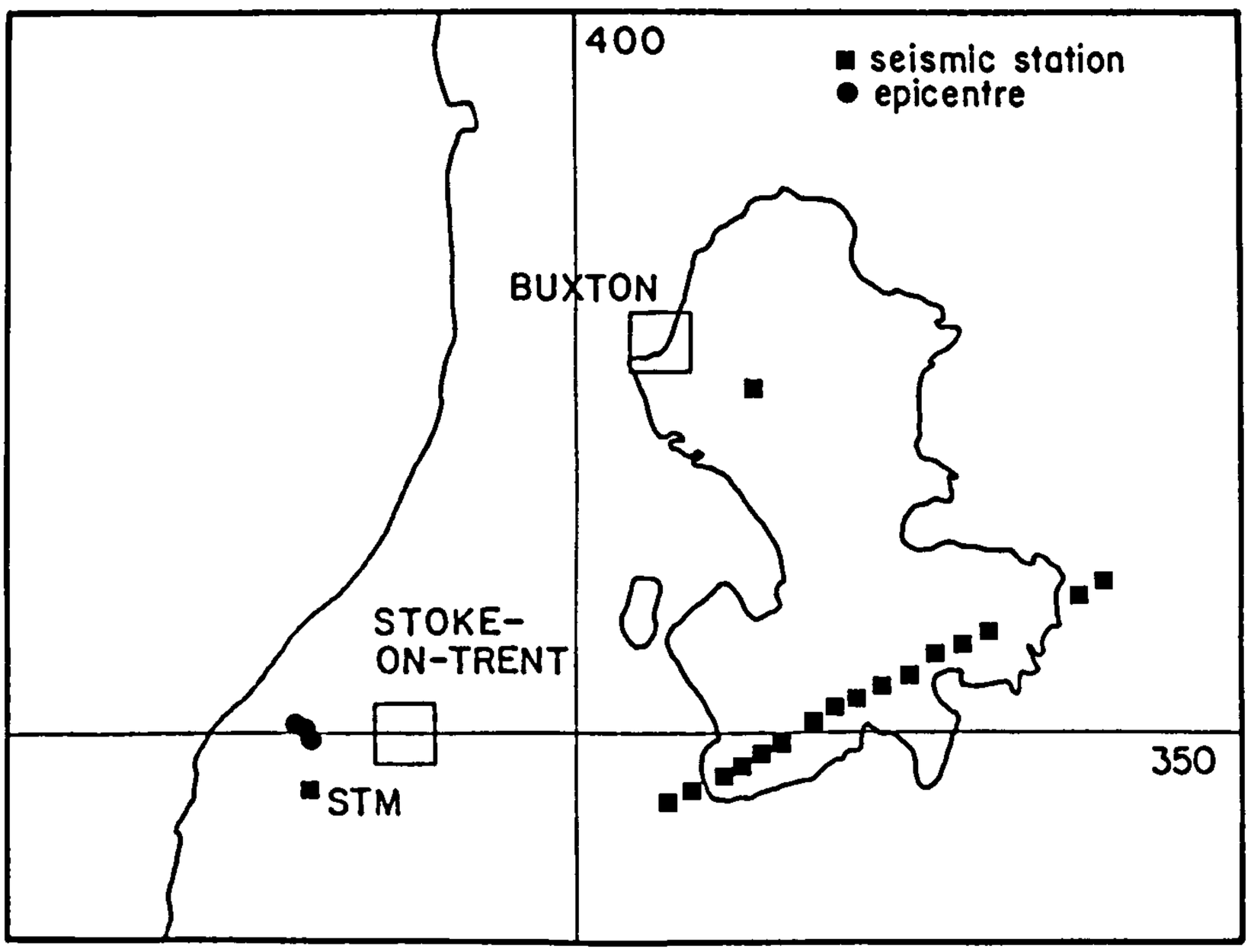

FIG 4-15 Location of Stoke tremors

these events is given in Table 4-5, the locations having been taken from the I.S.C. Monthly Bulletin.

Since the data recorded by the stations from the 1979 season specifically maintained for longer in order to record teleseisms (see Sections 3.3.1 and 3.3.2) could not be used for instrument problems, the data set was enlarged by records of the above events from stations in the Midlands seismic recording network (Midnet): Charnwood Forest (CWF), Haverah Park (HPK; J.D. Fairhead, University of Leeds), and Stoke-on-Trent (STM). The jet pen fast playouts of these were made available by GSU Edinburgh. In order to aid the picking of the onset times, the digitised data were plotted at the same time scale as these paper records (2.5cm/sec).

Of the twenty-nine earthquakes, eleven were from within teleseismic (30 to 100 degrees) distance, and nine from a distance greater than 100 degrees (most of which were from the Tonga Trench region).

Table 4-5

Global earthquakes recorded by experiment

Event no.	Date	Region	Distance degrees	Azimuth degrees
M2003	11.9.79	Azores	21	251
M2014	11.9.79	Romania	19.7	101
M2028	14.9.79	Komandorsky Is	73.3	5.3
M3021	19.9.79	Cen. Italy	14.3	130
M3044	21.9.79	Tyrrhenian Sea	18	135
M4001	23.9.79	Aleutian Is	74.8	2.7
M4002	24.9.79	Noveya Zemlya	30.7	28
M4037	27.9.79	New Hebrides	145	16
M5014	1.10.79	Mexico	77.8	280
M5040	2.10.79	Fiji Is	147.3	3.5
M6007	5.10.79	Fiji Is	148.7	2.6
F11011	10.10.80	Algeria	17.2	172
F11015	10.10.80	Algeria	17.2	171
F11017	10.10.80	Algeria	17.2	171
F11018	10.10.80	Algeria	17.3	172
F11019	11.10.80	Noveya Zemlya	30.6	28
F13016	24.10.80	Cen. Mexico	79.4	286
F13017	25.10.80	Loyalty Is	148	15
F13018	25.10.80	Loyalty Is	148.5	14
F31040	25.10.81	Mexico	81.8	289
F33003	3.11.81	Oregon coast	73.1	322
F34024	13.11.81	SW USSR	21.5	99
F34039	16.11.81	Loyalty Is	148.3	15.5
F35036	23.11.81	Kurile Is	80.3	23
F36011	24.11.81	Loyalty Is	148.9	13.8
F36012	24.11.81	Loyalty Is	148.8	13.8
F36020	25.11.81	Fiji Is	147.8	355
F36025	27.11.81	NE China	76	34
F37010	2.12.81	Honshu, Japan	81.4	26.6

CHAPTER FIVE

INTERPRETATION OF THE DATA

5.1 Introduction

This chapter concerns the interpretation of the quarry blast data processed in Chapter Four with the object of categorising the various recorded phases into direct, refracted and reflected waves. During this process a number of possible models will be forwarded in order to explain the data, and the most satisfactory model used as a basis for the time-term analysis of the next chapter.

As discussed in Chapter One, the Dome appears to be divided into two sub-Dinantian geological provinces separated by the Bonsall Fault zone. The interpretation of the data has been accordingly divided, starting with the north-south profile which crossed both provinces and which had the best data. Once ideas of the structure along this line have been formulated, the northern province will be investigated by considering the NEW and DASED2 profiles, and the southern province discussed by looking at the SEW line.

5.2 Display of data

All the picked events were plotted five ways. The first arrival times were plotted as 1) time-distance (T-X) graphs, 2) interstation apparent velocities against station position along the profile, and 3) reduced times, also against station position. 4) The log relative amplitudes were plotted against distance (lnA-X) both corrected and uncorrected for Heelan's ($1/X^2$) Law, but not for refracted raypaths as distances travelled in the basement refractor were unknown (see Section 2.4.1). Finally 5) the seismograms were plotted as reduced time sections.

Much of the interpretation used the reduced time graphs as they reflect the shape of the refractor so long as the reducing velocity is close to the true refractor velocity (see Section 2.3.2); examples of differing cases are simplistically sketched in Fig. 5.1. With a few exceptions, a reducing velocity of 5.6 km/s was used. This accords with both in situ velocity measurements of the Charnian (5.64 km/s for the Maplewell series; Whitcombe and Maguire 1980), and the solution velocity for the a_o refractor interpreted by the LISPB line (5.6 - 5.8 km/s; Bamford et al. 1977).

To facilitate comparison between events, the reduced times were plotted against station positions along the line, rather than true distance from the source. Since the deeper the refractor the greater the reduced time, the reduced times were plotted positive downwards so as to provide a pseudo-depth impression. All the plots were made with the same time and distance scales for convenience, and for untimed quarry blasts the origin time was arbitrarily calculated by assuming a direct arrival of 5.2 km/s at the nearest station. Errors in origin time thus show up as d.c. shifts on the time axis.

The reduced time seismogram section (see Section 4.3 (ii)) aids interpretation as the plot contains information for all the different phases, but events cannot be as easily compared as using the reduced time graphs. The reduced time seismograms were normally plotted against true distance from the source and with the same time scale as the fast replays, so that picked arrival times could be quickly checked or later arrivals accurately timed. Like the reduced time graphs, the seismograms were reduced at 5.6 km/s and the time origin arbitrarily given for untimed shots. The traces were plotted with as large a gain as possible without overlapping adjacent P waves.

For comparison, plots of first arrival times were also made for groups of blasts from the same quarry or closely grouped quarries, for which the data were usually superimposed by least-squares best fit. These multiple plots have two uses:

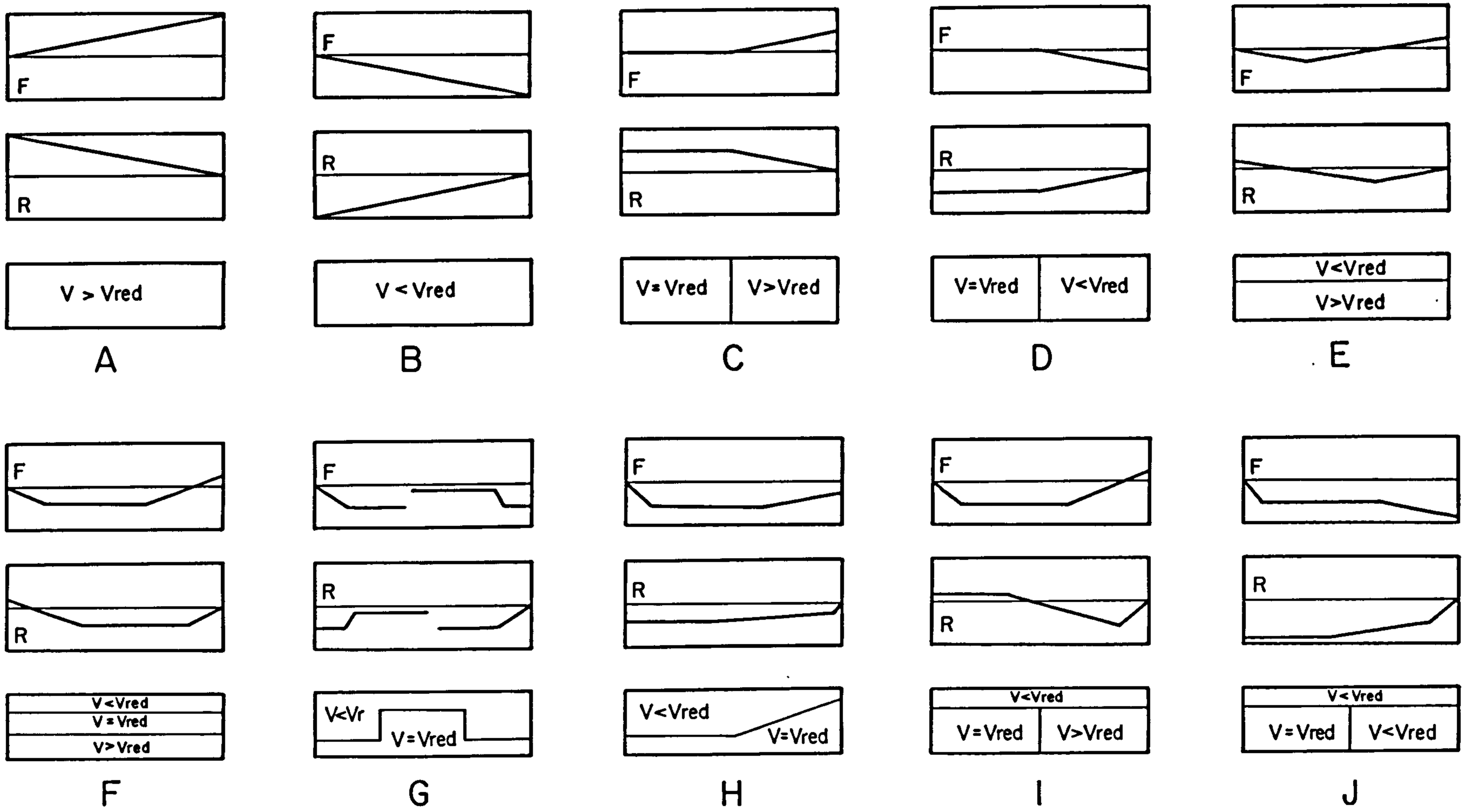

FIG 5-1 Reduce time graphs for various velocity models (not to scale) F Forward R Reverse

firstly to provide a convenient comparison between events from similar sources, and secondly to illustrate the margin of error within which the interpretation is being made.

Once all the data were plotted, observations which markedly differed from the norm were either repicked or deleted. On comparison with other reduced time graphs from a similar location, some events were judged to require re-locating, although only an extremely bad location will seriously corrupt the shape of a reduced time graph. For example, Fig. 5.2 illustrates the first arrival times of an event from Tunstead quarry, plotted also as if it were from Dow Low, some 10 km to the south-east.

5.3 Interpretation of the North-South Line

The north-south line passed the Woo Dale borehole, and linked the LISPB and the University of Leicester's Charnwood-Ballidon line, as shown in Fig. 1.1. Both the 1979 and 1981 (DASED1) experiments occupied this line, and jointly the distribution of data is extremely good; at least half a dozen events have been considered from each quarry group. The data set also includes local earthquakes from the Mansfield region (see Section 4.5.3), which provides a valuable addition to the quarry blast data.

5.3.1 Timed and Positioned Shots

The velocities used for the location of untimed quarry blasts were originally taken from the timed shots into the 1979 north-south profile (Section 4.5.1). There were five timed and positioned shots into this line: one each from Tunstead, Ballidon, Wardlow and Hindlow quarries, and the controlled shot at Shirley (Section 3.3.1). During the 1981 experiment a further nine timed and positioned quarry blasts were recorded along this profile: five from Tunstead, two from

FIG 5-2 Effect of poor location on reduced times

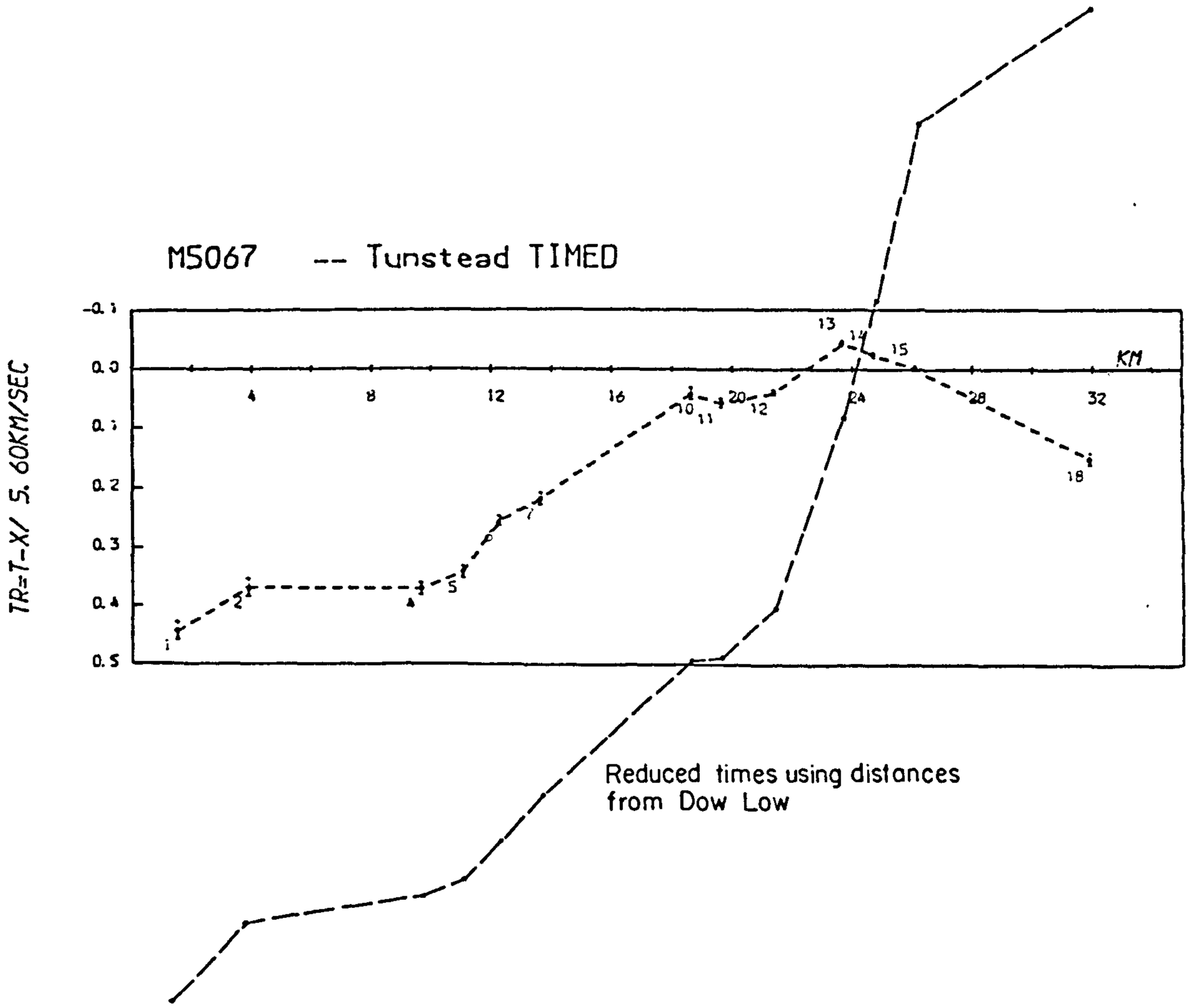

Dove Holes and one each from Ballidon and Shining Bank quarries. The picked times for the better recorded of these are plotted in Fig. 5.3.

The immediate striking factor of these picked times is the linearity of the T-X graphs and the high apparent velocities, even for the closest stations. There are no clear examples of classic two- or even three-layer T-X curves, so an intercept time analysis of these data would be difficult. Least-squares fits through the T-X points yield velocities of between 5.2 and 5.6 km/s for Tunstead and Doveholes quarries, and between 5.3 and 5.8 km/s for Ballidon and Wardlow. Within 10 km of some shotpoints, velocities of 5.6 - 5.7 km/s are commonly observed (e.g. Ballidon (M4035), and Tunstead (F34026)): either these velocities represent high velocity overburden, or basement refractions are observed at every station on the line.

The reduced time graphs are also difficult to interpret as the distinction between direct and refracted arrivals is not clear. If the first arrivals were all direct, then the reduced time variation would be expected to be related to surface geology. For example, stations 3 to 6 lie on Asbian Bee Low limestones, while station 7 and northwards are on younger limestones (see Fig. 1.5); this may explain the high velocity arrivals close to the Ballidon timed shot (M4035), and the lower velocities north of station 7. Similarly, stations 10 to 12 lie close to or upon the mud-rich facies of the Eyam Limestones, which can be correlated with increased reduced times for the Hindlow timed shot (M5064).

However, the reduced times generally decrease towards the northern end of the line for quarry blasts from south (Ballidon and Wardlow) and north (Tunstead, Doveholes, etc.). If the effects were totally due to lateral velocity variation in the overburden, then the reduced times for reversed shots should mirror each other (cf. cases C and D in Fig. 5.1), which is not seen here. Also the nature of the geology does not greatly change between stations 1 and 18, so it seems more

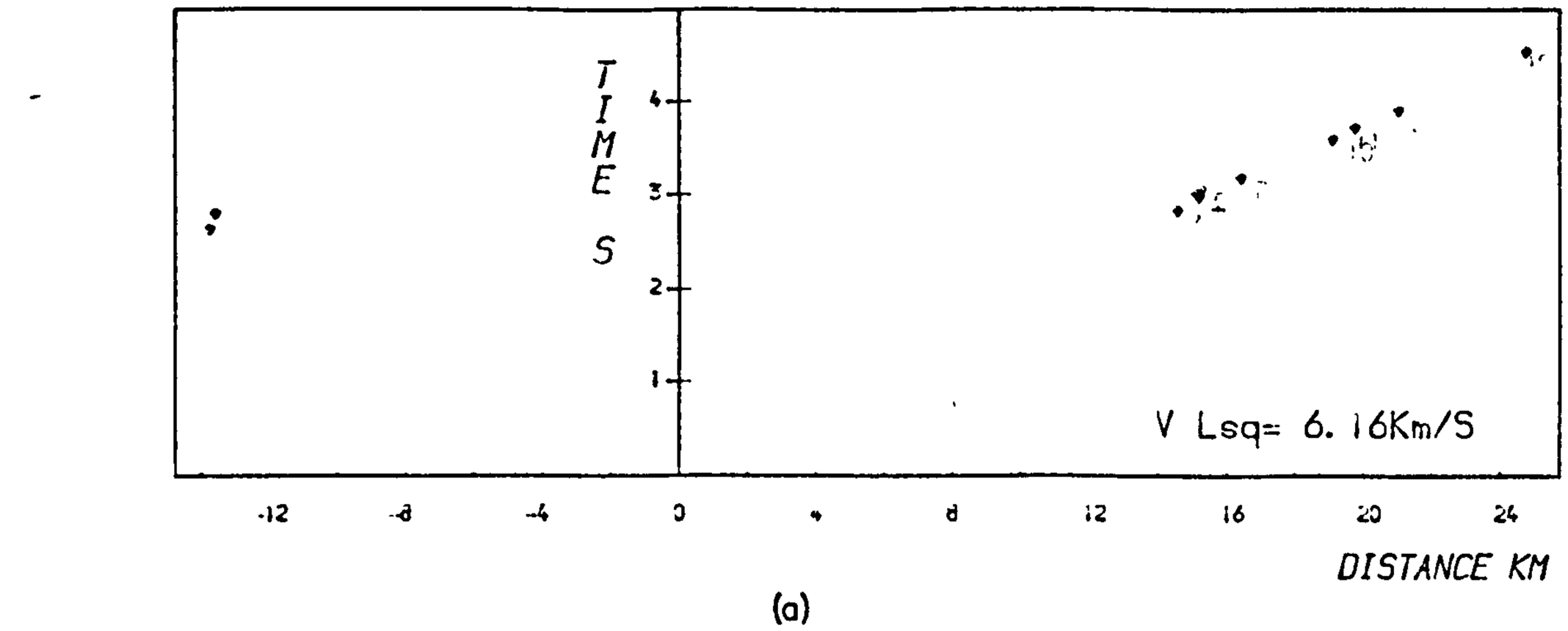

(a)

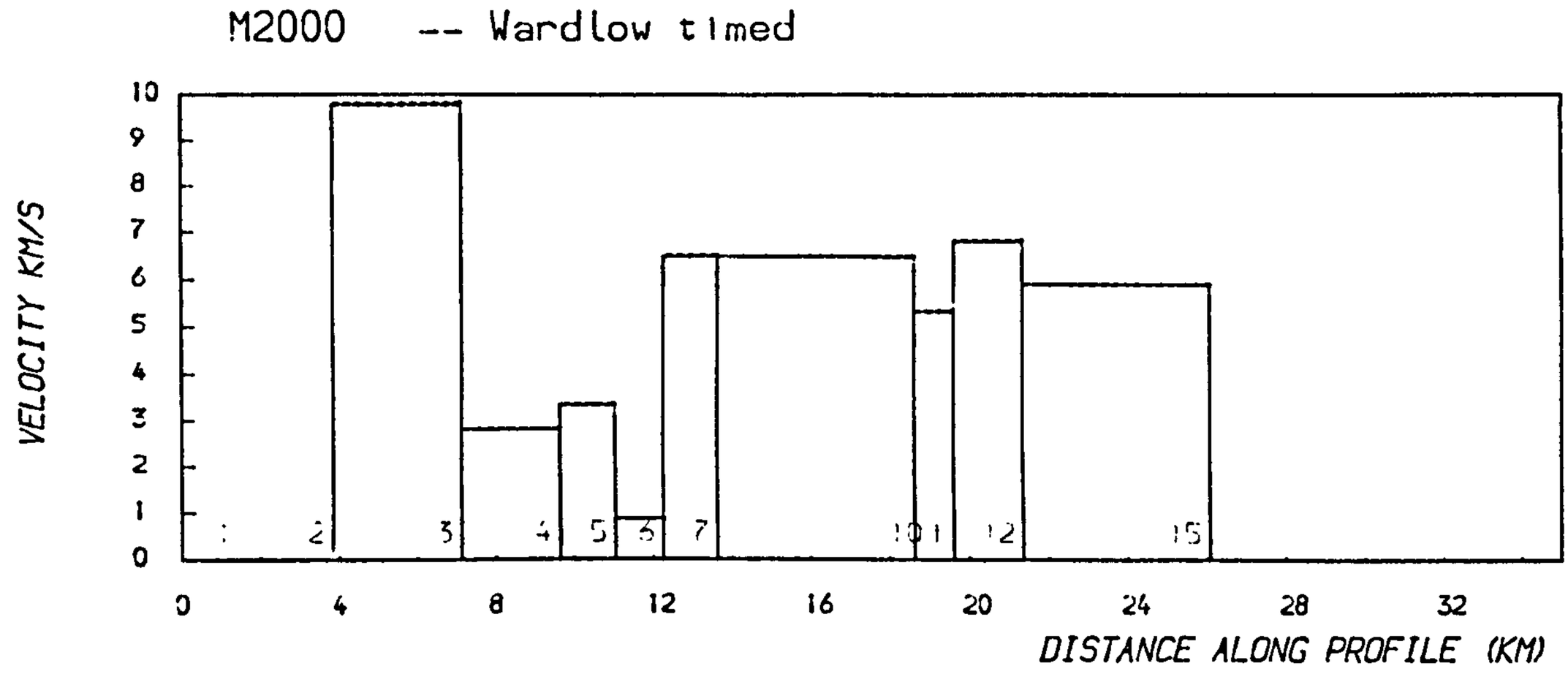

(b)

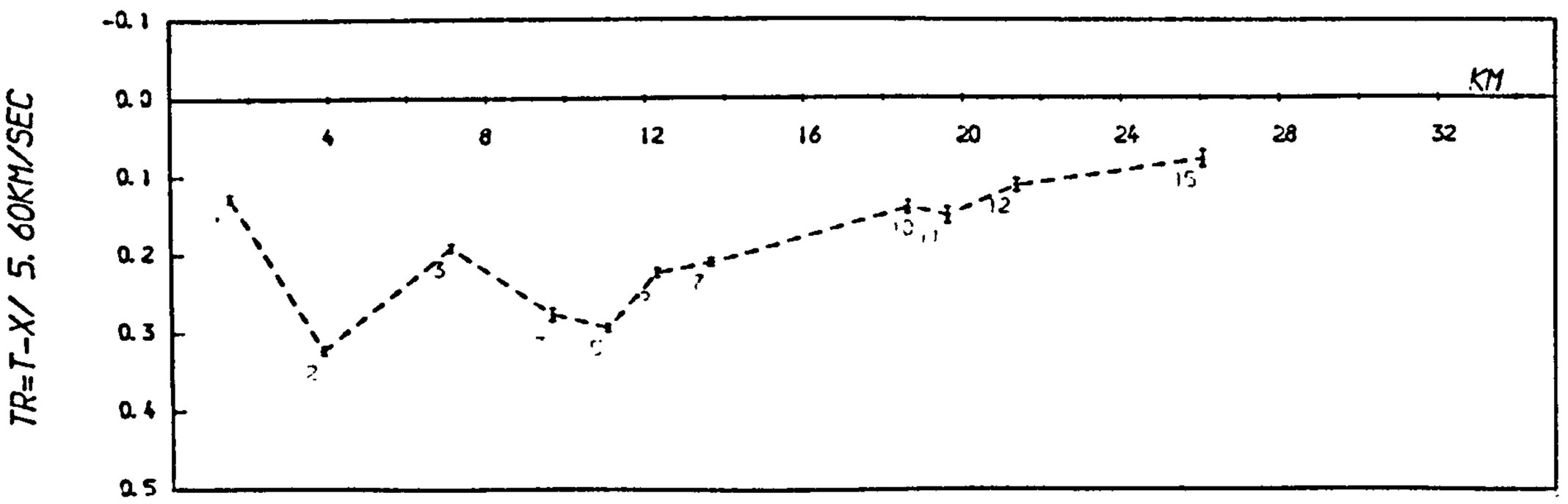

(c)

(a) T-X (b)apparent vel. (c)reduced

FIG 5-3

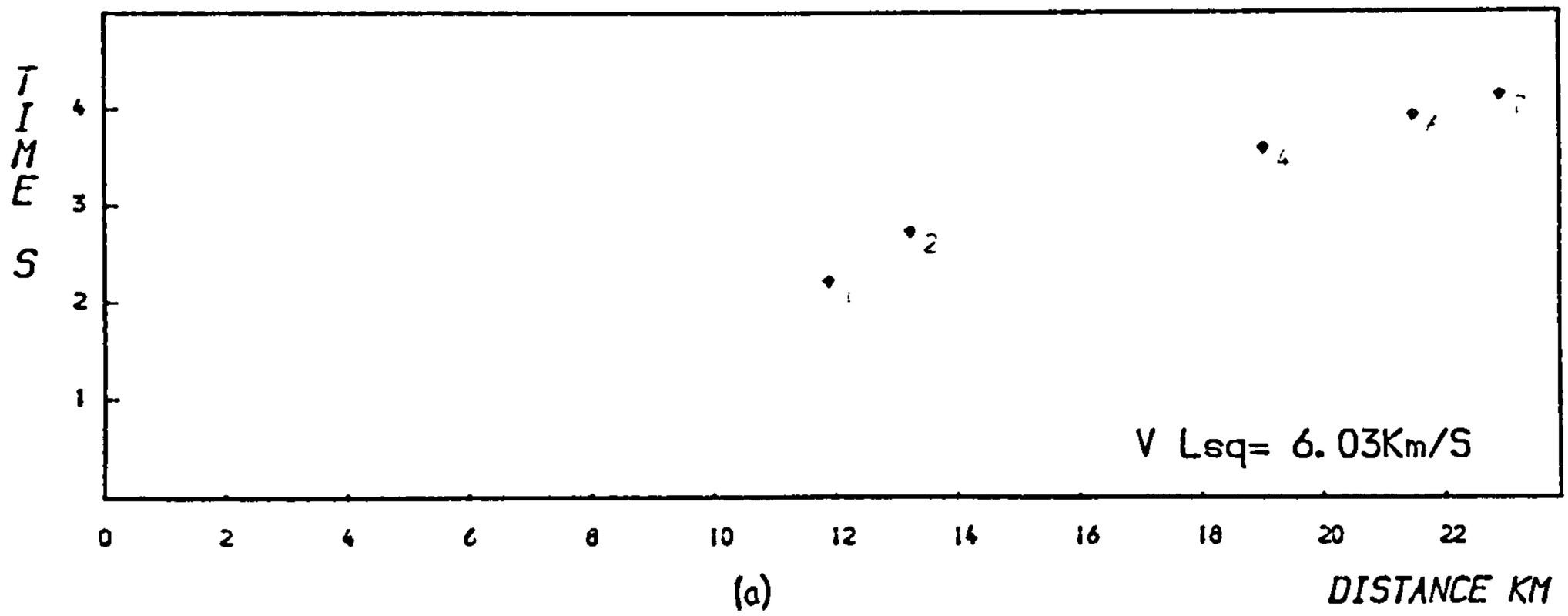

(a)

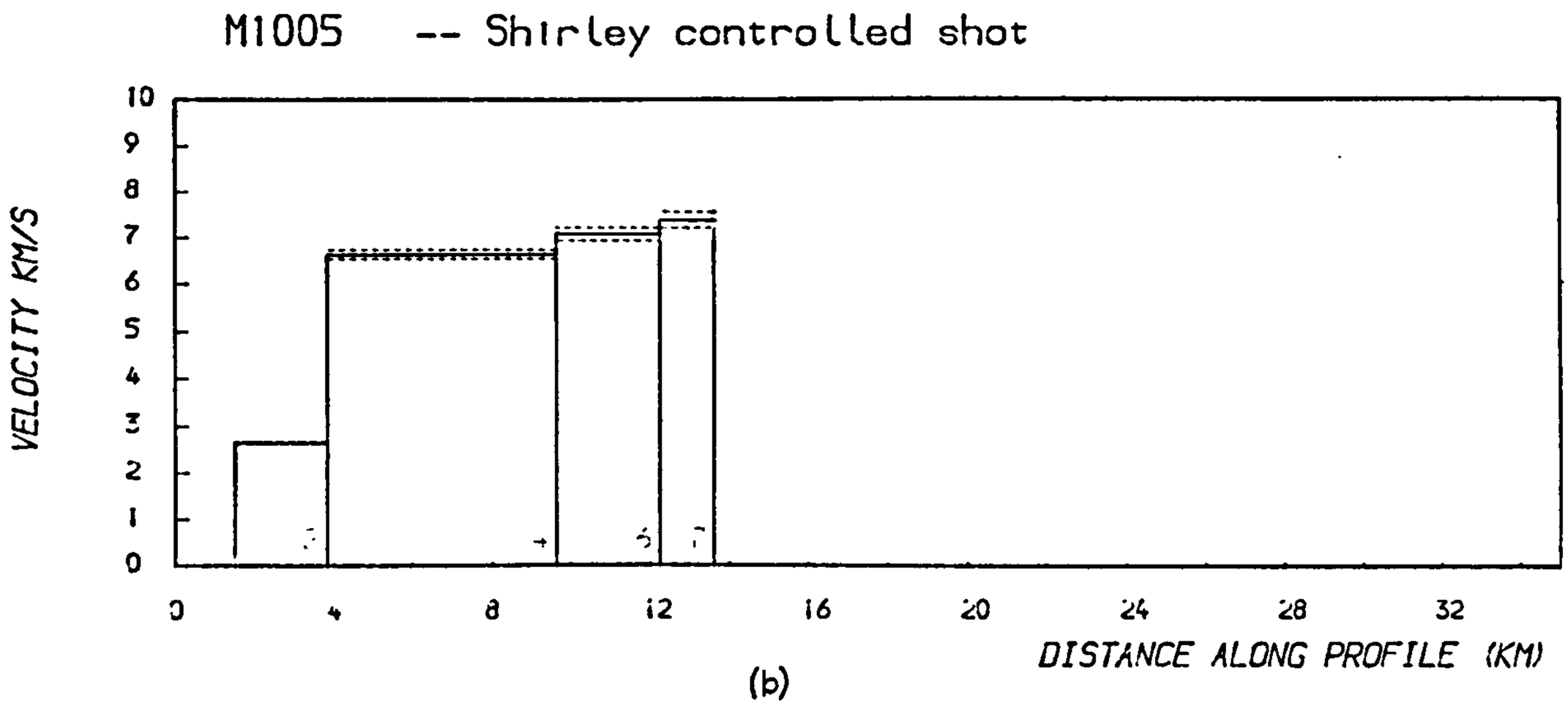

(b)

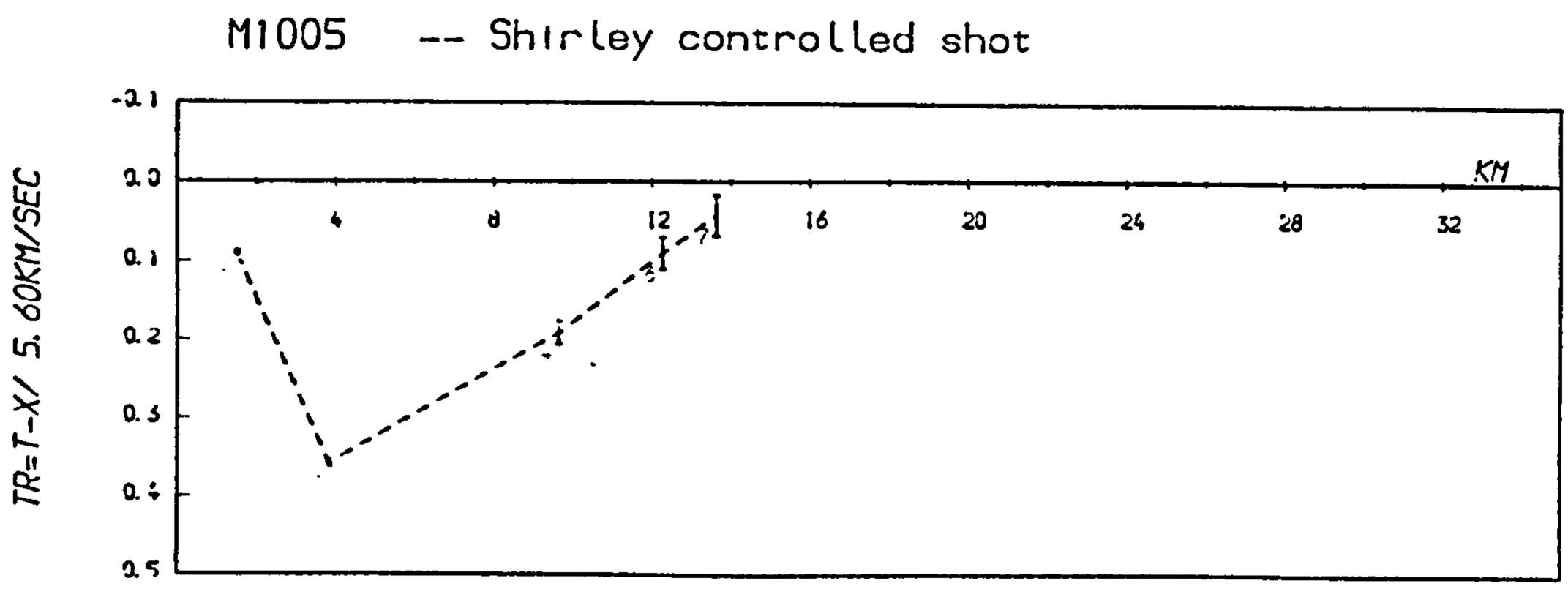

(c)

FIG 5-3 cont

M4035 -- Ballidon timed

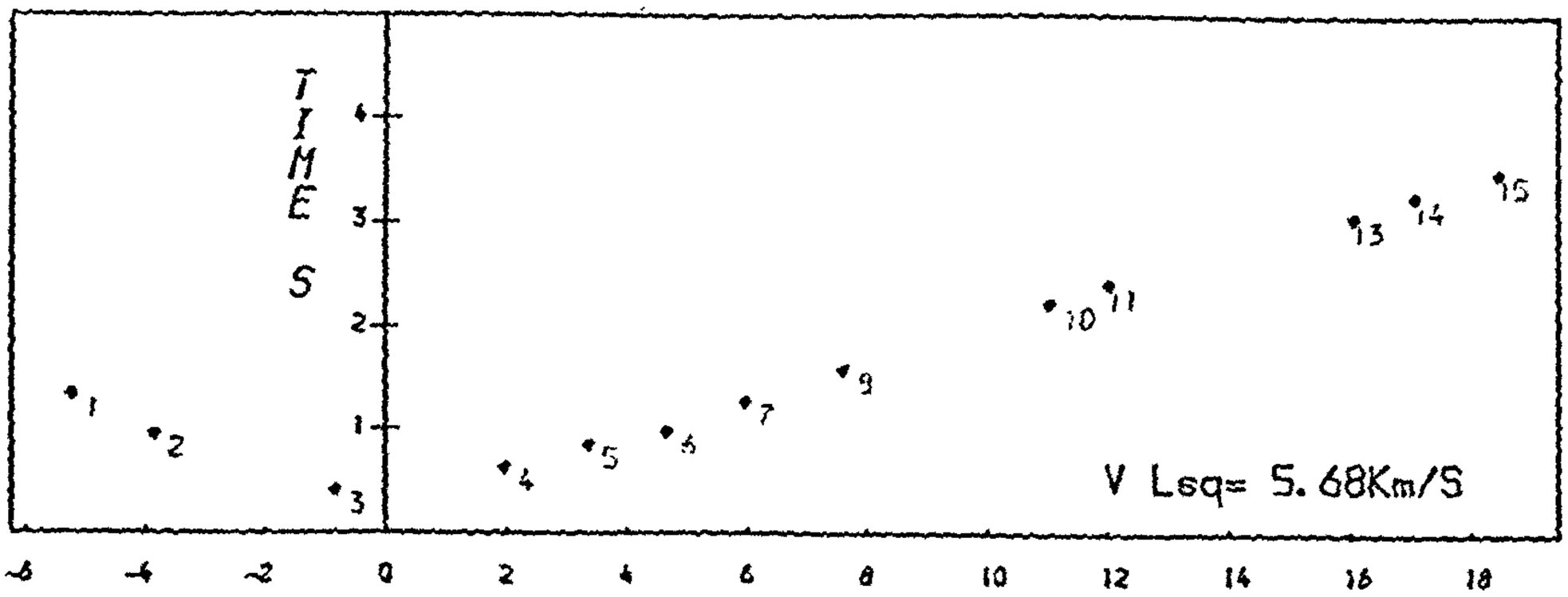

(a)

M4035 -- Ballidon timed

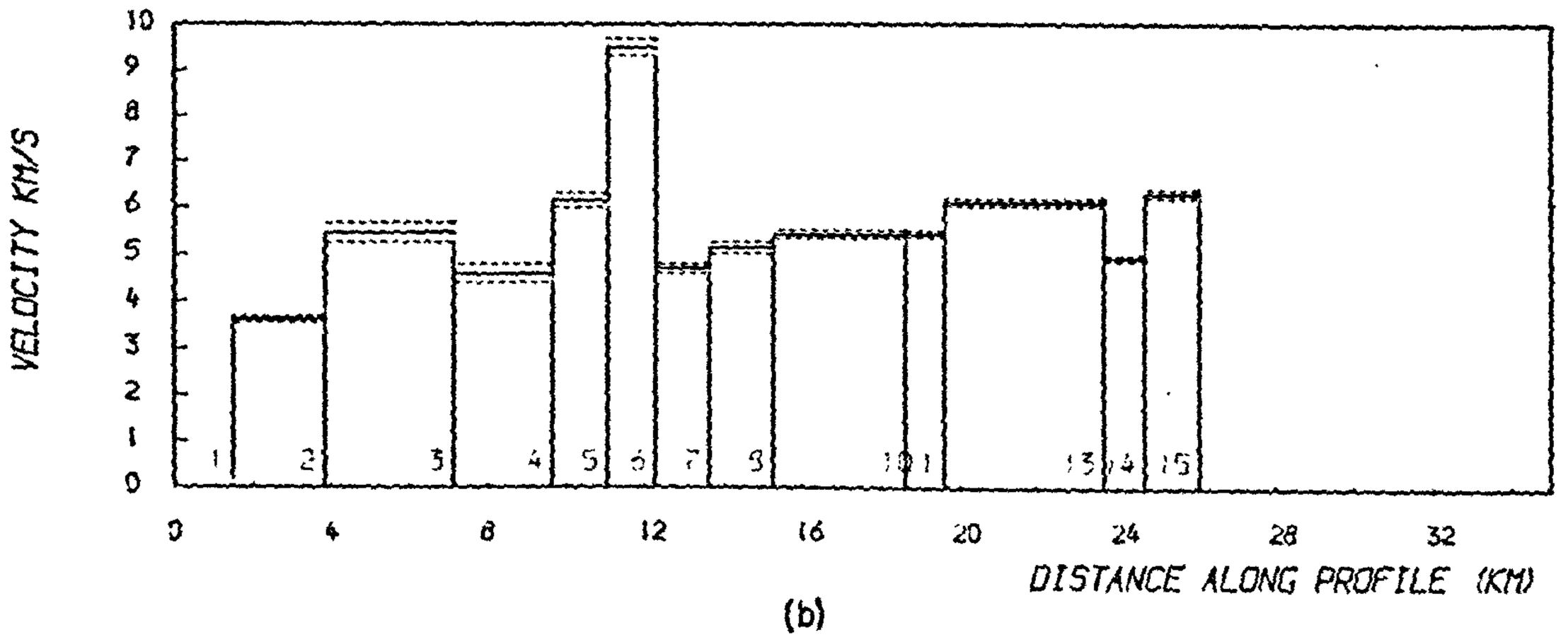

(b)

M4035 -- Ballidon timed

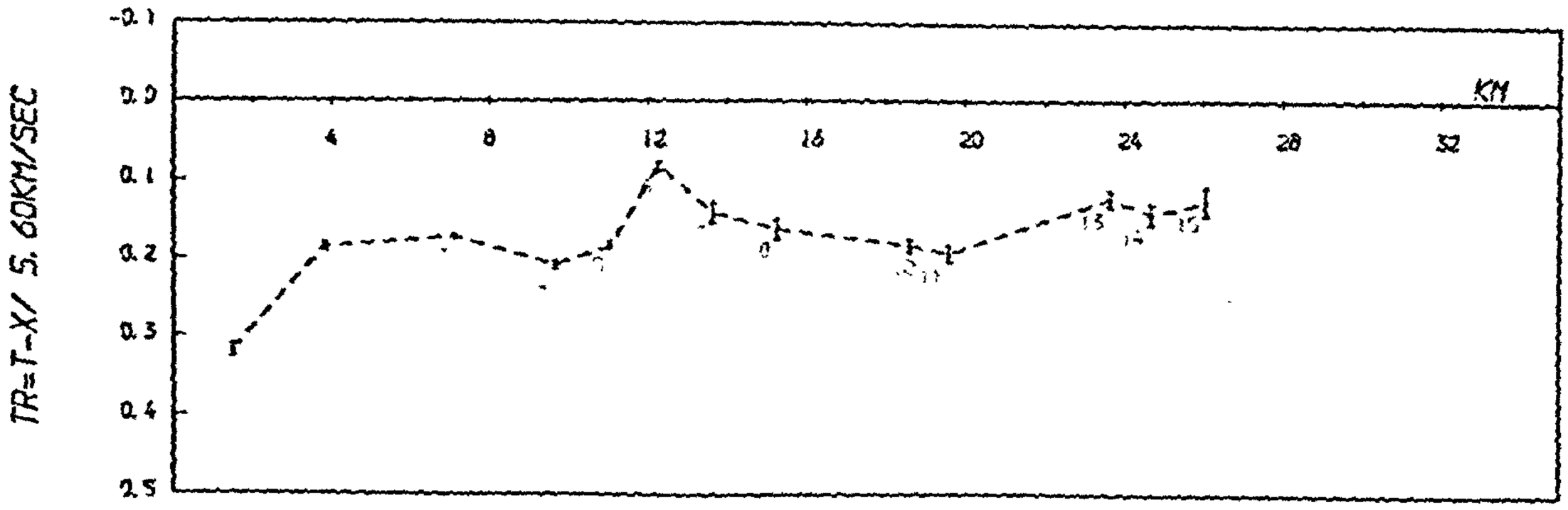

(c)

FIG 5-3 cont

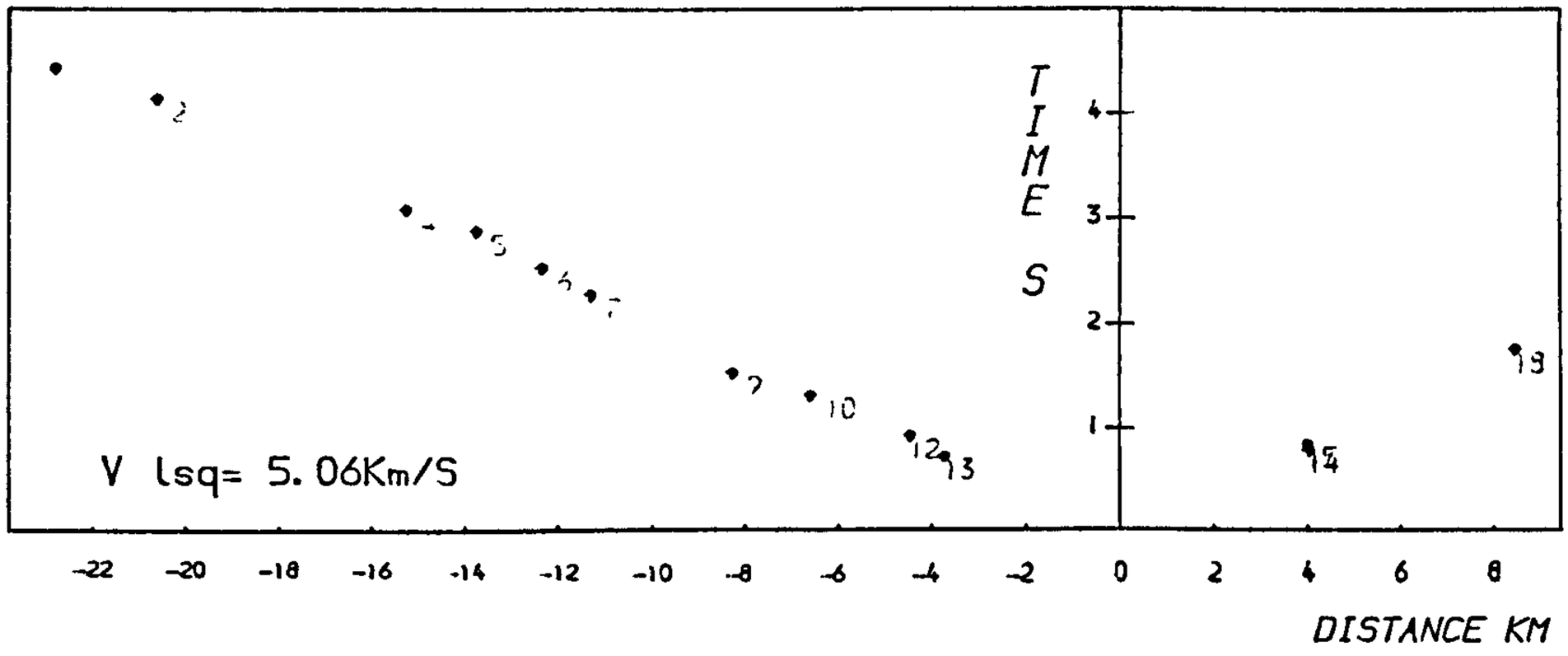

(a)

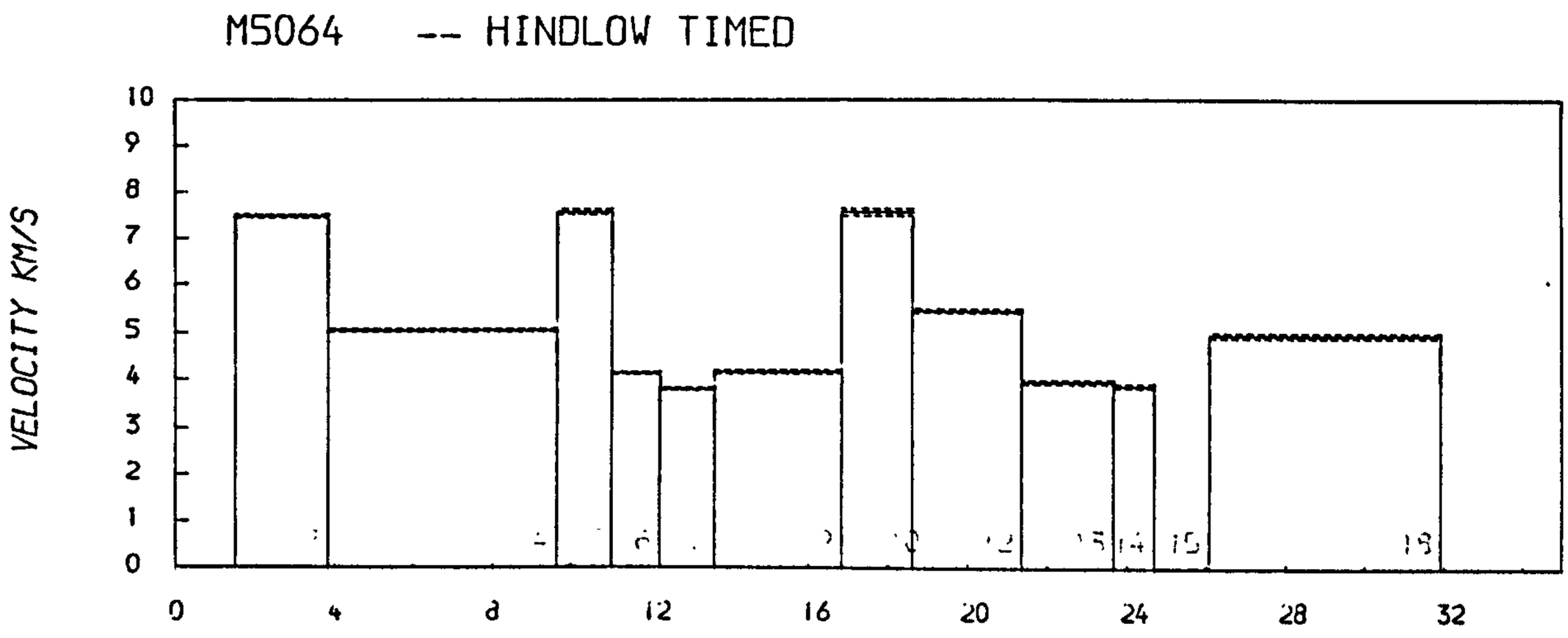

(b)

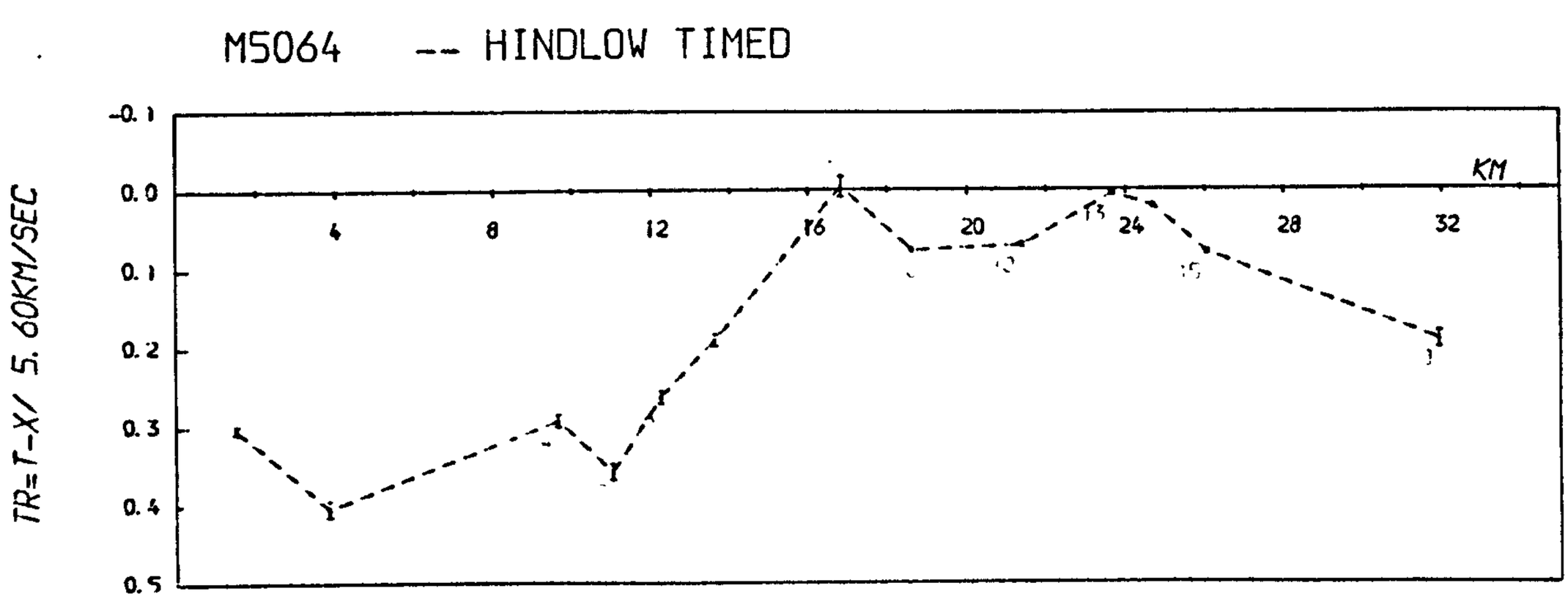

(c)

FIG 5·3 cont

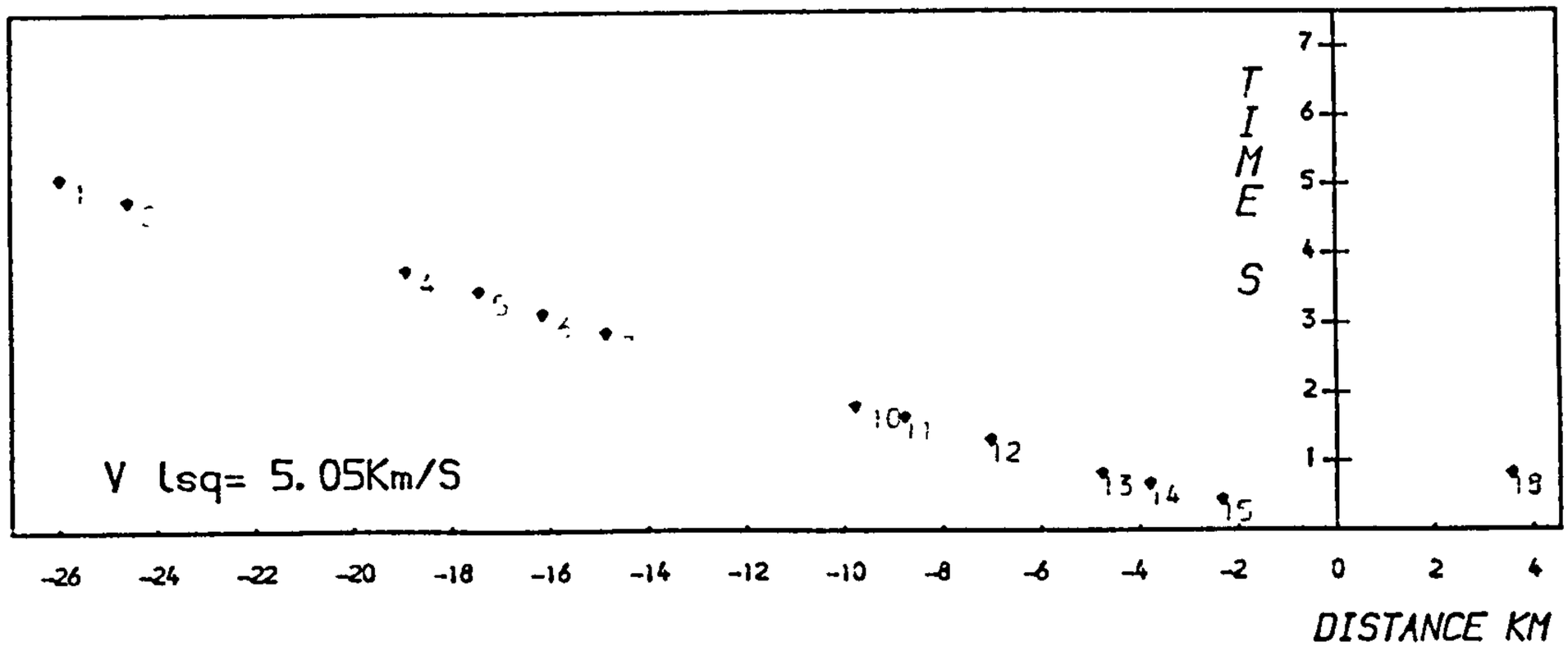

(a)

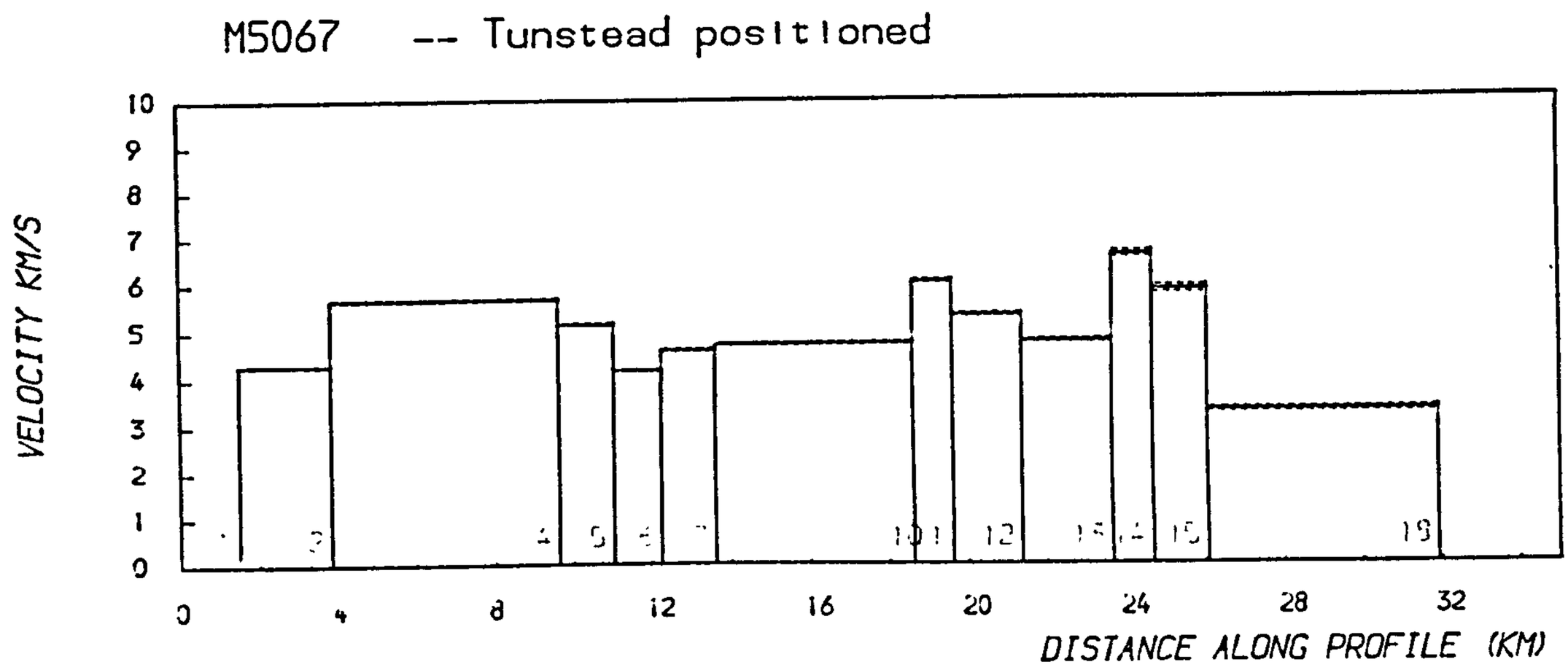

(b)

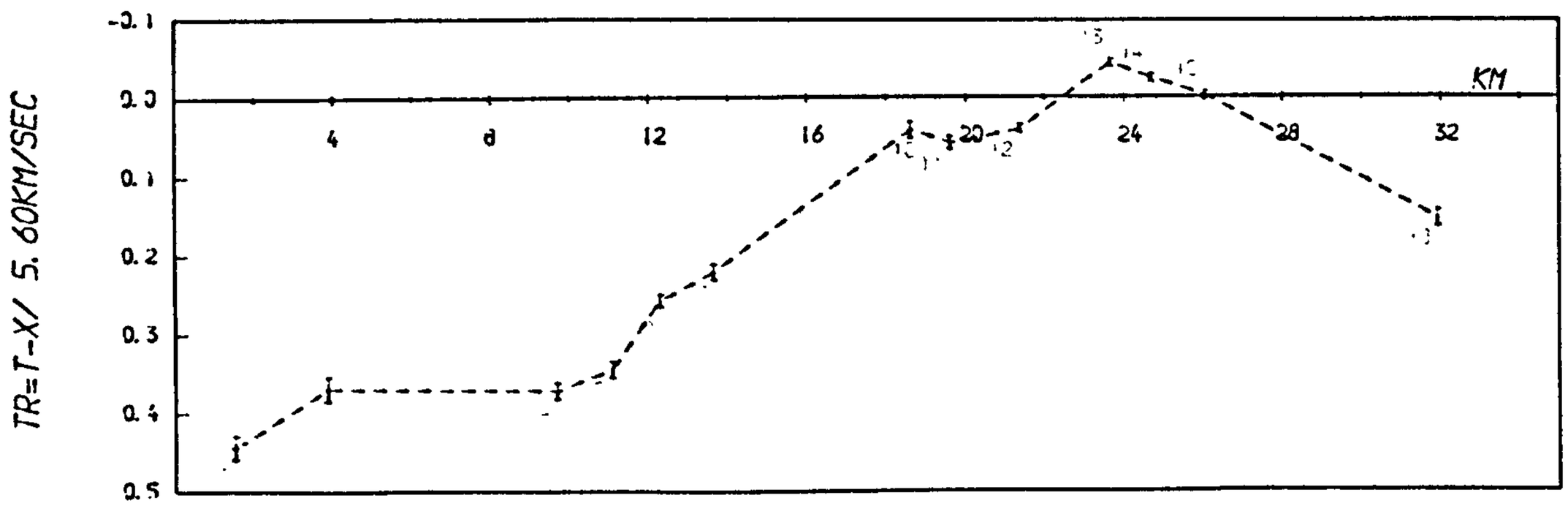

(c)

FIG 5-3 cont

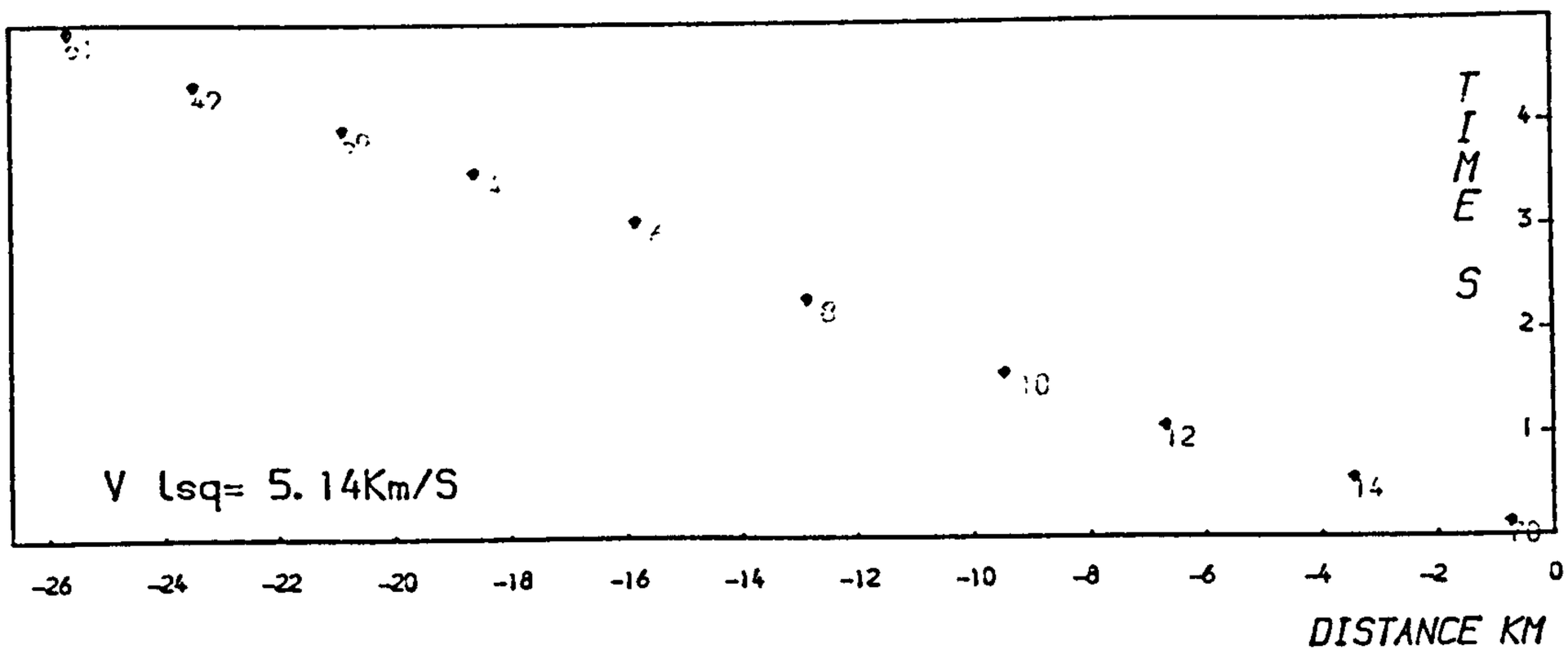

(a)

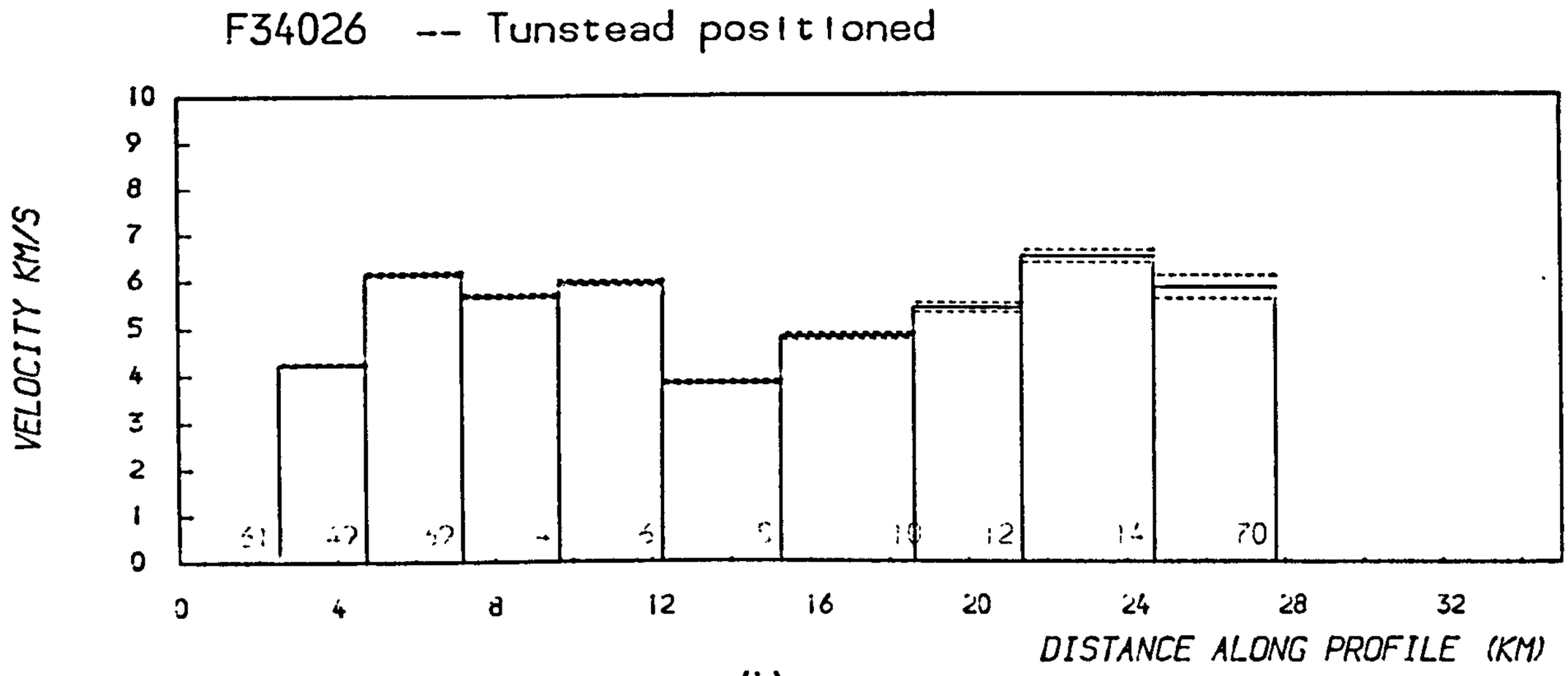

(b)

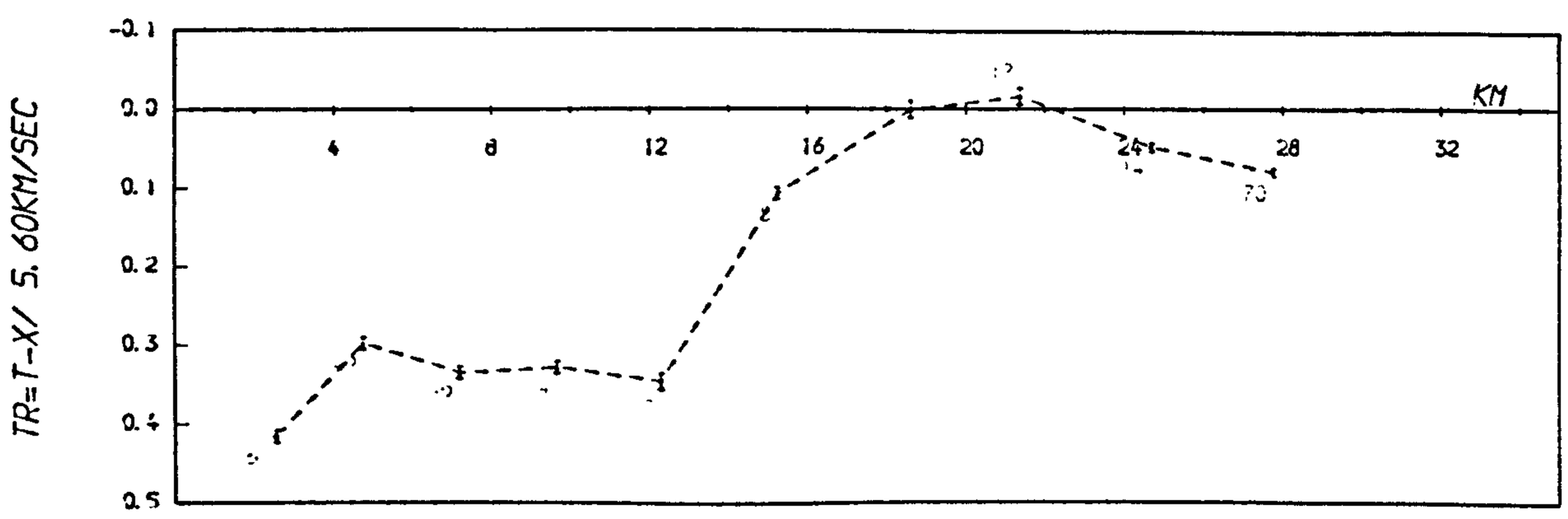

(c)

FIG 5-3 cont

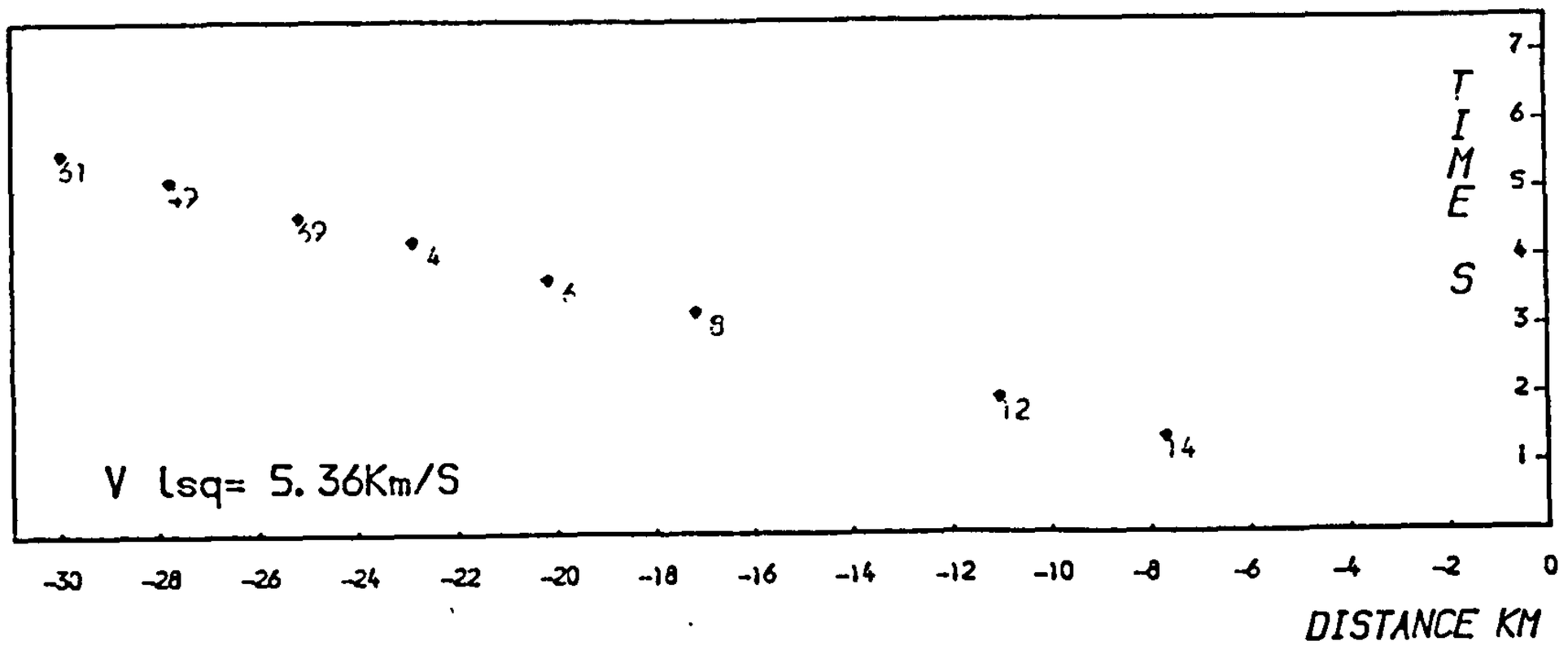

(a)

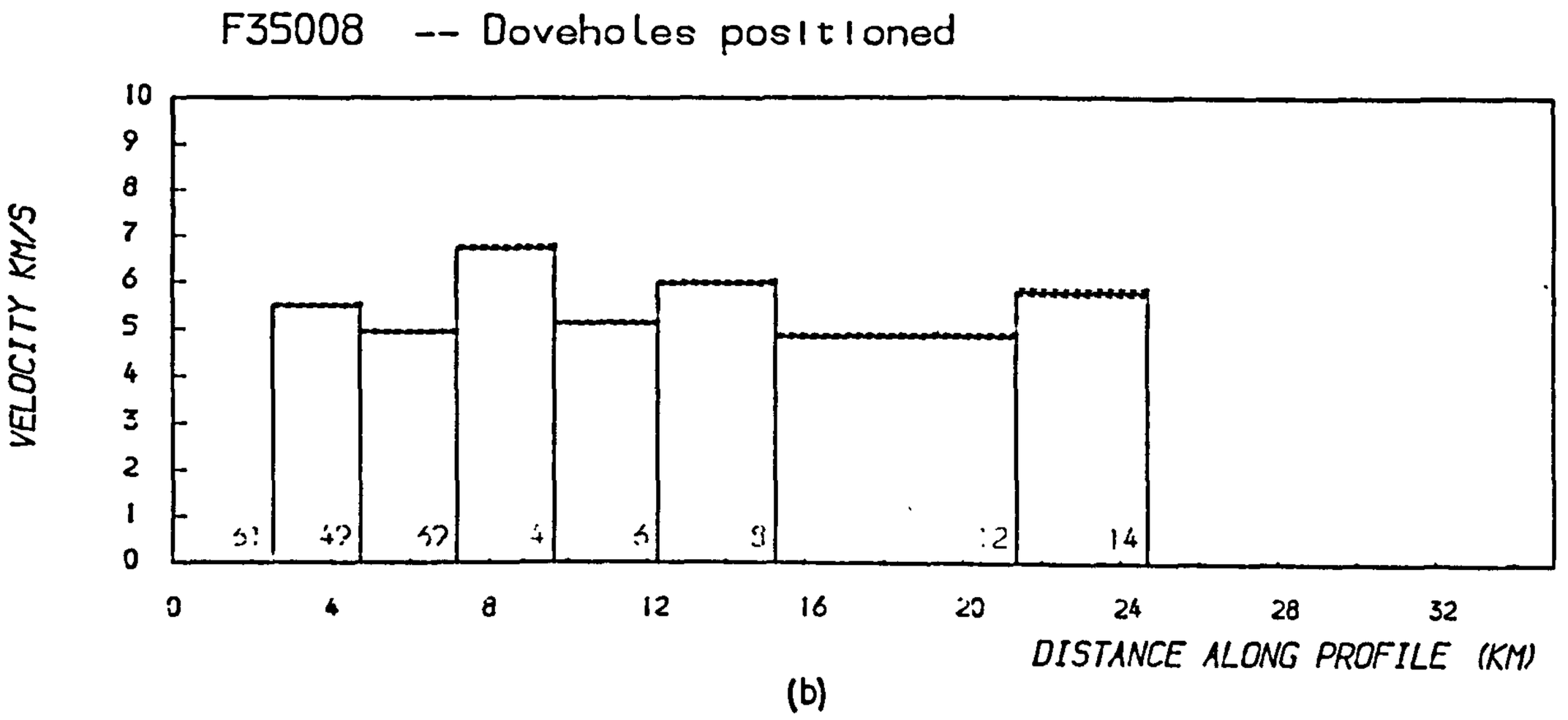

(b)

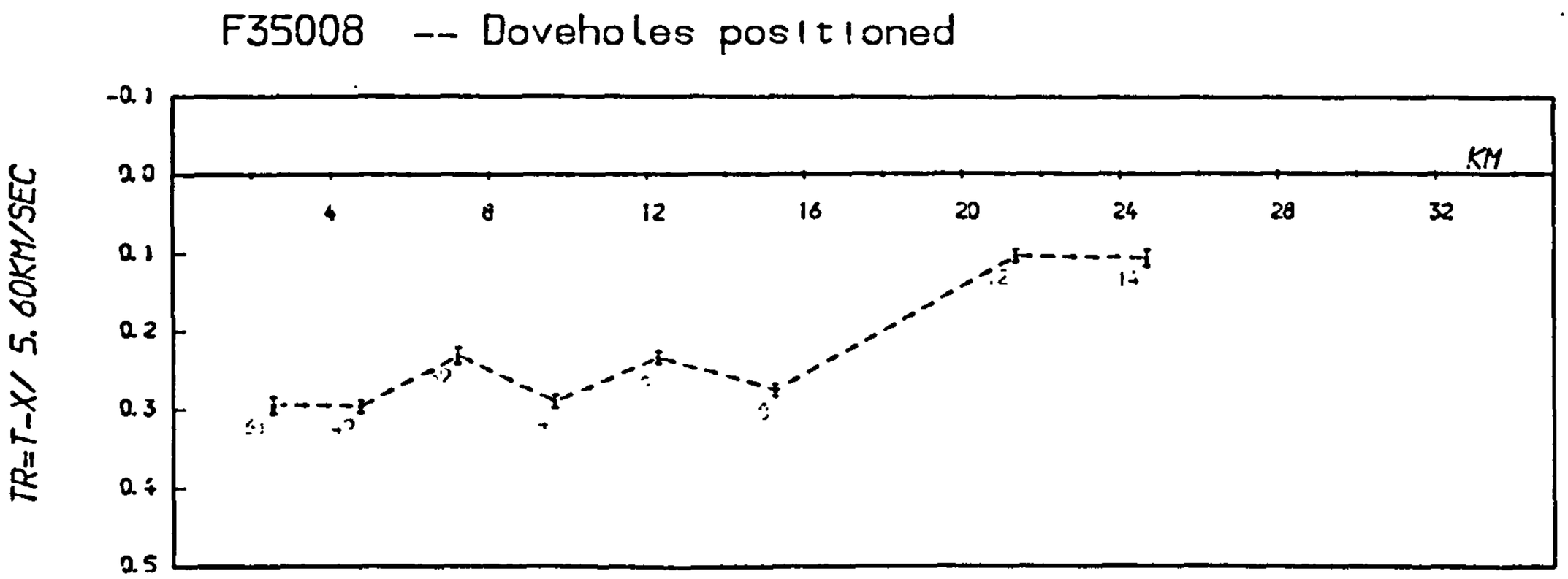

(c)

FIG 5-3 cont

likely that much of the variation in reduced times is due to deeper velocity structure.

Similar velocities for Carboniferous limestones have been measured in South Wales by Bayerly and Brooks (1980), who attributed 5.1 - 5.3 km/s and 5.6 - 5.7 km/s to clean and dolomitised limestones respectively. If one accepts direct arrival velocities of this magnitude, then at what distance are refractions from, say, a 5.6 - 5.8 km/s layer expected as first arrivals? For a horizontal two-layer case with an overburden of thickness h and velocity V_o,

$$X_c = \frac{2\,h\cos\theta_c}{V_o} \left(\frac{1}{V_o} - \frac{1}{V_r}\right)^{-1}$$

for cross-over distance X_c, refractor velocity V_r and critical angle θ_c. Table 5-1 lists the cross-over distances for various combinations of h, V_o and V_r, and also gives the critical distance, $2\,h\tan\theta_c$, at which the refracted phase first appears.

Table 5-1

Cross-over Distance Examples

Thickness h km	Overburden velocity V_o km/s	Refractor velocity V_r km/s	Cross-Over distance X_c km	Critical distance km
	5.3	5.7	5.24	2.52
0.5	5.6	5.7	10.6	5.27
	5.6	5.8	7.55	3.71
	5.3	5.7	10.5	5.05
1.0	5.6	5.7	21.2	10.54
	5.6	5.8	15.1	7.42
	5.3	5.7	21.0	10.10
2.0	5.6	5.7	42.4	21.10
	5.6	5.8	30.2	14.84

The depths used in Table 5-1 approximately correspond to the refractor depths implied by the Woo Dale borehole, LISPB and Charnwood-Ballidon profiles respectively. Since the limestone sequence is not as thick as 2 km everywhere on the Dome, and that not all limestones are dolomitised, then basement refractions are expected to be observed as first arrivals within the limits of a 30 km long profile. However, if there are laterally extensive dolomitic horizons, then high velocity 'direct' waves might prelude arrivals from a deeper refractor over substantial distances, as noted by Bayerly and Brooks (1980).

Taking the model further, a simple plane-layer ray-tracer has been used to plot T-X curves for the 1.0 km thick overburden case (above), shown in Fig. 5.4. Obviously, the smaller the velocity contrast the closer the phases arrive with respect to each other, and for the lowest velocity contrast there is a distance of some 20 km over which all the various arrivals fall within 0.1s. This presumably would result in much interference and loss of definition in the P wave coda.

5.3.2 Discrimination of Basement Refractions

It is apparent from the first arrival times plotted in Fig. 5.3 that T-X and apparent velocity plots alone are not well suited to distinguish between direct and refracted arrivals. However, the reduced time graphs suggest that not all the first arrivals are direct because the reduced times decrease towards the north of the line for shots from both directions. Also, there are consistent sudden increases in reduced time not clearly due to geological variation: for example, for the southern events from Shirley (M1005) and Wardlow (M2000), there is a 0.2 - 0.3s increase in reduced time between stations 1 and 2, while for the Ballidon timed blast (M4035) there is a 0.1s decrease in delay time between these stations. From northern quarries, examples include the 0.2s increase in reduced time between stations 9 and 7 for the timed

FIG 5-4

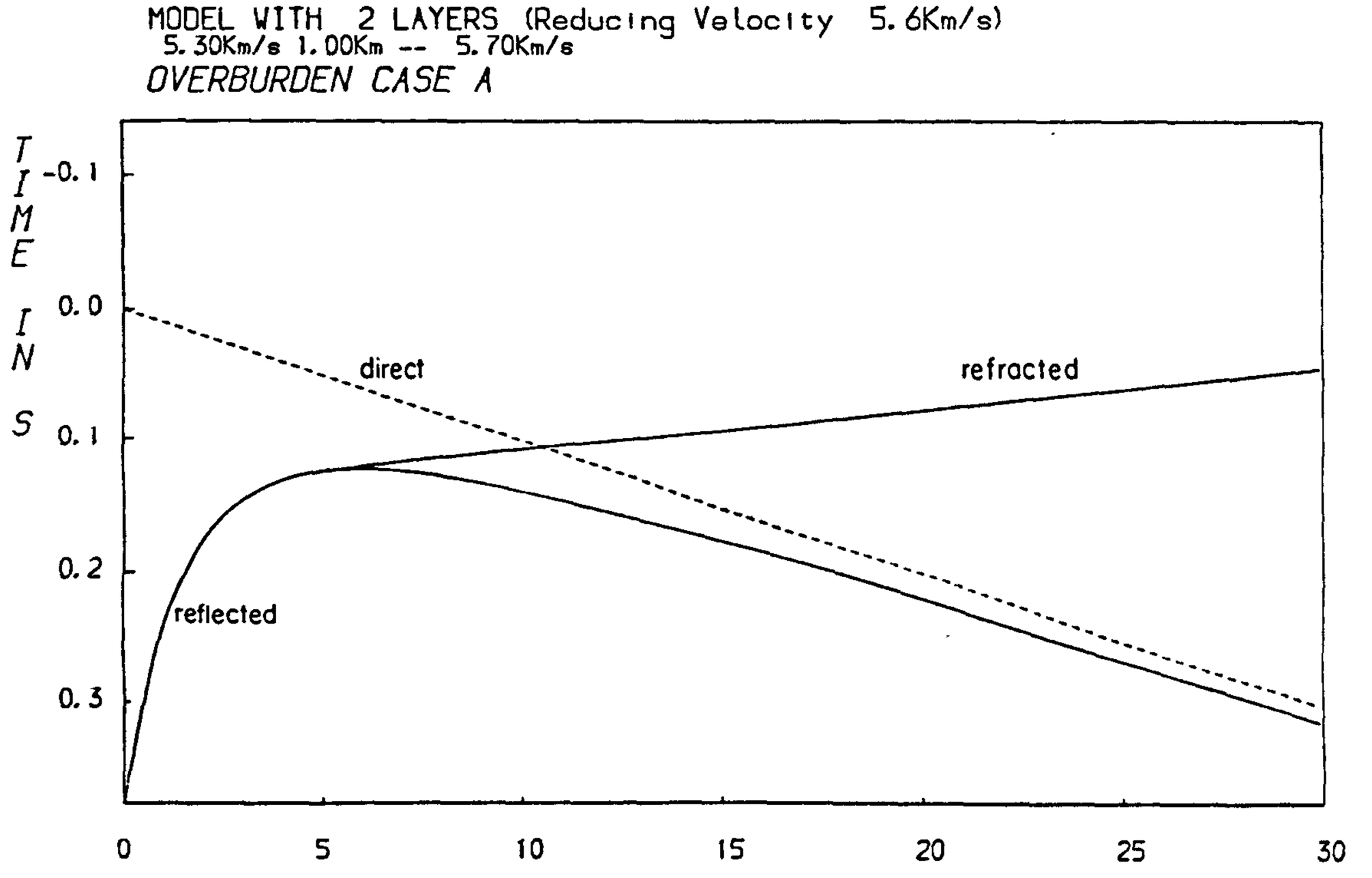
MODEL WITH 2 LAYERS (Reducing Velocity 5.6Km/s)
5.30Km/s 1.00Km -- 5.70Km/s
OVERBURDEN CASE A
TIME IN S
-0.1
0.0
0.1
0.2
0.3
direct
refracted
reflected
0
5
10
15
20
25
30
DISTANCE (KM)

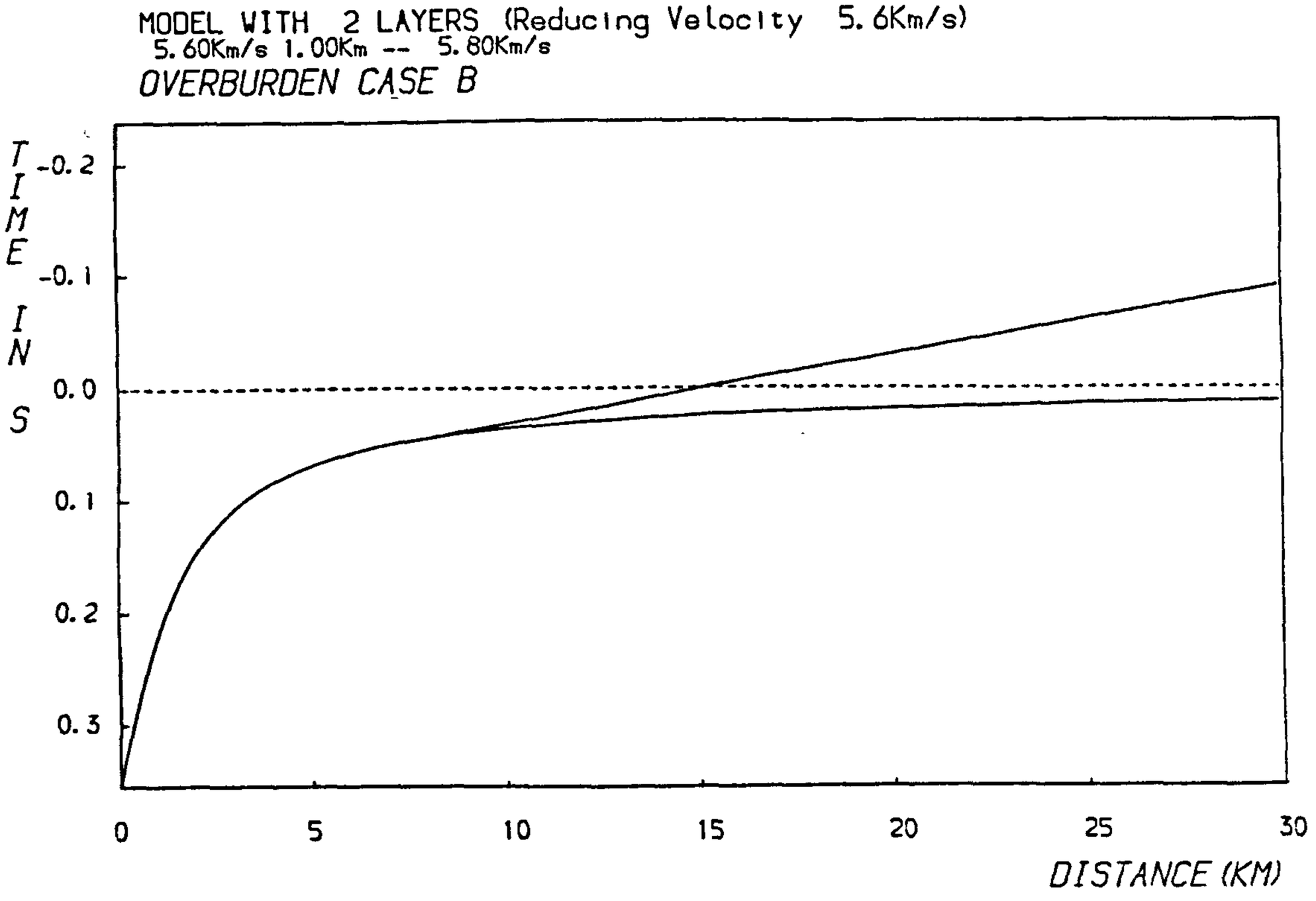
MODEL WITH 2 LAYERS (Reducing Velocity 5.6Km/s)
5.60Km/s 1.00Km -- 5.80Km/s
OVERBURDEN CASE B
TIME IN S
-0.2
-0.1
0.0
0.1
0.2
0.3
0
5
10
15
20
25
30
DISTANCE (KM)

Hinlow shot (M5064), and the 0.25s increase between stations 8 and 6 for the timed Tunstead shot (F34026).

The effect is illustrated by the good example of the untimed Tunstead blast M4027, the first arrival times for which are plotted in Fig. 5.5a. There is an increase in reduced time of about 0.2s between stations 8 and 7, which accompanies an increase in apparent velocity of about 0.3 km/s south of station 8. Plotting the relative amplitudes of the first arrivals (Fig. 5.5b), two rates of amplitude decay are evident: a residual decay of about 2 db/km between stations 15 and 8, and one of about 0.3 db/km between stations 7 and 1. The higher rate of amplitude decay may be due to either a thin or absorptive layer (Section 2.4.1); the Woo Dale borehole implies that the Dinantian limestones are thin, so the initial high residual attenuation may correspond to direct waves through them. Thus the delayed first arrivals south of station 8 with the lower attenuation rate may be for refractions from a thick basement refractor.

Two contrasting phases are evident from the reduced time seismograms for this Tunstead event (Fig. 5.5c), where the direct arrivals between stations 11 and 7 (full line) prelude longer period and proportionally greater amplitude basement refractions (dashed line). By station 7 these refractions are picked as 'first' arrivals since the amplitude of the high velocity direct waves has decayed to noise level.

As an example of a quarry blast from the south of the line, a similar contrast between direct and refracted wave residual attenuation is observed for the timed Ballidon event (M4035; Fig. 5.6a). Between stations 7 and 4 the residual attenuation is about 2db/km, while north of station 8 the rate is only 0.1 db/km. Unlike the untimed shot from Tunstead (above) however, this change in the rate of amplitude decay does not accompany any marked increases in reduced time, or change in apparent velocity (cf. Fig. 5.3). On the reduced time seismogram section (Fig. 5.6b) a basement arrival can be traced northwards from station 7.

M4027 -- Tunstead untimed

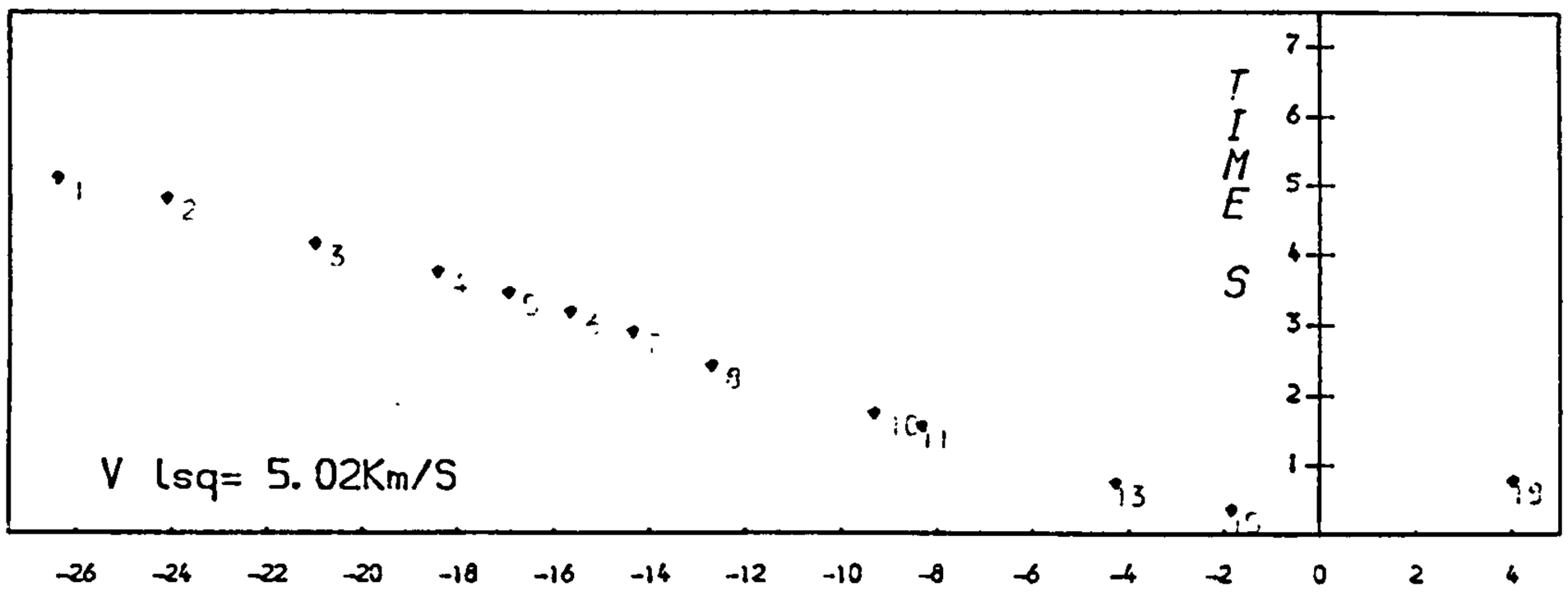

M4027 -- Tunstead untimed

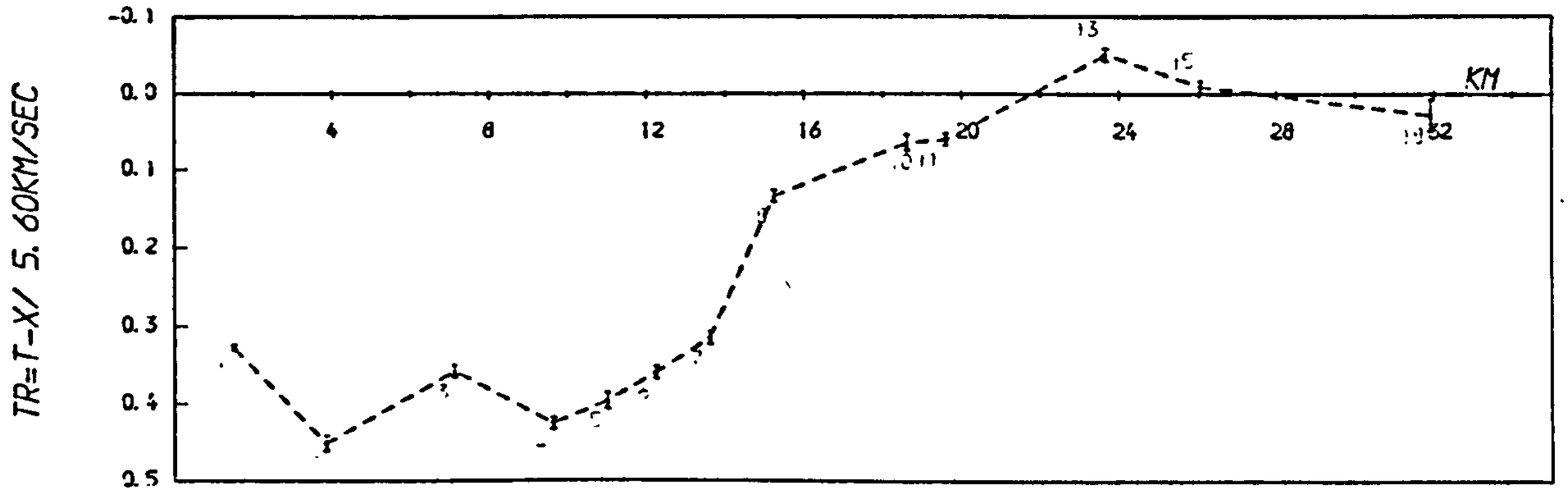

M4027 -- Tunstead untimed

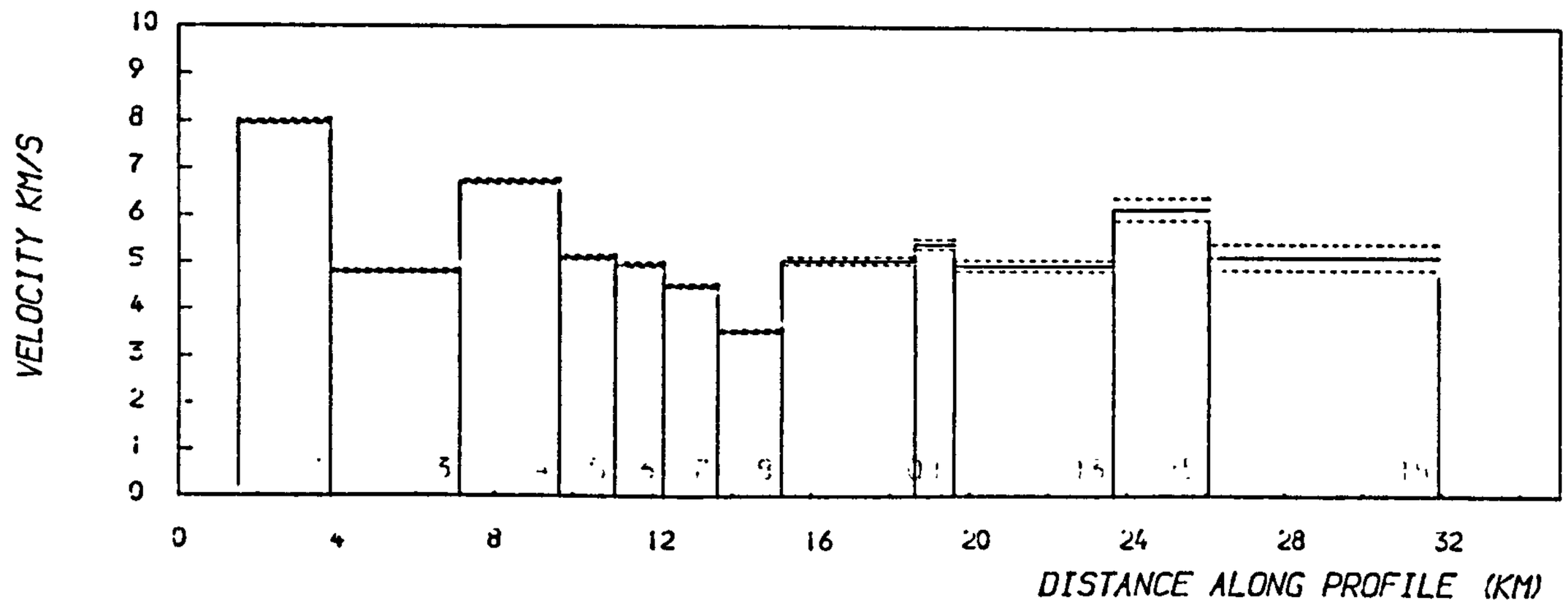

FIG 5-5a

FIG 5-5b Relative amplitudes, M4027 – Tunstead

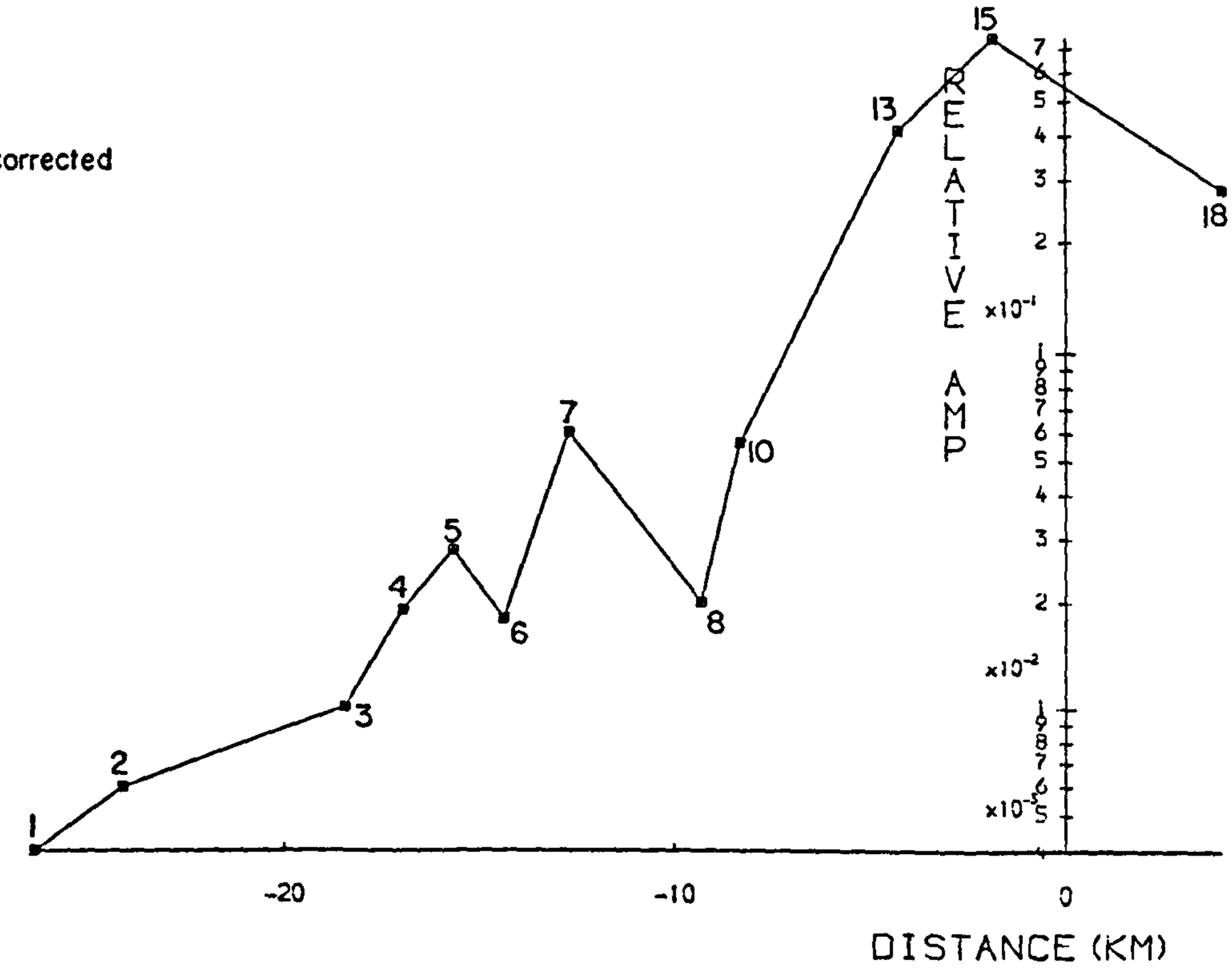

M4027 -- TUNSTEAD UNTIMED

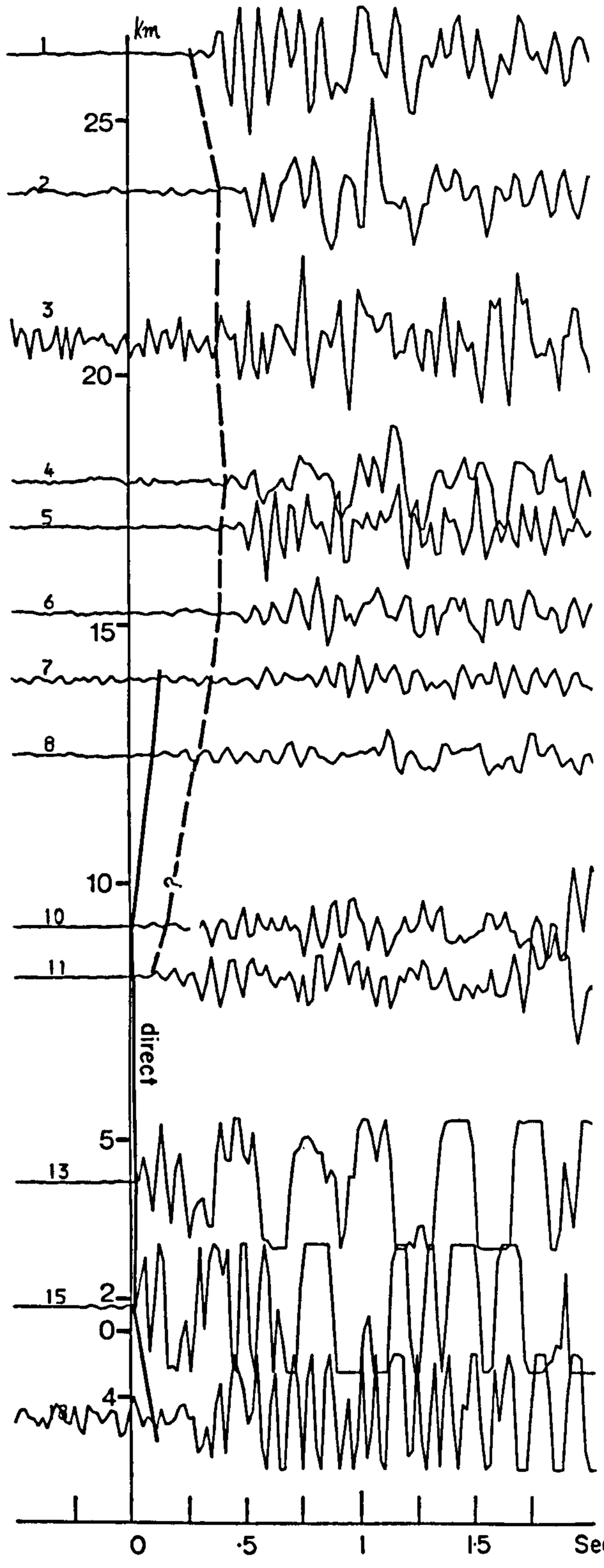

FIG 5-5c Seismograms reduced at 5·6km/s

(For repeated Tunstead shots, see end of Appendix A.)

FIG 5-6a Relative amplitudes - M4035 Ballidon

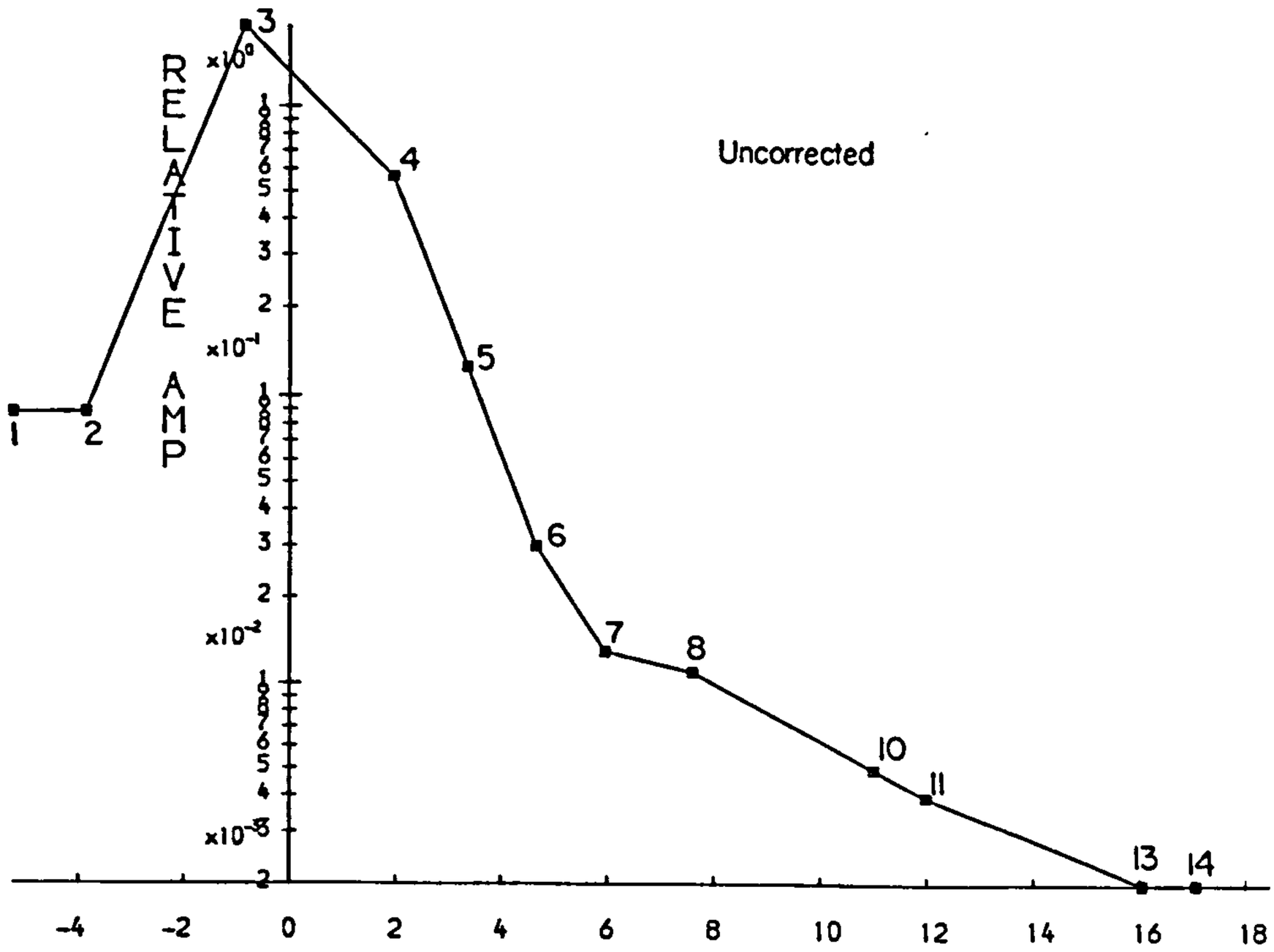

Uncorrected

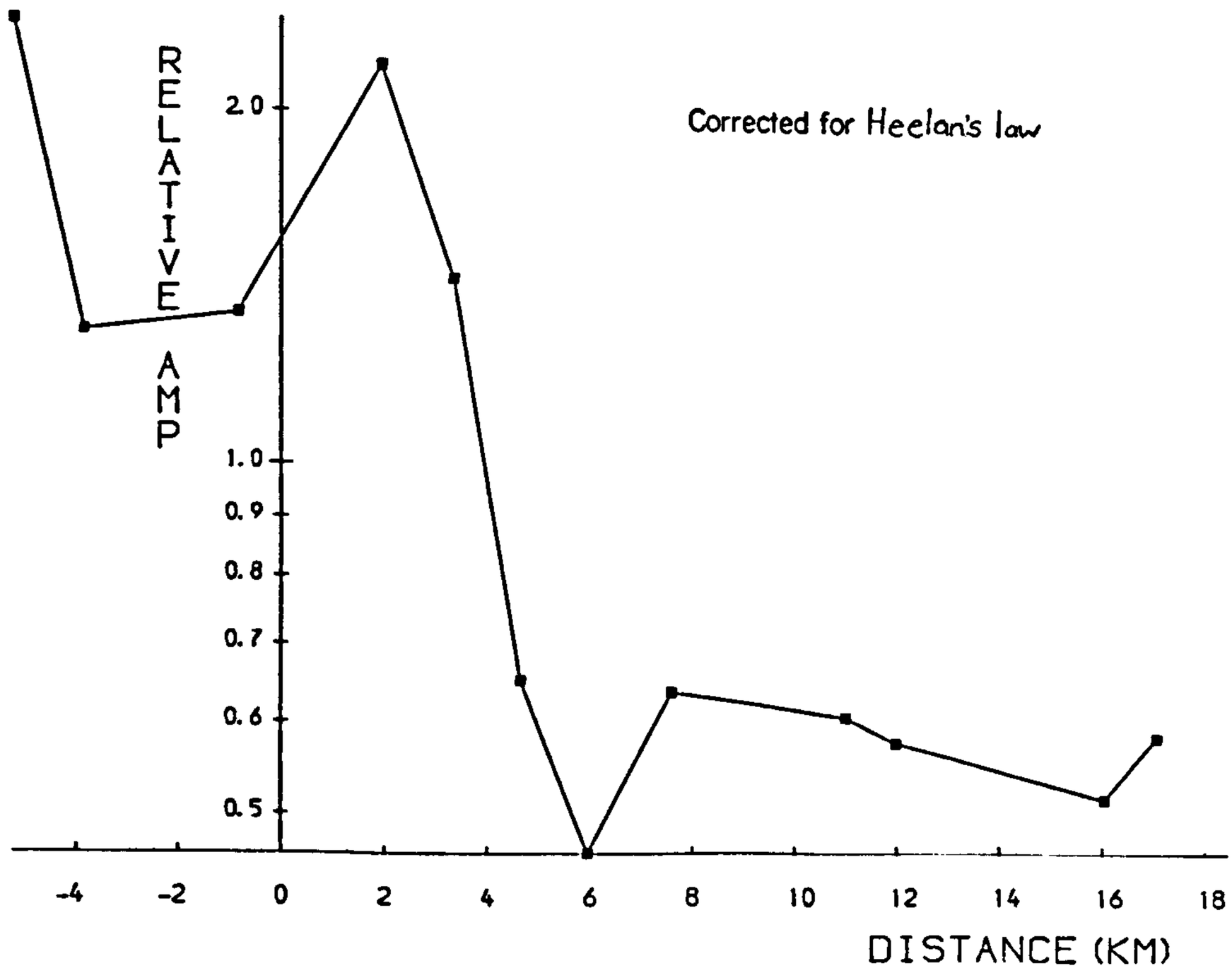

Corrected for Heelan's law

M4035 -- BALLIDON TIMED

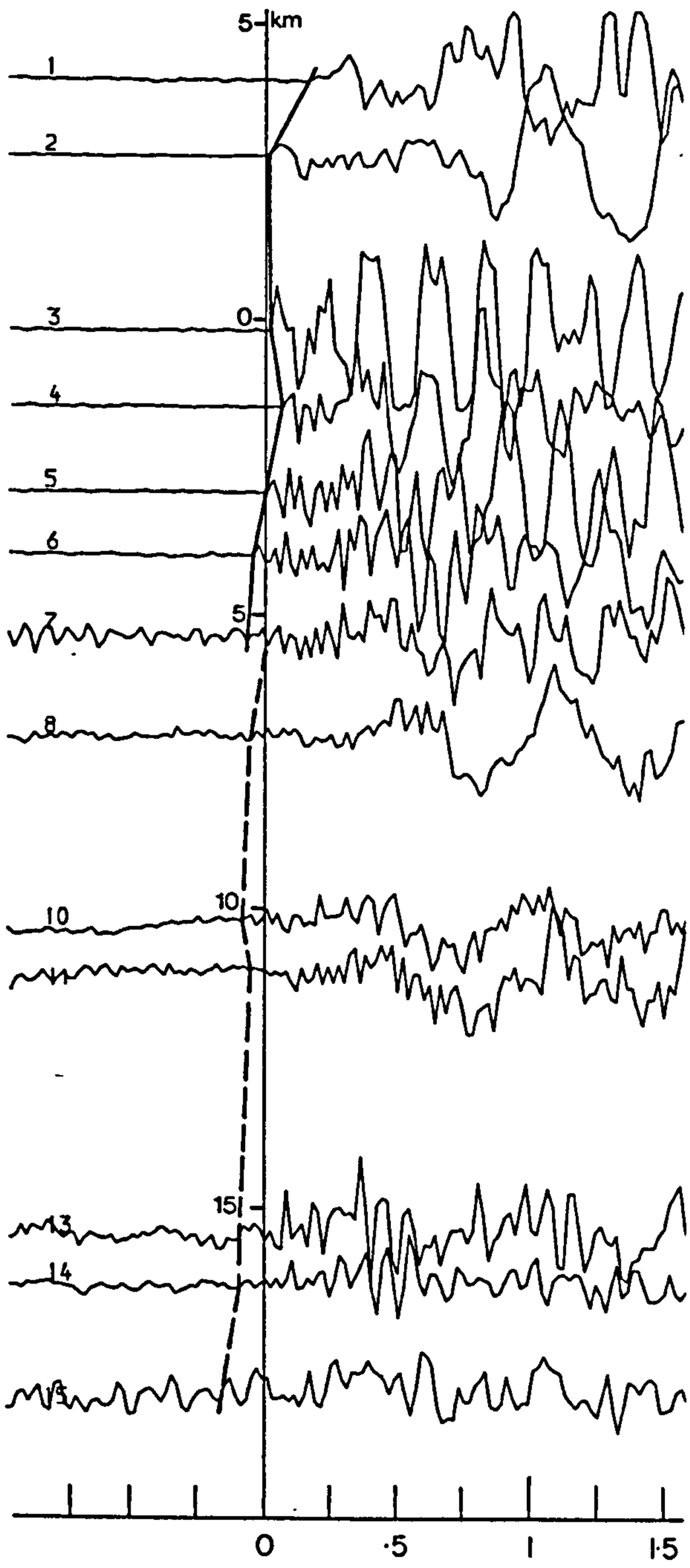

FIG 5-6b Seismograms reduced at 5·6 km/s

direct wave refraction

Note that the distance from each shot at which the basement refractions were picked as first arrivals differs between 15 km for the untimed Tunstead shot and about 7 km for the timed Ballidon. This may be because a) the refractor is much shallower around Ballidon, b) the overburden around Ballidon is more absorptive, or c) the distance over which high velocity direct waves mask the refractions is dependent upon the size of blast (the Tunstead blast was much larger).

To test possibility (c), the relative amplitudes for a number of blasts from Tunstead quarry are plotted in Fig. 5.7. Without other information, the size of blast has arbitrarily been expressed in terms of the number of overloaded cycles at station 15, which is also dependent on the distance of the shot from that station. The measured relative amplitudes vary from shot to shot, but the rate of amplitude decay generally abates between 4 and 6 km from the source. Therefore these data indicate that the distance at which basement refractions are picked as first arrivals is not necessarily related to charge size, although none of these blasts appear to be as large as M4027, which overloaded 14 cycles at station 15.

Generally, high velocity direct waves in this region appear to be characterised by higher attenuation rates than basement refractions and proportionally higher frequency content. The waveforms for direct waves also seem to change more rapidly between stations than basement arrivals. Sudden increases in reduced time were found to correspond with the picking of basement refractions, where the amplitude of direct waves had fallen below the ambient noise level. This case seems analogous to the high velocity shallow masking layers discussed by Trostle (1967) (see Section 2.1.1). The Carboniferous limestones in the Woo Dale borehole are thin (less than 300 m), but since a thicker sequence probably underlies Ballidon it is equally likely that these direct waves are transmitted along high velocity dolomitic horizons within the limestone succession. The lateral extent of these may determine the distance over which the basement refractions are preluded.

FIG 5-7 Relative amplitudes, Tunstead events

(a) uncorrected

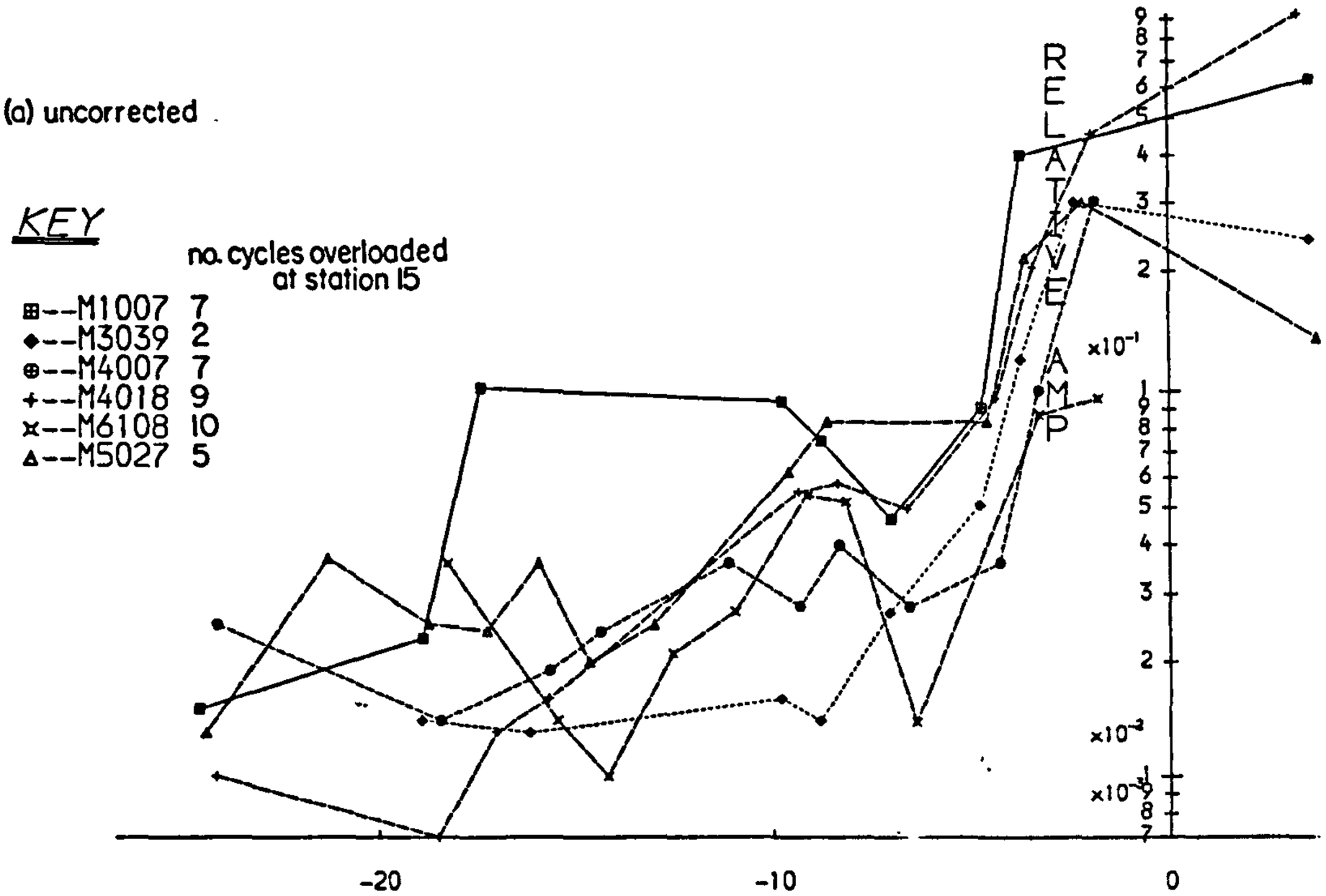

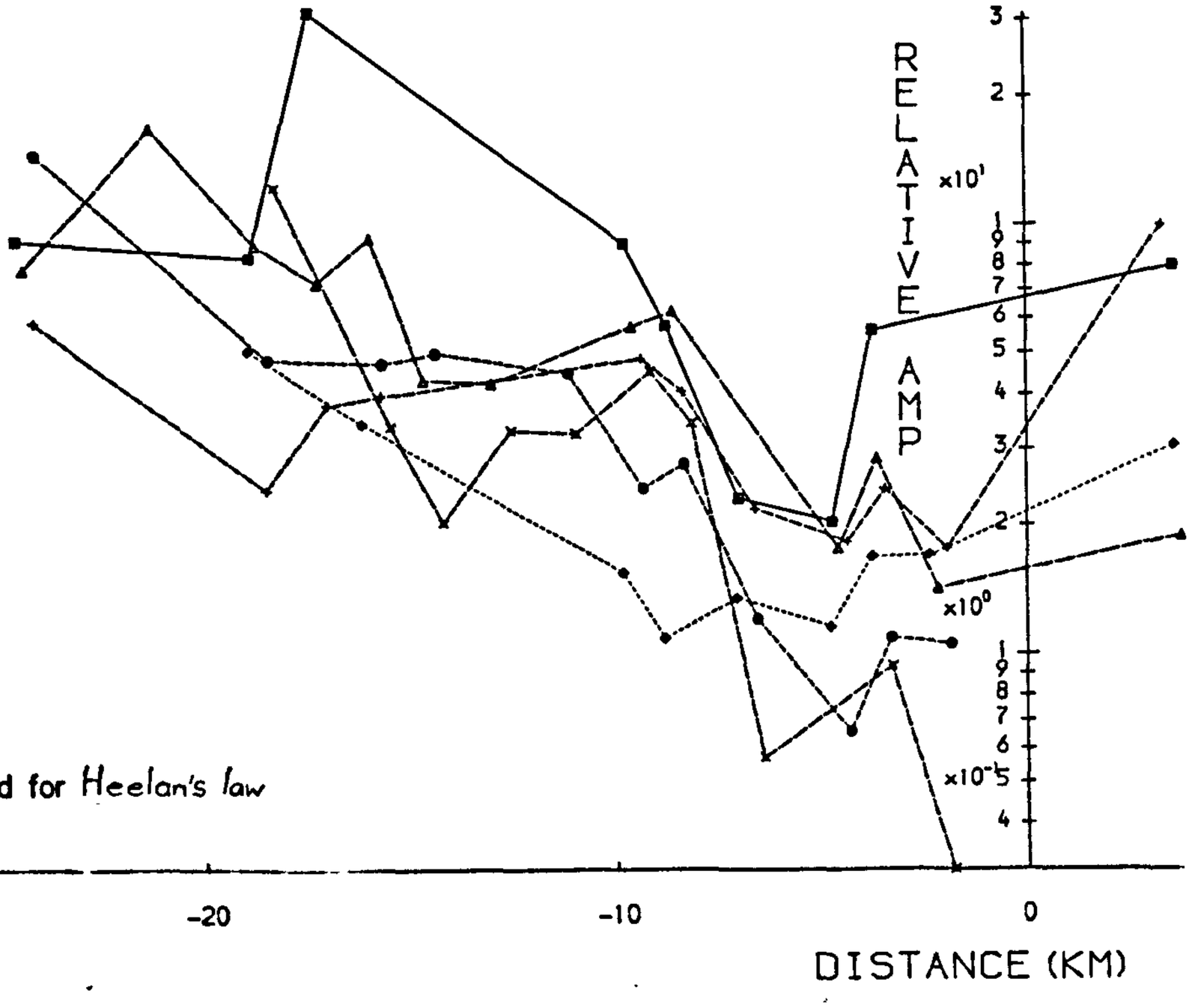

(b) corrected for Heelan's law

The simple ray-traced examples of Fig. 5.4 suggest that lags of 0.2 - 0.3s should not be expected between direct and refracted arrivals for uniform high velocity overburden. These delays therefore suggest a hidden layer: perhaps the main part of the limestone sequence itself masked by the shallow dolomitic layers.

5.3.3 First Model and the Interpretation of Refracted Arrivals

Most reduced time graphs were not easy to interpret unless different events were compared. Each quarry yielded a slightly different picture of the refractor topography according to its distance and azimuth to the line. Amplitude information was a useful diagnostic, but the inaccuracy of measurement (see section 4.4.4) rendered it unreliable. However, by examining a suite of events from the same or nearby quarries, a picture of the reduced time surface was gradually assimilated to facilitate the discrimination between direct and refracted arrivals, and to enable dubious observations to be identified and rejected.

To further help the interpretation a simple starting model was assumed which comprised a continuous refractor between the Leicester and LISPB profiles (as suggested by Whitcombe and Maguire (1981)), from which all the refracted waves originate. The model (Fig. 5.8) is broadly anticlinal and at a first approximation accords with the reduced sections of the timed shots from the 1979 experiment (Rogers 1980).

A selection of reduced time graphs of events from each quarry group are shown in Fig. 5.9. Like the plots of Fig. 5.3, the implied refractor structure is not simple and the variation between events suggests an azimuthal dependence for the reduced times. In order of distance north from station 15, the quarries of Tunstead, Waterswallows and Doveholes are approximately collinear with the north-south profile, such that direct waves from Doveholes were rarely

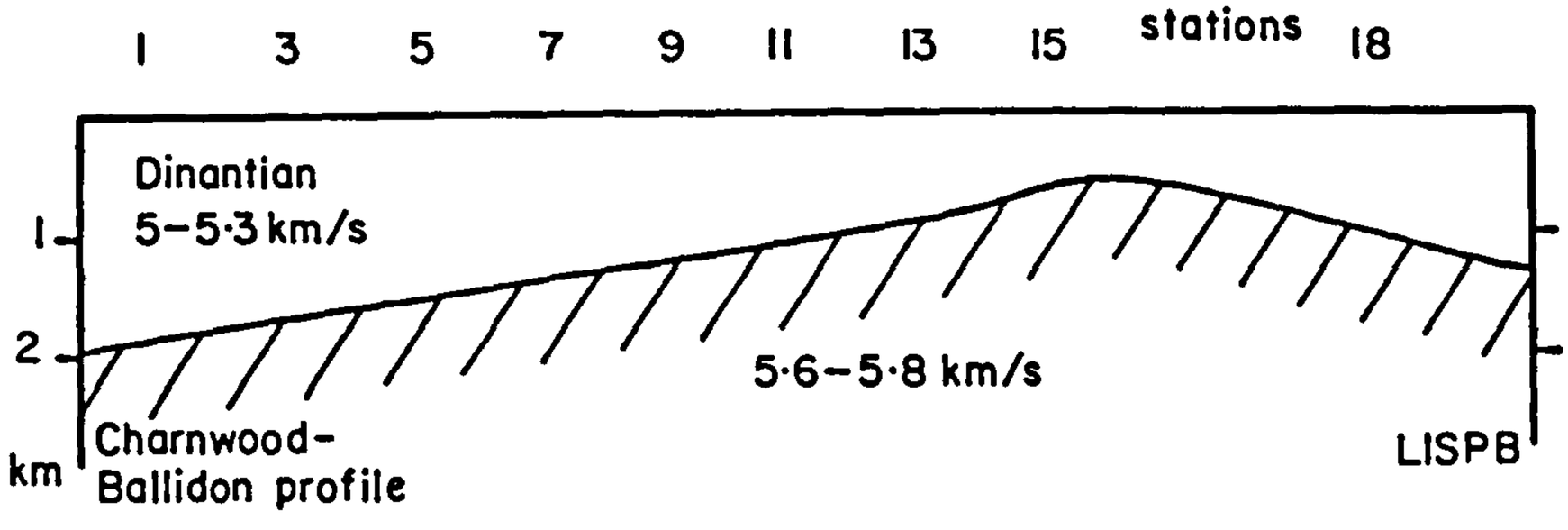

FIG 5-8 Simple starting model

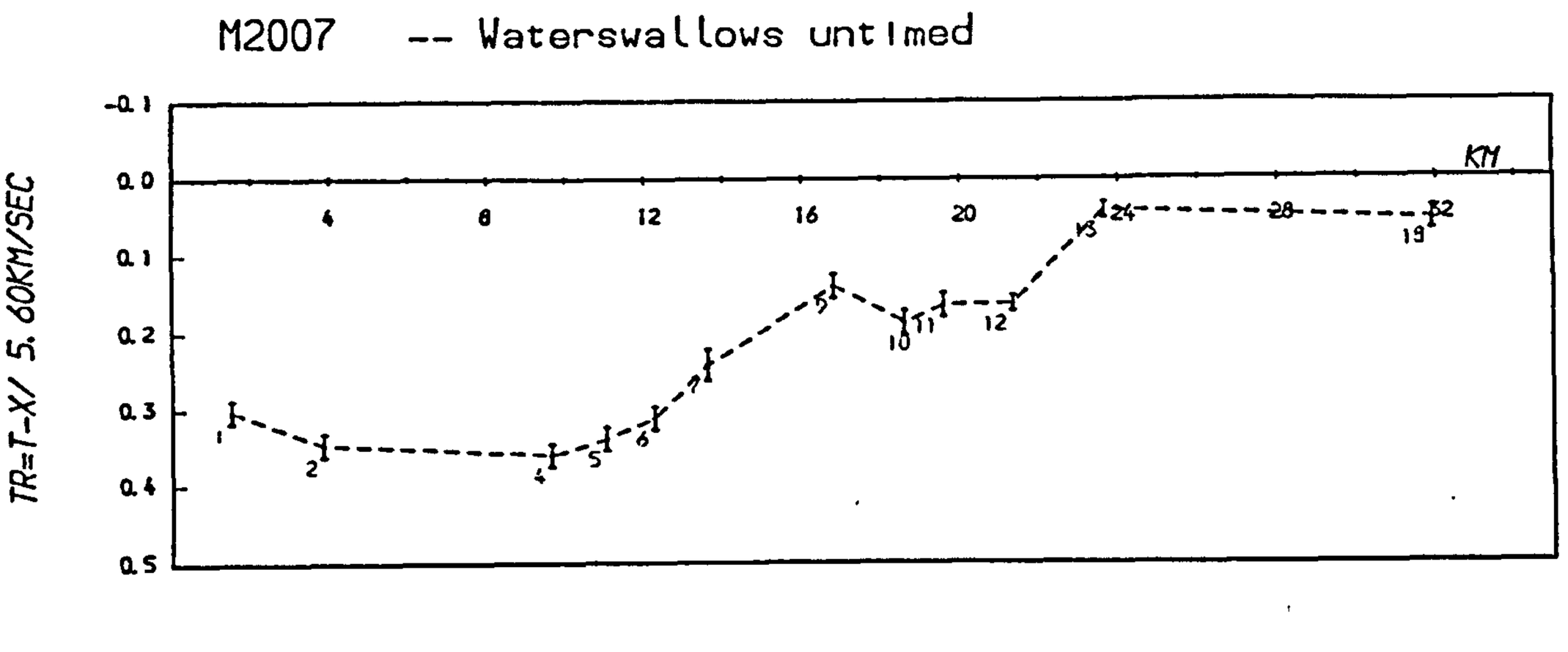

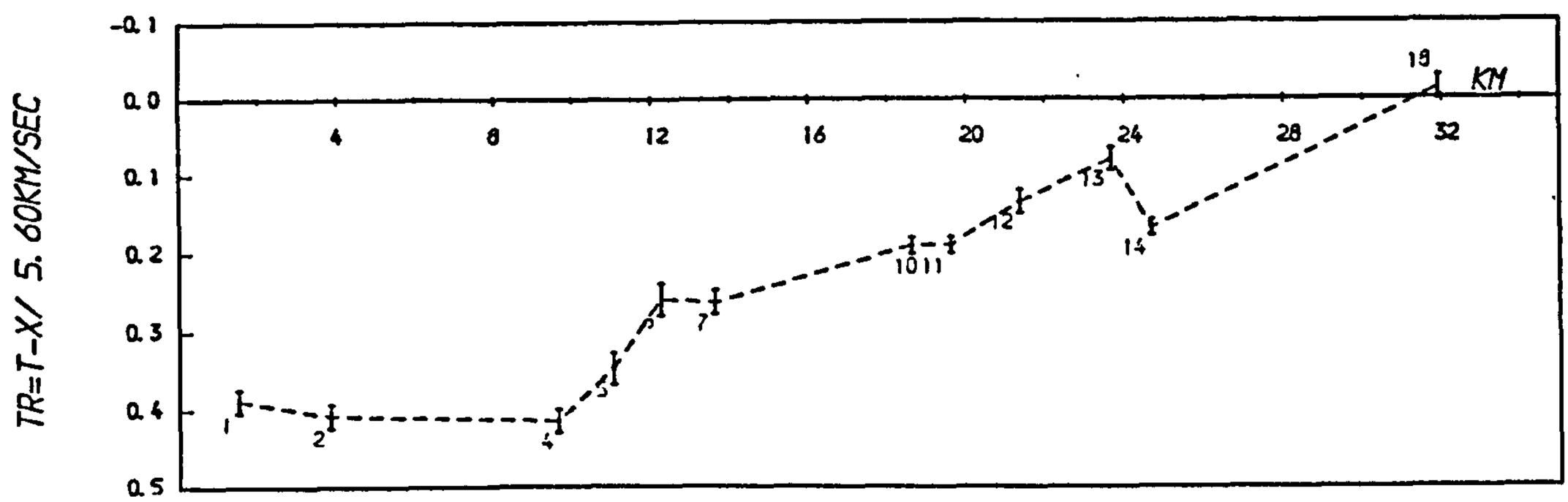

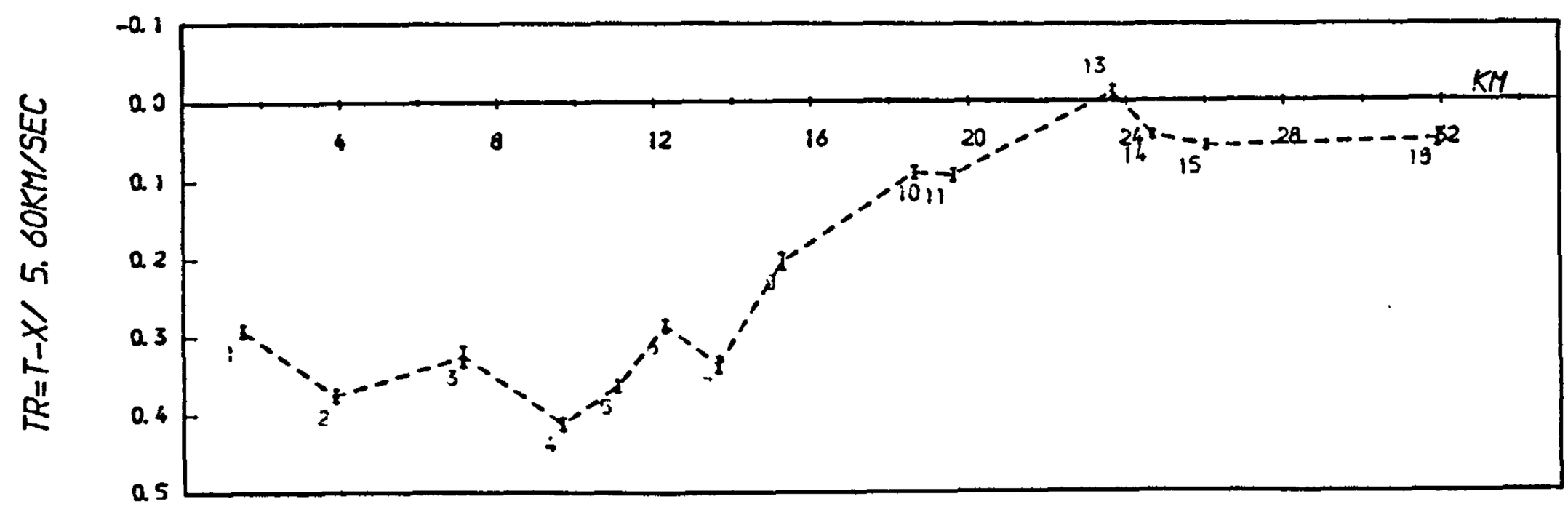

FIG 5-9 Reduced times

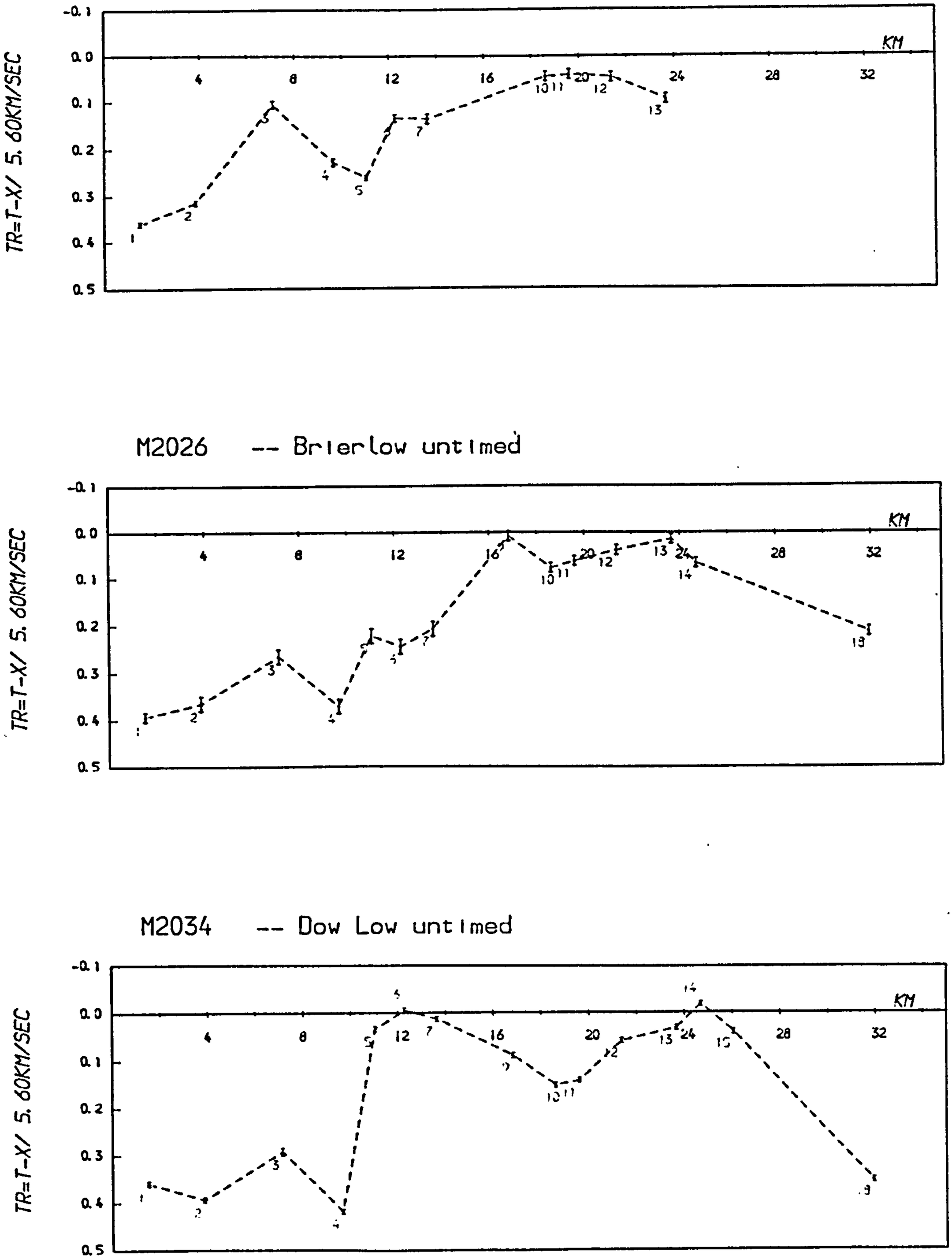
M2032 -- Dene untimed
M2026 -- Brierlow untimed
M2034 -- Dow Low untimed
TR=T-X/ 5.60KM/SEC
KM
-0.1
0.0
0.1
0.2
0.3
0.4
0.5
4
8
12
16
20
24
28
32

FIG 5-9 cont

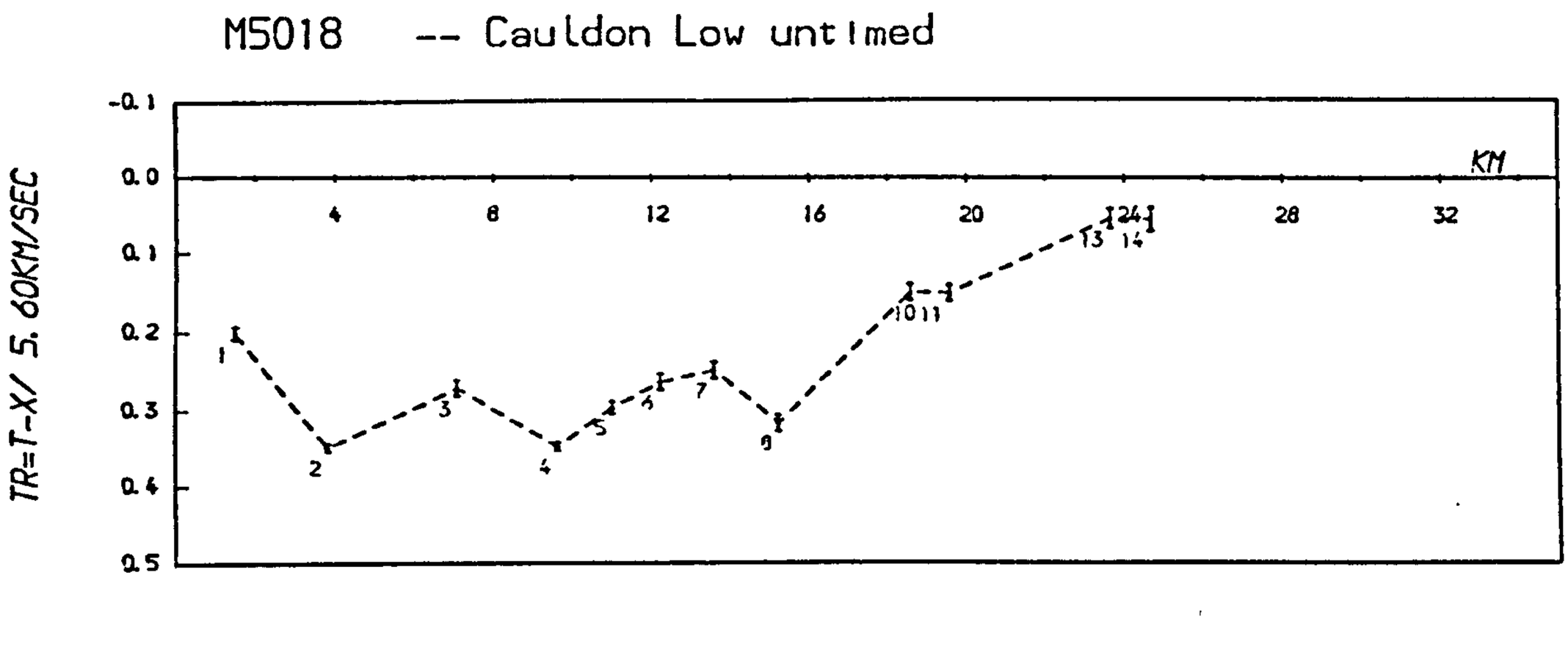
M5018 -- Cauldon Low untimed
TR=T-X/ 5.60KM/SEC
-0.1
0.0
0.1
0.2
0.3
0.4
0.5
KM
4
8
12
16
20
24
28
32

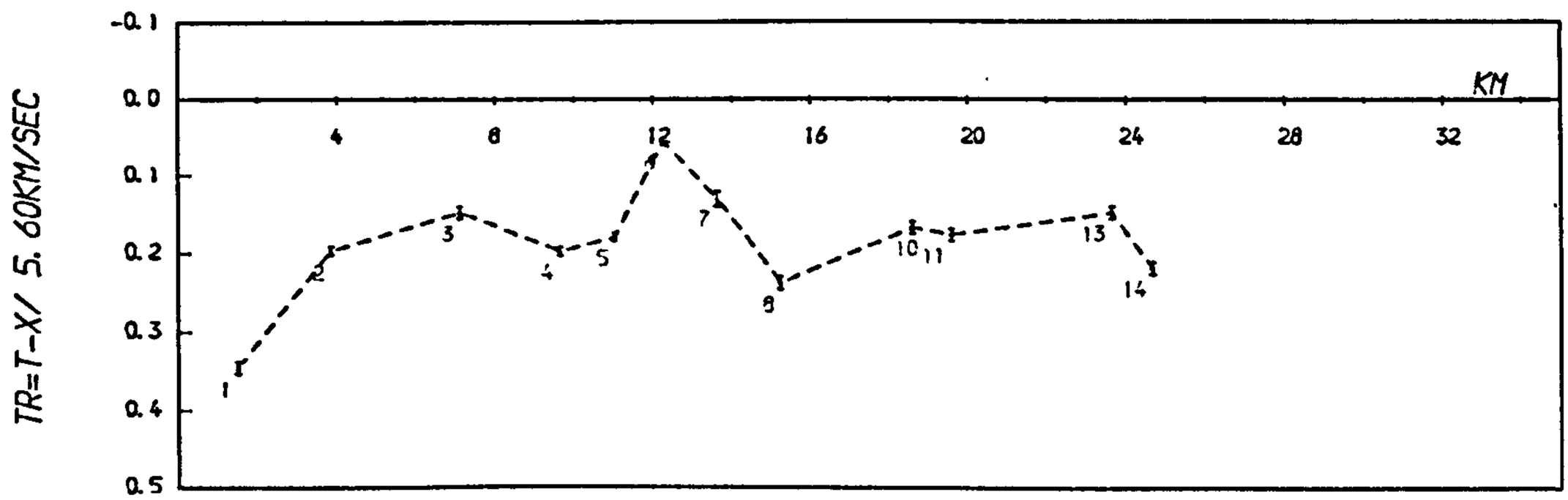
M5003 -- Ballidon untimed
TR=T-X/ 5.60KM/SEC
-0.1
0.0
0.1
0.2
0.3
0.4
0.5
KM
4
8
12
16
20
24
28
32

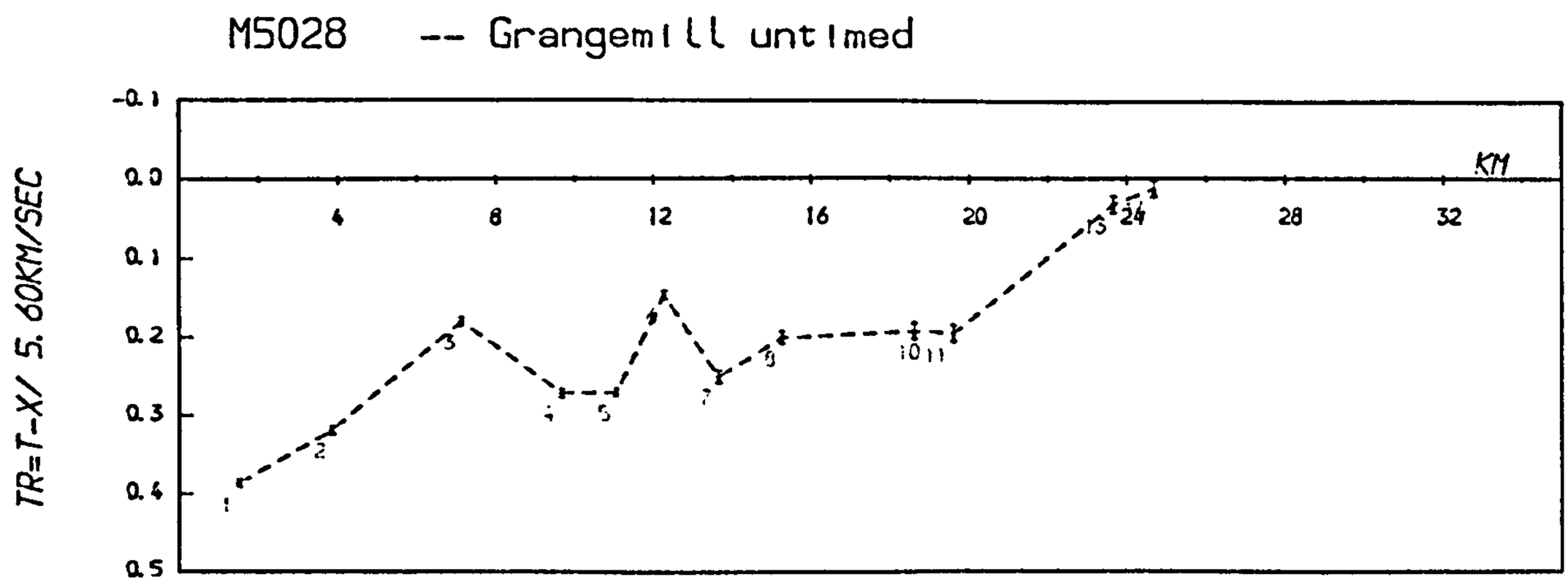
M5028 -- Grangemill untimed
TR=T-X/ 5.60KM/SEC
-0.1
0.0
0.1
0.2
0.3
0.4
0.5
KM
4
8
12
16
20
24
28
32

FIG 5-9 cont

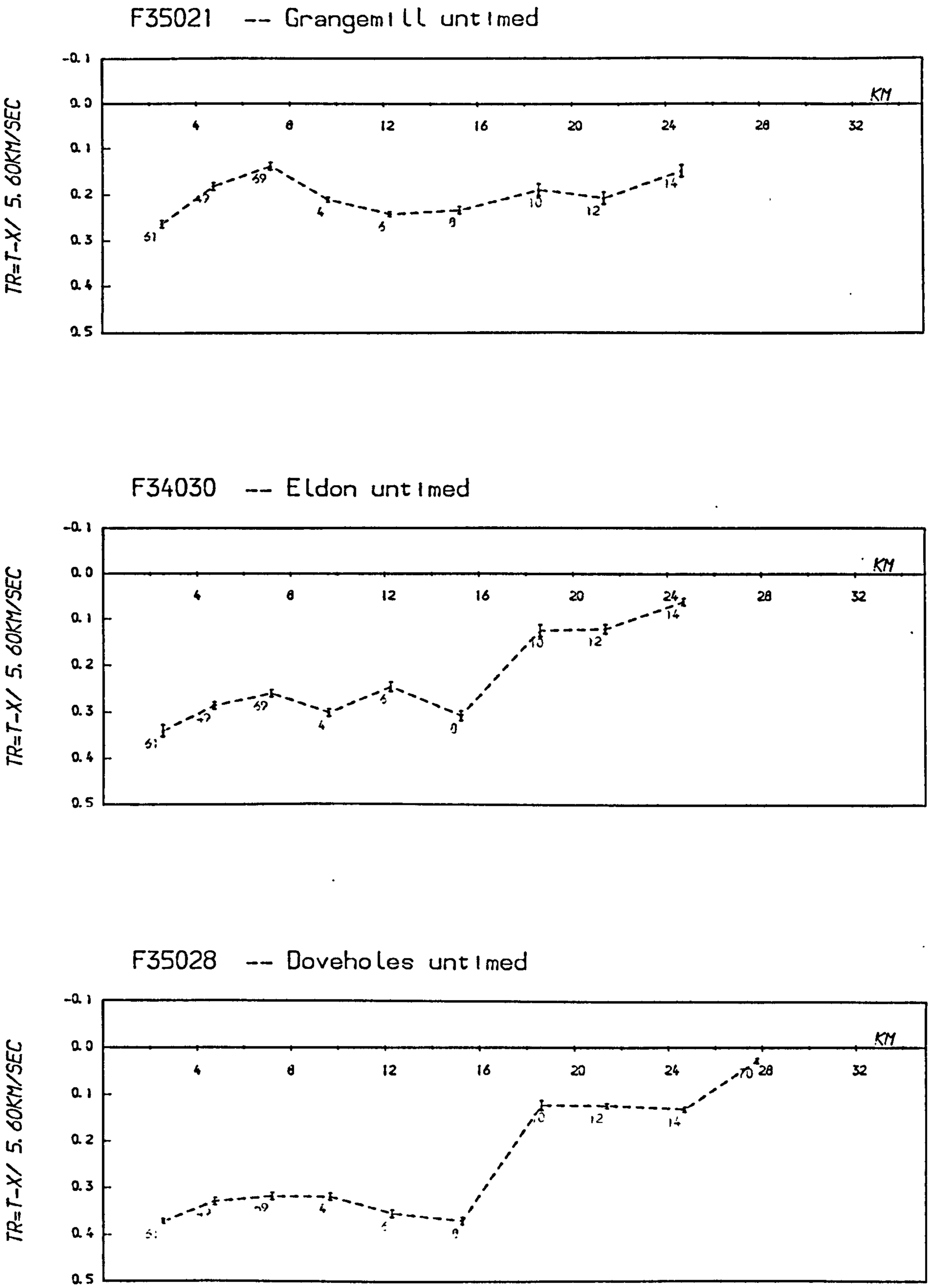
F35021 -- Grangemill untimed
TR=T-X/ 5.60KM/SEC
-0.1
0.0
0.1
0.2
0.3
0.4
0.5
KM
4
8
12
16
20
24
28
32
51
45
59
4
5
9
10
12
14
F34030 -- Eldon untimed
TR=T-X/ 5.60KM/SEC
-0.1
0.0
0.1
0.2
0.3
0.4
0.5
KM
4
8
12
16
20
24
28
32
51
45
59
4
5
9
13
12
14
F35028 -- Doveholes untimed
TR=T-X/ 5.60KM/SEC
-0.1
0.0
0.1
0.2
0.3
0.4
0.5
KM
4
8
12
16
20
24
28
32
10
12
14

FIG 5-9 cont

observed at station 12. If there was a vertical velocity gradient in the refractor, the reduced times for refracted arrivals would be expected to decrease with increasing distance from the shot. Comparing these events, however, the reduced times at the southern end of the line are much the same, so therefore any velocity gradient in the basement is minimal.

Reduced seismogram plots of untimed shots from Tunstead (M5027) and Waterswallows (M4006) are given in Fig. 5.10, where the full and dashed lines refer to interpreted direct and refracted arrivals respectively. Waterswallows quarry is situated on a dolerite intrusion and the source signal often contains more high frequency energy than shots from Tunstead or Doveholes. For both events the first break becomes lower frequency with distance and the attenuation of higher frequencies seems most marked between stations 10 and 8. The arrivals defining a hyperbolic reduced time curve near the source for M4006 may be reflections off the basement (cf. Fig. 5.4), although the phase is less easily identified with distance; the large amplitude later arrival at station 2 may be a wide-angle reflection. If so, the curve suggests that the average overburden velocity is about 5.2 km/s, not 5.6 km/s as those arrivals interpreted as direct for M5027. If so, then this reiterates the idea that the high velocity 'direct' waves are really transmitted along dolomitic layers in the limestone sequence.

The quarries of Dow Low, Brierlow, etc., are close broadside to the line (Fig. 3.7), and few basement refractions are identified as first arrivals except at the ends of the profile. Dow Low frequently detonates charges of 1 Tonne or more, such that the reduced times between stations 5 and 15 of M2034 reflect changes in direct wave velocity: note that the relatively lower velocities between stations 8 to 12 correlate with the younger Brigantian limestones. A similar velocity distribution is observed for the Brierlow shot (M2026), except that refracted arrivals are observed as first arrivals as close as station 7. The positive feature of station 3 is

FIG 5-10

M5027 -- TUNSTEAD UNTIMED*

M4006 - WATERSWALLOWS U/T

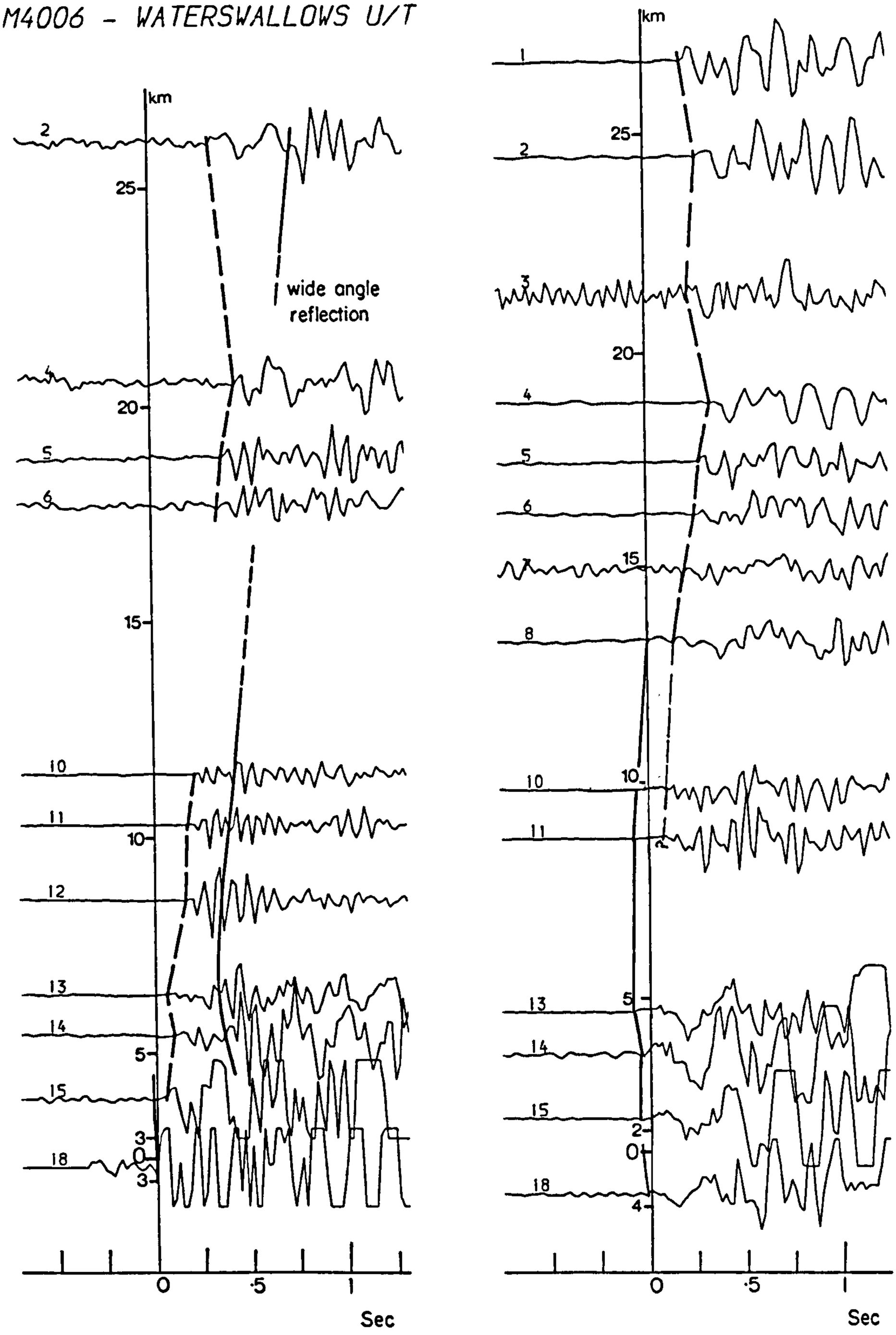

Reducing velocity 5·6 km/s —— direct wave — — — basement refraction

*For repeated Tunstead shots, see end of Appendix A.

also seen by Tunstead (M5027), Wardlow (M2000), Dene (M2032), etc.

Since shots from the south (e.g. Dene (M2032), Ballidon (M5003), Grangemill (M5028) and Cauldon (M5018)) also imply a refractor dipping south of station 15, it is less likely that the variation in reduced times is due to lateral velocity variation in the refractor (Fig. 5.1 cases I and J) than true refractor structure (Fig. 5.1 case H).

Refracted arrivals from both directions are only consistently observed between stations 7 and 14; since there is no characteristic short-wavelength feature commonly seen in the reduced time graphs for this region, the depth of the refractor cannot be reliably estimated from offset distances (see Section 2.3.2). However, the similarity of these data north of station 10 indicates that the offset may be less than the interstation separation, and the refractor consequently shallow in this area: that is, in the region of a few hundred metres, as expected from the Woo Dale borehole. A shallow basement is also supported by the fact that basement refractions are observed close to northern quarries.

Apparent offset can be estimated from the reduced times to give an idea of the area of basement beneath the line sampled by refractions from various azimuths. From Equation 2.15, offset o_i is related to the depth of refractor h by

$$o_i = h\tan\theta_c$$

where θ_c is the critical angle. Now a station's time-term is also related to h,

$$a_i = (h\cos\theta_c)/V_o$$

(from Equation 2.2) for overburden velocity V_o. By eliminating h,

$$o_i = a_i V_o \sin\theta_c$$

The differences between reduced times for an event are approximately equivalent to the differences in time-terms, the values

for which can therefore be estimated by normalising the reduced times against a known value for one station. For Fig. 5.11 the reduced times for refracted arrivals have been normalised against a value of 0.02s for station 15. This corresponds to a refractor at the depth of the Woo Dale volcanics. Overburden and refractor velocities of 5.2 and 5.6 km/s respectively have been assumed. Any negative values have been ignored.

Treating only those arrivals thought to be basement refractions, Fig. 5.12 summarises most of the data for the north-south profile from (a) Tunstead, Waterswallows, Dove-holes and Topley Pike quarries, (b) Ballidon, Longcliffe, Grangemill and the quarries of Matlock and Wirksworth, and (c) the quarries of the Cauldon Low group. The reduced time graphs have been superimposed by eye by shifting the time axes of the events with respect to each other in order to find a best match (rather than use an automatic technique, which might be too infuenced by poor observations). Obviously a certain amount of observational scatter is expected due to variation in azimuth, picking error, etc., but this does not explain the difference between stations with the smallest and largest range of values. For example, Fig. 5.12a considers quarries approximately collinear with the north-south line, yet the range of reduced times for station 8 is four times that of station 4.

Fig. 5.12 generally suggests that the geological structure beneath the north-south line is more complicated than the starting model of Fig. 5.8 assumes. The variation in reduced times may be due to mispicking of phases, or to short wavelength structure. Overall, stations 1 to 6 have the smaller range of reduced times, while the least consistent observations are for stations 9 to 15, particularly for southern quarries. In addition, the larger range of observations for stations 7 to 9 may be due to the Bonsall Fault which passes between them.

FIG 5-11 Reduced times for north–south line plotted as offsets towards shotpoint

+ southward ray

o northward ray

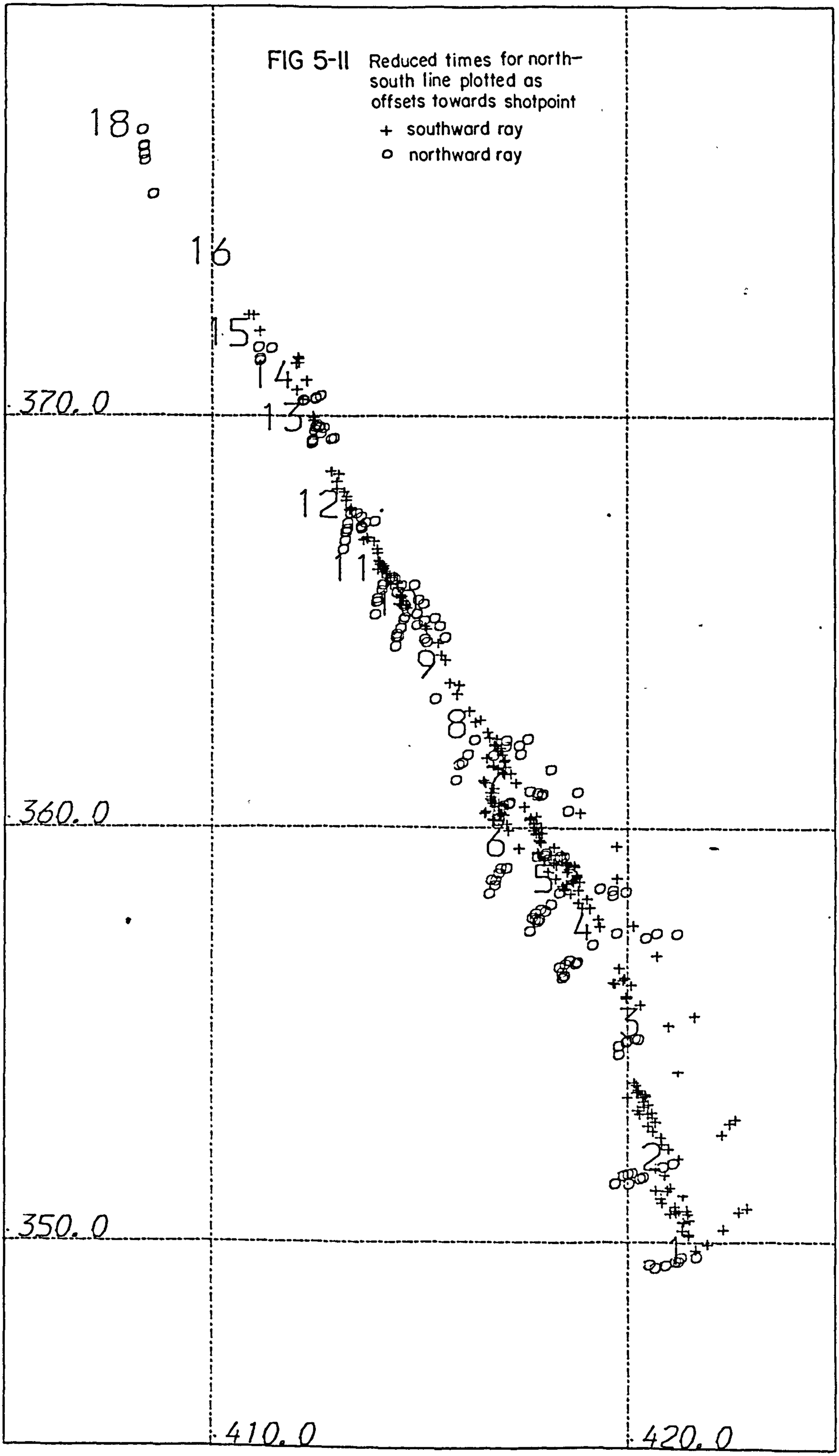

FIG 5-12

V_{red}=5·6km/s

(a) Tunstead, Waterswallows & Doveholes

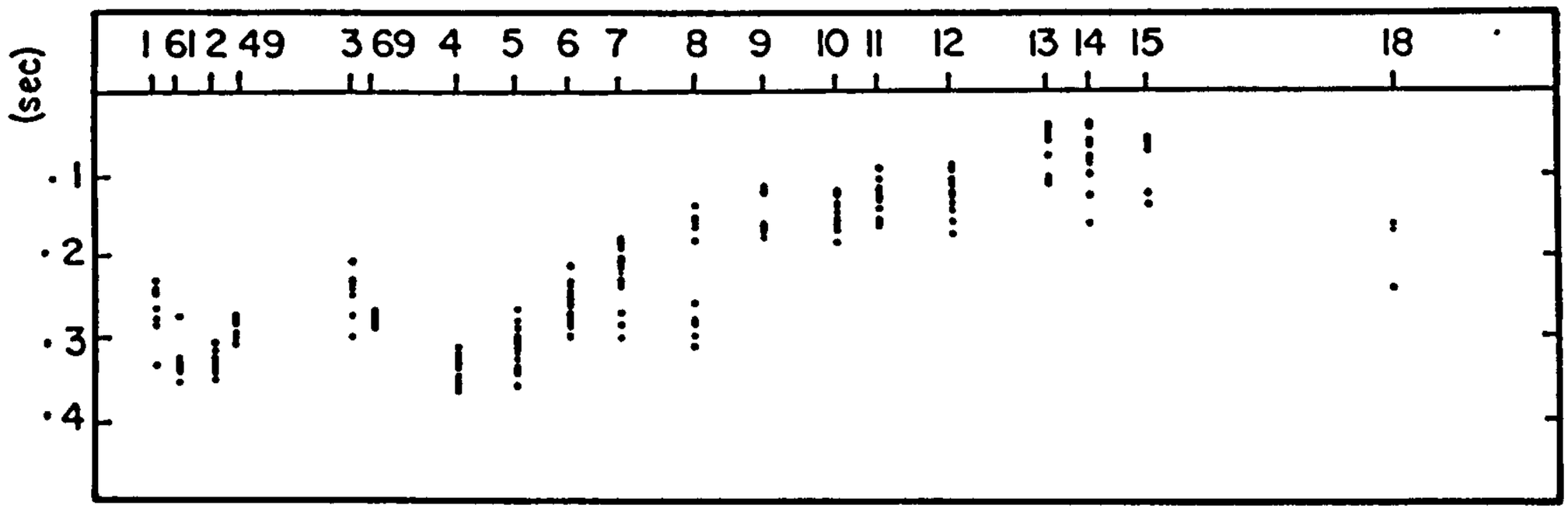

(b) Ballidon, Longcliffe, Matlock, Wirksworth

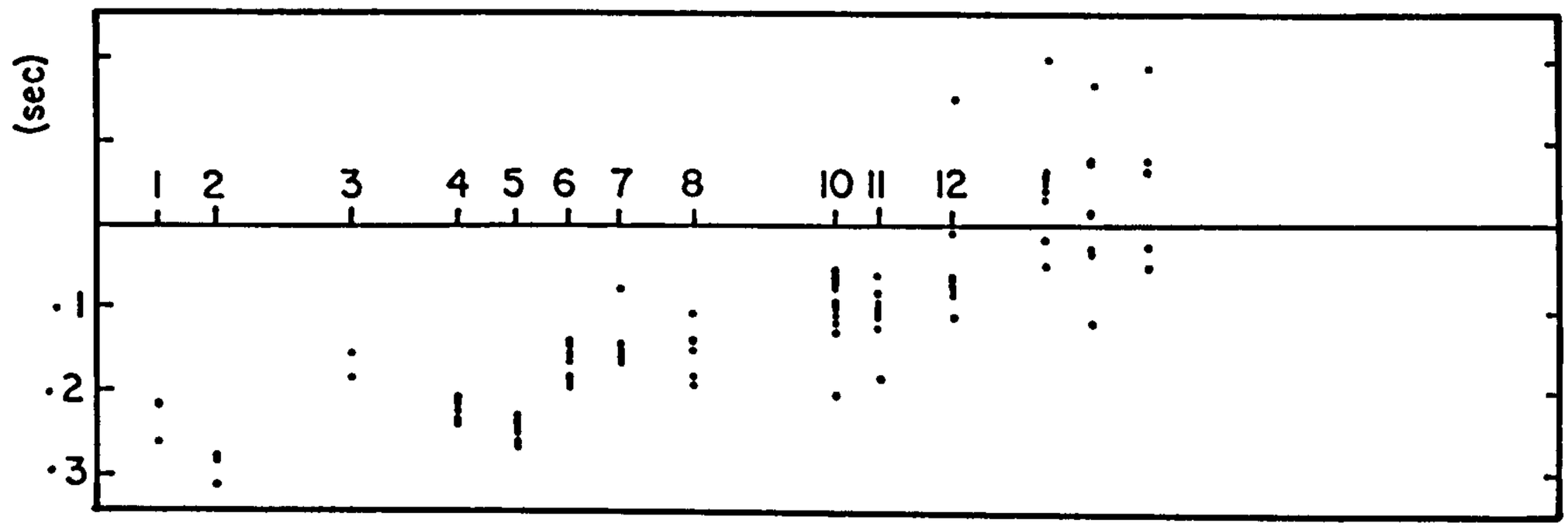

(c) Cauldon group

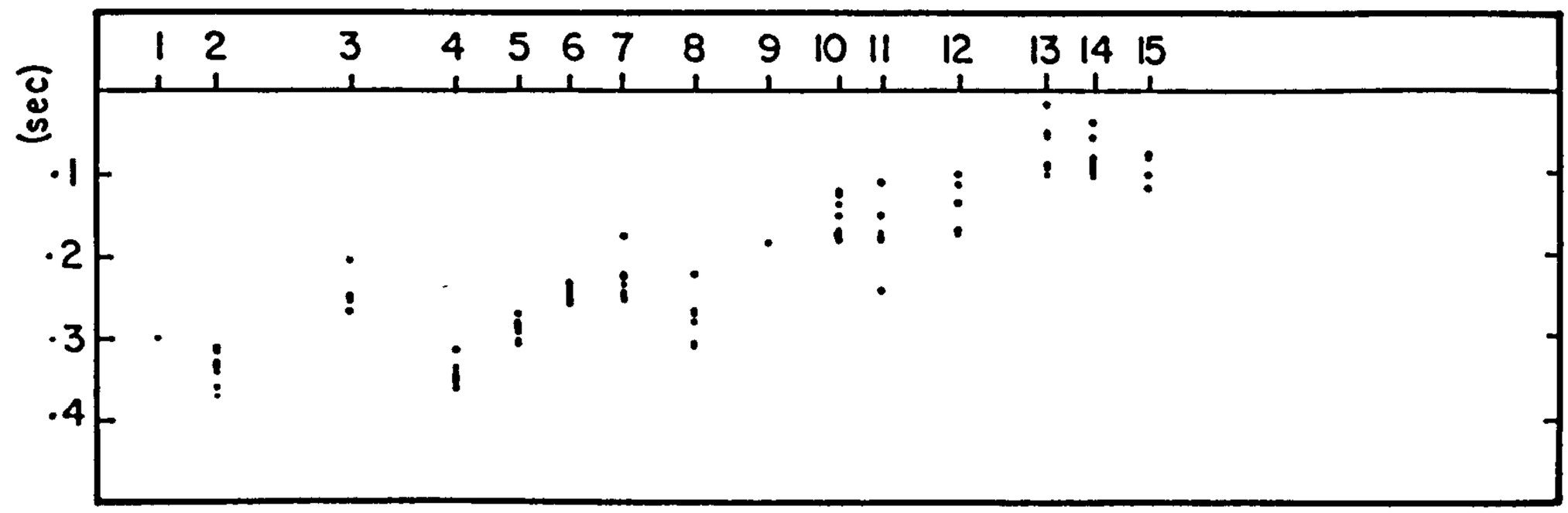

5.4 Towards a North-South Section of the Derbyshire Dome

The data suggests that the starting model of Fig. 5.8 needs to be refined. It is also hard to see how this model fits in with the Bouguer anomaly map, which suggests that the basement is deeper to the north of the Dome than it is to the south (Maroof 1976). However, the gravity model is not unique, and it is also possible that the anomaly is due to lateral density variation, or to a high density basement too deep to be resolved by this refraction experiment.

The Mansfield earthquakes (see Section 4.5.3) provide ideal additional sources to the quarry blast data since they were about 45 km from the north-south line and broadside from the east. The Mansfield region is within the same block environ as the Derbyshire Dome (Kent 1966), so it is likely that a continuous deep refractor connects the two regions. For this reason, and that the raypaths are azimuthally close to each other, any variation for the Mansfield events is expected to reflect the basement structure along the profile.

The first arrival times for the biggest of the Mansfield tremors, M6040, are plotted in the reduced time graph of Fig. 5.13a. Comparing this plot with the reduced time data from the quarry blasts (Fig. 5.12), the refractor structures generally concord. The only difference seems to be the reduced times for station 18, which is about 0.2s smaller for M6040 than the few refracted arrivals observed for the quarry blasts.

However, when the reduced time seismograms are plotted (Fig. 5.14), a contrast is evident between stations 7 and 10 such that to the north the P waves complicate and the first arrivals become more attenuated (with the exception of station 18, the response of the seismometer at which is known to be suspect; see Section 3.1.1). This would not be expected of the simple starting model because the effect suggests that either (a) the first arrivals to north and south originate from differing refractors, or (b) the rays have passed through overburden of differing characteristics. Since all the stations

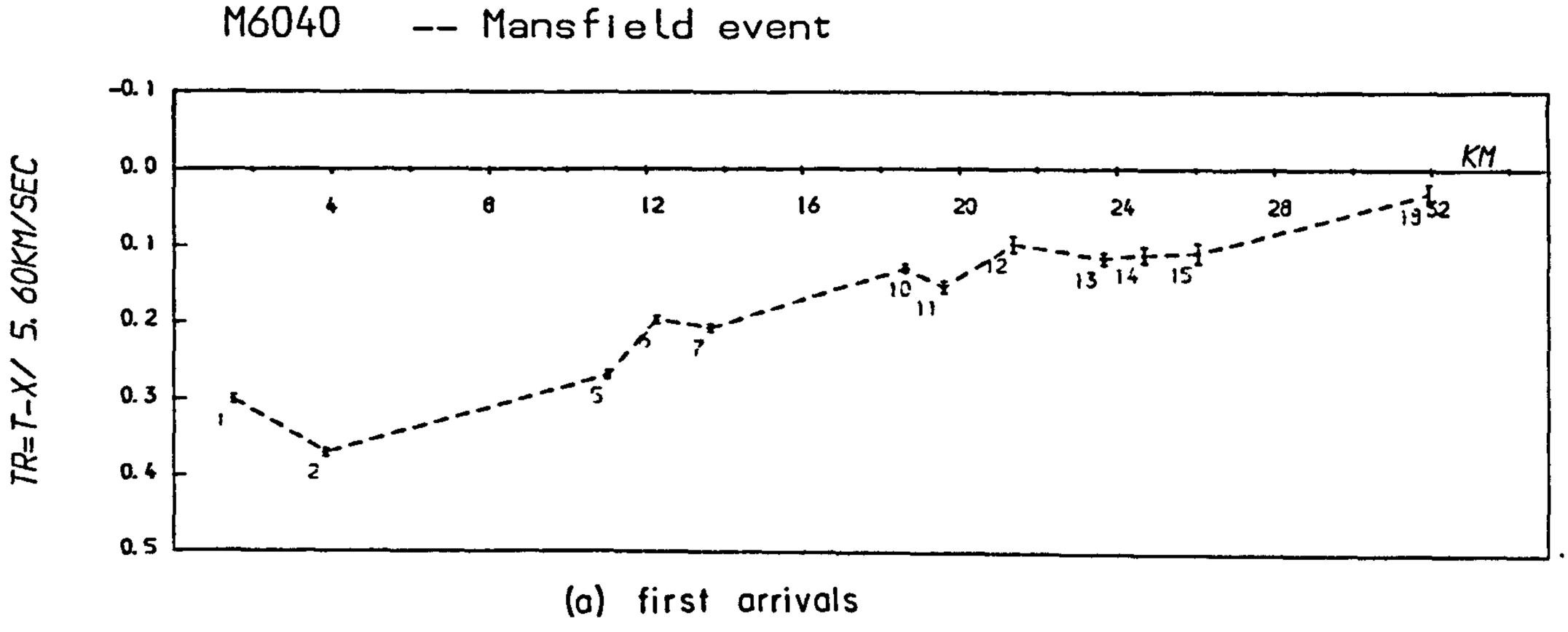

(a) first arrivals

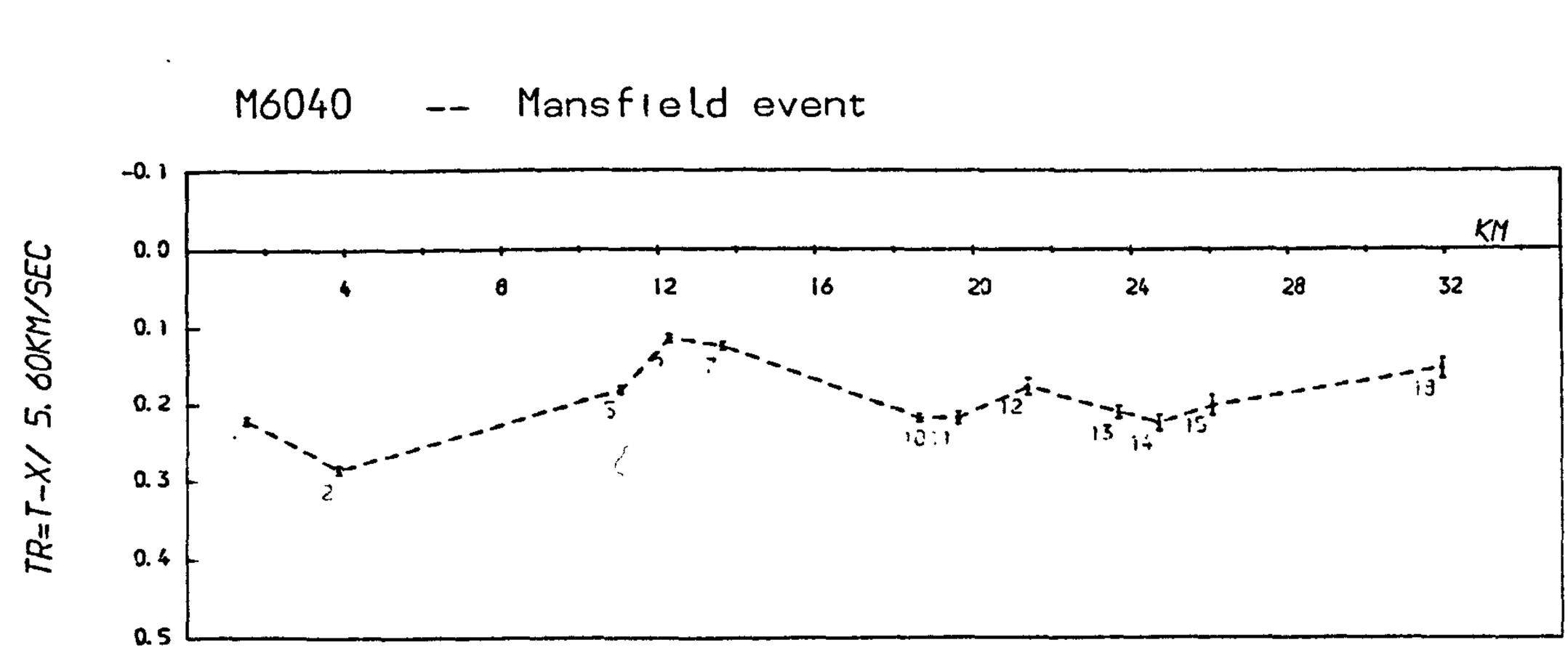

(b) with later arrivals

FIG 5-13

FIG 5-14 M6040 -- MANSFIELD TREMOR 7/10/79

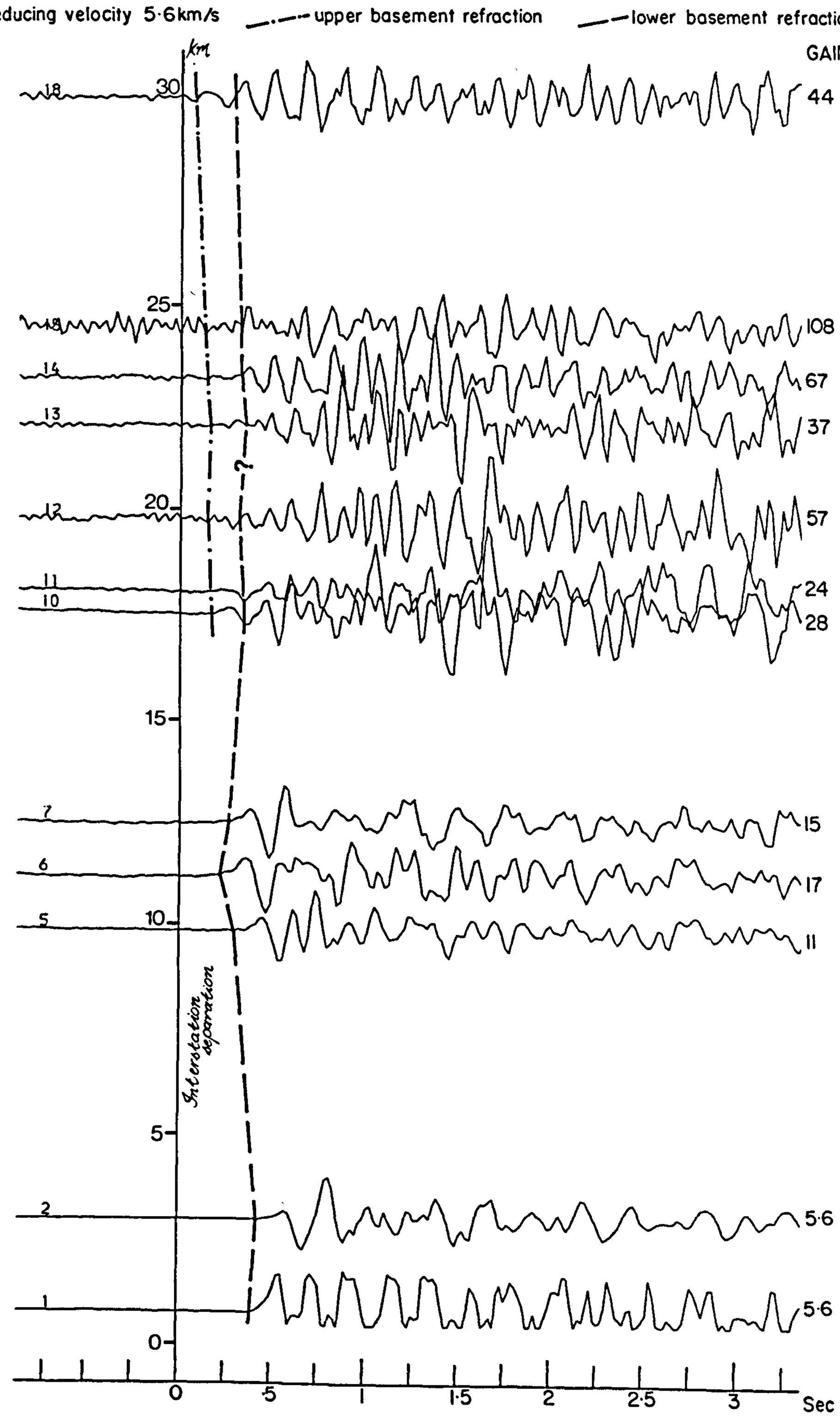

are situated on the limestone outcrop, then for case (b) there must be a deeper lateral change. For case (a), the first arrivals north of station 7 may originate from a thinner refractor than to the south: the first break is rapidly attenuated in proportion to the P wave coda, and its frequency content rises from about 5Hz at station 7 to about 10Hz at station 13. (Part of the attenuation is undoubtedly due to lower seismometer response to the higher frequencies; see response curve, Section 3.2.1). The thickness of this refractor will not be greater than the wavelength of the lowest frequency that it readily transmits, that is around 570m for a velocity of 5.7 km/s.

Furthermore, the first arrival observed for the southern stations of the line can be traced towards the north as a later arrival from station 10. Since this phase is delayed by a variable lag, it must be a separate arrival rather than a high amplitude component of the first arrival phase (which would lag by a constant delay). This later arrival to the north may be (a) a refraction from a deeper horizon (Fig. 5.15a), (b) a wide-angle reflection (Fig. 5.15b), (c) a reverberation (Fig. 5.15c), or (d) the two arrivals may be respectively diving and critically refracted rays (Fig. 5.15d). If the later arrivals were due to cases (b), (c) or (d), then they might also be expected south of station 10, which they are not. Therefore there may be a deeper refractor to the north not similarly present beneath the southern half of the line. The complicated nature of the arrivals to the north may also manifest interference between these refracted phases.

The reduced times for these later arrivals are plotted in Fig. 5.13b. It is tempting to consider that they originate from the same horizon as the first arrivals to the south. If so, then the sub-Carboniferous refractor in the south deepens north of the Bonsall Fault and is overlain by another refractor which shallows northwards to Woo Dale. The postulated relationship between this upper basement refractor and the lower basement refractor is depicted in Fig. 5.16. Several comments may be made about this model:

FIG 5-15 Possibilities for later arrivals

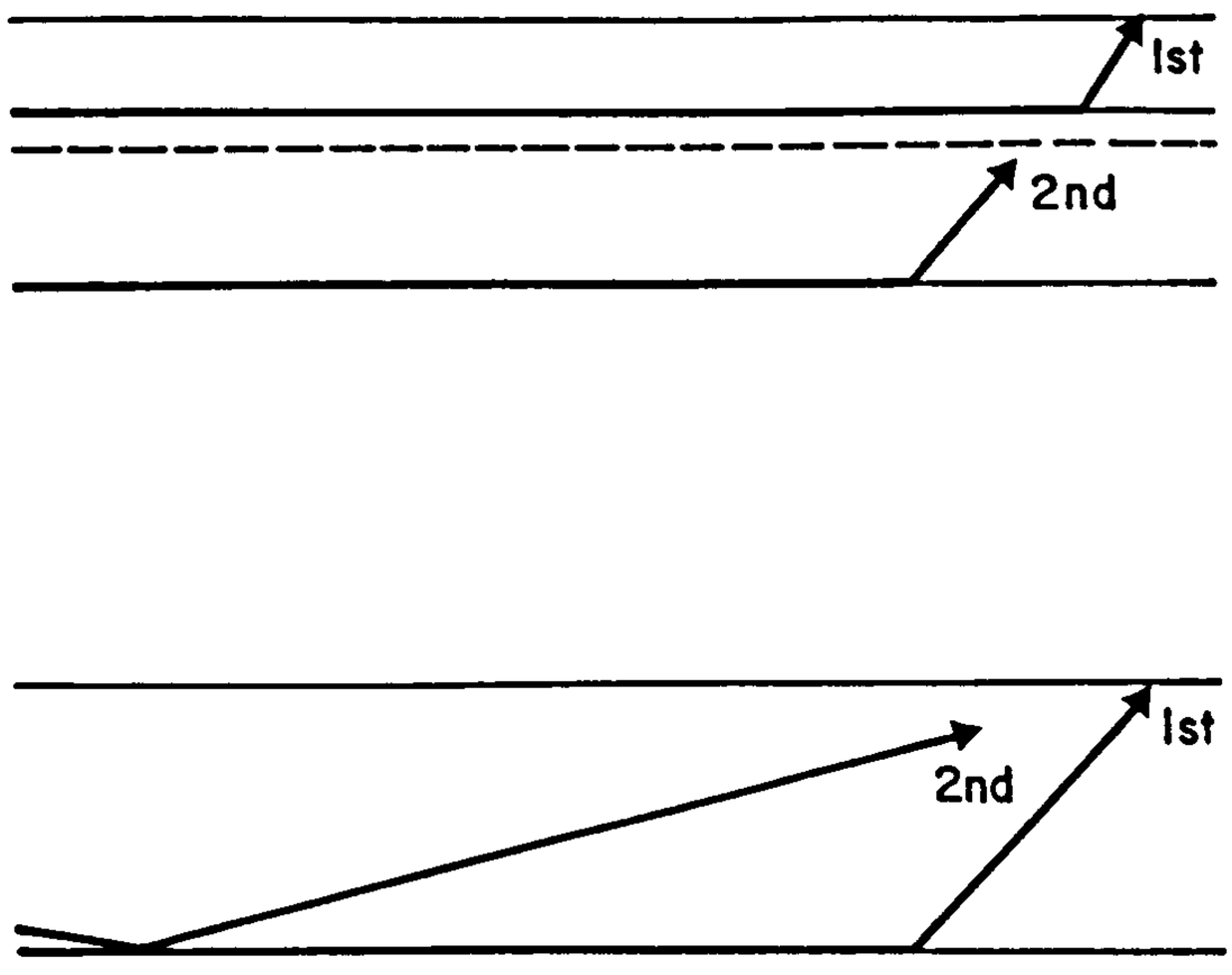

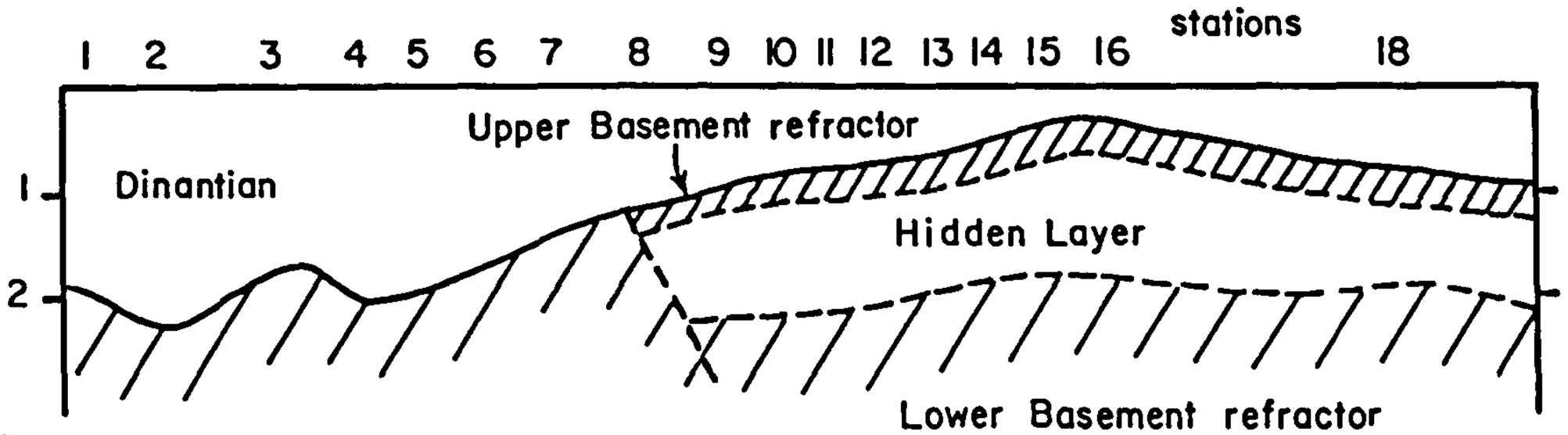

FIG 5-16 Refined model

a) the surface of the sub-Carboniferous outcrop is consistent with the starting model,
b) the basement deeper northwards implied by the Bouguer anomaly map is satisfied,
c) the shallow northern refractor may be equated with the volcanics of the Woo Dale borehole (or a similar shallow interface), and
d) the anomalously large range of reduced times observed at stations 7 to 9 (Fig. 5.12) suggest basement complexity between these stations.

In addition the model may be consistent with the interpretations of the Leicester and LISPB profiles. The continuous refractor model of Fig. 5.8 may accord with the first arrival data because the velocities of the two refractors are very similar. It is also possible that the larger range of reduced times north of station 6 (see Fig. 5.12) may in part be due to the picking of later arrivals where the refraction from the upper basement horizon was poorly recorded or lost in noise.

5.4.1 Testing the Refined Model

We wish to consider whether or not refractions from a down-faulted lower basement refractor can be observed as later arrivals from quarry blasts on the limestone outcrop. Fig. 5.17a simplistically represents the model for overburden of velocity V_o and thickness Z_o, basement of velocity V_r, and an intermediate refractor of velocity V_i which occurs to the right of a dipping interface BC. A line of detectors is considered along the surface, the first position of which lies above point B at X=O. The intermediate layer reaches full thickness Z_i at X=D, right of which a horizontal three-layer case is assumed. For a source far to the left, and ignoring direct waves, reflections and scattering from point B, P wave arrivals along the seismic line will comprise refractions from segments AB, CD and BE. For convenience, time equals zero at the emergence from point A of the first ray to strike X=O.

FIG 5-17

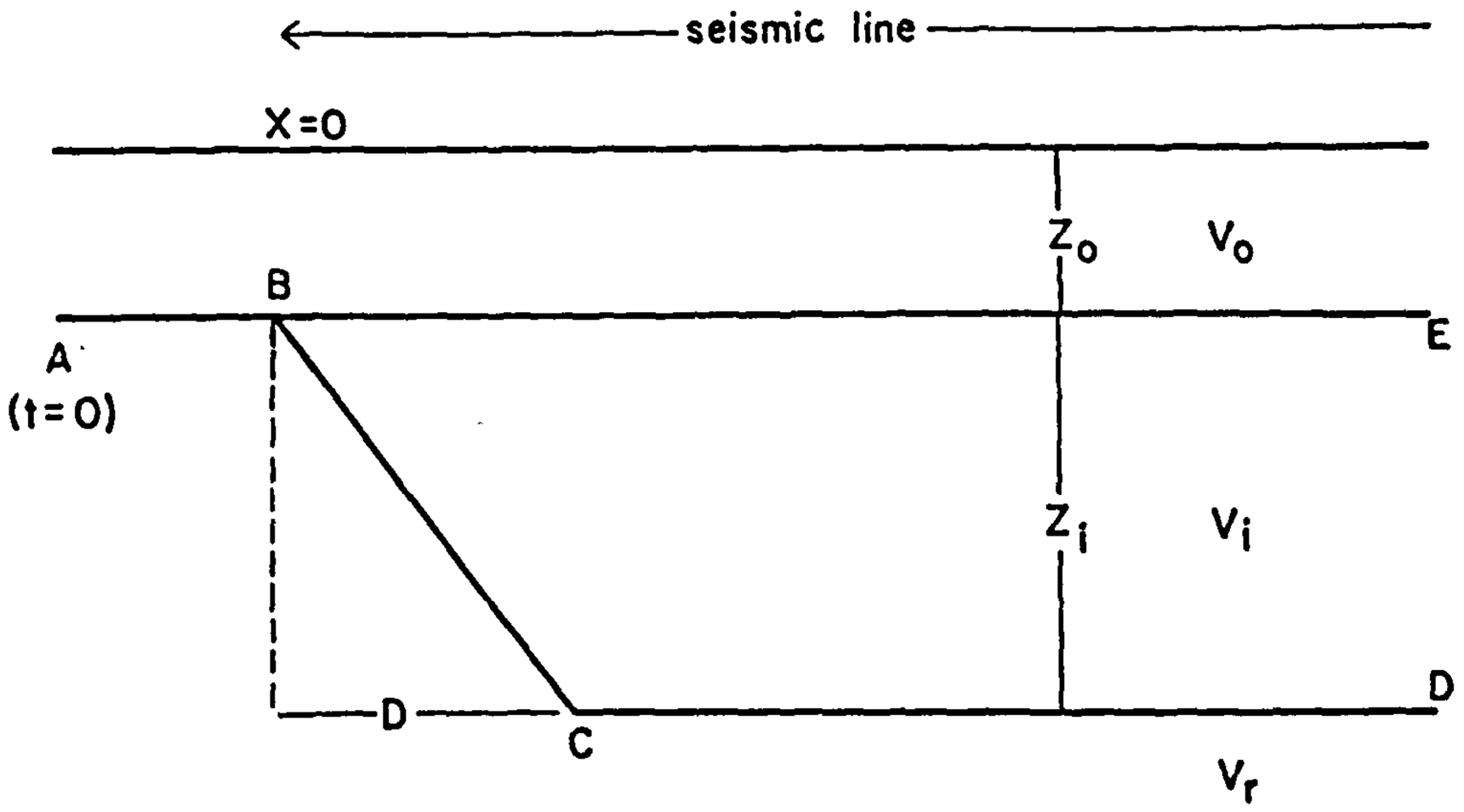

(a) Pinching layer model 1

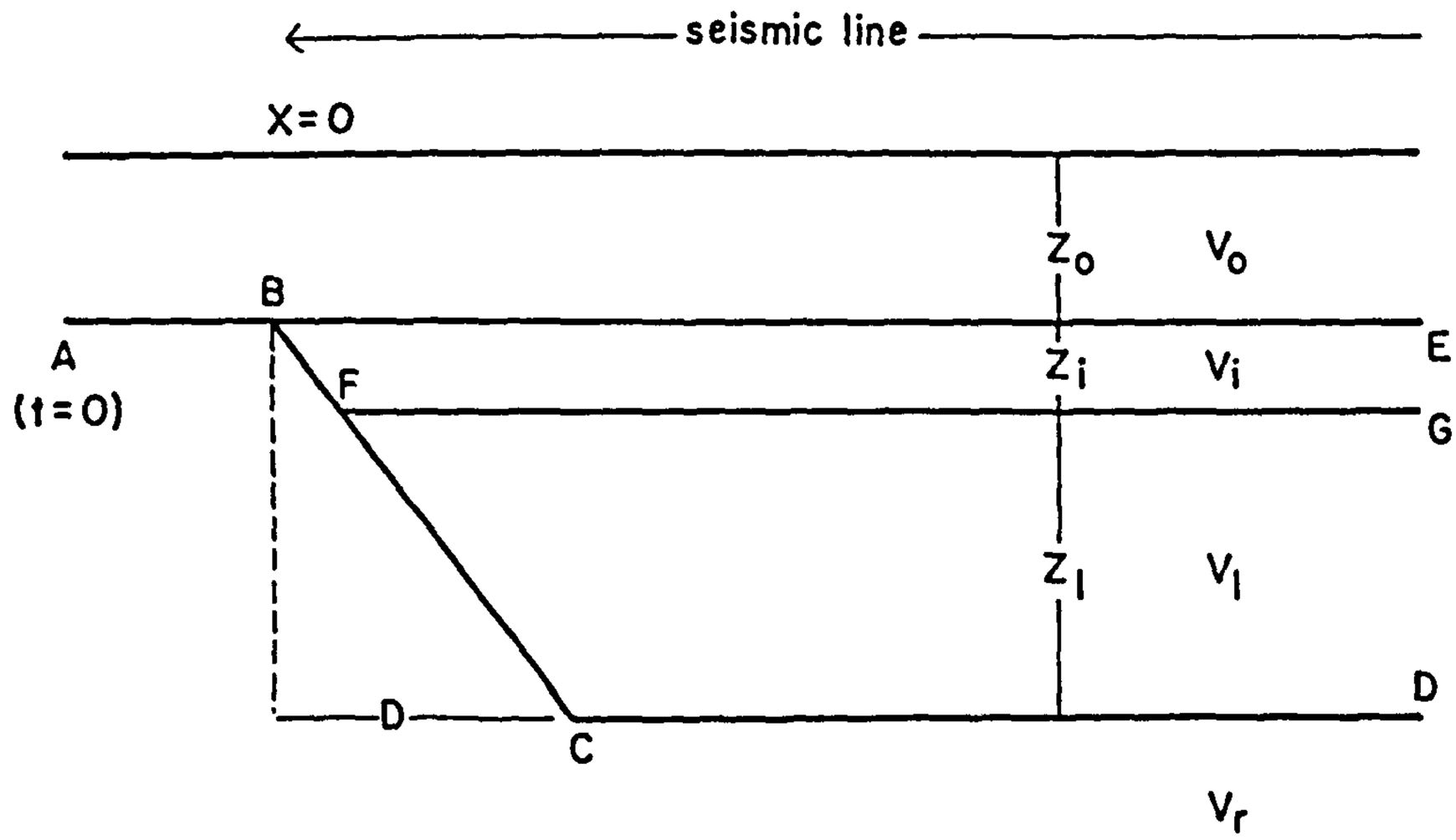

(b) Pinching layer model 2

Two such models have been ray-traced for Fig. 5.18. For each, overburden velocity $V_o = 5$ km/s, intermediate layer velocity $V_i = 5.5$ km/s, refractor velocity $V_r = 5.65$ km/s, overburden depth Z_c = 1 km and the three-layer case occurs after D=5 km. Two values for Z_i were used:

1) Z_i = 0.5 km Refractions from the lower basement refractor (segments BC and CD) arrive before those from the upper basement refractor (segment CE). The same result was obtained for various combinations of $V_o < V_i < V_r$ with the same depths, and implies that the first arrivals north of station 7 are really from the lower basement and that the later arrivals are from the shallower refractor. Clearly this cannot be the case since the lower basement refractions are known to be the higher amplitude of the two.

2) Z_i = 1 km Refractions from the lower basement refractor arrive first, but those from segment BC are largely coincident with refractions from the upper basement refractor. Refractions from the deepest level of the lower basement (CD) are offset by some 6 km from the base of the incline and for about 3 km they occur as later arrivals. Increasing the thickness of the intermediate layer increases the distance over which these refractions are observed as later arrivals, such that it is possible to model later arrivals from interface CD over long distances. However, to achieve this Z_i must be greater than 4 km, which is geologically unreasonable and which also contradicts the observation that the intermediate refractor is a thin layer.

Thus in order to model later arrivals more easily, the model requires further refinement by introducing a hidden layer of velocity V_l below the upper basement refractor such that $V_l < V_i$ and $V_i < V_r$. This makes BE the upper surface of a thin, shallow high velocity masking layer (Fig. 5.17b). Two models were ray-traced in Fig. 5.19, for both of which

FIG 5-18

(1)

PINCHING LAYER MODEL 1 (Reducing Velocity 5.6Km/s)
Vo 5.00Km/s (arrival not plotted), 1.00Km thick
Vi 5.50 ---------- Full thickness of 0.50Km, 5.00 Km from origin
Vr 5.65 ———— Off incline ------

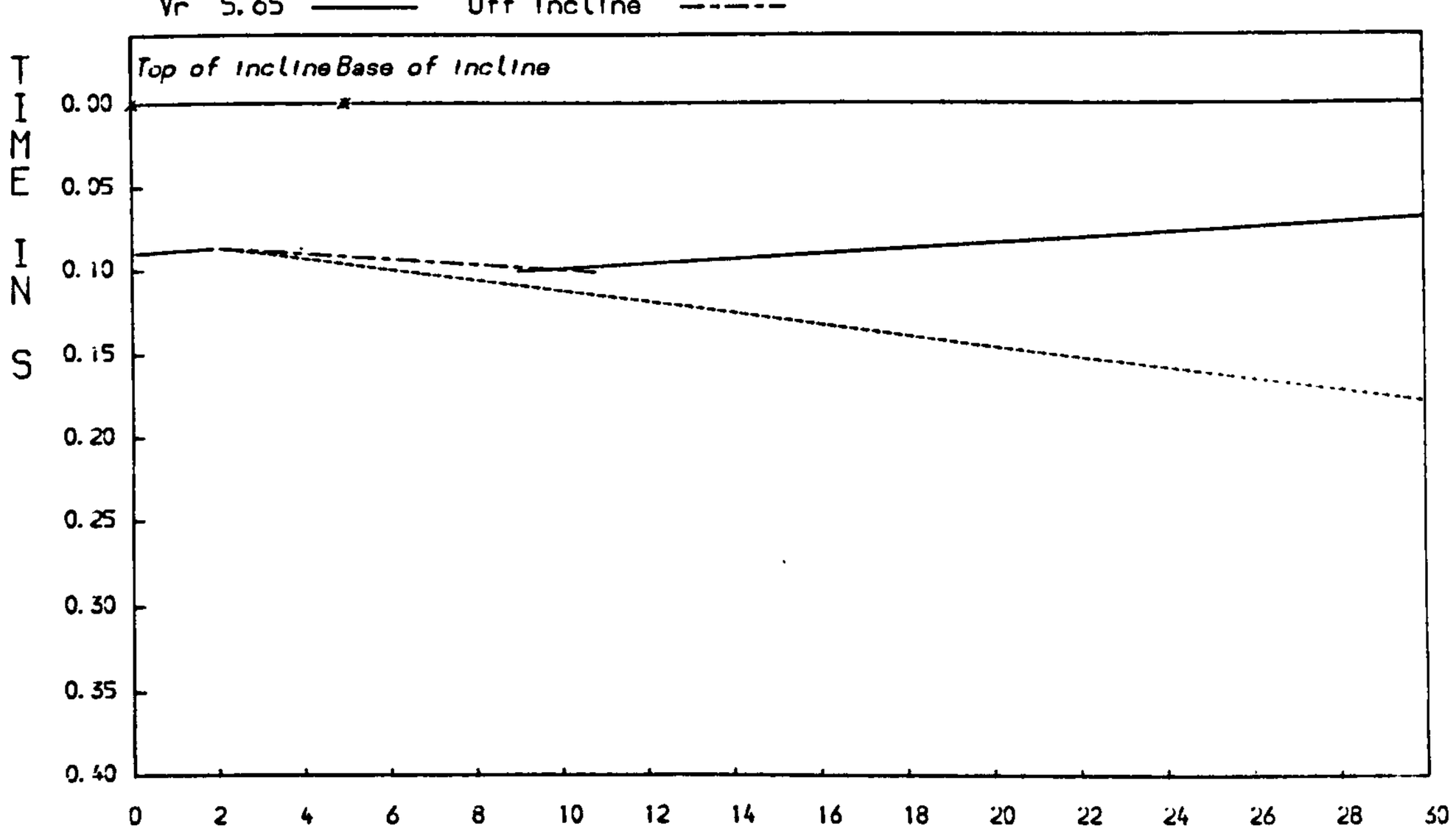

(2)

PINCHING LAYER MODEL 1 (Reducing Velocity 5.6Km/s)
Vo 5.00Km/s (arrival not plotted), 1.00Km thick
Vi 5.50 ---------- Full thickness of 1.00Km, 5.00 Km from origin
Vr 5.65 ———— Off incline ------

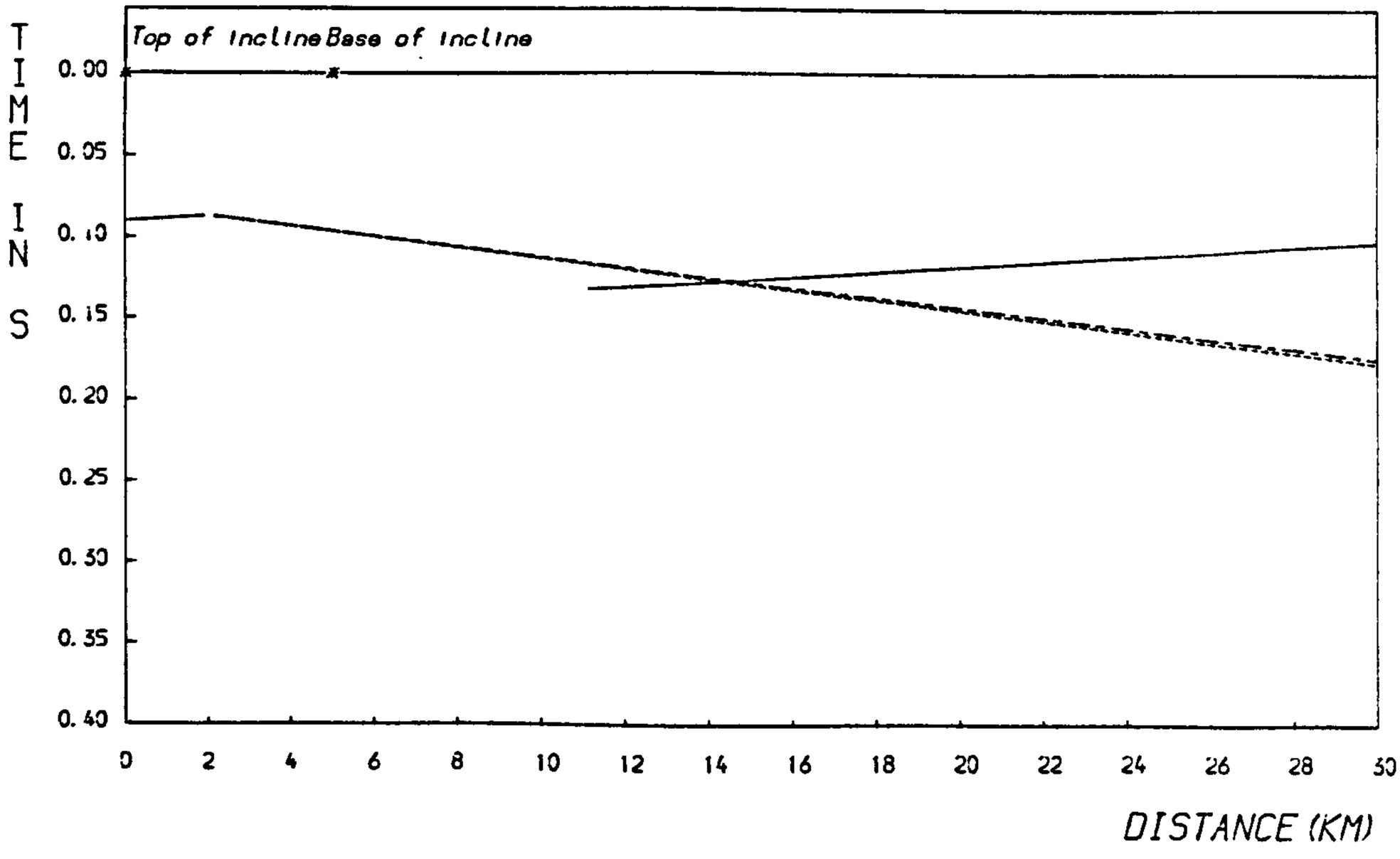

FIG 5-19

(1)

PINCHING LAYER MODEL 2 (Reducing Velocity 5.6Km/s)
Vo 5.00Km/s (arrival not plotted), 1.00Km thick
Vi 5.50 ——— Thickness 0.50Km,
Vl 5.40Km/s (no arrival), 1.50Km thick 3.00Km from origin
Vr 5.65 ——— Off incline ——---

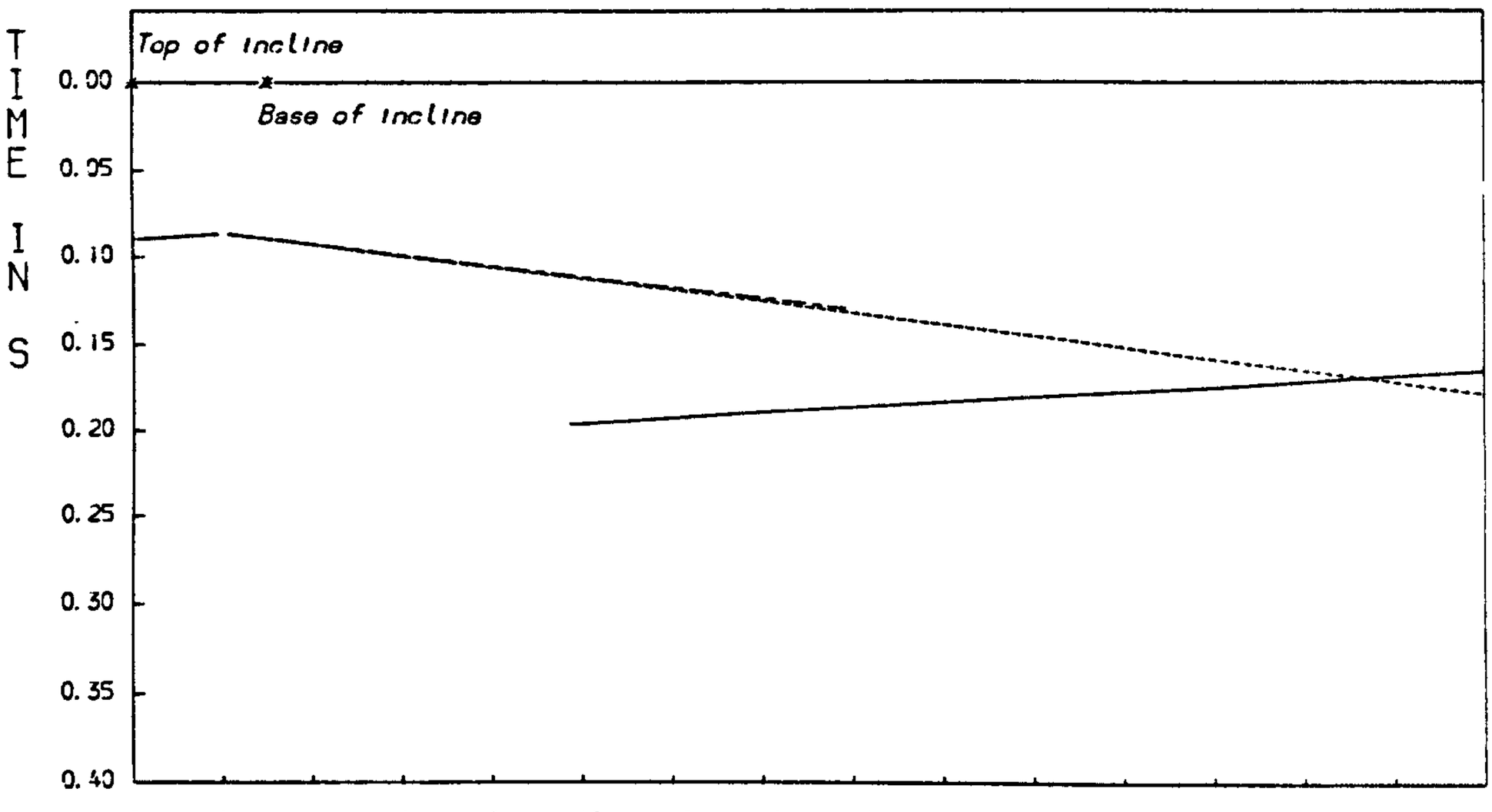

(2)

PINCHING LAYER MODEL 2 (Reducing Velocity 5.6Km/s)
Vo 5.00Km/s (arrival not plotted), 1.00Km thick
Vi 5.50 ——— Thickness 0.50Km,
Vl 4.80Km/s (no arrival), 1.50Km thick 8.00Km from origin
Vr 5.65 ——— Off incline ——---

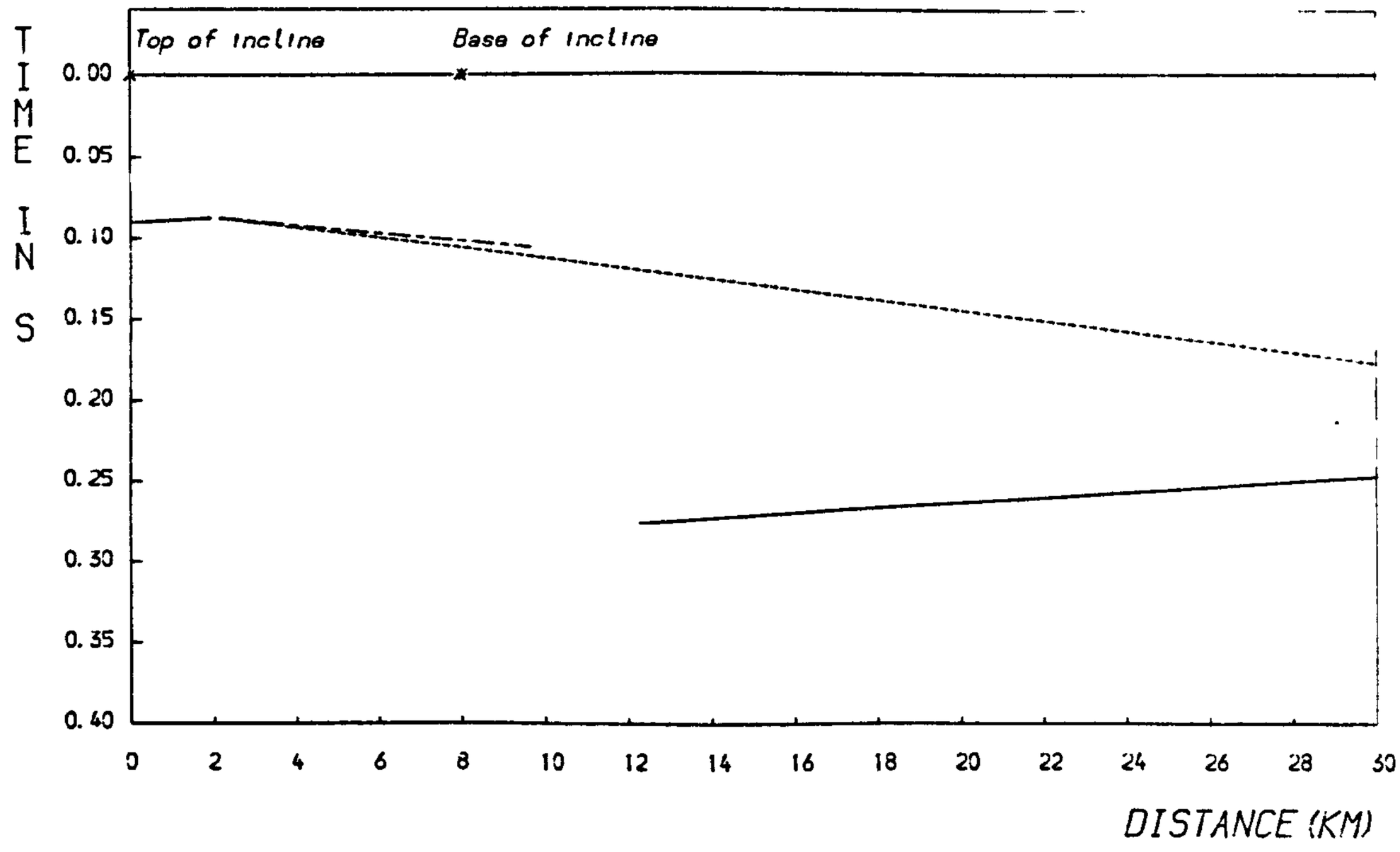

overburden velocity V_o = 5 km/s
thickness Z_o = 1 km
upper basement refractor velocity V_i = 5.5 km/s
thickness Z_i = 0.5 km
hidden layer thicknes Z_1 = 1.5 km
lower basement refractor velocity V_r = 5.65 km/s

The different values considered were:

1) V_1 = 5.4 km/s, D = 3 km

2) V_1 = 4.8 km/s, D = 8 km

With the introduction of V_1 it was easy to model a delay between refractions from upper and lower basement refractors without necessitating a large vertical displacement across the incline BC or a very low velocity V_1. Obviously there are many combinations of V_1, Z_1 which can produce delays of 0.1 - 0.2s compatible with those observed for the Mansfield event M6040.

For this third layer it was difficult to produce refractions from the segment BC that struck the surface within the length of the seismic line, unless D was very large. Thus the plotted refractions from the incline are from the segment BF; these are observed at larger X for smaller D. This result is the same whether critical refractions were shot off the incline, or diving waves from a distant source used, as they were here.

One problem common to both types of model is that of offset between the base of the incline and the first observation of the lower basement refraction. This may not affect observations for the Mansfield events whose rays travel subparallel to the strike of the Bonsall Fault line, but may be significant for quarries on the limestone outcrop whose rays travel perpendicular to the feature and for which lower basement arrivals would not be expected for several kilometres north of the fault. The effects of two lower velocity zone cases are depicted in Fig. 5.20 which plots the delays between upper and lower refracted arrivals for five values of Z_1. The

FIG 5-20

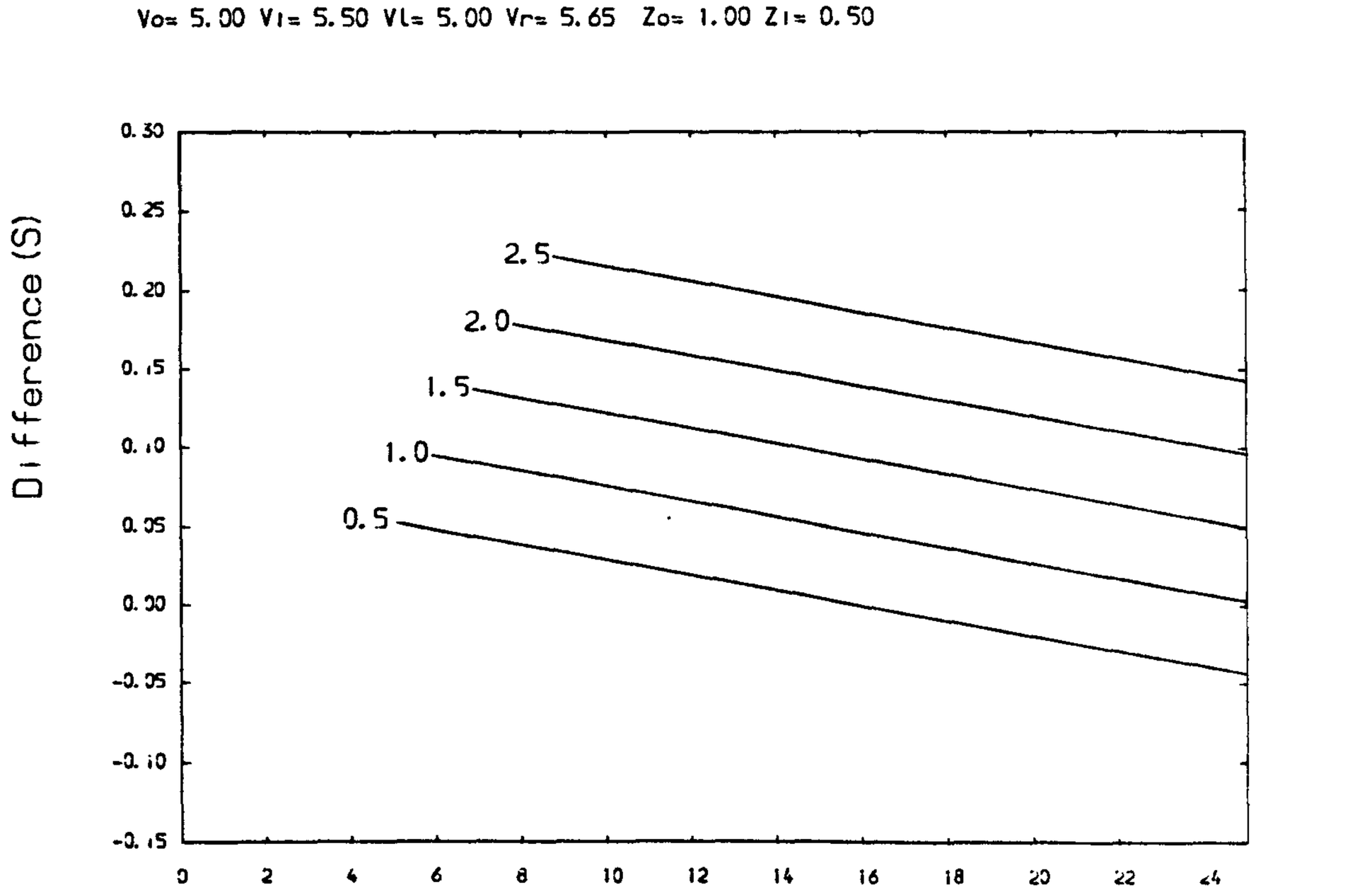
Vo= 5.00 V1= 5.50 Vl= 5.00 Vr= 5.65 Zo= 1.00 Z1= 0.50
Difference (S)
0.30
0.25
0.20
0.15
0.10
0.05
0.00
-0.05
-0.10
-0.15
2.5
2.0
1.5
1.0
0.5
0
2
4
6
8
10
12
14
16
18
20
22
24
Dist (Km) from basement origin

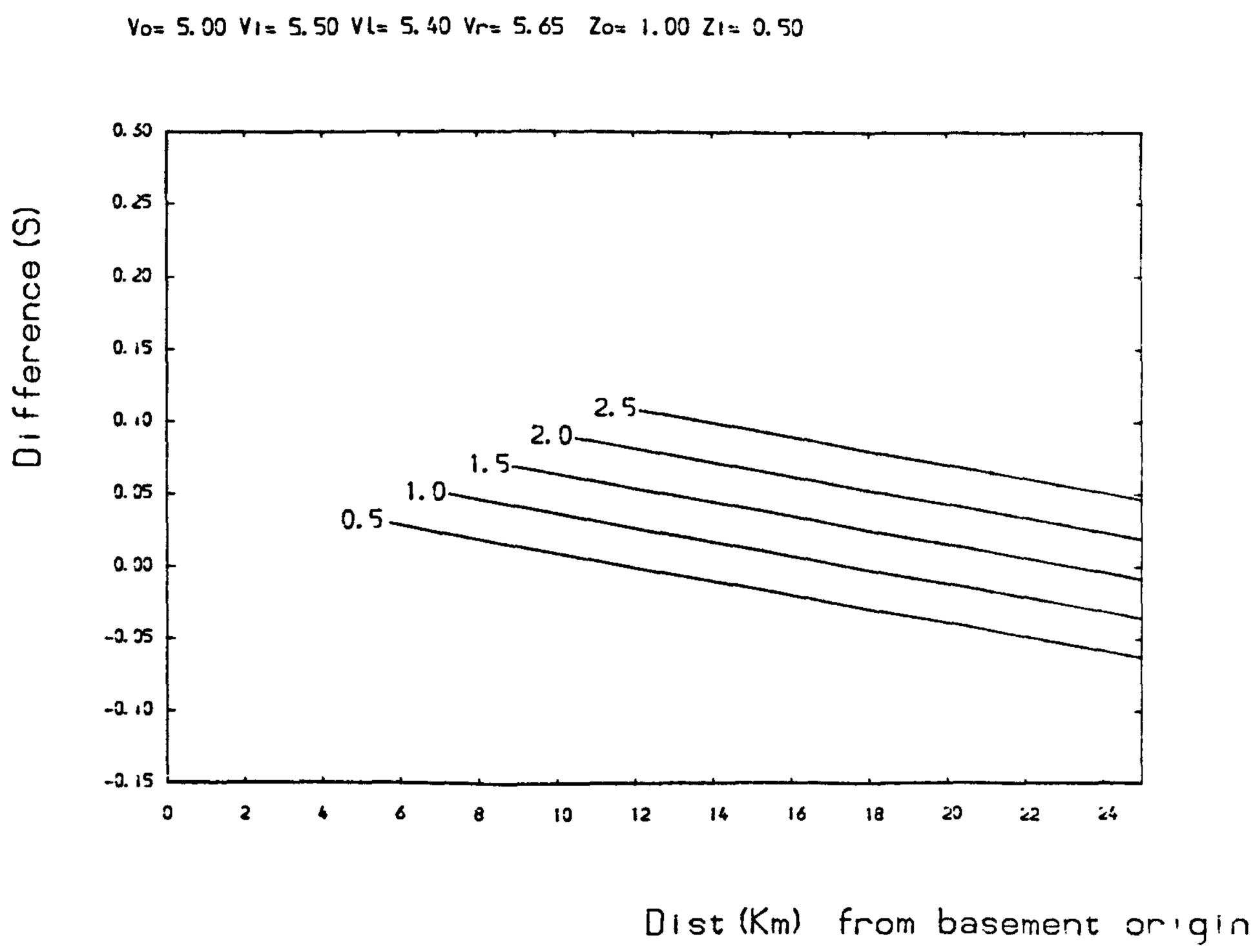
Vo= 5.00 V1= 5.50 Vl= 5.40 Vr= 5.65 Zo= 1.00 Z1= 0.50
Difference (S)
0.30
0.25
0.20
0.15
0.10
0.05
0.00
-0.05
-0.10
-0.15
2.5
2.0
1.5
1.0
0.5
0
2
4
6
8
10
12
14
16
18
20
22
24
Dist (Km) from basement origin

difference in arrival time is calculated from the first emergence of the lower basement refraction, and thus the first point on each curve occurs at the offset distance. The same values for V_c, V_i, V_r, Z_o and Z_i have been used for both cases, with the result that: for the higher value of V_1 the differences in Z_1 are principally manifest in degrees of offset, while for the lower value of V_1 the differences are mainly shown in the relative delays.

If there are two refractors to the north of the Bonsall Fault zone such that refractions from the deeper basement are only observed as later arrivals, then these models suggest that the delay is best modelled by introducing lower velocity material beneath the upper basement refractor. Obviously, the lower the mean velocity of this layer the shallower the lower basement refractor need be to produce the observed delays between refractions.

5.4.2 Later Arrivals from Quarry Blasts

A representative sample of quarry blasts from the area are plotted as reduced time seismograms in Fig. 5.21, where direct waves are denoted by the full line, arrivals interpreted as refractions from the upper basement refractor by the dotted and dashed line, and basement refractions by the full dashed line. The seismograms have not been plotted at the same gain.

Apart from the Mansfield events, the furthest sources considered to the north-south line are quarry blasts from the Cauldon Low region. Like the Mansfield event M6040, many of these show contrasts between the P waves recorded to north and south of the line. South of the Bonsall Fault, and nearer the quarry, the first arrivals correlate well with each other and are proportionally larger in amplitude than their P wave coda. To the north the amplitude of the first break decays rapidly, the first arrivals complicate and the first break is less easily picked. Comparing this event with the northern quarry blasts

M3008 -- DOVEHOLES UNTIMED

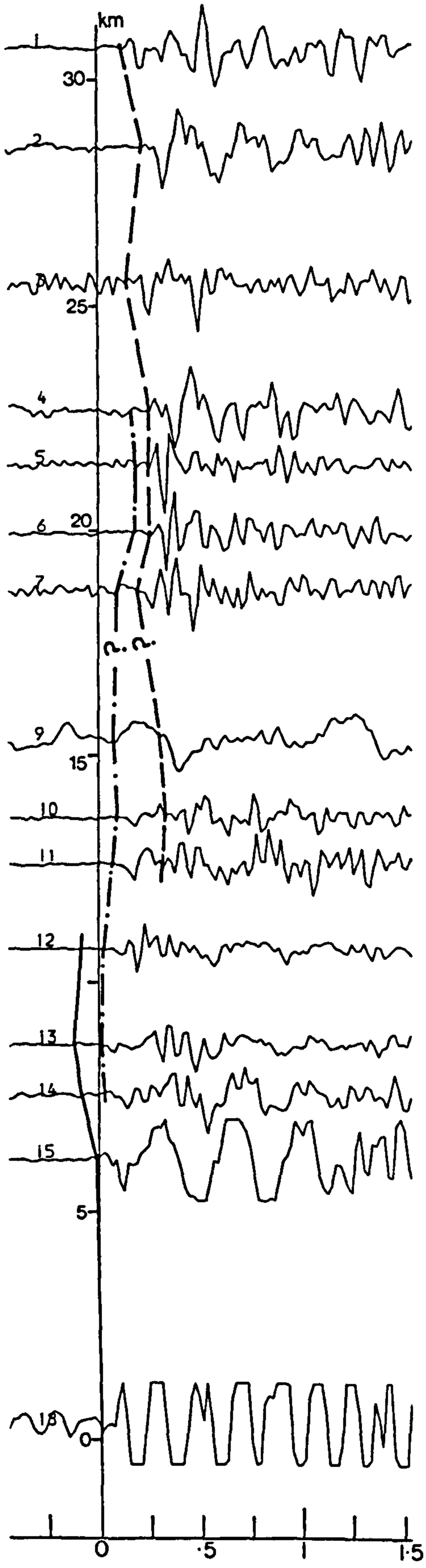

M4035 -- BALLIDON TIMED*

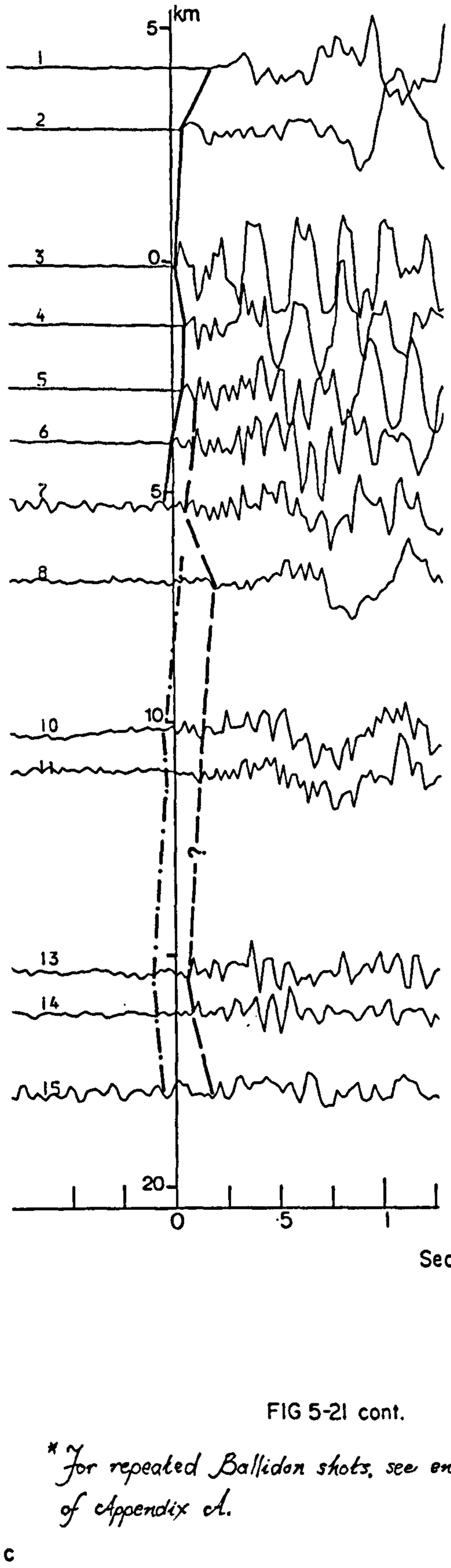

FIG 5-21 cont.

*For repeated Ballidon shots, see end of Appendix A.

FIG 5-21

M1010 -- CAULDON UNTIMED

—plotted against interstation separation

M4008 -- MIDDLEPEAK UNTIMED

— plotted against interstation separation

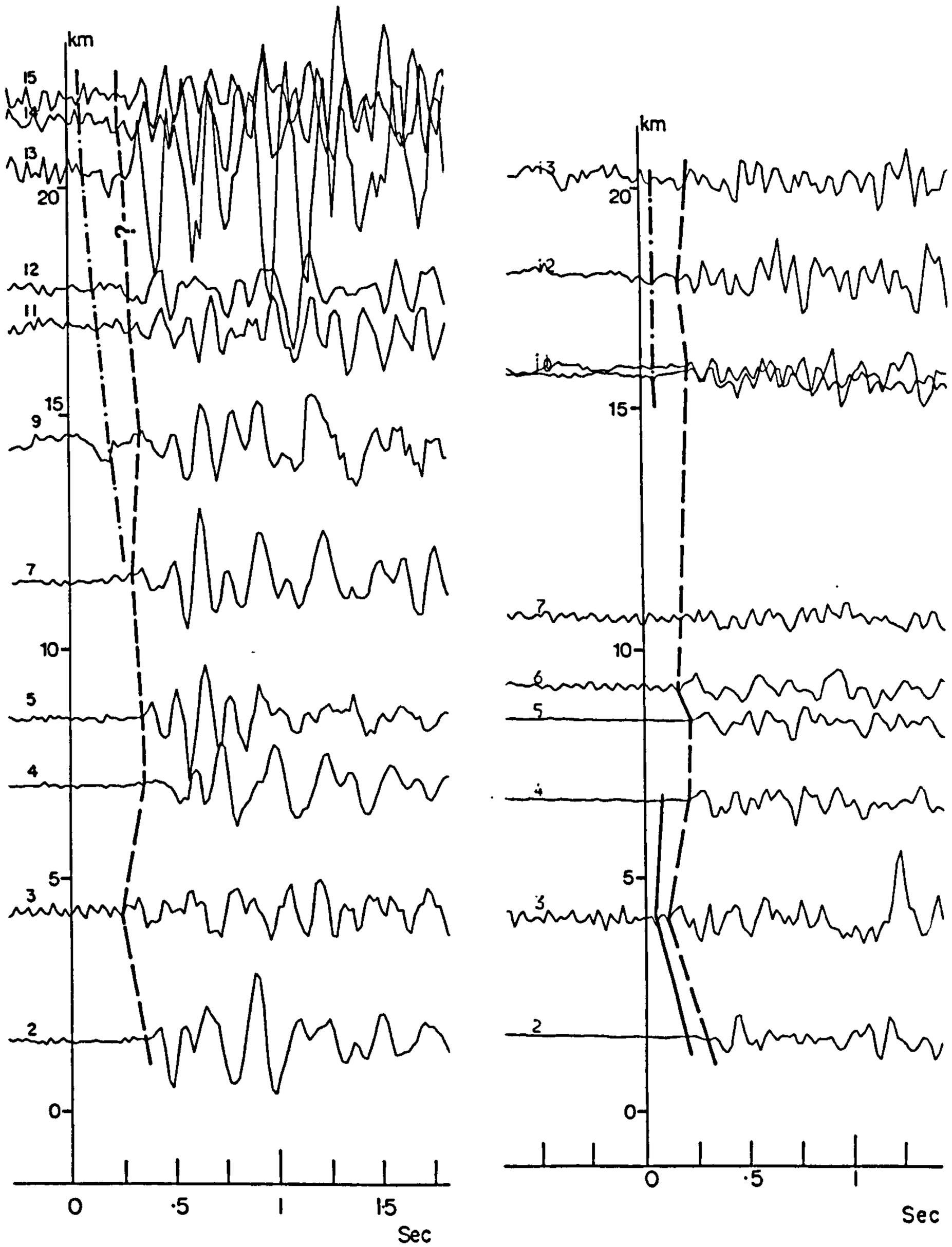

Reducing velocity 5·6km/s

direct wave

upper basement refraction

lower basement refraction

plotted in Fig. 5.10, lower frequency, more coherent basement refractions south of the Bonsall Fault are also observed. Thus these waveforms to the south are not only due to increased filtering of high frequency content with distance, but also reflect the nature of the basement refractor.

For this Cauldon shot, like the Mansfield event, later arrivals can be identified in the P wave coda for stations north of the Bonsall Fault that correlate with the first arrivals to the south, but which are not observed in the P wave coda for the southern stations. It could be argued that these later arrivals are not refractions from a deeper interface, but are either wide-angle reflections or direct waves. If they were direct waves this would imply that the first arrivals for the southern stations are also direct, which is unlikely.

In order to examine the possibility of wide-angle reflections, the simple model of Fig. 5.8 was ray-traced using a programme written by Cassel (1982; Fig. 5.22), but it proved difficult to produce these reflections with such a complicated refractor structure. As M4006 (Waterswallows) and other events show, coherent reflections are not often obvious on the reduced seismograms except for stations close to the source, so it is thought less likely that these later arrivals are reflections than lower basement refractions.

Fig. 5.21 also considers a re-interpretation of the timed Ballidon event M4035, where a proportionally larger amplitude, longer wavelength later arrival can be seen in the P wave coda north of station 7. Similar later arrivals can be identified within the first arrival coda for the Middlepeak event (M4008). For the Doveholes shot (M3008) the larger amplitude later arrival south of station 12 correlates with the first arrivals to the south and emerges about 13 km from the source. This is consistent with the model of Fig. 5.20a, where a hidden layer a kilometre thick resulted in an offset of about 6 km, equivalent to a critical distance of 12 km.

Several reduced time graphs with later arrival times are shown in Fig. 5.23. Although these arrival times are more

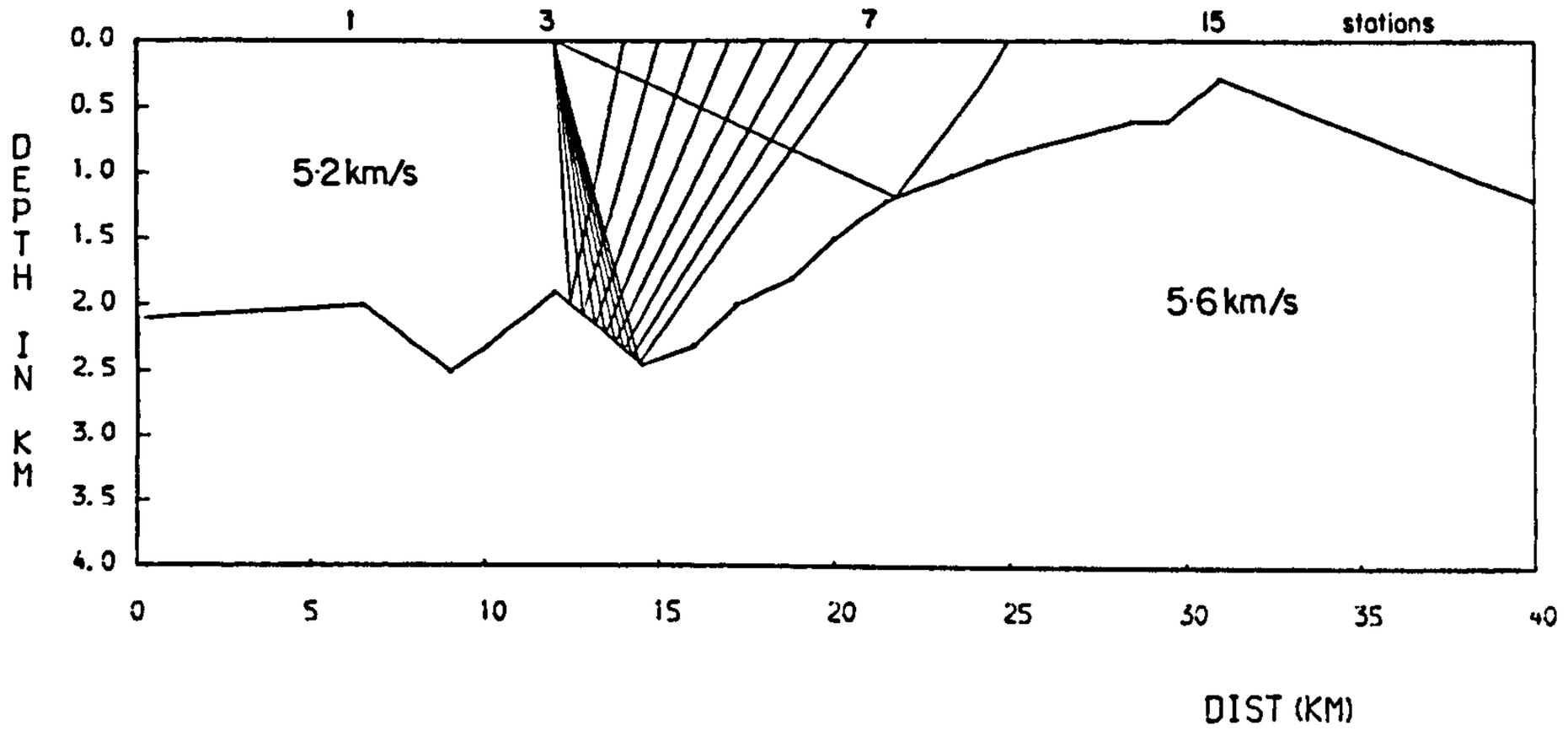

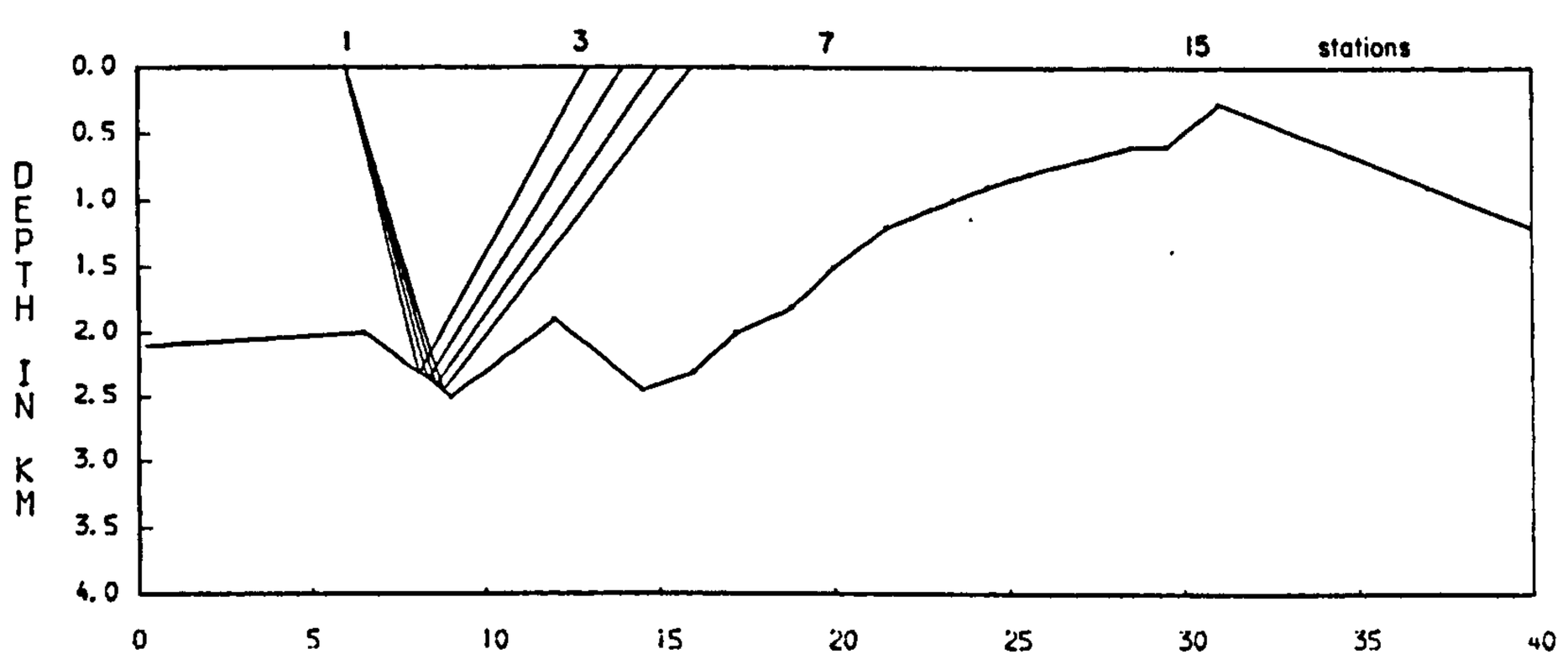

PRE-CARBONIFEROUS SURFACE MODEL

FIG 5-22 Attempts to ray-trace reflections using the 'box method' programme of Cassel (Geophys. J.R. astr. Soc., v.69(1982), 339-354). Rays traced to surface at 1km intervals between 12 and 38km. Run unsuccessful for source before 5km.

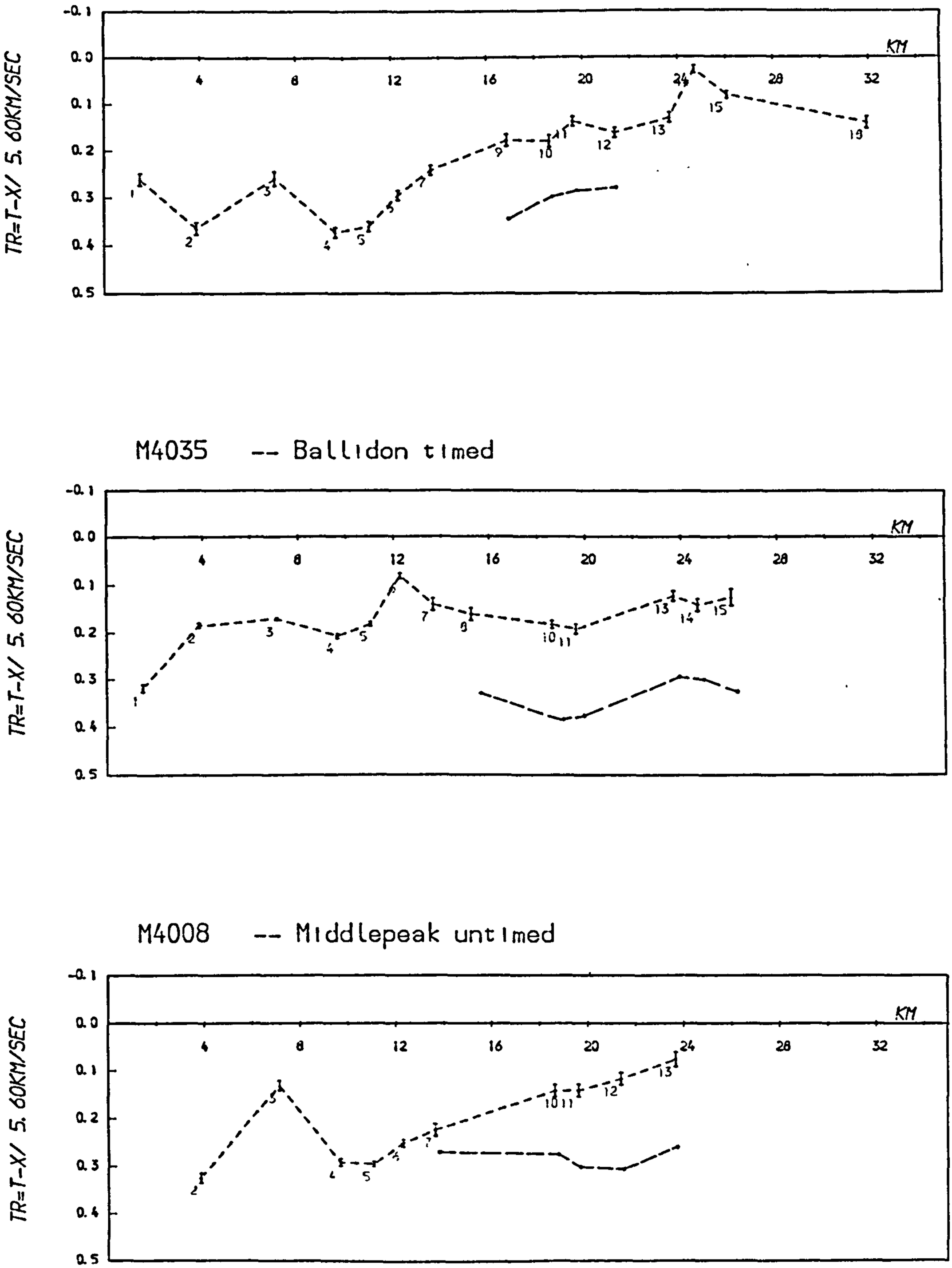

FIG 5-23 Reduced times including later arrival data (----)

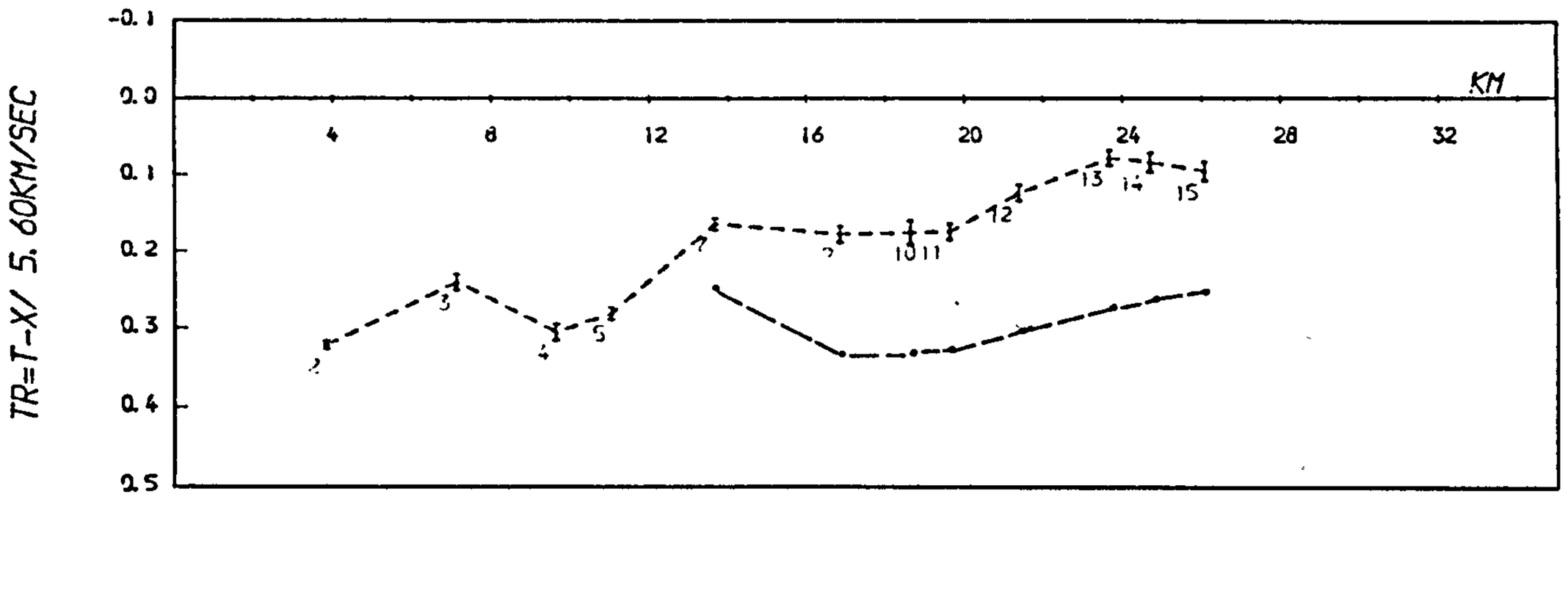
M1010 -- Cauldon Low untimed
TR=T-X/ 5.60KM/SEC
-0.1
0.0
0.1
0.2
0.3
0.4
0.5
KM
4
8
12
16
20
24
28
32

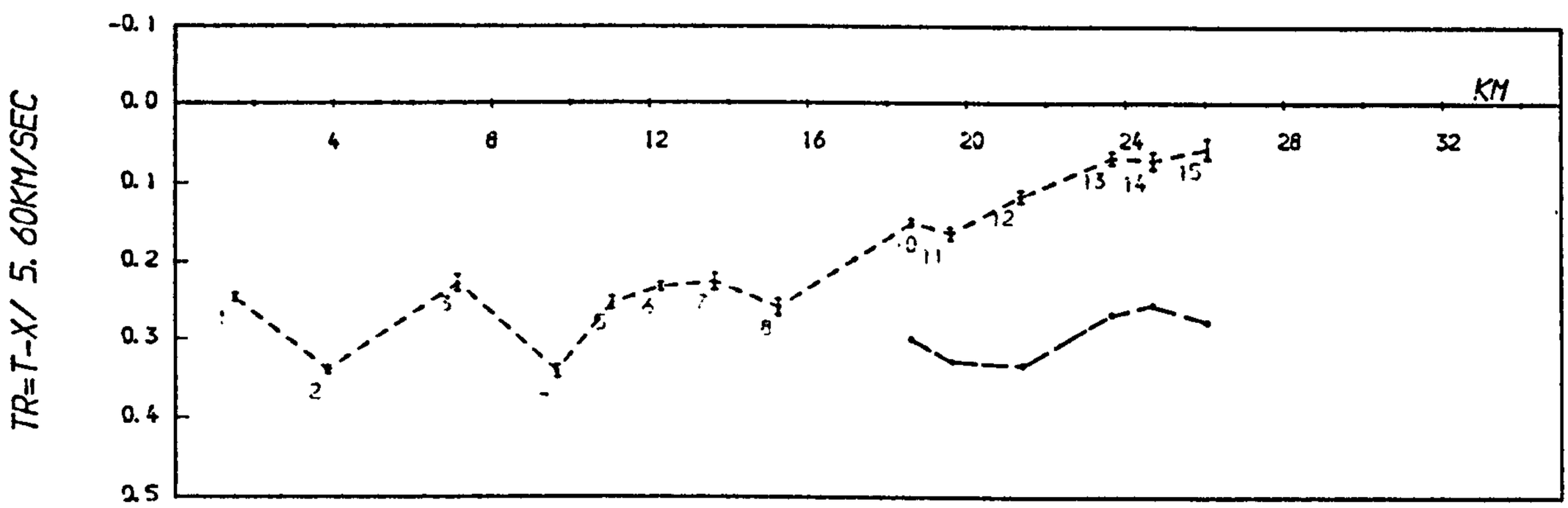
M4023 -- Ramshorn untimed
TR=T-X/ 5.60KM/SEC
-0.1
0.0
0.1
0.2
0.3
0.4
0.5
KM
4
8
12
16
20
24
28
32

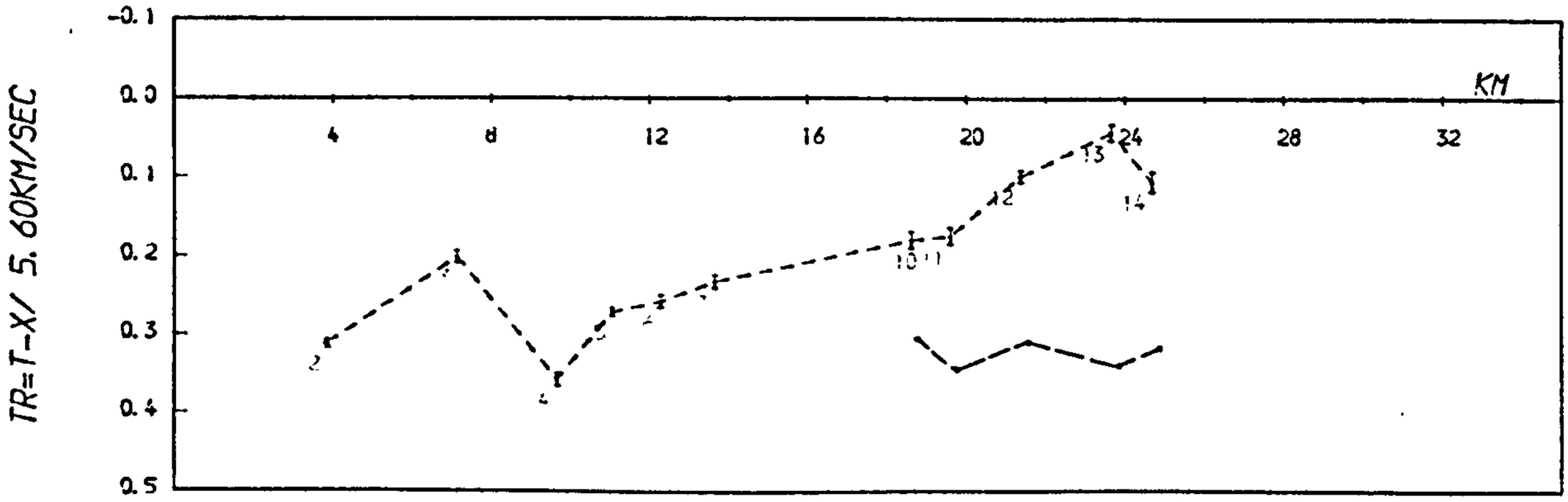
M4014 -- Cauldon Low untimed
TR=T-X/ 5.60KM/SEC
-0.1
0.0
0.1
0.2
0.3
0.4
0.5
KM
4
8
12
16
20
24
28
32

FIG 5-23 cont

subject to picking error than first breaks, some features are consistent in the data: for example the trough between stations 9 and 11, and the high between stations 13 and 15. Since later arrivals have been identified within 5 km north of the Bonsall Fault (that is within the problematical offset distance of Section 5.4.1), it is possible that they originated from the northward dipping lower basement interface itself, which may either have an irregular surface or is not too steeply inclined for refractions from it to strike the surface.

5.4.3 Summary - General Observations

The deeper structure along the north-south profile generally appears to be more complicated and of greater relief than the surface geology implies. The pre-Carboniferous surface is well-defined by first arrival data, which suggest a general shallowing towards the Woo Dale region (Fig. 5.12). Refractions from the basement are often observed within 3 km of quarries around Buxton, although these are frequently precluded for several kilometres by 5.6 - 5.8 km/s refractions from dolomitic horizons within the limestone sequence.

The profile appears to be underlain by two sub-Carboniferous refractors with differing seismic characteristics, but similar velocities. These refractors appear to be divided by the line of the Bonsall Fault, which may be related to a more important basement fault. To the south of this fault, basement refractions observed from quarry blasts are seen to be coherent and attenuate at a rate less than geometrical spreading. To the north the first arrivals are distinctly higher frequency and lower amplitude, but attenuate at a rate compatible with spherical spreading. These differences are illustrated by the relative amplitudes for several events from Doveholes quarry (Fig. 5.24). Note that refractions from the refractor to the north of the Bonsall Fault for quarry blasts do not attenuate as rapidly northwards as those from the

FIG 5-24 Relative amplitudes—various Doveholes blasts

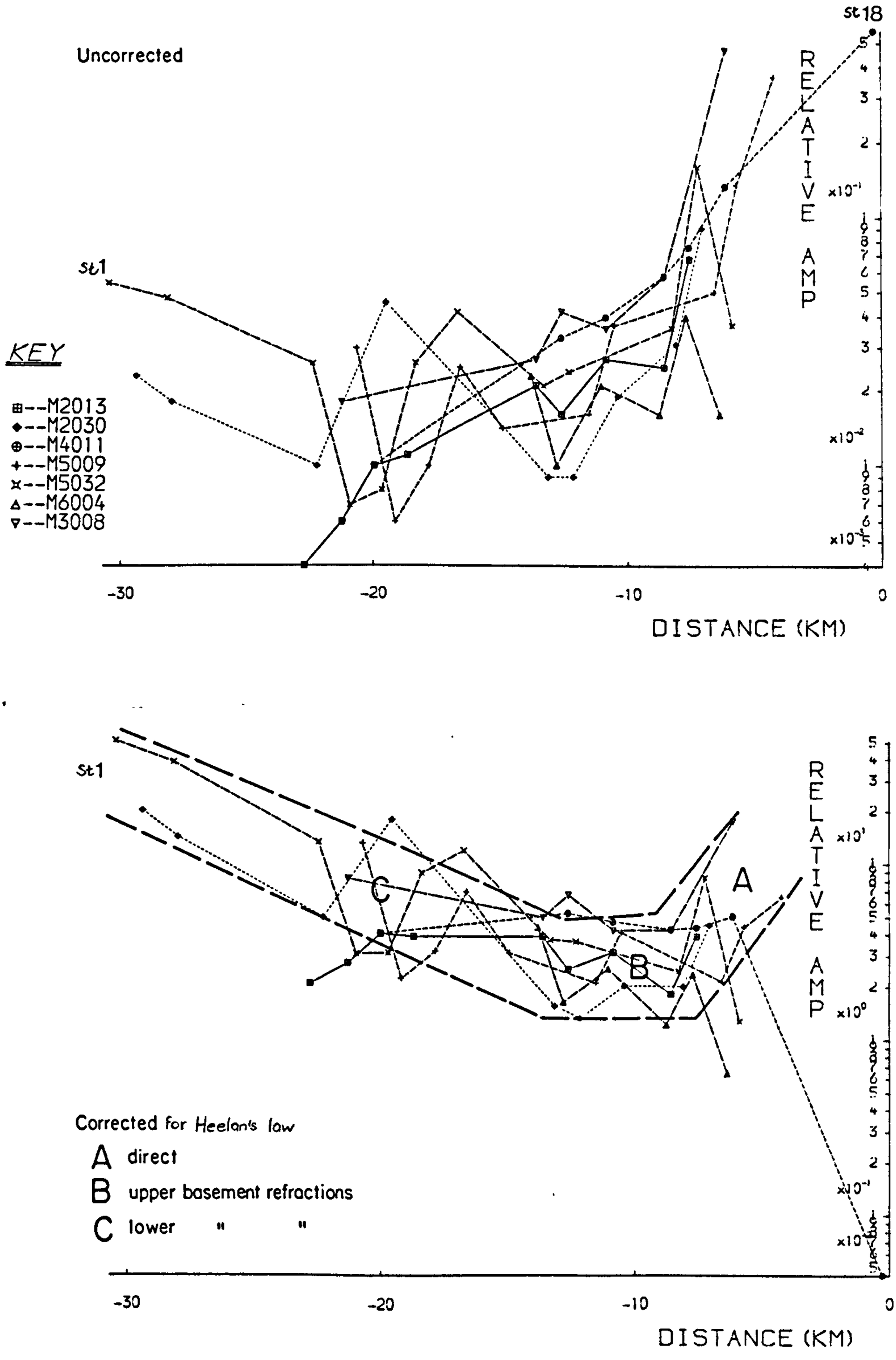

Mansfield event (Fig. 5.14). This may be because the latter signal is three to six times the wavelength of quarry blast P waves. The better transmission of signal of about 10 Hz suggests that the upper basement refractor is around 500 m or so thick.

Refractions observed as first arrivals to the south can often be traced as later arrivals to the north of the Bonsall fault. This is thought to indicate that the southern refractor is downfaulted northwards, and present at depth. The delay between refractions from upper and lower basement refractors to the north of the Bonsall Fault may suggest a hidden layer between the two. Similar later arrivals are not observed at the southern stations.

South of the Bonsall Fault the sub-limestone surface appears quite irregular and may be cut by faults not evident at outcrop. Smaller reduced times for stations 1 and 3, for example, are observed from a variety of azimuths, and the high at station 3 is similarly shown by station 69 from the DASED1 line. However the reduced times for station 61 seem as large as those for station 2, so that if there is a basement fault here it must lie between stations 1 and 61. That station 1 is on the upthrow side of a fault or syncline limb, may be linked with the difference in P wave character with station 2, the first arrivals at which are generally broader than those of station 1 even for northern events (e.g. Tunstead M5027 (Fig. 5.10)); thus there may be absorptive material beneath station 2 but thinned or absent from under station 1, which fills the basement low under station 2 and which filters the upward travelling P waves. Additionally, first breaks at station 4 are often similarly broadened.

5.5 The Northern Province

Two profiles lay completely within the northern province: the northern east-west (NEW) line, and DASED2. Both these profiles had station 14 (re-occupied as station 34 in

1980, see Fig. 3.1) in common with the north-south line. The NEW line additionally had station 51 in common with the southern east-west profile, and DASED2 was maintained during a repeat of the 1979 line. Thus the interpretation of these lines is well controlled by the results from the north-south profile.

This is fortuitous because the data for the NEW profile are not particularly well distributed with azimuth: most events are from the quarries around Buxton, to the west of the line. Although a few events were detected from Stoney Middleton, most reversal of the profile comes from shots at Hope Valley quarry (see Fig. 3.7).

5.5.1 Northern East-West (NEW) Line

The NEW profile crossed the north-south profile where the upper basement refractor is shallow and refractions from the lower basement only seen as later arrivals. The line passed both Woo Dale and Eyam boreholes, between which the sub-Carboniferous surface was expected to dip eastwards. The ends of the line also lay within the Namurian sedimentary basins of the Goyt Trough and the Edale Trough, and thus should manifest deeper basement than under the limestone massif.

i) Timed Events

Reduced time graphs for the timed and positioned shots are given in Fig. 5.25. These appear quite varied. Almost certainly the first arrivals for Ballidon, Longcliffe and Dene are all refractions, and it is possible that two different sets of arrivals have been picked: the smaller reduced times corresponding to the upper basement refractor. If so, then lower basement refractions appear to have been picked for stations 37 to 41 for all three events. Similarly the reduced times for station 34 are for upper basement refractions. Since the difference in reduced time between stations 34 and 37 is fairly consistent for these events, then a considerable delay

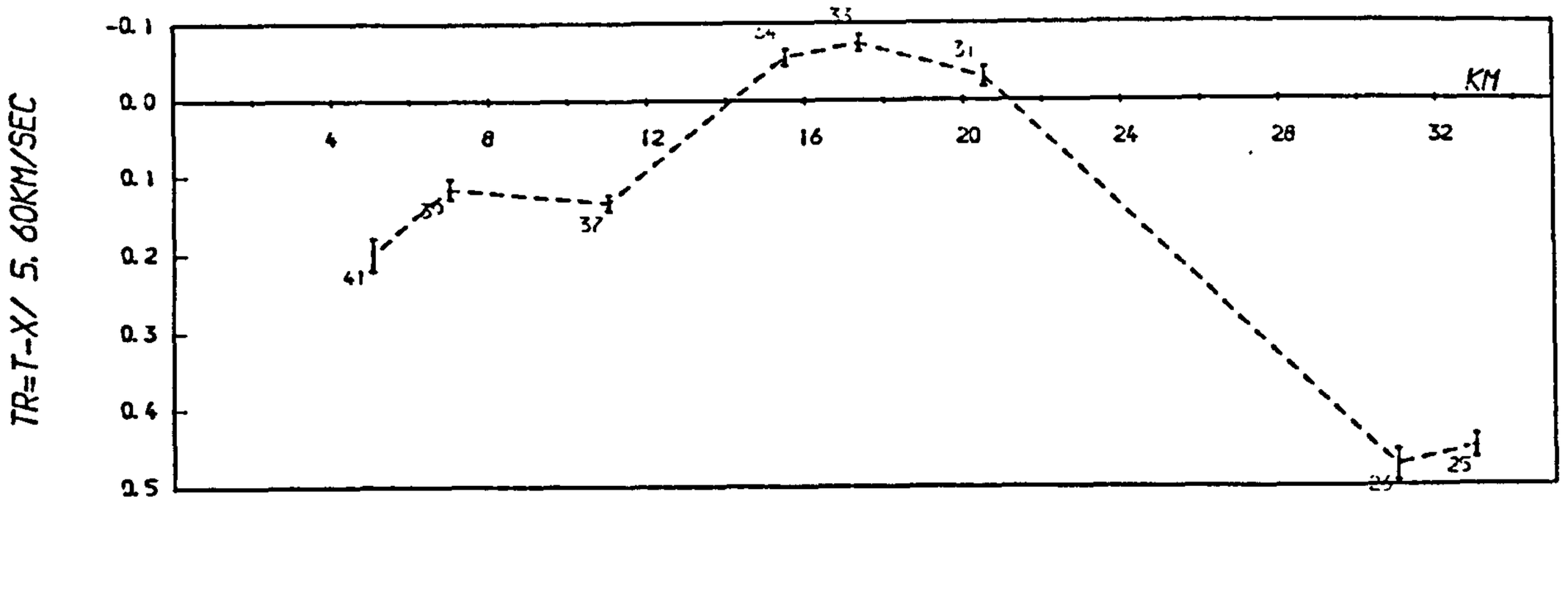

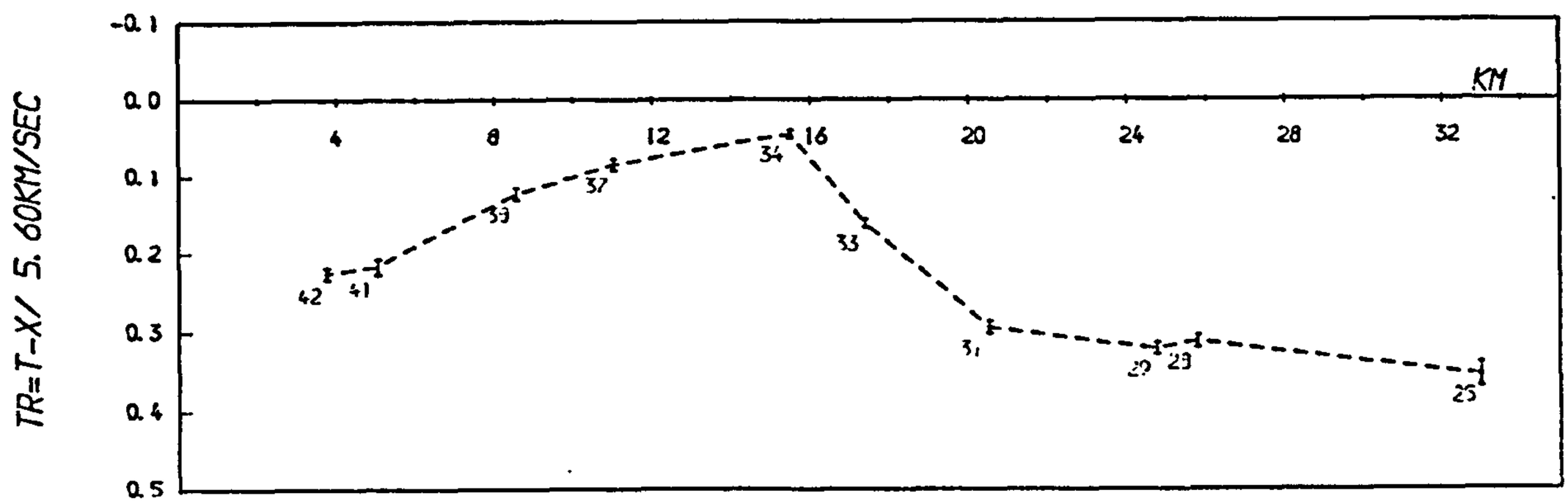

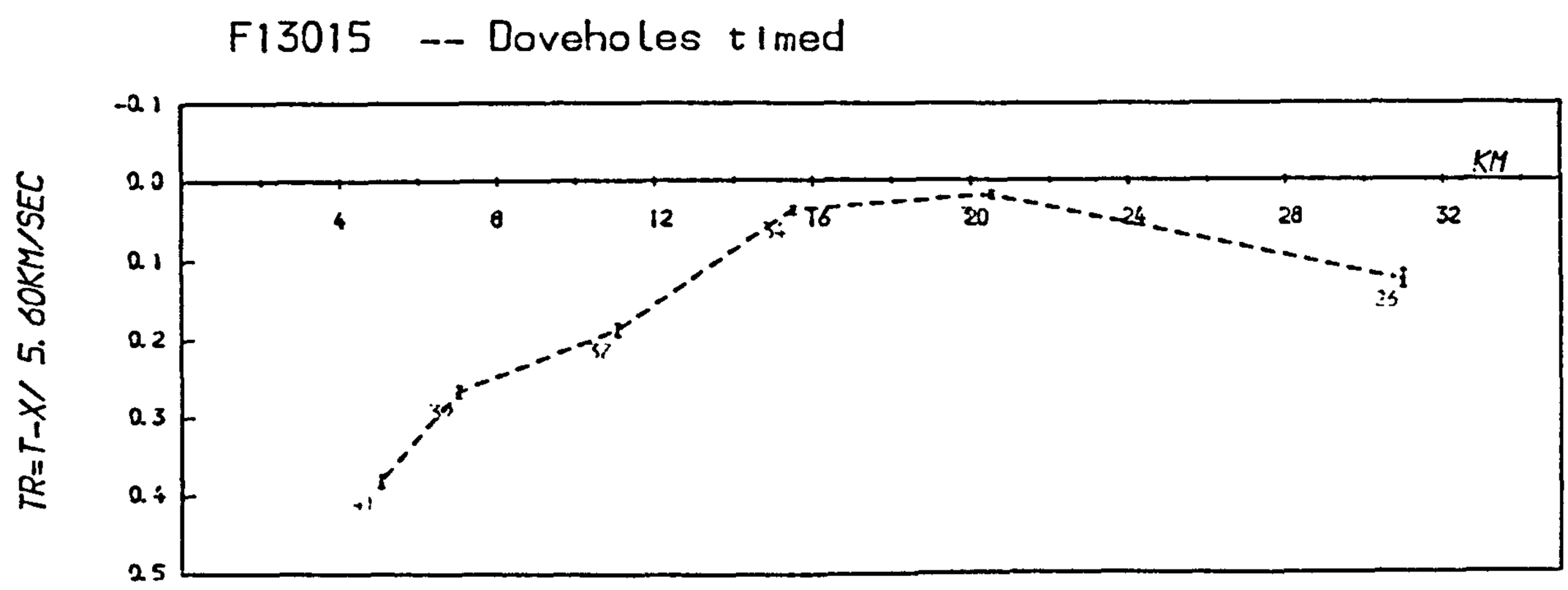

FIG 5-25 Reduced times

FIG 5-25 cont

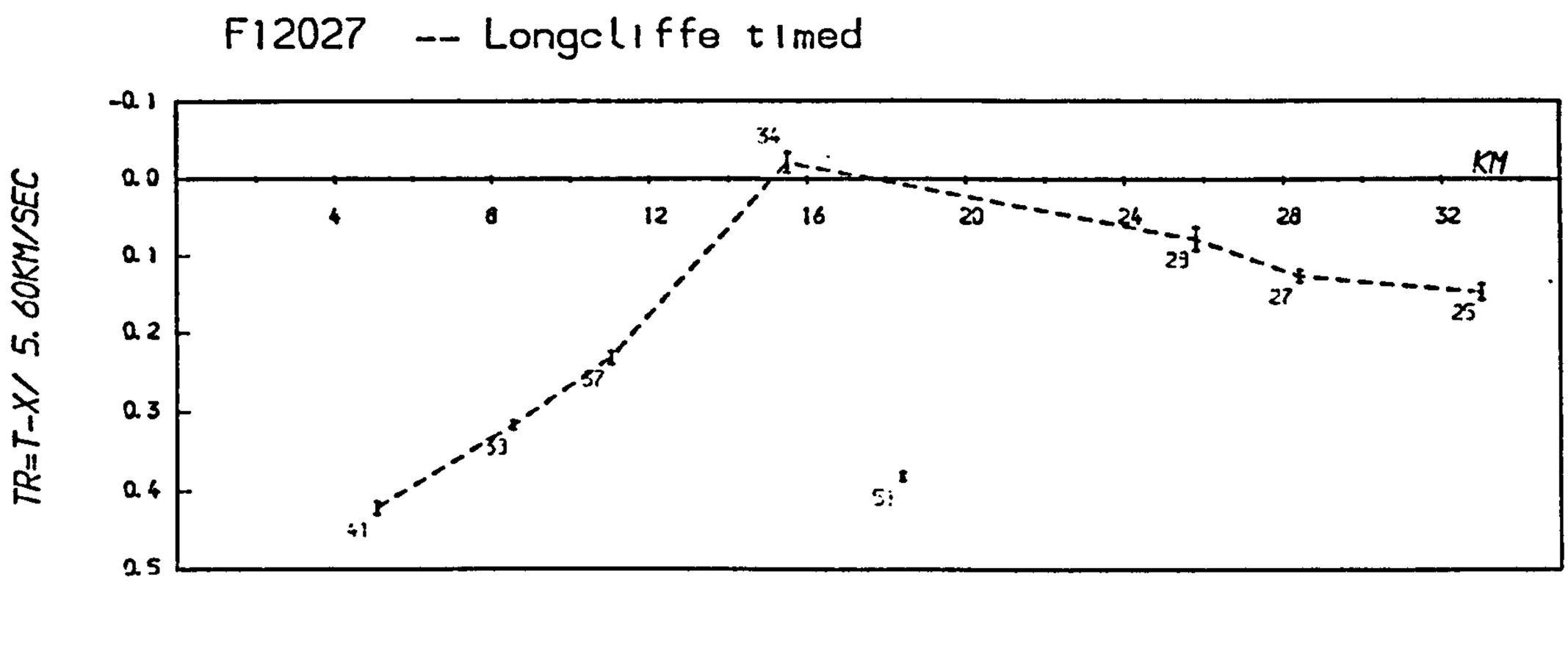
F12027 -- Longcliffe timed
TR=T-X/ 5.60KM/SEC
-0.1
0.0
0.1
0.2
0.3
0.4
0.5
4
8
12
16
20
24
28
32
KM
34
29
27
25
57
53
41
51

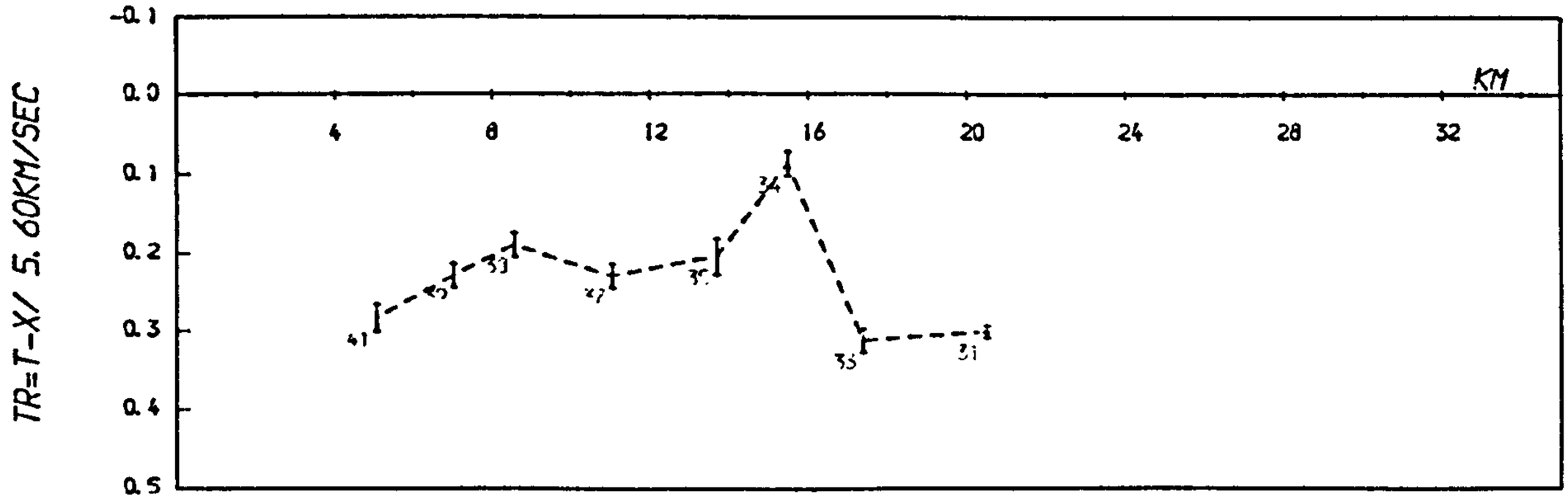
F13019 -- Ballidon timed
TR=T-X/ 5.60KM/SEC
-0.1
0.0
0.1
0.2
0.3
0.4
0.5
4
8
12
16
20
24
28
32
KM
41
43
33
37
35
35
31

between upper and lower refractor arrival times is inferred for stations 25 and 26 by events F12027 (Longcliffe) and F13004 (Dene).

The time shots from Tunstead and Doveholes are a little harder to interpret. The reduced times for the Doveholes event are similar to those from the Longcliffe shot. This may be credible for the upper basement arrival times, but not between stations 37 to 41 if it is considered that Doveholes is too close for lower basement refractions to be observed (cf. event M3008, Fig. 5.21).

The positioned Tunstead event F12015 is best considered in comparison with its reduced seismogram section (Fig. 5.26). The arrivals between stations 31 and 25 are interpreted as refractions from the upper basement refractor, while those between stations 33 and 38 as direct. The phase travelling at about 3.5 km/s west of station 38 may be a direct wave through the Millstone Grit, while the first arrivals at these stations are probably refractions from the top of the Carboniferous limestone (as their reduced times are less than those for the upper basement refractions, and the basement to the Goyt Trough is not expected to be shallower than that under the limestone massif).

The same features are evident from the reduced time seismograms for the larger untimed Tunstead blast F12010a, also plotted in Fig. 5.26, except that for this event an early high velocity first arrival is apparent until station 27. If this arrival is from an inter-limestone dolomitic horizon, it is strange that it is poorly observed at station 30. This may indicate that such layers are not laterally continuous and that the arrivals at stations 29 to 27 originate from a similar but deeper horizon than those for stations 32 and 31 (numerous dolomitic horizons occurred at depth in the Eyam borehole, see Fig. 1.7). These high velocity arrivals are apparent from the reduced time graph for this event (Fig. 5.27), and also for the Sterndale shot F12030 (Figs. 5.26 and 5.27).

The later arrivals for the Tunstead shot F12010a denoted by the full line are possibly reflections off the upper

FIG 5-26

F12010A -- TUNSTEAD UNTIMED

F12015 -- TUNSTEAD POSITIONED

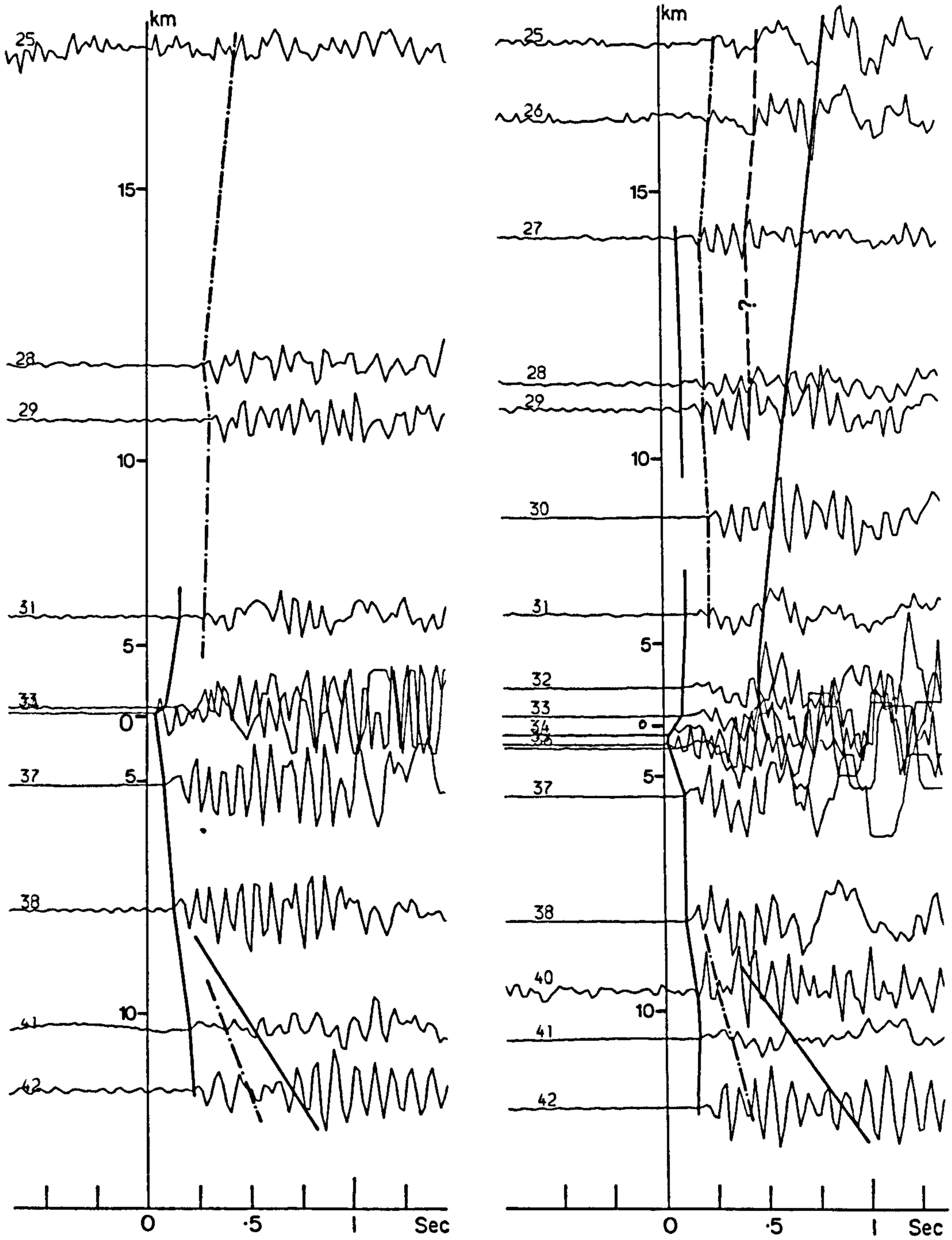

Reducing velocity 5·6km/s

direct wave & reflection

upper basement refraction

lower basement refraction

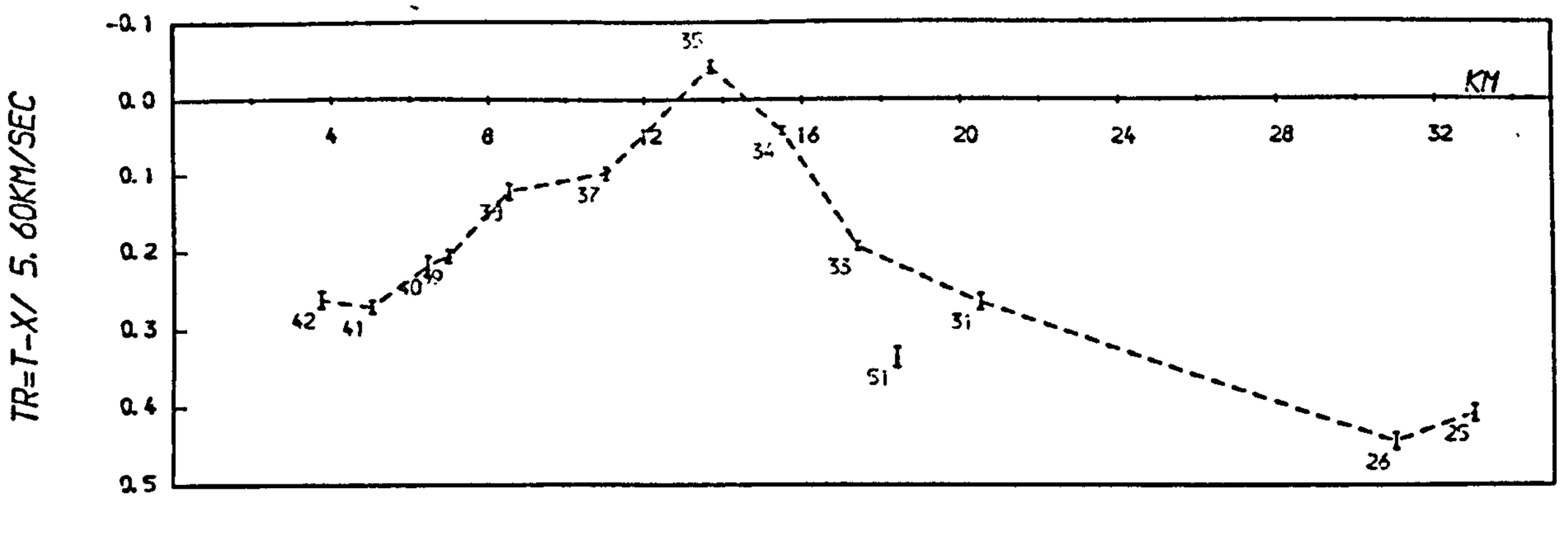

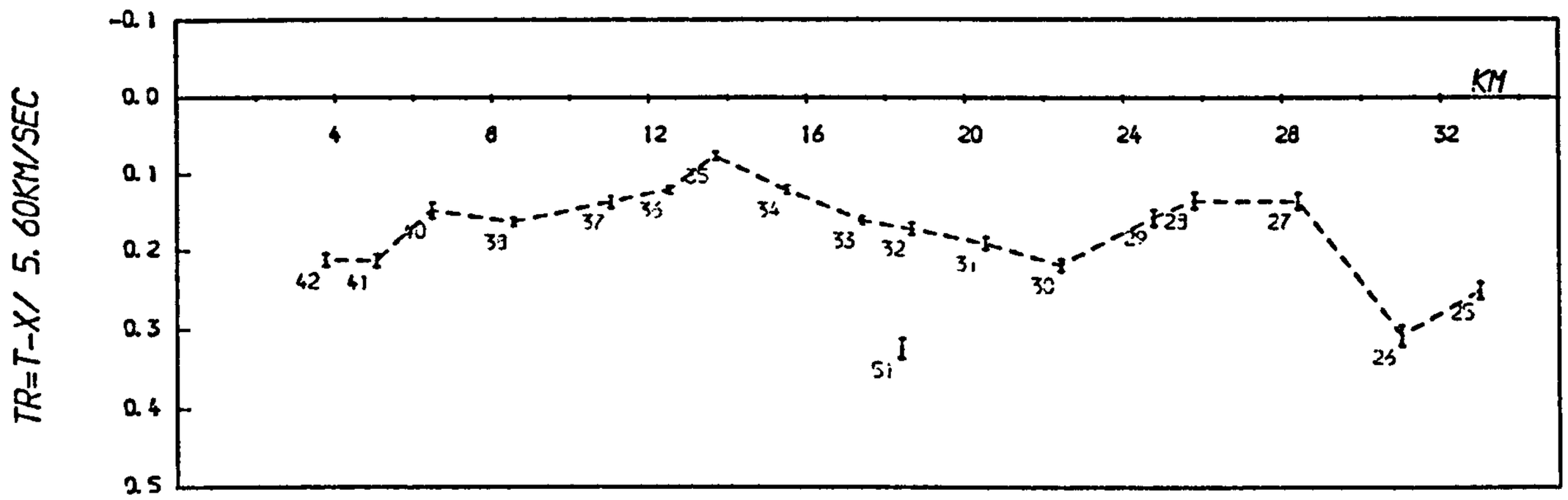

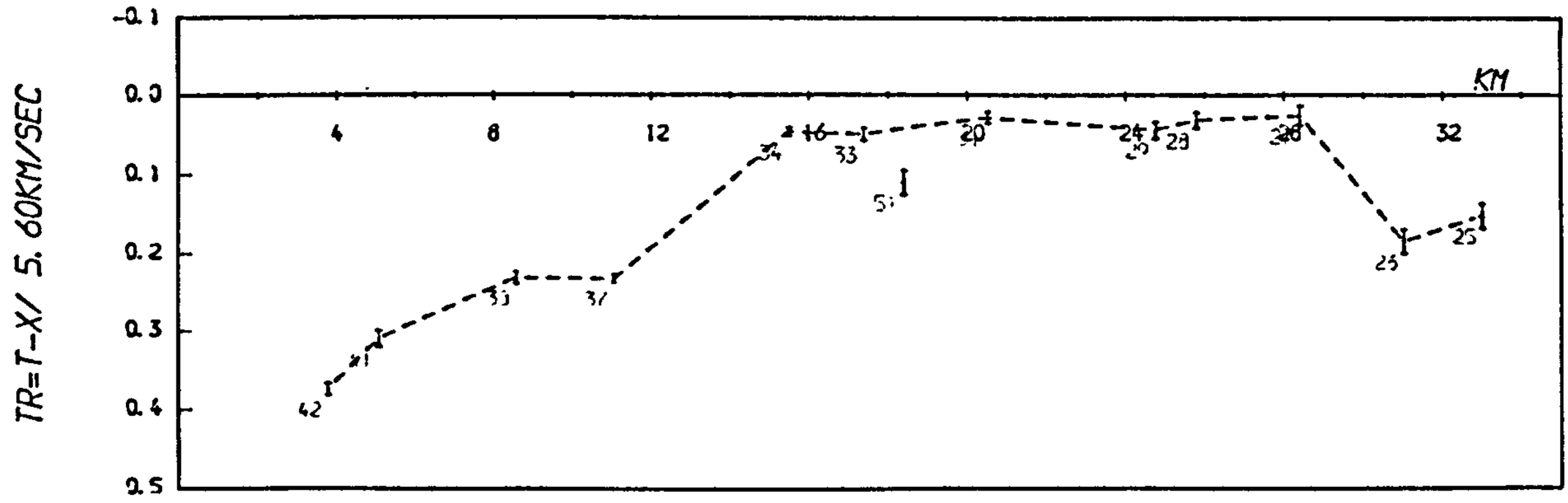

FIG 5-27 (a) Reduced time graphs

F12030 -- Sterndale untimed

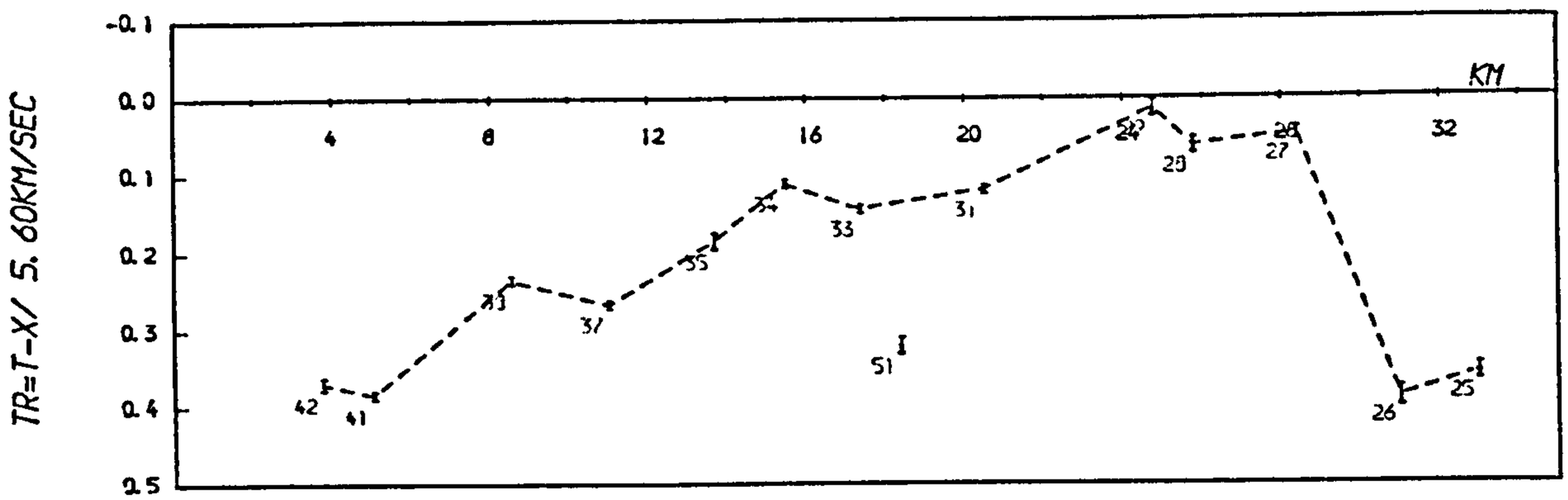

F12004 -- Brierlow untimed

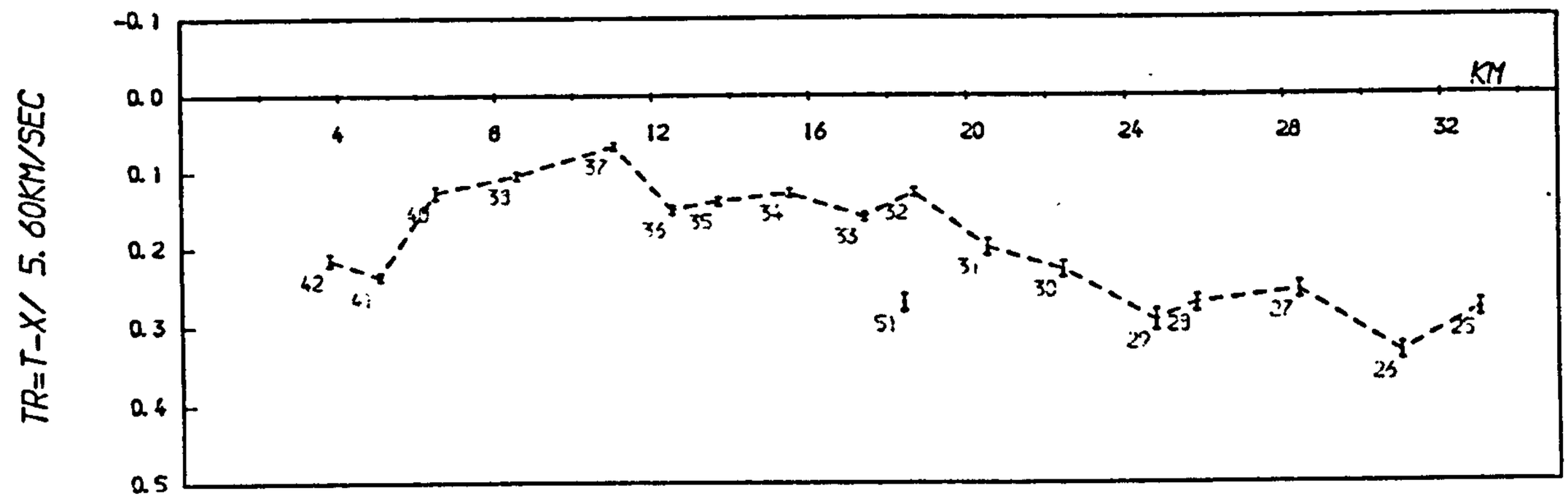

F12026 -- Waterswallows untimed

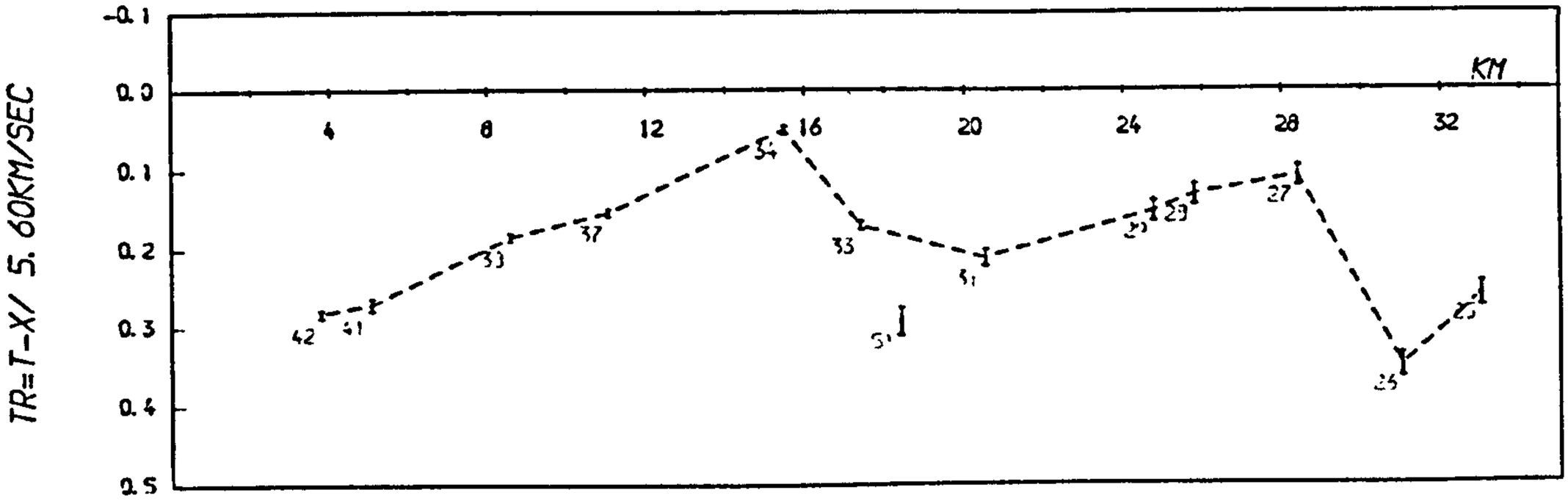

FIG 5-27(a) cont

F12028 -- Stoney Middleton untimed

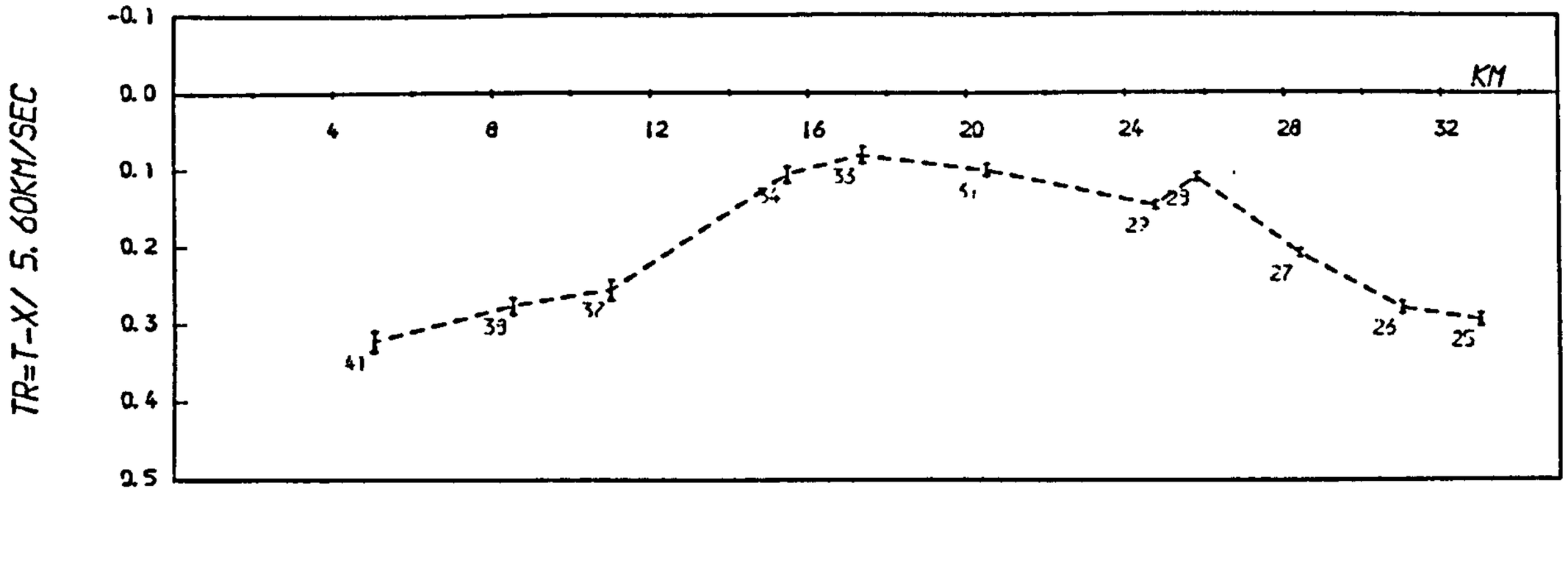

F11009 -- Smalldale untimed

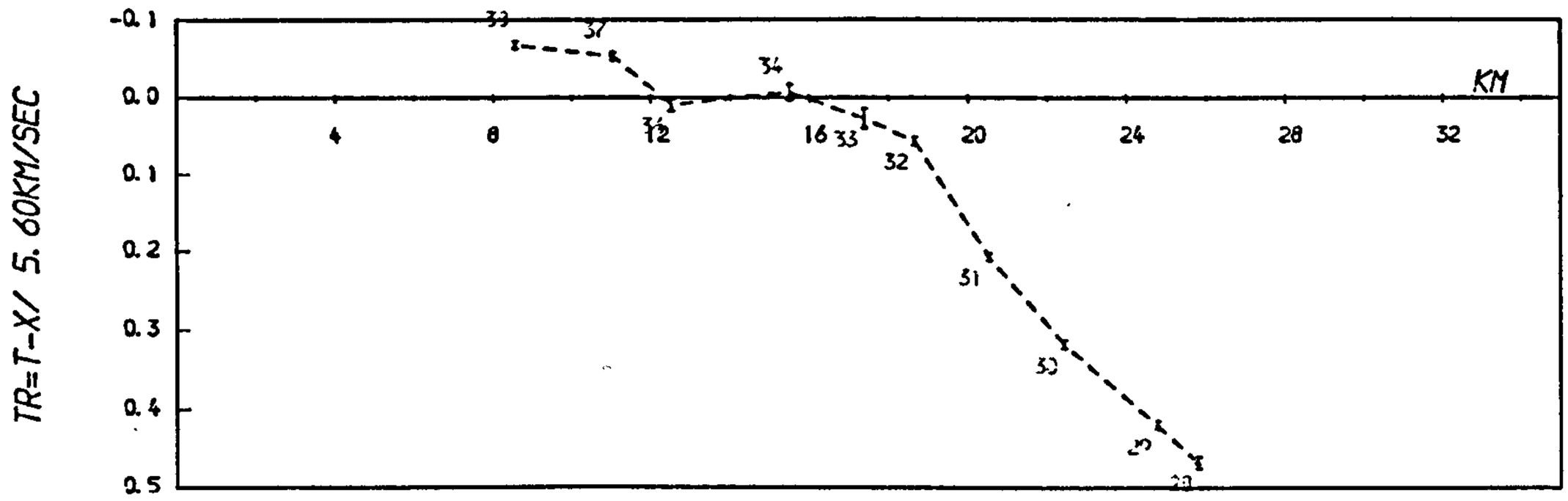

F12011 -- Hope Valley untimed

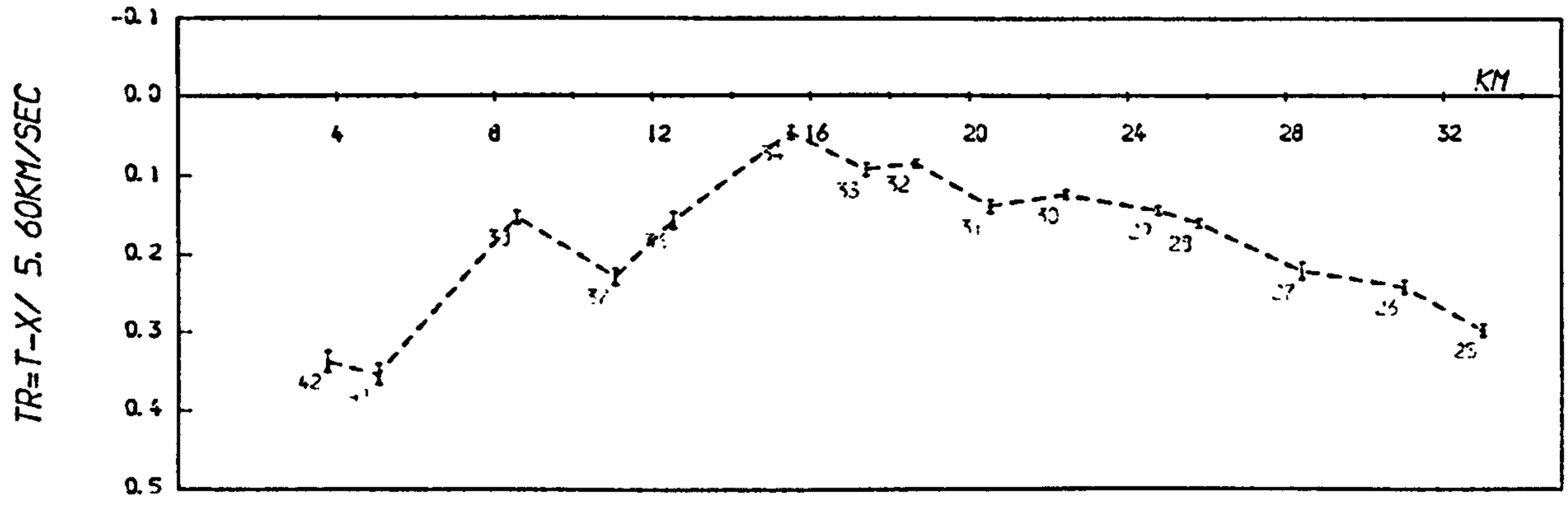

FIG 5-27(a) cont

FIG 5-27(a) cont

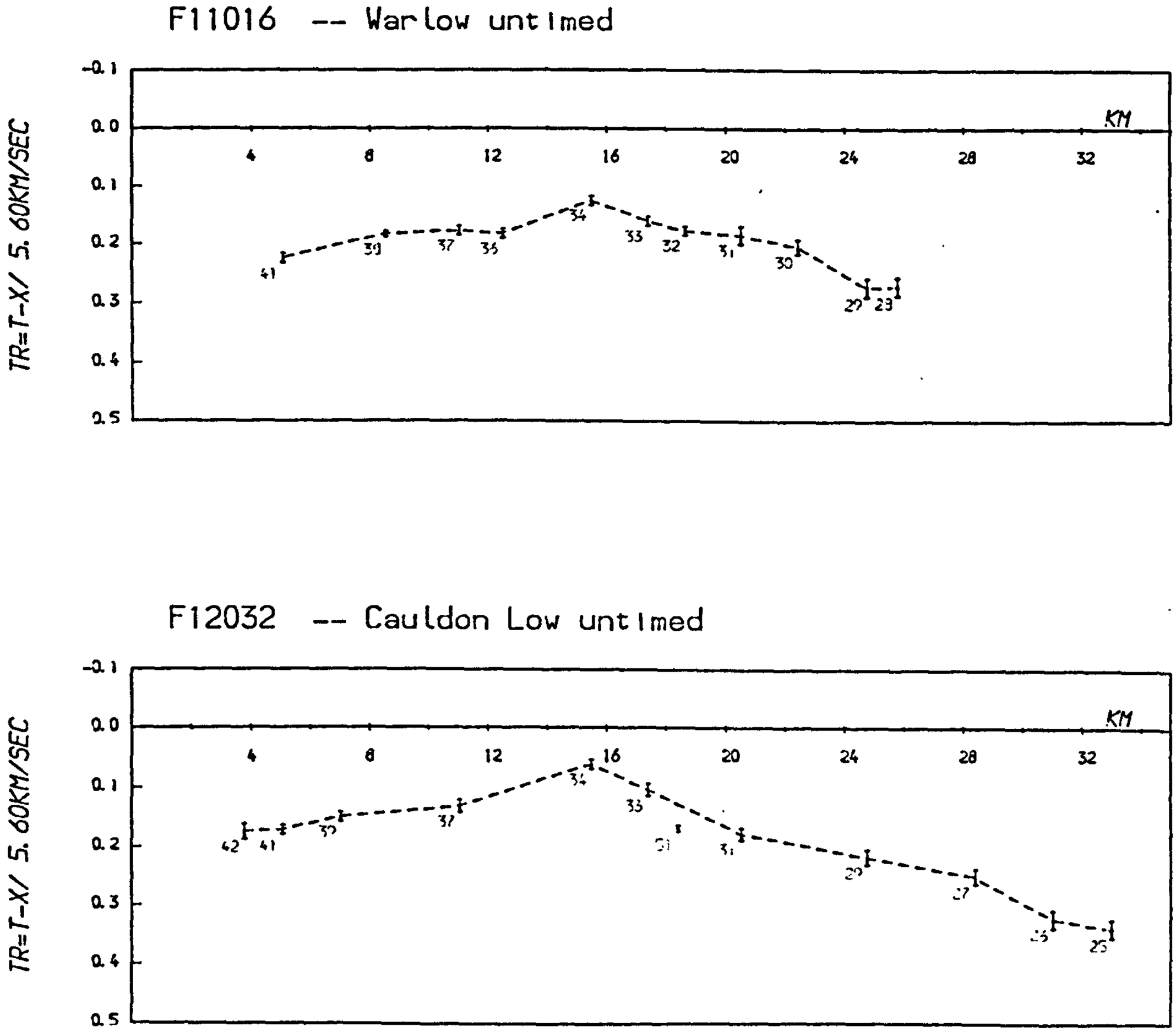

F13001A -- Tunstead untimed

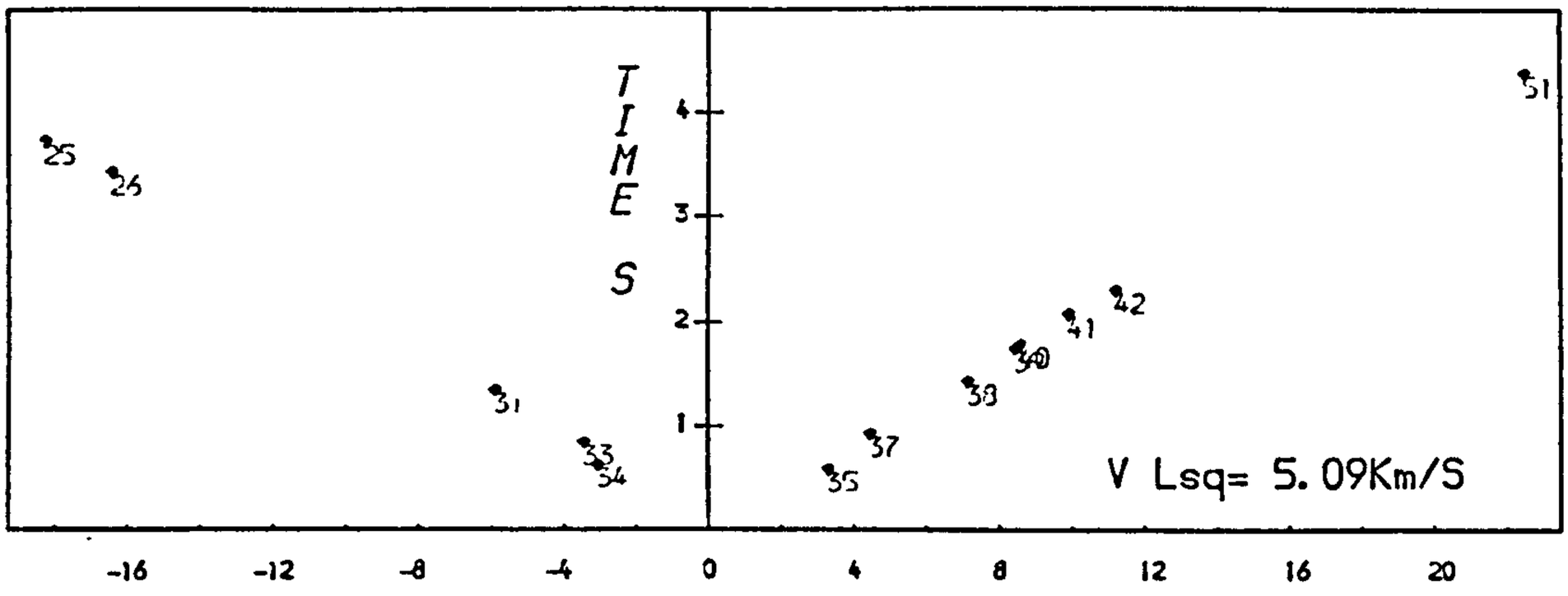

F12010A -- Tunstead untimed

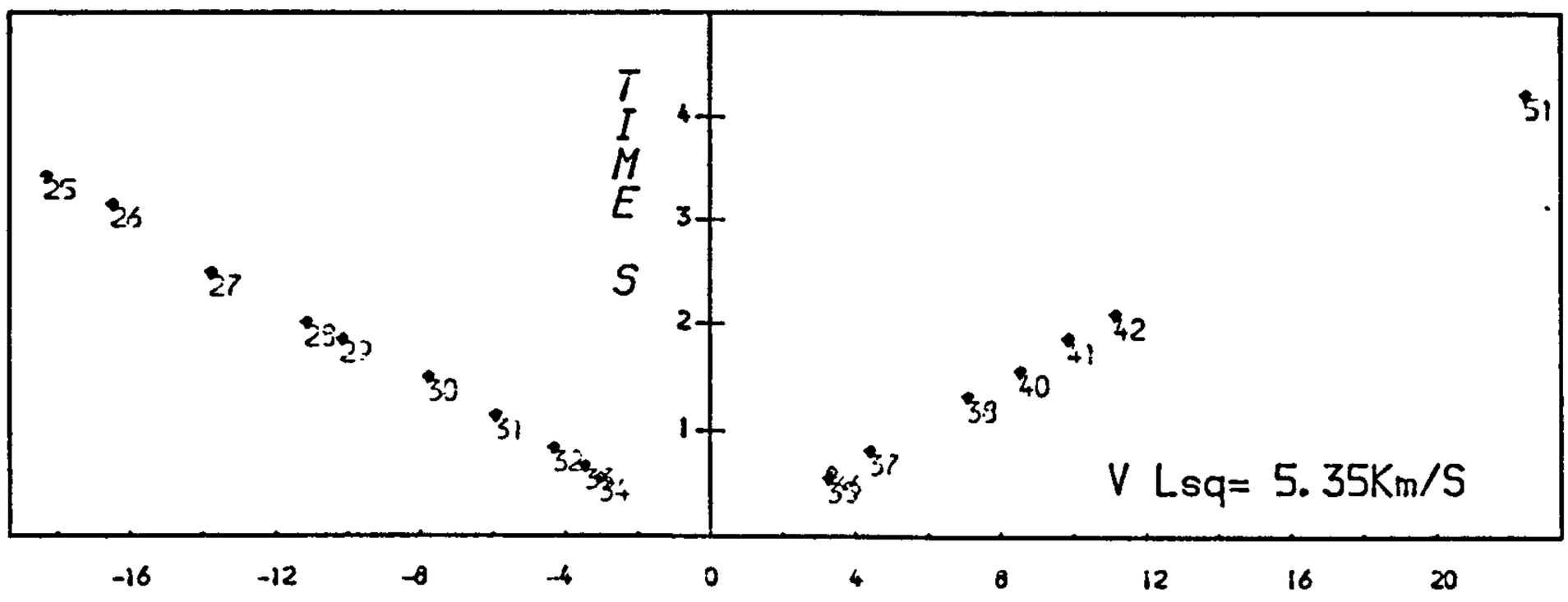

F12031 -- Doveholes untimed

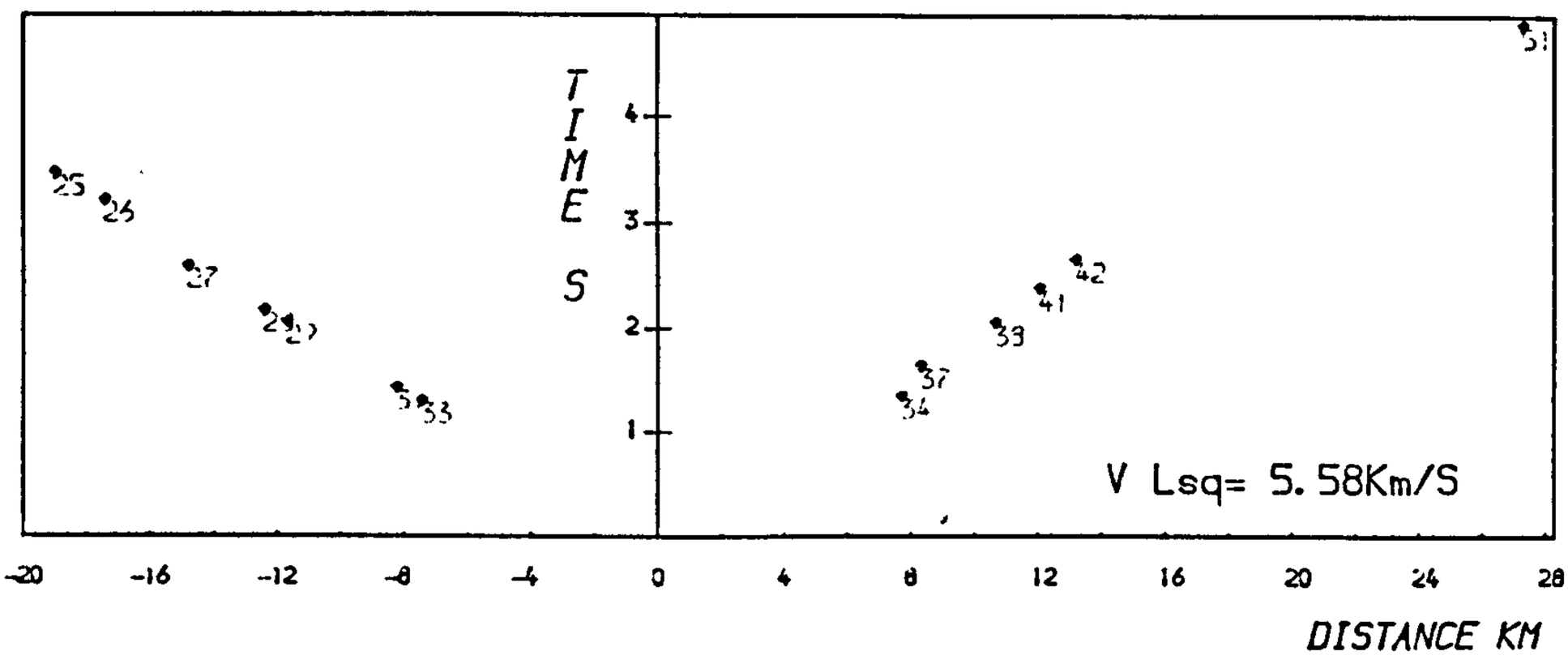

FIG 5-27 (b) T-X graphs

F12030 -- Sterndale untimed

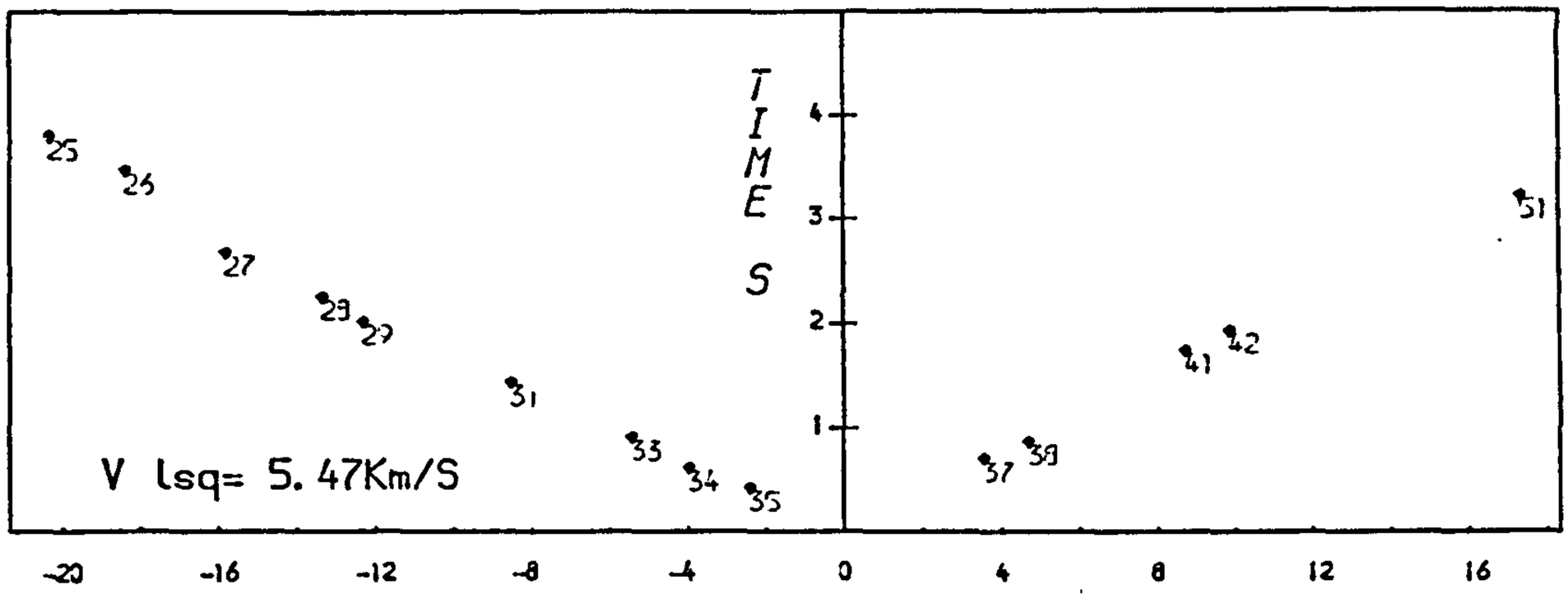

F12004 -- Brierlow untimed

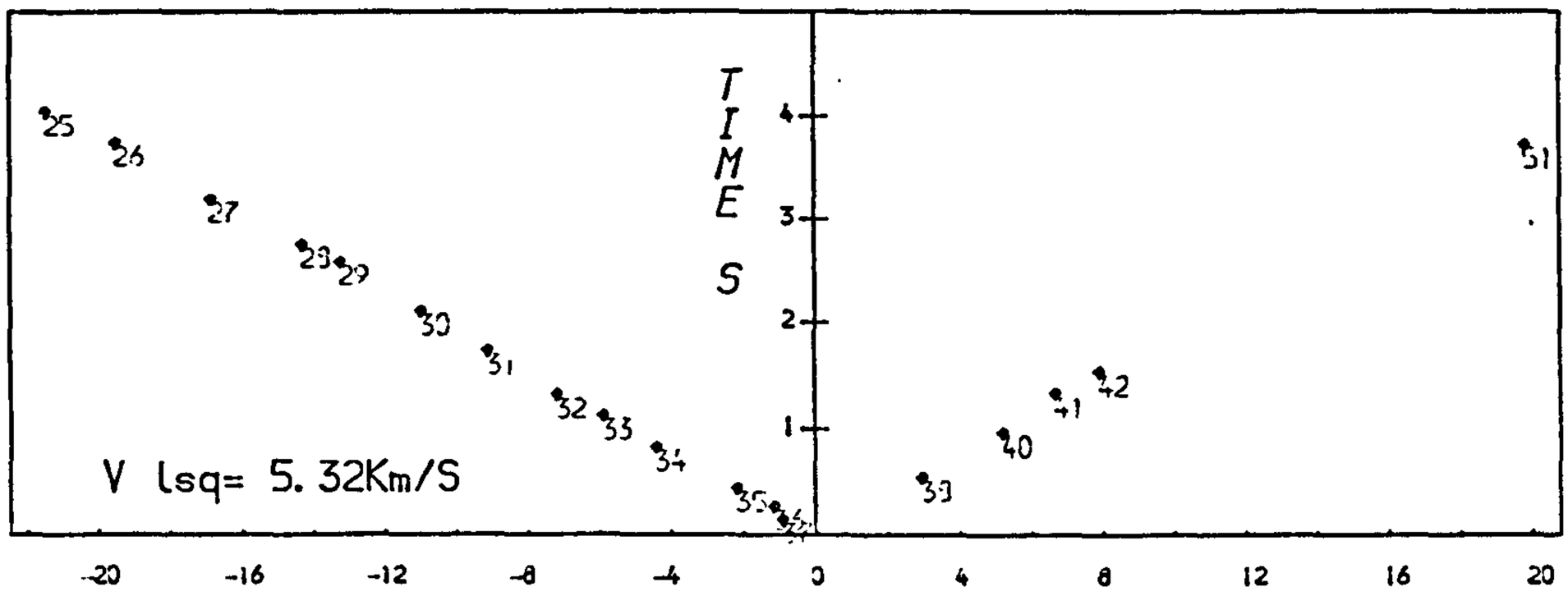

F12026 -- Waterswallows untimed

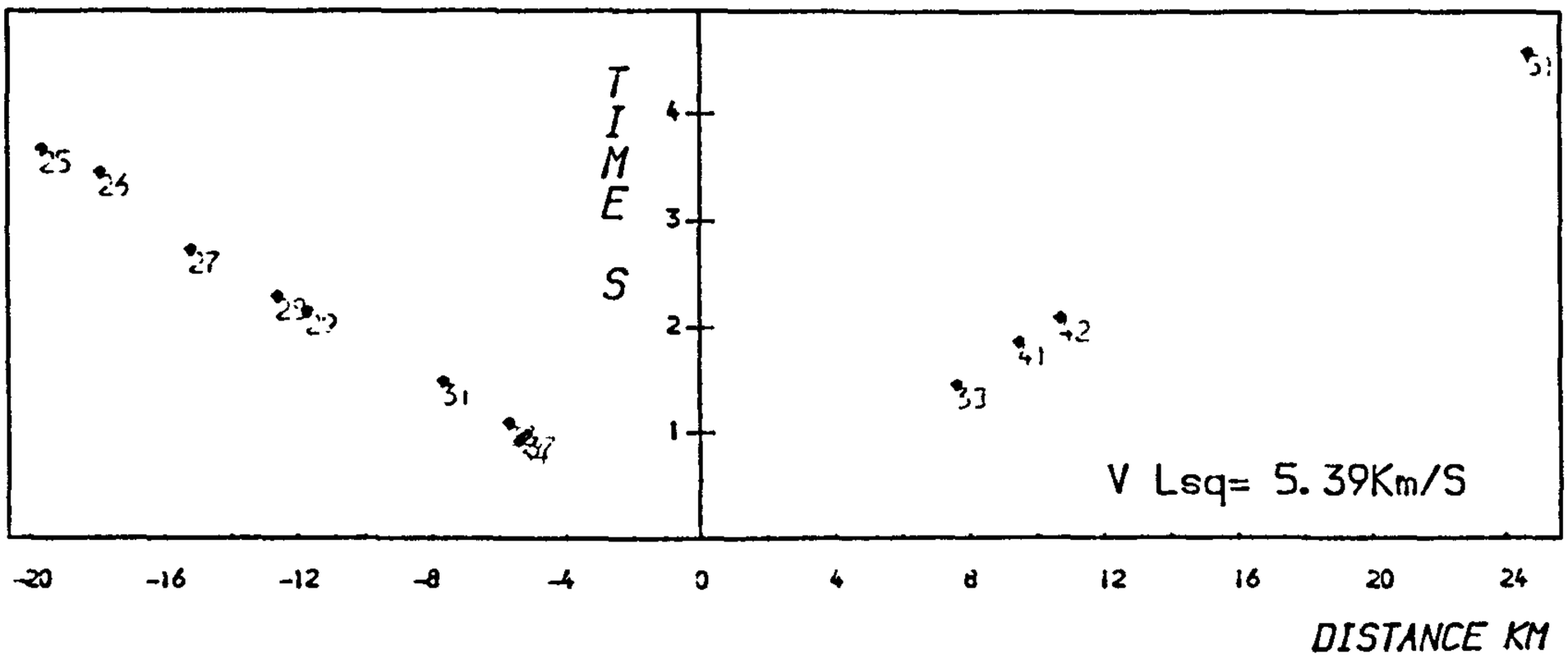

FIG 5-27(b) cont

F12028 -- Stoney Middleton untimed

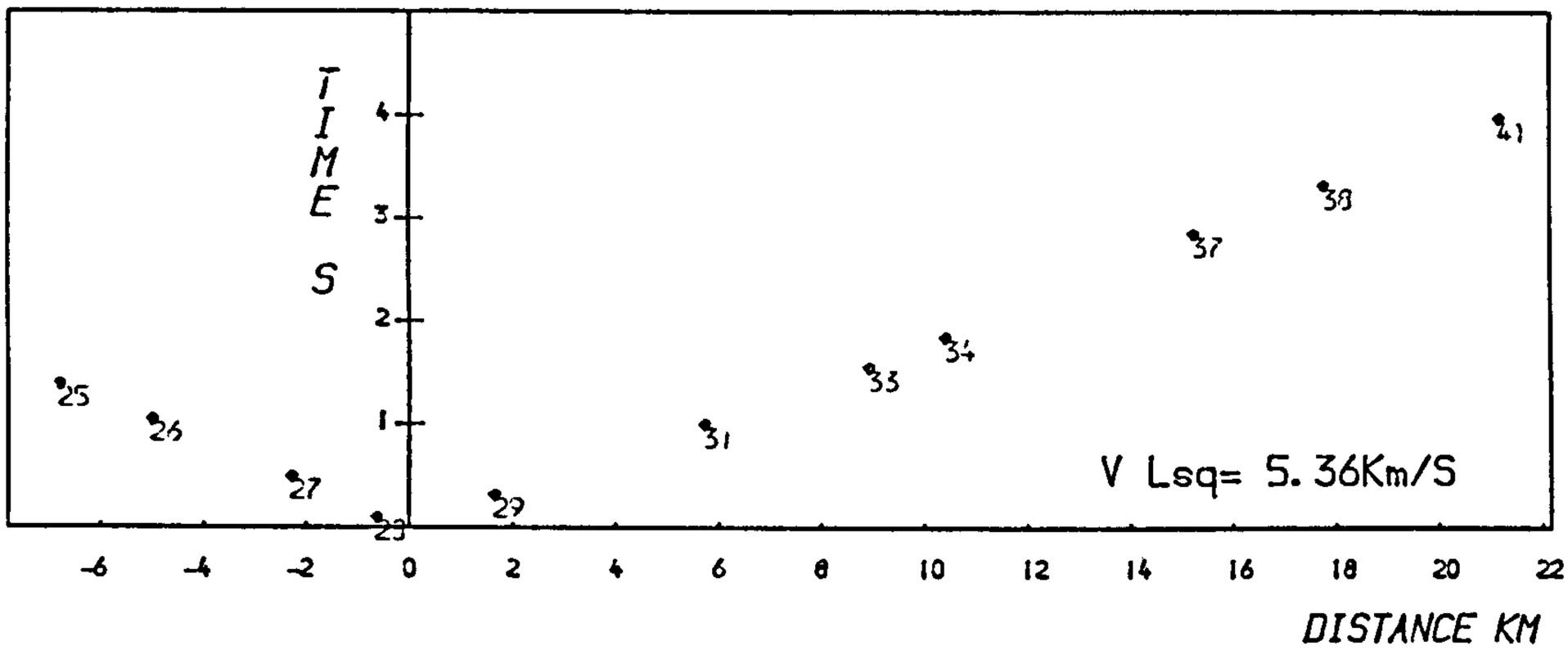

F11009 -- Smalldale untimed

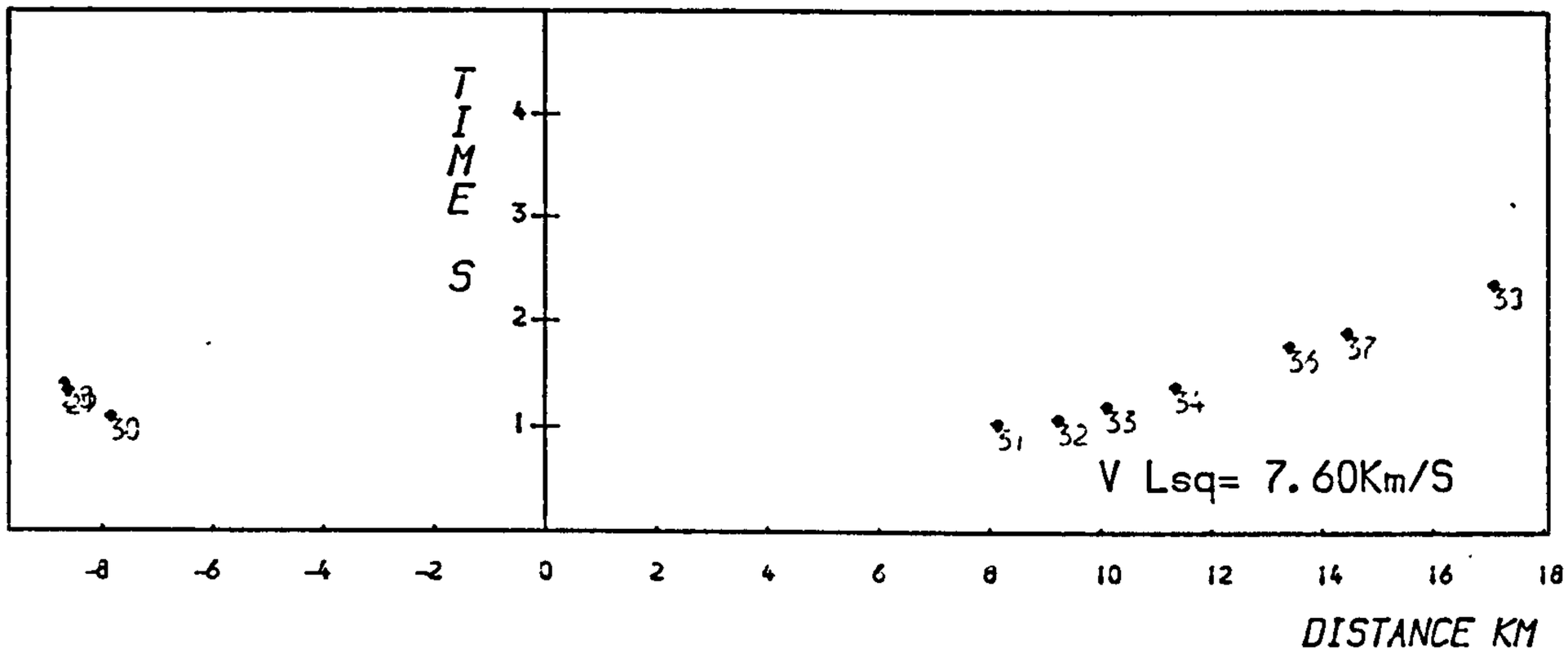

F12011 -- Hope Valley untimed

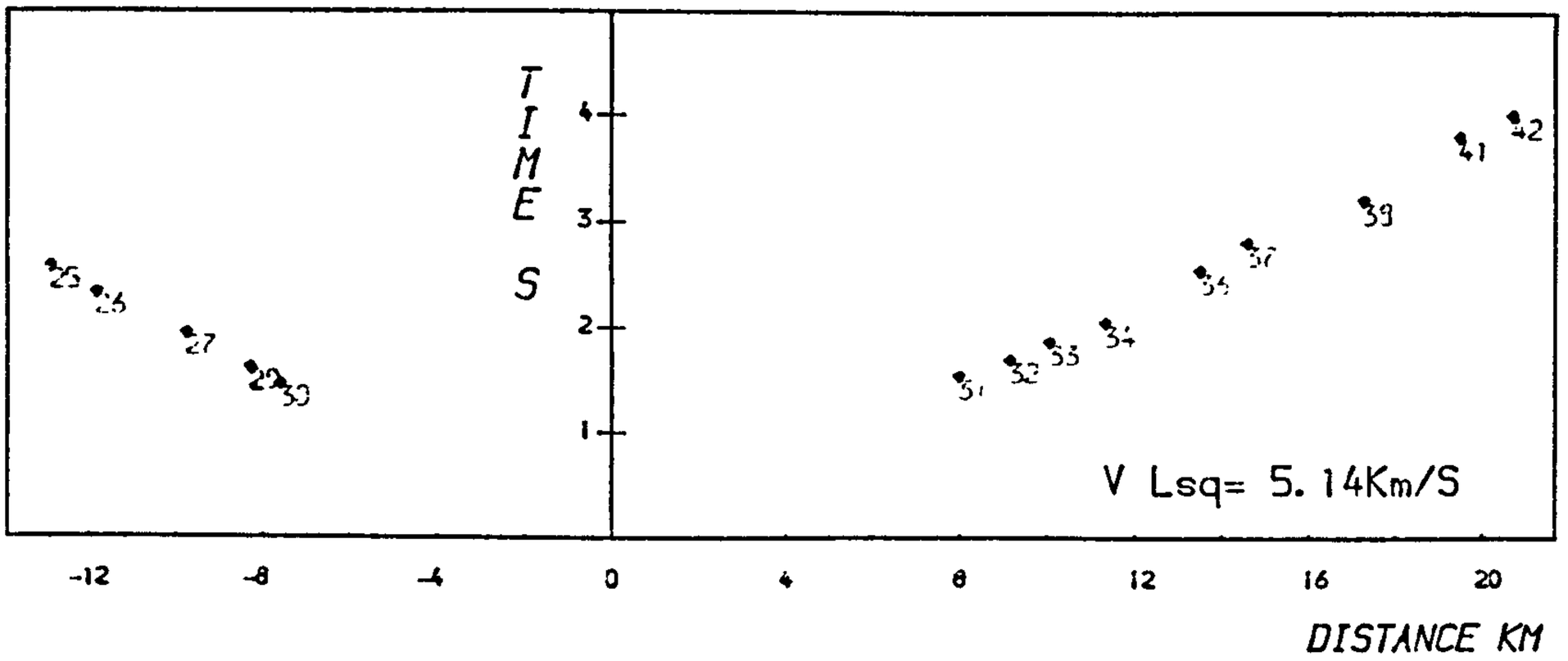

FIG 5-27 (b) cont

FIG 5-27(b) cont

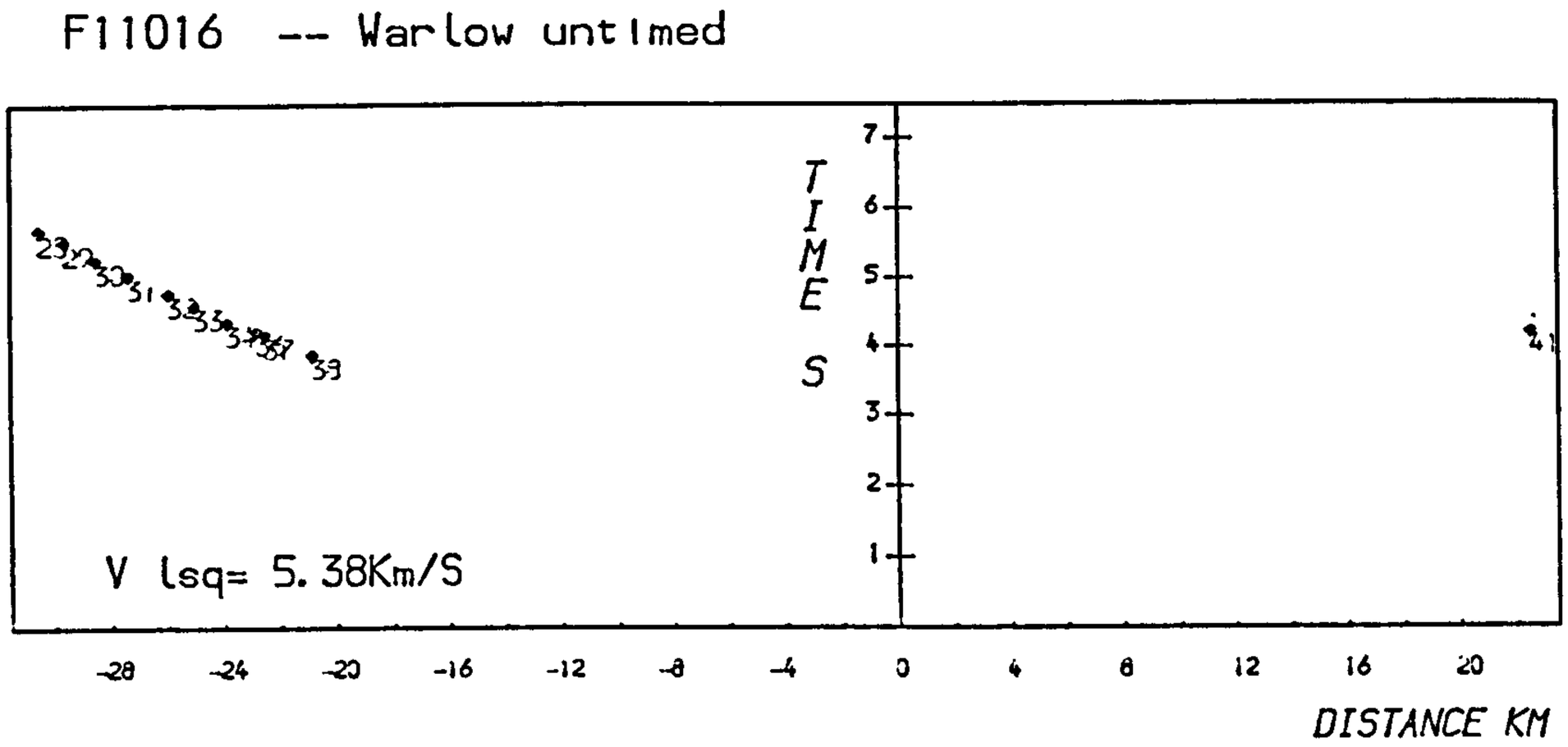

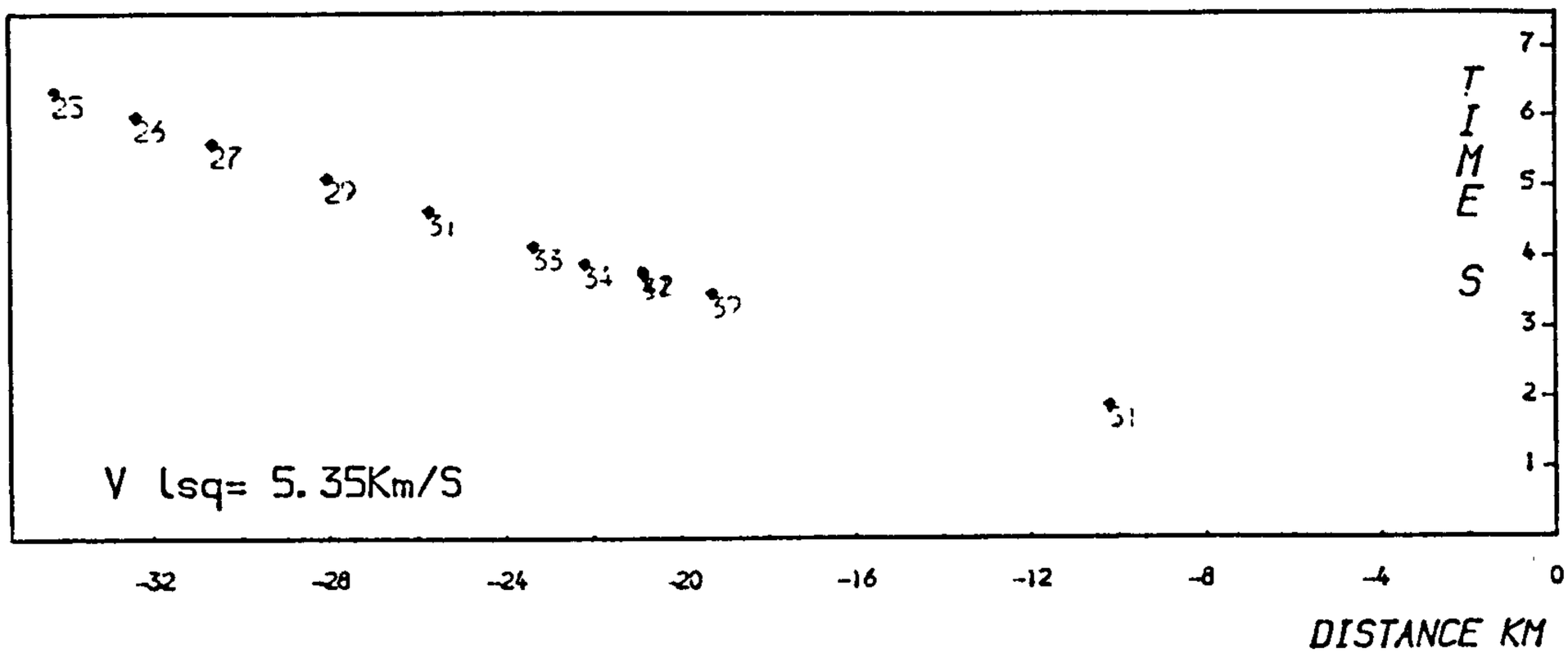

basement. If they can be correlated with the later arrivals seen in the P wave coda at stations 25 and 26, then the travel time curve suggests a mean overburden velocity of about 5.2 km/s. These wide-angle reflections must not be confused with the earlier large amplitude, lower frequency arrivals also seen in the coda (dashed line), which may be refractions from the lower basement.

ii) Northern Quarries

A selection of reduced time graphs and T-X plots for untimed blasts from northern quarries are given in Fig. 5.27. Except for those observations on the Millstone Grit, the T-X curves are as linear as those from the north-south line. Least-squares velocities for direct waves range from 5.2 to 5.8 km/s (for inter-limestone refractions), and 5.4 to 5.9 km/s for basement refractions, with no difference between eastward and westward shots. Direct wave velocities on the Millstone Grit vary between 4.6 and 4.9 km/s, but mainly these are down-dip velocities for refractions off the top of the limestone.

These reduced time graphs vary more between events from similar sources than those for the north-south profile, and consequently it is more difficult to discriminate against high velocity 'direct' waves from these plots alone. However, the same criteria for the discrimination of basement refractions discussed in Section 5.3.2 still apply, and the inter-limestone refractions are invariably higher frequency and lower amplitude than those from the sub-Carboniferous horizons. For example Fig. 5.28 illustrates the relative amplitudes for several Tunstead blasts, from which upper basement arrivals are commonly picked as first breaks east of station 31, and west of 39 (although the lnA-X relationship west of Tunstead is complicated by the anomalously high relative amplitudes between stations 35 and 39).

Interpreted refractions for quarry blasts from (a) Tunstead and Topley Pike, (b) Doveholes and Waterswallows, and (c) Dow Low, Brierlow and Sterndale have been plotted in

FIG 5-28 Relative amplitudes — various Tunstead blasts

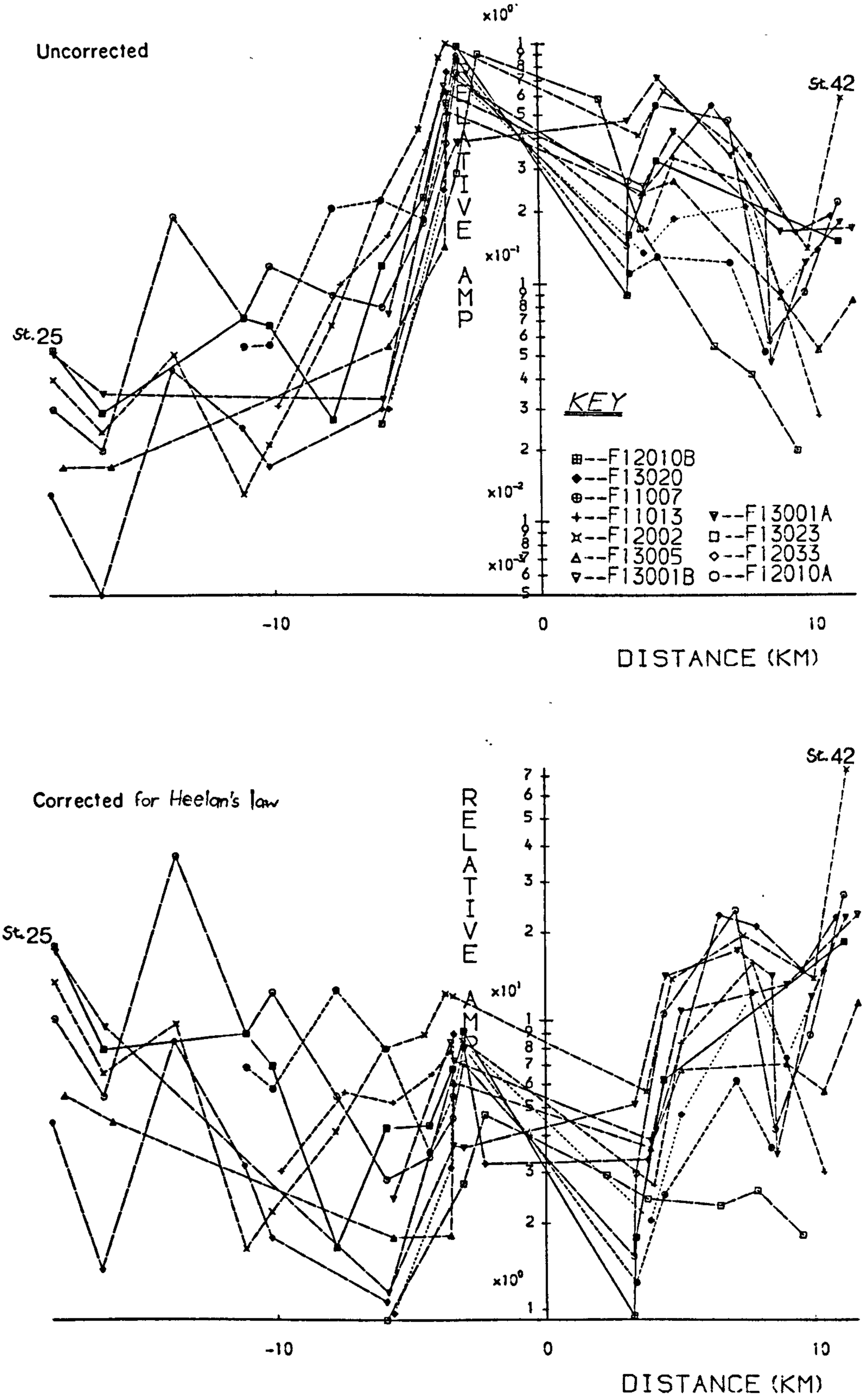

Fig. 5.29 in the same manner as Fig. 5.12. Both Tunstead and Dow Low accord with a refractor dipping eastwards of station 34, such that the reduced time for station 28 is greater by about 0.1s. This corresponds to an increase in depth of 1.4 km by inserting the delay, a, into $V_o.a/\cos\theta_c$ for V_o, V_r of 5.2, 5.6 km/s. The deepening sub-Carboniferous surface off the limestone outcrop is also manifest by these data, yet for the Doveholes events (Fig. 5.29b) the reduced times are greater for stations in the Goyt Trough region. However, as noted for the timed event F13015 (Fig. 5.25), it is possible that the first arrivals to the west of station 36 are from the lower basement refractor. The larger reduced times to the east of the profile may also correspond to lower basement refractions picked where upper basement arrivals were not well recorded.

Shots collinear with the line from Dow Low, Brierlow and Stoney Middleton quarries are plotted as reduced time seismograms in Fig. 5.30, where direct waves are denoted by the full line, upper basement refractions by the dotted dashed line, and interpreted lower basement refractions by the dashed line. Like the Tunstead events (Fig. 5.26), broadening of the P waves for stations 25, 26 and 38 to 42 is apparent, and probably indicates an increased attenuation of high frequencies by the cover of more absorptive Millstone Grit (assuming, that is, there is no facies change in the limestones off the massif).

Lower basement refractions can only be easily identified for eastern shots at stations west of about station 33, that is greater than around 12 km from the shot. This may correspond to the critical distance for refractions from the lower basement refractor. These arrivals are typically of lower frequency and higher amplitude than those from the upper basement refractor, and the delay between these two arrivals seems to lessen towards stations 37 and 38. For western quarries, lower basement refractions are observed east from about station 29 (e.g., Tunstead F12010, Fig. 5.26), although they can only be confidently identified east of station 28.

FIG 5-29

V_{red} = 5·6km/s

(a) Tunstead & Topley Pike

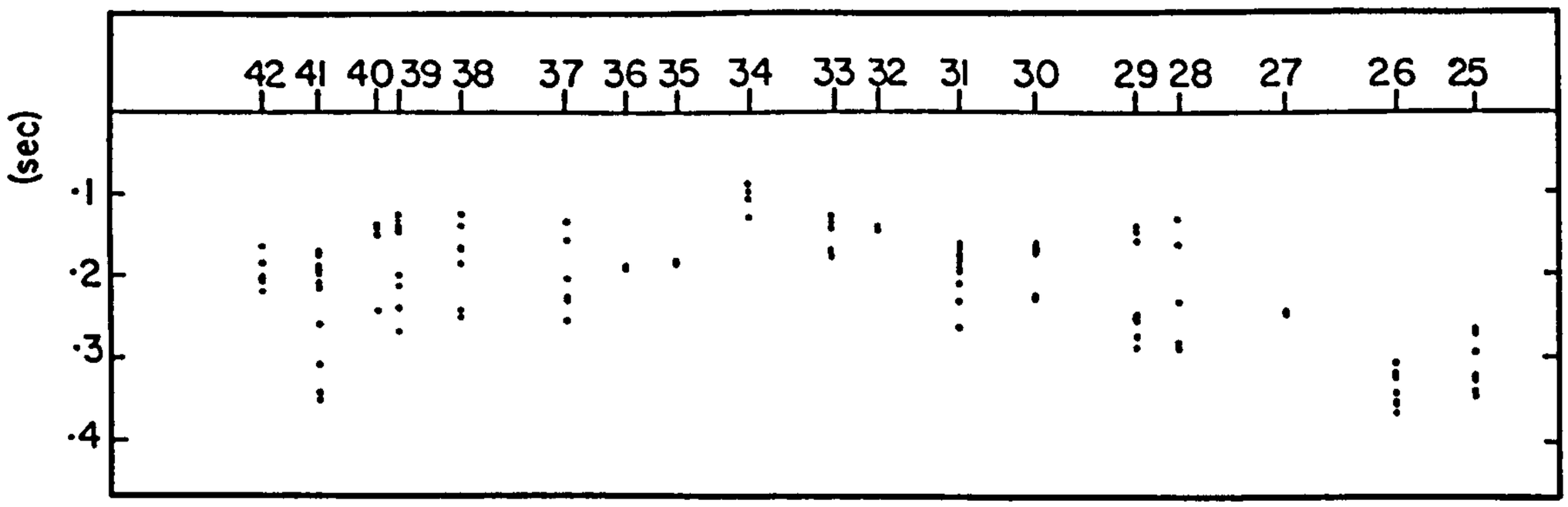

(b) Doveholes & Waterswallows

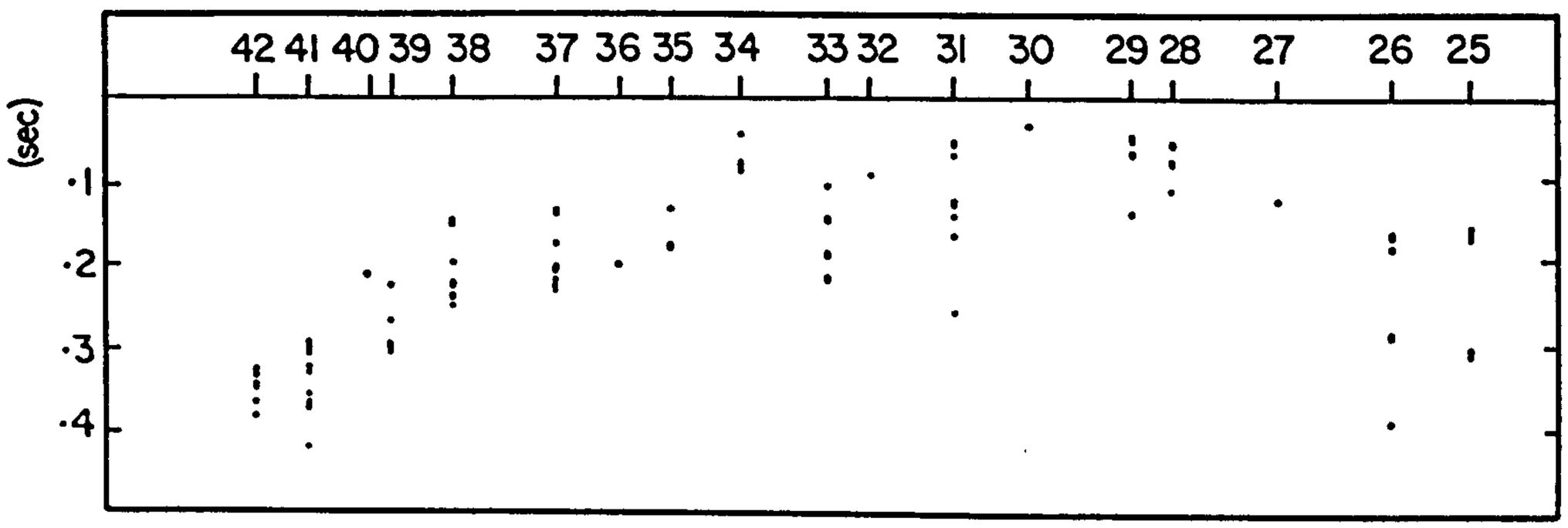

(c) Dow Low group

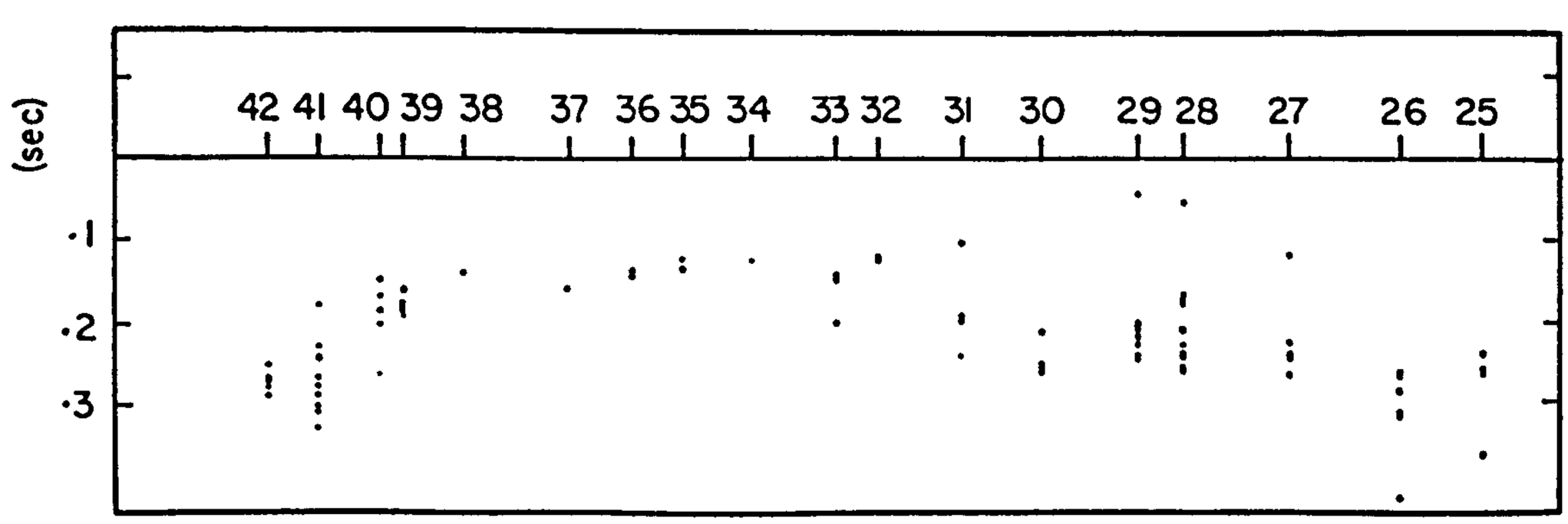

F12018 -- DOW LOW UNTIMED

F12004 -- BRIERLOW UNTIMED

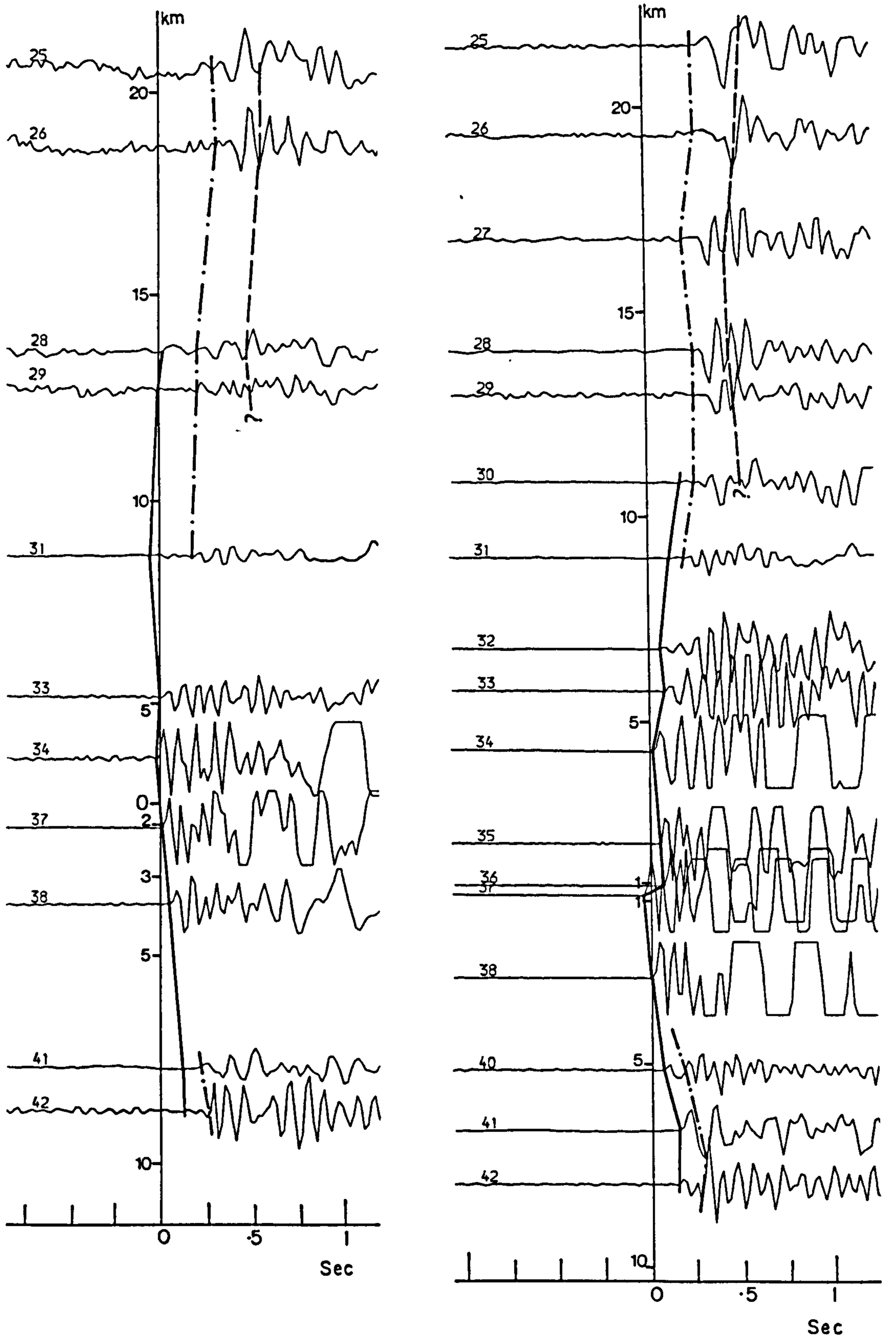

FIG 5-30 Key see FIG 5-26 (Vr=5·6km/s)

F12028 -- STONEY MIDDLETON

UNTIMED

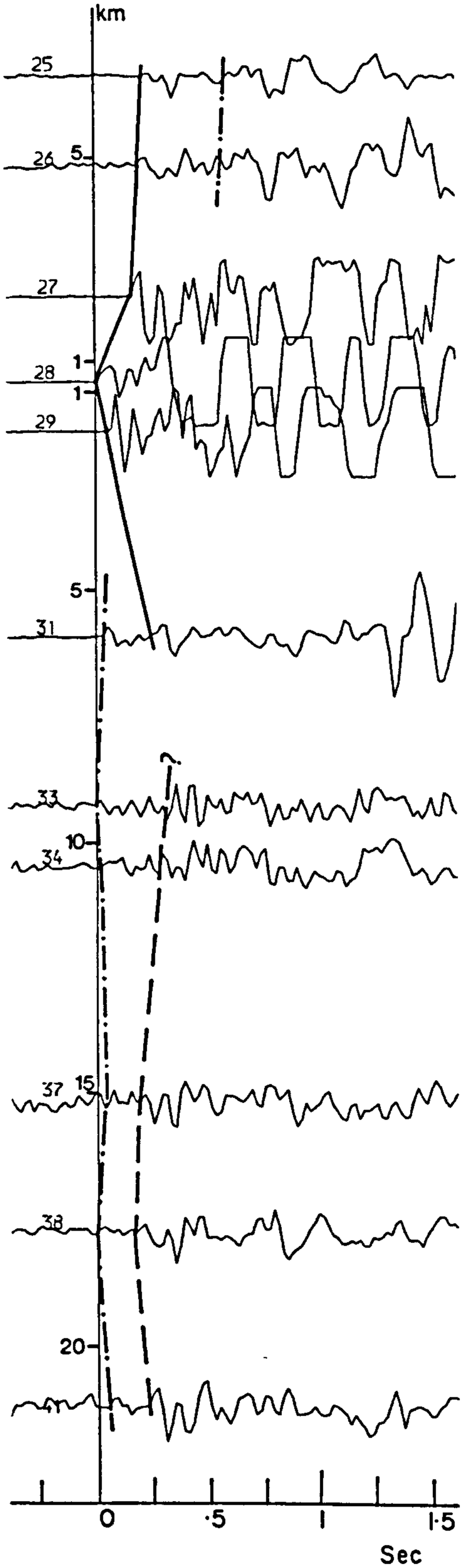

F12011 -- HOPE VALLEY

UNTIMED

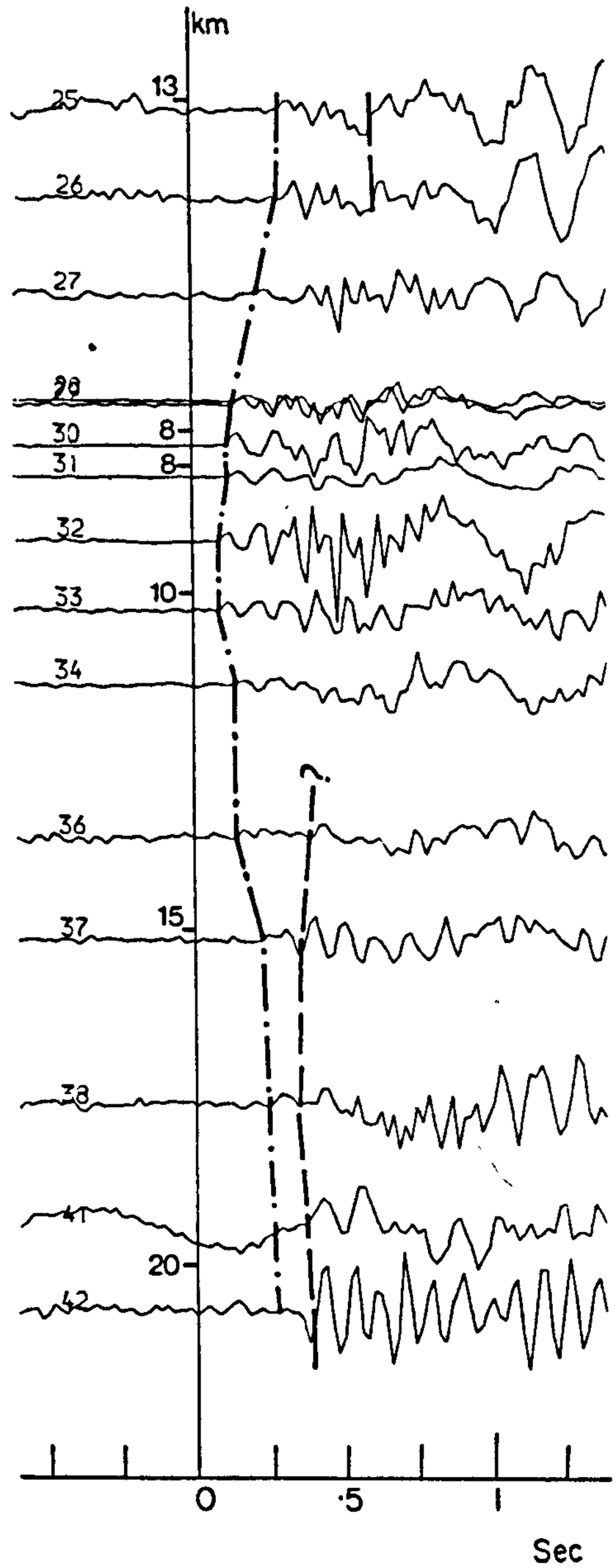

FIG 5-30 cont.

FIG 5-30 cont

F11009 -- SMALLDALE UNTIMED

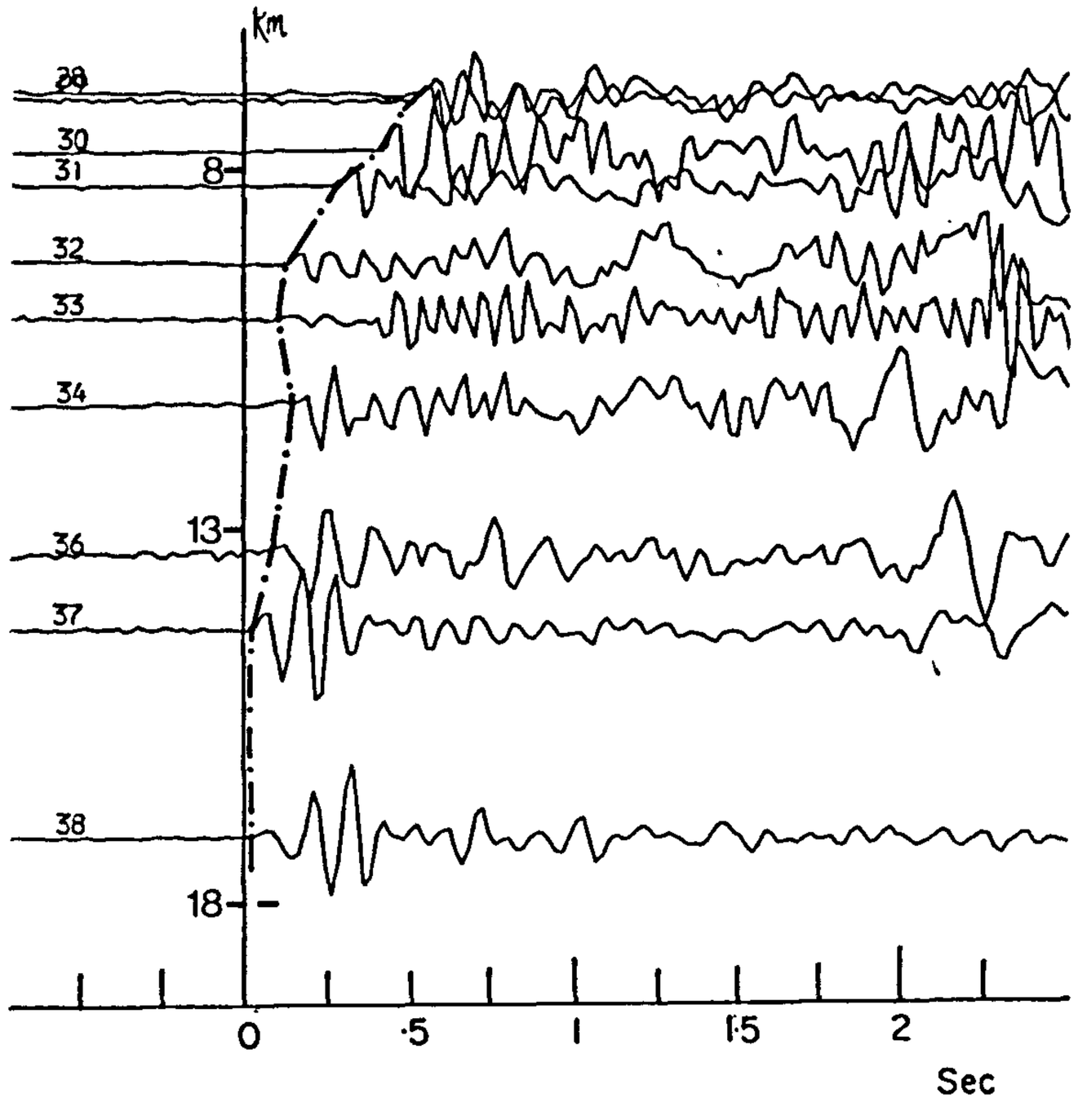

F12032 -- CAULDON UNTIMED

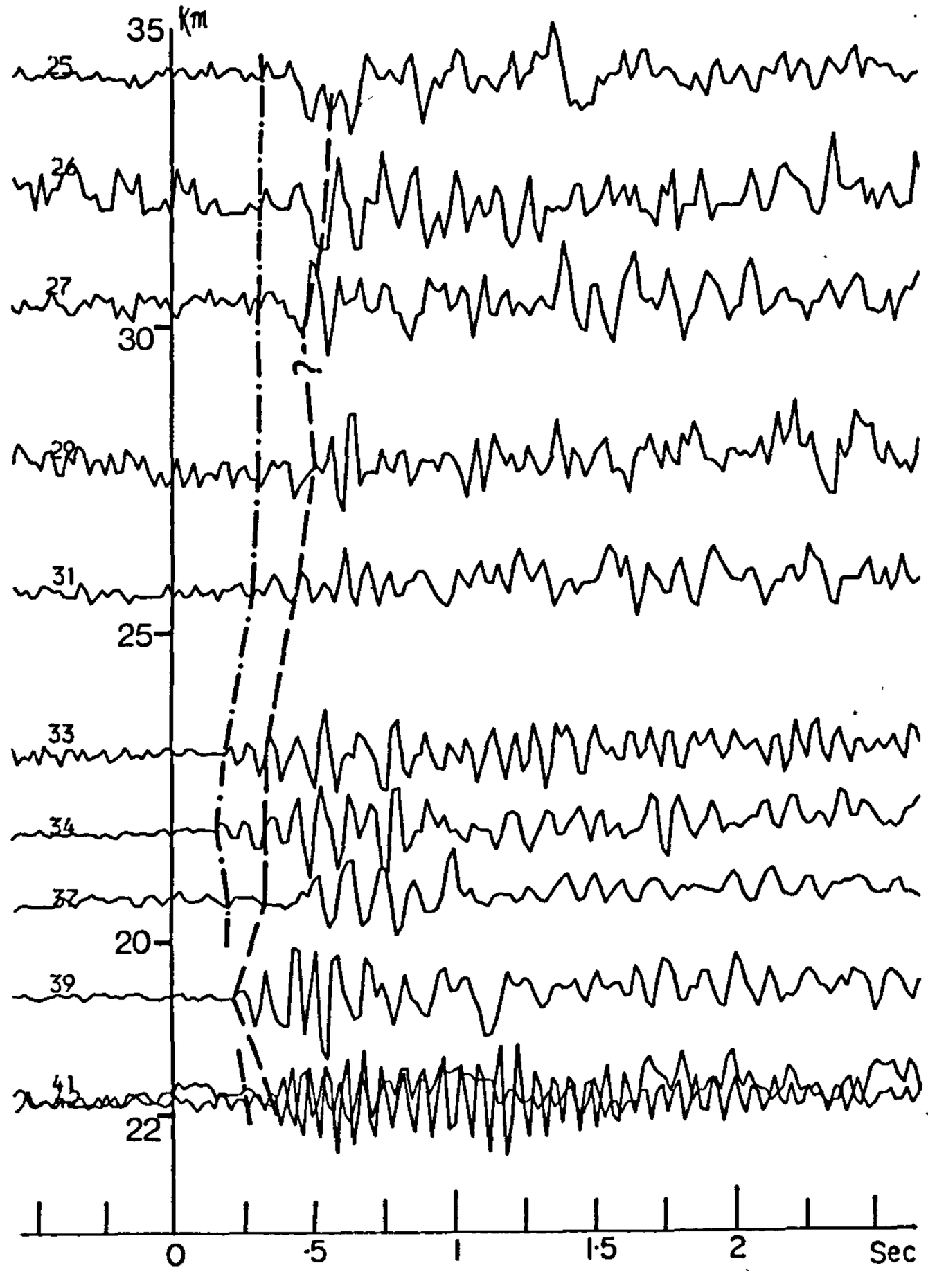

Broadside quarry blasts from the north such as Hope Valley, Smalldale and Eldon Hill (see Fig. 3.7) often manifest eccentric reduced time graphs such as F11009 (Smalldale) which cannot be resolved through picking error or mislocation of the source. The nature of the first arrivals at stations 34 to 38 (Fig. 5.30) suggest they may be from the lower basement, and that those at stations 32 and 33 from the upper basement refractor. The event contrasts with F12011 (Hope Valley), whose reduced time graph (see Fig. 5.27) is similar to those for events closer to the line. The reduced time seismograms for F12011 (Fig. 5.30) show higher frequency first arrivals consistent with an upper basement refractor origin, while west of station 34 broader later arrivals can be identified, interpreted as from the lower basement refractor.

iii) Cauldon Events

Apart from the timed events, only two shots from the southern province have been considered, both from Cauldon Low. All the first arrivals appear to come from the upper basement refractor, for which the reduced time graphs (Fig. 5.26) accord with the sub-Carboniferous surface suggested by the on-line events. Later arrivals interpreted as lower basement refractions can be traced along the entire line, although only with difficulty east of station 31 as the signal is close to the ambient noise level (Fig. 12032, Fig. 5.30).

5.5.2 Summary of Interpretation

Fig. 5.31 sketches the interpretation of these data. It is evident that the base of the Carboniferous between Woo Dale and Eyam is not smoothly dipping, but that there is an increase in slope roughly between stations 32 and 30. On the Bouguer anomaly map (Fig. 1.12) this corresponds to a belt of closer spaced contours, but the feature is not obvious from either the geological section (Fig. 3.10), or the surface suggested by the high velocity inter-limestone refractions, which probably originate from a much shallower horizon (e.g.,

the Woo Dale Dolomite, the Upper Millers Dale lava, etc.).

A similar three-layer interpretation of the deep geology along the NEW profile using gravity data has been received from R. Barker (University of Birmingham, pers. comm.). There is less seismic information on the lower basement refractor but the evidence suggests a general shallowing towards stations 37-38, which co-incides with the hinge region of the massif: marked by scattered Holkerian inliers and the high on the Bouguer anomaly map (Fig. 1.12). This region also co-incides with where the Bonsall Fault splits into several smaller faults, and where the strike of which turns towards the north (Fig. 1.9).

(Note that the northern profile was dog-legged between stations 39 and 40, such that any continuity of the time section here may be deceptive.)

5.5.3 DASED2

A representative selection of reduced time graphs for this line are given in Fig. 5.32. As the two 1981 profiles were principally designed to use blasts from Tunstead quarry (McDonald 1982), most data comprises events from the quarries around Buxton, although sufficient events from Shining Bank, Ballidon, etc. have been considered to give adequate reversal.

Like the NEW profile, all refractions observed as first arrivals can be interpreted either as from the upper basement, or refractions from layers within the limestone sequence. Few later arrivals have been identified as lower basement refractions for this line because a) only stations at the ends are outside the critical distance from shots close to the line, and b) quarry blasts from the southern province were not of good enough quality for later arrivals to be confidently picked.

Least-squares velocities along the profile are typical of most observations on the limestone massif, although the direct waves are slightly slower (5.1 — 5.5 km/s) as the line

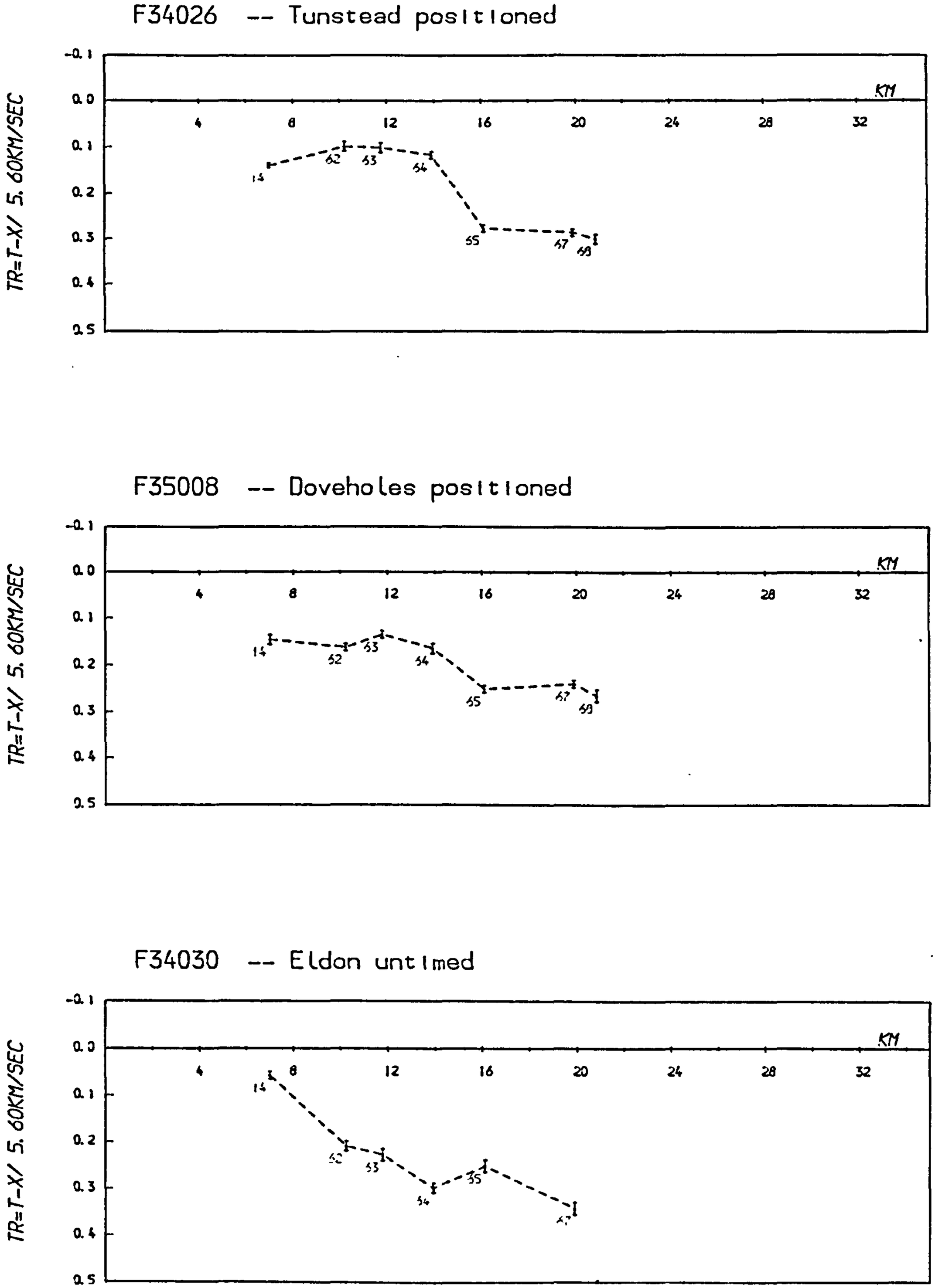

FIG 5-32 Reduced times

F33025 -- Dow Low untimed

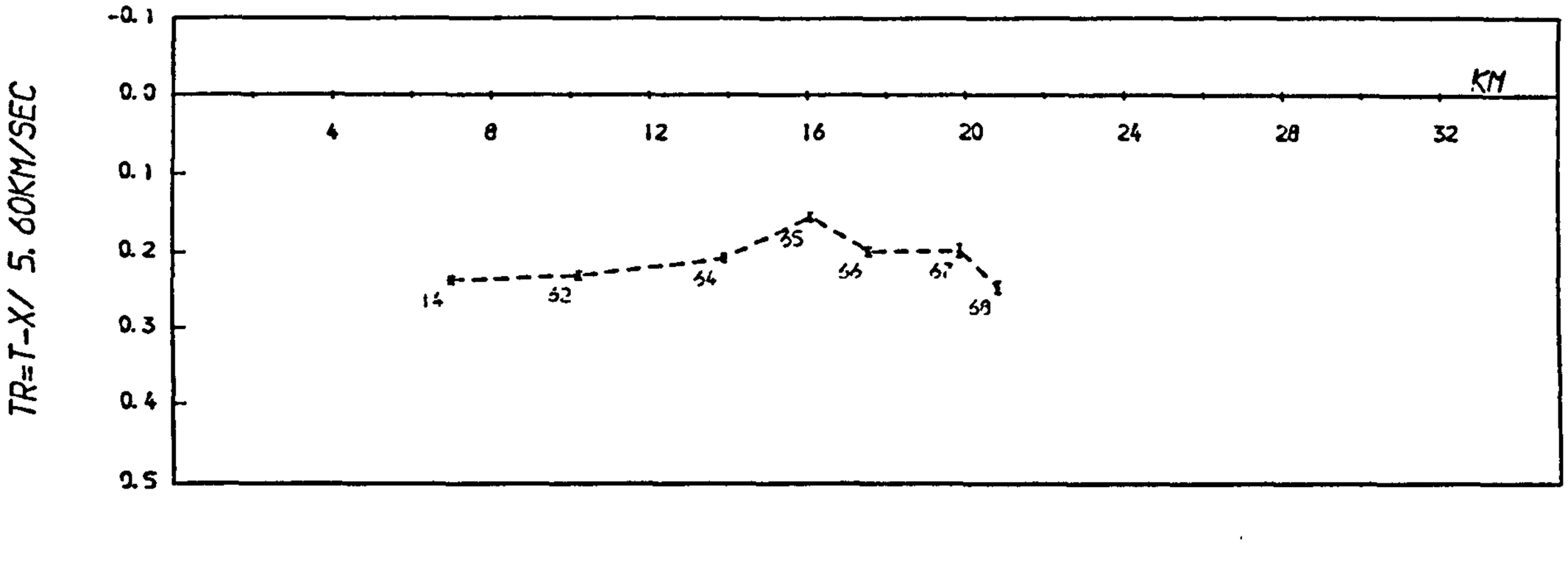

F33030 -- Brierlow untimed

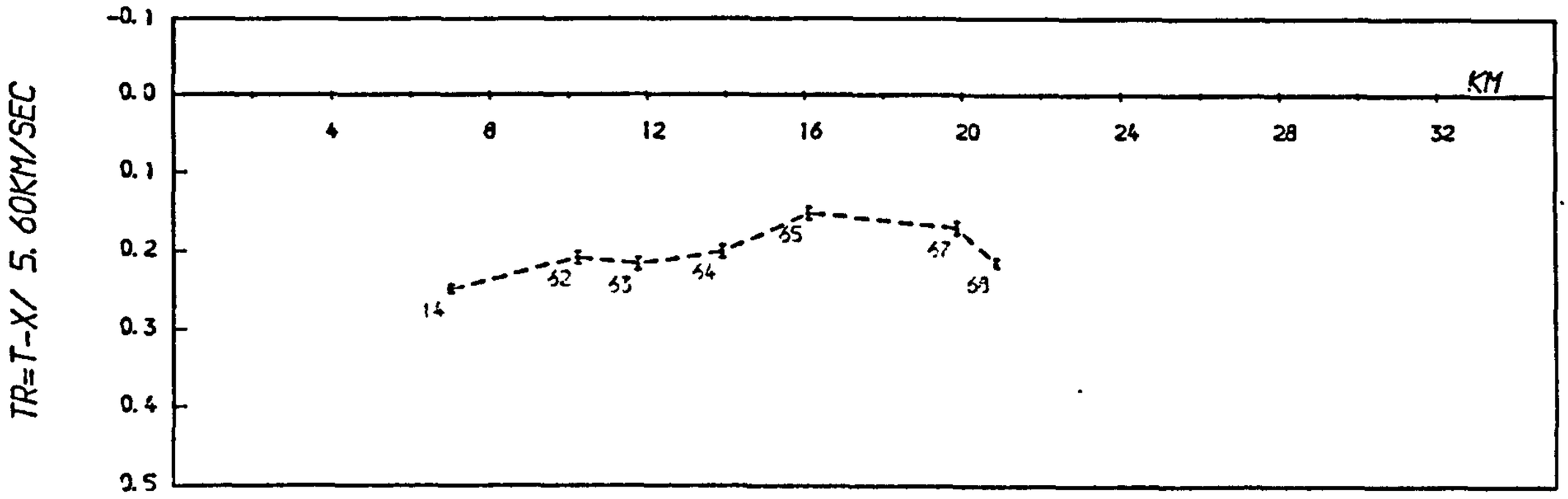

F37003 -- Tunstead untimed

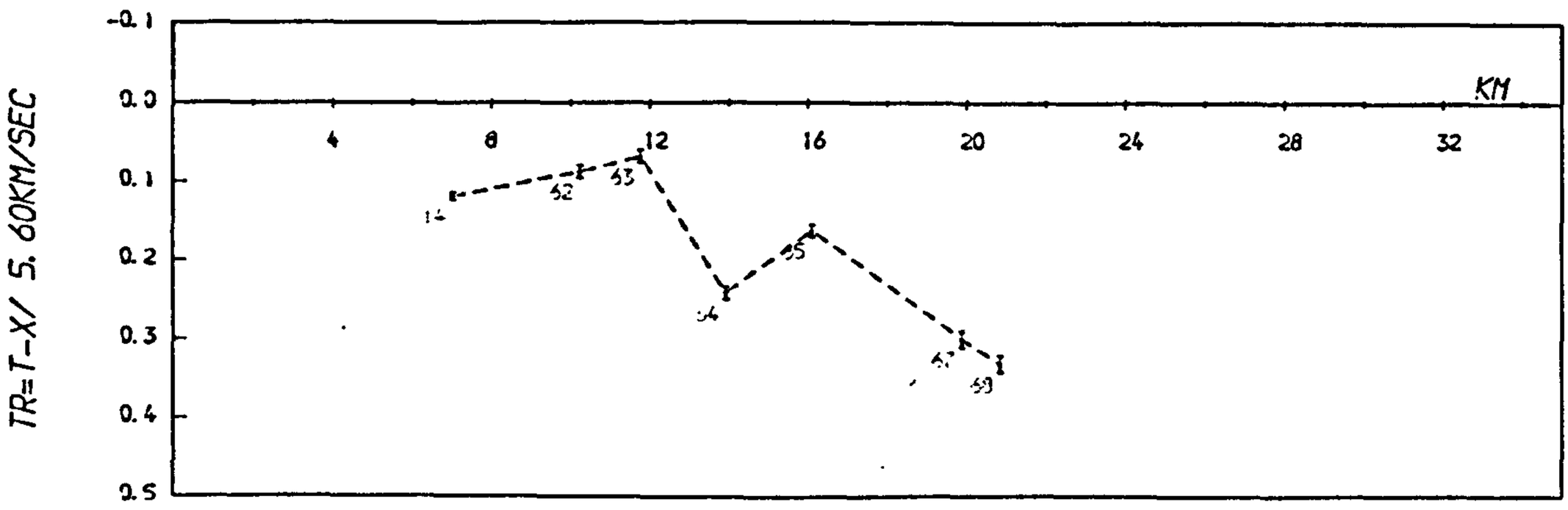

FIG 5-32 cont

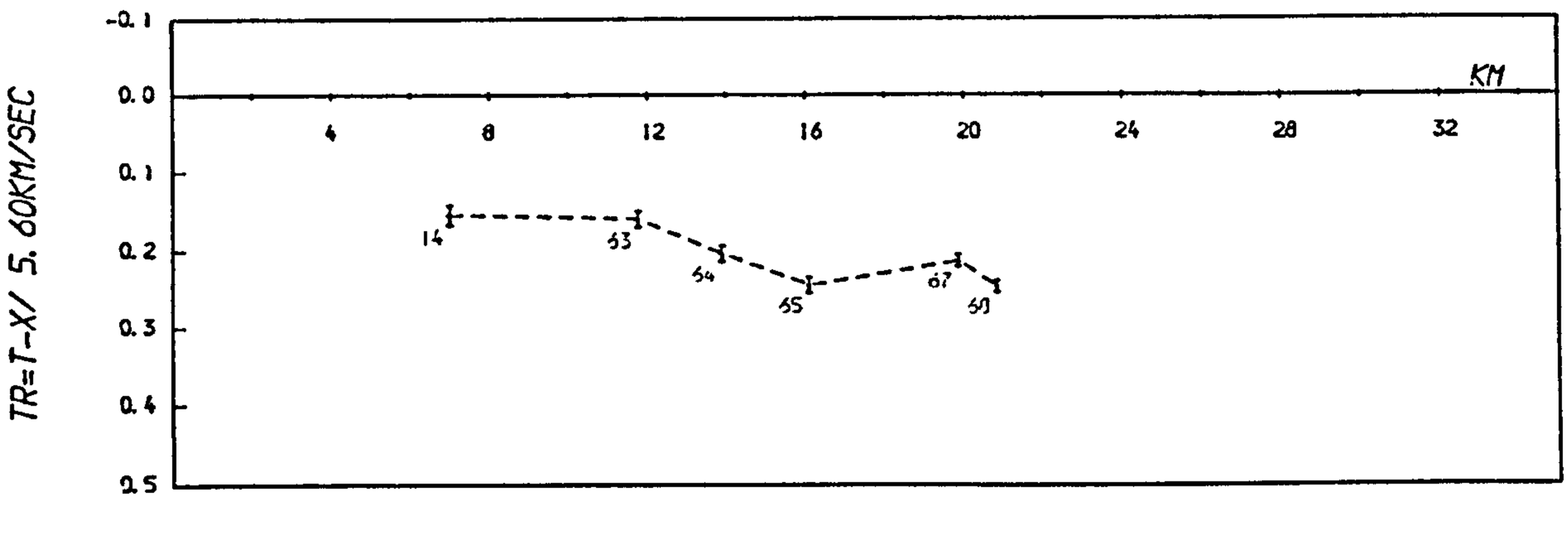
F37006 -- Longcliffe untimed
TR=T-X/ 5.60KM/SEC
-0.1
0.0
0.1
0.2
0.3
0.4
0.5
KM
4
8
12
16
20
24
28
32
14
53
54
55
57
59

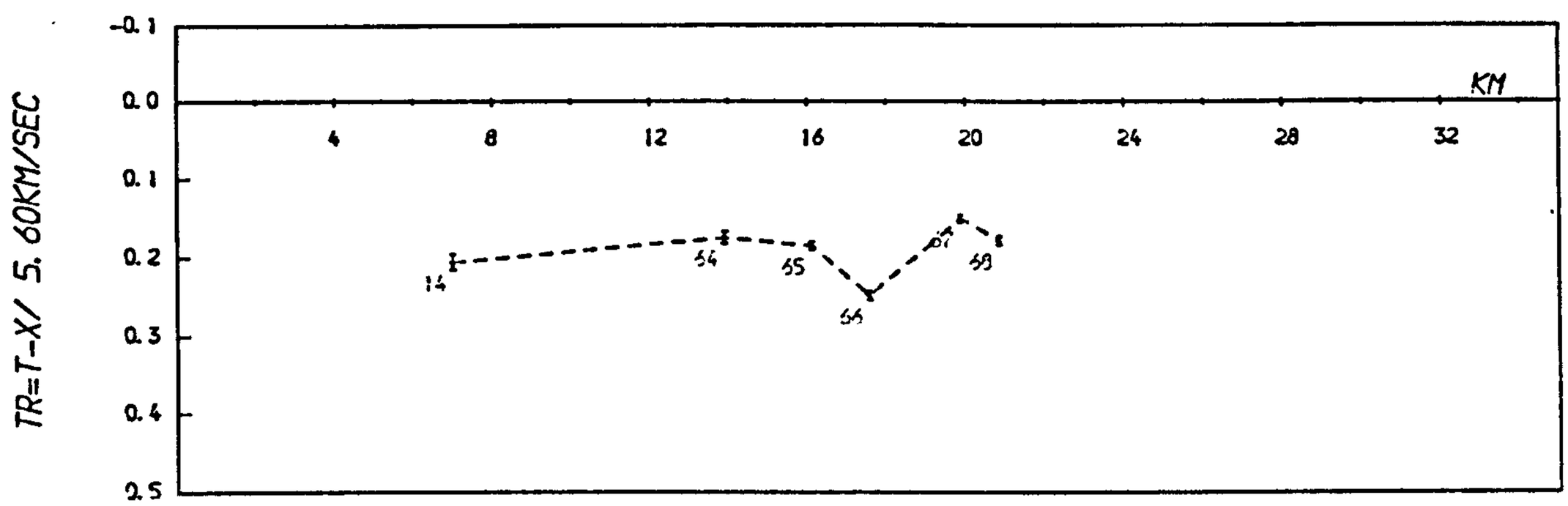
F33026 -- Shining Bank positioned
TR=T-X/ 5.60KM/SEC
-0.1
0.0
0.1
0.2
0.3
0.4
0.5
KM
4
8
12
16
20
24
28
32
14
54
55
56
57
58

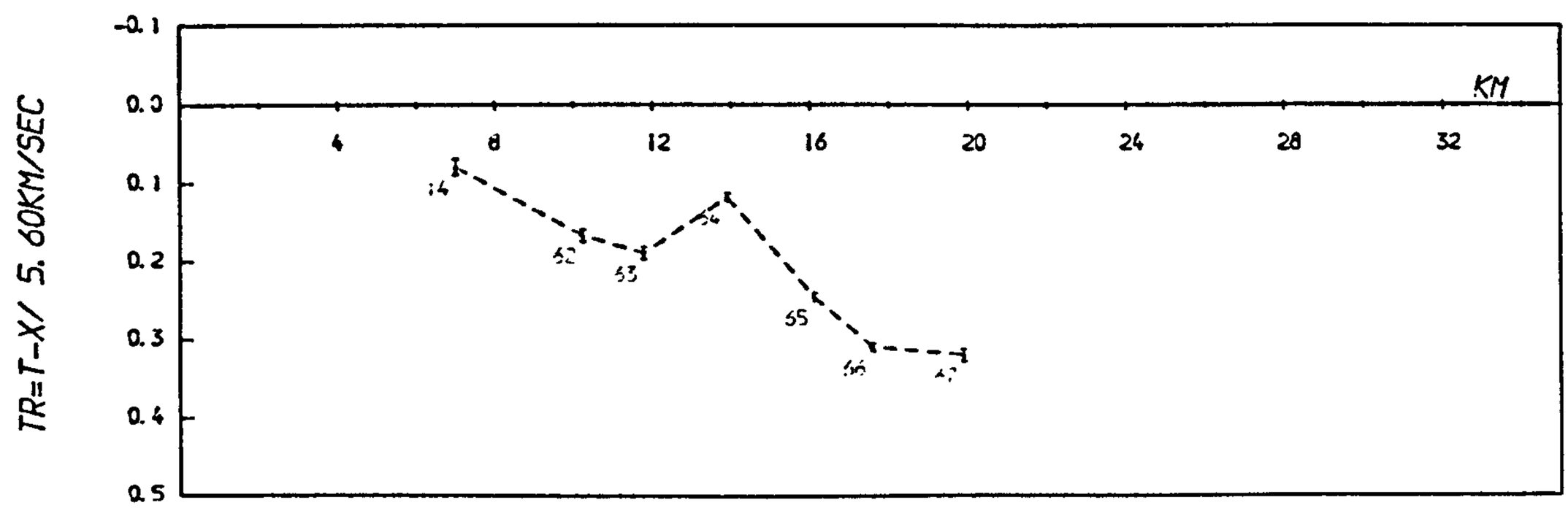
F32020 -- Stoney Middleton positioned
TR=T-X/ 5.60KM/SEC
-0.1
0.0
0.1
0.2
0.3
0.4
0.5
KM
4
8
12
16
20
24
28
32
14
52
53
54
55
56

FIG 5-32 cont

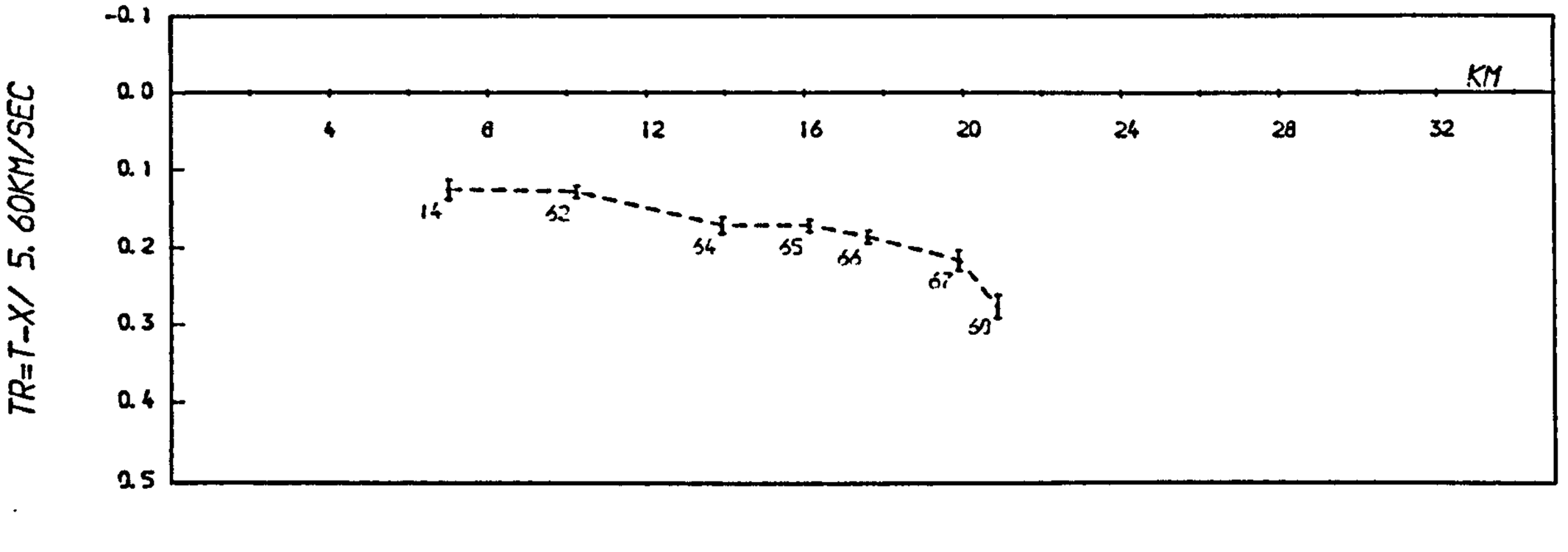
F32021 -- Cauldon Low untimed
TR=T-X/ 5.60KM/SEC
-0.1
0.0
0.1
0.2
0.3
0.4
0.5
KM
4
8
12
16
20
24
28
32
14
52
54
55
66
67
59

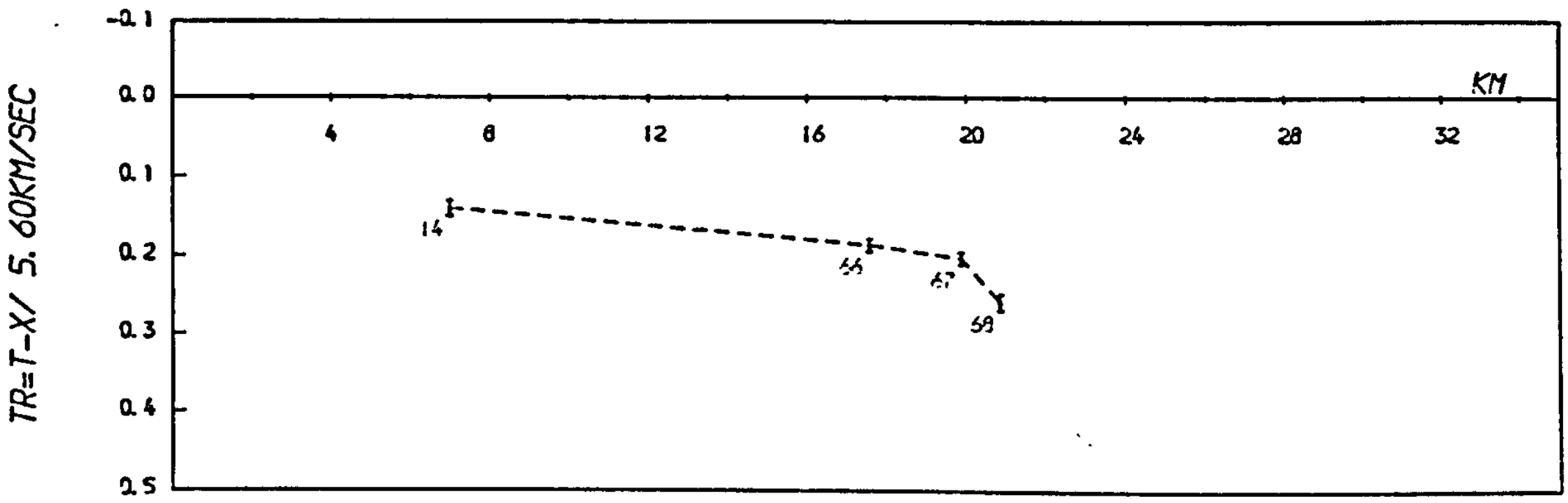
F32028 -- Cauldon Low positioned
TR=T-X/ 5.60KM/SEC
-0.1
0.0
0.1
0.2
0.3
0.4
0.5
KM
4
8
12
16
20
24
28
32
14
55
67
59

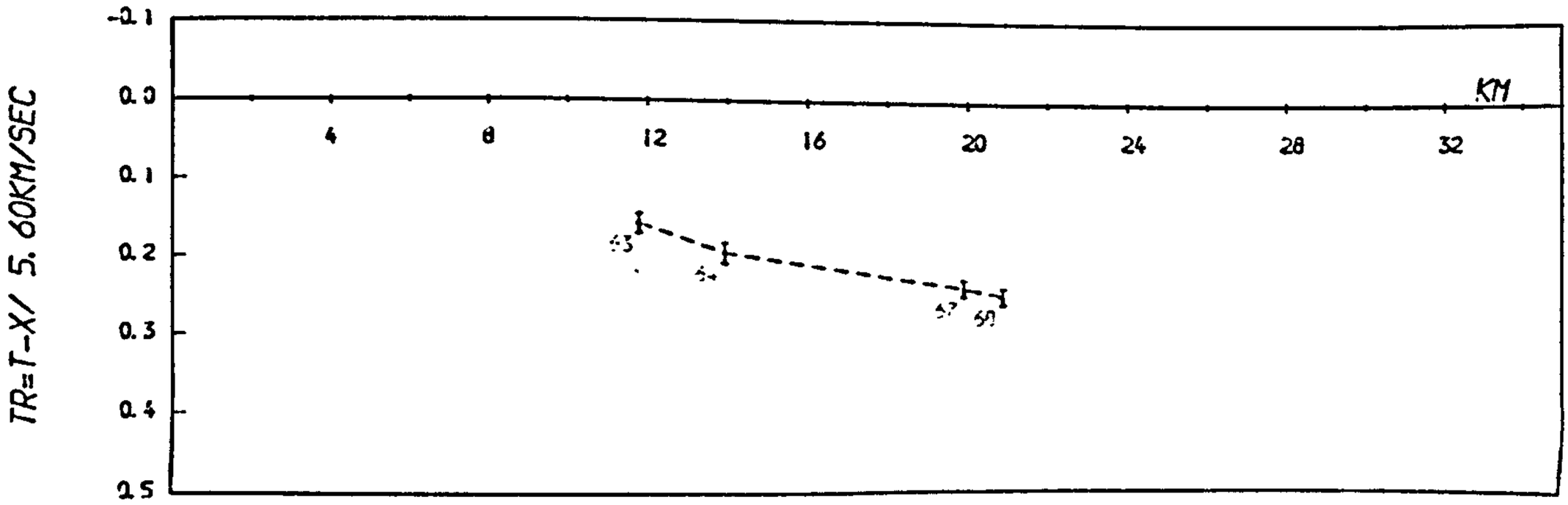
F34032 -- Ballidon untimed
TR=T-X/ 5.60KM/SEC
-0.1
0.0
0.1
0.2
0.3
0.4
0.5
KM
4
8
12
16
20
24
28
32
53
54
57
59

FIG 5-32 cont

mainly crosses Brigantian Monsol Dale and Eyam limestones (see Fig. 1.5). Direct wave velocities of 3.5 - 4 km/s are observed between stations 67 and 68, which lie on the Millstone Grit.

For the identified upper basement arrivals, the reduced time graphs indicate a gently dipping refractor between stations 14 and 67, while the reduced time for station 68 is consistently larger as the station lies upon the Stanton syncline (see Fig. 1.9). The most self-consistent reduced time plots are for shots from the Dow Low Group (e.g. F33025) the first arrivals from which (Fig. 5.33) are clean, of large amplitude relative to their P wave coda, and correlate well between stations. These arrivals contrast with the lower amplitude precursory direct waves of the Tunstead event F37003.

The first arrivals from Cauldon (F35021) are almost certainly upper basement refractions, and their reduced times concord with the basement topography implied by northern quarries. The shallow syncline between stations 14 and 65 agrees with the surface geology, where the line crosses a central outlier of Eyam limestone.

Even with the paucity of later arrival observations, it does not appear that the line crosses the postulated basement fault evident between stations 7 and 9 on the north-south line.

5.6 The Southern Province - Southern East-West (SEW) line

Data from south of the Bonsall Fault comprises events recorded by the southern half of the north-south line, and the whole of the SEW line. The closest stations between these profiles were 2 and 49 (see Fig. 3.1).

Most of the data recorded by the SEW profile consists of broadside shots from northern quarries, and shots close to the line from the Cauldon Low group to the west of the profile (see Fig. 3.7). A few eastern shots from Wirksworth

F33026 -- SHINING BANK TIMED

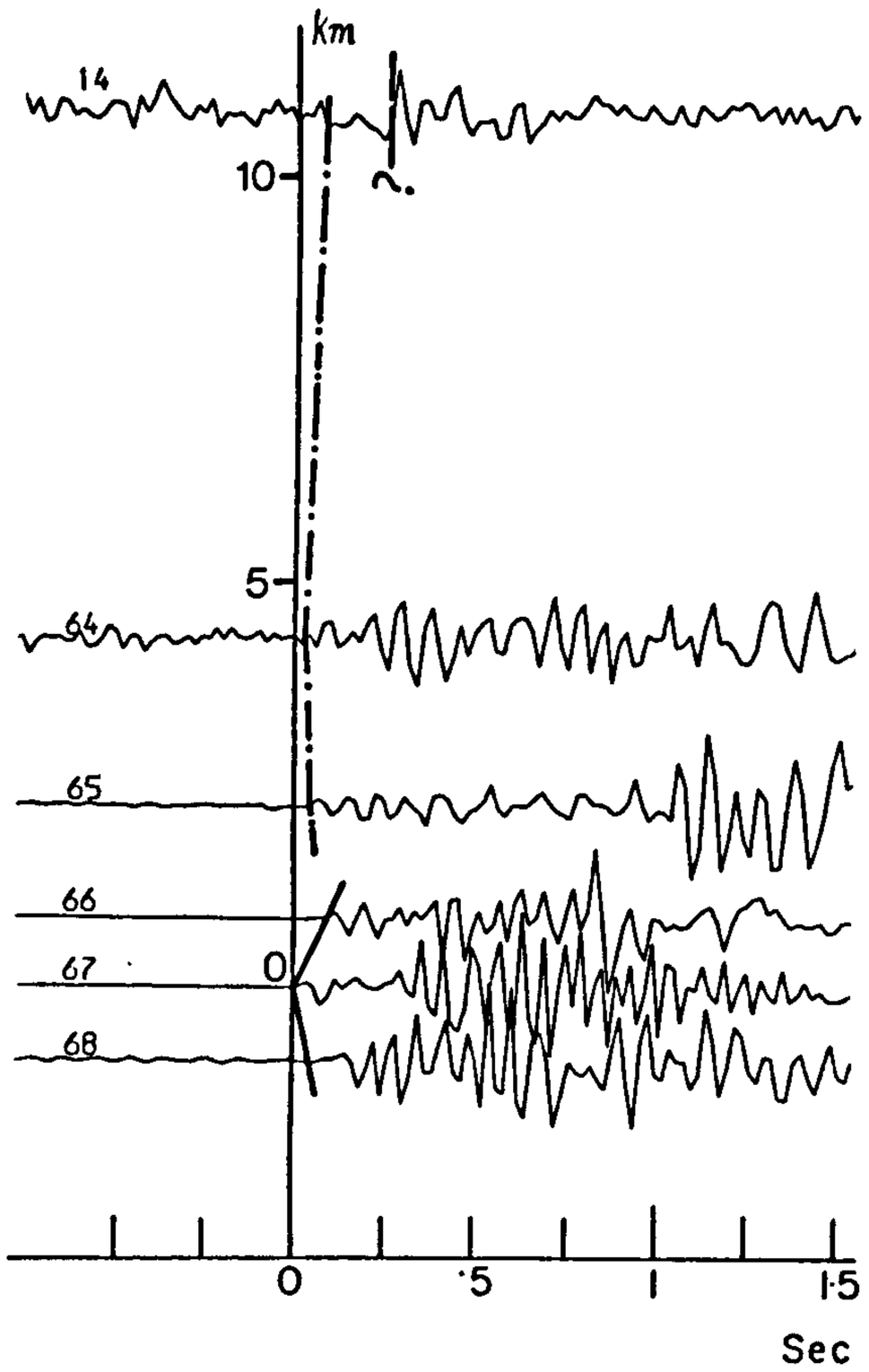

F37003 -- TUNSTEAD UNTIMED

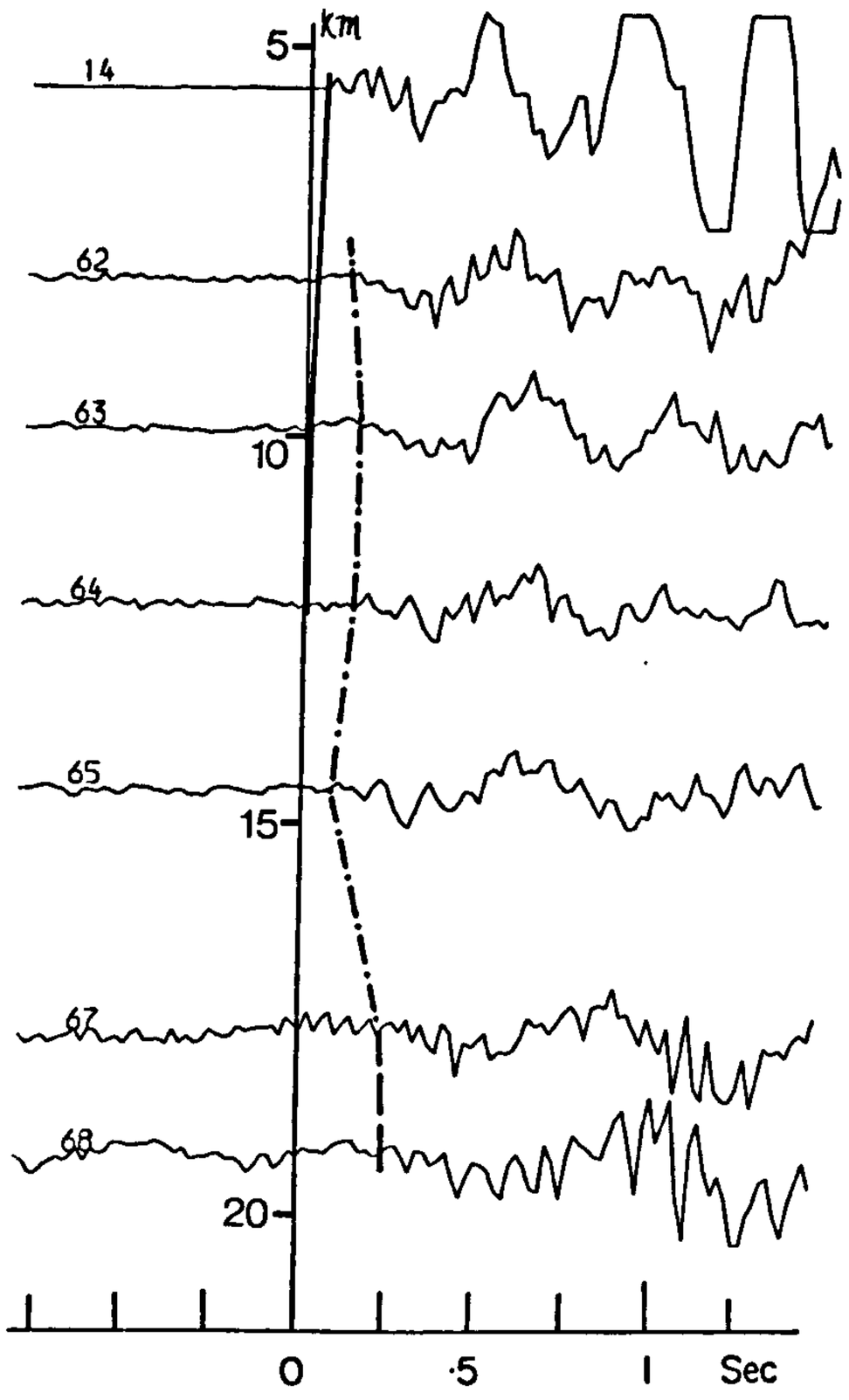

F33025 -- BRIERLOW UNTIMED

-plotted vs interstation separation

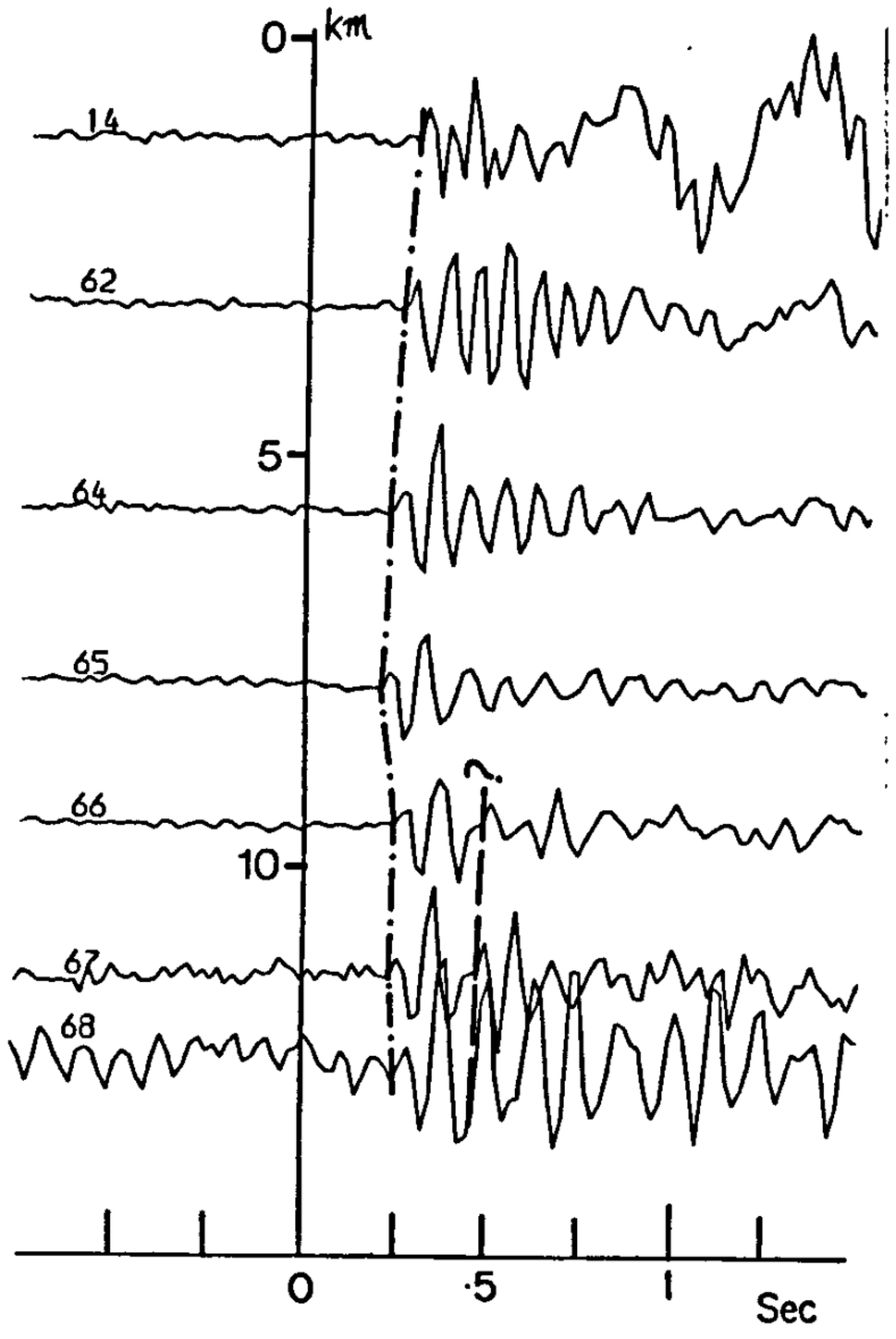

FIG 5-33 Vred=5·6km/s

and Ballidon have been considered, as well as the local earthquakes from Stoke-on-Trent (see Section 4.5.3) which provided seismic sources only about 25 km off the western end of the profile.

It is postulated that the refractor beneath the Carboniferous in the southern province is equivalent to the lower basement refractor to the north of the Bonsall Fault. The Caldon Low borehole (Fig. 1.7), to which station 58 was nearest, encountered sandstones under the limestone outcrop, and it is possible that these sub-crop beneath much of the southern province (Chisholm 1981; see Section 1.2.2). These sandstones probably thicken westwards into the North Staffordshire Deep (Fig. 1.4). The Bouguer anomaly map (Fig. 1.12) suggests the basement dips steeply west of Caldon Low, which is also inferred from the surface geology (Aitkinhead, IGS Leeds, pers. comm.).

5.6.1 Velocity Analysis - Shots close to the Line

Representative T-X plots are shown in Fig. 5.34. From the quarry blast data it is apparent that direct waves through the basinal facies are slower than those observed on the massif (i.e., for all stations north of 3). Consequently most T-X curves manifest distinct two-layer cases, and refracted arrivals are more easily identified. Eastwards from Cauldon Low and Wardlow, direct wave velocities are typically 4.6 - 4.8 km/s; westwards from Longcliffe and Ballidon (though slightly off line) also about 4.8 km/s, and westwards from Dene and Middlepeak, both east of the Dovedale transition, about 5.1 km/s.

Refracted arrival velocities from quarry blasts appear no different from those determined along the southern end of the north-south profile, and are interpreted as from the same (i.e., the lower basement) refractor. Eastwards from the Cauldon Low group, refractions arrive at about 5.7 - 5.8 km/s; westwards from Ballidon and Matlock the observed

C23015 -- Middleton untimed

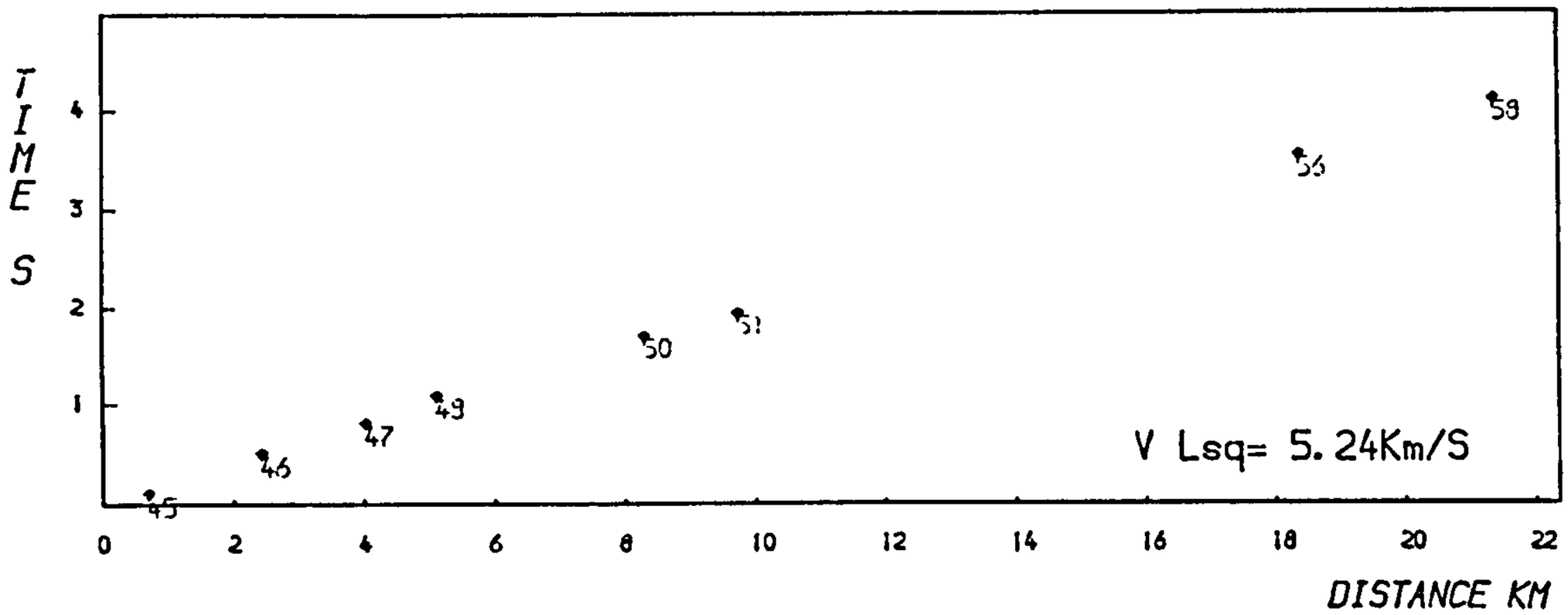

C22017 -- Upperwood untimed

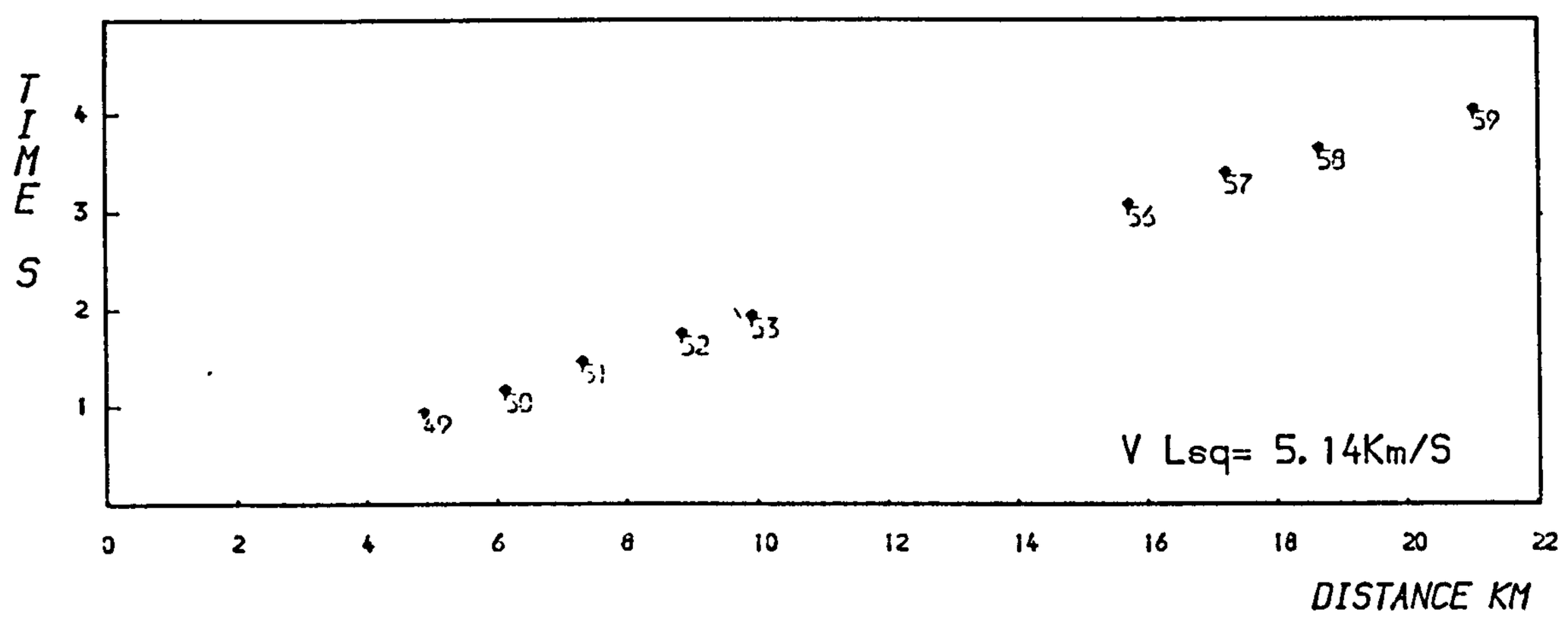

C23002 -- Dene timed

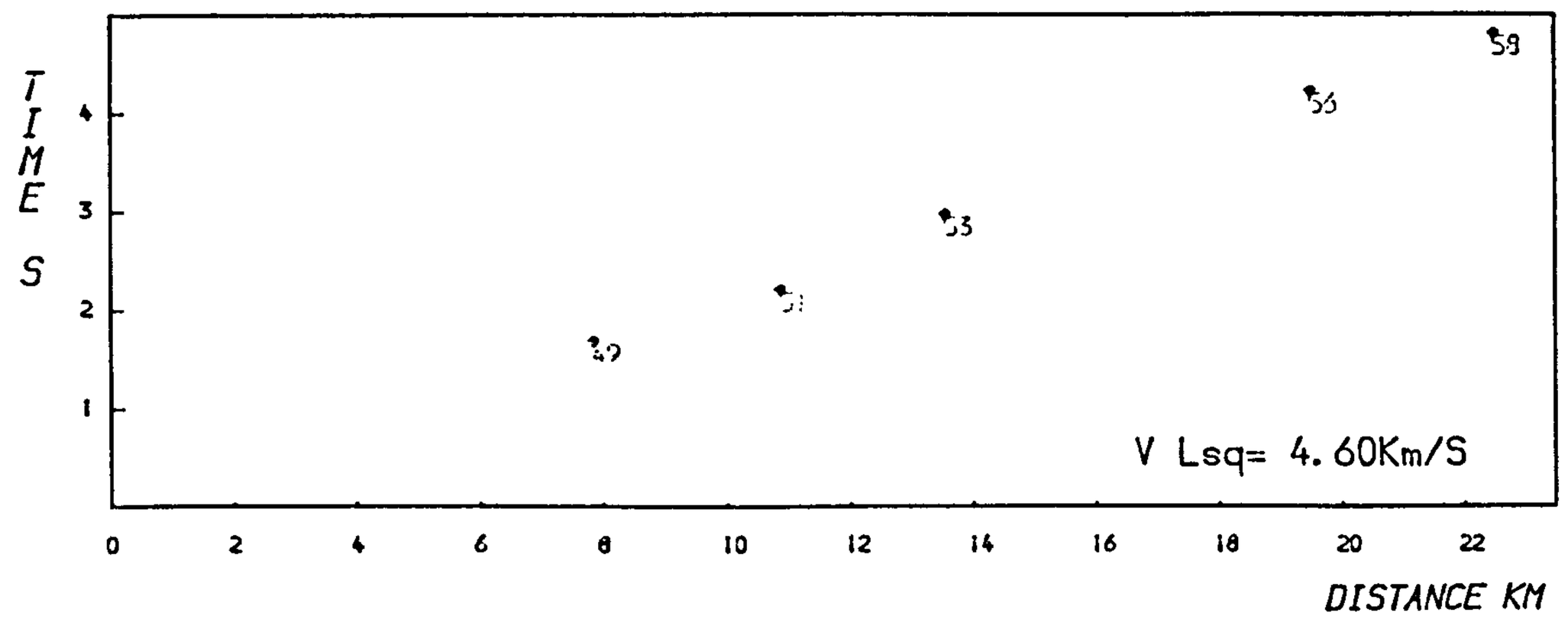

FIG 5-34 T-X graphs

C22009 -- Stoke Event

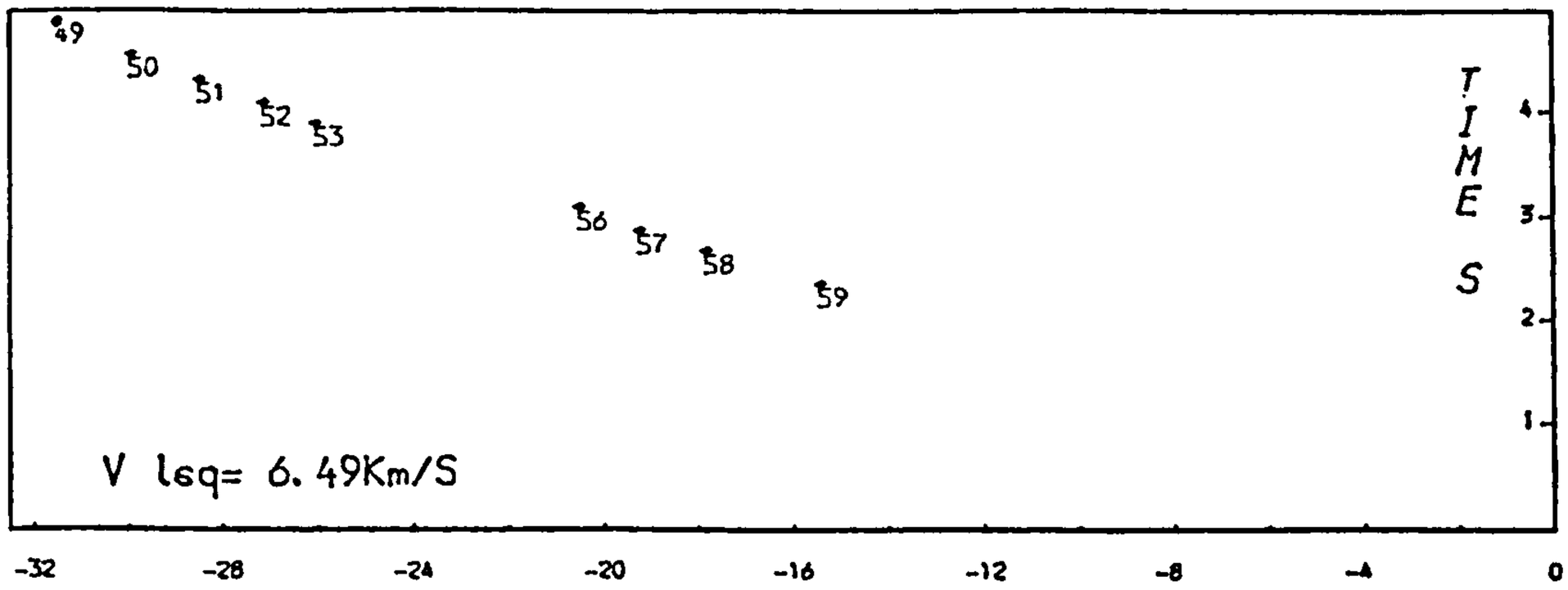

C21008 -- Cauldon untimed

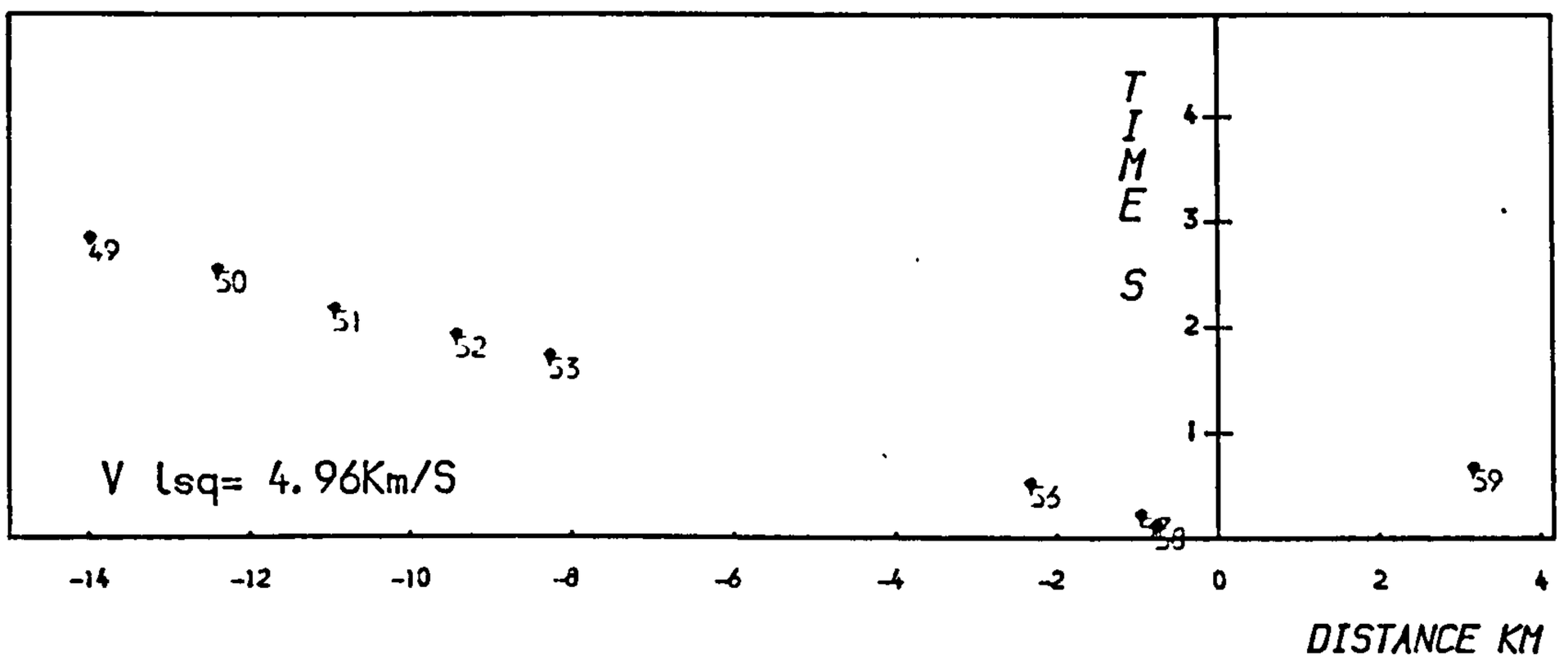

C21002 -- Ballidon untimed

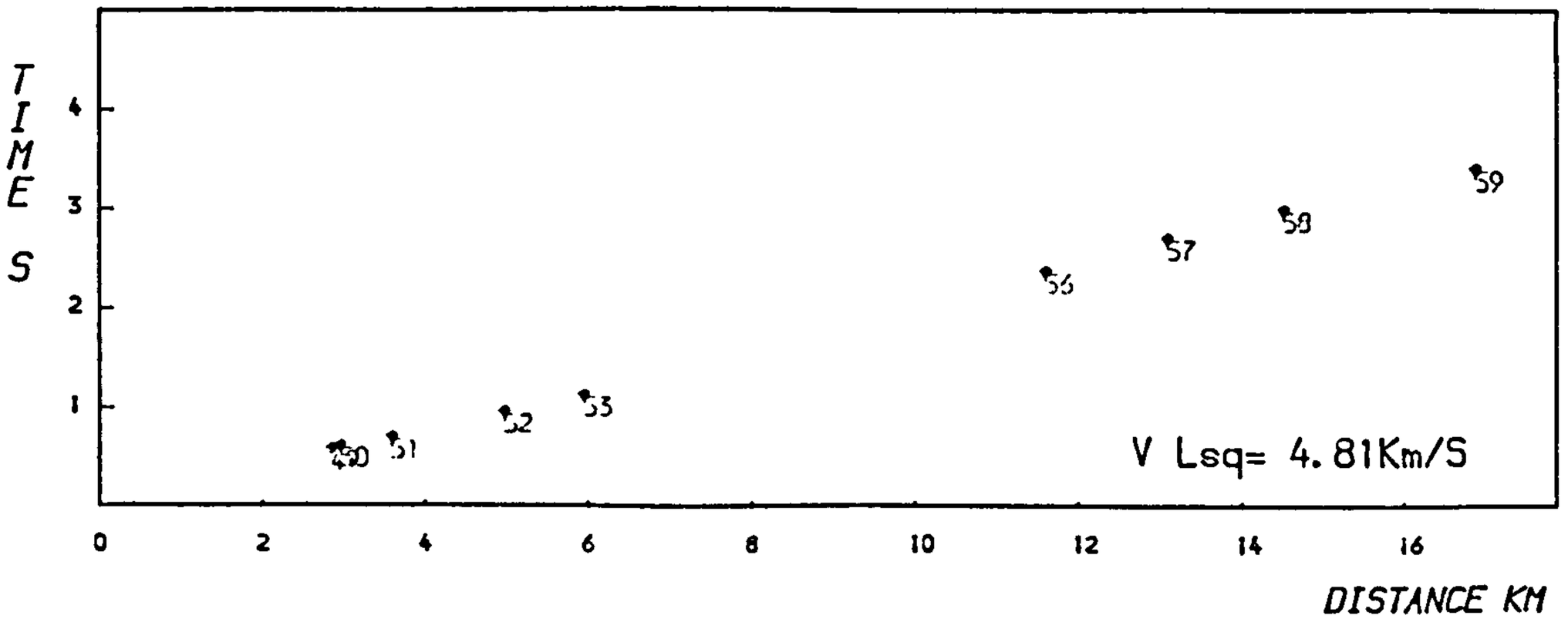

FIG 5-34 cont

velocities are slightly less, about 5.5 - 5.6 km/s. These may correspond to up- and down-dip velocities respectively for a westward dipping refractor.

Unlike the Mansfield events, those from Stoke-on-Trent were nearly collinear with the SEW line (see Fig. 4.15). Being about 25 km from the western end of the line, these first arrivals are almost certainly basement refractions. The apparent velocity of about 6.5 km/s is much higher than observed for the quarry blast data, and this may be because

(a) the arrivals originated from where the basement dips more steeply westward than the region sampled by the quarry blasts (i.e., a higher up-dip velocity). To give an apparent velocity of 6.5 km/s requires a dip of approximately 14 degrees for overburden and refractor velocities of 5.2 and 5.6 km/s respectively. For overburden of velocity 4.8 km/s, the dip needs to be about 20 degrees.

(b) the arrivals are from a deeper refractor of higher velocity.

Unfortunately because stations 54 and 55 never worked, it is difficult to estimate the cross-over distance for shots from Cauldon and Ballidon quarries. Certainly from Cauldon basement refractions are consistently first arrivals at station 53, which suggests a cross-over of a least 8 km. Thus taking the thickness of limestone from the Caldon Low bore-hole, and assuming the velocity of the Redhouse Sandstones as 4.5 km/s, this means the basement is at most about 1 km deep around station 53 for a limestone velocity of 4.8 km/s and a basement velocity of 5.65 km/s. Similarly, direct arrivals from Ballidon occur as first arrivals as far as station 53 (Fig. 5.34), 6 km from the shot.

5.6.2 Shape of the Basement - Reduced Time Graphs

A. Broadside Events from the North

The quarries to the north around Buxton are about the same distance from the NEW line as the Stoke tremors.

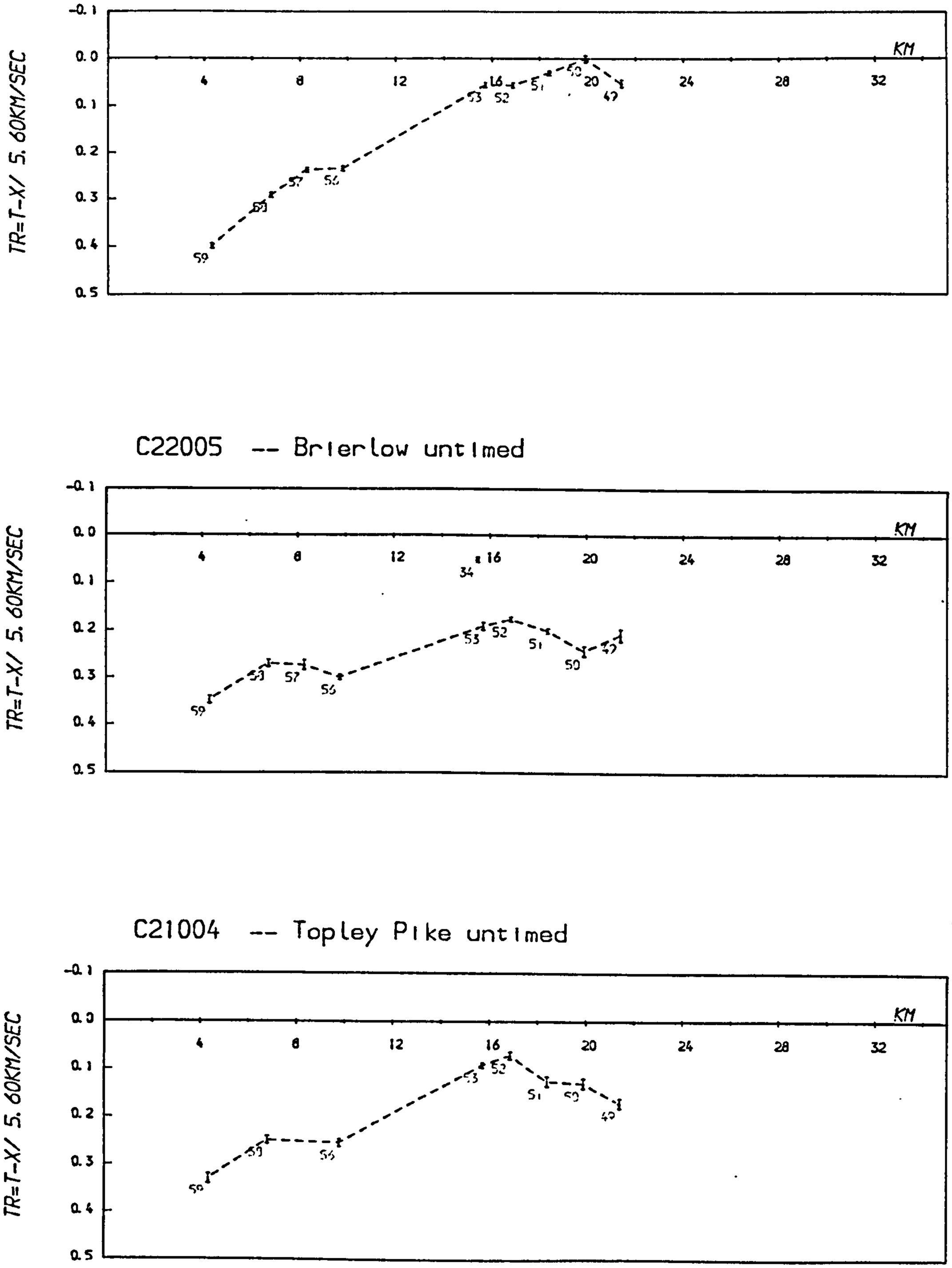

FIG 5-35 Reduced times

C22024 -- Doveholes positioned

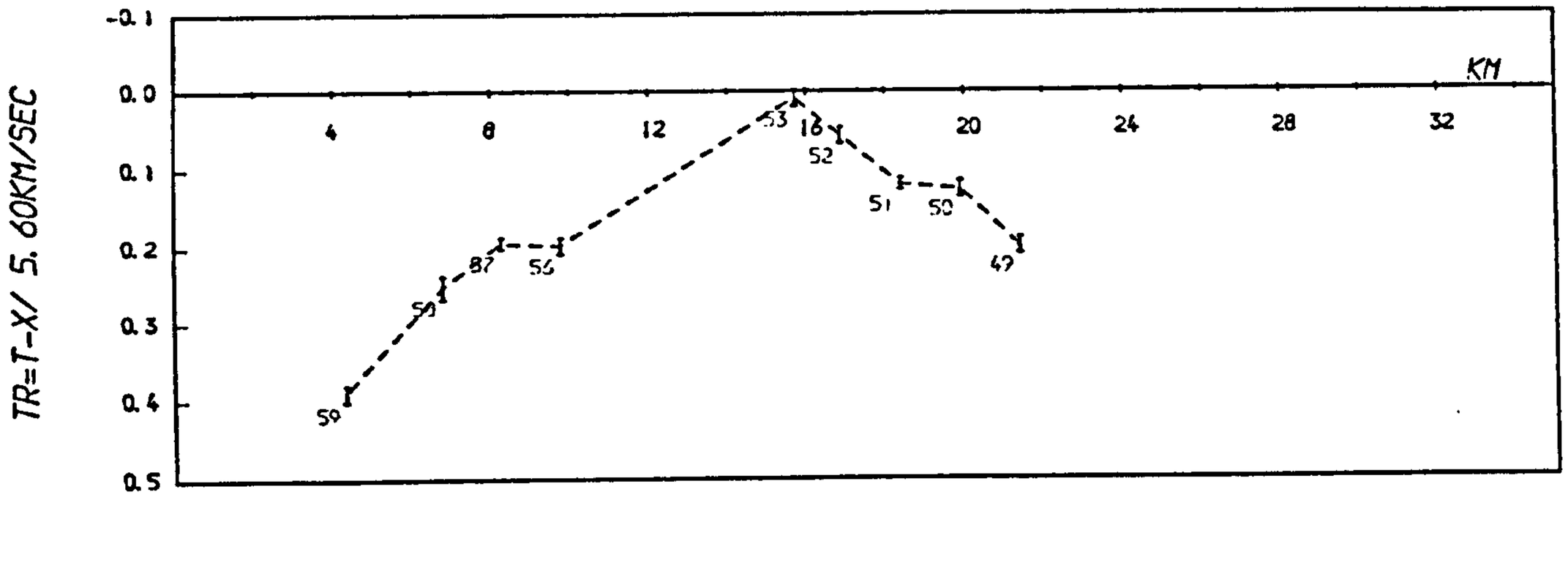

C23009 -- Hindlow timed

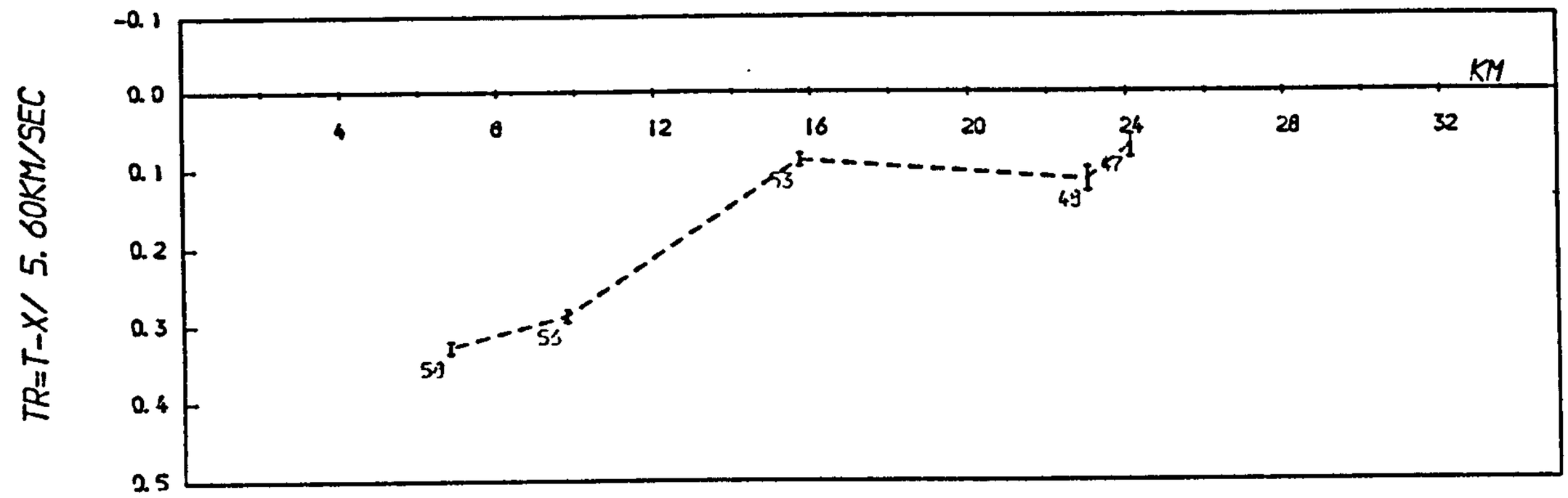

C22019 -- Tunstead timed

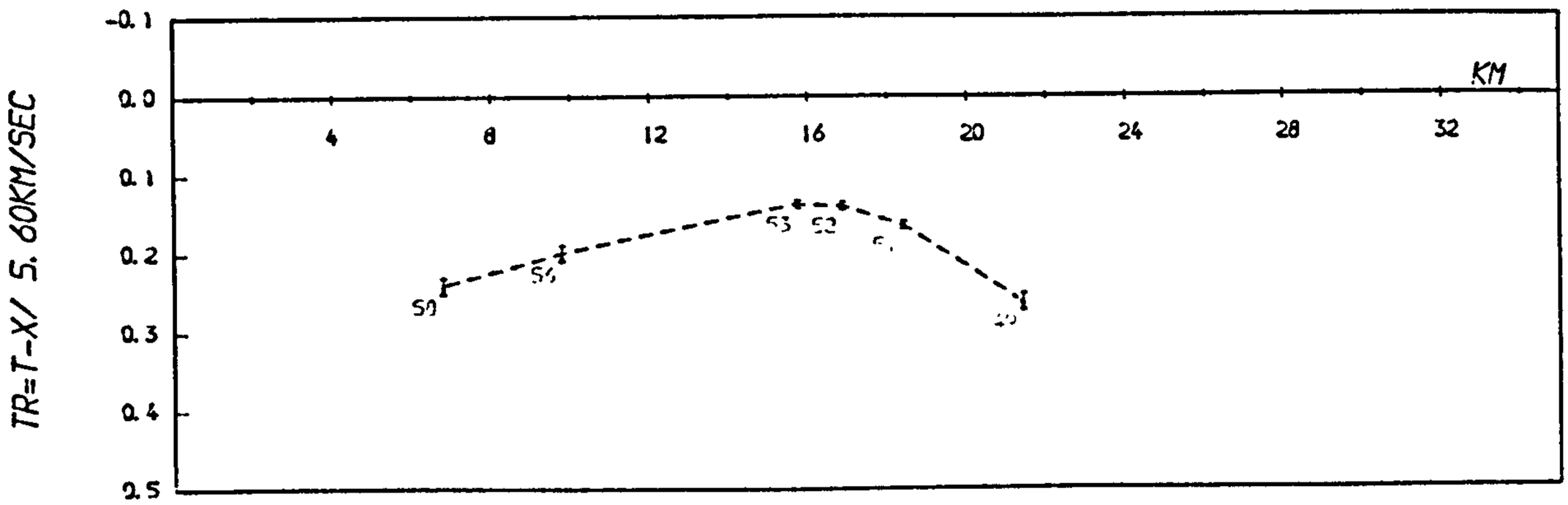

FIG 5-35 cont

C23015 -- Middleton untimed

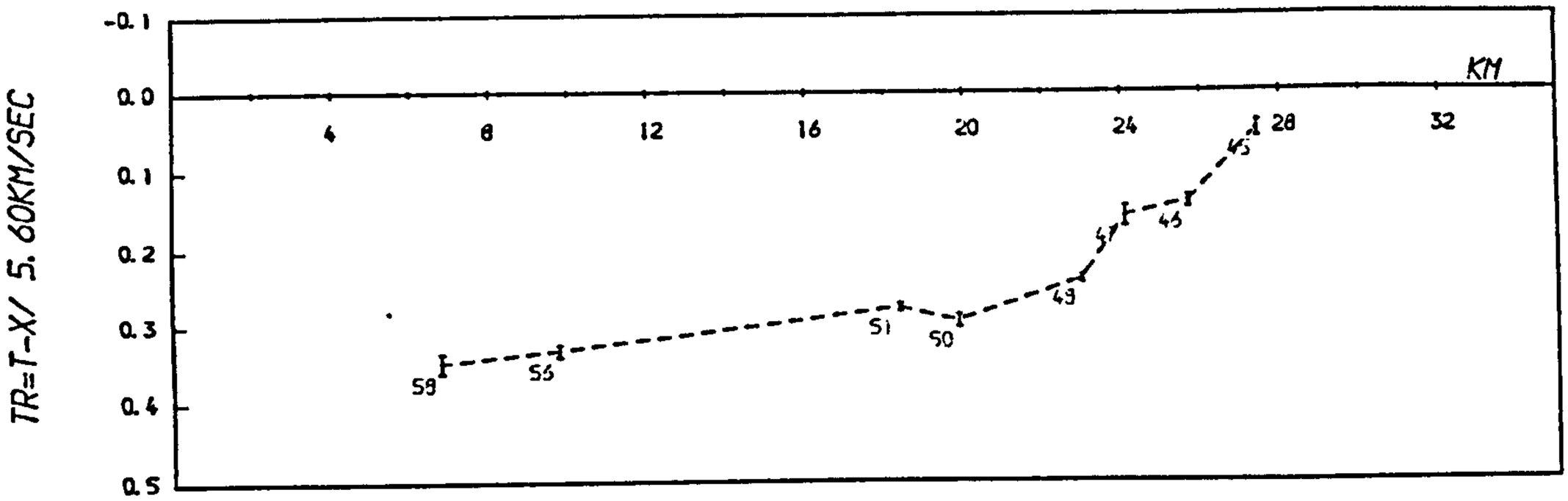

C22017 -- Upperwood untimed

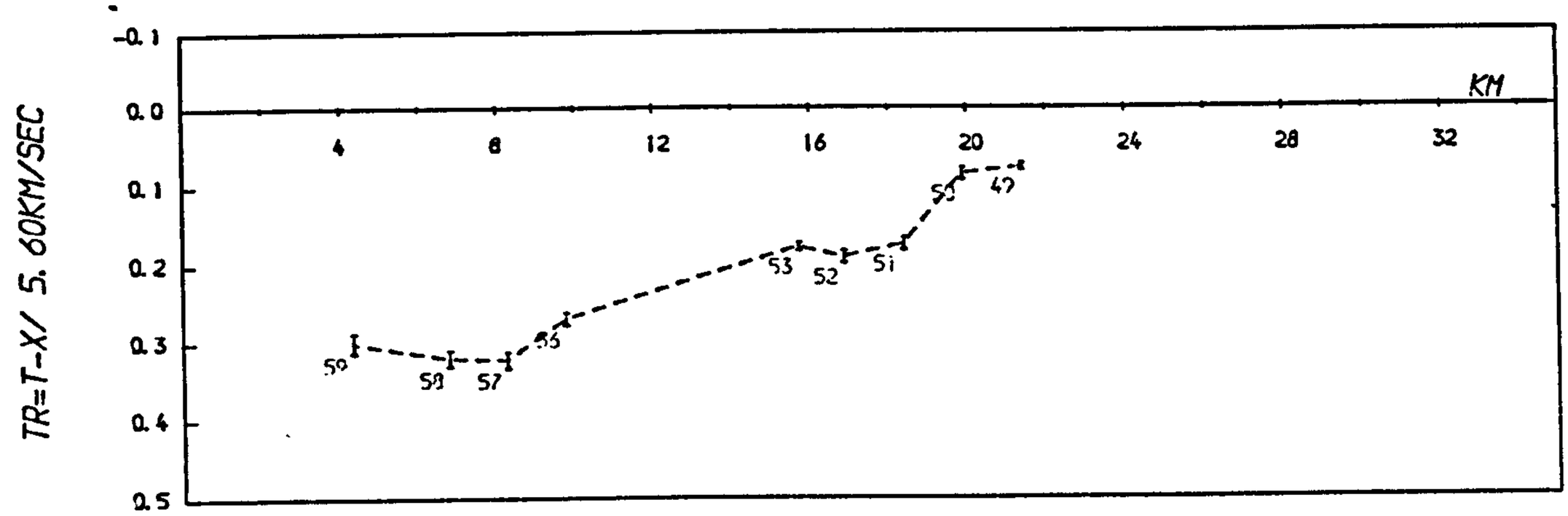

C23002 -- Dene timed

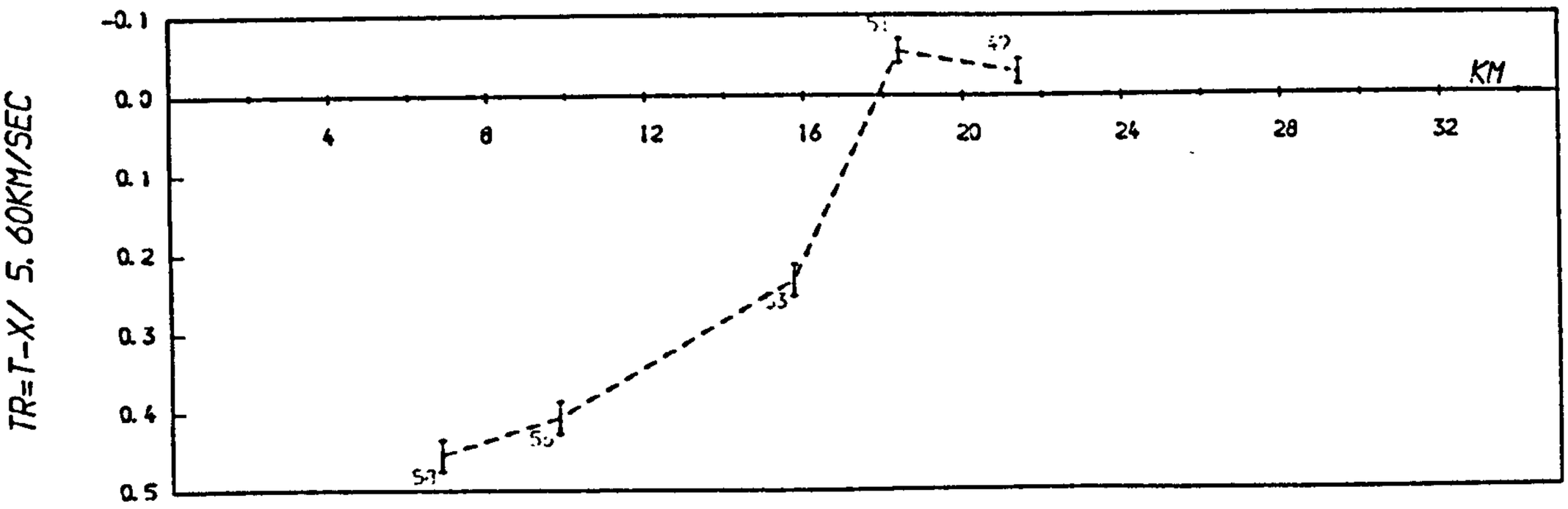

FIG 5-35 cont

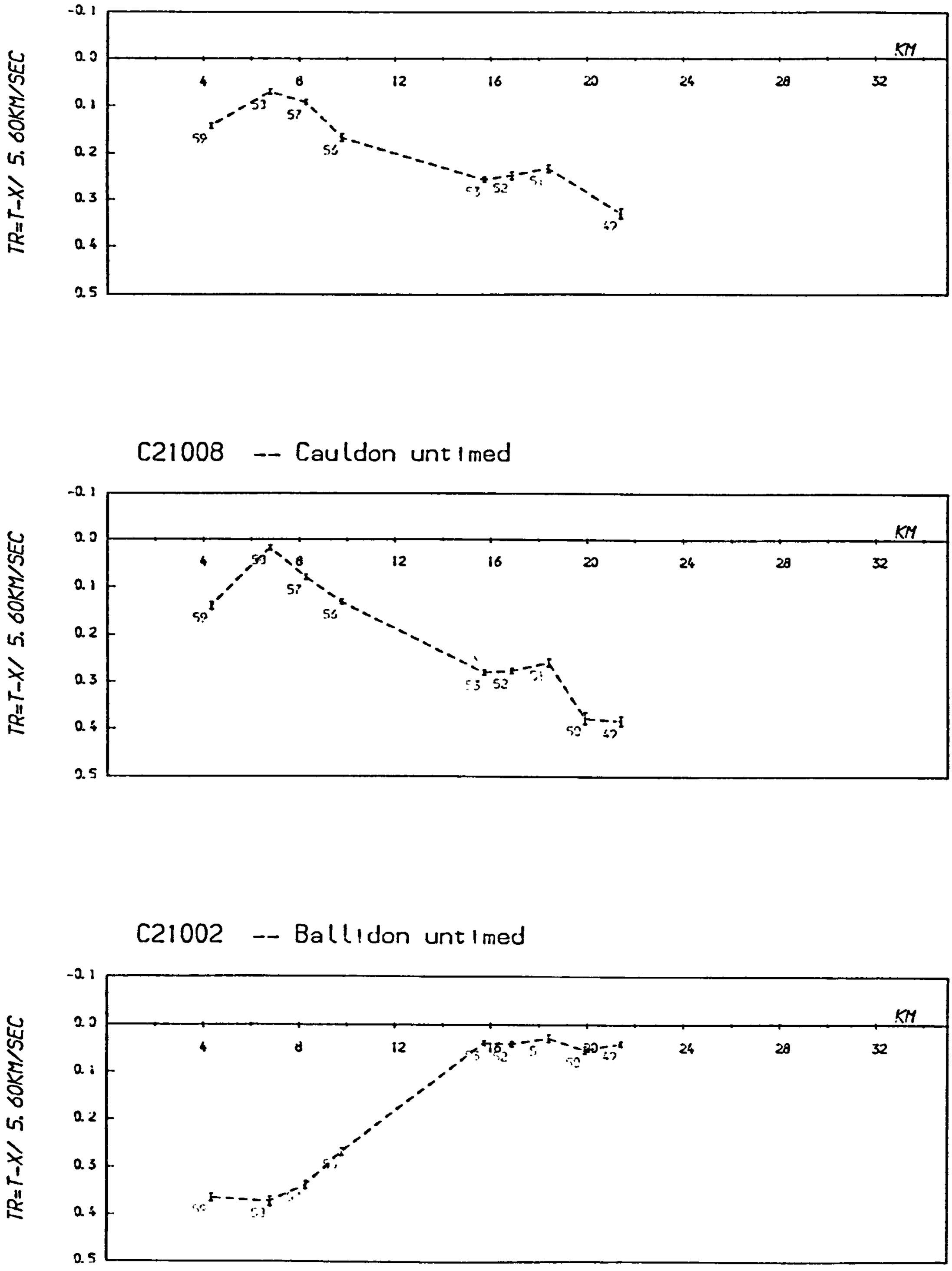
C22025 -- Wardlow untimed
C21008 -- Cauldon untimed
C21002 -- Ballidon untimed
TR=T-X/ 5.60KM/SEC
KM
-0.1
0.0
0.1
0.2
0.3
0.4
0.5
4
8
12
16
20
24
28
32

FIG 5-35 cont

The reduced times for these events (Fig. 5.35) all show a broadly anticlinal structure. For the northern quarries the axis appears to be between stations 52 and 53, while for the Stoke event it seems to be offset eastwards to station 50. The Cauldon Low anticline (see Fig. 1.9) also commonly appears on these plots between stations 57 and 58.

Not all events manifest as steep a dip westwards of station 53 as the Stoke tremor. Events C21004 (Topley Pike), C22024 (Doveholes) and C23009 (Hindlow) do, for example, but not C22005 (Brierlow) and C22019 (Tunstead). These differences are not systematic with distance or azimuth from the line.

An easterly dip between stations 52 and 49 is evident from most reduced time graphs, while events C22005 (Brierlow) and C23009 (Hindlow) suggest that this is the western limb of a shallow syncline, perhaps less than 8 km wide. If so then this feature may correspond with the syncline suggested between stations 1 and 3 on the north-south line (see Fig. 5.16), where stations 1 and 52 lie on the south and western (fault-bounded?) margin. This basin appears as a Charnoid-trending low on the Bouguer anomaly map.

B. Quarries close to the line

From Cauldon (e.g. C21008) and Wardlow (e.g. C22025), basement refractions are first observed at station 53. These data (Fig. 5.35) show the basement to shallow to station station 51: offset 2 km eastwards from between stations 52 and 53. For the velocity model discussed above in Section 5.6.1, this corresponds to a refractor about 1.3 km deep. Note that the reduced times for the Stoke event (C22009) this offset is about 3.5 km. The differing offset is either due to the different azimuth for the events, or that the first arrivals for the Stoke event originated from a deeper basement. This latter possibility is thought unlikely because a similar 3.5 km offset is not observed for the axis of the Cauldon Low anticline.

West of stations 52 and 53, the increase in reduced times for the Cauldon events (between stations 51 and 50) appears more pronounced than that for the quarries of Upperwood (C22017) and Middleton (C23015) to the east of the line. These data imply the depression to be a minor feature, and the Middleton event also shows the basement to shallow further eastwards to station 47. Generally, the quarries to the east of the line manifest a basement dipping west of station 53. The timed Dene shot (C23002) manifests as steep a westward dip as the Stoke event, but for the untimed Middleton blast (C23015) the incline appears far more gentle. For the Ballidon (C21002) and Upperwood (C22017) events, the basement seems to dip less steeply west of station 56 than it does between stations 53 and 56.

5.6.3 Reduced Time Seismograms

A selection of reduced time seismograms are plotted in Fig. 5.36. With the exception of station 50, basement refractions generally appear most coherent between stations 49 and 53. West of station 56 P waves often progressively broaden; this is presumably due to the filtering of the signal by the westwardly thickening sandstones beneath the limestone, and also by the Millstone Grit for signals recorded at station 59.

For the Stoke event C22009 the first arrivals between stations 59 and 56 are of lower amplitude relative to their coda than those recorded between stations 53 and 49. Their signal waveforms also appear more complicated and of higher frequency. These effects may be due to either interference by later arrivals from a shallower horizon not present beneath stations 53 to 49, or lateral change in the overburden.

In terms of frequency content and interstation coherency, the first arrivals at stations 49 to 53 from northern quarries are very similar to those from the Stoke event (e.g., Tunstead and Brierlow untimed, Fig. 5.36). It is thus thought likely that

C22009 -- STOKE-ON-TRENT EVENT

FIG 5-36

C21008 -- CAULDON LOW UNTIMED

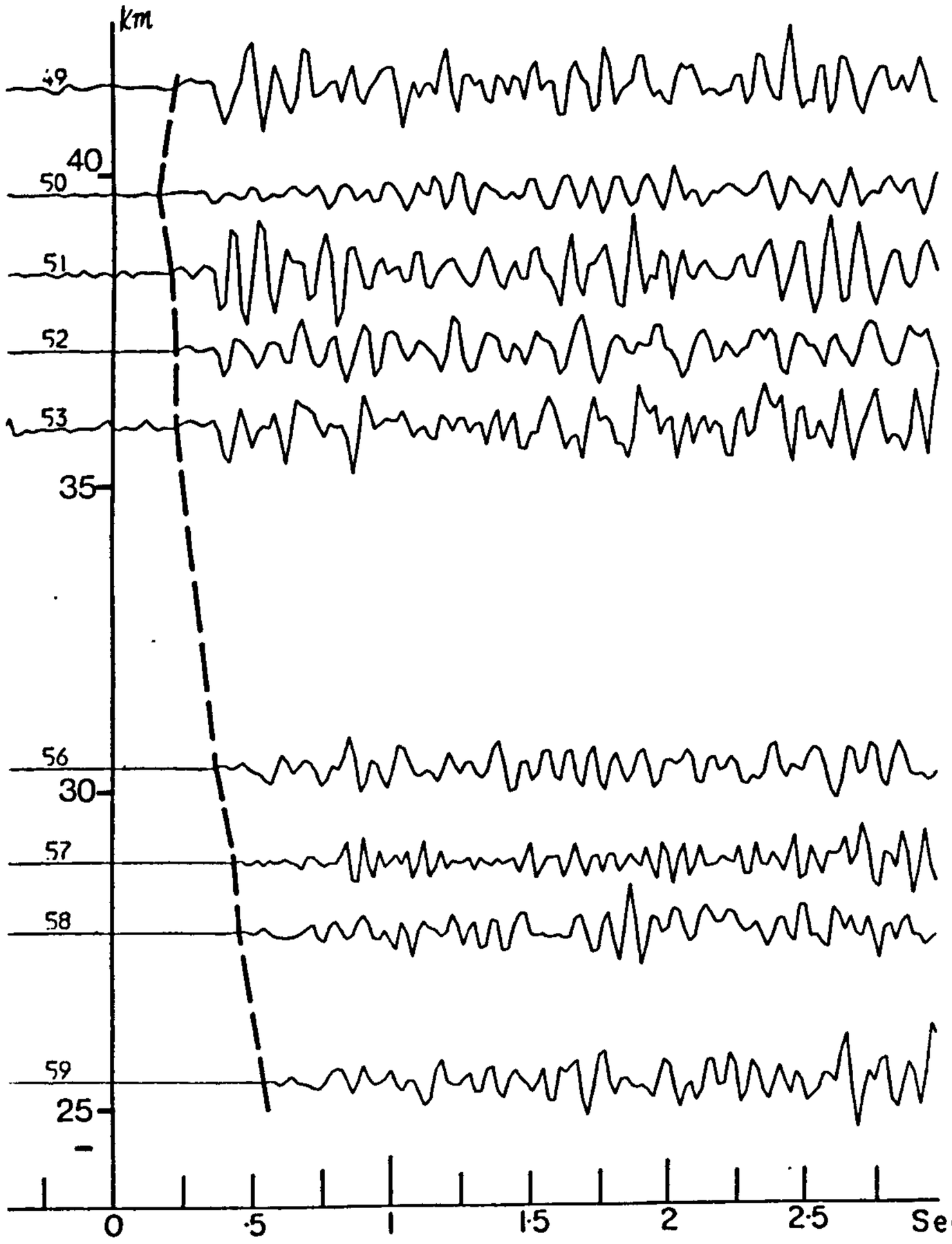

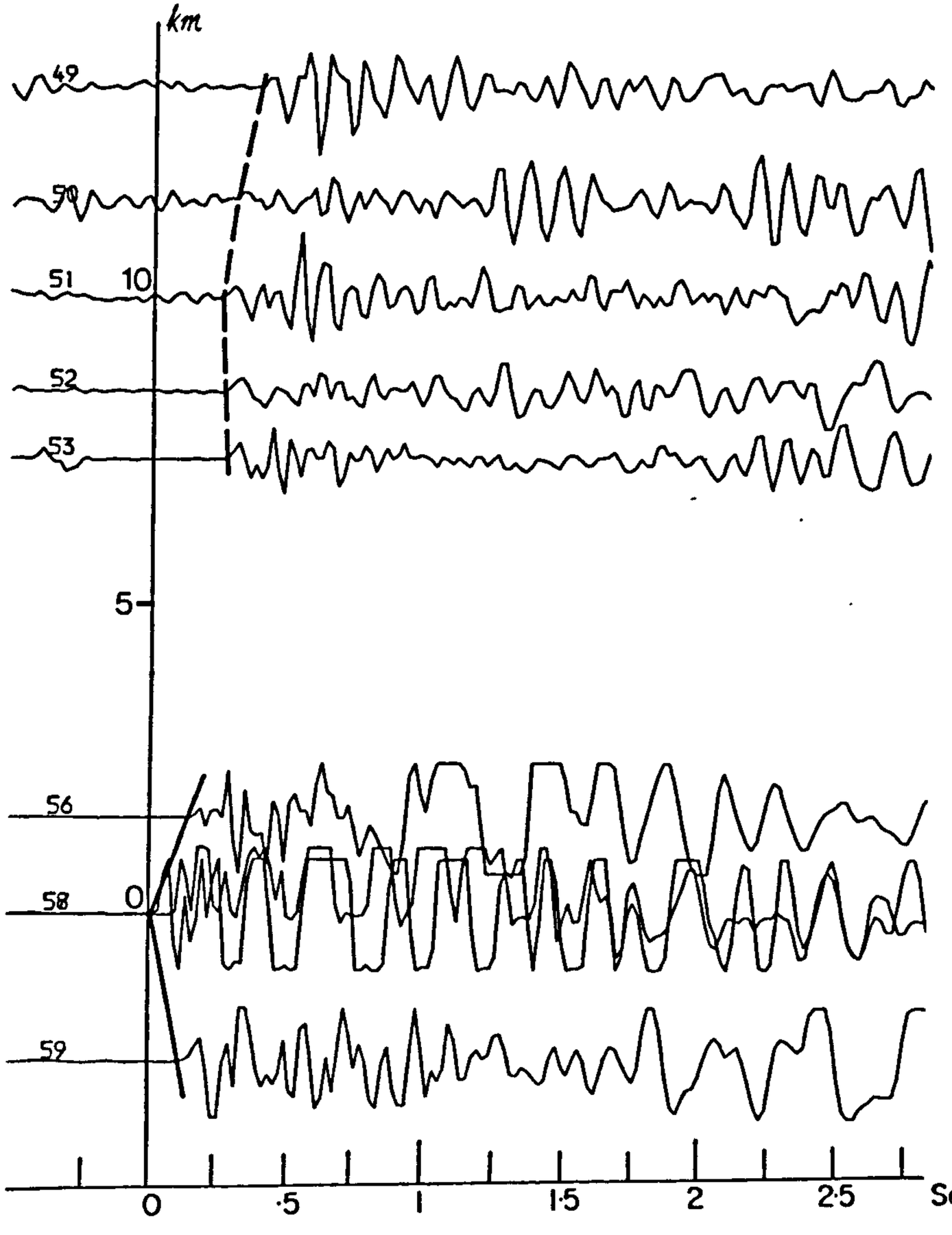

Reducing velocity 5·6km/s —direct wave – –lower basement refraction

FIG 5-36 cont.

lower Palaeozoic refractor

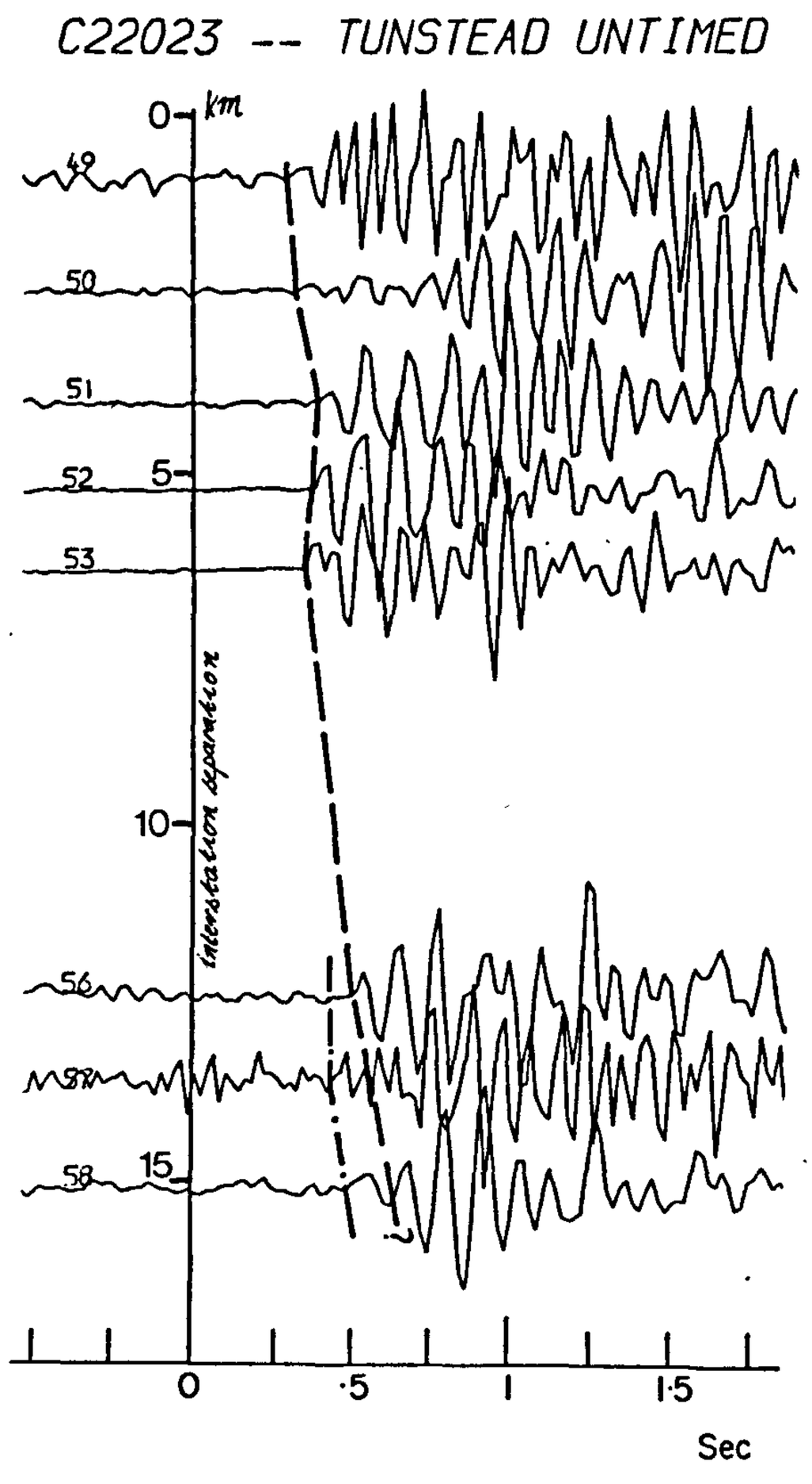

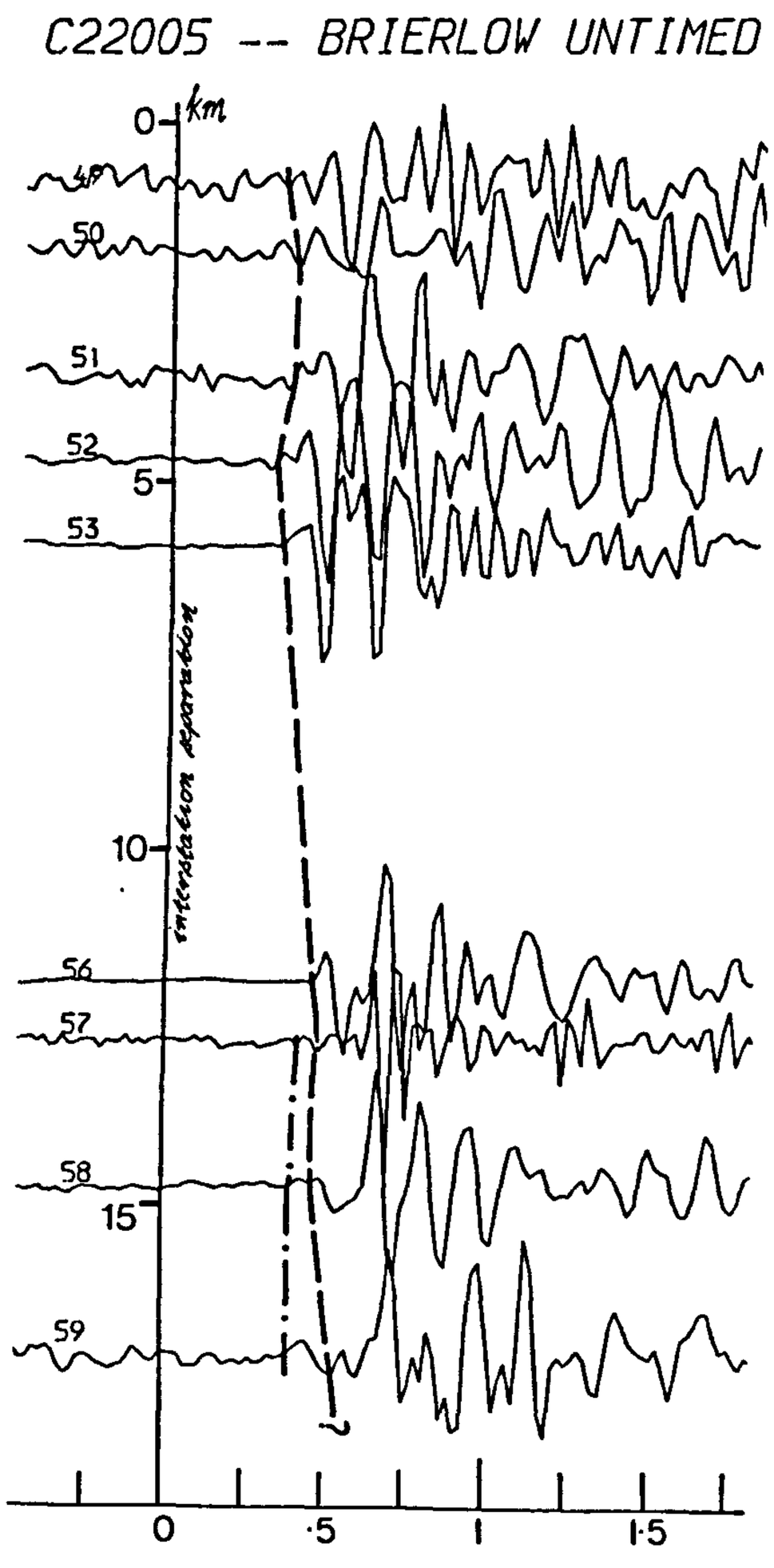

C22017 -- UPPERWOOD UNTIMED C23015 -- MIDDLETON UNTIMEL

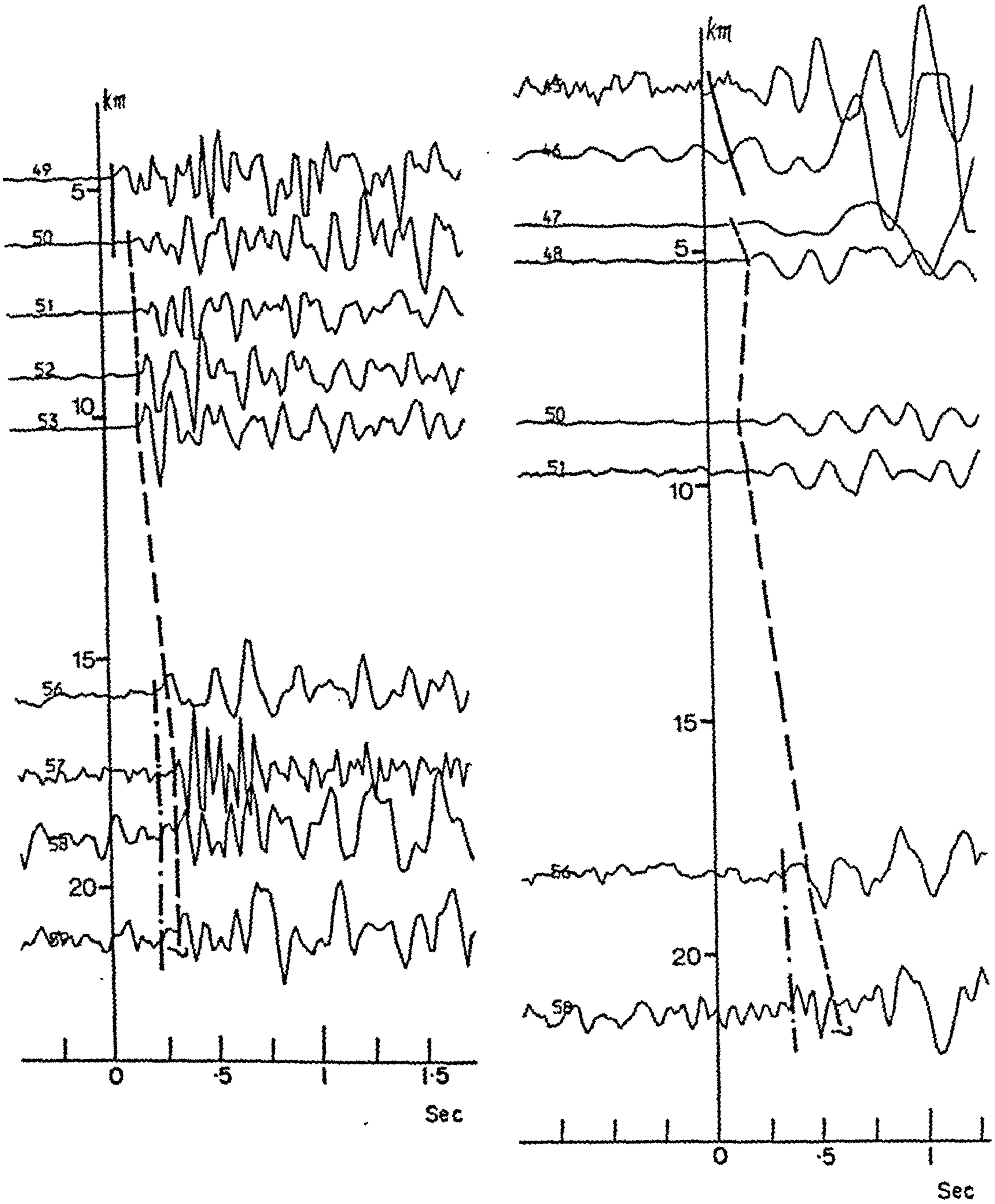

FIG 5-36 cont.

they originate from the same refractor. For these northern events, a lower amplitude, higher frequency precursor to these basement refractions can be traced west of station 56 (dotted and dashed line). This earlier arrival is interpreted as a refraction from a shallower horizon similar to the upper basement refractor under the northern province. Therefore for events whose reduced times manifest a refractor less steeply dipping west of station 53, this precursory phase was of large enough amplitude to be picked as a first arrival. The phase can also be observed for the blasts from Middleton and Upperwood quarries (Fig. 5.36). That it arrives progressively earlier than the deeper basement refractor suggests a westwardly thickening layer.

The refracted arrivals between 49 and 53 are generally similar in waveform to those observed between stations 1 and 6 on the north-south line, and suggest the presence of only one sub-Carboniferous refractor: i.e. no later arrivals interpreted as refractions from a deeper horizon. The signals recorded at station 50 are consistently atypical of the group: they are low amplitude, complicated and not easily correlated with adjacent stations. This may either be because the station lies close to a postulated basement fault (cf. Figs. 5.35) or because the station was situated on a small Millstone Grit outlier (see Fig. 3.1). Station 49 was sited on the same outlier, and the recorded first breaks are often (a) of lower frequency than the adjacent stations (e.g. the Stoke event), and (b) the P wave coda contains later, high frequency arrivals (e.g. Tunstead C22023), possibly reverberation.

5.6.4 Comments on Interpretation

The interpretation of the SEW profile is summarised by the cartoon of Fig. 5.37. The (Devonian?) sandstones encountered by the Caldon Low borehole are labelled as the Redhouse formation, and have been assumed to underly the

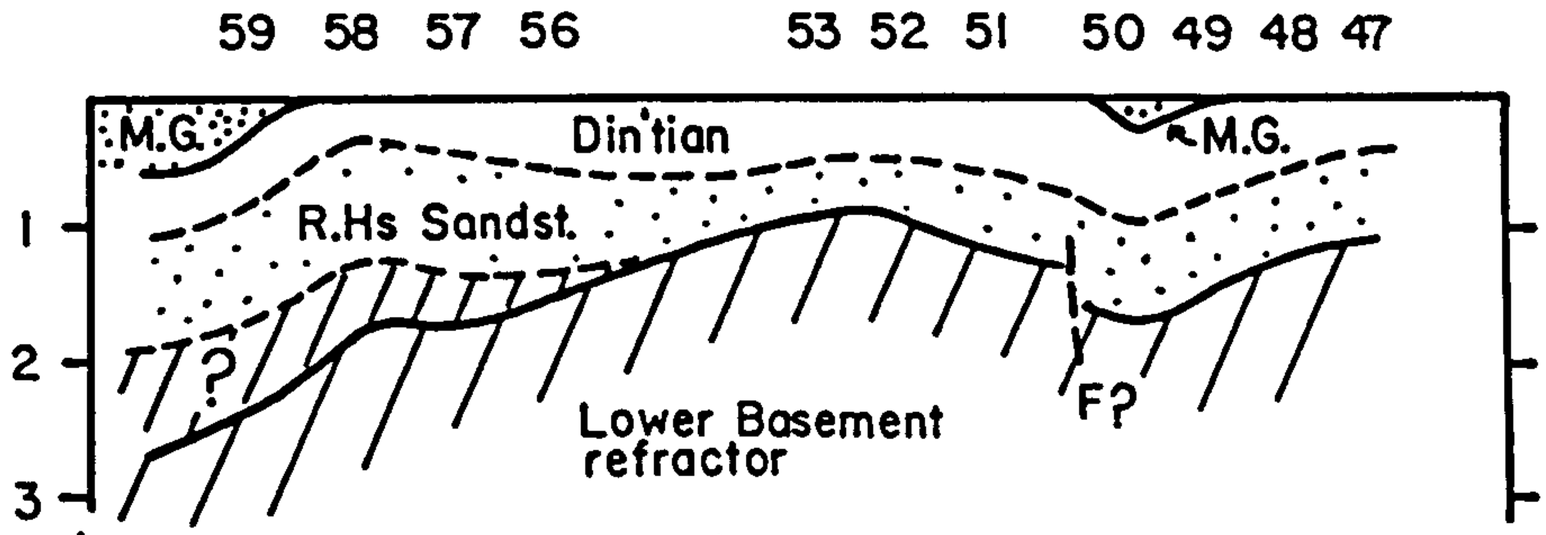

FIG 5-37 Sketch of interpretation — SEW line

length of the line. As the refractor velocities appear very similar to those measured for the north-south profile, the basement is taken to be the same. The arrival time suggests that the shallower refractor to the west also has a similar velocity.

Despite the lower velocity of the basinal limestone-shale sequence than its equivalent massif succession, the shallow Redhouse sandstones have not been considered as a refractive horizon because refractions are not noted for at least 4 km from Cauldon Low, and 6 km from Ballidon quarry, even as later arrivals. The distance at which basement refractions are observed implies a basement about a kilometre deep around stations 52 and 53. This is comparable with the depth of the basement under the massif and thus the basinal region is not necessarily marked by deeper basement.

The surface geology west of the Dovedale Transition is characterised by increasing high amplitude folding towards the west (see geological section, Fig. 3.11), which was possibly syntectonic with the tilt-block mechanism discussed by Miller and Grayson (1982). The general coherency of the basement refractions implies that the basement itself was not involved in this folding, although the Cauldon Low anticline seems to be a basement feature.

The shallower refractor towards the west of the line may correspond to the upper basement refractor to the north of the Bonsall Fault. This horizon either thins through overlap on the older basement, or was largely eroded at the base of the Devonian or Carboniferous. It is possible that the sequence thins completely eastwards, or may subcrop in patches under the southern province: in the basement depression between stations 47 and 52 perhaps.

5.7 General Notes

This interpretation of the seismic refraction data tends to vindicate the notion that the Dome can be divided

into two sub-Dinantian provinces, separated approximately by the line of the Bonsall Fault. To the north the sub-Carboniferous refractor appears to shallow towards Woo Dale. From Woo Dale to Eyam this refractor deepens by some 1.4 km to about 1.7 - 1.9 km, which is consistent with the depth to the Ordovician shales in the Eyam borehole. Thus this upper basement refractor is considered to be Ordovician, although these shales must either overlie the volcanoclastics encountered by the Woo Dale borehole, or vice versa.

In the southern province there is a strong Charnoid influence on the geology, and it is tempting to consider the sub-Carboniferous refractor in this region to be of Charnoid-type material. To the north this lower basement refractor may be downfaulted across the line of the Bonsall Fault by some 1-2 km, depending upon the mean velocity of the Lower Palaeozoic cover. The SEW line seems to be underlain by a similar refractor, although towards the west the lower basement refractor appears to dip beneath another lower Palaeozoic refractor.

Neither basement refractor appears to have any substantial vertical velocity gradient, which might have been expected were the Dome underlain by granodioritic material similar to the intrusions flanking Charnwood Forest (0.5 per sec determined by Whitcombe and Maguire (1981b)). Additionally, the near-surface velocities for the Leicestershire granites are about 4.7 - 4.9 km/s, or 5.2 - 5.4 km/s at a depth of 1 km; these are still lower than the 5.5 - 5.8 km/s determined for the refractors beneath the Dome. However, this does not completely rule out granitic plutons deeper than these data sample: that is, deeper than about 3 km, 'supporting' the Dome.

The velocities determined for the upper basement refractor under the northern province fall within those measured for the Ordovician in the Beckermonds Scar borehole: between 5.4 and 5.8 km/s (Wilson and Cornwell 1982). The velocity of the deeper hidden layer is unknown, though for the lower basement refractor to be shallower than about 4 km the mean velocity must be less than around 5.4 km/s. This

sequence may comprise Cambrian shales, sandstones and quartzites as found in the Dukes Wood borehole (Lees and Taitt 1946). Wills (1978) also postulated that the Carboniferous is underlain by Cambrian to the north and east of the Derbyshire Dome (see Fig. 1.16).

CHAPTER SIX

TIME-TERM ANALYSIS

6.1 Introduction

Having broadly classified and interpreted the arrival times, and roughly defined a working model, the data can now be more rigorously treated by the time-term method described in Section 2.2. The technique is well suited to spatially distributed data such as these, and the network of profiles can be treated together, as well as individually.

This chapter divides into four sections:

1. Application of the method
2. Time-Term solutions for individual profiles
3. Time-Term solutions for grouped profiles
4. General comments on solutions.

6.2 Application of Method

The analysis breaks down into three stages, each executed interactively on the computer: (1) the creation of an observations file, (2) the inversion of the observations matrix, and (3) the solution of the refractor velocity and station time-terms. These stages were considered separately in order to facilitate processing.

The three stages comprise:

(1) Choice of Data and Creation of the Observations File

Obviously for N unknowns there must be at least N observations for a least-squares solution (Willmore and Bancroft 1960), and there must be at least one observation for each shot and station otherwise the observations matrix [A] cannot be constructed (see Equation 2.7). For this

experiment there were sufficient data and no reduction of unknowns was required to satisfy these requirements (see Section 2.2.1).

Quarry blasts were selected from their reduced time graphs on the basis of the following criteria:

(a) The number of stations that observed refractions from the horizon of interest. Normally at least three observations per event were required.

(b) The distribution of observations along the profile; the greater the distribution the better the control on the solution velocity (see comments on reversal below).

(c) The inclusion of stations (and quarry groups) for which there were few observations overall, so they would not be omitted from the analysis.

(d) The quality of the arrival times; obviously the smaller the observational errors the better. Events with anomalous reduced time graphs were avoided.

In order to yield a good estimate of the refractor velocity, the line must be reversed and the observations file needs to consist of events from opposing directions along the profile. Ideally (though not necessarily), the number of observations from each end should balance, since a large number from one direction may bias the least-squares solution velocity. The observations must also be chosen so that the distance over which reversal occurs is as large as possible; if the stations which observed refractions from both directions are close together then the solution velocity might not be reliable.

At least one shot-shot time must be included in the observations file so that the time-terms can be solved uniquely. Since there were no quarry-based seismometers that recorded refracted arrivals (not even station 70 in Tunstead quarry, see Fig. 3.7), this time was estimated using the nearest station to a working quarry. For example, for the north-south line, the nearest basement refractions observed to the timed Ballidon shot (M4035) from the timed Tunstead blast (M5067) were at station 3, about 1.5 km to the east. By estimating

the refractor velocity the required shot-shot time was thus extrapolated from station 3. These shot-shot times were averaged using several events.

(2) Inversion of the Observations Matrix (programme TTINV)

The programme TTINV creates the matrix [A] which links observations with stations (Equation 2.7), and uses the NAG routine FO1ACF to invert [A]'[A], where [A]' is the transpose of [A]. The inverted matrix is then written to Disk.

This stage was executed independently of the calculation of the time-terms because the matrix inversion is common to the analysis whatever model is to be considered, whether constant velocity or velocity gradient. Thus once this step is completed, the time-terms could be calculated for a variety of velocity models.

(3) Calculation of the Solution Time-Terms (programme TIMET)

The solution velocities and time-terms were calculated using the programme TIMET, which employs the Disk files created by TTINV. The data may be solved according to various velocity models: a) a least-squares (uniform) refractor velocity, b) a linear vertical velocity gradient, or c) the refractor velocity can be constrained to a chosen value (uniform or velocity gradient).

If a velocity gradient is required, the user may constrain the gradient by stating a maximum velocity. Constrained or otherwise the solution variance σ_s^2 is minimised using the NAG routine E05JAF (see Section 2.2.3). The best values for the initial velocity and gradient terms are then used to calculate the solution time-terms.

A further option allows the addition of distance increments to each shot-station linkage as a means of iterating the solution.

The output from TIMET includes a full listing of each observation and its solution residual. Observations with

solution residuals greater than three times the standard error may be deleted from the observations file (Bamford, 1976), and steps (2) and (3) repeated for the 'cleaned up' data set.

6.2.1 Quality Check of Solutions

The quality of each solution is expressed in terms of the F ratio between the solution residual variance and the observational error variance, where the nearer this ratio to unity the more statistically similar the solution residuals and observation error populations (see Section 2.2.2). For these solutions, the F ratios have been tested against an F distribution chart, which gives the critical values below which the solution residuals and observational errors can be considered insignificantly different. These critical values depend upon the numbers of observations and unknowns, and upon the level of significance, α, considered, here taken to be the 0.05 probability point (the 95 per cent confidence limit).

Additionally, the ratio between two solution variances can be determined by dividing their F ratios (Fx/Fy). By this means a solution X is significantly different from solution Y if Fx/Fy is greater than the critical value for their respective nunbers of unknowns.

6.2.2 Display of Data

The tables of solutions are augmented by plotting the time-terms against station position along each profile, with time positive downwards to give the effect of depth. In order to avoid congestion, these values are plotted to only two decimal places.

The time-terms are converted to depths according to the relationship given by Equation 2.4:

$$a(h) = \int_{o}^{h} \frac{[V_r(h)^2 - V_o(z)^2]^{\frac{1}{2}}}{V_r(h)V_o(z)} dz$$

where a(h) is the time-term to the refractor at depth h, $V_r(h)$ the refractor velocity immediately below the interface and $V_o(z)$ the velocity structure of the overburden. The most simple depth conversion is for a constant velocity layer over half space, where the depth to the refractor z_o is given by

$$z_o = a_o \frac{V_o V_r}{(V_r^2 - V_o^2)^{\frac{1}{2}}} \qquad (6.1)$$

for time-term a_o. For two layers of thickness z_o, z_1 above a half space, the thickness of the second layer is given by

$$z_1 = \{a_1 \frac{z_o(V_1^2 - V_o^2)^{\frac{1}{2}}}{V_o V_1}\} \frac{V_r V_1}{(V_r^2 - V_1^2)^{\frac{1}{2}}} \qquad (6.2)$$

where a_1 is the time-term to the half space, and V_1 the velocity of the second layer.

The depths are plotted as 45 degree arcs to which the solution refractor surface is tangential.

6.3 Profiles Examined Individually

6.3.1 North-South Line

In Chapter Five it was proposed that the sub-Carboniferous surface of the Dome comprises two refractors of similar velocity. To the south of the Bonsall Fault zone the basement is thought to be of Charnoid-type material, and to the north the limestones are believed to be underlain by a Lower Palaeozoic refractor, possibly Ordovician shales and volcanics. North of the Bonsall Fault zone, the Charnoid-type refractor is thought to be present at depth, and has been traced through looking at later arrivals.

This model (see Fig. 5.8) is here tested by time-term analysis in four stages: (a) the refracted arrivals for the whole line are considered as a single data set; then observations from (b) north and (c) south of the Bonsall Fault are treated separately; and finally (d) later arrivals are incorporated to investigate lower basement refractions along the entire profile.

(a) Single Refractor

From the reduced time graphs discussed in Section 5.3 it was apparent that first arrival refractor velocities of 5.5 - 5.7 km/s were observed the length of the north-south line, and without any significant vertical velocity gradient. This supported the simple model of Fig. 5.8 where a continuous basement refractor was assumed the length of the line. At a first approximation the reduced time graphs for many events portray this refractor structure, and which can be used to give excellent reversal between stations 4 and 15.

A first solution considered 213 observations from 30 events, of which 14 were from northern quarries. The only completely unreversed stations were 1 and 18; basement refractions at station 18 were observed for shots from the Dow Low group of quarries only. The uniform solution velocity was 5.57 ± 015 km/s with an F ratio of 1.71. At the $\alpha = 0.05$ significance level the critical value is 1.58, so this result is significant. However, when twelve observations with a solution residual greater than 0.06 s were removed, the F ratio decreased to 1.38, for which the solutions residuals are statistically insignificantly different from the observational errors. This Solution A defined a least-squares velocity of 5.59 ± 012 km/s (see Table 6-1). A further solution allowed an unconstrained vertical velocity gradient, but defined no gradient term and exactly the same uniform velocity as Solution A.

The time-terms defined by Solution A are plotted in Fig. 6.1 alongside depths calculated by assuming a mean over-

Table 6-1 Time-terms in seconds

Station	Solution A Time term	Error	Depth km	Solution B Time term	Error	Depth km	Solution C Time term	Error	Depth (a)km	Depth (b)km	Solution D Time term	Error	Depth km
1	0.169	0.011	2.42				0.157	0.009	1.98	1.5	0.15	0.01	1.49
61							0.235	0.005	2.96	2.24	0.229	0.005	2.28
2	0.243	0.005	3.48				0.237	0.005	2.98	2.26	0.236	0.006	2.35
49							0.182	0.01	2.29	1.74	0.182	0.01	1.81
3	0.136	0.007	1.95				0.131	0.006	1.65	1.65	0.133	0.006	1.8
69							0.156	0.006	1.96	1.96	0.161	0.005	2.18
4	0.231	0.008	3.31				0.22	0.006	2.77	2.77	0.22	0.006	2.98
5	0.212	0.005	3.04				0.199	0.006	2.5	2.5	0.199	0.006	2.7
6	0.173	0.006	2.48				0.15	0.006	1.89	1.89	0.15	0.006	2.04
7	0.142	0.01	2.04				0.133	0.011	1.67	1.67	0.133	0.011	1.8
8	0.104	0.01	1.49	0.109	0.008	1.6					0.208	0.015	2.82
9	0.077	0.013	1.1	0.07	0.012	1.03					0.273	0.014	3.7
10	0.076	0.004	1.09	0.089	0.005	1.31					0.23	0.01	3.12
11	0.074	0.005	1.06	0.086	0.005	1.26					0.249	0.015	3.38
12	0.045	0.007	0.65	0.054	0.006	0.79					0.25	0.012	3.39
13	0.007	0.001	0.1	0.009	0.002	0.13					0.216	0.012	2.93
14	0.027	0.005	0.39	0.03	0.007	0.44					0.235	0.013	3.19
15	0.01	0.005	0.14	0.01	0.006	0.15					0.234	0.023	3.17
18	0.107	0.012	1.53	0.11	0.012	1.62							
	V_S= 5.59±0.012km/s F ratio 1.38			V_S= 5.55±0.034km/s F ratio 1.36			V_S= 5.71±0.038km/s F ratio 1.97				V_S= 5.63±0.024km/s F ratio 2.04		

FIG 6-1

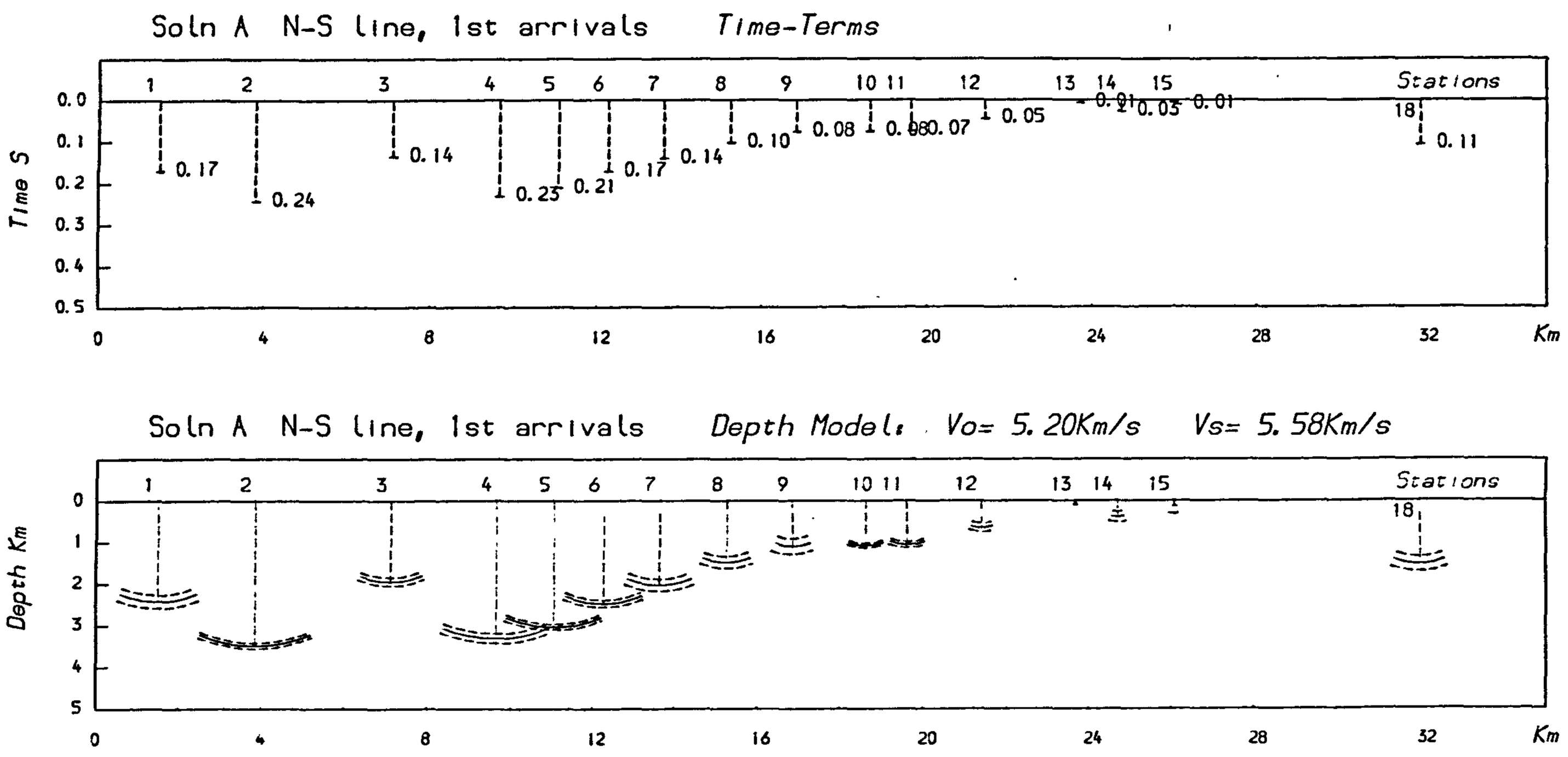
Soln A N-S line, 1st arrivals Time-Terms
Time S
Stations
1 2 3 4 5 6 7 8 9 10 11 12 13 14 15 18
0.17 0.24 0.14 0.25 0.21 0.17 0.14 0.10 0.08 0.08 0.07 0.05 0.01 0.03 0.01 0.11
0.0 0.1 0.2 0.3 0.4 0.5
0 4 8 12 16 20 24 28 32 Km
Soln A N-S line, 1st arrivals Depth Model: Vo= 5.20Km/s Vs= 5.58Km/s
Depth Km
Stations
1 2 3 4 5 6 7 8 9 10 11 12 13 14 15 18
0 1 2 3 4 5
0 4 8 12 16 20 24 28 32 Km

burden velocity of 5.2 km/s, estimated from the T-X curves for the wide-angle reflections discussed in Section 5.3.3. Between stations 4 and 14, where most of the data are reversed, the refractor appears to dip southwards at about 10 degrees. Thus the solution velocity may be $1/\cos\theta$ times the true refractor velocity, for angle of dip θ, and can be corrected to 5.5 km/s. Since this interface seems approximately planar, minimal structural influence is expected for the solution velocity gradient, and none occurs.

(b) North of the Bonsall Fault

The time-terms for Solution A reiterate the picture of a shallow basement refractor between stations 13 and 15 which can be tentatively correlated with the pre-Carboniferous volcanics in the Woo Dale borehole, as suggested in Chapter Five. Since the refractor in this region is so shallow, refractions from it are observed at short distances, so that the section of line north of the Bonsall Fault is well reversed.

Initially, 160 observations from 31 shots (sixteen from the north) were used, and defined a solution velocity of 5.53 ± 0.37 km/s with an F ratio of 1.84, which exceeds the critical value of 1.58 at the $\alpha = 0.05$ significance level. Seven observations with a solution residual greater than three times the mean error were deleted from the data set, for which Solution B (see Table 6-1) then gave a least-squares velocity of 5.55 ± .034 km/s with an F ratio of 1.36. This F ratio is less than the critical value so the solution residuals are insignificantly different from the observational errors. An unconstrained vertical velocity gradient solution yielded a velocity of 5.37 + .19z km/s with an F ratio of 1.3. This solution is insignificantly different from the uniform velocity solution (Fx/Fy=1.05, less than the critical value of 1.35), and the gradient may either be allowed because of short wavelength refractor structure, or because of the broad anticlinal crest between stations 8 and 18.

The time-terms for Solution B are plotted in Fig. 6.2 and converted to depths assuming an average overburden velocity of 5.2 km/s, although this velocity may be greater in the vicinity of Woo Dale where the Dinantian sequence is predominantly dolomite. The solution time-terms are very similar to those of Solution A, and any differences are probably due to the choice of different events used in the analysis.

(c) South of the Bonsall Fault

Basement refractions from southern quarries close to the line are only observed north of station 5 because (a) there are no on-line quarries south of Ballidon, and (b) because the pre-Carboniferous surface seems to be deeper along this section of the line than to the north (see Solution A, Fig. 6.1). Consequently this segment of the north-south line is not as well reversed as the stations north of the Bonsall Fault, although basement refractions from the quarries of Matlock and Cauldon have been observed north of station 1.

A first solution employed 106 observations from 20 events, ten apiece from north and south, and included five events from the 1981 experiment. This solution defined a least-squares velocity of 5.75 ± .041 km/s with an F ratio of 2.98, which is greater than the critical value of 1.68. With the deletion of ten observations with solution residuals greater than 0.06s, and the addition of thirty more, Solution C (Table 6-1) gave a uniform solution velocity of 5.71 ± .038 km/s with an F ratio of 1.97. This result is still significant and suggests unresolved short wavelength or azimuthally dependent basement structure.

The data also allow an unconstrained vertical velocity gradient of 5.48 + .178z km/s (F ratio 1.9), probably because any structurally related residuals are absorbed by the velocity gradient term. This solution is, however, insignificantly different from the uniform velocity solution (Fx/Fy = 1.04, less than the critical value of 1.35 at the $\alpha = 0.05$ significance level).

FIG 6-2

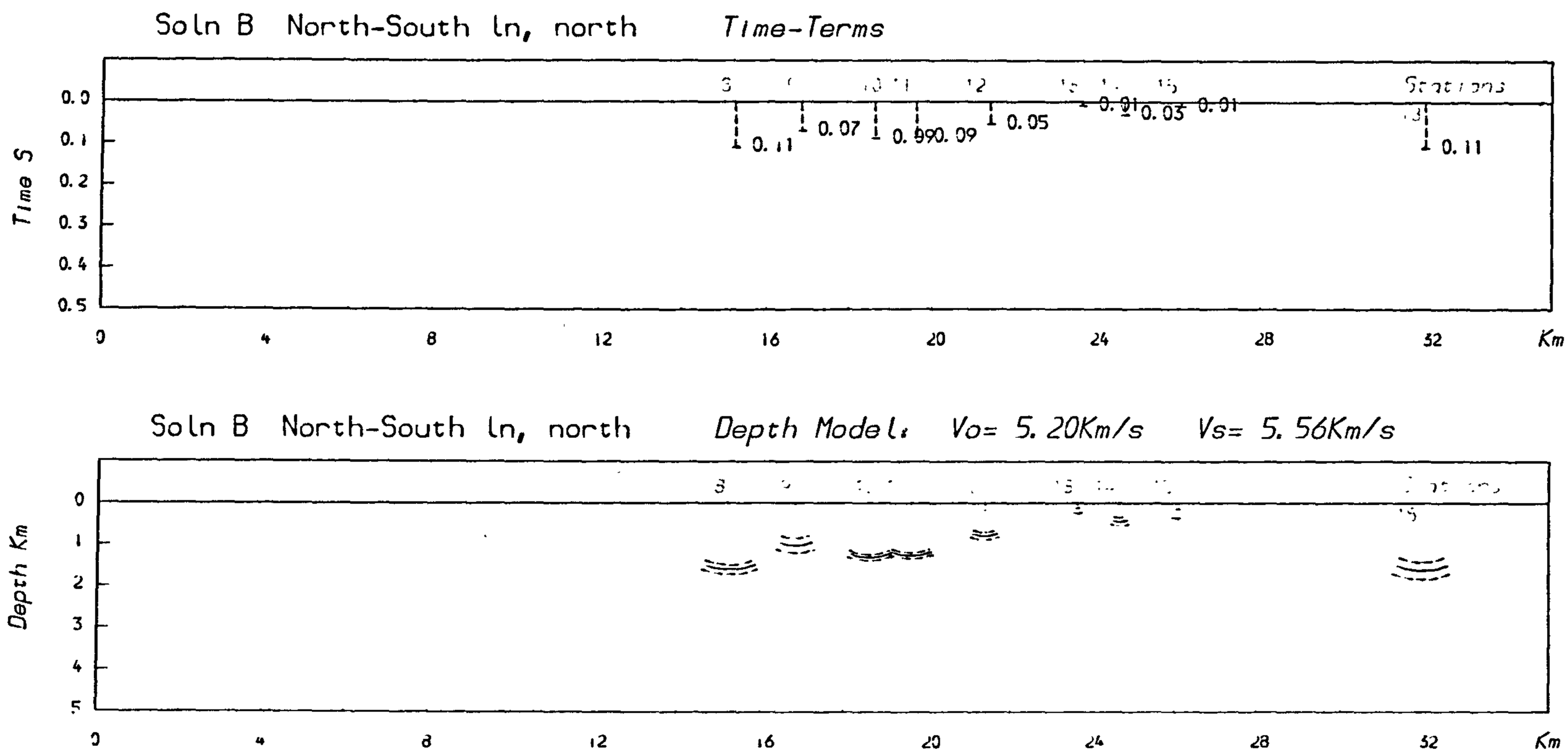
Soln B North-South ln, north Time-Terms
Time S
0.0
0.1
0.2
0.3
0.4
0.5
0.11
0.07
0.09
0.05
0.01
0.03
0.01
0.11
0
4
8
12
16
20
24
28
32
Km
Soln B North-South ln, north Depth Model: Vo= 5.20Km/s Vs= 5.56Km/s
Depth Km
0
1
2
3
4
5
0
4
8
12
16
20
24
28
32
Km

Plotting the time-terms for Solution C (Fig. 6.3), the refractor topography appears more irregular than that north of the Bonsall Fault (cf. Fig. 6.2). The three stations from the DASED1 line (viz 61, 49 and 69) concord with the structure manifest by the 1979 stations. (Station 69 was about a kilometre from station 3, and not as close as this plot suggests (see Fig. 3.1)). These time-terms are converted to depths

(a) by assuming an overburden velocity of 5.2 km/s throughout, and

(b) by using a mean overburden velocity of 4.9 km/s for stations situated within the basinal facies. This velocity has been estimated from the T-X plots of data from the SEW profile (see Section 5.2). If sandstones exist beneath the limestone, it has been assumed that their velocity is less than 5 km/s.

Obviously the larger the velocity contrast between overburden and basement, the shallower the calculated depths.

Since most data from this segment of the north-south line are reversed between stations 5 and 7, where the refractor appears to dip southwards at between 10 and 12 degrees, it is possible that the least-squares solution velocity is $1/\cos\theta$ times the true refractor velocity. If so then the solution velocity can be corrected to about 5.55 - 5.62 km/s.

(d) Lower Basement Refractor, Whole Profile

To follow the lower basement refractor north of the Bonsall Fault requires later arrival times (see Section 5.4.2). These are generally less reliable than those obtained from first arrivals, and there are consequently fewer of them, most of which from southern quarry blasts.

A first solution indiscriminantly used 259 observations from 41 events, of which 23 were from the north. The set included six events from southern quarries with later arrival times. These data gave a least-squares solution velocity of 5.65 ± .03 km/s with an F ratio of 3.38, which is significantly

FIG 6-3

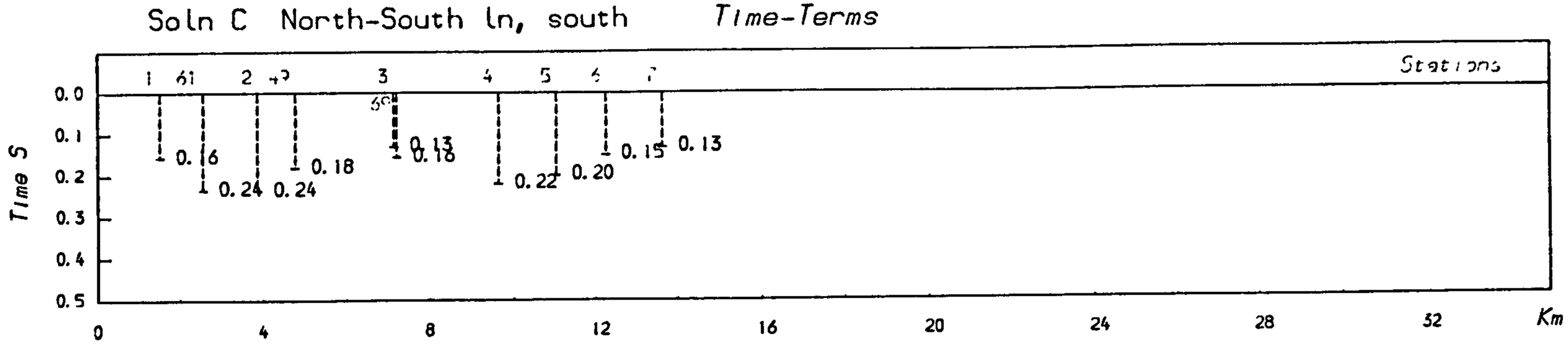
Soln C North-South ln, south
Time-Terms
Stations
Time S
0.0
0.1
0.2
0.3
0.4
0.5
1
61
2
3
4
5
6
7
0.16
0.24
0.24
0.18
0.13
0.18
0.22
0.20
0.15
0.13
0
4
8
12
16
20
24
28
32
Km

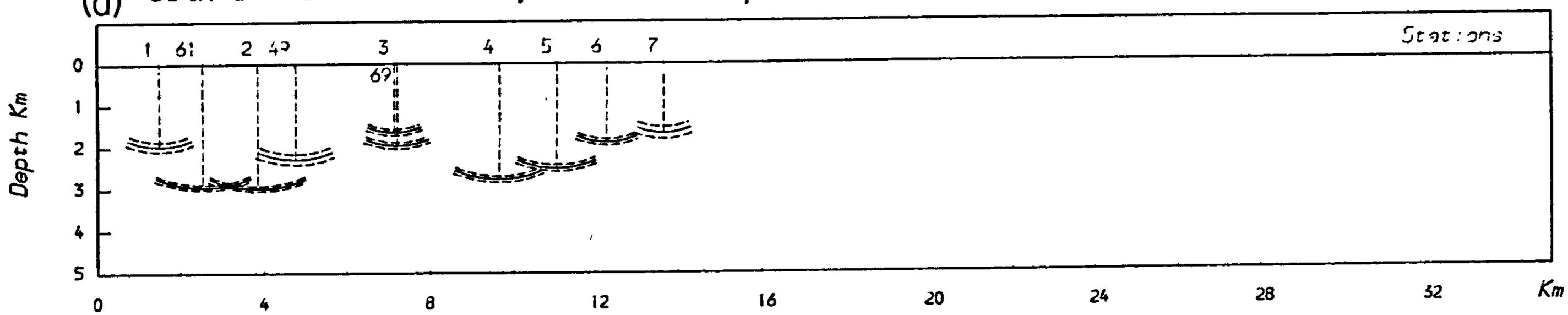
(a) Soln C North-South ln, south
Depth Model. Vo= 5.20Km/s Vs= 5.71Km/s
Stations
Depth Km
0
1
2
3
4
5
1
61
2
3
4
5
6
7
0
4
8
12
16
20
24
28
32
Km

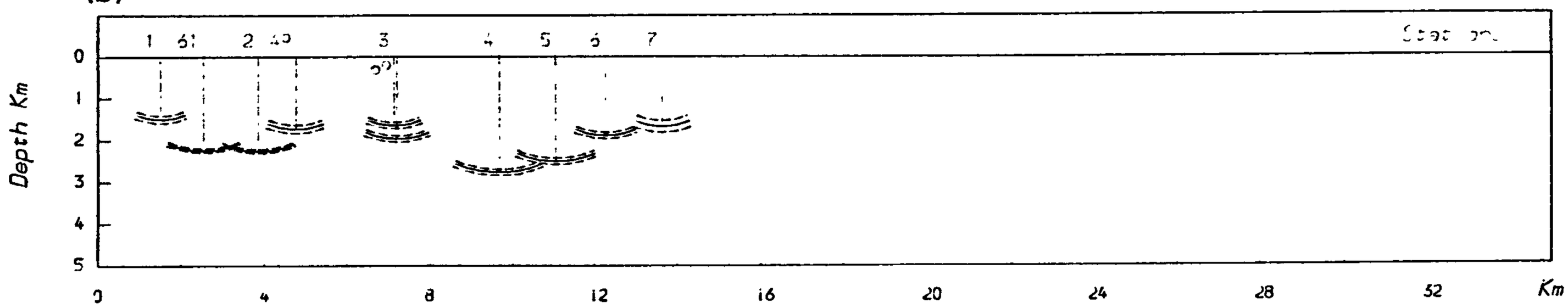
(b) Soln C North-South ln, south
Depth Model. Vo= 4.90Km/s Vs= 5.71Km/s
Depth Km
0
1
2
3
4
5
1
61
2
3
4
5
6
7
0
4
8
12
16
20
24
28
32
Km

greater than the critical value of 1.47 at the $\alpha = 0.05$ significance level. Solution D used the better 160 observations of this set, including two shots from Doveholes quarry with picked later arrival times. There were 80 observations from each direction. This solution defined a least-squares velocity of 5.63 ± .024 km/s with an F ratio of 2.04 (see Table 6-1). Although this solution is significantly different from the first solution (Fx/Fy = 1.65, greater than the critical value of 1.35), the F ratio is still greater than the critical value of 1.68. As well as unresolved short wavelength structure, lack of fit may also be due to the poorer resolution of the later arrivals.

The data also permit an unconstrained vertical velocity gradient of 5.46 + .15z km/s, the F ratio for which was 1.84. This result is insignificantly different from the uniform velocity solution (Fx/Fy = 1.1), and is probably induced through structurally related error.

The time-terms for Solution D are plotted in Fig. 6.4 with depths calculated for two uniform overburden velocities: 4.9 km/s for stations in the Dovedale region and 5.2 km/s for stations on the massif. The mean velocity of the Lower Palaeozoic intermediate layer to the north of the Bonsall Fault is likely to be greater than 5.2 km/s, in which case the depths to the lower basement refractor north of station 7 are probably underestimated. Note that the basement fault is smoothed by the averaging of the station delay times; the effect is best illustrated by the simulated data example of Smith et al. (1966; Fig. 6.5).

General Remarks - North South Line Solutions

The solution velocities for the two sub-Carboniferous refractors to north and south of the Bonsall Fault were 5.55 and 5.7 km/s respectively. The solution velocity for the southern segment may be too great because of poor reversal, in which case the solution velocity for the lower basement for the entire line, 5.63 km/s, may be closer to its true

FIG 6-4

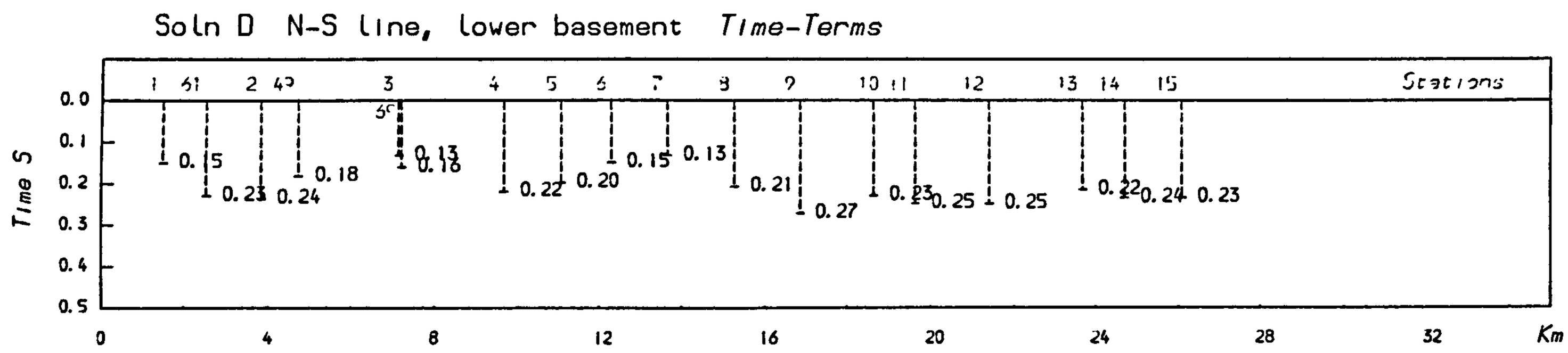
Soln D N-S line, lower basement Time-Terms
Stations
Time S
0.0
0.1
0.2
0.3
0.4
0.5
0
4
8
12
16
20
24
28
32
Km

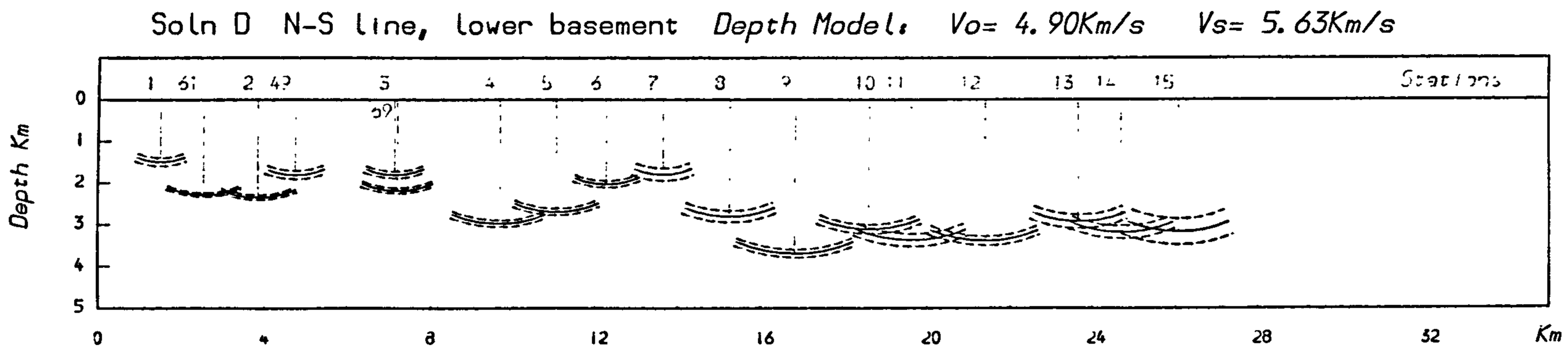
Soln D N-S line, lower basement Depth Model. Vo= 4.90Km/s Vs= 5.63Km/s
Stations
Depth Km
0
1
2
3
4
5
0
4
8
12
16
20
24
28
32
Km

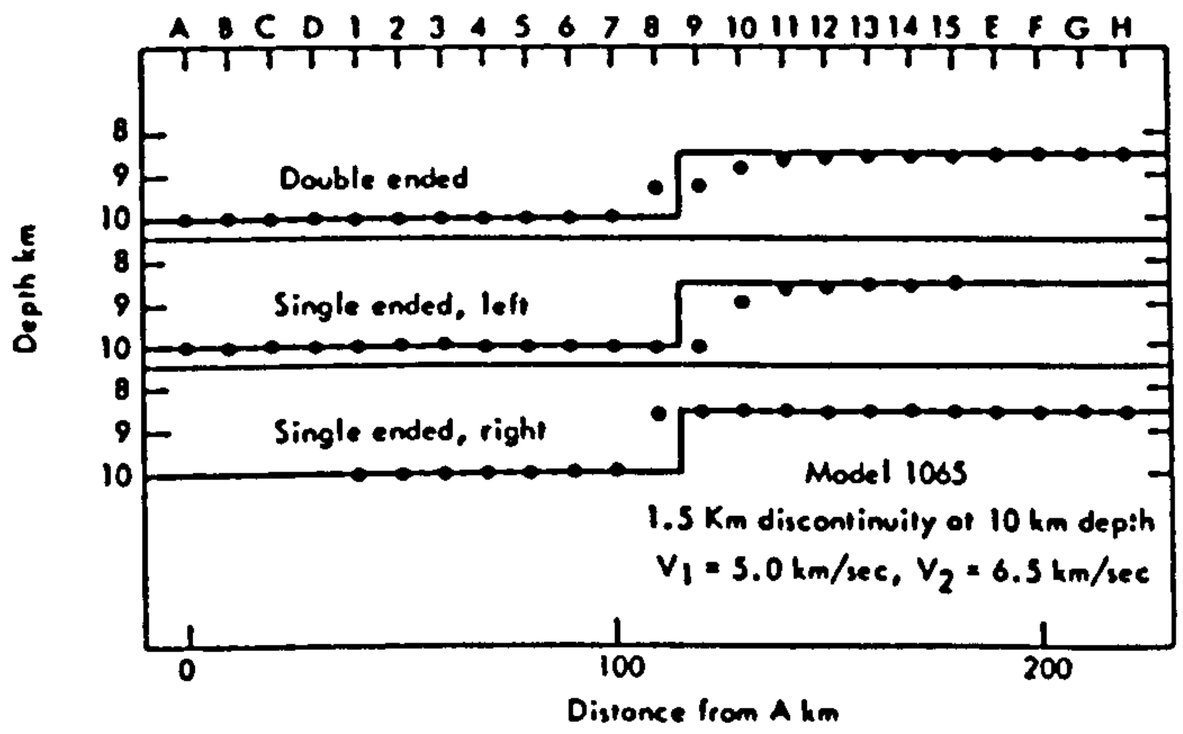

FIG 6-5 Theoretical time-term results across 1·5km fault (from Smith et al.(1966))

velocity. The solution which assumed a continuous refractor the length of the line yielded a uniform velocity of 5.59 km/s: approximately the mean of the two basement refractors.

The choice of events for any one solution was found to have less influence upon the solution velocity than on the time-terms for individual stations. This was particularly true where fewer than five observations were used from a station. The stations astride of the Bonsall Fault (viz 7 to 9) were most prone to choice of observations because there were fewer reliable observations than for other stations (cf. Fig. 5.12).

The quality of solutions for upper basement refractions were consistently better than those for lower basement refractions. This may be because the structure of the sub-Carboniferous surface is not as irregular to the north of the Bonsall Fault as it appears to the south, and thus there is less short wavelength structure to remain unresolved. The continuous refractor Solution A produced F ratios lower than the critical value, possibly because the observations used were drawn from the events which best defined the refractor structure.

6.3.2 Northern East-West Profile - Upper Basement Refractor

This profile was difficult to reverse adequately as most observations originated from quarries around Buxton to the west of the line. Eastern sources comprised the quarries of Stoney Middleton and Hope Valley only. Stations 25 to 27, and those west of stations 37 were completely unreversed. Nearly all observed refracted arrivals are thought to originate from the Lower Palaeozoic horizon defined by Solution B. Some first arrivals at the western end of the profile have been interpreted as lower basement refractions, and it is possible that some 'upper basement' refractions are actually from the deeper refractor (see Section 5.5.1). Another problem regarding choice of observations for this line concerns the danger

of including in the analysis high velocity refractions from dolomitic horizons within the limestone sequence. These had to be carefully discriminated against.

The lower basement refractions observed by this profile are discussed in Section 6.4.2.

A first solution employed 126 observations from 13 events, five of which were from the eastern end of the line. This solution defined a least-squares velocity of 5.46 ± .035 km/s with an F ratio of 4.36, which is significantly greater than the critical value of 1.68 at the $\alpha = 0.05$ significance level. From these data, two events whose solution residuals increased systematically from west to east by over 0.12s were removed, and a further two events from Cauldon Low quarries included. Thus, Solution E (see Table 6-2) yielded a uniform solution velocity of 5.47 ± .025 km/s with an F ratio of 2.19. This result is significantly different from the first solution ($F_x/F_y = 1.99$, i.e. greater than the critical value of 1.35), but the solution residuals are still significantly different from the observational errors. The solution velocity may be lower than that defined by Solution B either because the upper basement refractor is anisotropic, or because the data are biased towards events from the west (predominantly down-dip travel times).

A further solution allowed an unconstrained vertical velocity gradient, but failed to define one and gave the same uniform velocity as Solution E. Thus although the F ratio for Solution E was significant, any structurally induced error might not be great enough for it to be included in the velocity gradient term. Although the solution time-terms suggest a broad anticlinal structure (Fig. 6.6), most data are reversed from stations 34 to 27, between which the refractor is approximately uniformly dipping and expected to induce little structural effect on a velocity gradient solution.

The time-terms for Solution E are converted to depths in Fig. 6.6 using a mean overburden velocity of 5.2 km/s,

Table 6-2 Time-terms in seconds

Solution E				Solution F				Solution G			
Station	Time term	Error	Depth km	Station	Time term	Error	Depth km	Station	Time term	Error	Depth km
25	0.2	0.016	3.35	14	0.03	0.008	0.45	47	0.095	0.025	1.21
26	0.232	0.018	3.89	62	0.022	0.012	0.33	48	0.126	0.015	1.6
27	0.105	0.007	1.76	63	0.024	0.011	0.36	49	0.18	0.01	1.73
28	0.124	0.008	2.08	64	0.052	0.005	0.77	50	0.135	0.009	1.29
29	0.134	0.006	2.25	65	0.024	0.009	0.36	51	0.124	0.008	1.19
30	0.133	0.008	2.23	66	0.031	0.006	0.46	52	0.104	0.004	1.0
31	0.091	0.005	1.53	67	0.044	0.008	0.65	53	0.098	0.005	0.94
32	0.078	0.013	1.31	68	0.102	0.008	1.52				
33	0.052	0.004	0.87					56	0.273	0.008	2.62
(14)34	0.03	0.004	0.5					57	0.277	0.008	2.66
35	0.047	0.007	0.79					58	0.342	0.005	3.28
36	0.073	0.009	1.22					59	0.452	0.012	4.34
37	0.107	0.010	1.79								
38	0.104	0.009	1.74								
39	0.114	0.010	1.91								
40	0.117	0.008	1.96								
41	0.161	0.012	2.7								
42	0.139	0.013	2.33								
V_S= 5.47±0.025km/s F ratio 2.19				V_S= 5.55±0.03km/s F ratio 1.91				V_S= 5.7±0.035km/s F ratio 2.31			

FIG 6-6

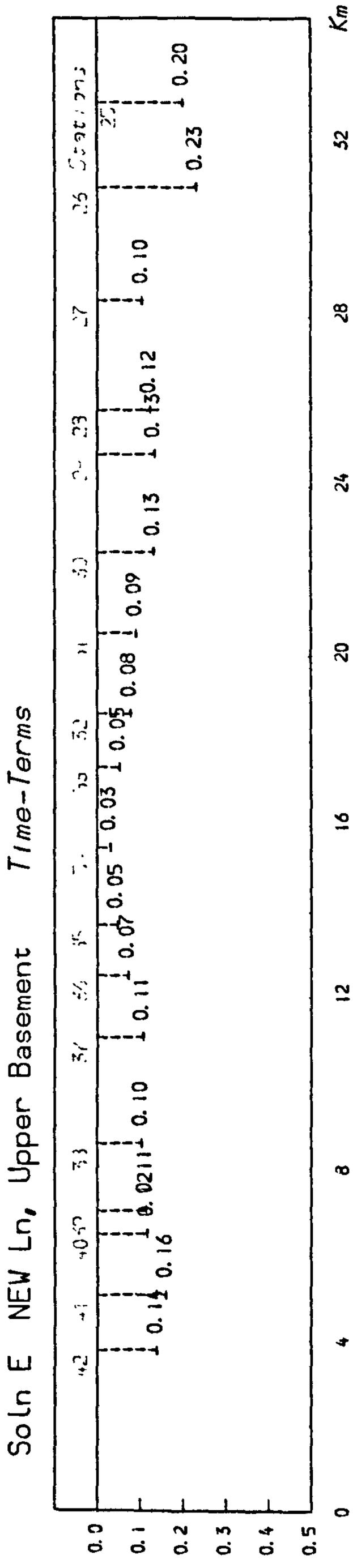
Time-Terms
Km
52
0.20
0.23
0.10
0.05
0.03
0.08
0.09
0.13
0.12
0.07
0.11
0.16
0.14
20
16
12
8
4
0
0.0
0.1
0.2
0.3
0.4
0.5
Time S
Depth Model: Vo= 5.20Km/s Vs= 5.47Km/s
So Lincoln E NEW Ln, Upper Basement
Depth Km
0
1
2
3
4
5

taken from the wide-angle reflection curves discussed in Section 5.5.1. Since no accurate end-to-end time could be determined, the time-terms have been baselined to the value defined for station 14(34) by Solutions A and B. For this model, the depth to the refractor at station 28, about a kilometre from Eyam borehole, is given as 2.08 km. However, if the Solution B velocity of 5.55 km/s is used instead of 5.47 km/s, this depth becomes 1.84 km, which is close to the depth at which the Ordovician shales were encountered (1.8 km). Thus it seems likely that these shales and the upper basement refractor are equivalent.

Although the increase in time-terms between stations 27 and 26 corresponds with the Edale Trough to the east, the estimated depths to the refractor are probably exaggerated (a) because of the lower velocity cover of Millstone Grit, and (b) because there might be a lateral decrease in limestone velocity into the Trough due to a facies change from massif to basinal. The Goyt Trough is also manifest in the time-terms west of station 38, and these values suggest the Goyt Trough is not as deep as the Edale Trough. Similarly, the cover of Millstone Grit means these depths are probably overestimated.

6.3.3 DASED2 - Upper Basement Refractor

All first arrivals interpreted as refractions for the DASED2 profile originated from the upper basement refractor. Reversal was between the quarries around Buxton and those of Shining Bank and Matlock, although far more events detected were from the north. Accordingly, the data used in the analysis were balanced to unbias the reversal.

The first solution used 71 observations from 14 events (seven in each direction, and about 35 observations apiece), and defined a uniform velocity of 5.558 ± .034 km/s with an F ratio of 2.66, which is greater than the critical value of 1.95. However, by removing three observations whose solution

FIG 6-7

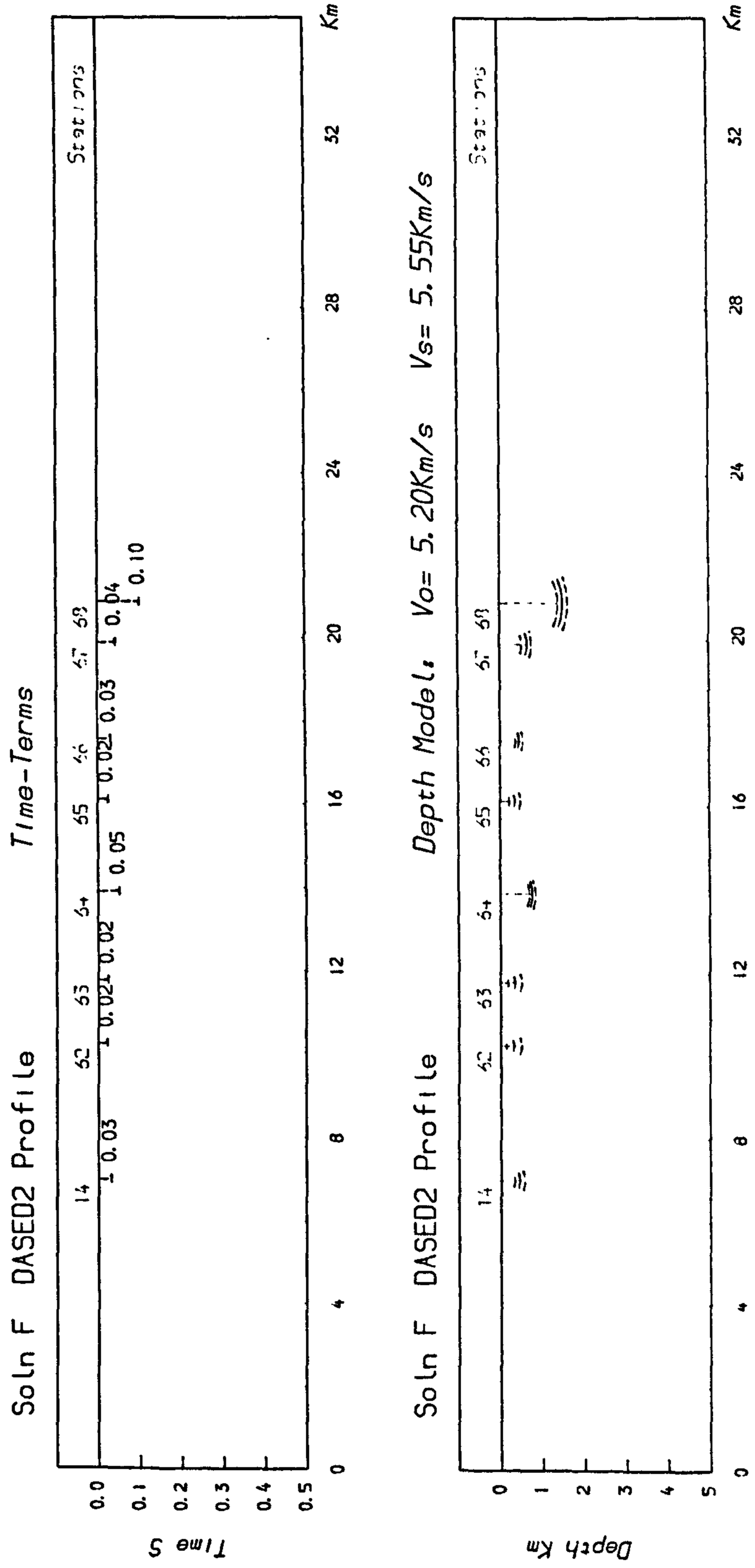
Time-Terms
DASED2 Profile
Soln F
Time S
0.0
0.1
0.2
0.3
0.4
0.5
0
4
8
12
14
52
53
54
0.03
0.02
0.01
0.05
0.04
0.10
16
20
24
28
32
Km
Depth Model, Vo= 5.20Km/s Vs= 5.55Km/s
Depth Km
0
1
2
3
4
5
55
56
57
58

residuals were greater than 0.055s, Solution F (see Table 6-2) gave a least-squares velocity of 5.55 ± .03 km/s with an F ratio of 1.91, which is insignificant. A solution which allowed an unconstrained vertical velocity gradient defined exactly the same velocity, without a gradient term.

The time-terms for this solution are plotted in Fig. 6.7 with depths calculated using a mean overburden velocity of 5.2 km/s. The implied refractor surface is only gently dipping south-eastwards so that the solution velocity must be quite close to the true refractor velocity, from which there is also minimal structural influence. The principal feature of the depth section is the increase in time-terms between stations 67 and 68, where the limestone dips beneath the Millstone Grit in the Stanton Syncline (see Fig. 1.9). Thus the increase in time-term for station 68 may be partly due to the cover of Millstone Grit, and also any lateral facies change in the Dinantian.

6.3.4 Southern East-West Line - Lower Basement Refractor

Like the NEW line, most data from sources close to the line are from the west (viz the quarries around Cauldon), while there are proportionally few quarry blasts that were considered from the east. Part of this problem was due to the largely inoperable eastern stations. However, there are ample broadside events from the quarries around Buxton, and the Stoke-on-Trent tremors provide good seismic sources some 25 km to the west of the line.

The Carboniferous is thought to be underlain by a Charnoid-type refractor for much of the line. There is evidence for a shallower (Lower Palaeozoic?) refractor thinning from the west to pinch out by station 53, although there are insufficient data to consider it for time-term analysis. The lower basement refractor itself is principally reversed by on-line events between stations 47 and 53, though the Stoke tremors reverse the line between stations 49 and 59.

The fewest observations of basement refractions are for eastern stations: there are none for stations 43 to 46, and only three observations each for 47 and 48 are recorded. All these were included in the first solution which employed 96 observations from 17 events, of which five each were from the east and west, and the remaining seven broadside from the north. This solution defined a least-squares velocity of 5.71 ± .04 km/s with an F ratio of 3.25. Taking out four observations with solution residuals greater than 0.055 s (including one observation at station 47), Solution G (Table 6-2) defined a uniform velocity of 5.7 ± .035 km/s with an F ratio of 2.31. This result is significant at the α=0.05 significance level (critical value 1.68), and implies unresolved refractor structure. The solution velocities are similar to those defined by Solution C for the southern half of the north-south line. Thus the basement velocity does not appear to be azimuthally dependent.

Structurally related solution residuals also probably influence the unconstrained vertical velocity gradient solution, which defined a velocity of 5.48 + .15zkm/s, with an F ratio of 2.09. This solution is insignificantly different from the uniform velocity solution (Fx/Fy = 1.1, less than the critical value of 1.35). When the time-terms for solution G are plotted (Fig. 6.8), a broad anticlinal structure is apparent, so it is possible that the velocity gradient is induced by this feature. Most data are reversed between stations 49 and 53 where the refractor appears to dip uniformly eastward, so the least-squares solution velocity may be similar to the true refractor velocity.

The time-terms are converted to depths assuming a mean overburden velocity of 4.9 km/s within the basinal facies and 5.2 km/s on the massif, although such an abrupt division is unlikely. The depths given for station 59 might be over-estimated due to the cover of lower velocity Millstone Grit. The Millstone Grit outlier between stations 49 and 50 (see Fig. 3.1) is probably too thin (less than 150 m) to have a pronounced effect on the time-terms. The values for station

FIG 6-8

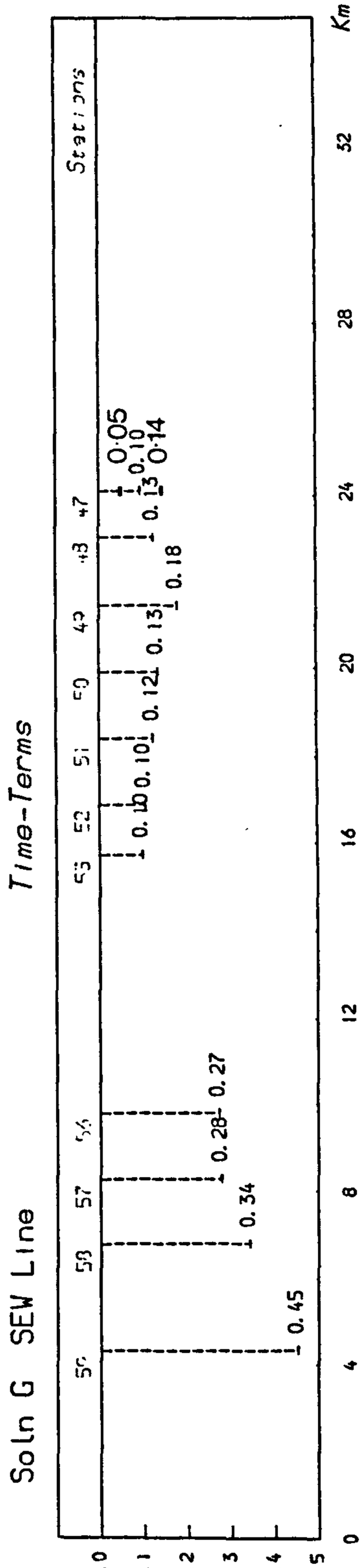
Time-Terms
Station
Km
52
28
0.16
0.10
0.12
0.13
0.18
0.05
0.10
0.13
0.14
16
20
24
Solution G SEW Line
56
58
57
54
0.45
0.34
0.28
0.27
4
8
12
0.0
0.1
0.2
0.3
0.4
0.5
0
Time S

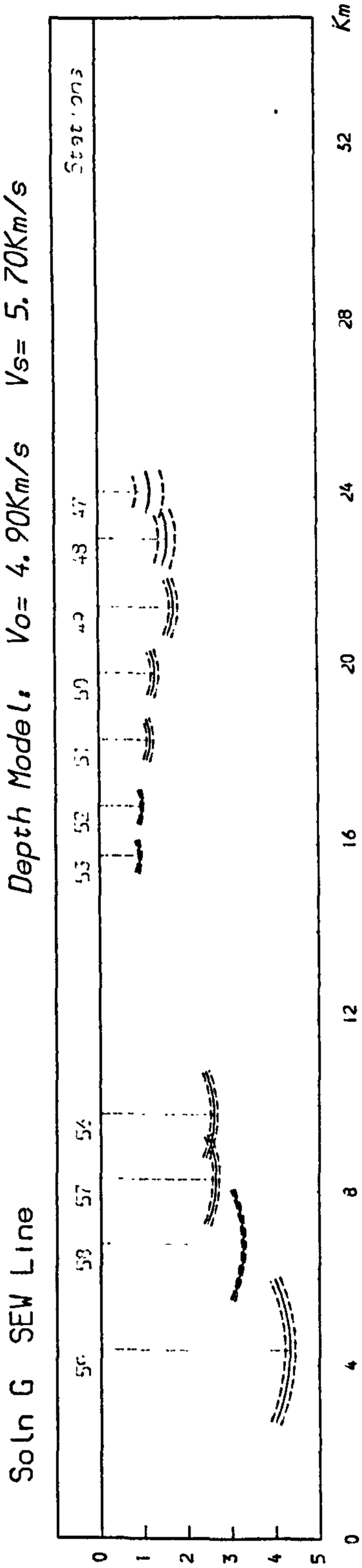
Depth Models Vo= 4.90Km/s Vs= 5.70Km/s
Station
Km
52
28
20
24
Solution G SEW Line
56
58
57
54
4
8
12
0
1
2
3
4
5
Depth Km

47 are given for three solutions using different permutations of its three observations; these time-terms vary between 0.059 and 0.132s.

6.4 Multiple Profile Analyses

The two advantages of solving time-terms for more than one profile at a time are: firstly that the solution time-terms for each line become tied into each other through common stations, and secondly that the observations become more spatially distributed, such that the solution velocities average between the constituent profiles.

The data have been grouped according to the respective refractors they observe. Thus there are two data sets:

1. Lower Palaeozoic: first arrival refractions from all stations north of the Bonsall Fault zone: viz North-South stations 7-18, and all stations from NEW and DASED2.
2. Charnoid-type basement: first arrival refractions from all stations south of the Bonsall Fault zone: viz North-South line stations 1-7, and all stations from the SEW profile. Mainly later arrivals observed north of the Bonsall Fault zone except for a few first arrivals from the western end of the NEW profile.

Owing to limitations of the NAG matrix inversion routine used, it was not possible to analyse all the data employed for the single lines solutions. Consequently the best data from each profile were chosen without biasing the observations in any one direction.

6.4.1 Lower Palaeozoic Refractor

Station 14 (re-occupied as station 34) was common to each of the three profiles grouped for these solutions. As the Lower Palaeozoic is quite shallow in the region of Woo Dale, upper basement refractions were observed at all the stations concerned, though stations 18, 25, 26 and 38 to 42 were unreversed.

Initially, 32 events (total 65 unknowns) comprising 187 observations were used of which 100 were from the NEW profile, 40 from DASED2 and 42 from the north-south line. These gave a uniform solution velocity of 5.46 ± .03 km/s (F ratio 3.99), but it was feared that the solution was too biased towards data from the NEW profile. Instead, a new data set of 218 observations was constructed with approximately 70 observations from each constituent profile. This solution defined a least-squares velocity of 5.5 ± .028 km/s with an F ratio of 2.91, which is greater than the critical value of 1.47. By taking out twelve observations whose solution residuals were greater than 0.06s, Solution H (see Table 6-3) defined a velocity of 5.53 ± .026 km/s with an F ratio of 2.04. This solution is also significant, and the lack of fit may be mainly due to data from the NEW line, the solutions for which were also significant, unlike those for data from the north-south and DASED2 lines (cf. Solution F with Solutions B and E).

The time-terms for Solution H are plotted in Figs. 6.9a-c. There are minor differences with the time-terms defined by the single line solutions, but these are probably more due to the choice of differing observations rather than the act of solving all lines together. These values have been converted to depths (a) by considering a uniform velocity overburden of 5.2 km/s, and (b) by allowing for any cover of lower velocity Millstone Grit, by which

$$d\left(\frac{1}{V_{mg}} - \frac{1}{V_o}\right)$$

has been subtracted from each station time-term where d is the thickness of Millstone Grit (taken from borehole information and geological sections), V_{mg} its velocity, and V_o the mean overburden velocity. For case (b), V_o has also been taken as 5.4 km/s for stations close to Woo Dale, which are assumed to be mostly underlain by Woo Dale Dolomite: viz stations 13 to 15, 33 to 35, 62 and 63. This overburden velocity bring the depth of the refractor for station 15 close to the depth at which the Woo Dale volcanics were encountered. These depths are listed in Table 6-3.

Table 6-3

Solution H

Station	Time-term (s)	Error	Depth(a) km	Depth(b) km
8	0.11	0.015	1.68	1.68
9	0.091	0.006	1.39	1.39
10	0.086	0.006	1.31	1.31
11	0.083	0.005	1.27	1.27
12	0.057	0.011	0.87	0.87
13	0.016	0.008	0.24	0.4
14	0.033	0.006	0.5	0.86
15	0.01	0.002	0.15	0.25
18	0.097	0.015	1.48	1.48
25	0.218	0.01	3.33	2.8
26	0.23	0.017	3.51	2.98
27	0.117	0.015	1.79	1.7
28	0.124	0.016	1.89	1.89
29	0.146	0.016	2.23	2.23
30	0.135	0.019	2.06	2.06
31	0.095	0.013	1.45	1.45
32	0.075	0.025	1.15	1.15
33	0.049	0.014	0.75	1.23
34	0.033	0.006	0.5	0.86
35	0.045	0.006	0.69	1.13
36	0.075	0.009	1.15	1.15
37	0.113	0.015	1.73	1.73
38	0.11	0.018	1.68	1.64
39	0.108	0.01	1.65	1.47
40	0.119	0.004	1.82	1.7
41	0.167	0.008	2.55	2.28
42	0.143	0.013	2.19	2.0
62	0.033	0.006	0.5	0.86
63	0.03	0.007	0.46	0.78
64	0.059	0.006	0.9	0.9
65	0.037	0.007	0.57	0.57
66	0.04	0.005	0.61	0.61
67	0.048	0.007	0.73	0.73
68	0.103	0.007	1.57	1.27

V_S= 5.53±0.026km/s
F ratio 2.04

FIG 6-9a

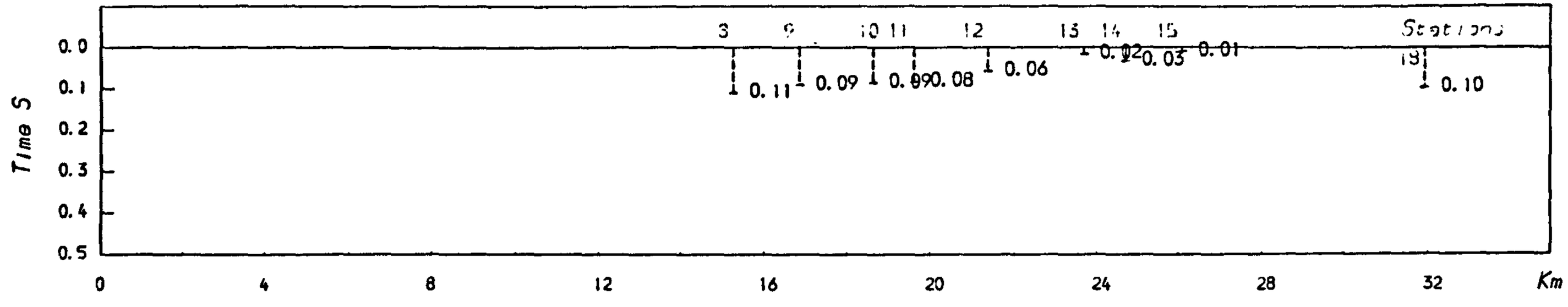
Soln H Upper Basement, all lines Time-Terms
Time S
0.0
0.1
0.2
0.3
0.4
0.5
3
9
10 11
12
13
14
15
Stations
18
0.11
0.09
0.09
0.08
0.06
0.02
0.03
0.01
0.10
0
4
8
12
16
20
24
28
32
Km

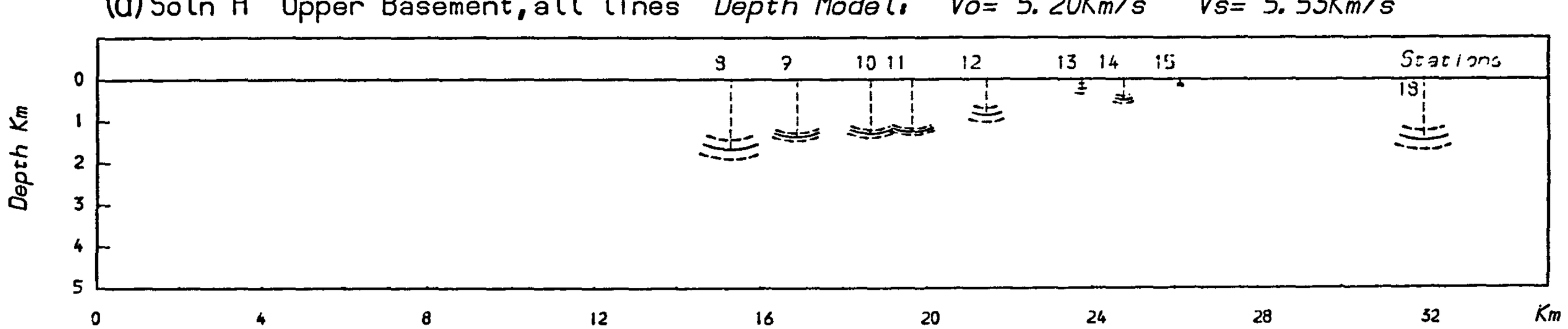
(a) Soln H Upper Basement, all lines Depth Model. Vo= 5.20Km/s Vs= 5.53Km/s
Depth Km
0
1
2
3
4
5
8
9
10 11
12
13
14
15
Stations
18
0
4
8
12
16
20
24
28
32
Km

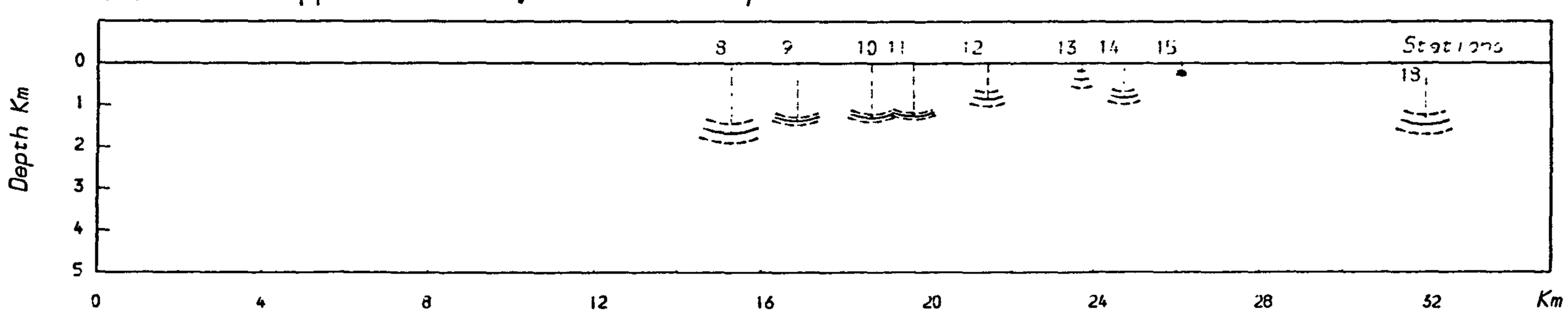
(b) Soln H Upper Basement, all lines Depth Model. Vo= 5.20Km/s Vs= 5.53Km/s
Depth Km
0
1
2
3
4
5
8
9
10 11
12
13
14
15
Stations
18
0
4
8
12
16
20
24
28
32
Km

FIG 6-9b

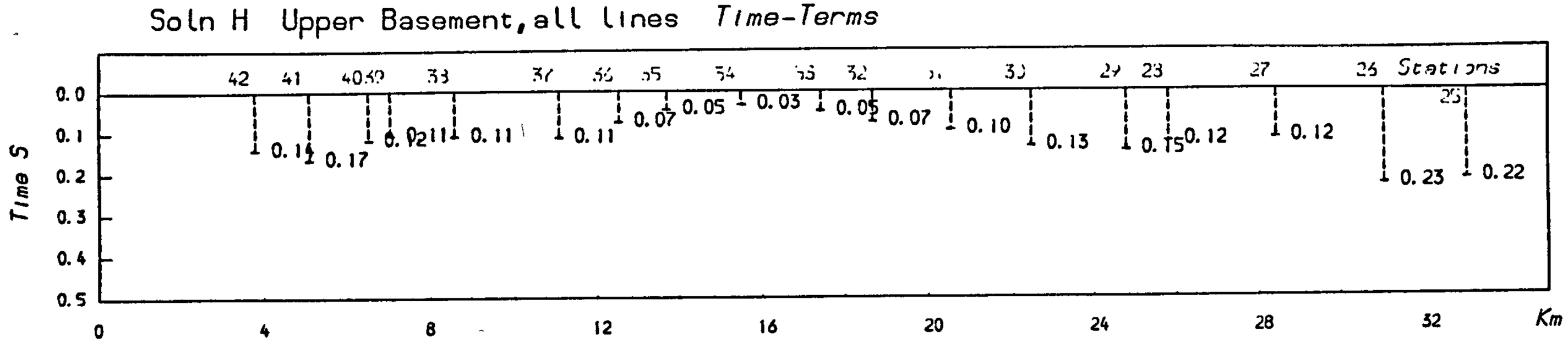

(a) Soln H Upper Basement, all lines *Depth Model* *Vo= 5.20Km/s* *Vs= 5.53Km/s*

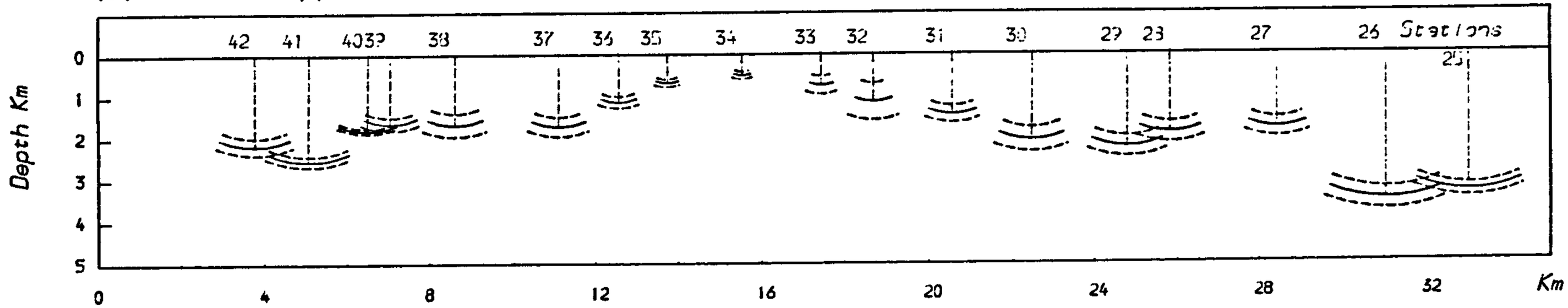

(b) Soln H Upper Basement, all lines *Depth Model* *Vo= 5.20Km/s* *Vs= 5.53Km/s*

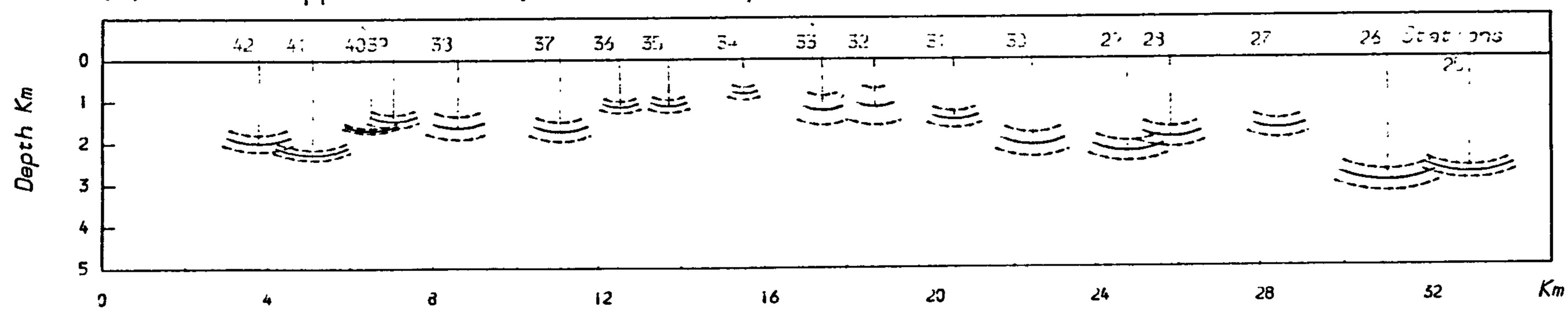

FIG 6-9c

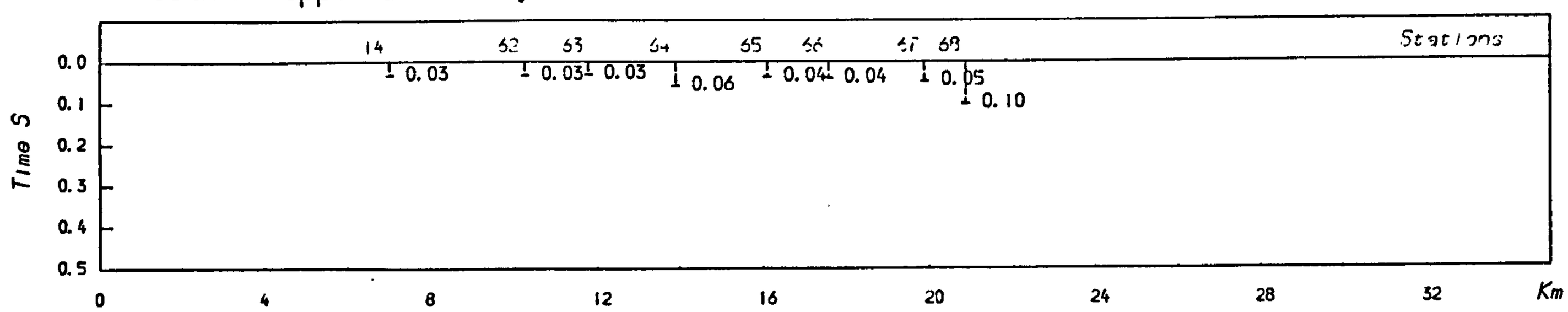

(a) Soln H Upper Basement, all lines *Depth Model.* *Vo= 5.20Km/s* *Vs= 5.53Km/s*

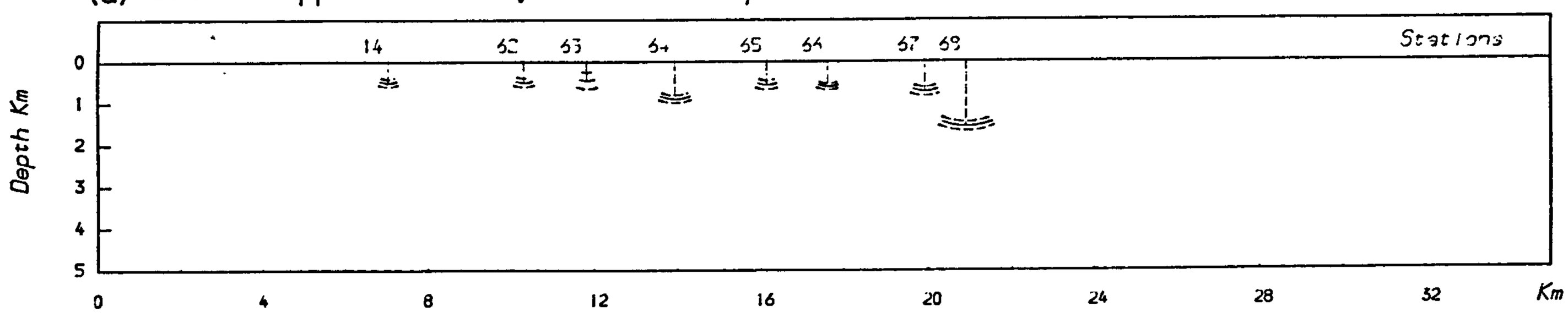

(b) Soln H Upper Basement, all lines *Depth Model:* *Vo= 5.20Km/s* *Vs= 5.53Km/s*

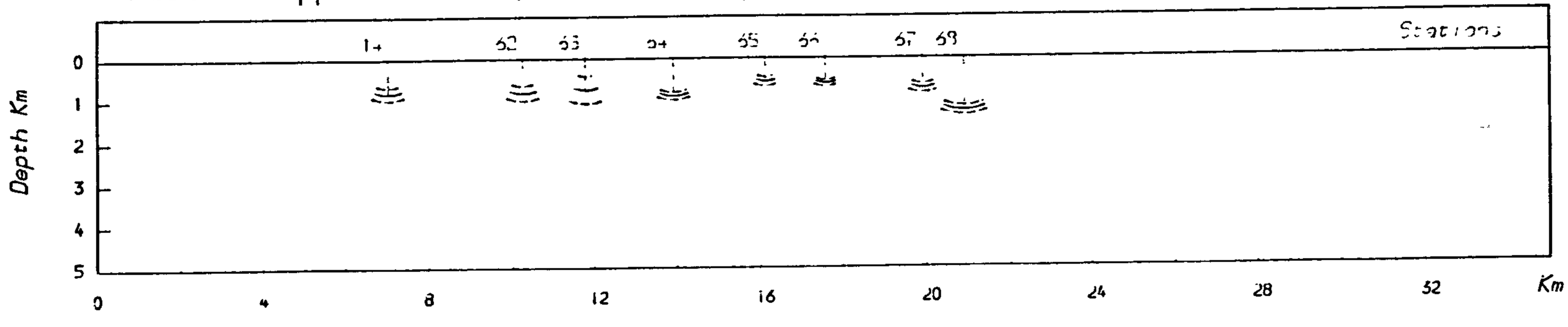

6.4.2 Charnoid-Type Basement

Most lower basement arrivals were observed for the north-south and SEW profiles; the later arrivals picked along the NEW line and interpreted as lower basement refractions were considered too speculative to be included in the first multiple profile anlaysis.

Since there were no common stations between north-south and SEW lines without incorporating data from DASED1 (when station 49 was re-occupied), the data may be treated by considering their two closest stations, 2 and 49 (1.2 km apart), as a single station. This is a very simple application of the MOZAIC technique (Bamford 1976). Thus there are three means by which the data can be solved: (a) stations 2 and 49 treated as one station, (b) stations 2 and 49 treated separately, and (c) including data from DASED1 to establish common stations between the two profiles.

The first solutions considered data from the southern province only; this was to exclude any untrustworthy later arrivals. Initially 143 observations from 36 events (twelve were from the south, and eight broadside from the north into the SEW line) were considered, for which a case (b) solution defined a velocity of 5.6 ± .038 km/s with an F ratio of 3.41 (i.e. greater than the critical value of 1.47). Taking out five observations with solution residuals greater than 0.06s, and including two more events from the north to balance the data set (total 153 observations), two solutions were obtained (also see Table 6-4):

Case(a) Least-squares velocity, 5.66 ± .036 km/s (F ratio 2.37; Solution I1)
With unconstrained velocity gradient, 5.51 + .127z km/s (F ratio 2.3)

case(b) Least-squares velocity, 5.65 ± .035 km/s (F ratio 2.22; Solution I2) With unconstrained velocity gradient, 5.4 + .16z km/s (F ratio 2.06)

Table 6-4 Time terms in seconds

Station	Solution I1 Time term	Solution I1 Error	Solution I2 Time term	Solution I2 Error	Solution I3 Time term	Solution I3 Error	Solution I4 Time term	Solution I4 Error	Solution I4 Depth km
1	0.176	0.013	0.177	0.013	0.178	0.013	0.172	0.011	1.69
61					0.243	0.005	0.241	0.01	2.37
2	0.235	0.006	0.243	0.007	0.234	0.006	0.243	0.008	2.39
3	0.13	0.009	0.131	0.009	0.131	0.009	0.131	0.013	1.74
69					0.169	0.005	0.168	0.016	2.23
4	0.23	0.01	0.231	0.01	0.224	0.007	0.222	0.005	2.95
5	0.207	0.006	0.207	0.006	0.206	0.006	0.201	0.007	2.67
6	0.17	0.009	0.17	0.009	0.172	0.007	0.168	0.007	2.23
7	0.138	0.011	0.138	0.011	0.137	0.011	0.129	0.01	1.72
8							0.209	0.006	2.78
9							0.271	0.012	3.6
10							0.237	0.008	3.15
11							0.269	0.01	3.57
12							0.209	0.02	2.78
13							0.224	0.011	2.98
14							0.241	0.011	3.19
15							0.24	0.012	3.19
47							0.097	0.021	1.29
48							0.129	0.014	1.53
49	0.235	0.006	0.165	0.01	0.188	0.007	0.191	0.006	2.05
50	0.197	0.009	0.141	0.009	0.16	0.008	0.167	0.009	1.79
51	0.164	0.009	0.107	0.009	0.126	0.009	0.133	0.008	1.31
52	0.146	0.005	0.089	0.005	0.107	0.005	0.115	0.006	1.13
53	0.146	0.008	0.09	0.007	0.108	0.007	0.116	0.006	1.14
56	0.312	0.007	0.256	0.007	0.275	0.007	0.282	0.006	2.78
57	0.308	0.009	0.251	0.009	0.28	0.009	0.277	0.008	2.73
58	0.368	0.007	0.312	0.007	0.331	0.007	0.338	0.007	3.33
59	0.464	0.022	0.407	0.023			0.432	0.026	3.93

Station	Solution J Time term	Solution J Error	Solution J Depth km
25	0.432	0.015	5.78
26	0.444	0.025	5.94
27	0.369	0.01	4.94
28	0.327	0.01	4.37
29	0.348	0.015	4.65
30	0.324	0.01	4.33
31	0.312	0.012	4.17
32	0.268	0.02	3.58
33	0.251	0.025	3.36
34	0.241	0.007	3.22
35			
36	0.207	0.01	2.77
37	0.161	0.015	2.15
38	0.196	0.008	2.62
39	0.188	0.008	2.51
40			
41	0.272	0.013	3.64
42	0.283	0.01	3.79

Solution Velocities:

I1 5.66±0.036km/s
I2 5.65±0.035km/s
I3 5.67±0.034km/s

J 5.65±0.025km/s

The velocities defined by these two cases are very similar and are comparable with the velocity given by Solution D for the whole north-south line. Setting stations 2 and 49 independent of each other obviously increases the degrees of freedom of the solution, hence the lower F ratios for case(b) solutions. However, the time-term for station 2 for case(b) is about 0.08s greater than that for station 49. If this is so, then within the accuracy required (about 10 ms), it is an unreasonable assumption to treat them as a single station.

By including events from DASED2, the data set grew to 171 observations. The case(c) Solution I3 gave a solution velocity of 5.67 ± .034 km/s with an F ratio of 2.24. As can be seen from Table 6-4, the solution time-term for station 2 is 50 ms greater than that for station 49. With an unconstrained velocity gradient, the best-fit velocity was 5.49 + .134z km/s with an F ratio of 1.99.

Those solutions allowing a vertical velocity gradient are statistically insignificantly different from the uniform velocity solutions. In common with the solutions for the constituent lines, the F ratios for the uniform velocity solutions are below the critical value of 1.47 at the α=0.05 significance level. The lack of fit probably reflects the generally irregular refractor topography, particularly around the basement depression between stations 1 to 3, and 48 to 50. The station time-terms in this region are also probably azimuthally dependent.

Including later arrivals from the north of the Bonsall Fault, 203 observations were considered to yield a least-squares solution velocity of 5.59 ± .026 km/s with an F ratio of 2.35. This velocity is atypically low for the lower basement refractor and reflects the inclusion of the less reliable later arrival data. Instead, Solution I4 constrained the refractor velocity to 5.65 km/s, for which the F ratio was 2.44 and the solution is insignificantly different from the unconstrained solution (Fx/Fy = 1.04).

The data also allowed an unconstrained vertical velocity gradient of 5.38 + .16z (F ratio 2.06), but the solution is statistically no different from the least-squares velocity solution.

The time-terms for Solution I4 are plotted in Figs. 6.10a,b. Like Solution H, any differences with the single line solutions probably reflect the choice of observations. The depths are calculated from mean overburden velocities of 5.2 and 4.9 km/s for massif and basinal facies respectively, with transitional stations (e.g. 48 and 49), given mean overburden velocities of 5.0 km/s. If the Redhouse sandstones are widespread under the region and of considerable thickness, then it is possible that these depths are overestimated. A mean overburden velocity of 5.2 km/s has been assumed for the overburden north of the Bonsall Fault; with no velocity information on the hidden Lower Palaeozoic sequence, this velocity has been estimated to keep the downward throw of the lower basement geologically feasible (see Section 5.4.1). Finally, the depth for station 59 has been corrected for a 200 m cover of Millstone Grit.

Lower Basement Time-Terms for the Northern East-West Profile

Since of the total 36 observations of basement arrivals for the NEW line, half are secondary refractions from two Cauldon events, and the remainder mainly from the unreversed outer stations of the line, these data were not considered good enough to include in the above solutions. However, once the time-term for station 14 (34) was well established, data from the NEW line were combined with the data used for the north-south line solution D.

A first solution used 166 observations from 28 events, and gave a least-squares velocity of 5.65 ± .029 km/s with an F ratio of 2.42. Taking out seven observations with solution residual greater than .06s, and including data from DASED1, Solution J (see Table 6-4) defined a least-squares velocity

FIG 6-10a

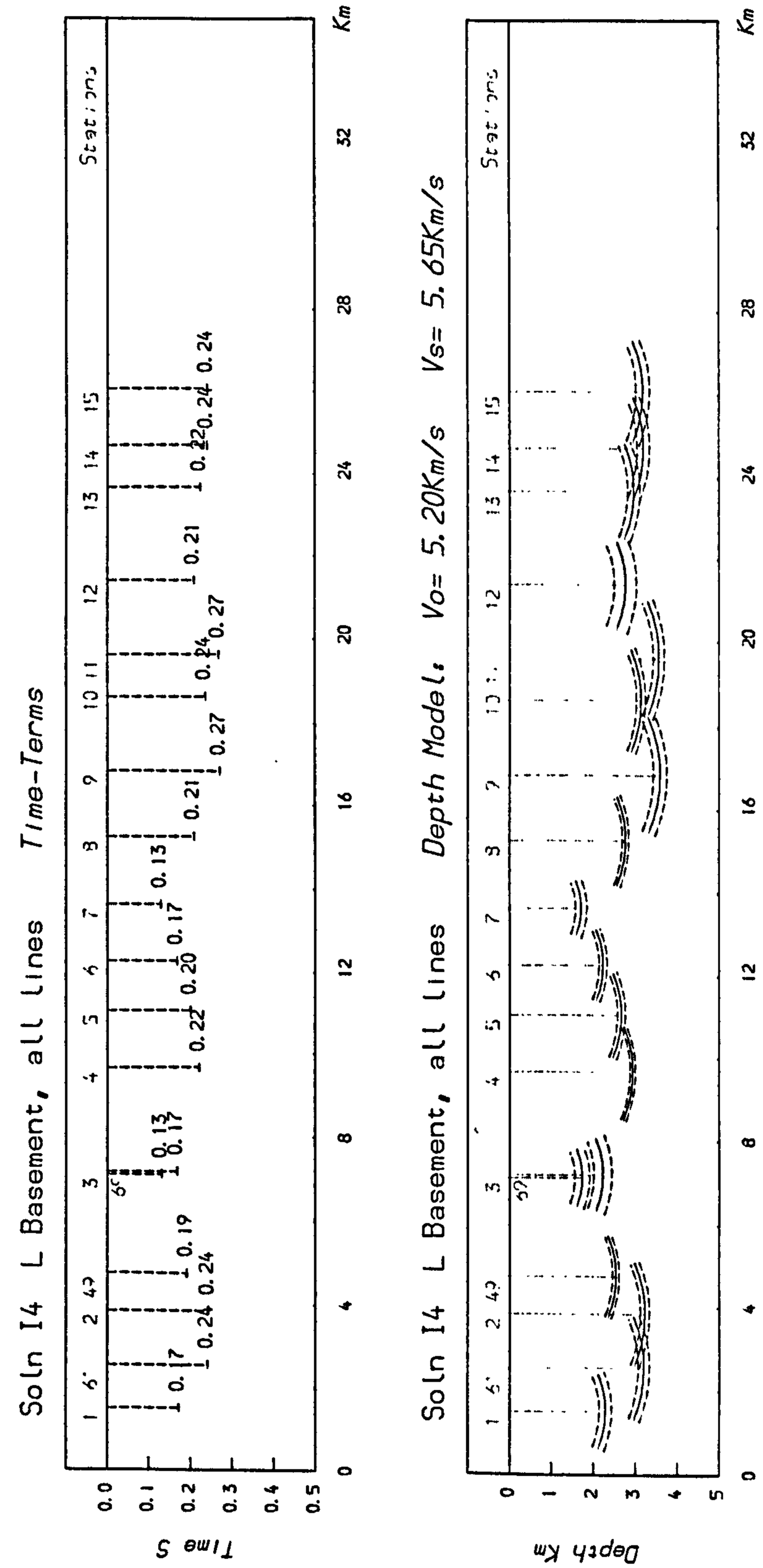
Time-Terms
Soln I4 L Basement, all lines
Stations
Km
32
28
24
20
16
12
8
4
0
0.0
0.1
0.2
0.3
0.4
0.5
Time S
Depth Model: Vo= 5.20Km/s Vs= 5.65Km/s
Depth Km

FIG 6-10b

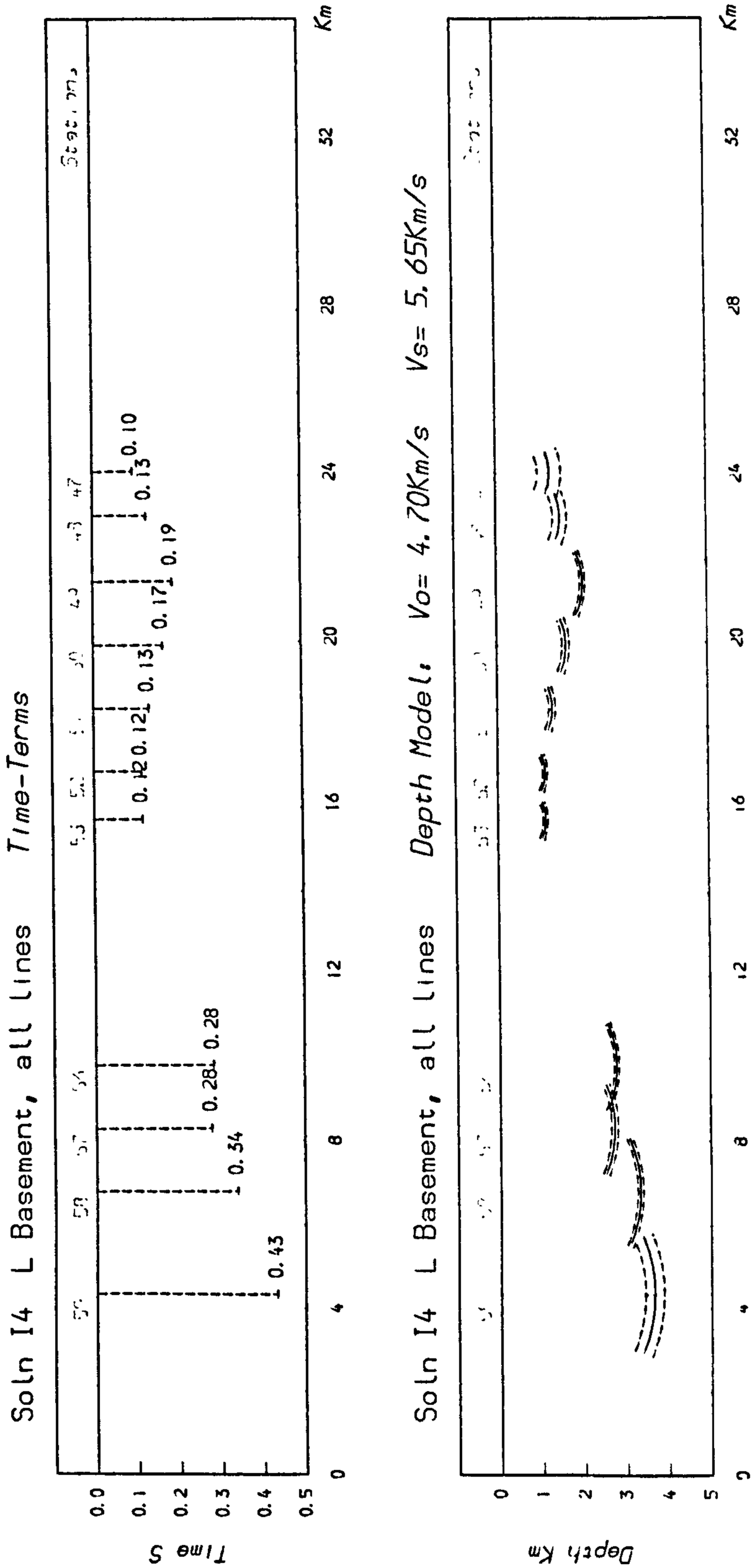
Time-Terms
Soln I4 L Basement, all lines
0.0
0.1
0.2
0.3
0.4
0.5
Time S
0.43
0.34
0.28
0.19
0.17
0.13
0.12
0.10
Km
0
4
8
12
16
20
24
28
32
Depth Model, Vo= 4.70Km/s Vs= 5.65Km/s
Soln I4 L Basement, all lines
0
1
2
3
4
5
Depth Km

of 5.65 ± .025 km/s with an F ratio of 1.78. At the α=0.05 significance level the critical value is 1.47, so this result is significant.

The time-terms for solution J are plotted in Fig. 6.11, alongside depths calculated for a mean overburden velocity of 5.2 km/s. Comparing these time-terms with those for Solution H(b), also plotted in Fig. 6.11, it is evident that the Lower Palaeozoic layer thins towards a basement high between stations 36 and 39. It could be argued that this feature is not real and that the 'basement' arrivals used in this region are actually poorly picked upper basement refractions. However,

(a) the refracted arrivals between stations 36 and 40 are often of higher amplitude, lower frequency, and less complicated than those towards the east (see Section 5.5.1)
(b) the range of reduced times was generally smaller between these stations than the rest of the line (see Fig. 5.29),
(c) the Bouguer Anomaly map implies a basement high between these stations (see Fig. 1.12), and
(d) the region co-incides with the 'hinge region' along the western margin of the Dome which marks the structural axis of the Dome, east of which the limestones thicken towards the Eyam borehole.

6.5 General Comments on Solutions

The method has contrasted the two sub-Carboniferous refractors interpreted in Chapter Five: to the north of the Bonsall Fault the Carboniferous is underlain by a refractor of velocity 5.5 -5.55 km/s which correlates with both the volcanics in the Woo Dale borehole and the Ordovician shales in the Eyam borehole. To the south of the Bonsall Fault the Carboniferous is underlain by a refractor of velocity 5.62 - 5.71 km/s, thought to be of Charnoid-type material; this refractor can be traced at depth beneath the northern province, downthrown by as much as a kilometre or more.

FIG 6-11

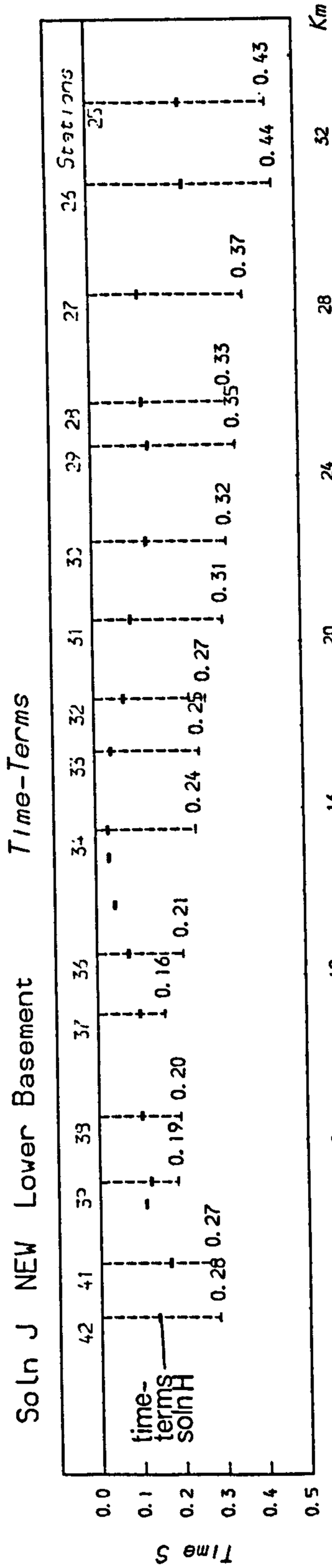
Time-Terms
Km
26 Stations
25
32
28
24
20
16
12
8
4
0.43
0.44
0.37
0.33
0.35
0.32
0.31
0.27
0.25
0.24
0.21
0.16
0.20
0.19
0.27
0.28
Soln J NEW Lower Basement
time-terms soln H
Time S
0.0
0.1
0.2
0.3
0.4
0.5
0

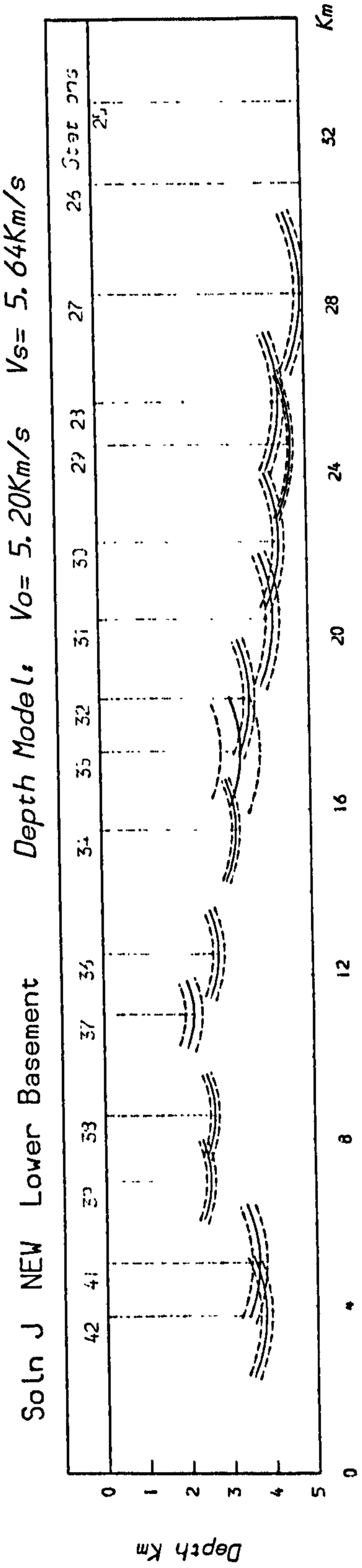
Depth Models Vo= 5.20Km/s Vs= 5.64Km/s
Km
26 Stations
25
32
28
24
20
16
12
8
4
Soln J NEW Lower Basement
Depth Km
0
1
2
3
4
5
0

The sub-Dinantian surface in the southern province generally appears more irregular than that under the northern province. This is reflected by the lower quality of the solutions for data from south of the Bonsall Fault, where the solution residuals are correspondingly greater. Also, data from the southern province consistently allowed a vertical velocity gradient term in the solution, while data from the north usually did not.

It is possible that the quality of the solution could be improved by carrying out an iteration by estimating Δ_{ij} from these first solutions. For example, those solutions which define velocity gradient terms may be structurally influenced by the broad anticlinal structure; this effect may be eliminated by iteration. However, this has not been attempted because

(a) most of the seismic sources are azimuthally distributed and untimed, for which only poor estimates of their time-terms could be made and Δ_{ij} inaccurately calculated,

(b) the process would be extremely time consuming, and only proportionally few events could be considered, and

(c) it is unlikely that the solution time-terms would change by much from these first solutions, especially since the quality was generally high (i.e. F ratios greater than 4 were rarely encountered).

Another problem inherent with these uniterated solutions is that rays crossing the Bonsall Fault zone will have necessarily travelled through refractors of differing mean velocities. Ideally their arrival times should be accordingly corrected for the distance travelled in both media. However,

(a) The mean velocities differ by only about 0.1 km/s. This corresponds to a delay of about 15 ms between rays whose paths in the media differ by 5 km. Since for any quarry on the Dome, this raypath difference cannot exceed 0.5 km between adjacent stations, so the error is small, and

(b) The effect on the least-squares solution velocity for the line segments must be minimal.

CHAPTER SEVEN

TELESEISMIC WORK, GRAVITY MODELLING AND GENERAL CONCLUSIONS

7.1 Introduction

Two peripheral facets of the project are briefly discussed in this chapter: a look at the teleseismic events recorded during the fieldwork, and an attempt to model Bouguer anomaly sections of the three longer profiles based on the interpretation of the seismic refraction data. Finally, general conclusions of the whole interpretation are drawn.

7.2 Teleseismic Work

The epicentres of recorded events within a distance of 120 degrees are plotted in Fig. 7.1, which excludes ten events from the Tonga Trench region. Of those shown, eleven occur within the teleseismic window of 30-100 degrees, all of which fall within azimuths of 270-40 degrees. This is, therefore, a limited data set, and the data recorded on the Dome have been supplemented by records from the Midlands seismic monitoring network (Midnet) stations of Haverah Park (HPK) near Leeds, Charnwood Forest (CWF) near Leicester, and Stoke-on-Trent (STM). These stations are within the presumed limits of the Precambrian microcontinent known as the Midland Craton (Thorpe 1974, Phillips et al. 1976), shown in Fig. 7.2.

These data have been considered on two scales: firstly variation in relative P wave delay between the Dome and the Midnet stations, and secondly variation among stations on the Dome itself. Relative delay times (Long and Mitchell 1970) provide a means of comparing crust and upper mantle structure between stations by eliminating common factors such as source effects, focal position, and much of the variation along the

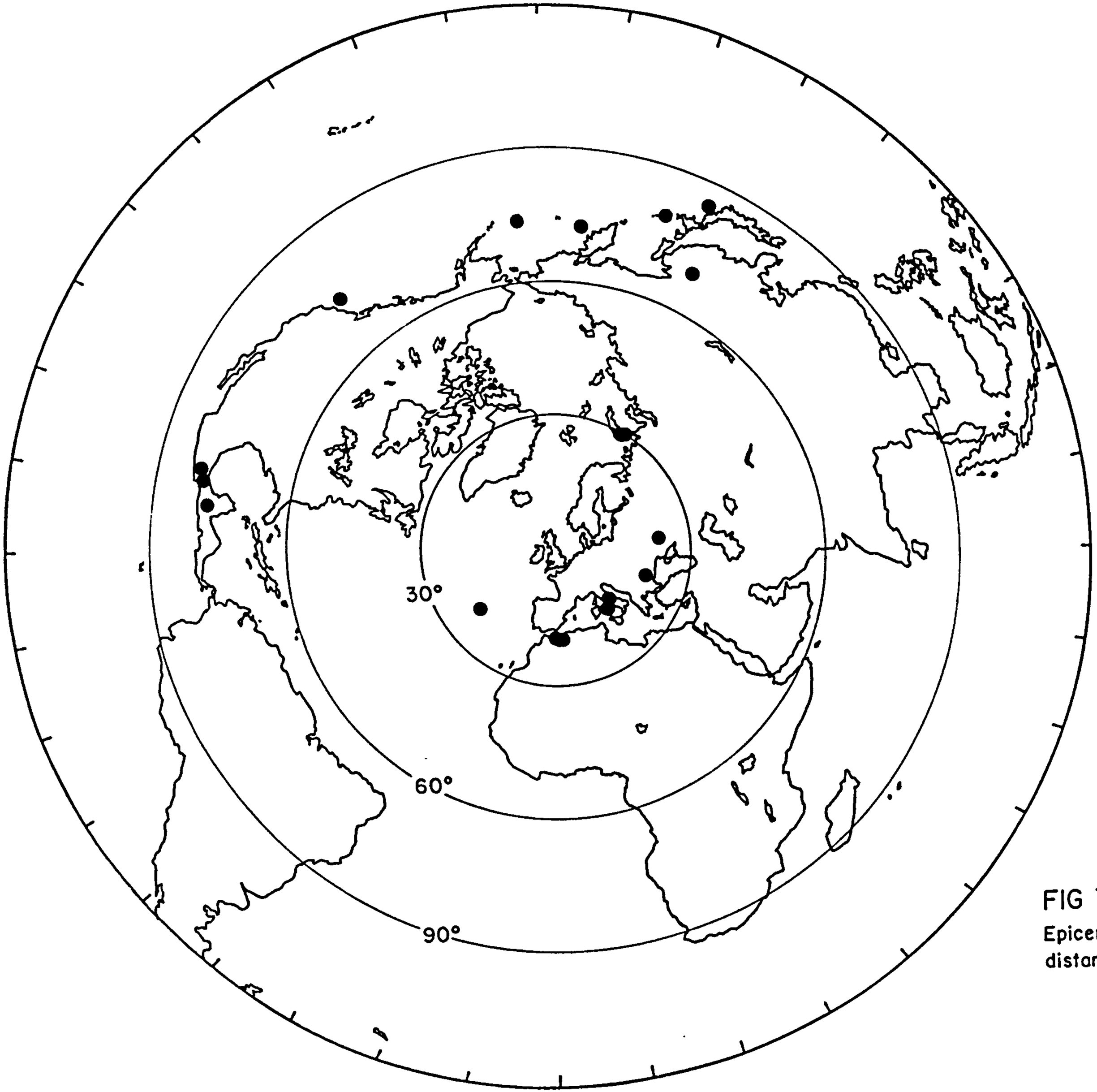

FIG 7-1
Epicentres within a distance of 120°

FIG 7-2 Principal tectonic units with seismic stations

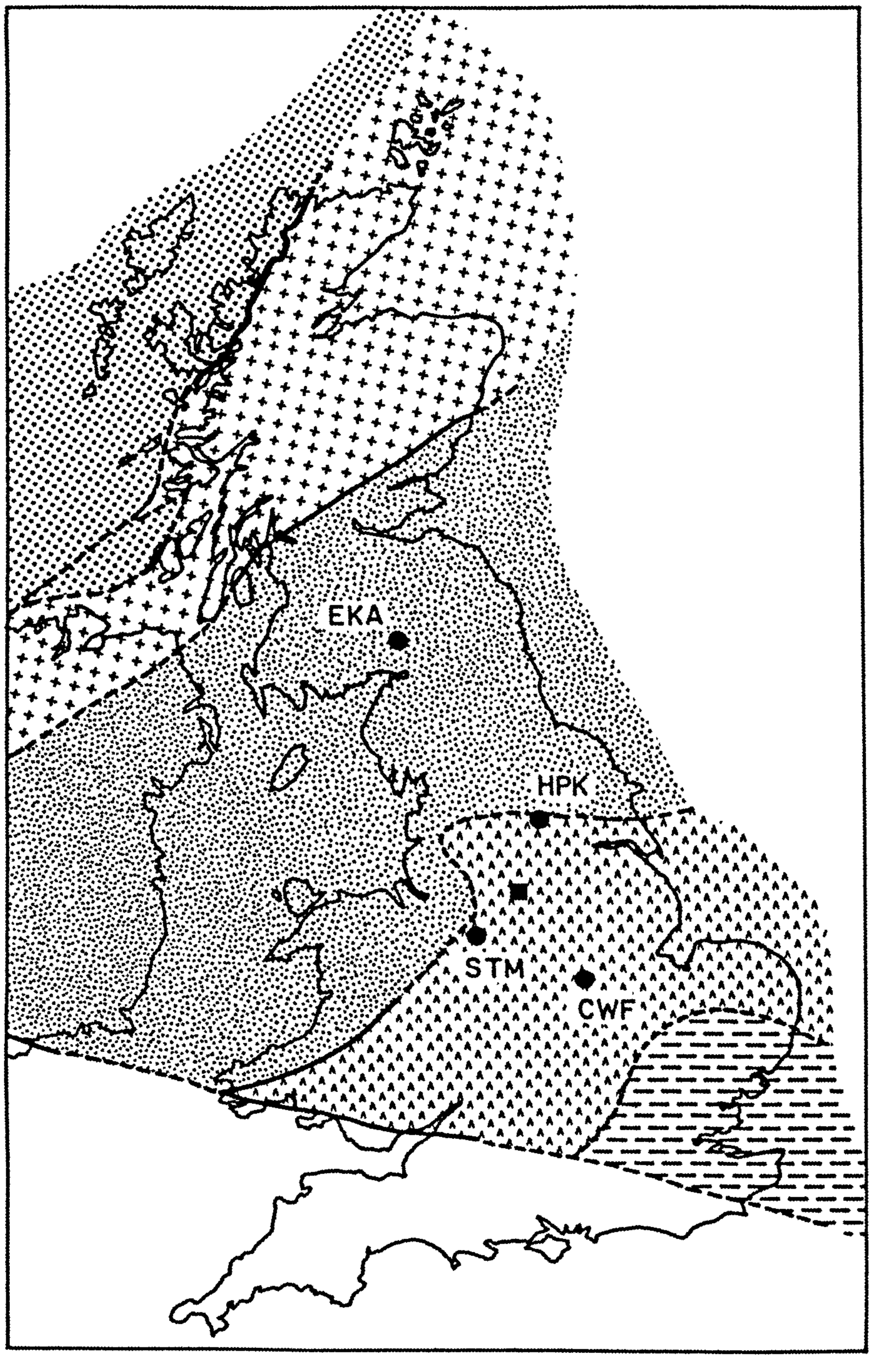

raypaths between source and receivers. The relative delay time, t_d, between station i and j is given by

$$t_d = (t_{i(obs)} - t_{j(obs)}) - (t_{i(calc)} - t_{j(calc)})$$

for observed arrival times $t_{(obs)}$ and estimated arrival time $t_{(calc)}$ calculated from a suitable earth model, such as Herrin (1968). A positive value for t_d implies either a delay under station i or a 'speeding up' under station j.

7.2.1 Comparison with Midnet Stations

Previous Work

The only published work concerning the region deals with a relative P wave delay study between Charnwood Forest and Eskdalemuir (EKA, Fig. 7.2) by Maguire et al. (1981) and between stations of the Charnwood Forest array (see Fig. 4.13; Maguire et al. 1982). Relative to EKA, they determined a mean delay of about -0.32s at CWF, which they associated with a thick, high velocity lower crust. The relative delay times were observed to increase with increasing epicentral distance (Fig. 7.3a), and also to vary with azimuth (Fig. 7.3b), particularly between 260 and 350 degrees. This azimuthal variation was thought to be due to structural complexity in the upper mantle to the north-west of EKA. Using data from the CWF array, they have also determined a strong NW-SE trend on the Moho, which was interpreted as dipping south-westwards.

Bermingham (1978) has examined teleseismic data recorded by the University of Leicester's Charnwood-Ballidon line, and observed a variation in delay relative to CWF of only $\pm$.05s, which he attributed to differences in thickness of the sediments in the Widmerpool Gulf. A brief examination of relative delay times between HPK and EKA has been made by Peasley (1980), who determined a 0.2s delay under HPK and thought it due to a c.7km thickness of Palaeozoic sediments (Ramsbottom 1974).

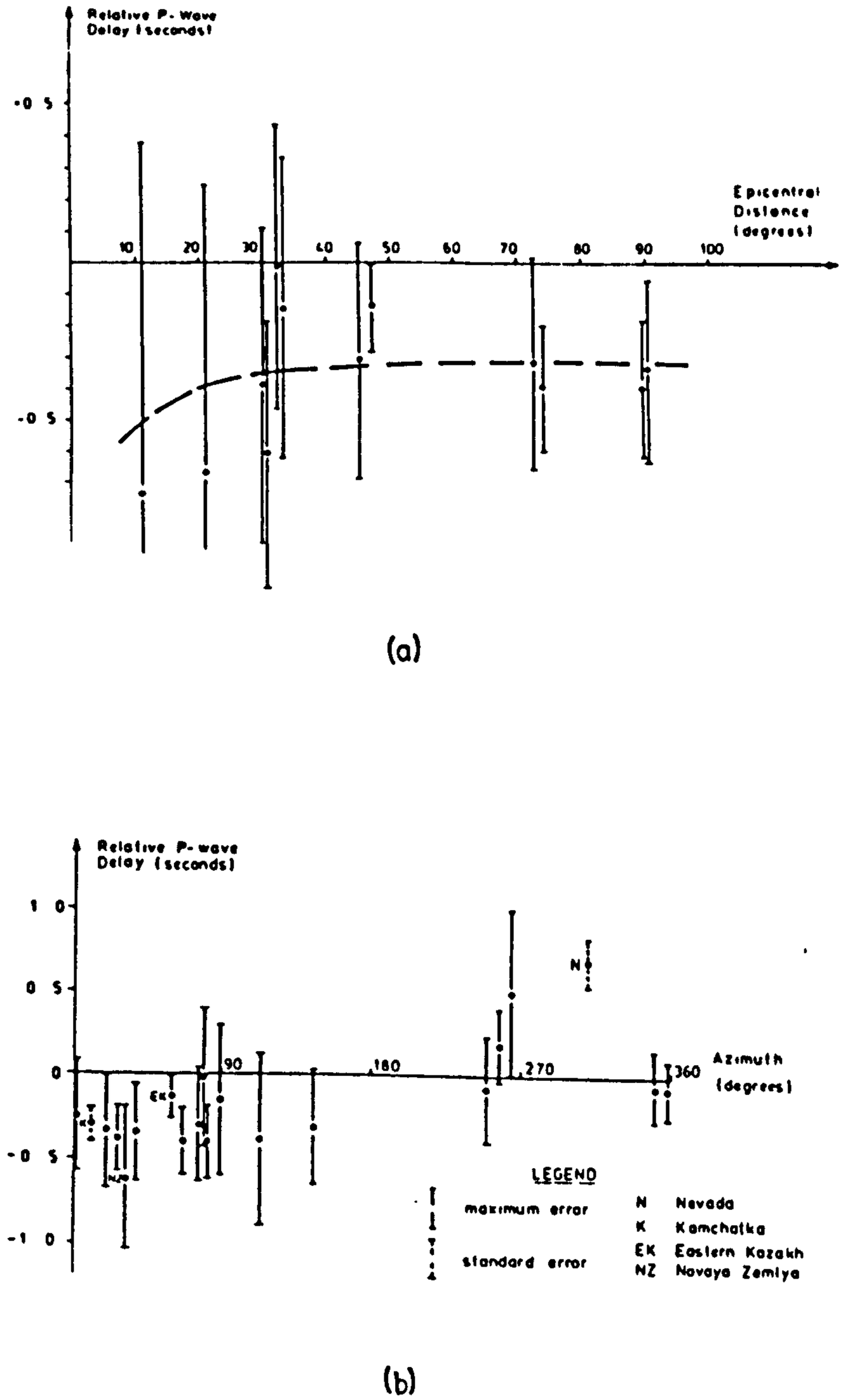

FIG 7-3 Relative P wave delays for CWF relative to EKA (a) vs epicentral distance (dashed line for theoretical delays using models), (b) vs azimuth (from Maguire et al. (1981))

Analysis

The P wave delays have been calculated for each Midnet station relative to the Dome, and have been plotted against (a) epicentral distance, (b) azimuth, and (c) azimuth and angle of incidence at the station, plotted on a polar projection. The angle of incidence, I, is given by

$$I = \sin^{-1} \left(\frac{V_c}{V_p}\right)$$

for upper crustal velocity V_c and phase velocity V_p (determined from the earth model by the computer programme GEDESS), and is dependent upon the epicentral distance. Since several stations on the Dome recorded each event, the mean relative delay has been plotted, and the root-mean-square deviation added to the estimated picking error to give the total estimated observational error.

(a) CWF vs Derbyshire Dome (Fig. 7.4)

For the seven events within the teleseismic window, the mean relative delay is about -0.15 $\pm$ .1s, which corresponds either to a delay beneath the Dome, or to higher velocity crust beneath CWF. From all the observations it is apparent that the delays increase with epicentral distance (cf. Fig. 7.3a), and that they vary with azimuth. With regards to the azimuthal variation noted between CWF and EKA (Fig. 7.3b), an anomalously positive delay is observed at 330 degrees.

(b) HPK vs Derbyshire Dome (Fig. 7.5)

Despite the fact that there are more data, the variation in delay times with distance and azimuth between HPK and the Dome appears greater than that observed between CWF and the Dome. This is either because HPK lies on the edge of the craton, or because its first arrivals were often difficult to pick through difference in waveform (also possibly due to deep structural complexity). For events within teleseismic distance all the delay times are positive

FIG 7-4 CWF relative to the Dome

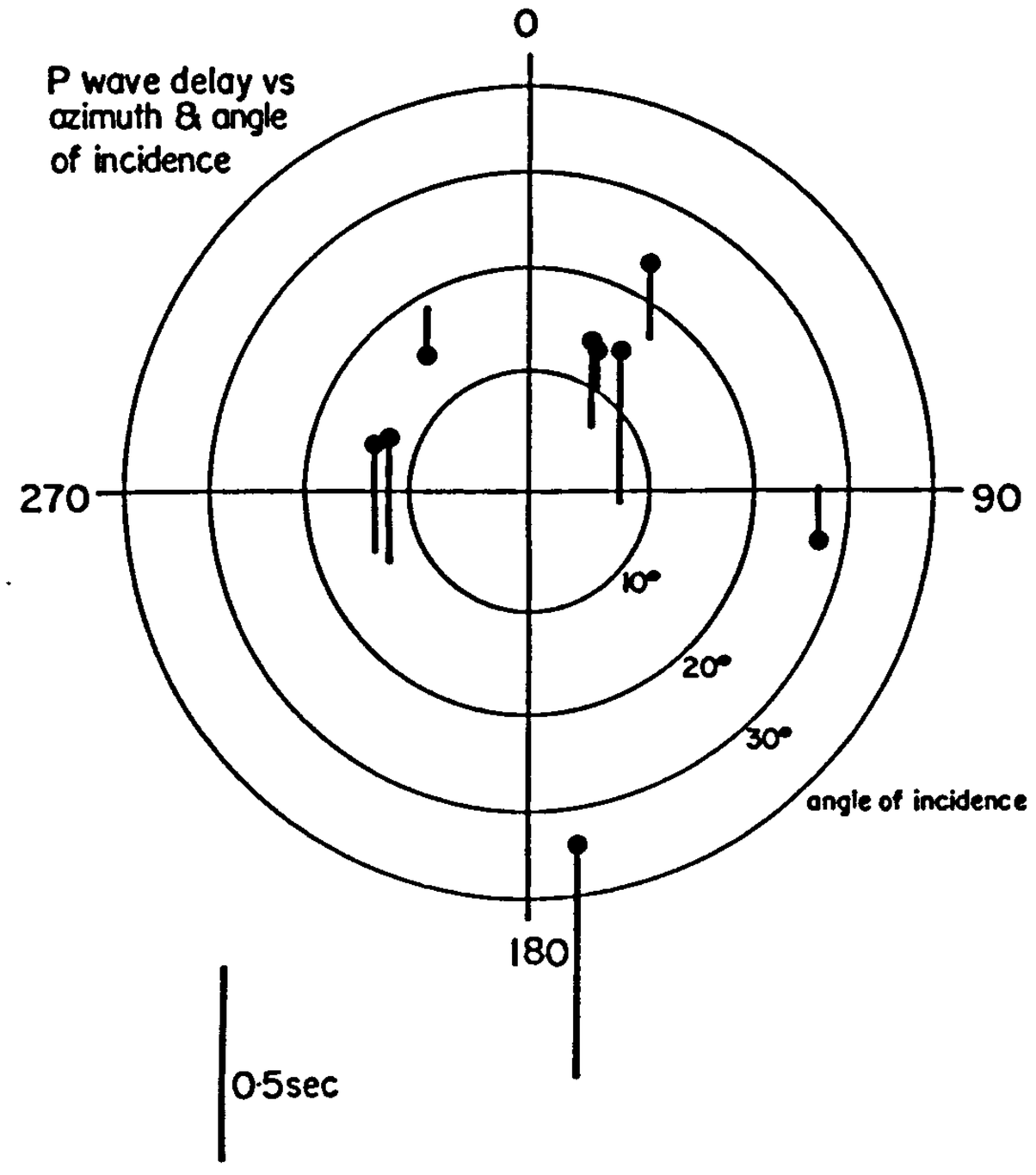

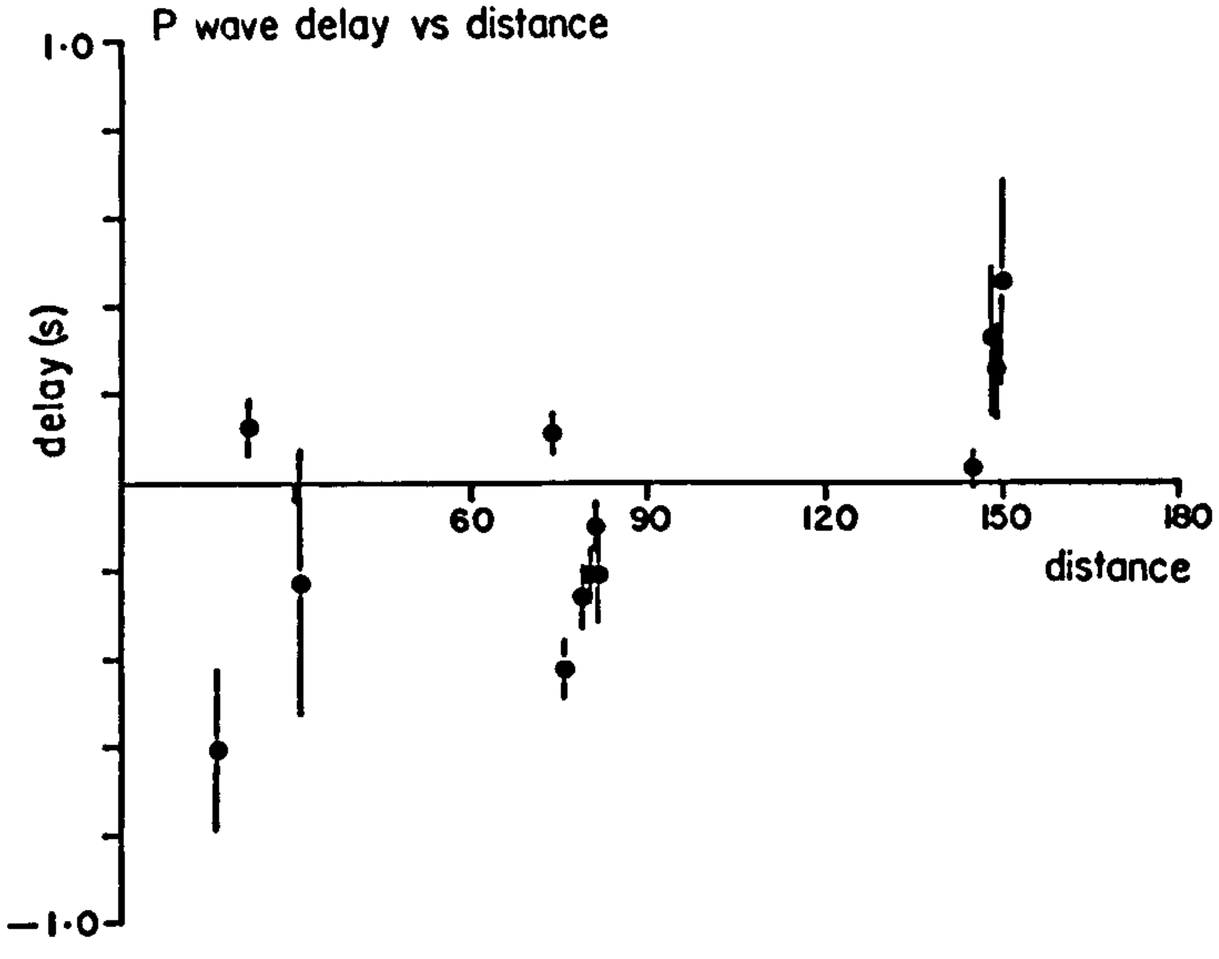

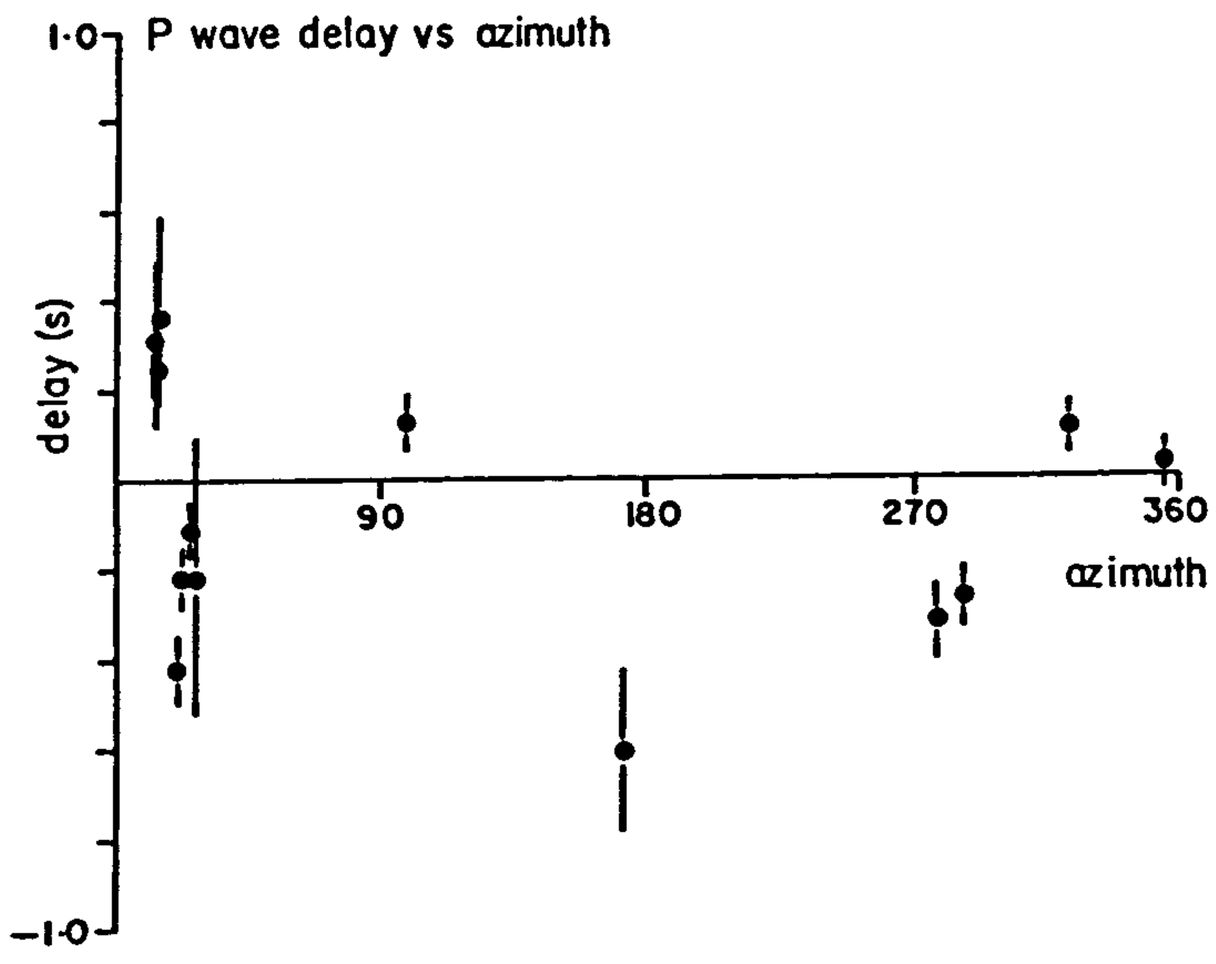

FIG 7-5 HPK relative to the Dome

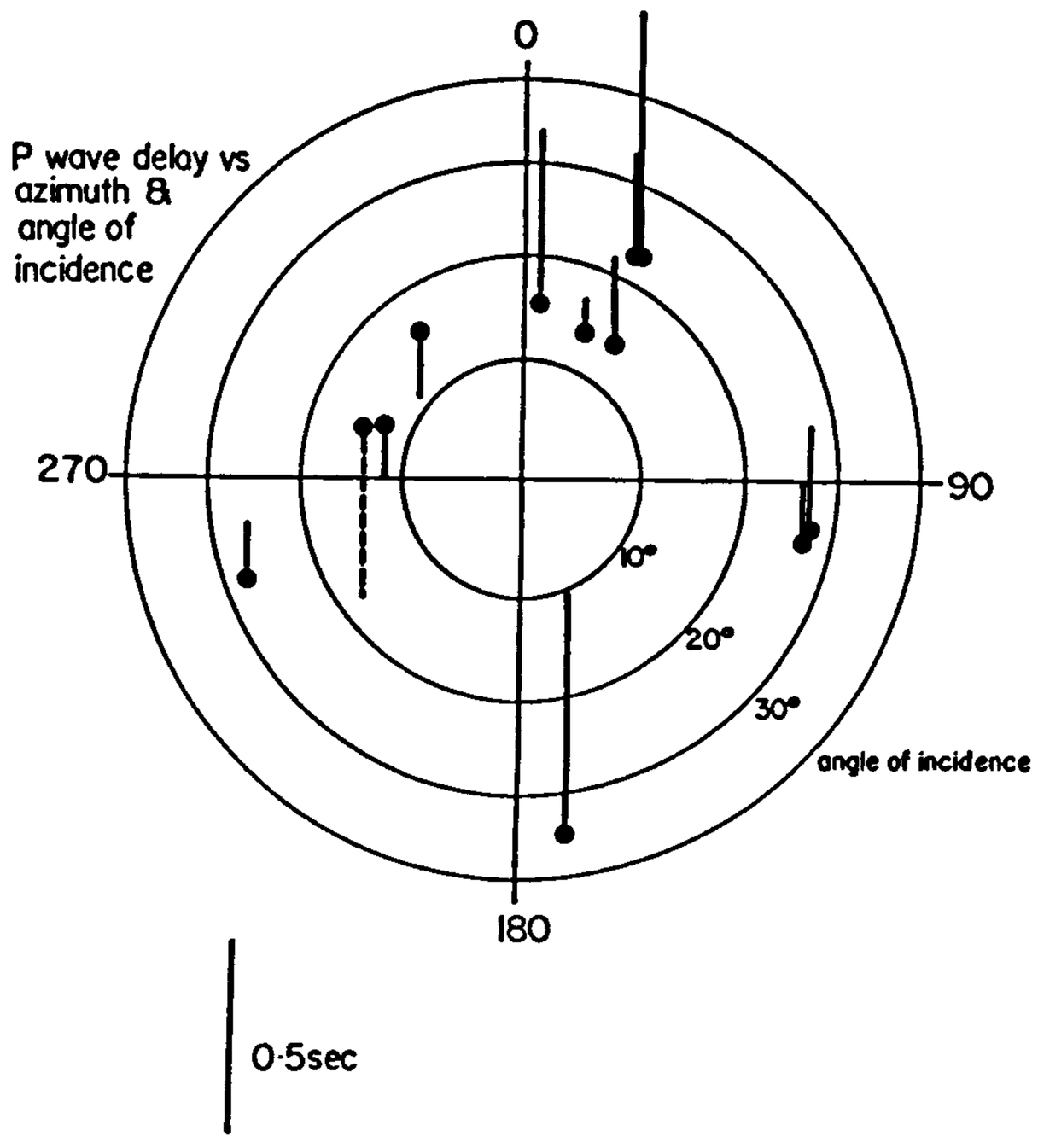

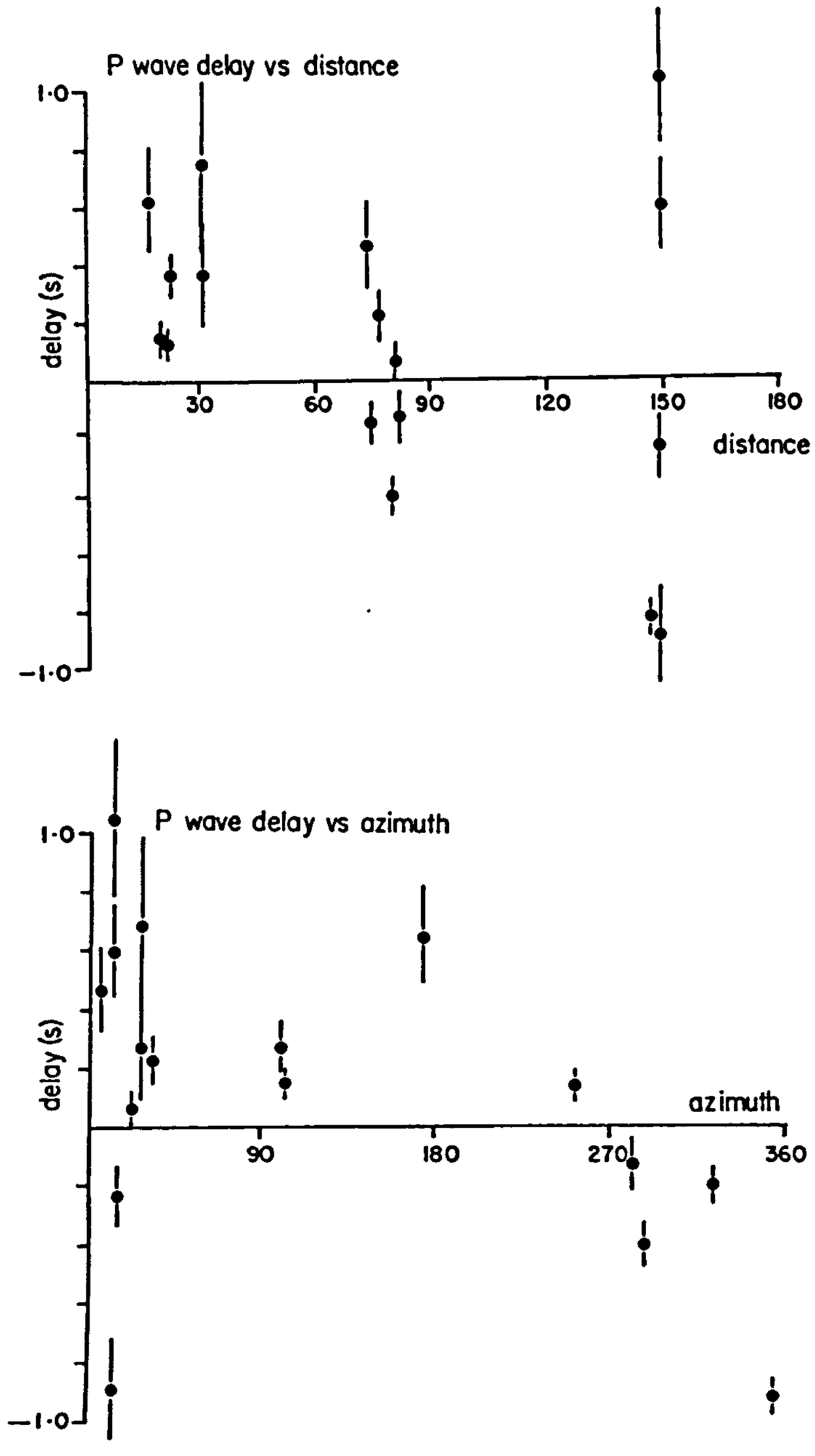

with respect to the Dome (delay under HPK), except in the azimuthal range 280-330 degrees. The mean delay time for all these events is about 0.18±.28s, and about 0.36±.15s for observations within 0-270 degrees azimuth. The delay times appear to decrease with increasing epicentral distance, except for the core phases for which there is much variation.

(c) Derbyshire Dome vs STM (Fig. 7.6)

The relative delay times between STM and the Dome vary with distance and azimuth almost identically to those for HPK. All relative delays except one (poor) observation are positive, but in the azimuthal range 270-330 degrees the values are very small. The mean value for events within teleseismic distance is approximately 0.34±.3s (delayed with respect to the Dome).

General Remarks

The delay times for these Midnet stations appear to be smaller further into the craton: arrivals at CWF are normally early relative to the Dome, while those at stations HPK and STM, close to the presumed perimeter of the craton, are delayed. The maximum delay between centre and margin is about 0.3-0.5s, which could be explained by the cover of Palaeozoic sediments under HPK and STM: as much as 7km beneath HPK (Ramsbottom 1974), and perhaps 3km or more under STM in the North Staffordshire Deep. To test that the observed azimuthal variation was not solely due to the data recorded on the Dome, the delay times for CWF relative to HPK have been plotted in Fig. 7.7 (negative delay means CWF early). Since this variation is still observed, the effect cannot be local to the Dome (or Charnwood Forest) only.

That the 270-350 degree azimuthal window is anomalous for these data throws doubt on the interpretation that the effect observed between CWF and EKA is local to EKA (Maguire et al. 1981). The Midlands are widely believed to be underlain by a Caledonian igneous province (e.g., Le Bas 1972, Dunham

FIG 7-6 STM relative to the Dome

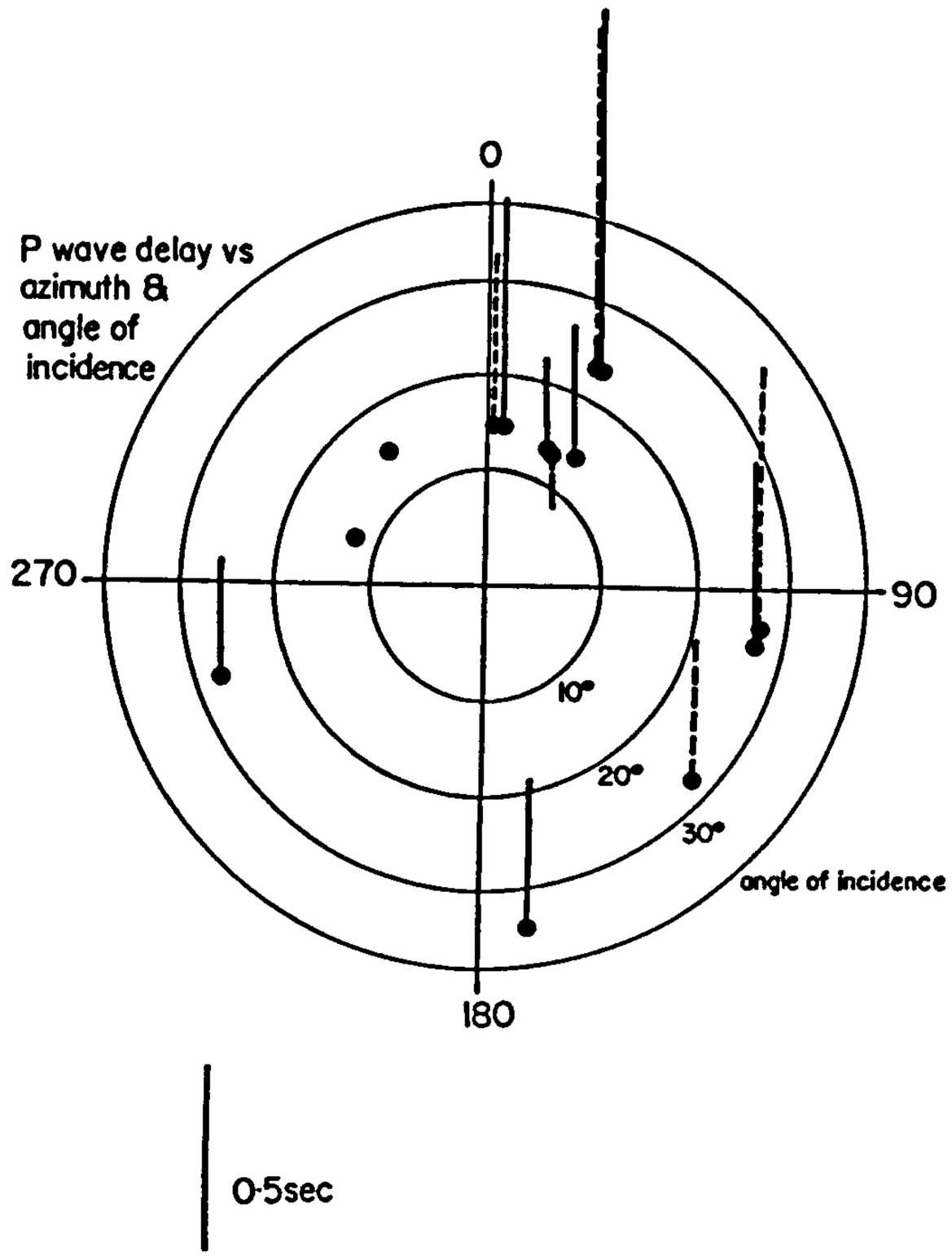

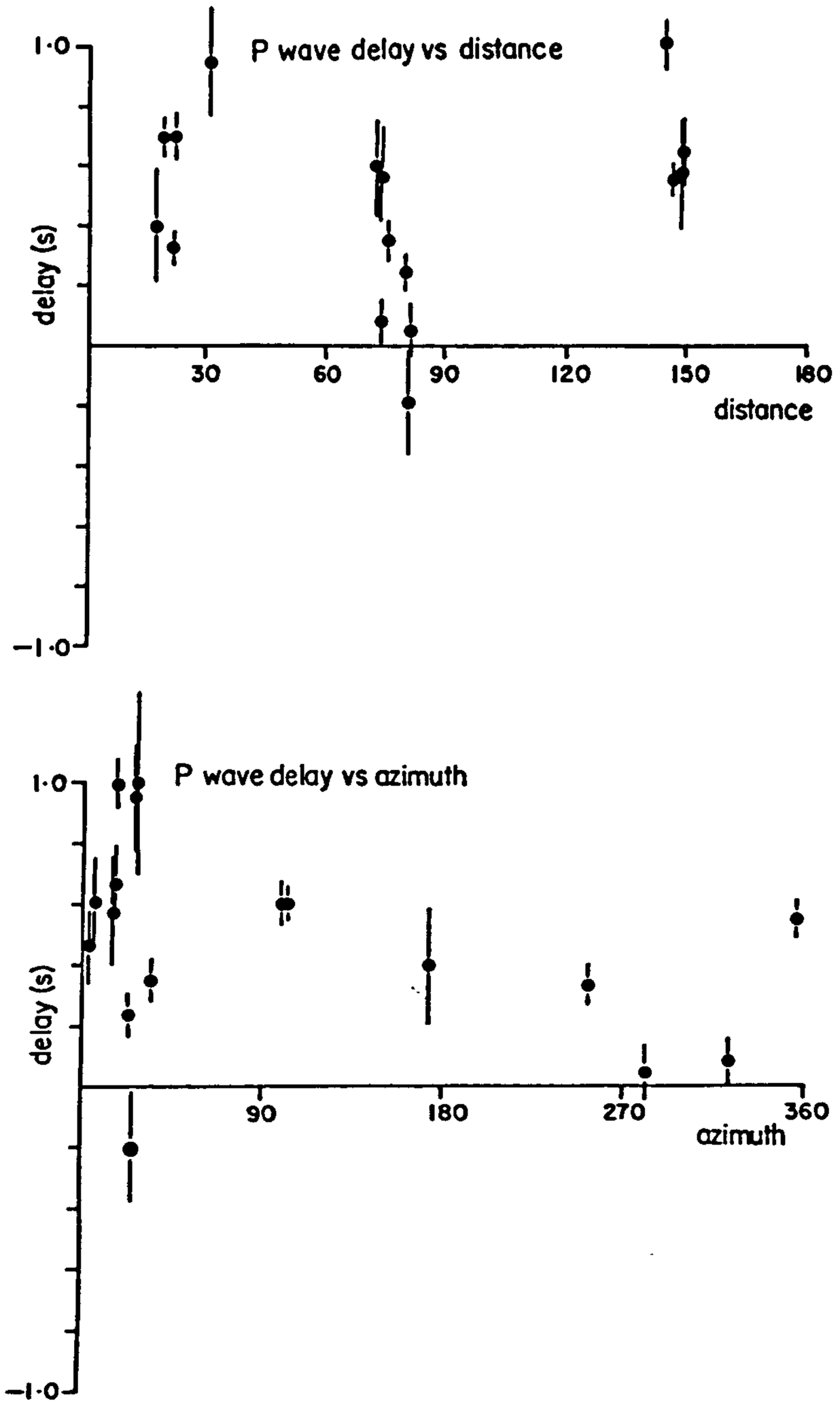

FIG 7-7 CWF relative to HPK

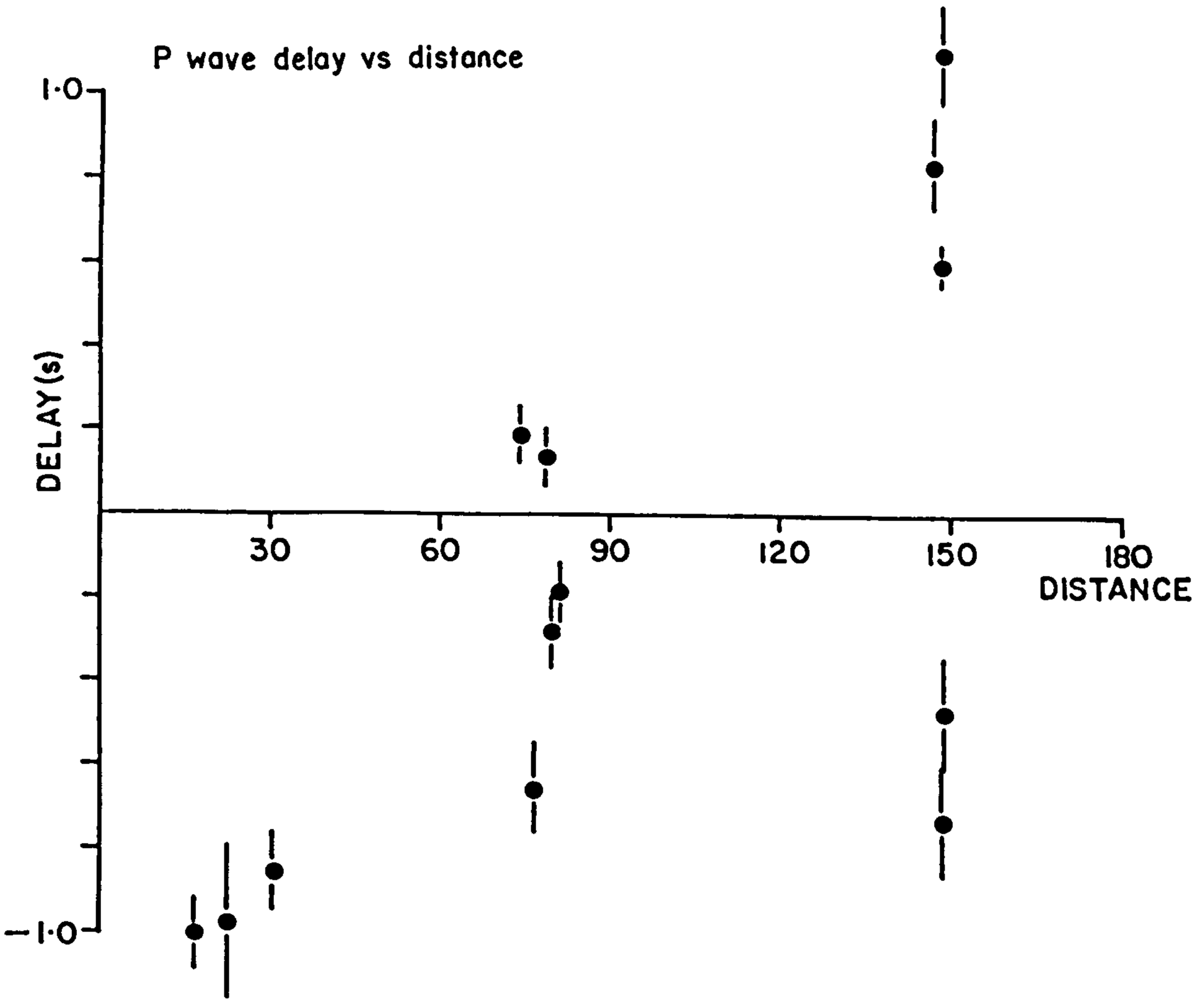

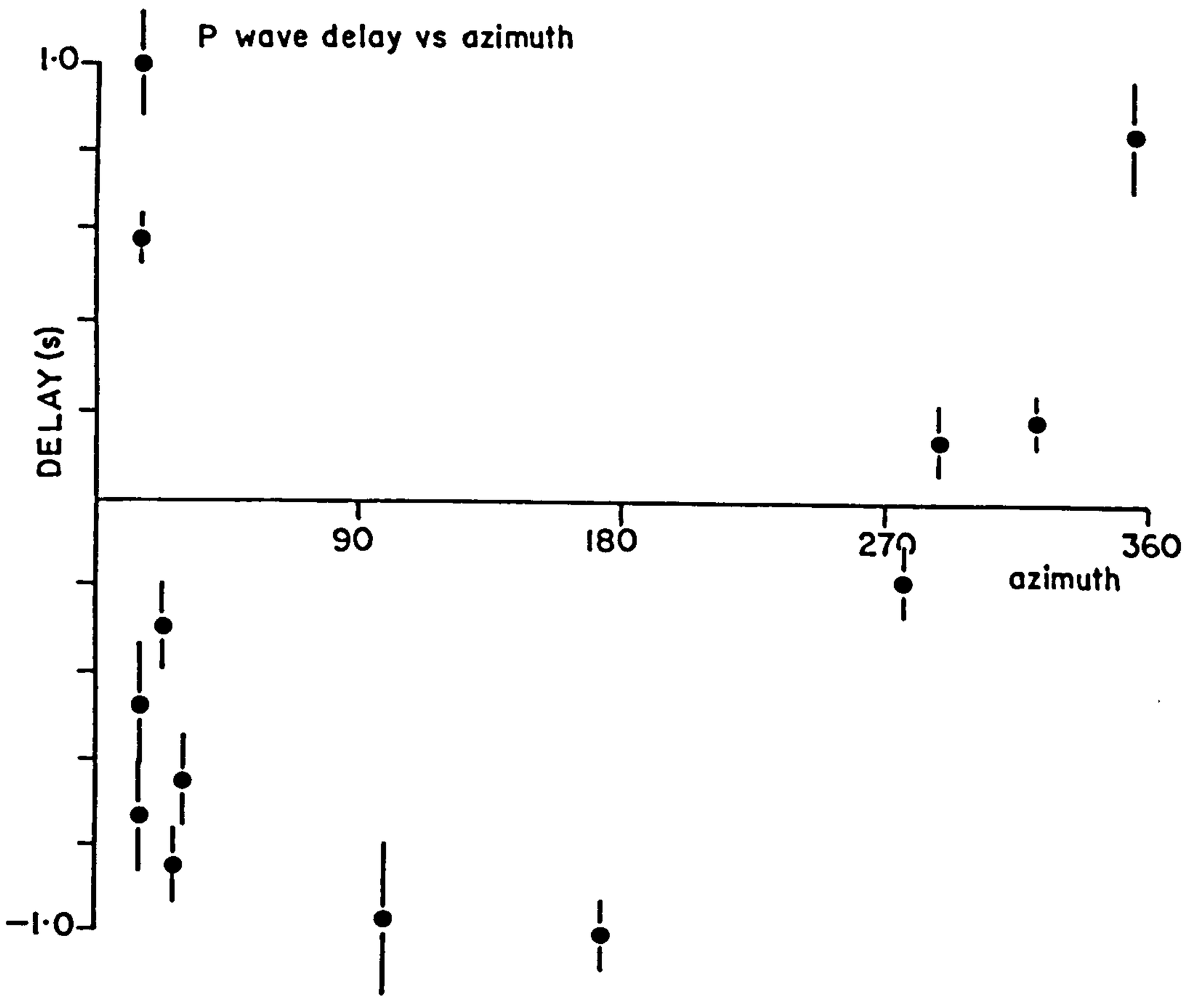

1974), which may have a pronounced effect on P wave delay times. Is it therefore coincidence that the anomalous azimuth window is in the direction of the Charnoid trend (Precambrian or Caledonian)? Obviously there is scope for a more thorough investigation of the region than attempted here.

7.2.2 Comparison of Stations on the Dome

The maximum separation of observations on the Dome is about 30km, and the differences in relative delay between stations is generally small, less than ± 0.1s. Events with larger relative delays are plotted in Fig. 7.8, where the delay times have been calculated relative to some base station, normally station 14. These have been plotted against station position along the profile. A positive value means the signal at the station is delayed relative to the base.

For the north-south line (Figs. 7.8a-c), the first arrivals at stations 1 to 8 are often earlier than stations 9-15 by 0.05-0.2s for events from various azimuths. It is thought unlikely that these delays are entirely due to the thickness of lower velocity Lower Palaeozoic to the north of the Bonsall Fault (see Fig. 5.16): for a 2km wedge of velocity 5km/s, the difference in travel time with 2km of velocity 5.65km/s to the south is only about 50ms, for a 20 degrees angle of incidence. It is possible the rays to the south are speeded up by an underlying region of high velocity: for example, shallow crystalline basement. Events M4002 and M2028 are both approximately from an azimuth of 20 degrees, but were 30 and 73 degrees distant respectively. For M2028 (Komandorsky Is) the negative relative delay between southern and northern stations is greater than that for the nearer event M4002 (Noveya Zemlya). Thus the more steeply incident P waves for M2028 have travelled relatively further in a higher velocity medium for the southern stations, or lower velocity for the northern stations.

The seismograms for the Noveya Zemlya event M4002 are plotted in Fig. 7.9, uncorrected for epicentral distance. A later phase is seen to emerge between station 13 and 12, which

FIG 7-7 Relative P wave delays between stations on the Dome

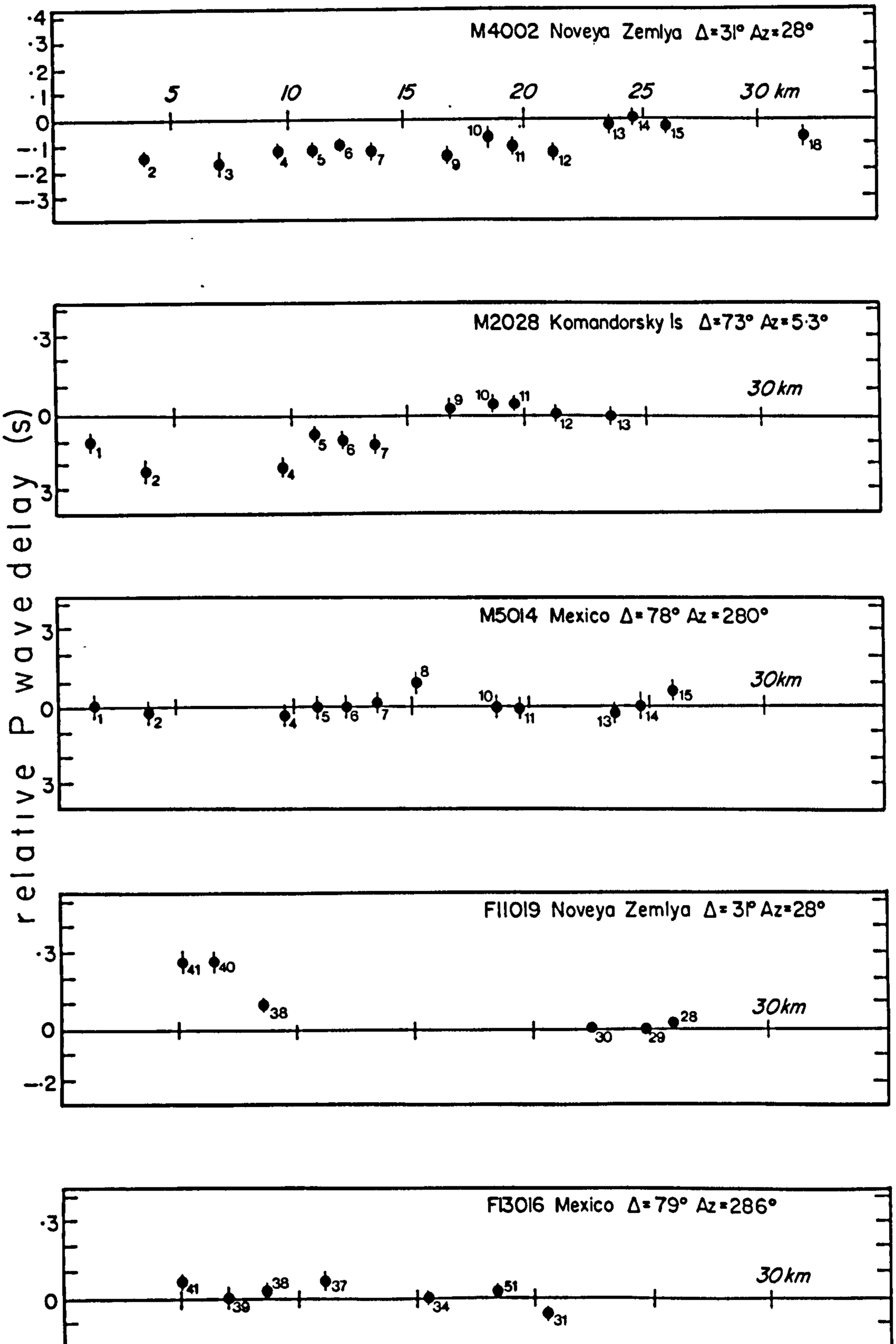

FIG 7-9 M4002 -- NOVEYA ZEMLYA 24/9/1979

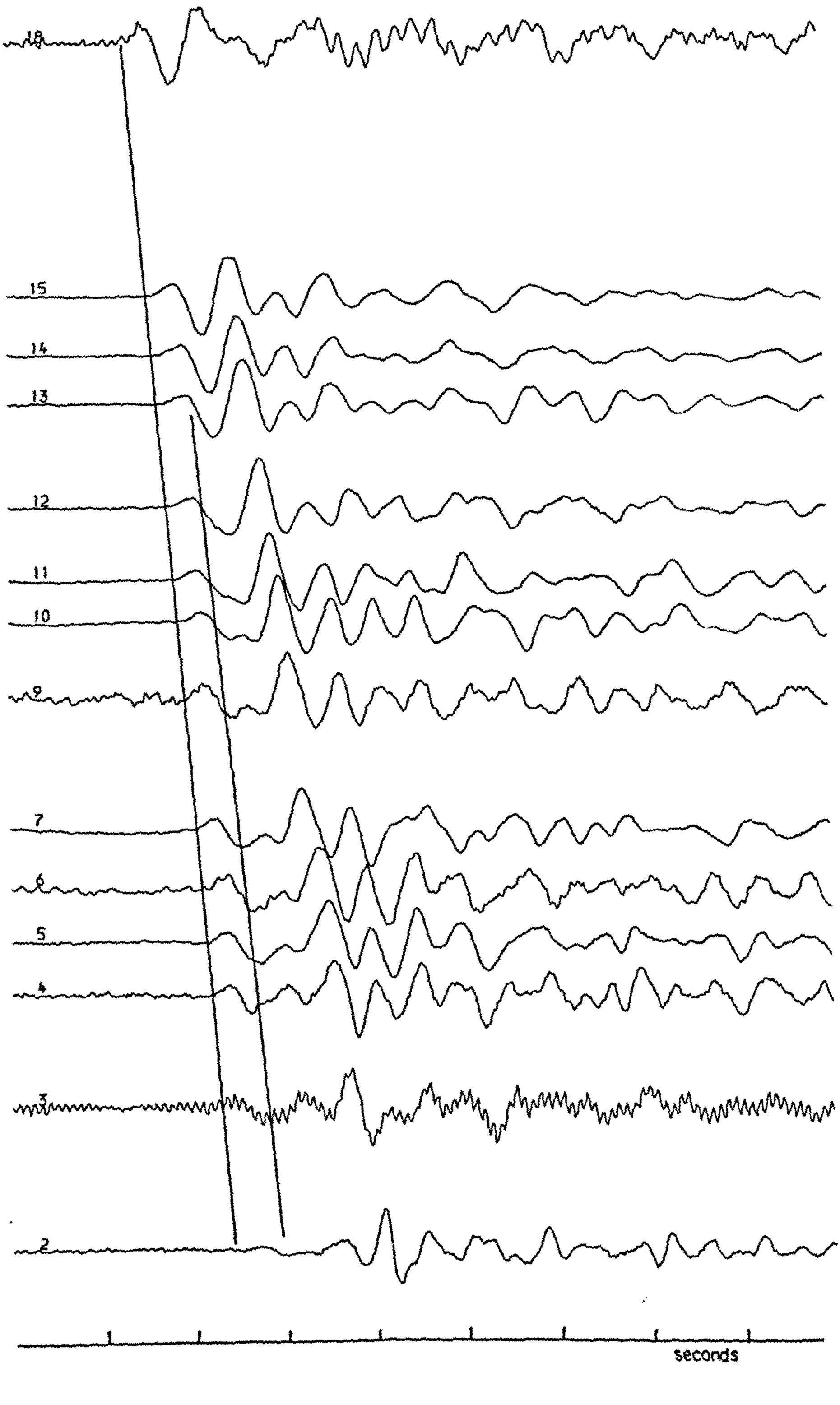

can be traced southwards as far as STM. M4002 is at the wrong distance for a triplication, and a deep origin for the later arrival is thought unlikely because (a) the delay between first and later arrivals is too small, and (b) the emergence of the phase does not correlate with any crustal feature deeper than 5km (see LISPB section Fig. 1.10). Rather, the later arrival is believed to be a free-surface multiple off the pre-Carboniferous surface, which dips southwards from stations 15 to 13. This is because (a) it may have a reversed polarity, and (b) the delay increases from zero at station 15 to 0.7s at station 2, a distance of 25km; thus the apparent dip, ϕ, is given by

$$\frac{d(Dt)}{dx} = \frac{0.7}{25} = \frac{2\tan\phi}{V_o} \quad \text{from which } \phi \simeq 8 \text{ degrees}$$

for overburden velocity, V_o of 5.2km/s. This value for ϕ is consistent with the upper crustal model (Fig. 5.16) at a first approximation.

The two teleseismic events recorded by the NEW profile are both shown. The delay at stations 38 to 41 relative to stations 28 to 30 for the Noveya Zemlya event A11019 may be due to the kilometre thick Millstone Grit in the Goyt Trough, although a similar delay is not observed for the Mexican event F13016.

These events serve to illustrate that some deeper crustal variation is observed by stations on the Dome. Note that were the relative delays between CWF and the Dome calculated using stations south of the Bonsall Fault zone only, the mean delay time between them would be smaller. Thus their underlying crustal structures may be more similar than considered above.

7.3 Gravity Modelling

The object of the exercise was to determine whether or not the interpretations of the seismic refraction profiles

could be used to model the Bouguer anomaly sections. For each of the three longer profiles, a best straight line was constructed through the station positions (except for the NEW profile, where this line was kinked to match the dog-leg between stations 39 and 40). Gravity values were then extrapolated by hand from the IGS Bouguer anomaly worksheet (kindly supplied by B. Chacksfield, IGS, Keyworth). Where possible, the gravity sections were drawn longer than the seismic profiles by about 5-10km at each end: firstly to accommodate edge effects, and secondly to sample as much above the 10mgal contour as possible. Smooth curves were then drawn through these points, and the data points read at kilometre intervals.

The modelling process employed the computer programme G2DPLOT, which calculates the anomaly for two-dimensional bodies on a flat earth (after Talwani et al. 1959). This programme was adapted by Smith (1980) at the University of Leeds for interactive use on a graphical VDU. For each profile a horizontal regional of between 7 and 10mgal was stripped off, assuming that the remainder of the anomaly was due to more dense crystalline basement deeper than sampled by the refraction profiles. These residual anomalies were then modelled until the fit was better than a root-mean-square error of 1mgal, the models being constrained by borehole and seismic data. For these sampled data it was considered unjustified to reduce this error further, nor to model gravity of variations less than about 2km wavelength.

The densities used for these models were:

Millstone Grit -- 2.5g/cc (Maroof 1976)

Carboniferous Limestone -- 2.7g/cc (Maroof 1976)

Upper basement refractor -- 2.74g/cc (consistent with the density of Ordovician shales in the Eyam borehole (Maroof 1976). Maroof measured the density of the Woo Dale volcanics as 2.6g/cc, but Schoefield (University of Manchester, pers. comm.) considers the borehole samples to be too altered to be representative)

Lower basement refractor -- 2.77g/cc (mean of the Charnian sediments listed in Table 1-3)
Redhouse Sandstones -- 2.6g/cc (assumed; Devonian?)
Lower Palaeozoic hidden layer -- 2.62g/cc (modelled, see below)

These densities were expressed as contrasts with the normal reduction density of 2.67g/cc.

7.3.1 North-South Line

The known parameters include the depth to the Woo Dale volcanics and where the Millstone Grit outcrops. A first model employed an undivided Dinantian overburden and a single layer above the lower basement refractor to the north of the Bonsall Fault zone. However, this could neither generate the northward fall in Bouguer anomaly nor maintain shallower basement to the south, so two deeper lower density layers were incorporated (Fig. 7.10).

The densities of the Lower Palaeozoic hidden layer to the north, and the Redhouse sandstones to the south were chosen to keep the depths of the lower basement refractor as consistent as possible with the seismic model. The density assumed for the Redhouse Sandstones is credible for an Old Red Sandstone formation. This layer has been defined north of the Bonsall Fault, but cannot exist as far north as Woo Dale (cf. borehole, Section 1.2.4). It is equally possible that the upper basement refractor subcrops south of the fault, but this has not been considered here.

The positive anomaly between 33 and 38km has been modelled without incorporating another body. It is likely that this anomaly is due to a shallow, high density mass: the feature occurs close to a dolerite intrusion north of Woo Dale (see Fig. 1.5).

Of course, this model is not unique, and the inclusion of a deeper, more dense body to the south of the line would

FIG 7-10 North-south line

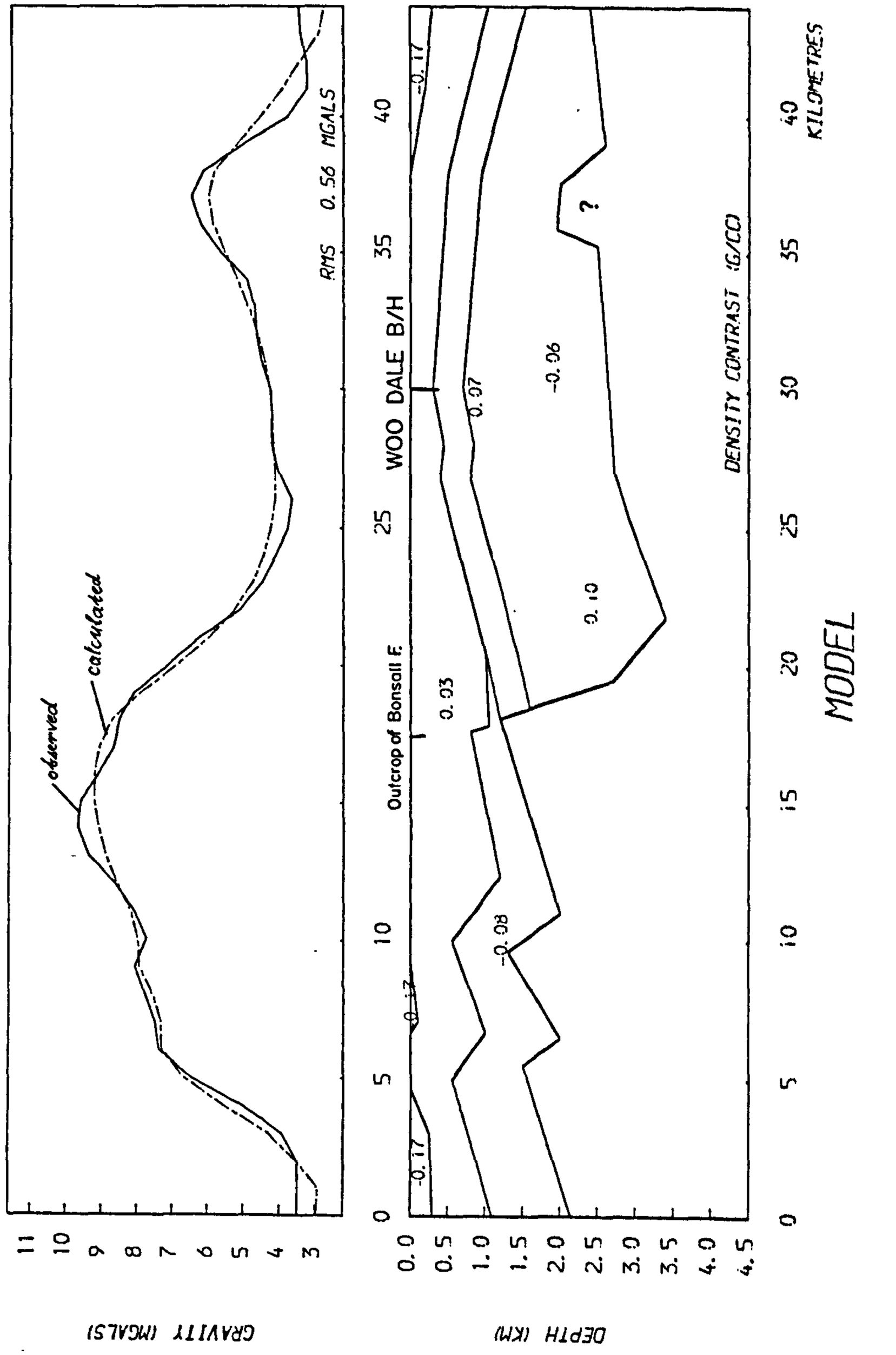

require no lower density material to the north. The sediments of the Charnwood Forest inlier have been estimated by Watts (1947) to be at least 2.3km thick, beneath which Whitcombe and Maguire (1980) determined a high (6.4km/s) velocity upper crustal refractor. Such a refractor may underly the Dome and be shallower to the south of the Bonsall Fault, although no refractions at that velocity were observed.

7.3.2 Northern East-West Line

The model of Fig. 7.11 assumes that the volcanics in the Woo Dale borehole and the Ordovician shales encountered by the Eyam borehole can be treated as a single horizon. The Bouguer anomaly high is about 8km west of the Woo Dale anticline, and this model employs the idea that the lower basement refractor is shallowest below the structural high between stations 36 and 39.

The model was mainly based upon the outcrops of Millstone Grit and the depths to the upper basement refractor, for which there is better geological and seismic control than the deeper horizons. Since the NEW and north-south lines were modelled at the same time, the thickness and density of the Lower Palaeozoic hidden layer was adjusted to maintain a consistent picture.

7.3.3 Southern East-West Line

The Bouguer anomaly section suggests a shallow, fairly flat basement between 8 and 32km. In order to allow a basement refractor to dip steeply west of station 56, a body of Lower Palaeozoic density was introduced to compensate (Fig. 7.12). The shallowing of the basement east of 25km has been inferred from the time-terms for stations 47 and 48, although there are no seismic data east of about 28km. It is also possible that the gravity high to the east is associated with volcanics around Matlock with which the feature correlates.

FIG 7-11 Northern east-west line

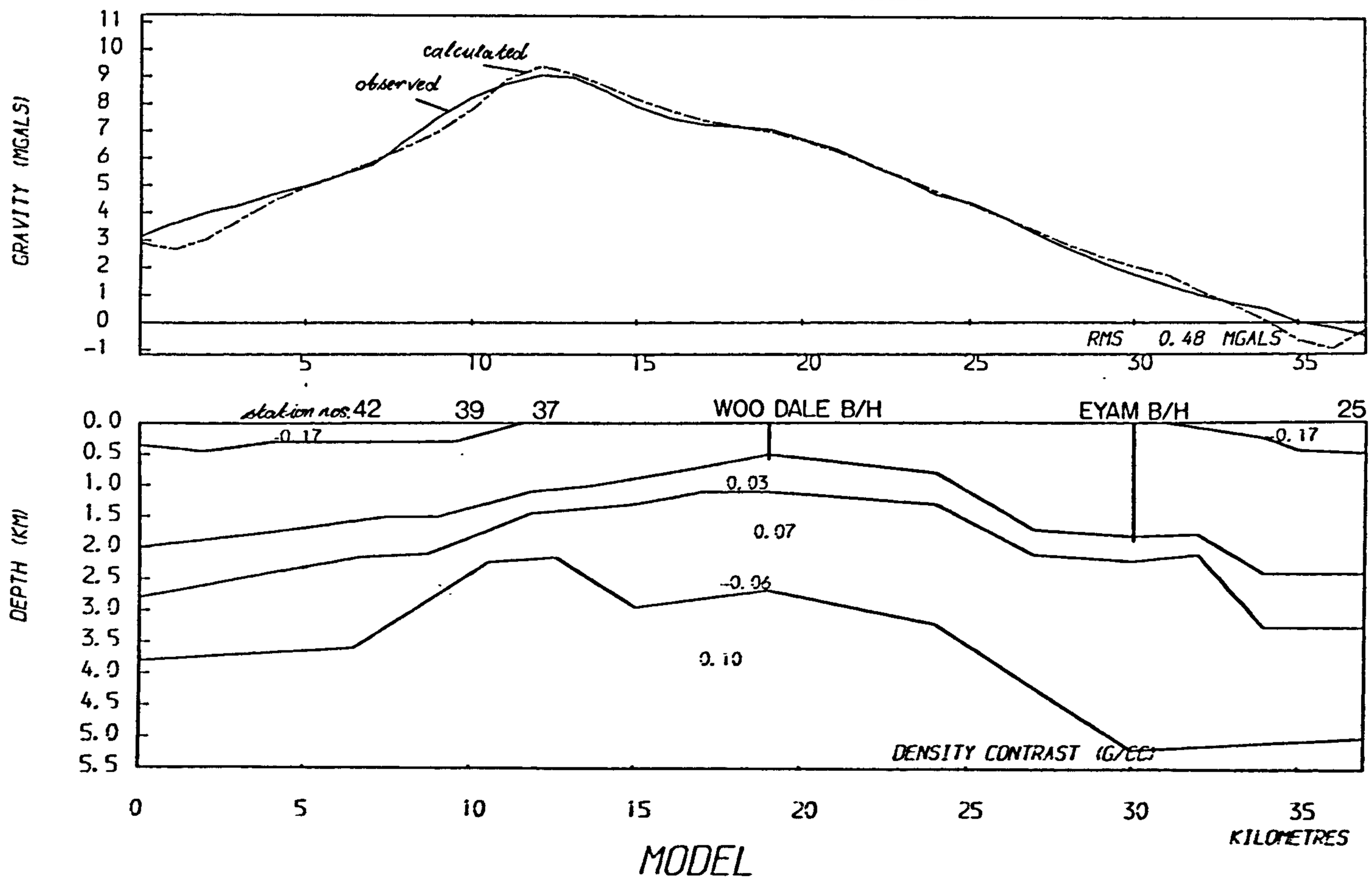

FIG 7-12 Southern east-west line

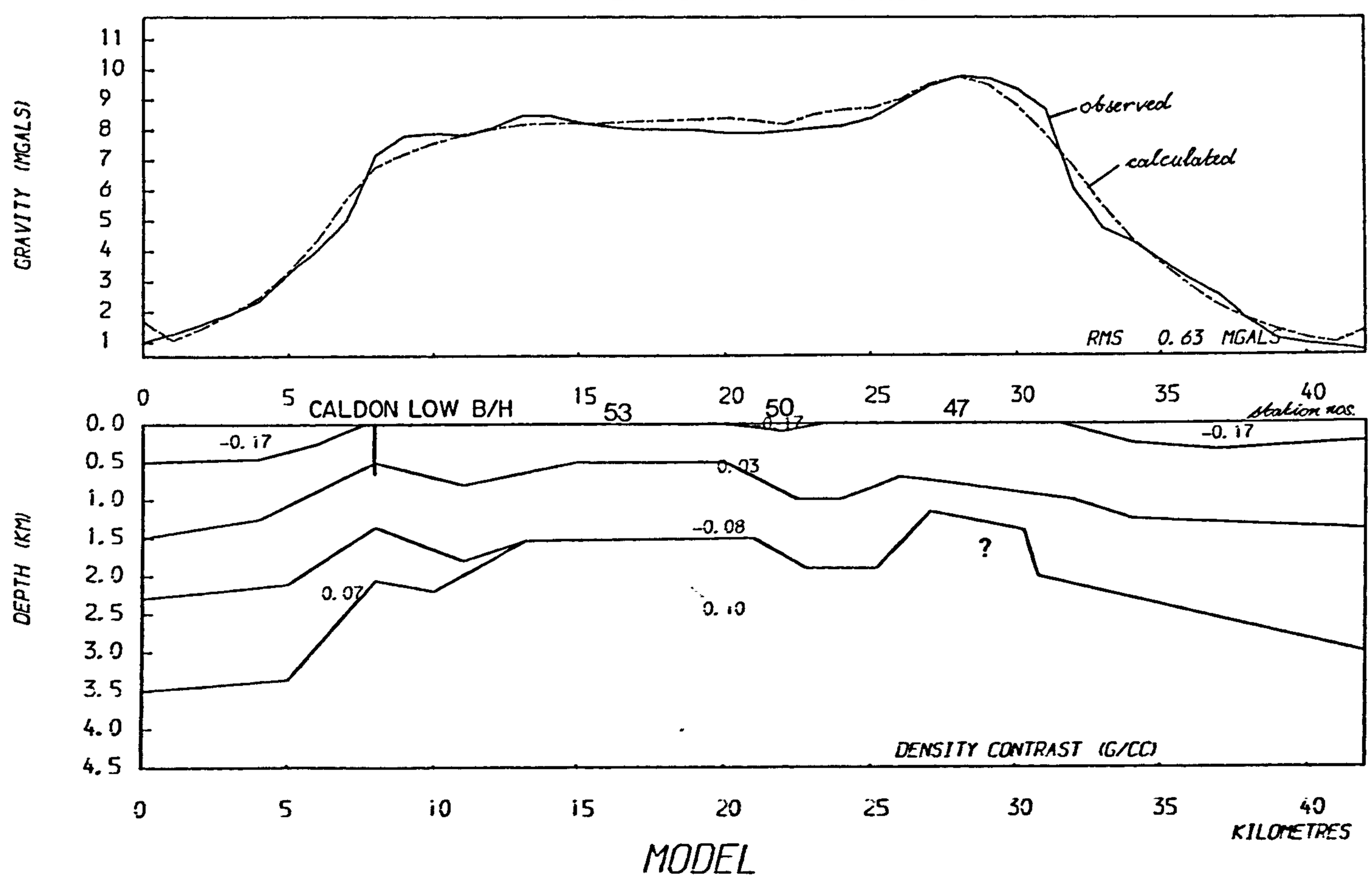

This model has not considered any decrease in density between limestones on the massif and those in the basinal region (west of about 22km). If the limestones were generally less dense, then a thinner sequence of Redhouse Sandstones would be required; the broadening of the P waves west of station 56 was thought to imply that these sandstones thickened westwards (see Section 5.6.3).

7.3.4 General Remarks

These models demonstrate that the structure of the Dome interpreted from the seismic refraction data can be used as a basis upon which to model the Bouguer anomalies. Changes in overburden density between massif and basinal facies, and also because of dolomitisation (which would increase limestone density), have not been taken into account. It could be argued that the density chosen for the hidden layer is too low. If so then the difference in Bouguer anomaly between southern and northern provinces may be due to a more dense crystalline basement shallower to the south, but still deeper than the refraction data have sampled.

7.4 General Conclusions - Comments on the Structure of the Derbyshire Dome

The interpretation of the four refraction profiles is depicted by the isometric projection of Fig. 7.13, which is based upon the time-term solutions of Sections 6.4.1 and 6.4.2. As suspected from previous geological and geophysical work, the cover of Carboniferous rocks disguises a more complicated deeper structure. The Dome appears to be divided into two basement provinces, separated approximately by the line of the NNW trending Bonsall Fault. To the north the Carboniferous appears to be underlain by a refractor of velocity 5.5-5.55km/s, which is believed to correlate with the volcanics in the Woo Dale borehole and the Ordovician

FIG 7-13 Isometric projection of the interpreted structure of the Derbyshire Dome

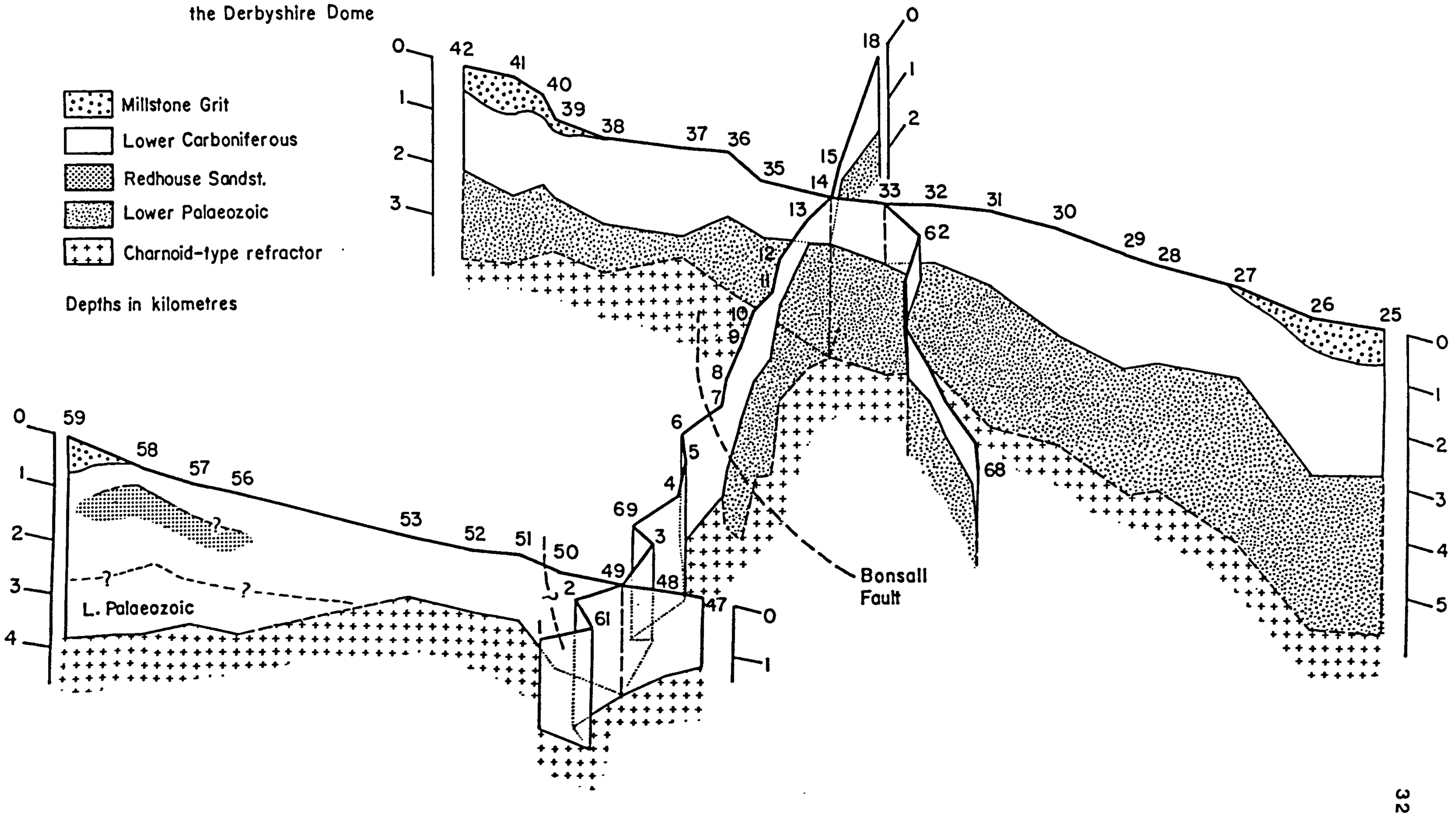

shales encountered at the base of the Eyam borehole, the relationship between which is uncertain. Characteristically, refracted P waves observed in the southern province are of lower frequency, less rapidly attenuated and correlate better between stations than those observed from the Lower Palaeozoic refractor to the north.

The Bonsall Fault appears to be the surface expression of a more important basement fault, to the north of which later arrivals are observed in the P wave coda which have been interpreted as refractions from the downfaulted Charnoid-type basement. Under the northern province the Lower Palaeozoic refractor may be less than 500m thick, deduced from the increased attenuation of refracted P waves of frequency less than about 10Hz. Refractions are not apparent from any horizon between this Lower Palaeozoic refractor and the Charnoid-type basement, so a hidden or low velocity zone has been inferred. The mean velocity of this hidden layer is uncertain but probably less than 5.3km/s in order for the calculated depth to the lower basement refractor to be geologically feasible (i.e., less than about 4km). Wills (1978) has postulated that beneath the Llanvirnian shales of the Eyam borehole there is a sedimentary sequence comparable with the quartzites, shales and sandstones at the base of the Duke's Wood borehole near Mansfield, thought to be Cambrian (Edwards 1967). The Cambrian Stockingford shales near Nuneaton were found to have a P wave velocity of about 4km/s (Whitcombe and Maguire 1981a), so it is possible that the Charnoid-type basement is even shallower to the north of the Bonsall Fault than shown by Fig. 7.13.

A speculative pre-Carboniferous palaeogeology of the Dome based upon these seismic data and the Bouguer anomaly map has been sketched in Fig. 7.14. The distribution of the sandstones encountered by the Caldon Low borehole is unknown, and their widespread occurrence beneath the southern province is inferred from (a) the pronounced high frequency filtering of basement refractions, (b) a shallow borehole near Matlock (Chisholm and Butcher, 1981), and (c) the modelling of the

FIG 7-14 Speculative pre-Dinantian geological outcrop

Bouguer anomaly (Section 7.3.1). These sandstones must thin or be faulted out south of the Woo Dale and Eyam boreholes, in which they were not found. They do not appear to have sufficient velocity contrast with the Dinantian limestones to produce refractions.

The area underlain by the Woo Dale volcanics is also uncertain. For Fig. 7.14 their subcrop has been constructed from those stations whose time-terms for the upper basement refractor were markedly smaller (less than .04s) than adjacent stations.

The fault drawn marking the western boundary of the Precambrian block is inferred from a north-south trending band of closely spaced gravity contours. The basement fault that divides north and south provinces is characterised by an eastward increasing gravity gradient, which suggests that its throw also increases eastwards.

At the surface, the maximum northward throw across the Bonsall Fault system is less than 150m. Thus most of the displacement across the basement fault associated with it must have taken place before the Asbian. It is possible that this fault was active concurrently with the eastward tilting of the pre-Carboniferous floor between Woo Dale and Eyam. If so, then the northern province can be considered as an independent tilt-block without necessitating a similar eastward tilting of the basement in the south, say between Ballidon and Matlock. This mechanism is sketched in Fig. 7.15, which is loosely based on the model of Miller and Grayson (1982; Fig. 1.8). The western margin of the Dome (Fig. 7.14) is thus considered to be a relatively stable 'hinge' zone. (Note: at outcrop the Bonsall Fault appears to be a scissor fault with a southerly downthrow in the Matlock region. Thus some retrograde displacement has occurred, possible during the Hercynian orogeny).

The pre-Carboniferous surface generally appears to be more irregular underneath the profiles that cross the southern province than those to the north. Surprisingly, the basement does not appear to deepen systematically across the

FIG 7-15 Postulated structural control of Dinantian sedimentation

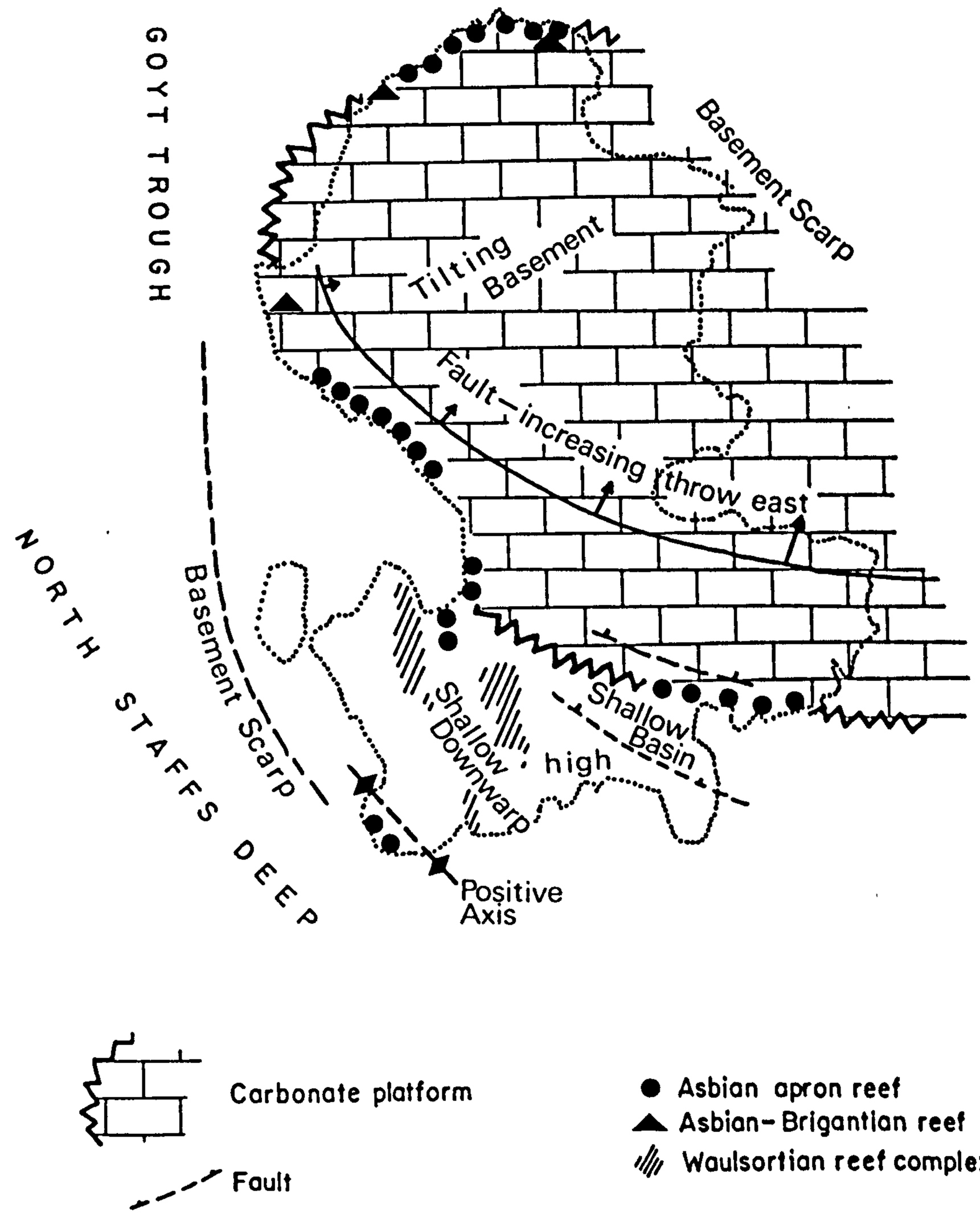

Dovedale transition from massif to basinal facies. The transition is, however, marked by a NW-SE trending, possibly fault-bounded, system of basins, which may represent tectonic complication between the two regions on the lip of the Widmerpool Gulf. The pre-Carboniferous basement is seen to deepen appreciably into the Gulf west of Cauldon Low, which is itself seen as a positive basement feature (Fig. 7.15).

The reason that the southern province may not have readily subsided like the north may be because it had greater support from underlying crystalline basement. This is also suggested by the relative teleseismic P wave delays, which showed speeding up under the southern province. However, if there is such a high velocity supporting basement, then it is too deep to investigate with these refraction data.

REFERENCES

BAMFORD, D., 1971, Applications of simulated data studies to crustal refraction studies, Bull. seism. Soc. Am., v61, 1013-1031

BAMFORD, D., 1973, An example of the iterative approach to time-term analysis, Geophys. J. R. astr. Soc., v31, 365-372

BAMFORD, D., 1976, MOZAIC time-term analysis, Geophys.J.R. astr. Soc., v44, 433-446

BAMFORD, D., FABER, S., JACOB, B., KAMINSKI, W., NUNN, K., PRODEHL, G., FUCHS, K., KING, R. and WILLMORE, P., 1976, A Lithospheric Seismic profile in Britain - I preliminary results, Geophys. J.R. astr. Soc., v44, 145-160

BAMFORD, D., NUNN, K., PRODEHL, C. and JACOB, B., 1977, LISP - III. Upper crustal structure of northern Britain, Jl. Geol. Soc. Lond., v133, 1977, 481-488

BAMFORD, D., NUNN, K., PRODEHL, C. and JACOB, B., 1978, LISB - IV. Crustal structure of Northern Britain Geophys. J.R. astr. Soc., v54, 43-60

BAMFORD, D. and PRODEHL, C., 1978, Explosion seismology and the continental crust-mantle boundary, Jl. Geol. Soc., v134, 139-152

BARRY, K.M., 1967, Delay time and its application to refraction profile interpretation, In Seismic Refraction Prospecting, Ed. A. Musgrave, S.E.G. (Tulsa)

BAYERLY, M., 1978, Quarry blast seismic studies in S. Wales, Unpubl. PhD thesis (University College of Wales, Cardiff)

BAYERLY, M. and BROOKS, M., 1980, A seismic study of deep structure in South Wales using quarry blasts, Geophys. J.R. astr. Soc., v60, 1-20

BENNISON, G.M. and WRIGHT, A.E., 1969, The Geological History of the British Isles, E. Arnold (London)

BERMINGHAM, P.M., 1978, Determination of teleismic P wave relative delay time between Eskdalemuir and Charnwood Forest, Unpubl. rep. (University of Leicester)

BERRY, M.J. and WEST, G.F., 1966, An interpretation of the first-arrival data of the Lake Superior experiment by the time-term method, Bull. seis. Soc. Am., v56, 141-171

BIRCH, A.F., 1958, Interpretation of the seismic structure of the crust in the light of experimental studies of wave velocities in rocks, In Contributions in Geophysics in Honour of Beno Gutenburg, Ed. Benioff International Series of Monographs in Earth Sciences, v1, 158-170

BOTT, M.H.P., 1961, Geological interpretation of magnetic anomalies over the Askrigg Blocks, Jl. Geol. Soc. Lond., v67, 481-495

BOTT, M.H.P., 1967, Geophysical investigations of the Northern Pennine basement rocks, Proc. Geol. Soc. Yorks., v36, 139-168

BRIDEN, J.C., WHITCOMBE, D.N., STUART, G.W., FAIRHEAD, J.D., DORBATH, C. and DORBATH, L., 1981, Depth of geological contrast across the West African craton margin, Nature, v292, 123-128

BROOKS, M. and AL-SAADI, R.H., 1977, Seismic refraction studies of geological structure in the inner part of the Bristol Chanel, Jl. Geol. Soc., v133, 433-446

BULLERWELL, W., 1965, Aeromagnetic map of Great Britain (Sheet 2) 1st Edition, I.G.S. (London)

CHISHOLM, J.I. and BUTCHER, N.J.D., A borehole proving dolomite beneath the Dinantian limestones near Matlock, Derbyshire, Mercian Geologist, v8, 225-228

CHROSTON, P.N. and SOLA, M.A., 1981, Deep boreholes, seismic refraction lines and the interpretation of gravity anomalies in Norfolk, Jl. Geol. Soc., v.139, 255-264

COPE, F.W., 1973, Woo Dale borehole near Buxton, Derbyshire, Nature, v243, 29-30

COPE, F.W., 1979, The age of the volcanic rocks in the Woo Dale borehole, Derbyshire, Geol. Mag., v116, 319-320

CRAMPIN, S., McGONIGLE, R. and BAMFORD, D., 1980, Estimating crack parameters from observations of P-wave velocity anisotropy, Geophysics, v45, 345-360

DONATO, R.J., 1960, Seismic model experiments on the shape and amplitude of the refracted wave, Geophys, J.R. astr. Soc., v3, 270-271

DUNHAM, K., 1973, A recent deep borebole near Eyam, Derbyshire, Nature, v214, 84-85

DUNHAM, K., 1974, Granite beneath the Pennines in N. Yorks, Proc. Yorks. Geol. Soc., v40, 191-194

EDWARDS, W.N., 1967, Geology of the country around Ollerton, Mem. Geol. Surv. U.K.

EDWARDS, W. and TROTTER, F.M., 1954, The Pennines and adjacent areas, Brit. Regional Geol., H.M.S.O.

EL-NIKHELY, ADLY, H.D., 1980, Seismic reflection, gravity and magnetic studies of the geology of the East Midlands, Unpubl. PhD. Thesis (University of Leicester)

EVANS, A.M., 1979, The East Midlands Aulacogen of Caledonian Age, Mercian Geologist, v7, 31-42

EVANS, A.M. and MAROOF, S.I., 1976, Basement controls on mineralisation in the British Isles, Mining Magazine, v134, 401.411

FALCON, N.L. and KENT, P.E., 1960, Geological results of petroleum exploration in Britain 1945-1957, Mem. Geol. Soc. Lond. no. 2

FAREY, J., 1817, A general view of the agriculture and minerals of Derbyshire

FEARNSIDES, W.G., 1933, A correlation of structures in the coalfields of the Midland Province, Rep. Brit. Assoc. (Leicester), 57-80

FORD, T.D., 1961, Recent studies of mineral distribution in Derbyshire and their significance, Bull. Peak Dist. Mines Hist. Soc., v2, 3-9

FORD, T.D., 1968, The Carboniferous Limestone, In Geology of the East Midlands, Ed. P.C. Sylvester-Bradley and T.D. Ford, Leicester University Press

FORD, T.D., 1972, Supplement to the bibliography of the Geology of the Peak District of Derbyshire, Mercian Geologist, v4, 109-137

FORD, T.D. and SARJEANT, W.A.S., 1964, The Peak District mineral index, Bull. Peak Dist. Mines Hist. Soc., v2, 122-150

FORD, T.D. and MASON, M.H., 1967, Bibliography of the geology of the Peak District of Derbyshire (to 1965), Mercian Geologist, v2, 133-244

FROST, D.V. and SMART, J.G.O., 1979, Geology of the country north of Derby, Mem. Geol. Surv. U.K.

GARDNER, L.W., 1939, An areal plan of mapping subsurface structure by refraction shooting, Geophysics, v4, 247-259

GEORGE, T.N., 1958, Lower Carboniferous palaeogeography of the British Isles, Proc. Yorks. Geol. Soc., v31, 227-318

GEORGE, T.N., 1962, Devonian and Carboniferous foundations of the Variscides in N.W. Europe, In Some Aspects of the Variscan Fold Belt, Ed. K. Coe

GEORGE, T.N., 1963, Tectonics and palaeography in Northern England, Sci. Progress Lond., v51, 32-59

GEORGE, T.N., JOHNSON, G.A.L., MITCHELL, M., PRENTICE, J.E., RAMSBOTTOM, W.H.C., SEVASTOPULO, G.D. and WILSON, R.B., 1976, A correlation of the Dinantian in Britain, Geol. Soc. spec. rep. no. 7

GREEN, G.W. and WELSH, F.B.A., 1965, Geology of the country around Wells and Cheddar, Mem. Geol. Surv. U.K.

GREENHALGH, S.A., 1980, Effects of delay shooting on the nature of P-wave seismograms, Bull. seism. Soc. Am., v70, 2037-2050

HABBERJAM, G.M. and THANASSOULAS, D., 1979. A deep resistivity sounding at Rookhope, N. England, Trans. Royal Soc. Edin., v70, 171-179

HAGEDOORN, J.G., 1959, The plus-minus method of interpreting seismic refraction sections, Geophys. Prosp., v7, 158-82

HEELAN, P.A., 1953, On the theory of head waves, Geophysics, v18, 871-893

HERRIN, E., TUCKER, W., TAGGART, J., GORDON, D. and LOBDELL, J., 1968, Estimation of surface focus P travel times, Bull. seism. Soc. Am., v58, 1273-1292

HESS, H., 1964, Seismic anisotropy of the uppermost mantle under oceans, Nature, v203, 629-631

HUDSON, R.G.S. and COTTON, G., 1945, The Lower Carboniferous in the boring at Alpont, Derbyshire, Proc. Yorks. Geol. Soc., v25, 254-330

INESON, P.R. and AL-KUFAISHI, F.A.M., 1970. The mineralogy and paragenetic sequence of Long Rake Vein at Raper Mine, Derbyshire, Mercian Geologist, v3, 337-351

INESON, P.R. and FORD, T.D., 1982, The South Pennine orefield: its genetic theories and eastward extension, Mercian Geologist, v8, 285-303

INESON, P.R. and MITCHELL, J.G., 1972, Isotropic age determinations on clay minerals from lavas and tuffs of the Derbyshire orefield, Geol. Mag., v109, 501-512

KENNET, B.L.N., 1977, Towards a more detailed seismic picture of oceanic crust and mantle, Marine Geophys. Res. v3(1)

KENT, P.E., 1957, Triassic relics and the 1000ft. surface in the Southern Pennines, East Midlands Geog., v1, 3-10

KENT, P.E., 1966, The structure of the concealed Carboniferous rocks of N.E. England, Proc. Yorks. Geol. Soc., v35, 323-352

KENT, P.E., 1974, Structural History, In Geology and Mineral Resources of Yorkshire, Ed. D.H. Rayner and E.M. Hemmingway, Yorks. Geol.Soc. (Leeds)

KUSZNIR, N.J., ASHWIN, D.P. and BRADLEY, A.G., 1979, Mining induced seismicity in the North Staffordshire coalfield, England, Jl. Rock Mech. Min. Sci. and Geomech. Abstr., v17, 45-55

KUSZNIR, N.J., FARMER, I.W., ASHWIN, D.P., BRADLEY, L.G. and AL-SAIGH, N.H., 1980, Observations and mechanics of seismicity associated with coal mining in N. Staffordshire, England (Unpubl.) 21st U.S. Rock Mech Symp.

LAYAT, C., 1967, Modified 'Gardner' delay time and constant distance correlation, In Seismic Refraction Prospecting, Ed. A. Musgrave, S.E.G. (Tulsa)

LE BAS, M.J., 1971, Caledonian igneous rocks beneath Central and Eastern England, Proc. Yorks. Geol. Soc., v39, 71-86

LEES, G.M. and TAITT, A.H., 1946, The geological results of the search for oil fields in G.B., Qt. Jl. Geol. Soc. Lond., v101, 255-317

LEWIS, G.D., 1971, Earliest times to Norman conquest, In Peak District, Ed. P. Monkhouse, H.M.S.O. National Park Guide No. 3

LEEDER, M.R., 1982, Upper Palaeozoic basins of the British Isles Caledonide inheritance versus Hercynian plate margin processes, Jl. Geol. Soc. Lond., v139, 479-491

LONG, R.E. and MITCHELL, M.G., 1970, Teleseismic P wave delay time in Iceland, Geophys. J. R. astr. Soc., v20, 41-48

MAGUIRE, P.K.H., BERMINGHAM, P.M. and FRANCIS, D.J., 1981, A relative P wave delay study between Eskdalemuir and Charnwood Forest, Geophys. J.R. astr. Soc., v65, 229-235

MAGUIRE, P.K.H., WHITCOMBE, D.N. and FRANCIS, D.J., 1982, Seismic Studies in the Central Midlands of England 1975-1980, Trans. Leic. Lit. and Phil. Soc., v75, 58-66

MAROOF, S.I., 1973, Geophysical investigations of the Carboniferous and pre-Carboniferous formations of the East Midlands of England, Unpubl. PhD thesis (University of Leicester)

MAROOF, S.I., 1976, The structure of the concealed pre-Carboniferous basement of the Derbyshire Dome from gravity data, Proc. Yorks. Geol. Soc., v41, 59-69

McDONALD, A.J.W., 1982, Surface waves over the Derbyshire Dome, Geophys. J.R. astr. Soc., v69, 278 (abstr.)

MEISSNER, R. and FAKHINI, M., 1977, Seismic anisotropy as measured under high-temperature conditions, Geophys. J.R. astr. Soc., v49, 133-143

MILLER, J. and GRAYSON, R.F., 1982, The regional context of Waulsortian facies in N. England (in press)

MURDOCK, J., 1980, Seismic velocity structure of the metamorphic belt of central California, Bull. seism. Soc. Am. v70, 203-221

O'BRIEN, P.N.S., 1967, The use of amplitudes in seismic refraction survey, In Seismic Refraction Prospecting, Ed. A. Musgrave, S.E.G. (Tulsa)

OWEN, T.R., 1976, The geological evolution of the British Isles, Pergamon Press (London)

PALMER, D., 1974, An application of the time section in shallow seismic refraction studies, Unpubl. MSc thesis (University of Sydney)

PARKINSON, D., 1950, The stratigraphy of the Dovedale area, Derbyshire and Staffordshire, Qt. Jl. geol. Soc. Lond., v105, 265-294

PARKINSON, D. and LUDFORD, A., 1964, The Carboniferous limestone of the Blore-with-Swinscoe district N.E. Staffordshire, with revisions to the stratigraphy of the neighbouring areas, Geol. Jl., v4, 167-76

PEASLEY, G.M., 1980, Travel time analysis between Eskdalemuir and two Leeds stations, Unpubl. MSc. thesis (University of Leeds)

PHILLIPS, W.E.A., STILLMAN, C.J. and MURPHY, T., 1976, Caledonide plate tectonic model, Jl. Geol. Soc. Lond., v132, 579-609

PIGOTT, C.D., 1965, Structure of limestone surfaces in Derbyshire, Geol. Jl., v131, 645-652

PRENTICE, J.E., 1951, The Carboniferous limestone of the Manifold Valley region, N. Staffordshire, Qt. Jl. geol. Soc. Lond., v106, 171-209

RAITT, R.W., SHOR, G.G., FRANCIS, T.J.G. and MORRIS, G.B., 1969, Anisotropy of the Pacific upper mantle, J. Geophys. Res., v74, 3095-3109

RAMSBOTTOM, W.H.C., 1973, Transgressions and regressions in the Dinantian: a new synthesis of British Dinantian stratigraphy, Proc. Yorks. Geol. Soc., v39, 567-607

RAMSBOTTOM, W.H.C., 1974, Carboniferous, In the Geology and Mineral Resources of Yorkshire, Ed. D.H. Rayner and J.E. Hemingway, Yorks. Geol. Soc. (Leeds)

REITER, L., 1970, An Investigation into the time-term method in refraction seismology, Bull seism. Soc. Am., v60, 1-13

ROGERS, D.E., 1980, Seismic studies on the Derbyshire Dome, Geophys. J.R. astr. Soc., v61, 199 (abstr.)

SAMSON, J.C., 1973, Descriptions of the polarisation states of vector processes; applications to ULF magnetic fields, Geophys. J. Royal astr. Soc., v34, 403-419

SAMSON; J.C., 1980, Comments on Polarisation and coherence, J. Geophys. Res., v48, 195-198

SAMSON, J.C. and OLSON, J.V., 1981, Data-adaptive polarisation filters for multichannel geophysical data, Geophysics, v46, 1423-1431

SCHEIDEGGER, A.E. and WILLMORE, P.L., 1957, The use of a least-squares method for the interpretation of data from seismic surveys, Geophysics, v22, 9-22

SCHMÖLLER, R., 1982, Some aspects of handling velocity inversion and hidden layer problems in seismic refraction work, Geophys. Prosp., v30, 735-751

SJÖGREN, B., 1979, Refractor velocity determination - cause and nature of some errors, Geophysical Prosp., v27, 507-538

SLOTNICK, M.M., 1959, Lessons in seismic computing, S.E.G. (Tulsa)

SMITH, E.G., RHYS, G.H. and EDEN, R.A., 1967, Geology of the country around Chesterfield, Matlock and Mansfield, Mem. Geol. Surv. U.K.

SMITH, P.M., 1980, Gravity program conversion using data from a survey across the Red Rock Fault, Unpubl. MSc thesis (University of Leeds)

SMITH, T.J., STEINHART, J.S. and ALDRICH, L.T., 1966, Lake Superior crustal structure, J. Geophys Res., v71, 1141-1172

STEPHENS, 1979, A deep electrical sounding on Big and Ramsley Moors, north of Baslow, N. Derbys, Unpubl. MSc thesis (University of Leeds)

STEVENSON, I.P. and MITCHELL, M., 1955, Geology of the country around Burton on Trent, Mem. Geol. Surv. U.K.

STEVENSON, I.P. and GAUNT, G.D., 1971, Geology of the country around Chapel-en-la-Frith, Mem. Geol. Surv. U.K.

TALWANI, M., WORZEL, J.L. and LANDISMAN, M., 1959, Rapid gravity computations for two-dimensional bodies with application to the Mendocino submarine fracture, J. Geophys. Res., v64, 49-59

TELFORD, W.M., GELDART, L.P., SHERIFF, R.E. and KEYS, D.A., 1976, Applied Geophysics, Cambridge University Press

THACH, T.K., 1965, Sedimentology of Lower Carboniferous (Visean) Limestones in North Staffordshire and S.W. Derbyshire, Unpubl. PhD thesis (University of Reading)

THORPE, R.S., 1974, Aspects of magmatism and plate tectonics in the Precambrian of England and Wales, Geol. Jl. v9, 115-136

WALKDEN, G.M., 1972, Mineralogy and origins of clay wayboards in the Derbyshire Dome, Geol. Jl. v8, 143-153

WALKDEN, G.M., 1974, Palaeokarst surfaces in Upper Visean limestone of the Derbyshire blocks, Jl. Sedim. Pet., v44, 1232-1247

WALTERS, S.G. and INESON, P.R., 1981, A review of the distribution and correlation of igneous rocks in Derbyshire, England, Mercian Geologist, v8, 81-132

WATTS, W.W., 1947, Geology of the ancient rocks of Charnwood Forest, Leicestershire, Leic. Lit. and Phil. Soc. (Leicester)

WHITCOMBE, D.N., 1979, Seismic studies of the upper crust in Central England, Unpubl. PhD thesis (University of Leicester)

WHITCOMBE, D.N. and MAGUIRE, P.K.H., 1979, The response of the time-term method to simulated crustal structures, Bull. seism. Soc. Am., v69, 1455-1473

WHITCOMBE, D.N., and MAGUIRE, P.K.H., 1980, An analysis of the velocity structure of the Pre-Cambrian rocks of Charnwood Forest, Geophys. J.R. astr. Soc., v63, 405-416

WHITCOMBE, D.N. and MAGUIRE, P.K.H., 1981a, A seismic refraction investigation of the Charnian basement and granitic intrusions flanking Charnwood Forest, Jl. Geol. Soc., v138, 643-652

WHITCOMBE, D.M. and MAGUIRE, P.K.H., 1981b, Seismic refraction evidence for a basement ridge between the Derbyshire Dome and the west of Charnwood Forest, Jl. Geol. Soc., v138, 653-659

WHITCOMBE, D.N. and ROGERS, D.E., 1981, The effects of refractor topography and overburden anisotropy on time-term solutions of refractor anisotropy, Geophys. J.R. astr. Soc., v67, 449-464

WHITE, P.H.N., 1948, Gravity data obtained in Great Britain by the Anglo-American Oil Company Ltd., Qt. Jl. Geol. Soc. Lond., v104, 339-364

WILLMORE, P.L. and BANCROFT, A.M., 1960, The time-term approach to refraction seismology, Geophys. J.R. astr. Soc., v3, 419-432

WILLS, L.J., 1977, A palaeogeological map of the Lower Palaeozoic floor below the cover of Upper Devonian, Carboniferous and later formations, Mem. Geol. Soc. Lond. no. 8

WILSON, A.A. and CORNWELL, J.D., 1982, The Institute of Geological Sciences borehole at Beckermonds Scar, N. Yorks, Proc. Yorks. Geol. Soc., v44, 59-88

WOLFENDEN, E.N., 1958, Palaeoecology of the Carboniferous reef complex and shelf limestones in N.W. Derbyshire, England, Bull. Geol. Soc. Am., v69, 871-898

WYROBEK, S.M., 1956, Application of delay and intercept times in the interpretation of multilayer refraction time distance curves, Geophys. Prosp., v4, 112-130

WYROBEK, S.M., 1959, Well velocity determinations in the English Trias, Permian and Carboniferous, Geophys. Prosp., v7, 218-230.

Appendix A Event data

Digitised quarry faces in red

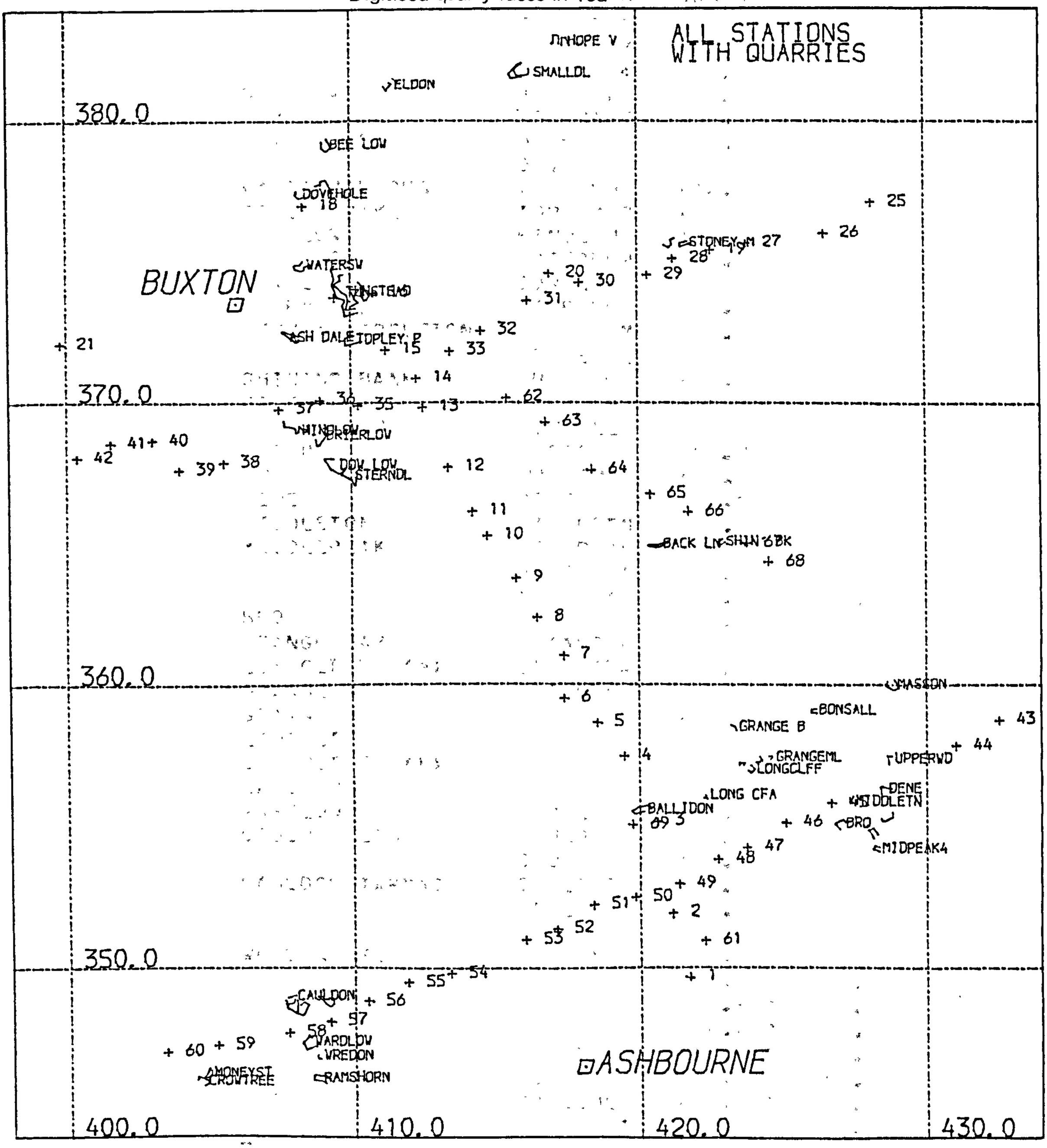

Summary of quarry positions & abbrieviations used by programme MODFIT

TUNSTEAD	TUNSTEAD	409.700	373.860
	TUNSTD 2	409.810	373.870
	TUNSTD 3	410.450	373.880
	TUNSTD 4	410.300	373.620
BEE LOW	BEE LOW	409.170	379.140
ASH DALE	ASH DALE	407.700	372.300
DOVEHOLES	DOVEHOLE	408.210	377.370
	DOVEH 2	409.120	377.650
WATERSWALLOWS	WATERSW	408.310	374.800
TOPLEY PIKE	TOPLEY P	410.050	372.200
HINDLOW	HINDLOW	408.120	368.980
BRIERLOW	BRIERLOW	408.970	368.800
DOW LOW	DOW LOW	409.440	367.760
STERNDALE	STERNDL	409.960	367.400
STONEY MIDDLETON	STONEY M	421.690	375.620
	STONEYM1	421.180	375.600
SHINING BANK	SHIN' BK	422.910	365.060
BACK LANE	BACK LN	420.720	364.970
BONSALL MOOR	BONSALL	426.100	359.100
MASSON	MASSON	428.830	360.000
UPPERWOOD	UPPERWD	428.720	357.410
DENE	DENE	428.520	356.360
MIDDLETON	MIDDLETN	427.360	355.900
MIDDLEPEAK	MIDDPEAK	428.140	354.770
	MIDD PK1	428.620	355.320
	MIDD PK2	427.950	355.050
BRO	BRO	427.020	355.100
GRANGE BAR	GRANGE B	423.320	358.500
LONGCLIFFE (a)	LONG CFA	422.310	356.100
GRANGE BAR	GRANGEML	424.590	357.450
GRANGE BAR	GRANGEM2	424.190	357.350
LONGCLIFFE	LONGCLFF	423.910	357.020
LONGCLIFFE (b)	LONGCL2	423.585	357.200
BALLIDON	BALLIDON	420.100	355.580
WARDLOW	WARDLOW	408.380	347.350
CAULDON LOW	CAULDON	407.800	348.960
	CAULD 2	407.720	348.770
CAULDON TARMAC	CAULD 3	407.800	348.620
	CAULD 4	408.140	348.560
	CAULD 5	409.040	348.830
WREDON HILL	WREDON	408.710	346.850
RAMSHORN	RAMSHORN	408.700	346.090
MONEYSTONE	MONEYST	404.870	346.240
CROWTREES	CROWTREE	404.670	345.960
ELDON HILL	ELDON	411.440	381.260
	ELDON 1	411.440	381.260
SMALLDALE	SMALLDL	416.300	381.700
	SMALLDL1	416.300	381.700
HOPE VALLEY	HOPE V	417.500	382.800
	HOPE V1	417.500	382.800

UNTIMED QUARRY BLASTS—SOLUTION LOCATIONS USING PROGRAMME MODFIT

(I) 1979 Experiment

Event	Quarry	Face	Coordinates		Soln variance	time'nearest station
M1004	STERNDL	2	410.150	367.060	0.00580	0.657
M1009	DOVEHOLE	3	408.100	377.400	0.00186	1.095
M1010	CAULD 4	1	408.080	348.660	0.00101	2.661
M1011	STONEY M	4	421.800	375.700	0.04925	1.350
M1012	RAMSHORN	2	408.800	346.000	0.00058	2.714
M2005	BALLIDON	6	419.940	355.670	0.00261	0.159
M2007	WATERSW	5	408.050	374.850	0.00153	0.401
M2009	TUNSTEAD	1	410.260	373.150	0.00268	0.801
M2013	BEE LOW	3	409.200	378.900	0.00216	0.393
M2015	RAMSHORN	1	408.970	345.920	0.00345	2.395
M2017	MASSON	3	428.900	359.800	0.01072	1.941
M2022	STERNDL	2	410.150	367.060	0.00702	0.611
M2023	MONEYST	5	404.900	346.460	0.00332	3.319
M2026	BRIERLOW	3	409.210	368.930	0.00458	0.682
M2029	UPPERWD	2	428.650	357.520	0.00987	1.929
M2033	BEE LOW	2	409.380	379.030	0.00195	0.427
M2032	DENE	3	428.460	356.460	0.00710	1.593
M2034	STERNDL	2	410.150	367.060	0.01608	0.657
M3003	BALLIDON	6	419.940	355.670	0.01146	0.164
M3008	DOVEHOLE	1	408.360	377.300	0.00230	0.058
M3010	RAMSHORN	4	408.530	346.220	0.00291	2.723
M3031	BRIERLOW	3	409.210	368.930	0.00347	0.682
M3033	HINDLOW	1	408.480	369.170	0.00318	0.769
M3034	CROWTREE	4	404.340	345.960	0.00142	3.407
M3036	BRIERLOW	3	409.210	368.930	0.00410	0.682
M3039	TUNSTD 3	3	410.420	374.110	0.00938	0.465
M4003	BALLIDON	4	419.710	355.530	0.02732	0.191
M4005	BRIERLOW	2	409.140	369.100	0.00861	0.688
M4006	WATERSW	3	408.400	374.630	0.00372	0.472
M4007	TUNSTD 4	4	410.050	373.380	0.01178	0.372
M4008	MIDDPEAK	4	428.300	354.700	0.00655	1.559
M4011	DOVEHOLE	2	408.230	377.260	0.01792	0.057
M4014	CAULD 3	2	407.970	348.380	0.00087	2.693
M4016	MIDDLETN	3	427.330	356.050	0.00688	1.357
M4017	GRANGE B	2	423.350	358.550	0.00365	0.804
M4018	TUNSTD 4	4	410.050	373.390	0.00564	0.428
M4020	DOVEH 2	5	409.380	377.280	0.00395	1.098
M4023	RAMSHORN	2	408.200	346.700	0.00720	2.682
M4025	GRANGE B	2	423.350	358.550	0.12109	0.804
M4027	TUNSTD 4	3	410.300	373.500	0.01850	0.372
M4028	MIDDPEAK	1	428.160	354.580	0.00394	1.692
M4029	WAPDLOW	1	406.630	347.220	0.00166	2.472
M4030	TOPLEY P	1	410.400	372.240	0.02419	0.177
M4031	UPPERWD	3	428.600	357.510	0.01014	1.705
M4034	DOVEHOLE	1	409.360	377.300	0.00984	1.408
M4038	BRIERLOW	5	408.790	368.500	0.00023	1.787
M4039	MIDDLETN	3	427.330	356.050	0.01074	1.359
M4040	MIDDPEAK	2	427.980	354.870	0.01706	1.640
M4043	UPPERWD	3	428.800	357.510	0.00904	1.705
M5003	BALLIDON	4	419.710	355.530	0.00217	0.180
M5008	STERNDL	2	410.150	367.060	0.00984	0.690
M5009	WATERSW	4	408.080	374.700	0.00242	0.792
M5013	STERNDL	2	410.150	367.060	0.00492	0.682
M5018	CAULD 4	1	408.090	348.660	0.00083	2.661
M5021	BRIERLOW	3	409.210	368.930	0.00449	0.643
M5027	TUNSTD 2	4	409.940	373.630	0.00520	0.432
M5028	GRANGEML	2	424.610	357.520	0.00966	0.929
M5032	DOVEH 2	5	409.360	377.470	0.00556	1.084
M5035	BALLIDON	4	419.710	355.530	0.00681	0.183
M5055	WAPDLOW	2	408.280	347.100	0.00287	2.708
M5060	GRANGEML	2	424.610	357.520	0.01412	1.029
M5061	BALLIDON	6	419.940	355.670	0.00229	0.359
M5067	TOPLEY P	3	409.820	372.300	0.00612	0.261
M5071	STERNDL	2	410.150	367.060	0.00787	0.600
M6004	DOVEH 2	2	409.900	377.730	0.00210	0.230
M6007	TUNSTEAD	7	409.380	374.160	0.00350	0.543
M6009	STERNDL	3	409.970	367.320	0.00322	0.694
M6050	WATERSW	3	408.400	374.630	0.00655	0.769
M6079	DOW LOW	4	409.060	368.020	0.00165	0.777
M6081	DOVEH 2	4	409.160	377.900	0.02249	1.272
M6087	MASSON	3	428.900	359.800	0.00581	1.941
M6093	UPPERWD	3	428.600	357.510	0.02133	1.866
M6092	MIDDPEAK	2	427.980	354.870	0.00093	1.609
M6101	DOVEH 2	4	409.160	377.900	0.02055	1.272
M6103	DOVEH 2	5	409.380	377.470	0.00701	1.116
M6104	UPPERWD	1	428.700	357.200	0.00316	1.709
M6111	STERNDL	2	410.150	367.060	0.02326	0.657
M6117	RAMSHORN	5	408.790	346.190	0.00033	2.675
M6121	WATERSW	5	408.050	374.850	0.00278	0.803
M6123	BALLIDON	4	419.710	355.530	0.00292	0.359

(2) NEW Line

Event	Quarry	Face	Coordinates		Soln variance	time nearest station
F11004	WATERSW	1	408.610	374.850	0.03475	1.042
F11005	BRIERLOW	4	408.900	368.460	0.00272	0.319
F11007	TUNSTEAD	1	410.260	373.150	0.00739	0.611
F11008	SMALLDL	4	415.900	381.600	0.00287	1.535
F11009	SMALLDL1	3	415.600	381.700	0.07247	1.572
F11012	TUNSTD 4	4	410.050	373.380	0.00175	0.439
F11013	TUNSTD 3	3	410.420	374.110	0.00353	0.691
F11014	DOVEH 2	5	409.380	377.470	0.01077	1.262
F11016	WARDLOW	1	408.630	347.220	0.00041	3.964
F11020	STONEYM1	4	421.200	375.750	0.00221	0.136
F11022	STERNDL	1	410.210	367.500	0.02759	0.941
F11023	BRIERLOW	1	409.030	369.070	0.00456	0.741
F12001	DOW LOW	5	409.400	368.000	0.04129	0.415
F12002	TUNSTD 4	2	410.170	373.600	0.00459	0.647
F12003	BRIERLOW	2	409.140	369.100	0.00865	0.191
F12004	HINDLOW	4	408.180	369.200	0.00177	0.184
F12010	TUNSTEAD	1	410.260	373.150	0.00290	0.576
F12010	TUNSTEAD	1	410.260	373.150	0.01757	0.619
F12011	SMALLDL1	1	416.050	381.550	0.00334	1.516
F12012	DOVEH 2	4	409.160	377.900	0.02382	1.489
F12014	WATERSW	1	408.610	374.850	0.00705	1.042
F12018	BRIERLOW	3	409.210	368.930	0.00585	0.366
F12026	WATERSW	1	408.610	374.850	0.00782	1.042
F12028	STONEYM1	2	421.130	375.460	0.00231	0.077
F12030	STERNDL	1	410.210	367.500	0.01607	0.441
F12031	DOVEH 2	4	409.160	377.900	0.01593	1.489
F12032	CAULD 5	2	409.710	348.950	0.00297	2.041
F12033	TOPLEY P	1	410.400	372.140	0.00308	0.455
F13001	TUNSTD 3	2	410.500	373.780	0.00939	0.684
F13002	BRIERLOW	3	409.210	368.930	0.01465	0.253
F13005	TUNSTD 3	2	410.500	373.780	0.00379	0.684
F13006	DOVEH 2	5	409.380	377.470	0.00167	1.476
F13007	HOPE W	3	417.450	382.350	0.01606	1.644
F13009	SMALLDL1	3	415.600	381.700	0.11607	1.629
F13011	TUNSTD 4	3	410.300	373.500	0.00426	0.551
F13012	WATERSW	1	408.610	374.850	0.00345	1.042
F13013	BRIERLOW	2	409.140	369.100	0.01056	0.362
F13020	TUNSTD 3	2	410.500	373.780	0.00375	0.743
F13021	DOVEH 2	6	409.380	377.280	0.01569	1.537
F13022	STERNDL	2	410.150	367.660	0.00267	0.590
F13023	TOPLEY P	1	410.400	372.140	0.00246	0.448
F14002	STERNDL	1	410.210	367.500	0.01792	0.881

(3) SEW Line

Event	Quarry	Face	Coodinates		Soln variance	time nearest station
C21002	BALLIDON	1	420.170	355.500	0.00821	0.571
C21004	TOPLEY P	1	410.400	372.140	0.00735	4.127
C21006	WARDLOW	5	408.460	347.500	0.00197	0.163
C21008	CAULD 4	4	408.180	348.290	0.00167	0.172
C21009	BRIERLOW	4	408.900	368.460	0.02612	0.762
C22004	TOPLEY P	1	410.400	372.140	0.00911	0.455
C22005	BRIERLOW	2	409.140	369.100	0.00423	0.720
C22007	CAULD 4	1	408.080	348.660	0.00245	0.230
C22017	UPPERWD	2	429.650	357.520	0.00151	1.608
C22018	CAULD 3	2	407.970	348.380	0.00183	0.146
C22020	WARDLOW	5	408.460	347.500	0.00137	0.182
C22023	TUNSTD 3	2	410.500	373.780	0.00089	4.282
C22025	WARDLOW	3	408.150	347.370	0.00160	0.118
C23014	WARDLOW	1	408.630	347.220	0.00046	0.224
C23015	MIDDLETN	3	427.330	356.050	0.00263	0.137
C23016	BRIERLOW	3	409.210	368.930	0.00681	3.792
C23018	CAULD 4	4	408.180	348.290	0.00206	0.172

(4) 1981 Experiment

F31046	WATERSW	1	409.610	374.950	0.01605	1.010
F32008	DOW LOW	3	409.290	367.650	0.04896	0.916
F32009	STONEY M	1	421.930	375.630	0.06154	1.699
F32019	DOW LOW	5	408.400	368.000	0.02577	0.796
F32021	CAULD 5	4	409.240	348.700	0.00906	2.453
F33016	GRANGE B	2	423.350	359.550	0.00544	0.804
F33020	BALLIDON	4	419.710	355.830	0.01124	0.352
F33030	BRIERLOW	3	409.210	368.930	0.01509	0.672
F33051	DOVEH 2	5	409.380	377.470	0.02612	0.750
F34007	DOVEHOLE	2	409.220	377.260	0.02483	0.679
F34013	BRIERLOW	2	409.140	369.100	0.03074	0.646
F34031	ELDON 1	1	411.700	381.400	0.07291	1.662
F34032	BALLIDON	4	419.710	355.530	0.07377	0.373
F34034	DOVEH 2	4	409.160	377.900	0.01230	0.779
F34041	BRIERLOW	3	409.210	368.930	0.02789	0.674
F34043	CAULD 3	3	407.670	348.370	0.00258	2.934

(4) 1981 cont.

Event	Quarry	Face	Coordinates		Soln variance	time nearest station
F34044	STERNOL	1	410.210	367.500	0.03027	0.633
F35001	BALLIDON	4	419.710	355.530	0.00251	0.094
F35005	BRIERLOW	3	409.210	368.930	0.04975	0.725
F35017	BALLIDON	7	420.300	355.720	0.01106	0.174
F35021	GRANGEML	1	424.530	357.480	0.00465	1.012
F35022	BRIERLOW	2	409.140	369.100	0.02300	0.688
F35028	DOVEHOLE	1	408.360	377.300	0.01199	0.747
F36010	DOVEH 2	4	409.160	377.900	0.02810	0.839
F36028	DOVEH 2	4	409.160	377.900	0.04214	0.838
F37006	LONGCL2	2	423.510	357.240	0.00964	1.575
F37009	TOPLEY P	1	410.400	372.140	0.01310	0.372
F37023	DOW LOW	4	409.060	368.020	0.00760	0.859
F37035	DOW LOW	3	409.290	367.650	0.03043	0.816
F38005	DOW LOW	4	409.060	368.020	0.02331	0.859

BLASTS FROM TUNSTEAD QUARRY LOCATED USING A NETWORK OF SHOTPOINTS (100m GRID)

Event			Co-ordinates(km)		Soln. variance	Time to nearest station
1979						
M1007	TUN 2	18	410.300	374.000	0.01075	0.489
--FIRST ITERATION, V1= 5.069						
M1007	TUN 2	18	410.300	374.000	0.01075	0.489
M6103	TUNSTEAD	3	409.400	374.800	0.00859	0.687
--FIRST ITERATION, V1= 5.272						
M6108	TUN 5	18	409.800	373.300	0.00378	0.342
New line						
F13001A	TUN 5	12	410.300	373.200	0.02257	0.613
--FIRST ITERATION, V1= 5.094						
F13001A	TUN 5	12	410.300	373.200	0.02257	0.613
SEW line						
C21010	TUN 6	1	410.500	373.900	0.02003	0.705
--FIRST ITERATION, V1= 5.247						
C21010	TUN 6	1	410.500	373.500	0.02003	0.705
1981						
F33021	TUN 4	5	410.200	373.600	0.00701	0.159
--FIRST ITERATION, V1= 5.104						
F33021	TUN 5	4	410.000	373.300	0.00583	0.140
F33033	TUN 4	6	410.200	373.500	0.00714	0.162
--FIRST ITERATION, V1= 5.199						
F33033	TUN 4	6	410.200	373.500	0.00714	0.162
F33047	TUN 4	14	410.100	373.400	0.00815	0.150
--FIRST ITERATION, V1= 5.046						
F33047	TUN 4	7	410.100	373.500	0.00813	0.142

1981 cont

F33021	TUN 4	5	410.200	373.600	0.00701	0.159
--FIRST ITERATION, V1= 5.104						
F33021	TUN 5	4	410.000	373.300	0.00583	0.140
F33033	TUN 4	6	410.200	373.500	0.00714	0.162
--FIRST ITERATION, V1= 5.199						
F33033	TUN 4	6	410.200	373.500	0.00714	0.162
F33047	TUN 4	14	410.100	373.400	0.00815	0.150
--FIRST ITERATION, V1= 5.046						
F33047	TUN 4	7	410.100	373.500	0.00813	0.142
F34005	TUN 6	4	410.400	373.900	0.00713	0.199
--FIRST ITERATION, V1= 5.034						
F34005	TUN 4	6	410.200	373.500	0.00711	0.161
F34020	TUN 6	10	410.300	374.000	0.00897	0.185
--FIRST ITERATION, V1= 5.065						
F34020	TUN 6	9	410.300	374.100	0.00895	0.189
F34038	TUN 6	4	410.400	373.500	0.01296	0.199
--FIRST ITERATION, V1= 5.145						
F34039	TUN 6	4	410.400	373.500	0.01296	0.199
F35030	TUNSTEAD	1	409.600	374.800	0.00791	0.219
--FIRST ITERATION, V1= 5.200						
F35030	TUNSTEAD	1	409.600	374.800	0.00791	0.219
F35032	TUN 5	12	410.300	373.200	0.01935	0.204
--FIRST ITERATION, V1= 5.119						
F35032	TUN 5	12	410.300	373.200	0.01636	0.200
F35040	TUN 5	18	409.800	373.000	0.00610	0.163
--FIRST ITERATION, V1= 5.418						
F35040	TUN 5	18	409.800	373.000	0.00610	0.163
F36005	TUN 5	12	410.300	373.200	0.00565	0.204
--FIRST ITERATION, V1= 5.325						
F36005	TUN 5	10	410.100	373.200	0.00394	0.161
F37003	TUN 5	12	410.300	373.200	0.00314	0.204
--FIRST ITERATION, V1= 5.188						
F37003	TUN 5	12	410.300	373.200	0.00314	0.204
F37012	TUN 6	2	410.500	373.800	0.00209	0.217
--FIRST ITERATION, V1= 5.235						
F37012	TUN 4	15	410.200	373.400	0.00127	0.161
F37033	TUN 5	12	410.300	373.200	0.00465	0.204
--FIRST ITERATION, V1= 5.329						
F37033	TUN 6	1	410.500	373.900	0.00213	0.205

1979

Event	Quarry	Easting	Northing
M1005	SHIRLEY SHOT	423.29	338.89
M2000	WARDLOW	408.36	347.28
M4035	BALLIDON	419.86	355.58
M5064	HINDLOW	408.97	368.62
M5067	TUNSTEAD	409.87	373.79

1980

Northern East-West Line

Event	Quarry	Easting	Northing
F12015	TUNSTEAD	410.02	373.40
F12016	DOW LOW	410.35	369.40
F12027	LONGCLIFFE	423.91	357.00
F13003	CAULDON	408.95	348.90
F13004	DENE	428.44	356.28
F13014	MIDPEAK	428.50	355.10
F13015	DOVEHOLES	409.30	377.15
F13014	BALLIDON	420.04	355.71

Southern East-West Line

Event	Quarry	Easting	Northing
C22019	TUNSTEAD	410.49	373.86
C22022	WATERSWALLOWS	408.26	374.69
C22024	DOVEHOLES	409.30	377.19
C23002	DENE	428.45	356.29
C23009	HINDLOW	409.06	368.95

1981

Event	Quarry	Easting	Northing
F31043	BALLIDON	409.94	355.67
F32002	TUNSTEAD	410 07	374.00
F32020	STONEY MIDDLETON	421.13	375.46
F32027	TUNSTEAD	409.63	373.40
F32028	CAULDON	409.05	348.86
F33005	DOVEHOLES	409.04	377.74
F33014	TUNSTEAD	409.81	373.76
F33026	SHINING BANK	422.90	365.00
F33037	CAULDON	409.24	348.89
F34009	TUNSTEAD	409.79	373.28
F34026	TUNSTEAD	410.17	373.60
F35008	DOVEHOLES	377.93	377.93
F35013	TUNSTEAD	410.09	373.99
F35024	TUNSTEAD	409.73	373.80
F36019	DOVHOLES	409.29	377.81
F36024	BALLIDON	419.84	355.59
F36031	BALLIDON	419.71	355.53
F36041	STONEY MIDDLETON	421.20	375.75
F37024	TUNSTEAD	410.29	374.26
F38004	TUNSTEAD	409.83	373.70
F39012	TUNSTEAD	409.31	373.24

Repetitivity of quarry blast sources (a) Tunstead shots V_{red} = 5·6 Km/s

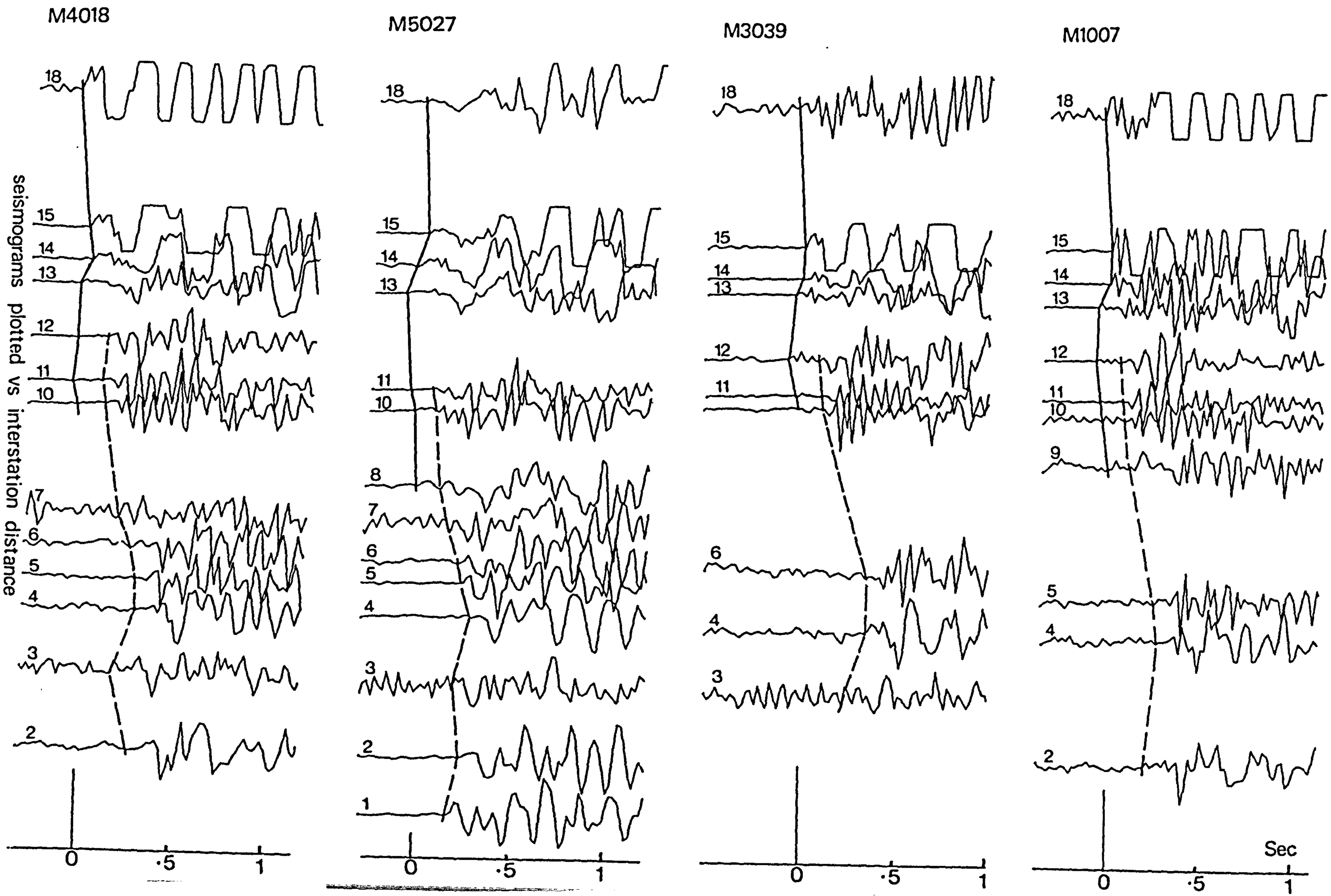

(b) Ballidon shots

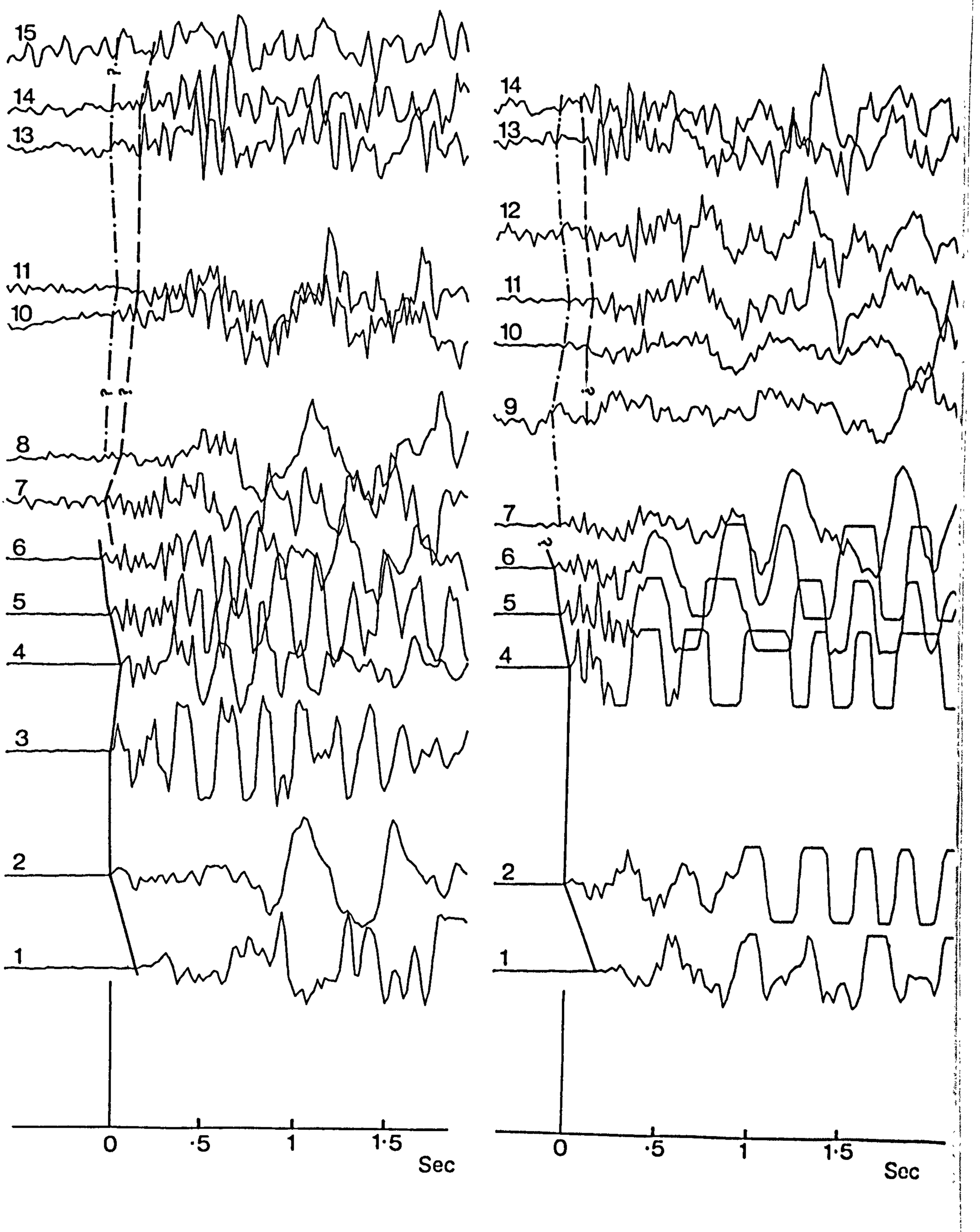

APPENDIX B

POLARISATION FILTERING

Polarisation filters were first developed by Samson and Olson (1981) for the enhancement of three-component, fluxgate magnetometer data. The technique essentially calculates the degree of polarisation for all channels in order to design a filter which operates on each channel separately in the frequency spectrum. The process is data-adaptive because the filter is slid through the data, at each position of which the degree of polarisation is recalculated and the filter accordingly redesigned.

The principals are given in Samson (1973), Samson (1980), and Samson and Olson (1981), of which the following is a brief summary: consider a set of N seismometers, the information from which can be represented by the time-dependent vector

$$[X(t)] = [x_1(t), x_2(t) \ldots x_N(t)] \tag{B1}$$

which represents N-dimensional data whether $x_j(t) j=1,N$ is an N-component set or N vertical seismometers. The discrete transform of X(t) is

$$[Z(\omega)] = \left(\frac{1}{2\pi}\right) \sum_{k=0}^{n-1} [X(t)] e^{ikw} \quad (0 \leq \omega \leq 2\pi) \tag{B2}$$

where $[Z(\omega)]$ is normally calculated using a fast-Fourier transform algorithm. n may be the number of points in the time series, or the length of filter chosen. The data may be conveniently written as the spectral matrix [S], where

$$[S(\omega)] = \sum_{\alpha=\omega_1}^{\omega_2} [Z(\alpha)][Z^{\dagger}(\alpha)] \quad \omega_1 \leq \omega \leq \omega_2 \tag{B3}$$

Where (†) denotes complex conjugate of the transpose. Now, [S] can be expanded

$$[S(\omega)] = \sum_{j=1}^{N} \lambda_j(\omega)[u_j(\omega)][u_j^{\dagger}(\omega)] \qquad (B4)$$

where λ_j and $[u_j]$ are the eigenvalues and eigenvectors of [S]. We wish to consider the case where the signal is highly polarised, that is when [S] has only one non-zero eigenvalue, or

$$[S(\omega)] = \lambda_1[u_1][u_1^{\dagger}] \qquad (B5)$$

In this sense the vector [u] is the complex representation $[u] = [r_1] + i[r_2]$, where r_1, r_2 are the major and minor axes of the polarisation ellipse. Thus a measure of the degree of polarisation, P, is given by

$$P = \frac{N(T_r S^2) - (T_r S)^2}{(N-1)(T_r S)^2} \qquad (B6)$$

where T_r denotes the sum of the diagonal elements. Having determined P, $[Z(\omega)]$ may be operated upon to give the filted output $[Y(\omega)]$, where

$$[Y(\omega)] = \frac{1}{n} \sum_{k=0}^{n-1} [Z(k)]P^q(k)e^{2\pi ik} \quad \text{for} \quad [Z(k)], k=1,n \qquad (B7)$$

and $Y(\omega)$ may be transformed to yield the filtered time dependent matrix [Y(t)]. Variants on the filtering process include the polarisation bias (set by exponent g above), the smoothing of $[S(\omega)]$, modification for a sliding filter, and the allowance for lagged arrivals between channels. These are all discussed in Samson and Olson (1981).

The degree of polarisation is analogous with the quality of coherence, except that P is not limited to two dimensions nor the orientation of the instruments (Samson 1980). The essence of the technique is to discriminate against that part of the data not observed to be well polarised (i.e. random noise, which should be incoherent between the

N-channels), and to enhance that part of the data which is well linearly polarised (i.e. seismic signal). Thus the method sets out to represent coherent seismic data as a linearly polarised state, and differs from other multi-channel data-adaptive filters by that for N input channels there are N output channels, and not just one best filtered channel.

For a system of vertical seismometers, the signal rarely arrives at more than one instrument at the same time. While the method can accommodate lagged arrivals by using a correlation matrix to estimate the lag between each instrument (and accordingly maximise the value of P), if the lags are greater than the length of the sliding window then problems arise. Few difficulties occur for a teleseimic event recorded on a small array, where total lag is unlikely to exceed one and a half wavelengths, but for a close high-frequency source (such as a quarry blast), the lag between adjacent instruments may be several wavelengths or more. A further problem with local-scale data is that the signal changes rapidly between instruments because of velocity filtering, dispersion and the interference of phases.

For these reasons, the part of a seismic refraction signal most suited to polarisation filtering is the first arrival: it is least affected by interfering later phases, and is often of similar amplitude and frequency to the ambient noise. Furthermore, the time of arrival is known within measurement error, so that the seismograms can be easily time shifted so that the arrivals are lined up to within one wave-length or so (the alignment need only be within the length of filter to be used).

For the University of Leeds Amdahl V7, the polarisat-ion filter programme MRCLEAN has been set up to run in conjunction with PLOTTER (see Fig. 4.2). Operative details are expounded in its relevant Manual, which exists as a Disk file.